UNIVERSIDAD DE VALENCIA-CSIC
DEPARTAMENTO DE FÍSICA ATÓMICA, MOLECULAR Y NUCLEAR
INSTITUTO DE FÍSICA CORPUSCULAR

TAGS measurements for neutrino physics and applications

Víctor Guadilla Gómez

DOCTORADO EN FÍSICA
July 2017

Supervisors:
Alejandro Algora
José Luis Taín Enríquez

Alejandro Algora, Científico titular del Consejo Superior de Investigaciones Científicas (CSIC) y **José Luis Taín Enríquez**, Investigador Científico del Consejo Superior de Investigaciones Científicas (CSIC)

CERTIFICAN: Que el presente trabajo **"TAGS measurements for neutrino physics and applications"** ha sido realizado bajo su dirección en el Instituto de Física Corpuscular (Centro Mixto Universitat de València - CSIC) por **Víctor Guadilla Gómez** para su presentación como Tesis Doctoral dentro del programa de doctorado en Física de la Universitat de València.

Y para que así conste, en cumplimiento con la normativa vigente, firman el presente certificado en Burjassot (Valencia) a 10 de julio de 2017.

Alejandro Algora

José Luis Taín Enríquez

This thesis has been funded by:

FPA2011-24553
FPA2014-52823-C2-1-P

FPU12/01527

A los grandes amores de mi vida:
mi padre, mi madre, Silvia, Irene
y Karolinka

Tablero de dirección

Table of instructions

A su manera este libro es muchos
libros, pero sobre todo es dos libros

In its own way, this book consists of
many books, but two books above all

Rayuela/Hopscotch, Julio Cortázar

Como en *Rayuela*, el lector puede optar por una de las dos posibilidades siguientes, dependiendo de su interés científico o su interés sentimental:

El primer libro sigue un curso normal, comenzando en el Abstract y pasando en orden por todos los capítulos que se enuneran en el índice.

El segundo libro comienza en los Agradecimientos y continúa con el Poemario científico. A continuación se invita al lector a leer los epígrafes de los distintos capítulos y apéndices siguiendo el orden aquí propuesto:

Conclusions - 12 - 11 - 14 - 1 - 2 - 3 - D - 5 - 7 -
8 - 4 - 13 - 6 - C - 10 - B - Resumen - A -9

As in Hopscotch, the reader can choose one of the two following options, depending on the scientific or sentimental interest:

The first book is read normally, starting in the Abstract and going through all the chapters presented in the Contents.

The second book starts in the Acknowledgements, and continues with the Scientific Collection of Poems (unfortunately only in Spanish). Next, the reader is invited to read the epigraphs of the chapters and appendixes in this suggested order:

Conclusions - 12 - 11 - 14 - 1 - 2 - 3 - D - 5 - 7 -
8 - 4 - 13 - 6 - C - 10 - B - Resumen - A -9

Poemario científico

Canto a la Idea Madre

I
¡Vamos¡ ¡En pie! ¡Surge! ¡Escucha!
¡Escucha! ¡Despierta! Rompe tus cadenas; sé.
Sal de las sombras, de los limbos, de las partes infinitas,
¡oh separado en la inmovilidad total!
Arráncate de la paz, de la noche; emerge;
mueve los codos, las manos, los dedos. ¡Desperézate,
bosteza!
¡En pie! ¡En pie! ¡Endurécete; que aparezca tu fuerza!
¡Aprieta los dientes,
recrea una estatua y una altura; ponte en guardia, afirma
tus piernas!
Y que tus ojos sean una corona de los más claros ojos.
Corónate. Compón tu mirada. Siéntete todo
el instrumento de este día que empieza y del acto que te
llama.
Yo que te llamo. Yo que nada puedo sin ti.
Yo, la Idea
que todo lo puedo contigo,
estaba en tu sombra y en tu composición.
Esta dispersa, cerca y lejos (como una gota de vino
en una cuba de agua clara), en tu substancia.
¡Ven en mi ayuda! Sé carne y osamenta,
sé mi forma, mis ojos, mi lengua, mis tendones.
Sé para que yo sea. ¡Sé para ser!
Obedece:; que sea yo la orden que tú profieras.
Mi voz es la tuya y tú sabes distinguir
mi voluntad. Pero tú quieres... ¡YO! ¡La Idea!

II
Al principio yo no existía. Luego, entre tus
pensamientos.
Yo era uno más entre ellos. Infusa, vaga.
Pero ahora tú ya no eres enteramente tú mismo,
tú mismo, tu vida, tu sangre, tus temores, tus horas, tu
voz,
sino el esclavo de la ocasión favorable, ¡mi oportunidad!
Soy la única idea que está conforme con tu ser, y tú
eres el hombre que me conviene.
Tú eres mi suerte; yo, tu pérdida única e inmortal.
He surgido como al acaso en la agitación de tu cabeza.
Pero otros acasos y otra faz de las cosas
te hicieron como para mí.
¡En marcha! ¡Disponte a cazar! ¡Persigue lo que te
anima!
Me vas a tomar por ti; creerás que soy tú mismo,
no tropezarás más que con un obstáculo oculto...

Tus ojos verán lo que yo quiero ver.
Tu inteligencia ordinaria se asombrará de sí misma,
hallará caminos tales que te parecerás insensato.
Dirás lo que te sorprende. Te encontrarás después de
haber realizado
tu imposible.
No comprenderás tu propia perspicacia.
Te disculparás de tu clarividencia y de tu potencia.
Te avergonzarás de lograr tales ganancias.
¡Humildemente murmurarás cosas maravillosas!...

III

¡Oh! Sin embargo, para mí ¡qué milagro!
un pobre cuerpo, ese individuo mezquino,
esa salud vacilante,
esos nervios siempre irritados contra sí mismos,
precisamente los necesitaba.
¡Milagro que me hizo ser! ¡Oh circunstancia! ¡Oh,
humano!
¡Única oportunidad!
¡Tantos otros hombres no me han tenido!
He hallado en tu estructura y en tu substancia
la hora, el ser, la hora del ser y el ser de la hora.
La coincidencia de tus recuerdos, del tiempo que hacía,
la naturaleza de tu sueño, de tu vagar, de tus manías.
He hallado
mi alimento en tu flaquezas,
mi posibilidad en tus ignorancias,
una ocasión en tus repugnancias...
Ahora nos pertenecemos. Nos confundimos.
Nos amamos.
Tú eres mis *Loco por mi causa*: TU IDEA.

Paul Valéry

La vida aprende su lección
del movimiento de lo que no vive:
las constancias del agua,
las decisiones del viento,
los ritmos mudos de una piedra.

La vida aprende su lección
de los movimientos más seguros que ella.

Roberto Juarroz

(...)
Éstos son los pensamientos de todos los hombres en
todas la épocas y países, no son originales míos,
si no son tuyos tanto como míos no son nada o casi
nada,
si no incluyen todo, son poco
menos que nada,
si no son el enigma y la resolución del enigma, nos son
nada,
si no son al mismo tiempo cercanos y remotos, no son
nada.

(...)
Todas la verdades esperan en todas las cosas,
ni se apresuran a pronunciarse ni se demoran,
no precisan el fórceps obstétrico del cirujano,
lo insignificante es tan importante para mí como lo demás
(...)

Walt Whitman

El primer peldaño

El joven poeta Eumenes
se lamentó un día a Teócrito:
"Llevo escribiendo dos años
y sólo he compuesto un idilio.
Mi simple obra completa.
Veo, con tristeza, que alta,
extremadamente alta, es la escalera de la Poesía;
y que hallándome ahora en el primer peldaño
nunca alcanzaré otro más alto".
A lo que Teócrito replicó: "Palabras como ésas
son impropias, blasfemas.
Feliz y orgulloso deberías sentirte
de estar en el primer peldaño.
Haber llegado hasta ahí no es ningún pequeño logro:
lo que acabas de hacer es algo maravilloso.
Incluso ese primer peldaño
es un largo camino sobre el mundo ordinario.
Para estar en ese peldaño
has de ser por derecho propio,
de la ciudad de las ideas, miembro.
Y no es nada fácil, sino algo inusual
obtener la ciudadanía de esa ciudad.
Sus consejos están llenos de legisladores
a los que ningún charlatán puede engañar.
Haber llegado hasta ahí no es ningún pequeño logro:
lo que acabas de hacer es algo maravilloso".

Konstantin Kavafis

Dentro del mundo

¿Hubo un primer segundo, nació el tiempo
de la naciente Creación enorme,
estalló en un segundo una materia?

¿Esa materia natural del orbe
se habrá bastado lúcida a sí propia,
siempre según novel iniciativa?

¿Ímpetu irracional se arroja armónico?
¿Cómo se pasa del azar a ciegas
al postrer desenlace matemático?

¿Estalló de repente desde el Cero?
¿Desde qué, desde quién?
- Yo sé.
- Yo no.
¿Hasta dónde se llega con un Yo?

Esa lenta paciencia de la Naturaleza
se reproduce. Dura la soledad triunfante,
entregada a sí misma. Soledad creadora.
Soledad- y misterio.

La variedad prodigiosa
de la flora y de la fauna
va aludiendo a ese misterio
de una Creación fantástica:
trabajo imaginativo
de Alguien con mucha maña,
de Nadie con invención
absurda pero atinada.
¿Cómo sucedió?
Quién sabe,
quién entiende esta maraña...

(. . .)
Mortal soy de minúscula morada,
hombre libre-si puedo-al fin humano.
La gran Naturaleza me contiene,
dentro, muy dentro a gusto,
para mí ya bastante y con sentido.

¿Qué sentido? Muy ardua tentativa
que habremos de inventar a nuestro paso
por la Tierra. Será gran aventura,
destinada a su círculo terrestre.

(. . .)
Estupendo este viaje
que va desde el impulso hasta la meta.
Mucha vida nos reta.

Que el esfuerzo mortal jamás relaje
su afán de posesión si está a la vista
lo que ya Es.
Conquisto. Me conquista.

Jorge Guillén

El cultivo de la Filosofía

Sembré en la tierra llana
de un taburete de madera
la idea del infinito
mirad cómo crece
- dice el filósofo frotándose las manos

Realmente crece
como un guisante
Después de tres o tal vez cuatro
cuartos de hora de eternidad
sobrepasará incluso
la altura de su cabeza

Hice también una chapucilla con el cilindro
- dice el filósofo
en lo alto del cilindro un péndulo
ya entendéis de qué se trata
el cilindro es el infinito
el péndulo es el tiempo
tic – tic - tic
- dice el filósofo y riendo sonoramente
agita sus pequeñas manos

al final inventé la palabra ser
palabra dura e incolora
hay que estar largo tiempo apartando las hojas cálidas con manos vivas
hay que pisotear las imágenes
llamar fenómeno a la puesta del sol
para poder descubrir detrás de todo esto
muerta y blanca
la piedra filosofal

esperaríamos ahora
que el filósofo rompiera a llorar por su sabiduría
mas no llora
el ser empero no se inmuta
el espacio no se disuelve
y el tiempo no se detendrá en su enloquecida carrera

Zbigniew Herbert

Supernova

Hace 21 millones de años
estalló una ardiente supernova
y hoy, airado, el firmamento
escupe un diamante, congelado,
luminoso, de blancura cegadora
y no hay niños en pesebres
que nos salven del naufragio.

A veces te dará por pensar
que todo es piedra negra y afilada
y que difícilmente podremos trepar
el acantilado contra el que las olas
empujan los botes salvavidas.
Pero habrás de ver que la noche
pare nuevas estrellas,
supernovas ancianas,
más que el rencor y los abrazos.

(...)
Hace 21 millones de años estallaba
una estrella blanca, pequeña y somnolienta,
cansada de dormir el sueño de otros,
y el cielo a veces es una alambrada
o el agua de piscinas que en invierno
recogen hojas secas, renacuajos
y todo trae la sombra de cipreses.
Menos mal que tú viniste un día
para alumbrar con tu luz de supernova
viejas constelaciones desgastadas
por el arañazo inútil de deseos
que fueron persiguiendo a otras estrellas.

Ismael Serrano

La medida

Como un amanecer
desvelando siluetas
impregnadas de noche.

Como abrir un libro
escrito en caracteres extraños
intentando, pese a todo,
seguir el hilo de su historia.

Como ese fuego que aturde
el espíritu al recordar
que nuestro tiempo en el mundo se agota.

Así, así de potente y misterioso,
de escurridizo e inevitable,
es el acto de medir.

Medir, buscar, excavar,
en los entresijos de la realidad,
destilando la expresión precisa de cada rincón.
Tallando el recipiente capaz de contener
la sangre que fluye, inperceptible,
en todas las cosas;
el recipiente que se amolde
a la forma cambiante y relativa del misterio.

Medir, anhelar, mirar,
con los ojos bien abiertos
para no perderse el milagro
de lo que siempre sucede.
Extender nuestros sentidos
para llegar donde nadie llegó
y acariciar así la verdad que nos estuvo buscando.
Invocar al silencio que permite oír
el susurro de los engranajes que giran sin cesar,
sin preguntarse cómo ni por qué,
sin necesitar ser medidos.

Medir, amar, entender,
lo que nos sorprende, lo que somos,
lo que no supimos siquiera imaginar.
Lo que pide a gritos incendiar
nuestra mente con nuevas ideas.

Como un acto de libertad,
como un evocador poema
que trasciende el reflejo del mundo
y transmite lo que queda de nosotros
al final de la jornada, tras un largo día
de camino y búsqueda y esperanza. Medir.

Víctor Guadilla

Radioactividad

Donde el ojo no llega,
allá donde se alcanza sin remedio
la frontera de nuestros sentidos.
Cuando la silueta del mundo
se desdibuja, y palpamos
torpemente entre la bruma
sin hallar el relieve de las cosas,
desconsoladamente ciegos.

Donde el lenguaje no llega,
allá donde se tornan impotentes
la gramática y la rima,
por cruel ausencia
de realidad conocida que nombrar.
Cuando el perfil huidizo del mundo
se esconde en el silencio,
sin dejarnos siquiera
una huella palpable
sobre la que soñar
y crear formas.

Donde la naturaleza aguarda
con un fulgor inimaginable,
capaz de prender
la sagrada mecha de las ideas.
Allí, donde alargamos el brazo
y solo hallamos un aire estéril.
Allí, la extensión del ojo
y del lenguaje
nos desvela la riqueza del silencio,
la luz invisible del cosmos.
El eco del mundo
siempre cambiante.

Víctor Guadilla

Relojes

Si lográramos imaginar durante un segundo
un universo carente de vida,
vacío de esos diminutos fragmentos
de materia autoconsciente,
sin esas ramificaciones pensantes
a través de las cuales, ancestralmente,
el universo recorre el extenuante
camino del autoconocimiento,
buscando explicarse a sí mismo,
su sentido, su forma.
Si de verdad fuéramos capaces, durante un segundo,
entonces podríamos atrevernos a pensar
que hemos aislado ese espacio inerte
del tiempo que fluye a ritmo de sístole
y diástole en nuestra mente mortal.
Sin embargo, ese segundo
sería tan suyo como nuestro,
pues miríadas de diminutos relojes
se agazapan en los rincones mas secretos
de núcleos atómicos inconformistas
invocando, al son de un débil latido,
la danza de la materia.

Víctor Guadilla

Abstract

Nowadays, many exciting topics in nuclear physics need information from β-decay studies to expand our knowledge on nuclear structure, nuclear astrophysics and reactor technology. The precious β-intensity distributions have been shown to be affected by the *Pandemonium* systematic error when they are derived from measurements with germanium detectors in high resolution experiments, and the Total Absorption γ-ray Spectroscopy (TAGS) technique is an effective way to overcome this problem. In this work, the new segmented Decay Total Absorption γ-ray Spectrometer (DTAS), designed for FAIR, will be presented. The first measurements with this detector have been performed at IGISOL (Finland), and a detailed characterization by means of Monte Carlo simulations of the full set-up employed in the experiments will be presented. In these first experiments with DTAS an ambitious physics programme was addressed, covering two challenges in neutrino physics: the description of the double β-decay process, and the understanding of the shape of the reactor antineutrino spectrum. In addition important reactor decay heat calculations have been improved by obtaining results free from the effects of *Pandemonium* for fission fragments that are required with high priority. Some of the target decays of this work are also of paramount relevance from the point of view of nuclear structure, as in the case of β-delayed neutron emitters.

In this work we will focus on ten β-decays of relevance measured at IGISOL with DTAS. They will be analyzed in the framework of the TAGS technique to extract the corresponding β-intensity distributions. The analysis will show differences with respect to previous high resolution experiments, with a remarkable amount of β-intensity that was not detected before in the majority of them. Furthermore, the β-intensity distributions of two fission fragments will be obtained for the very first time. Finally, the impact of these TAGS data on the mentioned topics will be discussed. For this, theoretical double β-decay calculations, and summation calculations for decay heat and the reactor antineutrino spectrum will be presented with the data provided by this work.

Contents

Part I

Introduction

Chapter 1

Overview

No se puede desatar un nudo sin saber cómo está hecho

You can not untie a knot without knowing how it is tied

Aristóteles

1.1 β-decay

One of the most successful tools in nuclear structure studies over the years has been β-decay. Unlike the other two most common types of radioactivity, the α-decay and the γ-decay, β-decay was not so straightforwardly understood at the beginning due to its continuum nature. It was not until Pauli explained it as a three-body process in 1931 with a new particle involved, the neutrino [1], that a formulation of β-decay was at last undertaken. In 1934 Fermi presented his theory [2] based on a relativistic formalism with the underlying idea of a zero range weak force responsible for the process, and this theory was completed by Gamow and Teller in 1936 [3].

The β-decay concept refers to three closely related processes, summarized in Equation (1.1). The first one is the emission of electrons observed in the early experiments after the discovery of radioactivity by Bequerel in 1896. This process is due to the conversion of a neutron into a proton with the emission of an electron and the corresponding antineutrino, the so-called β^- process. The second process consists in the conversion of a proton into a neutron with the emission of a positron and the corresponding neutrino, and it was discovered by Irène Curie and Frédéric Joliot in 1934 (two years after the discovery of the positron in cosmic rays by Anderson). This process is known as β^+ decay and is strongly related to the third process grouped under the common name of β-decay: the capture of an electron by a nucleus, observed for the first time by Alvarez in 1938. It also corresponds to the conversion of a proton into a neutron, but in this case by means of the absorption of an electron from an atomic orbital and the emission of a neutrino. It is known as electron capture (EC).

$$\begin{aligned} \beta^- &: {}^{A}_{Z}\mathrm{X}_N \rightarrow {}^{A}_{Z+1}\mathrm{X}_{N-1} + e^- + \overline{\nu}_e \\ \beta^+ &: {}^{A}_{Z}\mathrm{X}_N \rightarrow {}^{A}_{Z-1}\mathrm{X}_{N+1} + e^+ + \nu_e \\ EC &: {}^{A}_{Z}\mathrm{X}_N + e^- \rightarrow {}^{A}_{Z-1}\mathrm{X}^{*}_{N+1} + \nu_e \end{aligned} \tag{1.1}$$

In Equation (1.1) ${}^{A}_{Z}\mathrm{X}_{N}$ represents a nucleus with chemical symbol X (note that the chemical element changes when Z changes), proton number Z, neutron number N and mass number $A = Z + N$. ${}^{A}_{Z-1}\mathrm{X}^{*}_{N+1}$ represents the resulting excited atomic state after the electron capture process, which leads to the emission of the characteristic X-rays (or the emission of Auger electrons) from the daughter element following the EC. The maximum energy available for the β-particles (e^{-}/e^{+}, $\overline{\nu}_e/\nu_e$) corresponds to the $Q_{\beta/EC}$ value that characterizes the decay; this energy window is calculated as the difference in total energy (in nuclear mass) between the initial and the final systems.

From a more fundamental point of view, β-decay can be viewed microscopically as the transformation of one type of quark into another through the exchange of charged weak currents ($W^{\pm}$ bosons) as depicted in Figure 1.1.

$$\begin{aligned} \beta^{-} &: n \rightarrow p + e^{-} + \overline{\nu}_e \Rightarrow (udd) \rightarrow (uud) + e^{-} + \overline{\nu}_e \\ \beta^{+} &: p \rightarrow n + e^{+} + \nu_e \Rightarrow (uud) \rightarrow (udd) + e^{+} + \nu_e \\ EC &: p + e^{-} \rightarrow n + \nu_e \Rightarrow (uud) + e^{-} \rightarrow (udd) + \nu_e \end{aligned} \tag{1.2}$$

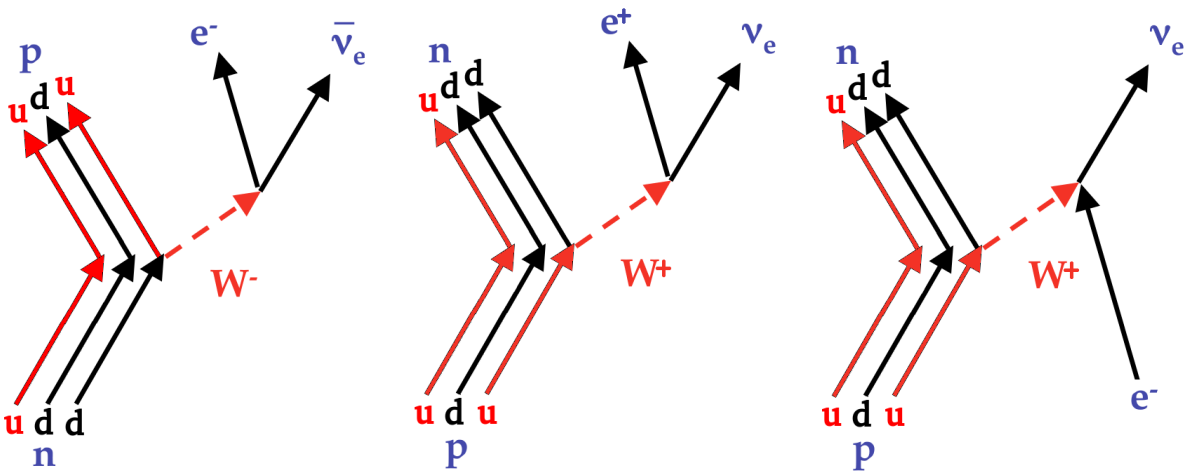

Figure 1.1: β-decay diagrams from a microscopical point of view.

1.1.1 Fermi theory of β-decay

Fermi assumed that both the electron and the antinetrino were created in the process of the β^{-} decay (for simplicity β^{-} will be assumed hereafter, but all results are equivalent for β^{+} and EC), and that the interaction was point-like (which was confirmed years later with the measurement of a mass of 80 GeV [4] for the $W^{\pm}$ bosons). The starting point for his theory is the transition rate calculated by treating the interaction causing the β-decay, $v_\beta(\mathbf{x}, t)$, as a weak perturbation compared with the interaction that forms the quasi-stationary states in the nucleus, $V(\mathbf{x})$ [5], so that the total potential can be written as $V'(\mathbf{x}, t) = V(\mathbf{x}) + v_\beta(\mathbf{x}, t)$. The transition rate ($\lambda$) is evaluated in the framework of

time-dependent perturbation theory [6, 7], and it is known as the Fermi Golden Rule:

$$\lambda = \frac{2\pi}{\hbar}|M_{fi}^{\beta}|^2\rho(E_f) \tag{1.3}$$

where M_{fi}^{β} is the β-decay matrix element between the initial (ψ_i) and the final (ψ_f) states, and $\rho(E_f) = dn/dE_f$ is the density of final states, defined as the number of accessible final states in the energy interval dE_f.

The three main ingredients to calculate the β-decay transition rate according to Fermi theory have been already presented i.e. the interaction matrix elements M_{fi}^{β}, the density of final states $\rho(E_f)$ and the interaction $v_\beta(\mathbf{x}, t)$. Now, some details about these three quantities will be explained.

- In the matrix elements calculation, the wave function of the final state must include not only the nucleus, but also the electron, φ_e, and antineutrino, $\varphi_{\overline{\nu}}$, wave functions. Likewise, for electron capture the corresponding wave function of the electron would appear in the initial state. With these ideas in mind, the matrix elements can be written as:

$$M_{fi}^{\beta} = \langle \psi_f \varphi_e^* \varphi_{\overline{\nu}}^* \,|\, v_\beta \,|\, \psi_i \rangle = \int [\psi_f \varphi_e^* \varphi_{\overline{\nu}}^*] v_\beta \psi_i d\mathbf{x} \tag{1.4}$$

  where electron and antineutrino have momentum $\mathbf{p}$ and $\mathbf{q}$ respectively and their wave functions are approximated by plane wave forms normalized within the volume V [5]:

$$\begin{aligned} \varphi_e &= \frac{1}{\sqrt{V}} e^{i\mathbf{p}\cdot\mathbf{x}/\hbar} \simeq \frac{1}{\sqrt{V}}(1 + i\frac{\mathbf{p}\cdot\mathbf{x}}{\hbar} + \ldots) \\ \varphi_{\overline{\nu}} &= \frac{1}{\sqrt{V}} e^{i\mathbf{q}\cdot\mathbf{x}/\hbar} \simeq \frac{1}{\sqrt{V}}(1 + i\frac{\mathbf{q}\cdot\mathbf{x}}{\hbar} + \ldots) \end{aligned} \tag{1.5}$$

  where the expansion of the exponential term is justified by $\mathbf{p}\cdot\mathbf{x}/\hbar \ll 1$ (which is valid for energies up to a few MeV [5, 8]). Taking only the first term of the expansion corresponds to the so-called *allowed* approximation [5], and it implies that the orbital angular momentum carried by the electron and the antineutrino is zero, $L = 0$. If J_i and J_f are the initial and final spins of the nuclear states involved in the β-decay, then:

$$\overrightarrow{J}_f = \overrightarrow{J}_i + \overrightarrow{L} + \overrightarrow{S} \tag{1.6}$$

  where S is the total intrinsic spin that can be 0 or 1, since 1/2 particles are involved. $S = 0$ (anti-parallel spins) corresponds to the first assumption made by Fermi, and it is known as Fermi decay, whereas $S = 1$ are the so-called Gamow-Teller transitions [8].

  For cases with $L \neq 0$ the transition probabilities will be smaller, and they are called forbidden transitions (the degree of "forbiddenness" corresponds to the value of L). The parity of the electron plus antineutrino wave functions is given by $(-1)^L$, and it

will imply a change in parity for transitions with odd L. A summary of the selection rules for allowed and forbidden transitions, in the case of Fermi and Gamow-Teller modes, is presented in Table 1.1

Transition type	$\log ft$	L	$\Delta\pi$	ΔJ (Fermi)	ΔJ (Gamow-Teller)
Super allowed	2.9-3.7	0	No	0	0
Allowed	4.4-6.0	0	No	0	0,1
First forbidden	6-10	1	Yes	0,1	0,1,2
Second forbidden	10-13	2	No	1,2	1,2,3
Third forbidden	>15	3	Yes	2,3	2,3,4

Table 1.1: Selection rules and characteristics of the different types of β-decay transitions. Super allowed transitions correspond to transitions between isobaric analogue states. The meaning of the $\log ft$ will be explained later, and the values in the second column are taken from [9].

A pure free-particle approximation as in Equation (1.5) is not realistic for an electron, and the distortion caused by the electrostatic field of the nucleus (with Z protons) in the electron wave-function has to be taken into account. Quantitatively, the main effect is to modify the electron wave-function at the origin [9]:

$$|\varphi_e^*(0,Z)|^2 \simeq \frac{1}{V}\frac{2\pi\eta}{1-e^{2\pi\eta}} \simeq \frac{1}{V}F(Z,p) \tag{1.7}$$

where $F(Z,p)$ is the so-called Fermi function and

$$\eta = \pm\frac{Ze^2}{4\pi\varepsilon_0 h}\frac{\sqrt{m_e^2+p^2/c^2}}{p} \text{ for } \beta^{\mp} \text{ decay} \tag{1.8}$$

with e and m_e the charge and the mass of the electron respectively, h the Planck constant, c the speed of light, and ε_0 the vacuum permittivity.

- The density of final states will depend on the final states accessible for the decay products, both the electron and the antineutrino, and it can also be written as $\rho(E_f) = \frac{dn}{dE_f}(e^-,\overline{\nu}_e)$. The number of levels for a particle with three degrees of freedom is [5,9]:

$$\begin{aligned} dn_e &= \frac{4\pi V}{h^3}p^2dp \\ dn_{\overline{\nu}} &= \frac{4\pi V}{h^3}q^2dq \end{aligned} \tag{1.9}$$

The number of final states which have simultaneously an electron and an antineutrino is the product of the independent number of states [9]:

$$dn(e^-,\overline{\nu}_e) = dn_e dn_{\overline{\nu}} = \frac{(4\pi)^2V^2p^2q^2dpdq}{h^6} \tag{1.10}$$

If the density of states is evaluated for electrons emitted with momentum between 0

and p_{max}, then p is kept constant, and the variation of the final energy only affects the antineutrino observables [9]:

$$\rho(E_f) = \frac{dn}{dE_f}(e^-, \overline{\nu}_e) = \frac{(4\pi)^2 V^2 p^2 q^2 dp}{h^6}\frac{dq}{dE_f} \tag{1.11}$$

- With respect to the interaction v_β, its mathematical character was unknown for Fermi, and all the possibilities for the character of the operator consistent with special relativity were considered: vector (V), axial vector (A), scalar (S), pseudoscalar (P) or tensor (T). The only way to find out which was correct was through experiments. In this line, it was shown that β-decay does not conserve parity (P) nor charge conjugation (C), although the combined CP operation is conserved. This established the V-A combination of operators as the representation of the interaction for β-decay. V and A are characterized with different coupling constants, g_V and g_A respectively.

  In the isospin formalism, the vector part can be represented by the operator τ, which can change isospin T, while the axial vector part is represented by a product of τ and σ, which can flip spin S [10]. The interaction can be written, therefore, as Equation (1.12):

$$v_\beta = \sum_{j=1}^{A}[g_V \tau_j + g_A \overrightarrow{\sigma}_j \cdot \overrightarrow{\tau}_j] \tag{1.12}$$

With all these considerations in mind, the partial decay rate for electrons emitted with momentum between 0 and p_{max} results from writing $d\lambda$ in Equation (1.3) instead of λ. It can be evaluated by replacing $\rho(E_f)$ with Equation (1.11), and with the *allowed* approximation of Equation (1.5) (considering the correction of the Fermi function):

$$d\lambda = \frac{2\pi}{\hbar}|M_{fi}|^2 F(Z,p)\frac{(4\pi)^2 p^2 q^2 dp}{h^6}\frac{dq}{dE_f} \tag{1.13}$$

being $M_{fi} = \langle \psi_f \,|\, v_\beta \,|\, \psi_i \rangle$ the nuclear matrix element.

The total decay rate is obtained after integration of Equation (1.13) for all values of the electron momentum. For each of them the momentum of the antineutrino will be fixed, according to $q = \frac{Q_\beta - T_e}{c}$ (for a β-decay to the ground state of the daughter nucleus the maximum energy window is available, Q_β), with T_e the kinetic energy of the electron, and assuming that $m_{\overline{\nu}} = 0$. Moreover, since $E_f = E_e + E_{\overline{\nu}} = E_e + qc$, hence $dq/dE_f = 1/c$, and the total decay rate has the form:

$$\lambda = \frac{|M_{fi}|^2}{2\pi^3 \hbar^7 c^3}\int_0^{p_{max}} F(Z,p)p^2(Q_\beta - T_e)^2 dp \tag{1.14}$$

If Equation 1.14 is written in terms of the reduced energy of the electron [9] $\varepsilon = \frac{E_e}{m_e c^2}$, with $E_e = T_e + m_e c^2 = \sqrt{p^2c^2 + m_e^2 c^4}$, then $p = m_e c\sqrt{\varepsilon^2 - 1}$, and therefore $p^2 dp =$

$m_e^3c^3\sqrt{\varepsilon^2-1}\varepsilon d\varepsilon$:

$$\lambda = \frac{|M_{fi}|^2 m_e^5 c^4}{2\pi^3\hbar^7}\int_1^{\varepsilon_{max}} F(Z,\varepsilon)\varepsilon\sqrt{\varepsilon^2-1}\left(\frac{Q_\beta}{m_e c^2}-\varepsilon+1\right)^2 d\varepsilon \tag{1.15}$$

In general, the integral has to be evaluated numerically, and it is called the Fermi integral:

$$f(Q_\beta, Z) = \int_1^{\varepsilon_{max}} F(Z,\varepsilon)\varepsilon\sqrt{\varepsilon^2-1}\left(\frac{Q_\beta}{m_e c^2}-\varepsilon+1\right)^2 d\varepsilon \tag{1.16}$$

Taking into account the relationship between the partial half-life and the transition rate: $\lambda = ln2/t$, with $\sum_{\text{all } t} 1/t = 1/T_{1/2}$, it can be written:

$$ft = \frac{2\pi^3\hbar^7 ln2}{|M_{fi}|^2 m_e^5 c^4} \tag{1.17}$$

where ft is the so-called comparative half-life or ft value, that allows the comparison of β-decay probabilities in different nuclei. Different ft values are related to differences in the nuclear matrix elements and therefore in the nuclear wave functions. Due to the incredibly wide range of half-lives in β-decay, normally the $\log ft$ values are compared, as shown in Table 1.1 for different types of transition.

If the form of the β-decay interaction from Equation (1.12) is taken into account in (1.17), and reduced transition probabilities are defined as:

$$\begin{aligned} B(F) &= |\langle\psi_f|\tau|\psi_i\rangle|^2 \\ B(GT) &= |\langle\psi_f|\tau\sigma|\psi_i\rangle|^2 \end{aligned} \tag{1.18}$$

then:

$$ft = \left(\frac{2\pi^3\hbar^7 ln2}{m_e^5 c^4}\right)\frac{1}{g_V^2 B(F) + g_A^2 B(GT)} \tag{1.19}$$

The inverse of Equation (1.19) only for a GT transition (since Gamow-Teller transitions are much more common than Fermi transitions) is:

$$\frac{1}{ft} = \left(\frac{m_e^5 c^4 g_V^2}{2\pi^3\hbar^7 ln2}\right)\left(\frac{g_A}{g_V}\right)^2 B(GT) \tag{1.20}$$

In order to define a quantity related to experimental observables, a summation over some of the quantum numbers is performed to get an average quantity. Although the matrix elements may fluctuate from state to state, their total strength over the energy interval from E_x to $E_x + \Delta E$ is assumed to be constant[1] [11–14]. Therefore, the strength function $S_\beta(E_x)$ or reciprocal ft-value, calculated per MeV of final levels at the excitation

[1] if the width of the strength function is small compared to the characteristic energies associated with variations in the interaction.

energy E_x in the daughter nucleus, is defined as:

$$S_\beta(E_x) = \sum_{E_f \in \Delta E} \frac{\frac{1}{\Delta E}}{f(Q_\beta - E_x, Z)t} = \frac{1}{6146 \pm 7} \left(\frac{g_A}{g_V}\right)^2 \sum_{E_f \in \Delta E} \frac{1}{\Delta E} B(GT)_{i \to f} \qquad (1.21)$$

where it has to be noted that the energy available for the β-particles, Q_β, has been replaced by $Q_\beta - E_x$ in the Fermi integral (Equation (1.16)) to consider the general case where a level at E_x is populated, and not only the ground state of the daughter. The constant factor has been evaluated with g_V which is known from superallowed Fermi decays [15]. The ratio of the axial vector to the vector coupling constant is known from [16], g_A/g_V = -1.27399(19).

If the definition of partial half-life, $t = T_{1/2}/I_\beta(E_x)$, is now taken into account in Equation (1.21), with $I_\beta(E_x)$ the absolute β intensity to level E_x, an expression that relates the theory with quantities that can be measured experimentally is found:

$$S_\beta(E_x) = \sum_{E_f \in \Delta E} \frac{\frac{1}{\Delta E} I_\beta(E_x)}{f(Q_\beta - E_x, Z)T_{1/2}} = \frac{1}{6146 \pm 7} \left(\frac{g_A}{g_V}\right)^2 \sum_{E_f \in \Delta E} \frac{1}{\Delta E} B(GT)_{i \to f} \qquad (1.22)$$

Equation (1.22) relates the theoretical reduced transition probabilities, where nuclear structure information is carried by the matrix elements, and three experimental observables: the Q_β value, the half-live $T_{1/2}$ and $I_\beta(E_x)$. The details of the experimental measurements of Q_β and $T_{1/2}$ are beyond the scope of this work. Concerning the I_β intensities, one has to measure the feeding probability to each individual state of the daughter nucleus in the β-decay. For this, the intensities of the β-delayed γ-rays can be used, as will be explained in the next section.

1.2 TAGS technique

Conventionally, I_β distributions have been obtained from the γ-ray intensity balance of the β-delayed γ-rays coming from the electromagnetic de-excitation of the levels fed in the β-decay. The measurement of these γ-rays is normally performed with high resolution HPGe detectors. Special care is taken in the analysis to consider the appropriate corrections for internal conversion or internal pair production, and it is assumed that if a β-transition is not seen with a γ-ray, its contribution to the excited part of the decay scheme is negligible. However, in 1977 J.C. Hardy *et al.* [17] tested this methodology by means of Monte Carlo (MC) simulations, with a fictional nucleus called *Pandemonium*. The I_β distribution of the decay of this nucleus was fixed in the MC, and real resolutions and efficiencies of HPGe detectors were considered. By applying the conventional tools mentioned before, they found that 14% of the true γ-ray intensity above 1.7 MeV was completely undetected in the analysis when compared with the simulation. They pointed out that this effect would increase for more complex level schemes, and they stated that "Every complex β-decay scheme that is based on γ-ray peak analysis and intensity balances must now be regarded

as doubtful". The problem is related to the modest efficiency of the HPGe detectors, and the lack of sensitivity for this unobserved intensity implies a systematic error in the calculation of the I_β distributions that is known as the *Pandemonium* effect. This effect is depicted in Figure 1.2, and it shifts the apparent I_β distribution to lower excitation energies.

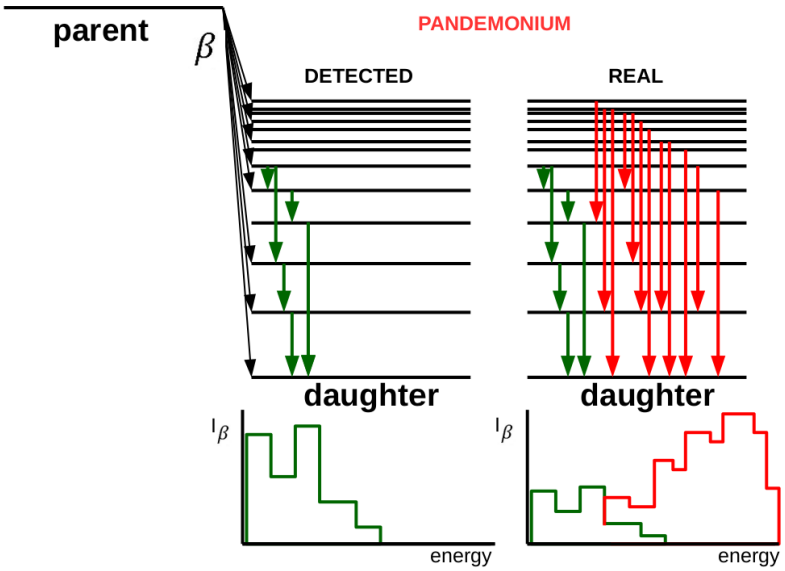

Figure 1.2: *Pandemonium* effect shown schematically. Red γ-rays coming from feeding to high excitation are missed, thus shifting the apparent β-intensity distribution to lower energies.

One solution to overcome this problem is Total Absorption γ-ray Spectroscopy (TAGS), which relies on a completely different philosophy: instead of measuring the γ-rays with a high resolution detector with modest efficiency, measuring with a high efficiency detector with (in general) modest energy resolution. As shown in Figure 1.3 for a toy level scheme, TAGS aims to detect the full β-delayed electromagnetic cascade in order to avoid the *Pandemonium* systematic error, in contrast with high resolution spectroscopy, where HPGe detectors are used to detect individual γ-rays.

TAGS has been shown to be an effective tool to determine β-decay intensity distributions for nuclei far from the valley of β stability. The main requirement for a Total Absorption Spectrometer (TAS) detector is to maximize the efficiency. This is normally achieved by using large scintillator crystals covering a solid angle as close as possible to 4π. For an ideal detector, with 100% γ-ray efficiency, the measured energy spectrum would provide directly the β-intensity distribution convoluted with the instrumental resolution. However, as depicted in Figure 1.3, the spectrum of a real spectrometer shows escape peaks and Compton regions, since neither the peak efficiency nor the total efficiency are 100%. As a consequence, the determination of the β-intensity distribution is not straightforward, and it is obtained by deconvolution of the experimental spectrum with the response function of the spectrometer. Mathematically it can be reduced to the solution of a linear

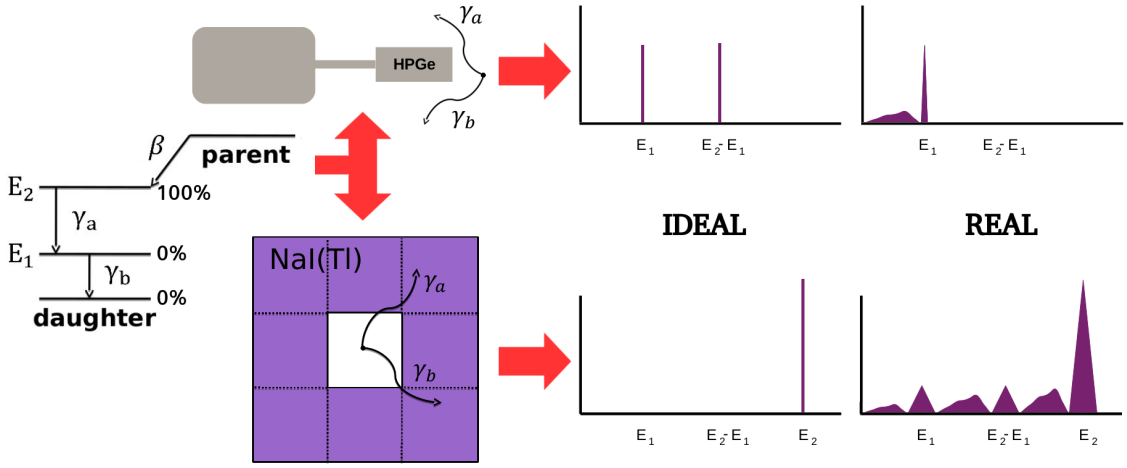

Figure 1.3: Comparison of high-resolution measurements and TAGS technique for a toy level scheme. For real HPGe detectors high energy γ-rays may be missed due to *Pandemonium*, whereas for real spectrometers a complex total absorption spectrum is defined by the response function of the detector.

inverse problem represented by Equation 1.23:

$$d_i = \sum_{j}^{levels} R_{ij}(B) f_j \tag{1.23}$$

where d_i is the number of counts in the experimental channel i of the spectrum, f_j represents the number of events that feed level j in the daughter nucleus, and R_{ij} is the response function of the detector, that depends on the branching ratio matrix of the decay (B) and is calculated by means of MC simulations [18]. The explanation of the procedure to calculate the response function and details about the algorithms used in the deconvolution process will be presented in Chapter 2.

Traditionally, NaI(Tl) has been chosen as scintillator material for the vast majority of TAS detectors constructed over many years. In the 1970s, the pioneering total absorption measurements were performed with large cylindrical NaI(Tl) crystals at ISOLDE [13] and OSIRIS [14] (Figure 1.4 (a)). They were continued by other measurements in the 1980s at the IRIS mass separator with a set-up of one NaI(Tl) crystal [19] later expanded to three crystals [20] (Figure 1.4 (b)). In the 1990s, at the ^{252}Cf based INEL ISOL facility, Greenwood et al. [21] carried out an extensive total absorption study of fission fragments with a large NaI(Tl) crystal (Figure 1.4 (c)). In the meanwhile, a combination of two NaI(Tl) crystals was operated at LNP JINR [22] (Figure 1.4 (d)), and a NaI(Tl) total absorption spectrometer constructed to be operated at LBL was coupled to the GSI on-line separator [23] (Figure 1.4 (e)). At that point, the group of Valencia became familiar with this technique by participating in the measurements at GSI. This was the starting point that led to the development of the algorithms and analysis tools for TAGS that will be employed in this work. Furthermore, it motivated the construction of a TAS installed at ISOLDE based on a large NaI(Tl) crystal that has been working since then as

a permanent set-up [24] (Figure 1.4 (f)). The technique rose to prominence because of the decay heat problem that will be treated in Section 1.3.3, giving rise to new measurements with a NaI(Tl) detector designed at the Nuclear Institute of Saint Petersburg that was used by the group of Valencia at IGISOL [25] (Figure 1.4 (g)). From this time onward, designing segmented spectrometers has been the tendency, due to the extra information that can be extracted with them. A 12-fold segmented detector constructed by the groups of Valencia and Surrey, made of BaF_2, has been the first spectrometer with segmentation [26–28] (Figure 1.4 (h)). In the last five years, a 50-fold BaF_2 detector has been developed for VECC [29] (Figure 1.4 (i)), and three NaI(Tl) segmented spectrometers have been constructed: SuN for NSCL-FRIB [30] (Figure 1.4 (j)), MTAS for Oak Ridge [31] (Figure 1.4 (k)), and the one starring in this work, DTAS for FAIR [32] (Figure 1.4 (l)).

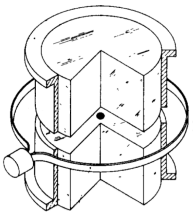

(a) Two cylindrical crystals of 15 cm diameter and 10 cm length, each of them read by a PMT

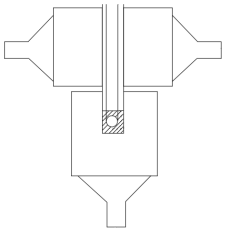

(b) Three crystals with 20 cm diameter. One with 20 cm length, and the other two with 10 cm length. Each crystal read by a PMT

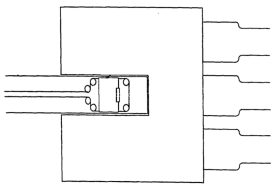

(c) A crystal of 25.4 cm diameter and 30.5 cm length with a well of 5.1 cm × 20.3 cm read by 7 PMTs

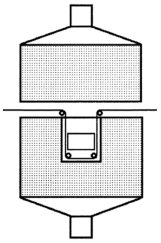

(d) Two crystals. One with 20 cm diameter and 11 cm length, and other with 21 cm diameter and 14 cm length. Each crystal read by a PMT

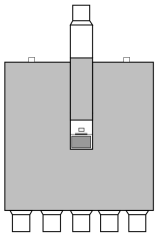

(e) A cylindrical crystal of 35.6 cm diameter and 35.6 cm length with a well of 5.1 cm × 20.3 cm read by 11 PMTs

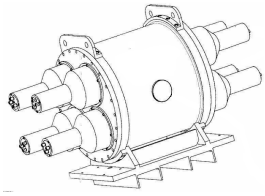

(f) A cylindrical crystal of 38 cm diameter and 38 cm length with a 7.5 cm × 38 cm hole, read by 8 PMTs

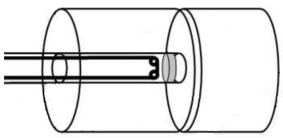

(g) A crystal of 20 cm diameter and 20 cm length with a well of 4 cm × 20 cm read by 5 PMTs plus another crystal of 20 cm diameter and 10 cm length read by a PMT

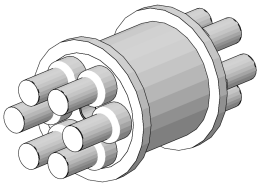

(h) 12-fold segmented detector with pentagonal crystals, each read by a PMT. The total detector has 25 cm diameter and 25 cm length with a 5 cm × 25 cm hole

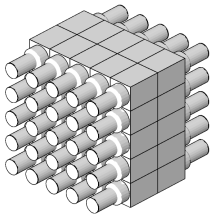

(i) 50-fold segmented detector with rectangular crystals of 3.5 cm × 3.5 cm × 5 cm/35 cm each read by a PMT. No details known about the hole

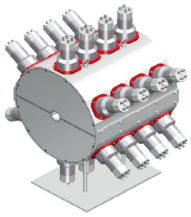

(j) 8-fold segmented detector with semi-cylindrical crystals of 40.64 cm diameter and 10.16 cm length, each read by 3 PMTs. The total detector has a 4.57 cm × 40.64 cm hole

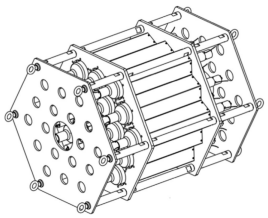

(k) 19-fold segmented detector with hexagonal crystals of 53.34 cm length and 17.6 cm width, each read by 2 PMTs. The central one is read by 12 PMTs, and has a 6.35 cm × 53.34 cm hole. Honeycomb like structure

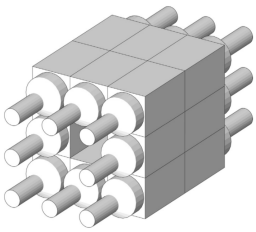

(l) 16/18-fold segmented detector with rectangular crystals of 15 cm × 15 cm × 25 cm, each read by a PMT. With 16 modules a hole of 15 cm × 15 cm × 50 cm is left. With 18 modules it depends on the set-up

Figure 1.4: TAS detectors along the years.

1.3 Motivations: β-decay measurements of interest

1.3.1 Double β-decay

Double β-decay is a radioactive decay process in which a nucleus ${}^{A}_{Z}\mathrm{X}_{N}$ undergoes a transition to the nucleus ${}^{A}_{Z\pm2}\mathrm{X}_{N\mp2}$. It can be observed for some nuclei where the nucleus ${}^{A}_{Z\pm1}\mathrm{X}_{N\mp1}$ has a smaller binding energy, and the single β-decay is forbidden. If the nucleus ${}^{A}_{Z\pm2}\mathrm{X}_{N\mp2}$ has a larger binding energy, then the double β-decay process is allowed energetically [33], as shown in Figure 1.5 left.

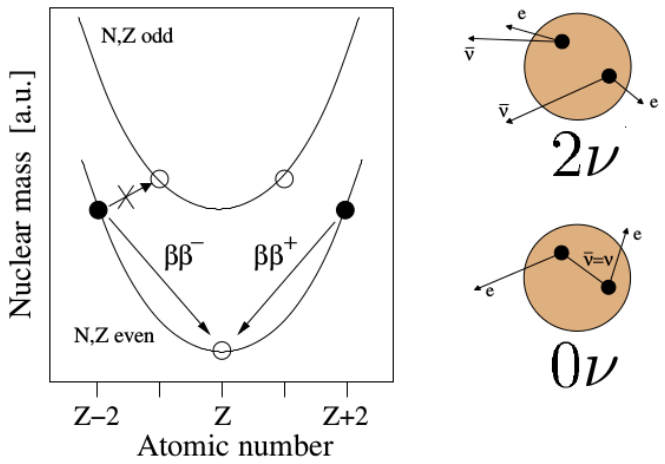

Figure 1.5: Scheme of the double β-decay from [34]. Atomic mass as a function of Z for isobar multiplets with even A is shown on the left hand side, while a scheme for 2ν mode and 0ν mode is presented on the right hand side.

This mode is of second order Fermi-theory (it can be seen as two simultaneous decays), and therefore the expected half lives are long compared to single β-decay. In fact, the decay rates are extremely slow, $\sim 10^{21}$ times slower than single β-decays, with half-lives of the order of 10^{18}-10^{22} years [34].

Double β-decay comprises the so-called 2ν mode, and the 0ν mode, which would only occur if neutrinos are Majorana particles (if they are their own antiparticles), as depicted in Figure 1.5 right. Double β-decay has only been detected until now in the 2ν mode, with the exception of one unconfirmed case [35]. The possible 2ν transitions are summarized in Equation (1.24).

$$\begin{aligned}
&\beta\beta^{-} : {}^{A}_{Z}\mathrm{X}_{N} \rightarrow {}^{A}_{Z+2}\mathrm{X}_{N-2} + 2e^{-} + 2\overline{\nu}_{e} \\
&\beta\beta^{+} : {}^{A}_{Z}\mathrm{X}_{N} \rightarrow {}^{A}_{Z-2}\mathrm{X}_{N+2} + 2e^{+} + 2\nu_{e} \\
&ECEC : {}^{A}_{Z}\mathrm{X}_{N} + 2e^{-} \rightarrow {}^{A}_{Z-2}\mathrm{X}^{*}_{N+2} + 2\nu_{e} \\
&EC\beta^{+} : {}^{A}_{Z}\mathrm{X}_{N} + e^{-} \rightarrow {}^{A}_{Z-2}\mathrm{X}^{*}_{N+2} + e^{+} + \nu_{e}
\end{aligned} \tag{1.24}$$

This 2ν decay mode conserves lepton number, it occurs whether or not neutrinos are their own antiparticles, and does not depend significantly on the masses of the neutrinos

[36]. The rate of the 2ν mode can be written as:

$$(T^{2\nu}_{1/2})^{-1} = G_{2\nu}|M^{2\nu}|^2 \tag{1.25}$$

where $M^{2\nu}$ are the nuclear matrix elements of this second order process, and $G_{2\nu}$ is the four-particle phase-space factor, involving Fermi integrals. A detailed calculation of this factor is presented in [33], where a dependence on $Q^5_{\beta\beta}$ is found ($Q_{\beta\beta}$ is the energy window available for a $\beta\beta^-$ process, and equivalently for the other three 2ν transitions of Equation (1.24)).

The neutrinoless case of the decay (0ν) is considered one of the best candidates to provide information about the absolute neutrino mass scale and the Dirac or Majorana nature of the neutrino, as shown in [36,37]. To extract information about the mass scale, the half-life of this very slow process needs to be determined experimentally. Then, the obtained half-life is converted into a neutrino mass by means of the relationship presented in Equation (1.26):

$$(T^{0\nu}_{1/2})^{-1} = G_{0\nu}|M^{0\nu}|^2|\langle m_\nu\rangle|^2 \tag{1.26}$$

where $M^{0\nu}$ are the nuclear matrix elements of the nucleus undergoing the decay, $G_{0\nu}$ is the phase-space factor for the emission of the two electrons (if $\beta\beta^-$), and $\langle m_\nu\rangle$ is the effective Majorana mass, with $\langle m_\nu\rangle = |\sum_k m_k U^2_{ek}|$ [36], for the electron neutrino (if $\beta\beta^-$), being m_k the masses of the three neutrinos and U the matrix that transforms states of mass into states of flavour.

Nuclear transition matrix elements are involved in the conversion process from half-life to neutrino mass and, in the end, they constitute the major source of uncertainty. A precision of about 20% on the nuclear matrix elements is required for a reasonable conversion from half-lives to neutrino masses, allowing discrimination between the different neutrino mass models [38]. The calculations of the nuclear matrix elements require a knowledge of the wave functions of the nuclear states involved. Theoretical calculations of double β-decay have been performed in the past using several approaches: the quasiparticle-random-phase-approximation (QRPA)-in particular in its proton-neutron variant (pnQRPA)-, the interacting shell model (ISM), the proton-neutron interacting boson model (IBA-2), the energy density functional approach (EDF) and the projected Hartree-Fock-Bogoliubov (HFB) mean-field scheme. In both modes of double β-decay basically the same kind of nuclear matrix elements are involved [39]. It has been suggested that it is possible to test the accuracy of the neutrinoless (0ν) double β-decay calculations by comparing the two-neutrino (2ν) double β-decay calculations (within the same theoretical frameworks) with measured 2ν double β-decay rates. The parameters of the model can be reduced in double β-decay calculations (mainly in QRPA) by looking at the information on the single β-decay rates (β^+/EC, and β^-) for the intermediate nucleus. In QRPA equations, the particle-particle matrix elements are multiplied by the g_{pp} parameter that takes values between 0.6 and 1.2. Moreover, the axial vector coupling constant, g_A, is sometimes quenched, and the effective value of g_A can also be studied together with the value of g_{pp} within a QRPA

framework [40]. Precise single β-decay data for the associated intermediate nuclei of the double β-decay process can help to fix these parameters that play a crucial role in double β-decay calculations.

It should also be noted that constraining the parameters of the calculations is not just possible by means of β-decay studies. In recent years a great effort has also been invested in studies of the properties of ground-state wave functions of double β-decay candidates, the occupancies of valence single-particle orbitals and pairing correlations of the states of interest by means of transfer reactions (see for example [41,42]).

The requirement for a double β-decay is $Q_{\beta\beta} > 0$. However, since the decay rate is proportional to $Q^5_{\beta\beta}$, as mentioned, in general only isotopes with $Q_{\beta\beta} > 2.0$ MeV are under consideration in experiments of neutrinoless double β-decay: ^{48}Ca, ^{76}Ge, ^{82}Se, ^{96}Zr, ^{100}Mo, ^{110}Pd, ^{116}Cd, ^{124}Sn, ^{130}Te, ^{136}Xe, and ^{150}Nd. From these cases, one of the best known is the A=100 double β-decay system depicted in Figure 1.6 (^{100}Mo, ^{100}Tc, ^{100}Ru) [43–47].

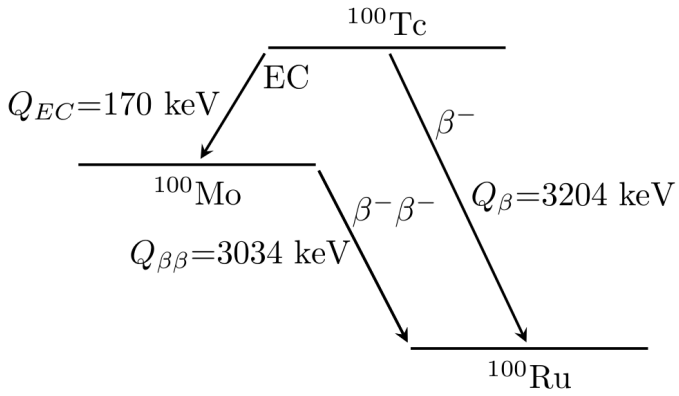

Figure 1.6: Schematic picture of the A=100 double β-decay system. The $Q_{\beta/EC}$ values are taken from [48].

Double β-decay rates have been measured to the ground state and to the first excited 0^+ state of ^{100}Ru [49] in the NEMO 3 experiment [50]. Concerning the other possible experimental constraints for the calculations (single β-decay rates) the EC branch of the decay $^{100}\text{Tc} \rightarrow {}^{100}\text{Mo}$ has been measured recently with much higher precision than before [51]. Also in a recent measurement using charge-exchange reactions the $^{100}\text{Ru} \rightarrow {}^{100}\text{Tc}$ transitions have been measured, indicating the nature of the single-state dominance in the double β-decay process [45,52]. On the other hand, the decay of $^{100}\text{Tc} \rightarrow {}^{100}\text{Ru}$ has only been measured up to now using the high-resolution technique [53,54].

Theoretical calculations for this system in the QRPA framework [55] concluded that it was difficult to describe both the EC/β^- and the 2ν double β-decay observables at the same time, using the same set of parameters, as can be seen in Table 1.2.

Recent QRPA calculations suggest that not considering a common g_A effective value for both the single β-decay and 2ν double β-decay, could improve the reproduction of the observables [40, 57]. In these calculations, g_{pp} and g_A are treated as independent parameters that can be fixed by reproducing the experimental $\log ft$ values of the EC and β^- branches. The g_{pp} value obtained in this way can be used to calculate the nuclear

Final state	Energy [MeV]	logft (exp)	logft (theo)	$t_{1/2}$ (exp)	$t_{1/2}$ (theo)
$0^+_{g.s.}$	0.000	4.6	4.4-4.6	5.9-10.5×10^{18}	1.7-3.8×10^{18}
2^+_1	0.540	6.5	4.5-5.3	>1.1×10^{21}	5.2×10^{20}-2.1×10^{21}
0^+_{2-ph}	1.130	5.0	5.2-5.4	6.7×10^{20} [a]	6.7×10^{19}-1.9×10^{20}
2^+_{2-ph}	1.362	7.1	6.1-6.7	>1.3×10^{21}	1.8×10^{23}-7.1×10^{24}
0^+_{1-ph}	1.741	6.3	4.1	5.7×10^{20}	1.7-1.8×10^{20}
EC($0^+_{g.s.}$)	0.000	4.29 [b]	3.5-3.7	-	-

Table 1.2: Comparison between experimental and theoretical QRPA logft values and partial half-lives for the A=100 system. Data are taken from [55]. The logft values correspond to the single EC/β^- branches, whereas the half-lives correspond to the 2ν double β-decay from ^{100}Mo to ^{100}Ru.

[a] from [56]
[b] from [51]

matrix elements of the 2ν double β-decay, and a new value for the effective g_A value is obtained by reproducing the half-life of the 2ν double β-decay. A summary of the resulting values from [57] is presented in Table 1.3.

g_{pp}	$g_A(\beta)$	$g_A(\beta\beta)$
0.820-0.838	0.61-0.70	0.75-0.85

Table 1.3: Extracted values of g_{pp} and g_A for the A=100 system in [58].

From the point of view of the study of 0ν double β-decay in ^{100}Mo, apart from the NEMO 3 experiment, already mentioned, that uses a tracking device and a calorimeter to measure different sources of double β-decay isotopes, there are two experiments aiming to search for the 0ν in ^{100}Mo. One is AMoRE (Advanced Mo based Rare process Experiment) [59] based on ^{40}Ca^{100}MoO$_4$ scintillator crystals. The other is MOON (Mo/Majorana Observatory Of Neutrinos) [60], that uses a ^{100}Mo sheet inserted between two NaI(Tl) detectors. Both experiments exploit the reasonable cost of enrichment in ^{100}Mo that makes this isotope attractive for double β-decay studies.

Finally, the decay of ^{100}Tc $\rightarrow$ ^{100}Ru is also important because it has been identified as an important contributor to a new type of flux-dependent correction to the antineutrino spectrum produced in nuclear reactors [61]. This correction takes into account the contribution of the β-decay of nuclides that are produced by neutron capture of long-lived fission products. The correction is non-linear in neutron flux, because the process depends on a fission process to produce the fission product (^{99}Tc) followed by a neutron capture. For that reason, a better knowledge of the individual β-branches of this decay can also contribute to a better determination of this correction, of interest for neutrino-oscillation experiments.

Bearing all these ideas in mind, since the decay of ^{100}Tc $\rightarrow$ ^{100}Ru has only been measured using HPGe detectors [53,54], one of the aims of the present work will be the study of this decay employing the total absorption technique. If β-intensity at high excitation energies in the daughter was not detected because of the *Pandemonium* effect [17], it could

be important in order to constrain theoretical models, as explained before, when comparing calculations and experiment. A description of the experiment performed to measure the β-decay of ^{100}Tc will be presented in Chapter 6, and the results of the TAGS analysis will be shown in Chapter 7.

1.3.2 β-delayed neutron emission

For neutron-rich nuclei far from the stability, the Q_β windows can reach values large enough to cover the neutron separation energy S_n. In those cases with $Q_\beta > S_n$, neutron emission competes with γ-ray emission in the de-excitation process of all excited levels populated above S_n in the β-decay. This decay mode was discovered in 1939 by Roberts et al. [62]. As we go further from stability, this competition increases, becoming dominant when the neutron excess is high enough. Furthermore, for large Q_β, two neutron emission (and in general x-neutron emission) become possible if $Q_\beta > S_{xn}$. A schematic view of the process is depicted in Figure 1.7.

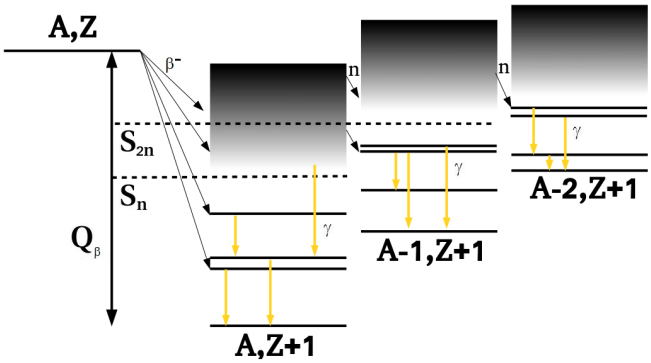

Figure 1.7: Schematic picture of the β-delayed neutron emission process.

This process is important in nuclear technology, since in a nuclear reactor some fission products are β-delayed neutron emitters. The amount of delayed neutrons represents a small fraction of the total neutrons in the reactor (below 1% considering the prompt neutrons from fission). However, these neutrons help to slow the dynamic time response of the reactor, making it controllable. Moreover, the decay of these fission products contributes to the decay heat calculation, as explained in Subsection 1.3.3, and the competition between the neutron and γ-ray emission is crucial for the determination of the β-intensity, and average γ and β energies.

In Astrophysics this process plays a crucial role in the explosive nucleosynthesis scenario. Heavy nuclei beyond Fe can be produced by means of the rapid-neutron-capture process, the so-called r-process. The main characteristic of the r-process is the availability of a large number of neutrons in a short time interval that are added to elements of the iron group in successive neutron capture processes. Around 50% of the solar abundances are thought to be produced with this process [63]. The conditions are large neutron fluxes, with very high neutron densities (10^{20} up to 10^{30} neutrons/cm^3) and short time-scales of the order of 10-100 s, and moderate temperatures of 1-2 GK. The astrophysical sites for

the r-process are still under debate, however these conditions can be fulfilled in different astrophysical environments such as core collapse supernovae of massive stars [64] or neutron star mergers [65].

The r-process path runs from iron through very short-lived nuclei up to the transactinide region within a few seconds, as shown in Figure 1.8. Once the neutron source ceases, the progenitor nuclei undergo fission or decay by β or α emission towards stability, and they produce the stable isotopes of elements up to the heaviest species that define the abundance distributions.

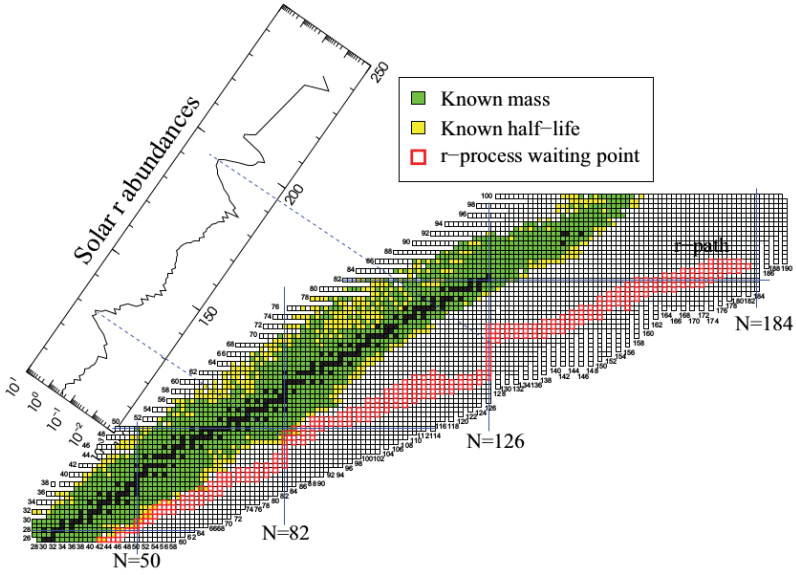

Figure 1.8: r-process paths, defined by their waiting point nuclei, and solar r-process abundances after the decay to stability, from [66].

Calculations of the r-process try to reproduce the solar-system abundance distribution. The detailed study of the r-process requires nuclear data that are many times obtained theoretically from nuclear models. Some of the most important parameters for these calculations are the nuclear masses, that determine the path of the r-process, the half-lives, $T_{1/2}$, that influence the speed of the process and the shape of the abundance distribution, and the β-delayed neutron emission probability values, P_n, that modify the abundance distribution. P_n is defined mathematically by Equation (1.27), and it depends on the β-strength distribution, S_β.

$$P_n = \frac{\sum_{S_n}^{Q_\beta} S_\beta(E_i) f(Q_\beta - E_i, Z)}{\sum_{0}^{Q_\beta} S_\beta(E_i) f(Q_\beta - E_i, Z)} \tag{1.27}$$

One of the difficulties related to these calculations is to test these nuclear models far from stability. This is also of paramount interest from the point of view of nuclear structure, since β-decay strength distributions are particularly sensitive to the details of the nuclear model. For example, predictions of $T_{1/2}$ and P_n from QRPA calculations [67,68] have been compared in recent years with experimental results. However, the ideal test of the accuracy of nuclear models implies the comparison of β-strength distributions. The characterization

of the complete β-strength distribution can be achieved by combining 4π neutron counter detectors, that provide P_n values, n-ToF arrays, that provide the energy distribution of the neutrons, and the TAGS technique to obtain the β intensity distribution followed by γ-ray emission without the systematic *Pandemonium* error.

While in the classical picture of equilibrium flow the (n,γ) reaction does not play a role, in non-equilibrium conditions this process has to be considered [69]. After neutrons are almost exhausted and matter decays to stability it has been shown in neutrino-driven wind simulations that neutron captures are key for determining the final abundance distribution [70]. However these cross sections are not experimentally accessible for the very unstable isotopes involved (it would require unstable targets that are not available). When no experimental information is available, statistical calculations using the Hauser-Feschbach formalism (HFF) [71] are used. These calculations rely on parameters obtained close to the valley of β stability for Nuclear Level Densities (NLD), Photon Strength Functions (PSF) and Neutron Transmission Coefficients (NTC) [72]. In recent years the connection between the β-delayed neutron emission process and (n,γ) reactions as a possible source of the missing experimental information has been highlighted [73–76], as depicted in Figure 1.9.

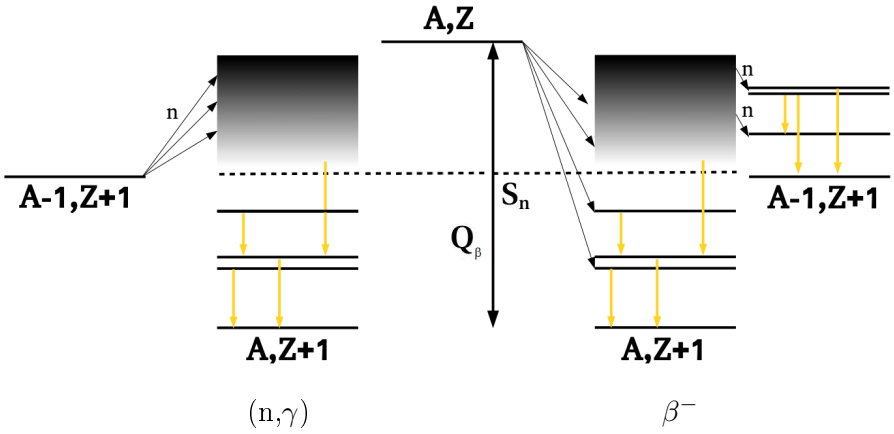

Figure 1.9: Schematic comparison between β-delayed neutron emission and the neutron capture process.

This connection is clear when comparing the cross section of the (n,γ) process and the β intensity distribution with γ emission above S_n, proportional to the following ratios of the widths:

$$\begin{aligned} \sigma_{n\gamma} &\propto \frac{\Gamma_\gamma \Gamma_n}{\Gamma_\gamma + \Gamma_n} \\ I_{\beta\gamma} &\propto \frac{\Gamma_\gamma}{\Gamma_\gamma + \Gamma_n} \end{aligned} \tag{1.28}$$

where Γ_γ and Γ_n are the partial γ and partial neutron widths respectively, defined as in [74].

In both processes similar resonances are populated, though they usually have different spin-parity values. The difficulty when taking advantage of this connection, is related to the

accurate measurement of the $I_{\beta\gamma}$ above S_n. Again, the TAGS technique applied to study β-delayed neutron emitters has proved to be capable of extracting this β intensity [73,74,77].

With all these ideas in mind, two β-delayed neutron emitters were studied in this work. The decay of ^{137}I will be presented in Chapter 13 and the decay of ^{95}Rb will be presented in Chapter 14. These measurements follow the line of previous TAGS measurements performed by the Valencia group, with the study of the decays of ^{87,88}Br and ^{93,94}Rb [73,74,78].

1.3.3 Decay heat problem

In the 1930s Fermi, and then Otto Hahn and Fritz Strassman, bombarded with neutrons uranium targets trying to produce a transuranic element. However, the results of these experiments did not seem to create any transuranic element. Lisa Meitner and Otto Frisch realized in 1939 that in reality the uranium nucleus was divided into two nuclei of approximately equal size after the absorption of the neutron. The fission process had been discovered, and, although it would lead to the horrifying development of nuclear weapons, it was also the seed of a promising source of energy for human beings. Since then, nuclear power plants based on fission have been constructed and operated all over the world. In nuclear reactors, there are three main sources of energy (without considering the energy taken by the neutrinos): the kinetic energy of the fission products and the neutrons, the prompt neutrons and prompt γ radiation of the de-excitation of fission fragments, and the γ and β energy released in the natural decay of the fission products [79,80]. This last source contributes approximately between 8% and 12% [79] to the total energy generated and is known as decay heat. Decay heat is, thus, an important factor when designing nuclear facilities, as well as when handling nuclear fuels and nuclear wastes.

It is possible to measure directly the decay heat by means of radiation detection experiments or calorimetric experiments. Some of the experimental measurements were done at Oak Ridge National Laboratory (ORNL), [81,81], at Lowell [82] and at Yayoi [83] for a number of fissionable isotopes and neutron energies. However, due to the diversity of existing reactors and fuel compositions, theoretical estimates are needed because of their flexibility. In order to test these calculations, a comparison with experimental measurements is carried out. Some reviews of the existing experimental data have been made in the past, and the benchmarks of Tobias [84] have been considered for a long time the decay heat standards. The Tobias standards are based on least-squares fits to 54 measurements of ^{235}U and 28 measurements of ^{239}Pu. In the last reports of the IAEA [85], however, direct comparison of the calculations with the three experimental measurements cited before were made, as can be seen in Figure 1.10.

The theoretical calculation of the decay heat can be made with two approaches: the statistical method and the summation method [80,86]. The statistical method, historically introduced by Way and Wigner [87], is based on considering the fission products as a statistical ensemble, and then using empirical relations for half-lives and atomic masses to calculate the γ and $\gamma+\beta$ components. This method is less accurate for longer cooling times. The alternative summation calculation method is applied over an inventory of radioactive

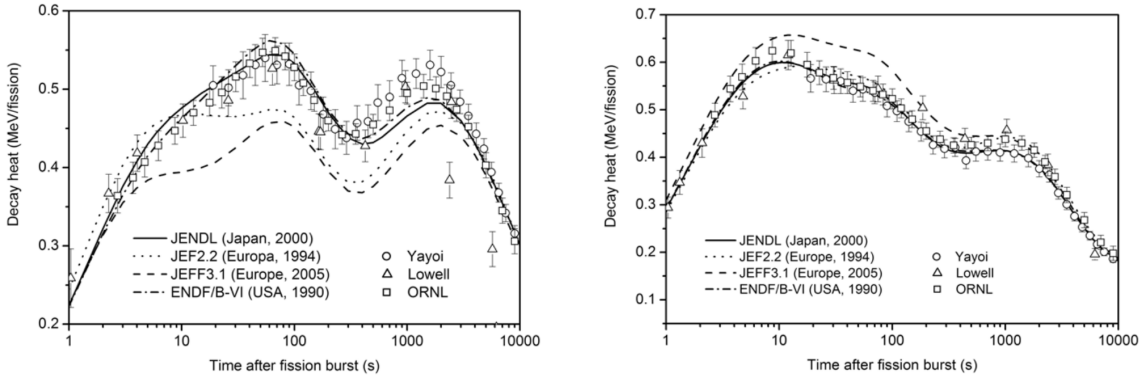

Figure 1.10: Decay heat calculation for ^{239}Pu with data from JENDL, JEF-2.2, JEFF-3.1 and ENDF/B-VI decay-data libraries in comparison with experimental data from Yayoi, Lowell and Oak ORNL. Extracted from [85]. The electromagnetic component (left) and the light particle component (right) are shown.

isotopes, which is obtained by solving the linear system of coupled first order differential equations that describe the creation and decay of fission products [79,80,88]. This system is given in Equations 1.29:

$$\begin{aligned} &\text{Build up: } \frac{dN_i}{dt} = -(\lambda_i + \sigma_i\phi)N_i + \alpha_i F + \sum_j f_{j\to i}\lambda_j N_j + \sum_k \mu_{k\to i}\sigma_k\phi N_k \\ &\text{Decay: } \qquad\qquad \frac{dN_i}{dt} = -\lambda_i N_i + \lambda_{i-1}N_{i-1} \end{aligned} \tag{1.29}$$

where N_i is the number of nuclide i, λ_i is the decay constant of nuclide i, σ_i is the average capture cross section of nuclide i, ϕ is the neutron flux, α_i is the independent fission yield of nuclide i and F is the fission rate. $f_{j\to i}$ is the branching ratio of the decay from nuclide j to i, whereas $\mu_{k\to i}$ is the production rate of nuclide i per one neutron capture of nuclide k. The decay of the nuclide i depends on the number of nuclei of the predecessor in the decay chain.

With this inventory, the decay heat as a function of time can be computed by summing the energy released by each nucleus weighted by the activity at this time, according to Equation (1.30):

$$f(t) = \sum_i (\overline{E}_{\beta,i} + \overline{E}_{\gamma,i} + \overline{E}_{\alpha,i})\lambda_i N_i(t) \tag{1.30}$$

where $f(t)$ is the power function, $\overline{E}_i$ is the mean decay energy of the ith nuclide (β, γ and α components), λ_i is the decay constant of the ith nuclide, and $N_i(t)$ is the number of nuclide i at cooling time t. The mean γ and β energies are defined as:

$$\overline{E}_\gamma = \sum_i I_\beta(E_i)E_i \quad , \quad \overline{E}_\beta = \sum_i I_\beta(E_i) < E_{\beta i} > \tag{1.31}$$

with $I_\beta(E_i)$ is the probability of β feeding to level E_i and $\langle E_{\beta i}\rangle$ is the mean energy of

the β particles emitted when level i is fed.

The main uncertainties associated with this method concern the neutron cross sections, the fission yields and the available decay data. The discrepancy between the experimental measurements and the summation calculations using the three reference databases, JEFF, ENDF/B and JENDL, is shown in Figure 1.10. In order to reduce the uncertainties in data for β-decay intensities, that may suffer from the *Pandemonium* effect, TAGS technique was proposed for the study of the decay of fission fragments. As a consequence, a review of the most important contributors from 10 to 10000 s for the U/Pu fuel cycle to decay heat was carried out. Indeed, TAGS measurements of some of the decays of highest priority in a list elaborated by the International Atomic Energy Agency (IAEA) and the Nuclear Energy Agency (NEA) [85], were shown to improve dramatically the reproduction of experimental data [89], as shown in Figure 1.11, proving the capability of the summation method to identify the most important contributors, and confirming the potential of the TAGS technique to measure undetected β intensity.

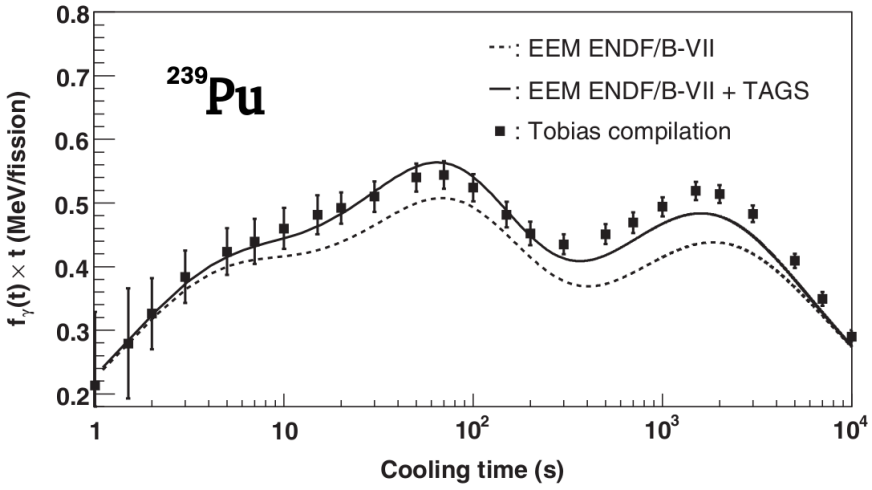

Figure 1.11: Impact of TAGS data for the decays of ^{102,104,105,106,107}Tc, ^{105}Mo, and ^{101}Nb in reactor decay heat reproduction with summation calculations, from [89]. The electromagnetic component for ^{239}Pu calculated with ENDF/B-VII is compared with the evaluation of Tobias [84].

From that time onward, further TAGS measurements of important contributors to the decay heat have been undertaken by the group of Valencia [26–28, 74] and by the group of ORNL. In this work, the first TAGS measurements of some important fission products for the decay heat will be presented. The list of cases studied in this work is presented in Table 1.4, where the contribution of each nucleus to the decay heat as a function of time after shut-down is taken from [90] for the main fissile isotopes of the U/Pu and Th/U fuels.

Nuclide	Priority U/Pu	Priority Th/U	Contribution [%] ^{235}U		Contribution [%] ^{239}Pu		Contribution [%] ^{232}Th	
			10 s	100 s	10 s	100 s	10 s	100 s
^{103}Tc	1	2	-	1.2	-	3.3	-	-
^{103}Mo	1	2	-	1.9	1.3	5.0	-	-
^{137}I	1	2	1.6	1.5	1.4	1.1	2.0	1.8
^{100}Nb	1	1	5.7	-	6.9	-	1.3	-
^{102}Nb	2	2	3.9	-	4.7	-	-	-

Table 1.4: List of high priority decays studied in this work that are important contributors to the decay heat. The priority of the TAGS measurements for U/Pu [85] and Th/U [91] fuels, as well as the contribution to the decay-heat of the main fissile isotopes at different cooling times (from [90]) are presented.

1.3.4 Reactor antineutrino spectrum

Nuclear power plants produce on average 6 antineutrinos per fission due to the β-decay of fission products, which means an electron antineutrino flux of $\sim 10^{20}$ $\overline{\nu}$/s with energies up to $\sim$10 MeV from a reactor of 1 GW thermal power. This amount of antineutrinos can be used in reactor based experiments related to antineutrino oscillation. In the Standard Model of fundamental interactions there are three neutrino flavours, the weak interaction states associated with the eigenstates of neutrinos when they are detected, that are a linear superposition of the mass eigenstates, associated with the propagation of neutrinos [92]. The unitary matrix linking both sets of eigenstates is called the Pontecorvo-Maki-Nakagawa-Sakata (PMNS) matrix. Due to the non-zero mass of the neutrinos, there is a neutrino oscillation between flavours when neutrinos propagate, implying that individual lepton charge is not conserved. The oscillation probability is described by three mixing angles (θ_{12}, θ_{23}, θ_{13}), two independent mass square differences (Δm^2_{31}, Δm^2_{23}), and one CP violation phase phase, δ_{CP}. Reactor based neutrino oscillation experiments are disappearance experiments where the oscillation probability is given by Equation 1.32 in a 2ν oscillation framework.

$$P_{\text{oscillation}} \simeq \sin^2\theta_{13}\sin^2\left(1.27\frac{\Delta m^2_{31}L}{E_\nu}\right) \tag{1.32}$$

where θ_{13} is the neutrino mixing angle, Δm^2_{31} is the mass square difference in eV^2, L is the distance that the neutrino travels [93] in m, and E_ν is the energy of the neutrino measured in MeV.

Nowadays there are three running reactor based neutrino oscillation experiments aiming to improve the value of the neutrino oscillation mixing angle θ_{13}: Double Chooz [94], Daya Bay [95], and Reno [96]. The experimental θ_{13} in these experiments is independent of δ_{CP}, which turns out to be an advantage in comparison with accelerator based experiments.

The detection of antineutrinos is based on the inverse-β reaction $\overline{\nu}_e + p \rightarrow e^+ + n$, with an energy threshold of 1.8 MeV. In the three experiments mentioned, this reaction is detected using liquid scintillator detectors loaded with gadolinium in order to increase the neutron capture probability. The prompt energy deposition and the e^+ annihilation with

an electron followed by a neutron capture give the signals that enable the identification of a ν event. The reconstruction of the energy of the antineutrino is carried out according to Equation 1.33.

$$E_{\overline{\nu}} = E_e - 2m_e + m_n + m_e - m_p \tag{1.33}$$

where E_e is the prompt energy detected, and m_p, m_e and m_n are the masses of the proton, electron and neutron, respectively.

A two detector concept is applied in the three experiments, with a measurement of the antinetrino energy spectrum with a near detector (depending on the experiment it is placed 290-525 m from the reactor) and a far detector (1050-1900 m from the reactor). Identical near and far detectors are used in order to cancel most of the systematic uncertainties. They are located underground to reduce the background coming from cosmic rays (a cosmic muon spallation in the surrounding materials of the detector, for example, can trigger the detection system in the same way as a true neutrino signal). All three experiments employ pressurized water reactors (PWR): RENO consists of six reactors, Daya Bay operates on three separate sites, each with two reactors, and Double Chooz consists of two reactors, as it is depicted in Figure 1.12.

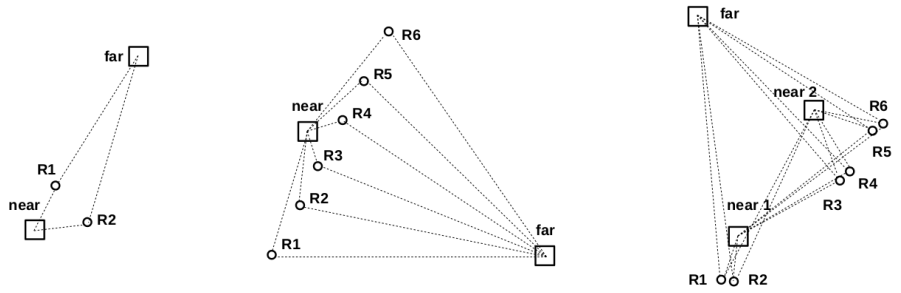

(a) Double Chooz (b) RENO (c) Daya Bay

Figure 1.12: Experimental set-ups of Double Chooz, RENO and Daya Bay experiments, from [97]. Squares depict the detectors and circles depict the reactors. Dotted lines represent the baselines between detectors and reactors.

The three experiments use as an input to their oscillation analyses the predicted antineutrino spectrum. A correction with the antineutrino spectrum prediction has to be applied due to the effect of the non-isoflux conditions. Moreover, the first phase of the Double Chooz experiment collects data only with the far detector, and results are obtained from comparison of the measurement with the predicted antineutrino spectrum emitted by the two reactors. The total emitted antineutrino flux is given by Equation 1.34.

$$S_{total}(E_{\overline{\nu}_e}) = \sum_k f_k S_k(E_{\overline{\nu}_e}) \tag{1.34}$$

where k represents the fissile nuclei, f_k is the contribution to the total number of fissions of fuel k, and S_k is the reference antineutrino spectrum per fission.

In pressurized water reactors (PWR), UO_2 is used as fuel enriched 3-5% in ^{235}U (natural

uranium is 99.274% ^{238}U and 0.7205% ^{235}U). In the reactor core, thermal neutrons induce fission in ^{235}U giving rise to fission fragments and a few neutrons. A fraction of the neutrons is captured in ^{238}U, producing ^{239}U that in the end decays to ^{239}Pu. More neutron captures can also produce ^{240}Pu and ^{241}Pu. ^{239}Pu and ^{241}Pu also fission with thermal neutrons, whereas ^{238}U only fissions with high energy neutrons. The fission cross section of ^{240}Pu is quite small in comparison with the neutron capture cross section. As a consequence, 99% of all PWR reactor antineutrinos are coming from the fission of four isotopes, ^{235}U, ^{238}U, ^{239}Pu and ^{241}Pu. The total emitted spectrum in Equation 1.34 will be, therefore, the sum of these four fissile nuclei.

The reference spectra $S_k(E_{\overline{\nu}})$ can be obtained with two different approaches: the so-called conversion method based on cumulated β spectra measurements, and the ab initio or summation method that relies on the information available in the databases.

- Conversion method:

  This is the standard method, and it uses cumulative β^- spectra measured with the magnetic beta spectrometer BILL [98] at the High Flux Reactor of the Institute Laue-Languevin (ILL) in Grenoble. Those measurements were performed with thermal neutrons for ^{235}U, ^{239}Pu and ^{241}Pu [99–102], and the spectra were recorded in bins of 250 keV up to 8 MeV. Until 2014 there was no available measurement for ^{238}U, that undergoes fission with fast neutrons, and only the summation calculations explained below were used for this contributor. It was finally measured at the scientific neutron source FRM II in Garching [103].

  The antineutrino spectra of each fissile nucleus is deduced from these β spectra by means of a conversion procedure, where β branches are fitted and converted to antineutrino branches. These fits were originally performed by considering 30 virtual branches [99–102] and dividing the β spectrum in 30 bins.

  The antineutrino spectrum for each branch can be obtained by substituting the energy of the electron (E_e) by the energy of the antineutrino (E_ν), $E_\nu = E_0 - E_e$, in the expression of the β spectrum. For an allowed transition this expression is given in Equation (1.35) according to [104]:

$$N(E_e) = k \times E_e p_e (E_0 - E_e)^2 \times F(Z, E_e) \times L_0 \times C \times S \times G_\beta \times (1 + \delta_{WM} E_e) \quad (1.35)$$

  where k is a normalization constant, p_e is the momentum of the electron, $F(Z, E_e)$ is the Fermi function, L_0 is the electromagnetic finite-size correction, C is the weak-interaction finite size correction, S is correction due to the screening of the nuclear charge by the atomic electrons, G_β is the radiative correction for the β spectrum that has to be replaced by a much simpler radiative correction for neutrinos, G_ν. Finally, one of the largest corrections to the shape of the β spectrum is the weak-magnetism term, $1 + \delta_{WM} E_e$, related to the interference of the magnetic moment distribution of the vector current with the spin distribution of the axial current. Its value is

deduced from the $M1$ γ decay width in isobaric analogue states, under the conserved vector current (CVC) hypothesis. This last term is supposed to be the same for all β-decays [105]. As can be observed the conversion depends on the nuclear charge Z, thus assumptions have to be made in order to apply this method.

- Summation method:

  This method, also known as the *"ab initio"* approach, uses information from nuclear databases to calculate the total antineutrino spectrum as the sum of the spectra associated with the decay of each fission product weighted by the corresponding fission yield, in the line of decay heat summation calculations. For each of the fissile nuclei, as presented in Equation (1.34), the antineutrino spectrum is calculated according to Equation (1.36).

$$S_k(E_{\overline{\nu}_e}) = \sum_i \left(Y_i \times \sum_j I_{ij} S_{ij}(E_{\overline{\nu}_e}) \right) \tag{1.36}$$

  where Y_i is the cumulative fission yield of the fission product i, I_{ij} is the decay intensity to the daughter level j, and $S_{ij}(E_{\overline{\nu}})$ is the antineutrino spectrum for the transition with endpoint energy $Q_\beta - E_j$.

  Fission rates and activities may be determined with the simulation package MCNP Utility for Reactor Evolution (MURE) [106], whereas β intensities are obtained from the decay data available in the databases [106, 107].

  Due to its flexibility, the summation approach is the only predictive method that can be used for any reactor fuel type, and the only one that can predict the shape of the antineutrino spectra beyond 8 MeV. One of the main advantages of this method, is the possibility to identify the most important contributors to the spectrum in any energy range [107, 108], as shown in Figure 1.13. On the other hand, the main disadvantage of this method is related both to the inaccuracy of the fission yields, to the incompleteness of the decay schemes, and to the lack of information for very unstable nuclei. For these reasons, while the current uncertainty in the conversion method is about $2-3\%$ [109], the summation approach is estimated to have an appreciably larger uncertainty ($10-20\%$ [109]).

There are three important hot topics concerning the current level of knowledge in the reproduction of antineutrino spectrum. All of them are complex problems that involve many different experimental and theoretical questions:

- Reactor antineutrino anomaly

  Recently, Mueller *et al.* in a mixed version of the conversion and the summation methods, took into account the information available in the databases to use real β branches with perfectly known nuclear charge, and reduced the number of virtual branches to 5 [106], with Z=46. This last evaluation led to a mean normalization shift of about +3% in the antineutrino rate with respect to the original value. An improved

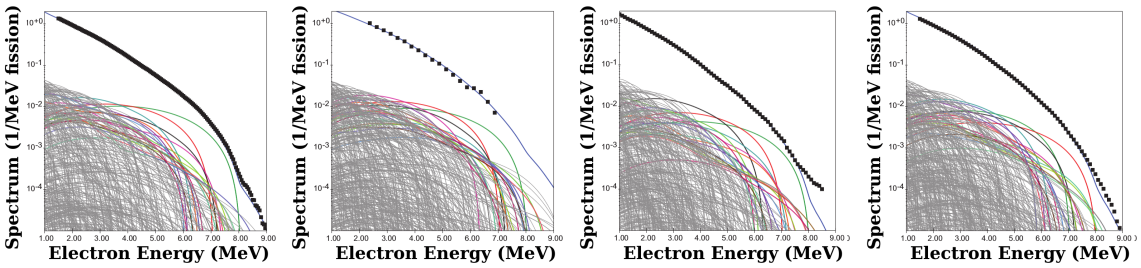

(a) ^{235}U (b) ^{238}U (c) ^{229}Pu (d) ^{241}Pu

Figure 1.13: Calculated electron spectra compared with the data from ILL and Garching, from [107]. The thin gray lines represent the individual β spectrum from each fission fragment. The thick color lines represent the most important individual contributors at 5.5 MeV.

application of the original conversion method done by Huber *et al.* [104] confirmed this shift by using only virtual branches, but taking into account the information in the databases on the mean nuclear charge of the fission fragments as a function of the energy. The effect of a realistic description of the average nuclear charge on the shape of the antineutrino spectrum deduced from the β spectrum, especially between 4 and 8 MeV, had been already pointed out in [110]. Although in [110] errors of $\sim 1\%$ were obtained when comparing a calculation of the antineutrino spectrum with the calculated β spectrum converted to antineutrino spectrum, in reality, the error is larger because of all the corrections in Equation (1.35), the statistical fluctuation and binning of real data etc., as explained in [104]. In Figure 1.14 from Huber *et al.* [104] the comparison of the original ILL conversion with the two new conversion methods mentioned here is shown. Indeed, the shift with respect to the original normalization can be seen for the re-examinations from Mueller *et al.* [106] and Huber *et al.* [104]. The green line in Figure 1.14 corresponds to the conversion from Huber *et al.* [104] with a simplified expression of the β spectrum that is used in Mueller *et al.* [106], without some of the corrections in Equation (1.35).

The effect of this re-examination of the fluxes was to decrease the normalized ratio of observed to expected event rates in short baseline reactor experiments. If the predicted rates are re-evaluated for all the experiments performed in the eighties and nineties [111], a deficit with respect to the new predictions is found, thus unveiling a reactor antineutrino anomaly [111]. In addition, the re-evaluation of the neutron mean lifetime (that affects the predicted cross section per fission) and the inclusion of long lived isotopes (non-equilibrium correction) were also shown to increase this deficit. As a result, a 6% deficit was calculated in [111], as shown in Figure 1.15, where $\sim 50\%$ is coming from the re-examination of the fluxes, $\sim 25\%$ from the neutron mean lifetime and $\sim 25\%$ from the non-equilibrium correction. This deficit of antineutrinos relative to the predictions in short baseline experiments, could imply an oscillation mixing with sterile neutrinos [112]. Nevertheless, the uncertainty associated with the treatment of forbidden transitions could be comparable with the anomaly, according to [113], since they represent $\sim 25\%$ of the total transitions. An-

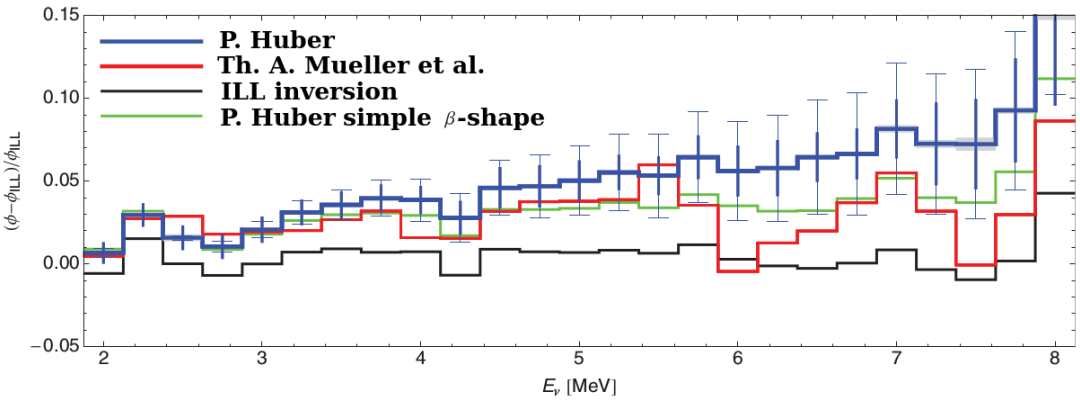

Figure 1.14: Differences between the recent applications of the conversion method and the original one for ^{235}U, from Huber *et al.* [104]. The original conversion from [101] is compared with the re-examinations of Mueller *et al.* [106] and Huber *et al.* [104].

other possible explanation suggested in [106,113] is related to the uncertainty in the weak magnetism term. Very recently, the Daya Bay collaboration suggested that the evolution of the reactor antineutrino flux, especially in ^{235}U, could account for the anomaly [114]. Regardless of its origin, one of the main conclusions highlighted by this anomaly is that new measurements like those carried out at ILL would be useful, since a problem with their normalization could also account for this discrepancy. Moreover, a better knowledge of the β-decay of the fission fragments is crucial to understand and reproduce the antineutrino spectrum when a summation approach or a mixed approach is used.

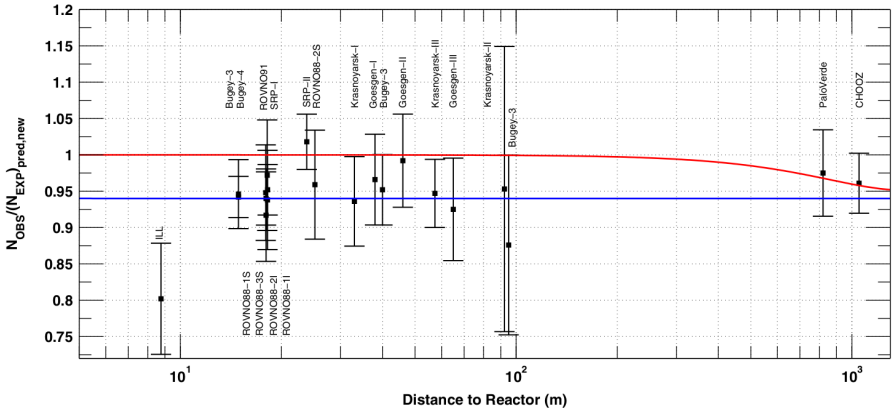

Figure 1.15: Short baseline reactor antineutrino anomaly for the reactor experiments performed since the eighties, from [111]. The ratio between prediction and experimental results is presented. The red line corresponds to a three-active neutrino mixing scenario, whereas the blue line corresponds to a solution including a new neutrino mass state

- Reactor antineutrino shape distortion

  Apart from the neutrino anomaly, RENO, Daya Bay and Double Chooz experimental antineutrino spectra have shown an excess (a shoulder) relative to the predictions in

the range of 5-7 MeV [115–117], as shown in Figure 1.16 from [118].

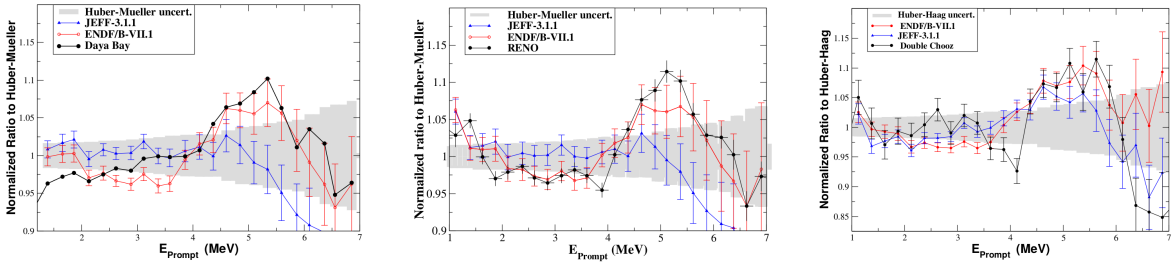

(a) Daya Bay (b) RENO (c) Double Chooz

Figure 1.16: Experimental excess in antineutrino spectra with respect to predictions from [118].

This excess has attracted a lot of attention in the last few years, and different possible origins have been considered. Since it has been observed at two different baselines (near and far detectors) by Daya Bay and RENO, any kind of oscillation is excluded. The most important explanations are related to the forbidden nature of the β-decays dominating this energy region of the antineutrino spectrum, and to the contribution of ^{238}U. In a detailed study on all the uncertainties [118], a proper treatment of forbidden transitions is discarded as having a relevant impact in the region of the shoulder, whereas ^{238}U could account for a significant fraction of this structure. Another study [119] claimed to obtain a similar bump with summation calculations, in agreement with experimental measurements, but not compatible with conversion calculations. Similar results were obtained by [118], and both studies suggest that this could be due to problems with the original integral β measurements at ILL.

Moreover, an effect of the fission yields has been observed in the reproduction of the shoulder with summation calculations. In [118], the results with the two recommended fission yield data sets, from the JEFF-3.1.1 and ENDF/B-VII.1 nuclear databases, are compared (the other reference nuclear database, JENDL, has essentially the same fission yields than ENDF/B). The conclusion, as shown in Figure 1.16, was that JEFF-3.1.1 only reproduced the shoulder for the Double Chooz experiment, since this experiment is the only one that uses the recent experimental information for the spectrum of ^{238}U [103], instead of a summation calculation. On the contrary, ENDF/B-VII.1 obtained a shoulder for the three experiments. However, a careful review of ENDF/B-VII.1 fission yields was performed in [120], and several errors were identified. The correction of these errors in the fission yields excluded any excess with summation calculations, and a 6% uncertainty in summation calculations up to 7 MeV from the fission yield component was concluded.

Recently, studies with a new generation of experiments based on Highly Enriched Uranium (HEU) fuels in experimental reactors, such as Stereo [121] or NEOS [122], have been combined with the experiments already mentioned, that are based on Low Enriched Uranium (LEU) fuels. These new experiments offer the possibility to approximate all the production of antineutrinos exclusively to ^{235}U. A combination

of measured reactor antineutrino spectrum in Double Chooz and in Stereo, first suggested the scenario of ^{235}U as the only nucleus responsible for the distortion [123]. Another study combining Daya Bay data and NEOS supported the idea of ^{235}U as the leading contributor to the shoulder [124]. In addition, the NEOS experiment has also reported an excess in the region of 5 MeV similar to the bump seen by RENO, Daya Bay and Double Chooz [122].

- Non proliferation of nuclear weapons

  ^{239}Pu for nuclear weapons may be obtained in conventional water moderated reactor resulting from neutron capture on ^{238}U. In order to detect unreported plutonium production, different safeguard methods have been promoted by the IAEA. Conventional methods rely on the collection of several hundred samples across the reactor to reconstruct the three dimensional distributions of the burn-up [125]. These methods provide information only after the shut down of the reactor. An alternative to such a complex procedure is a real-time measurement of the reactor antineutrino spectrum [126]. By applying the basics of the summation approach, the relative contribution to fission from each of the fissile isotopes can be obtained [125, 127], and undeclared refueling of plutonium could be detected. For these applications, neutrino detectors have to work with minimal background and ensure reasonable dimensions for transport and placement. New detectors are being developed for this purpose, such as PANDA (Plastic Anti-Neutrino Detector Array) [128]. The feasibility of the antineutrino monitoring also relies on the nuclear data used in the summation method. A review of the current efforts in this field can be found in [129].

In the light of the unprecedented accuracy needed in the experimental search for the θ_{13} mixing angle, the accuracy in antineutrino spectrum calculations turned out to be critical. The observation of discrepancies between experiments and calculations in absolute flux and spectral shape have revealed possible uncertainties both at the level of the experimental measurements of the β spectra used in conversion calculations, and at the level of nuclear data used in summation calculations (apart from a careful review of the uncertainties in the experimental reactor antineutrino measurements that is not mentioned here). From the point of view of nuclear data, improvements in fission yields and decay data are mandatory in order to reduce the uncertainty of the summation approach. In particular, decay data free from the *Pandemonium* effect for the most important contributors to the regions of the antineutrino spectrum where the level of understanding and reproduction is more questionable, would benefit any discussion in this field.

An improvement in decay data can be achieved by using the TAGS technique, as in the case of decay heat calculation. A valuable source of data unaffected by *Pandemonium*, is coming from the β spectra measurements of fission fragments performed by Tengblad *et al.* at ISOLDE and OSIRIS [130]. In those experimental campaigns 111 fission products were measured with charged particle telescopes, and in fact a calculation of the integral β-spectrum emitted from thermal-neutron induced fission of ^{235}U was performed with them. These data together with TAGS data of fission fragments from the measurements

performed by Greenwood *et al.* at the INEL ISOL facility [131], were included in the summation calculations done in Mueller *et al.* [106], obtaining a better agreement with ILL data, as shown in Figure 1.17.

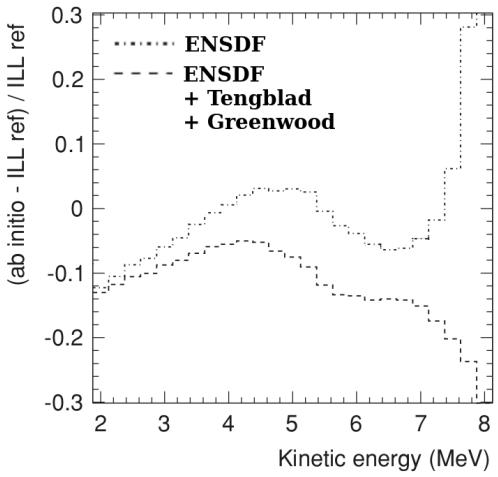

Figure 1.17: Residues of the comparison of the ILL data and the summation calculation from Mueller *et al.* [106] for ^{235}U with and without including data free from *Pandemonium*.

Likewise for decay heat calculation, TAGS measurements have been promoted to improve antineutrino spectrum calculations, and a list of priorities has been also defined by the IAEA [91]. The inclusion of new TAGS data (the decays of ^{102,104,105,106,107}Tc, ^{105}Mo, and ^{101}Nb from [89,132]) in the summation approach, had a relevant impact in the antineutrino spectrum [133], reaching 8% in the 2-4 MeV energy range for the plutonium isotopes, 3.5% for ^{238}U, and 1.5% for ^{235}U. Since then, new TAGS measurements have been performed motivated by the antineutrino spectrum predictions. The target cases have been selected by considering that among the ∼1000 fission fragments involved, around 20 play an important role in the regions in question. These most relevant cases have been identified [107,108] and some of them are listed in Table 1.5.

The majority of the important cases have a relevant ground state to ground state β intensity, which has been pointed out as something crucial due to the first forbidden nature of many of these transitions and the corresponding effect in the shape of the β spectrum [107]. A β-γ counting method for TAGS data developed by Greenwood *et al.* [134] will be revisited in this work in order to study precisely those cases with large ground state feeding β intensity.

The first three rows in Table 1.5 correspond to the most important contributors at medium and high energies. ^{92}Rb is considered to be of paramount relevance, and it was studied recently at IGISOL [108], giving an impact of between 1.5% and 4.5% depending on the fissile isotope. A 6% impact around 7.2 MeV has been recently found with TAGS measurements of ^{88}Br and ^{94}Rb from the same campaign at IGISOL [74]. Another TAGS measurement of ^{92}Rb at ONRL [135] confirms the previous numbers, and includes a measurement of the decays of ^{96}Y and ^{142}Cs. These last two cases were measured in the experimental campaign of the cases presented in this work, and they are under analysis by

Nuclide	^{235}U			^{238}U			^{239}Pu			^{241}Pu		
	FY [%]	@4 [%]	@5.5 [%]	FY [%]	@4 [%]	@5.5 [%]	FY [%]	@4 [%]	@5.5 [%]	FY [%]	@4 [%]	@5.5 [%]
^{92}Rb	0.048	6.1	21.6	0.042	3.3	10.8	0.020	4.0	16.8	0.019	2.5	10.8
^{96}Y	0.047	6.3	14.5	0.054	4.5	9.5	0.029	6.0	16.5	0.032	4.5	12.5
^{142}Cs	0.029	3.5	6.8	0.044	3.2	5.9	0.016	3.0	7.1	0.031	3.9	9.2
^{140}Cs	**0.060**	**3.4**	**2.4**	**0.060**	**2.1**	-	**0.044**	**3.9**	**3.4**	**0.056**	**3.2**	**2.8**
^{100}Nb	**0.056**	**5.5**	**4.7**	**0.064**	**3.8**	**3.1**	**0.052**	**7.8**	**8.2**	**0.051**	**5.1**	**5.4**
^{102}Nb	**0.028**	**1.9**	-	**0.049**	**2.2**	-	**0.028**	**3.1**	**1.2**	**0.041**	**3.0**	-
^{95}Rb	-	-	-	**0.022**	**1.8**	-	-	-	-	-	-	-
^{137}I	-	-	-	**0.036**	**2.2**	-	**0.023**	**2.2**	-	**0.045**	**2.9**	-

Table 1.5: Table with the most important contributors to the antineutrino spectrum calculation and other important contributors measured in this work. Fission yield (FY) and contributions at 4 MeV (@4) and 5.5 MeV (@5.5) are presented for each fissile isotope. The cases studied in this work are presented in bold. Data taken from [107] based on ENDF/B-VII.1.

the group of Subatech [136].

The rest of the cases highlighted in bold in Table 1.5, will be studied in this work. Among them, ^{100}Nb is considered to be amongst the most important contributors together with ^{92}Rb, ^{96}Y and ^{142}Cs. The TAGS measurement for this decay will be presented in Chapter 11, while in Chapters 10, 12, 13 and 14 the results for the rest of the cases will be presented.

Chapter 2

TAGS Data Analysis

Lo fácil o lo difícil no es el problema
en sí, sino nuestro modo de resolverlo

Easy or difficult is not the problem itself, but our way of solving it

Javier Fresán

In this chapter, the procedure to extract the β-intensity distribution from TAGS measurements developed by the Valencia group will be explained. The algorithms used in the de-convolution process using the spectrometer response to the decay, will be addressed. Finally, the different steps is the construction of the response matrix will be detailed, as well as the reference information used as input.

2.1 The solution to the TAGS inverse problem

As it was shown in Equation (1.23) from Chapter 1, the measured spectrum and the β-feeding distribution are related by:

$$d_i = \sum_{j}^{levels} R_{ij}(B) f_j + C_i \tag{2.1}$$

where now C_i, the contribution of all contaminants to channel i, has been added to present the realistic scenario of a TAGS analysis. As explained in Chapter 1, d_i is the number of counts in channel i of the spectrum, and f_j is the number of events that fed level j in the daughter nucleus. $R_{ij}(B)$ is the response function of the detector that represents the probability that feeding to the level j gives a count in channel i of the experimental spectrum. This response function is calculated by means of MC simulations, and it is unique for each detector and each decay scheme [137] as will be shown in Section 2.3.

A careful study of the performance of different methods to solve the linear inverse problem of a TAGS analysis, was carried out in [137]. Among the algorithms studied in [137], two were selected as good algorithms for TAGS analysis, and they will be summarized here. The Expectation-Maximization algorithm has been traditionally used by the Valencia group, and it will be the one used by default in the analysis presented in this work. However, as a part of the estimation of the uncertainties, the Maximum-Entropy algorithm will also be used in order to see the impact of the deconvolution method on the results.

2.1.1 Expectation-Maximization algorithm

The easiest way to derive the Expectation-Maximization (EM) algorithm is through Bayes theorem, following the line of [138] and previous works [139, 140]. This theorem is formulated to link m independent causes (in our case, the β-feedings, f_j) with n effects (the experimental counts, d_i, in our case). If a single effect i is observed, the probability that it has been due to the cause j is thus given by Equation (2.2):

$$P(f_j|d_i) = \frac{P(d_i|f_j)P(f_j)}{\sum_{j=1}^{m} P(d_i|f_j)P(f_j)} = \frac{P(d_i|f_j)P(f_j)}{\sum_{j=1}^{m} R_{ij}P(f_j)} \tag{2.2}$$

where the denominator ensures the normalization of the probability to 1. $P(f_j) = \frac{f_j}{\sum_{j=1}^{m} f_j}$ is the β-intensity distribution, I_β. $P(d_i|f_j)$ is the conditional probability that the cause f_j produces the effect d_i, which in the TAGS analysis is nothing but the response function $R_{ij}(B)$ of the spectrometer.

The evaluation of $P(f_j|d_i)$ depends on the initial probability of the causes. Bayes theorem allows a better knowledge of $P(f_j)$ with the increasing number of observations. However, if there is no a priori information, initially it can be assumed to be a uniform distribution.

Concerning the possible contaminants present in the experimental spectrum, such as the activity from the decay of the daughter, the environmental background or the pileup, they can be treated by adding them to the causes responsible for the observables, as in Equation (2.1). The nature and normalization procedure for the different contaminants will be explained in next chapters. A subtraction of the contaminants is not contemplated, since it enhances the statistical fluctuations [141] and could lead to negative counts, which does not make sense when dealing with probabilities.

Experimentally, the distribution d_i is obtained after observing a number of events. The expected number of those events associated with each cause will be written as in Equation (2.3):

$$\widehat{f_j} = \sum_{i=1}^{n} P(f_j|d_i)d_i \quad j = 0, ..., m \tag{2.3}$$

taking into account the experimental efficiency for observing the cause j (the efficiency for detecting a decay to level j), $\varepsilon_j = \sum_{i=1}^{n} R_{ij}$, it will be written as:

$$\widehat{f_j} = \frac{1}{\varepsilon_j}\sum_{i=1}^{n} P(f_j|d_i)d_i = \frac{1}{\sum_{i=1}^{n} R_{ij}}\sum_{i=1}^{n} \frac{P(d_i|f_j)P(f_j)}{\sum_{j=1}^{m} R_{ij}P(f_j)}d_i \quad j = 0, ..., m \tag{2.4}$$

where $P(f_j|d_i)$ is replaced by using Bayes theorem from Equation (2.2). From expression (2.4) feedings can be obtained iteratively from the initial assumption of a uniform distribution. The convergence of this iterative process is checked by applying Equation (2.1), so that the feeding intensities obtained are multiplied by the response function, and the result is compared with the experimental spectrum. A χ^2 can be defined with this difference, and several stopping criteria can be chosen to finish the iterations. A limit in the number of iterations has been proved to be a good criterion, and normally after $\simeq$200

iterations, the reproduction of the experimental spectrum is quite good and the χ^2 does not improve significantly with more iterations.

The EM algorithm has several advantages: it does not imply any assumption on the statistical distribution of the data, it always gives a positive solution (a physical requirement fulfilled by working with normalized probabilities), and it does not need any regularization parameter.

2.1.2 Maximum-Entropy algorithm

The solution to the linear inverse problem proposed by the Maximum-Entropy (ME) algorithm is based on maximizing the Shannon information entropy [142], that represents our a priori knowledge about the solution, when considering some constraints. The constraint associated with the TAGS problem is related to the reproduction of the experimental data (a χ^2 condition).

There are different formalizations of the information entropy, and the one chosen in [137] is based on [143], the entropy for a positive additive feeding distribution f given in Equation 2.5.

$$S[\mathbf{f}] = -\sum_{j=1}^{m}\left(f_j ln\frac{f_j}{h_j} - f_j + h_j\right) \tag{2.5}$$

where $\mathbf{h}$ is a positive definite trial distribution.

The maximization of the entropy corresponds to the minimization of Equation (2.6) after considering the constraint:

$$\chi^2[\mathbf{f}] - \lambda S[\mathbf{f}] = \sum_{i=1}^{n}\left(\frac{d_i - \sum_{k=1}^{m} R_{ik}f_k}{\sigma_{d_i}}\right)^2 - \lambda\sum_{j=1}^{m}\left(f_j ln\frac{f_j}{h_j} - f_j + h_j\right) \tag{2.6}$$

This minimization was performed numerically in [137] with an algorithm based on [144]. The result obtained for the iterative calculation of the β-feeding distribution is presented in Equation (2.7):

$$f_j^{(s+1)} = f_j^{(s)} exp\left(\frac{2}{\lambda}\sum_{i=1}^{n} R_{ij}\frac{\left(d_i - \sum_{k=1}^{m} R_{ik}f_k^{(s)}\right)}{\sigma_{d_i}^2}\right) \qquad j = 0, ..., m \tag{2.7}$$

The result of this algorithm, as in the case of the EM method, leads to positive solutions. The main problem here is associated with the choice of the parameter λ, for which there is not any fixed criterion.

2.2 Response function calculation

The calculation of the response function R_{ij} of the decay is performed in two steps: the construction of the branching ratio matrix of the de-excitation in the daughter nucleus, and the recursive convolution of MC responses according to this branching ratio matrix.

2.2.1 Branching ratio matrix

The calculation of the branching ratio matrix is based partly on the known decay information of the levels at low excitation, that is taken from the literature, assuming that they are well known from high-resolution measurements. A source of information about the completeness of the decay scheme is the Reference Input Parameter Library (RIPL-3) [145]. By consulting this library and checking the quality of the available data, one can make a decision about the known part of the level scheme that is included in the branching ratio matrix. From the last known level included up to Q_β, a continuum region with 40 keV bins is defined with branching ratios based on the statistical model [146]. This complements the known decay scheme in the energy window of the β-decay. The statistical model uses average quantities such as level densities and photon strength functions [147].

- Nuclear Level Density (NLD)

  For the description of the level densities, three phenomenological models are frequently used: the Gilbert-Cameron approach, which combines the Constant Temperature model at low excitation energies and the Fermi-gas model at high energies, the back-shifted Fermi-gas model, and the generalized superfluid model (see [148] for a brief explanation of them). The parameters for all these models are conventionally obtained by fitting the available experimental data. The main disadvantage of these methods is related to the lack of experimental information, especially at high excitation energy. In addition, the capability of extrapolating these models beyond the experimentally known region is very limited.

  A microscopic Hartree-Fock-Bogoliubov (HFB) plus combinatorial (HFB+c) approach by Goriely *et al.* [149] has been found to provide a robust prescription for NLD that includes a spin and parity dependence, which in our particular case of a branching ratio matrix calculation, could provide a better reproduction of the de-excitation pattern and its multiplicity. The comparison with available experimental data makes possible the renormalization of the calculations with the correction of Equation (2.8):

$$\rho(E, J, \pi)_{renorm} = e^{\alpha\sqrt{E-\delta}} \times \rho(E - \delta, J, \pi) \tag{2.8}$$

  where $\rho(E, J, \pi)$ is the nuclear level density at energy E for spin J and parity π, and δ is the energy shift extracted from the comparison with the experimental cumulative numbers of low-lying levels (in MeV), while α is extracted from the experimental s-wave neutron spacing (in $\text{MeV}^{-1/2}$).

  The level densities calculated with this microscopic approach together with the corresponding corrections from [149] can be found at RIPL-3 [145]. These will be the input NLD information used in this work to compute the branching ratio matrix in the unknown region. An example of the accumulated number of levels calculated with the theoretical level density normalized to the data, in comparison with the experimental information from the Evaluated Nuclear Structure Data File (ENSDF) [150], is shown in Figure 2.1 for ^{100}Mo.

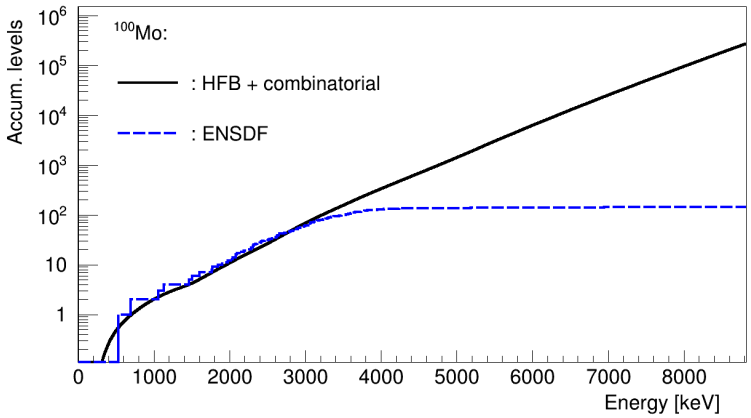

Figure 2.1: Accumulated number of levels in ^{100}Mo calculated with the HFB plus combinatorial approach compared with the experimental information from ENSDF.

- Photon Strength Functions (PSF)

  The branching ratios of the known part of the level scheme are typically taken from the information for the adopted levels of the daughter nucleus of the decay available at ENSDF [150]. The branching ratios for transitions between levels of the unknown part, and between these levels and the known levels, are calculated from the γ-strength functions [146]. A γ-strength function is a distribution of the average reduced width as a function of the γ-ray energy for transitions of a particular multipole type XL, where X can be E for electric transitions and M for magnetic transitions, whereas L is the multipolarity [151]. In our case, only the most likely transitions are considered [146], namely $E1$, $M1$ and $E2$ transitions.

  The strength function for the γ-decay of an excited state to the ground state is well described by a giant resonance Lorentzian model. The description of the γ-decay from other states is made under the Brink-Axel hypothesis [151], which says that an excited state has a giant resonance built on it as in the case of the ground state, but shifted upwards in energy by the energy of the excited state. The strength functions have, therefore, Lorentzian shape [152], and are characterized by the giant resonance parameters E_0 (MeV), Γ_0 (MeV) and σ_0 (mb). However, for $E1$ transitions this shape has been shown to be inadequate at energies close to the neutron binding energy (S_n), and a generalized Lorentzian shape is used [146, 152]. The expressions

for the γ-strength functions are given in Equation (2.9).

$$
\begin{aligned}
f_{E1}(E_\gamma) &= 8.68 \times 10^{-8}[\mathrm{mb}^{-1}\mathrm{MeV}^{-2}]\sigma_0\Gamma_0 \times \left(\frac{E_\gamma \Gamma(E_\gamma)}{(E_\gamma^2 - E_0^2)^2 + E_\gamma^2 \Gamma(E_\gamma)^2} + \frac{2.8\pi^2 T^2 \Gamma_0}{E_0^5} \right) \\
f_{M1}(E_\gamma) &= 8.68 \times 10^{-8}[\mathrm{mb}^{-1}\mathrm{MeV}^{-2}] \frac{\sigma_0 E_\gamma \Gamma_0^2}{(E_\gamma^2 - E_0^2)^2 + E_\gamma^2 \Gamma_0^2} \\
f_{E2}(E_\gamma) &= 5.22 \times 10^{-8}[\mathrm{mb}^{-1}\mathrm{MeV}^{-2}] \frac{\sigma_0 E_\gamma^{-1} \Gamma_0^2}{(E_\gamma^2 - E_0^2)^2 + E_\gamma^2 \Gamma_0^2}
\end{aligned}
\tag{2.9}
$$

where $\Gamma(E_\gamma) = \Gamma_0 \dfrac{E_\gamma^2 + 4\pi^2 T^2}{E_0^2}$, with $T^2 = \dfrac{S_n - E_\gamma}{a}$, and a is the level density parameter at the neutron binding energy in MeV^{-1}.

In Figure 2.2 the shape of these functions is shown for the $E1$, $M1$ and $E2$ transitions in the case of ^{103}Ru.

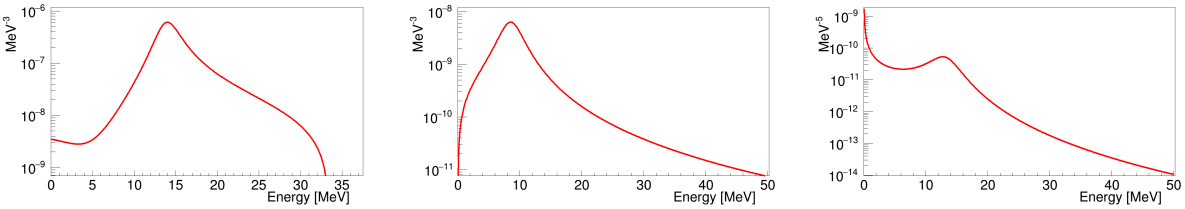

$E1$ $M1$ $E2$

Figure 2.2: Example of the shape of the γ-strength functions for $E1$, $M1$ and $E2$ transitions in ^{103}Ru.

With the strength functions presented above, the γ-ray transmission coefficients for transitions of multipole type XL are defined as in Equation (2.10) [152]:

$$
T_{XL}(E_\gamma) = 2\pi E_\gamma^{2L+1} f_{XL}(E_\gamma) \tag{2.10}
$$

Finally, the branching ratios for each level at excitation energy E_x are calculated with the average total radiation width of states with excitation energy E_x, and spin-parity J^π into levels within the interval $(E, E+\Delta E)$, where ΔE=40 keV in our case. This average total radiation width uses the NLD mentioned before, and is given by equation (2.11) [152]:

$$
\langle \Gamma_\gamma \rangle = \frac{1}{2\pi\rho(E_x, J, \pi)} \sum_{XL} \sum_{J_f^{\pi_f}} \int_{E_x - E - \Delta E}^{E_x - E} T_{XL}(E_\gamma) \rho(E_x - E_\gamma, J, \pi) dE_\gamma \tag{2.11}
$$

In Table 2.1, the parameters for the evaluation of the Photon Strength Functions based on [152] are collected for all the nuclei that will be studied in the present work. The quadrupole deformation parameter, β, plays a role when calculating the parameters for $E1$ transitions [153], and it is obtained from experimental measurements when possible [154] or

with the Finite Range Droplet Model (FRDM) calculations available at RIPL-3 [145]. The level density parameter a given by the TALYS nuclear reaction code [155] is generally used. When it was possible, we used the value obtained from Enhanced Generalized Superfluid Model (EGSM) calculations available at RIPL-3 [145].

	Level-density parameter	Deformation parameter	γ-strength function parameters								
			E1			M1			E2		
Nucleus	a(S_n) [MeV^{-1}]	β	E [MeV]	Γ [MeV]	σ [mb]	E [MeV]	Γ [MeV]	σ [mb]	E [MeV]	Γ [MeV]	σ [mb]
^{100}Ru	8.4341[a]	0.2148	14.531 17.416	4.201 5.926	78.421 111.167	8.847	4.000	2.277	13.594	4.910	2.358
^{103}Ru	9.836[a]	0.235	14.290 17.417	4.070 5.927	82.797 113.708	8.760	4.000	0.629	13.461	4.874	2.307
^{103}Tc	17.6002	0.3	13.866 17.826	3.843 6.194	87.143 108.132	8.760	4.000	0.867	13.461	4.874	2.203
^{140}Ba	15.657	0.126	14.041 15.629	3.936 4.824	114.134 186.221	7.909	4.000	0.510	12.153	4.430	3.025
^{100}Nb	18.1677	0.358	13.610 18.344	3.709 6.541	87.187 98.891	8.847	4.000	0.639	13.594	4.901	2.048
^{100}Mo	16.594	0.231	14.418 17.513	4.139 5.989	78.680 108.750	8.847	4.000	0.850	13.594	4.910	2.149
^{102}Nb	17.600	0.378	13.431 18.400	3.617 6.578	90.620 99.662	8.789	4.000	0.634	13.504	4.886	2.017
^{102}Mo	17.680	0.311	13.829 17.939	3.824 6.269	86.385 105.375	8.789	4.000	0.879	13.504	4.886	2.117
^{137}Xe	7.118[a]	-0.018	15.279 15.043	4.621 4.487	94.649 194.973	7.966	4.000	0.329	12.241	4.466	2.851
^{95}Sr	15.802	0.31	14.069 18.236	3.951 6.467	77.156 94.264	8.999	4.000	0.476	13.828	4.970	1.829

Table 2.1: Parameters for the γ-strength functions involved in the branching ratio matrix calculations for the nuclei that will be studied in this work.

[a] Value from EGSM calculations.

2.2.2 Monte Carlo convolution

Once the level scheme and the branching ratio matrix are built, MC simulations of all the mono-energetic γ-rays, β-particles and X-rays corresponding to all the transitions are performed. For this, the Geant4 package is used [156], including the geometry of the spectrometer and all other details of the set-up. The calculation of the response function with MC simulations relies on the validation of the MC code with the implemented geometry by comparing with measurements of well-known radioactive sources, as will be shown in Chapter 5.

The response of the spectrometer, R_{ij}, represents the probability of registering a count in channel i when level j of the daughter nucleus is fed. The probability of not registering any count is treated by considering a channel zero in the responses for the non-interaction probability. The integral of the response to a level from channel zero gives the maximum probability, 1. In the case of a TAGS spectrum in coincidence with a β-detector, the integral of the response to level j is normalized to the efficiency of the β-detector for the energy of the corresponding β end-point $Q_\beta - E_j$.

The response to the β-decay to each of the levels of the daughter nucleus is the convolution of the β emission and the subsequent electromagnetic de-excitation, as described in [18]. For the case of a β^- decay it is given by Equation (2.12), with b_j^- the response of the electrons emitted in the decay to level j (analogously for β^+ and EC decays replacing b_j^- by b_j^+ and x, respectively):

$$R_j^{\beta^-} = b_j^- \otimes r_j \tag{2.12}$$

where r_j is the response to the electromagnetic de-excitation of level j given by Equation (2.13):

$$r_j = \sum_{k=0}^{j-1} B_{jk} g_{jk} \otimes r_k \tag{2.13}$$

where B_{jk} represents the branching ratio for the transition from level j to level k, and g_{jk} is the response to the γ-ray corresponding to this transition. If there are conversion electrons, the response g_{jk} is replaced according to Equation (2.14):

$$g_{jk} \leftrightarrow \left(\frac{1}{1+\alpha_{jk}^{total}} g_{jk} + \frac{\alpha_{jk}^K}{1+\alpha_{jk}^{total}} e_{jk}^K \otimes x_K + \frac{\alpha_{jk}^L}{1+\alpha_{jk}^{total}} e_{jk}^L \otimes x_L + ... \right) \tag{2.14}$$

where α_{jk}^{total} is the total conversion coefficient for the transition from level j to level k, while α_{jk}^K,α_{jk}^L,... are the conversion coefficients associated to electrons from $K, L, ...$ shells. The responses to the corresponding conversion electron transition and to the X-ray are e_{jk} and x respectively.

In Figure 2.3, an example of the resulting response function R_{ij} calculated with this procedure for the decay of ^{140}Cs is shown.

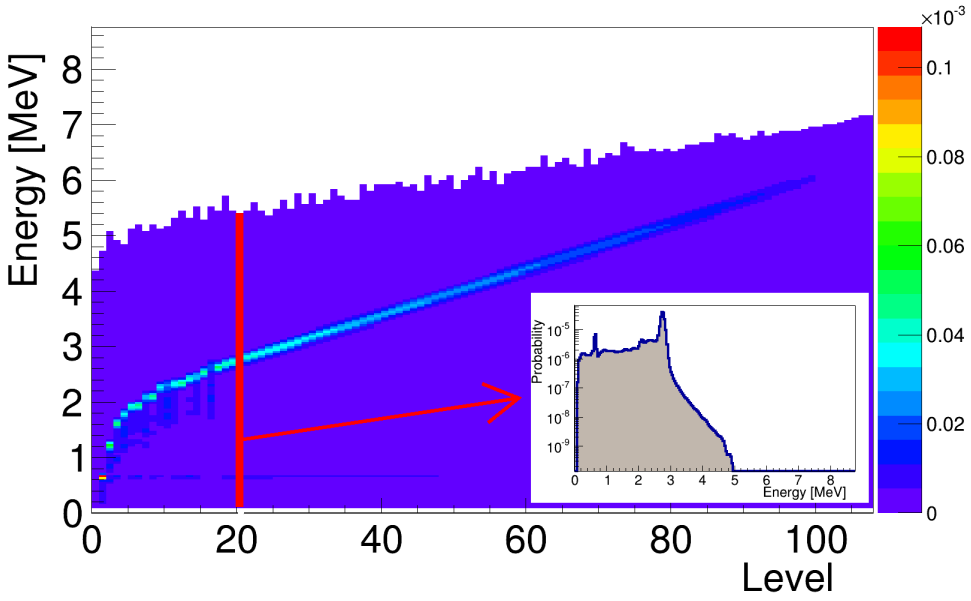

Figure 2.3: Response matrix for the decay of ^{140}Cs calculated by means of MC simulations. The inset shows the response of the spectrometer when level 20 is fed.

Part II

Characterization of the DTAS detector

Chapter 3

The DTAS detector

Conviene adiestrarse en el arte de imaginar lo que existe

It is convenient to be trained in the art of imagining what exists

Belén Gopegui

Experimental studies of nuclear structure by means of β-decay, require at the very first step the availability of the desired beams. In order to provide stable and radioactive nuclear beams, a considerable number of facilities have been designed, constructed and operated over the years. The new generation of radioactive beam facilities is aimed at the production of very exotic nuclear species to test our knowledge of nuclear structure. Among them, the FAIR fragmentation facility will inherit the leading role of GSI in Europe. A brief description of the main goals and characteristics of this facility will be presented in this chapter. Furthermore, the second requirement for such nuclear structure studies is based on a detection technique and a detection system that enables us to extract the precious nuclear structure information. For this reason, the new DTAS spectrometer designed for FAIR will be presented in this chapter.

3.1 The new FAIR-NuSTAR facility

The FAIR facility consists of a configuration of machines for accelerating and storing particle beams, and creating new particles by colliding or bombarding targets with the beams. The experimental programme proposed at FAIR is complementary to other planned next generation radioactive beam facilities such as FRIB (USA), the upgraded RIKEN facility (Japan) and the next generation European ISOL facility (EURISOL). The facility has been designed for a wide range of experiments and it is centred around two large synchrotrons, SIS100 and SIS300, with a circumference of 1100 m and built one above the other in a subterranean tunnel. The UNILAC and SIS18 accelerators from GSI will pre-accelerate the ions before they are injected into the first ring SIS100. The goal of SIS100 is to generate intense pulses of ions for the conversion to secondary beams of rare nuclei and also for the conversion of proton beams into antiprotons. Accelerated uranium ions stripped of their electrons will also be fed into SIS300 where their energy will be increased for experiments involving collisions between heavy nuclei.

The concept and layout of FAIR can be seen in Figure 3.1, where the complex system

of rings to guide, accelerate, store and refine beams for specific experiments, is shown. The operation of FAIR is designed to carry out four scientific programmes (NuSTAR, PANDA, CBM and APPA) with different particle beams at the same time. This will be achieved by coordinating the beam operation in both the synchrotrons and adjacent storage and accelerator rings.

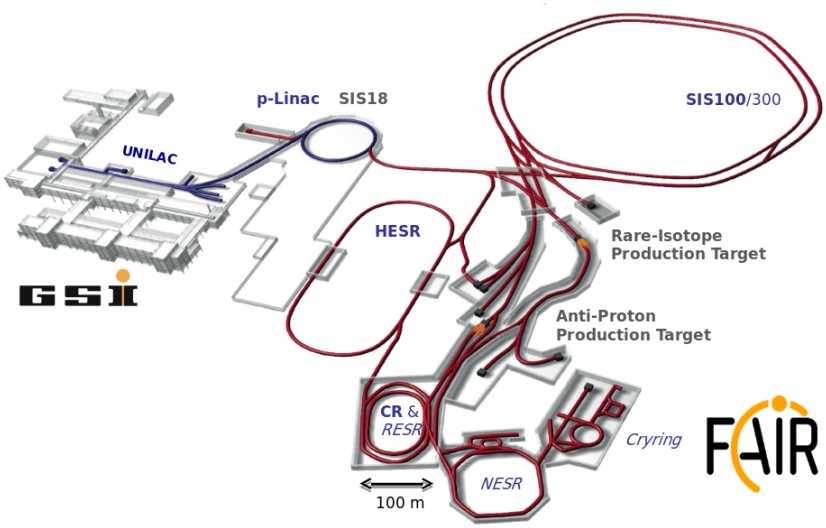

Figure 3.1: Scheme of the future FAIR facility extending the current GSI laboratory. From [157].

One of the main objectives of FAIR, personified by the NuSTAR (Nuclear Structure, Astrophysics and Reactions with Rare Isotope Beams) collaboration, is to create secondary beams of highly unstable nuclei to study nuclear structure properties and the nucleosynthesis of elements in the universe. These beams will be produced by passing the primary heavy-ion beam through a target. The ions break up into other nuclei which are separated in a magnetic separator, the Super-FRS (Fragment Recoil Separator) whose layout can be seen Figure 3.2.

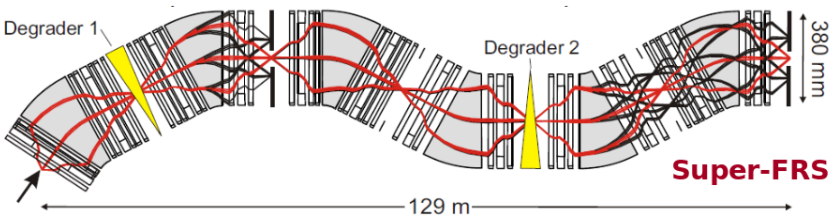

Figure 3.2: Scheme of the Super-FRS fragment separator designed for FAIR. From [157].

The Super-FRS will be an essential part of the FAIR facility since it will be a very powerful in-flight separator for exotic nuclei produced in the fragmentation process. Its design and performance are based on the experience gained with the present FRS separator

at GSI. The gain in beam intensity compared with the present FRS beams will be of the order of 10^3 for fragmentation and 10^4 for fission products. The Super-FRS will deliver beams of exotic nuclei to three different experimental areas, as shown in Figure 3.3.

- The high-energy branch where reactions of high-energy heavy nuclei relevant to astrophysical processes will be investigated.
- The low-energy branch where properties of nuclei such as decay modes and energy levels can be explored using low-energy beams.
- The ring branch where exotic nuclei are collected, cooled and stored in the FAIR ring system (CR-RESR-NESR). There, experiments will measure the masses and lifetimes of unknown nuclei or probe their structure using electron or antiproton beams.

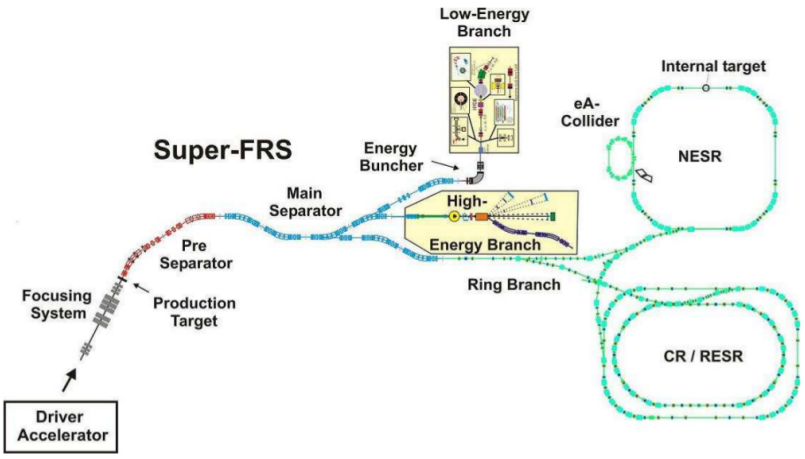

Figure 3.3: Scheme of the Super-FRS and the experimental areas of NuSTAR. From [158].

At the low energy branch of the Super-FRS several thousands of isotopes between uranium and hydrogen with lifetimes down to a few ns will be delivered with enough intensities to perform nuclear spectroscopy studies.

3.1.1 DESPEC

The DESPEC (Decay spectroscopy) collaboration is part of the NuSTAR collaboration and will address the spectroscopy of very short-lived nuclei which are not available at ISOL based radioactive beam facilities. The DESPEC experiments will be located at the low energy branch of the Super-FRS facility (see Figure 3.3). To study the decay properties, beams will be stopped in a sensitive stopper, a Double Sided Silicon Strip Detector (DSSSD), producing a large signal in a given pixel (identified by two orthogonal strips). The implanted ion can be identified in Z and A with the information obtained from the Super-FRS ancillary detectors, whereas the signal produced in the same pixel by the emitted β-particle in the subsequent decay (it will be a smaller signal) can be used to tag the β-delayed radiation detected with appropriate instruments.

Decay spectroscopy far from stability with implanted radioactive beams will give information on the nuclear structure of exotic nuclei, and will provide data relevant for astrophysics. In particular, key information such as particle decay branching ratios, half-lives, first excited states or isomeric decays can be extracted even from a relatively small number of events. Moreover, the expected intense beams provided by the SFRS will allow complete decay studies where delayed particle and γ emission branching ratios can be extracted, as well as detailed spectroscopic information, such as nuclear moments, spins, electro-magnetic transition probabilities and β-strength functions.

3.2 The DTAS detector

The study of exotic nuclear species at the focal plane of the FAIR-NuSTAR Super Fragment Separator in the DESPEC experiment [158] will give information on the nuclear structure and the astrophysics impact of exotic nuclei. In these studies, far from stability, the Q_β values are very large, and the corresponding increase in level density implies, on the one hand, the fragmentation of the β-feeding into many levels populated in the decay and, on the other hand, the fragmentation of the γ-intensity in many possible cascades. TAGS has been shown to be an accurate tool to determine β-decay intensity distributions avoiding the *Pandemonium* effect, as explained in Chapter 1.

For this reason, a new spectrometer has been designed and constructed for the DESPEC experiment [32]. The Decay Total Absorption γ-Ray Spectrometer (DTAS) is a segmented detector that consists of a maximum of eighteen rectangular NaI(Tl) crystals with dimensions 150 mm $\times$ 150 mm $\times$ 250 mm. The selection of the materials, and all the details of the design process are specified in [32]. The modules have been manufactured by Scionix [159], and the main characteristics are shown in Figure 3.4 as well as summarized here with the information from [32]:

- NaI(Tl) high quality crystals with high optical transmission and uniform response. Tolerance in crystal dimensions: 3 mm in transverse dimension, 1 mm in the longitudinal dimension. Rounded side edges with a radius of 10 mm.
- Reflector: Few layers of Teflon on all five active faces.
- Damping material: 1 mm thick, low Z elastic material (silicone putty) on all five active faces.
- Canning: 1 mm thick aluminium on all five active faces. Side face edges reinforced internally. Front face edges reinforced externally.
- Optical window: 14 mm thick, 130mm diameter borosilicate glass window.
- Fixing plate: 15 mm thick aluminium plate. Four symmetrically distributed M6 fixing holes separated by 138 mm.
- Photomultiplier tube (PMT): 5" diameter 9390B PMT from Electron Tubes (ETL). Ten stage, linear-focused SbCs dynode structure, bi-alkali photocathode. Removable.

- Voltage divider: Resistor chain (R1=2MΩ, R2-R10=470kΩ) with charging capacitors C8- C10=10nF. Wired for positive high voltage (SHV connector). Output signals: anode and last dynode (BNC connector).
- Magnetic shield of the PMT housing: 0.64 mm thick mu-metal.
- Light pulser port: Connector type SMA 905 for optical fibre coupling on the fixing plate. Illuminating the optical window.

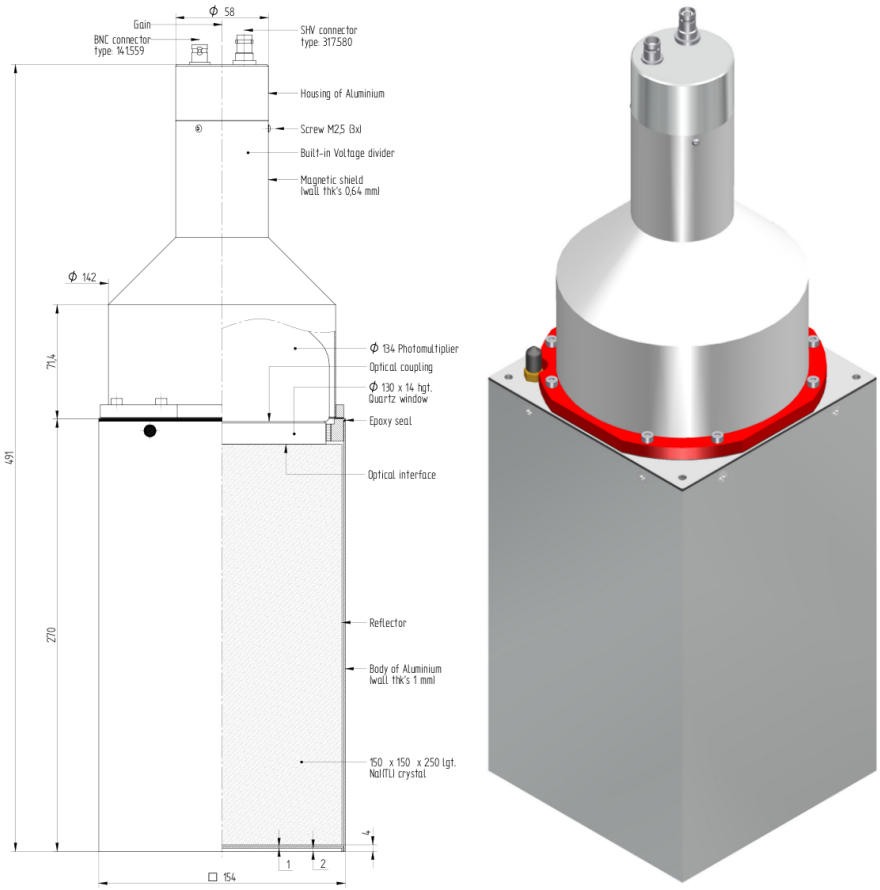

Figure 3.4: Drawings and characteristics of the modules manufactured by Scionix for DTAS.

The advantage of the segmentation in this case is twofold: the possibility to extract information from the multiplicity spectra, as will be explored in the following chapters, and the flexibility of the set-up that allows the use of the spectrometer at other facilities than FAIR. In fact, two main configurations are considered for DTAS: a sixteen-module configuration that has been designed for fragmentation facilities, and an eighteen-module configuration for ISOL type ones. Both configurations without shielding can be seen in Figure 3.5. In the eighteen-module configuration a hole is produced by removing the modules of the horizontal central plane, thus allowing access from both sides of the detector, as shown in Figure 3.5 left, in order to combine DTAS with ancillary detectors and to

allocate the beam pipe in its centre. On the other hand, the configuration foreseen for FAIR [32], with sixteen modules, will be coupled to the Advanced Implantation Detector Array (AIDA) [160].

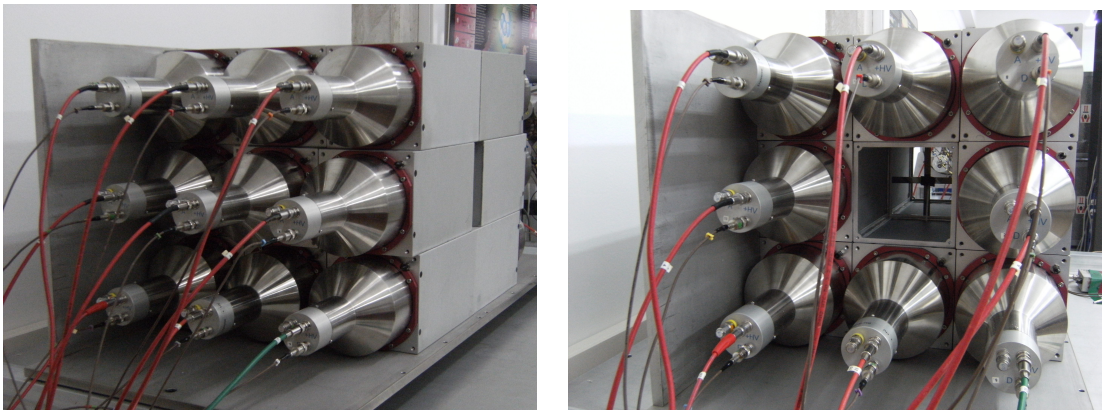

Figure 3.5: DTAS detector in the 18-crystal configuration (left) and 16-crystal configuration (right).

AIDA is a multi-plane Si DSSD array shown in Figure 3.6 left, with 8 cm×8 cm (128×128 strips) DSSSD detectors of 1 mm thickness. The possible configurations of AIDA are: rows of single DSSSD detectors or rows of 3 detectors side by side, covering 24 cm×8 cm (384×128 strips). The enclosure of AIDA in the configuration foreseen to be coupled to DTAS has transverse dimensions of 10 cm×10 cm. In order to place AIDA in the center of DTAS, the two central modules in the eighteen-module configuration are removed and the two modules above the central hole are supported by a specially designed aluminium frame with external dimensions identical to a module, as shown in Figure 3.5 right.

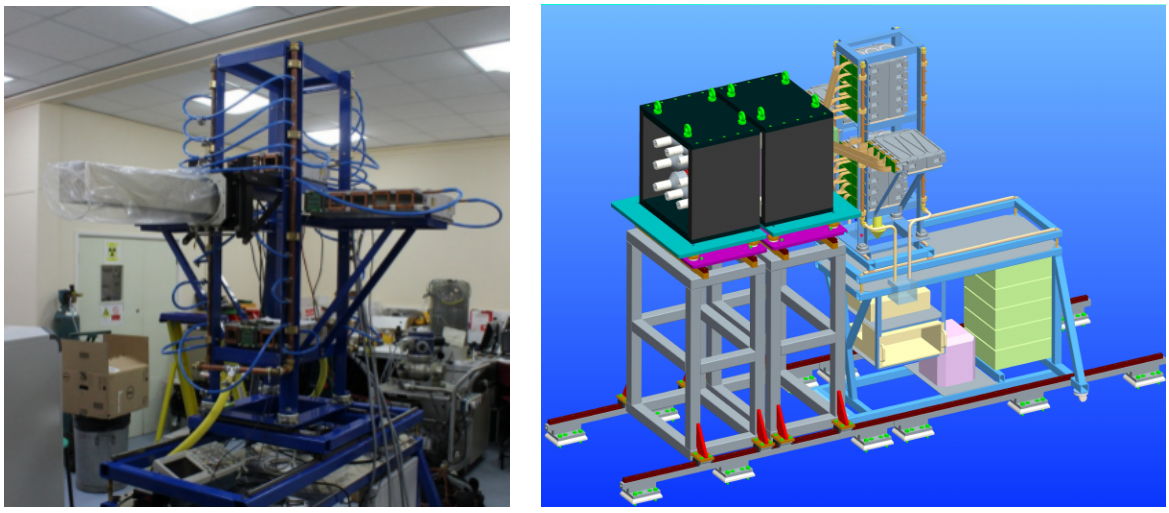

Figure 3.6: The left hand side shows the AIDA detector enclosure for 8 cm×8 cm DSSSDs with FEE cards mounted in the mechanical structure (from [161]). The right hand side shows the combination of DTAS with AIDA that is foreseen for use at FAIR.

Chapter 4

Commissioning of DTAS

No es ver, sino hacer lo que resulta esencial para la Física

It is not seeing, but doing what is essential for Physics

Günter Ludwig

Since DTAS is a new spectrometer, details about the different steps of the commissioning will be summarized in this chapter. First, the most important information from the study of the behaviour of the individual modules will be presented. Then, a review of the main steps concerning the reconstruction of the total sum of the spectrometer will be done, based on the tests performed at IFIC with both the eighteen-module and the sixteen-module configurations. Finally, details about the commissioning in a radioactive beam facility will be presented, with dedicated explanations of the treatment of the main contaminants.

4.1 Individual module study

The 18 individual modules of DTAS and the prototype module were studied separately with calibration sources. In order to minimize the amount of dead material, the sources were stuck on a magnetic tape placed at 12.2 cm in front of the detector, as shown in Figure 4.1. A very simple electronic chain was used for the readout of the signal of the modules. As mentioned in Chapter 3, each PMT has two outputs, one for the anode and the other for the last dynode. If only one of them is used, it has been found that the other must be terminated with a 50 Ω terminator in order not to disturb the signals. In this case, we used the dynode signal. It was preamplified by a CANBERRA 2005 preamplifier [162] and shaped with an ORTEC 671 spectroscopic amplifier [163]. The final signals were acquired with a Palmtop Multichannel Analyzer (MCA) [164]. The gain settings were fixed for all the measurements and the high voltage of each PMT was adjusted to measure all the modules approximately in the same energy range. In order to correct the possible change in gain of the PMT that will be studied in Section 4.2.2, we measured each source in runs of 2 hours divided in intervals of 5 minutes.

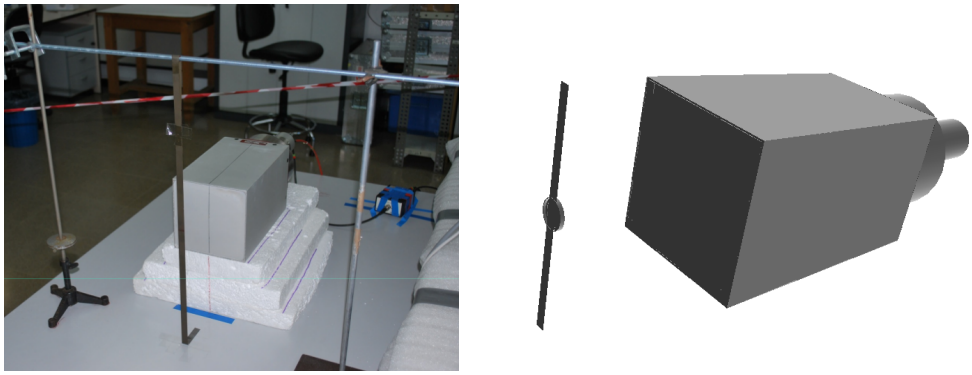

Figure 4.1: Set-up for the study of the individual modules. Each module was placed in front of the calibration source that was stuck on a magnetic tape. A picture of the set-up at IFIC (left) together with the geometry included in the MC (right) are shown.

The resulting background subtracted spectra for the ^{137}Cs and ^{22}Na calibration sources corresponding to the 18 detectors + the prototype are shown in Figure 4.2 together with the environmental background spectra used for the subtraction.

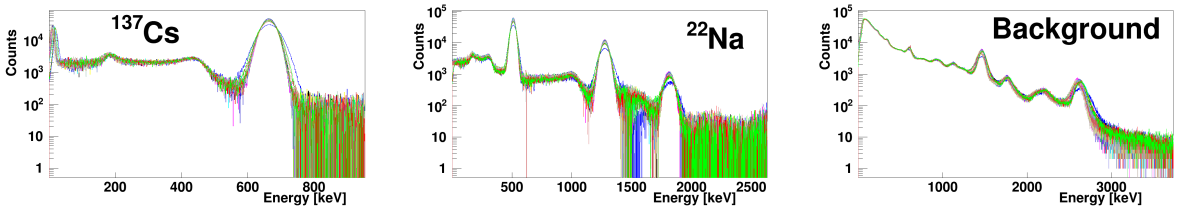

Figure 4.2: Individual crystal measurements for a ^{137}Cs calibration source (left), a ^{22}Na source (middle), and environmental background (right).

The main goal of these measurements was to obtain useful information about the behaviour of each module that could be helpful for the total DTAS configuration. For example, an evaluation of the energy resolution could indicate the best placement of each module in the total arrangement. The individual resolutions at the ^{137}Cs 661.7 keV peak, as well as the total efficiencies calculated with the ^{137}Cs and ^{22}Na calibration sources, are displayed in Table 4.1 and plotted in Figure 4.3.

Finally, the last piece of information related to the study of the individual modules concerns the MC simulations. In order to identify possible problems in the description of the geometry of the modules, it is worth comparing the individual measurements with the corresponding MC simulations. This could be useful before studying the response function of the whole DTAS detector, that is a key step in order to perform a TAGS analysis, as explained in Chapter 2. For this, the Geant4 simulation package [156] was used, including the geometry of the modules and details of the non-proportionality light-yield in NaI(Tl) that will be explained carefully in Chapter 5. After subtracting background in the experimental spectra and widening the MC with the experimental resolution, the quality of the reproduction can be seen in Figure 4.4. Although a better calibration at

Module #	Resolution [%]	Efficiency (^{137}Cs) [%]	Efficiency (^{22}Na) [%]
1 (281)	7.37	5.25	17.34
2 (282)	7.85	5.38	17.97
3 (283)	7.81	5.28	17.54
4 (284)	7.55	5.21	17.22
5 (285)	7.65	5.30	17.47
6 (286)	8.20	5.29	17.68
7 (287)	7.60	5.16	17.10
8 (288)	9.01	5.43	18.07
9 (289)	7.90	5.24	17.48
10 (290)	7.59	5.22	17.38
11 (353)	7.57	5.11	17.03
12 (354)	8.72	5.27	17.13
13 (355)	7.60	5.32	17.76
14 (356)	7.56	5.24	17.55
15 (568)	7.15	5.25	17.74
16 (569)	7.84	5.36	17.80
17 (570)	7.17	5.40	17.88
18 (571)	7.33	5.39	17.83
19 (850)	10.42	5.19	17.10

Table 4.1: Table with characteristics of the individual modules: resolution at 661.7 keV, and total efficiencies for the ^{137}Cs and ^{22}Na calibration sources. The numbers in brackets for the modules correspond to the reference numbers in their data-sheets.

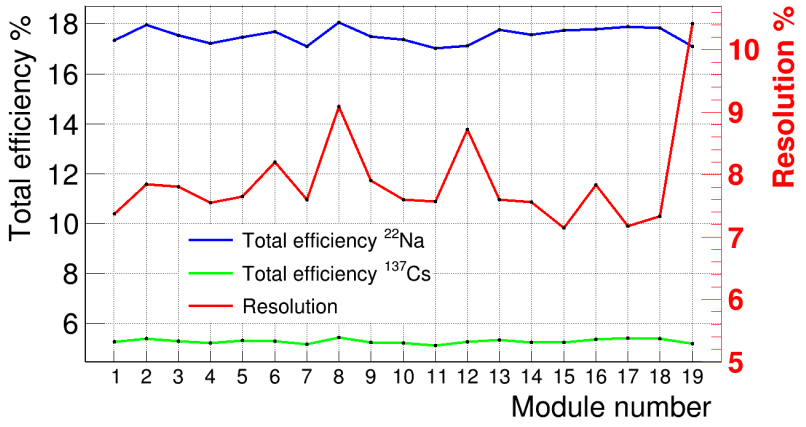

Figure 4.3: Characteristics of the individual modules: resolution at 661.7 keV is plotted in the right y-axis, whereas total efficiencies for the ^{137}Cs and ^{22}Na are plotted in the left y-axis. The x-axis shows the module numbers from 1 to 18, and the prototype (module 19).

low energies would improve the reproduction, and the backscattering peaks due to the surrounding materials are not reproduced in the MC, for our purposes at this stage both MC and experimental spectra are considered to be in good agreement.

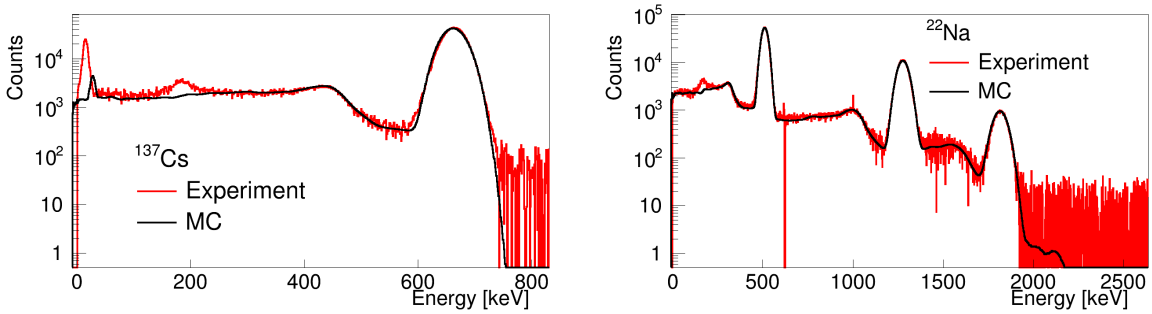

Figure 4.4: Individual module spectra of ^{137}Cs and ^{22}Na compared with MC simulations.

4.2 Commissioning at IFIC

The first assembly of the full detector was performed in 2013. First, the sixteen-module configuration and afterwards the eighteen-module one were mounted with shielding around them, as can be seen in Figures 4.5 and 4.6.

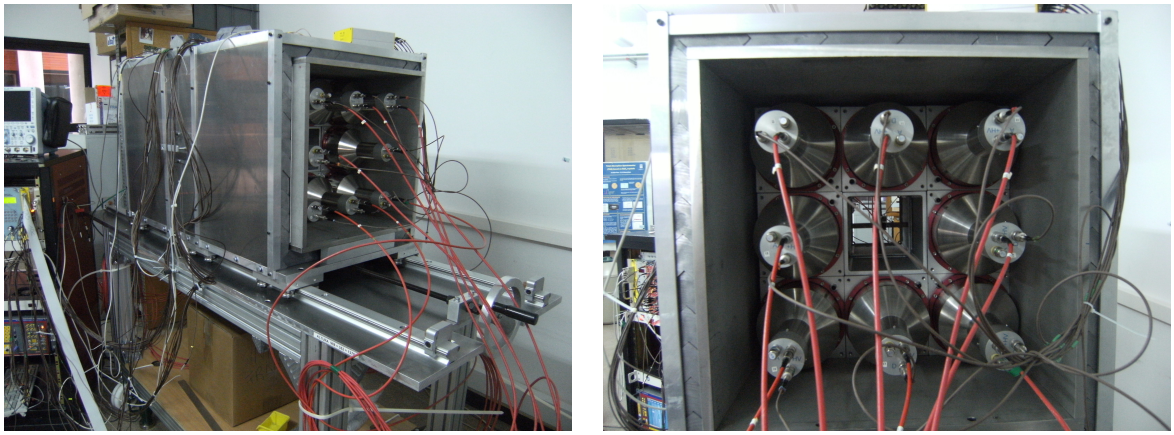

Figure 4.5: DTAS16 configuration mounted with the shielding around it.

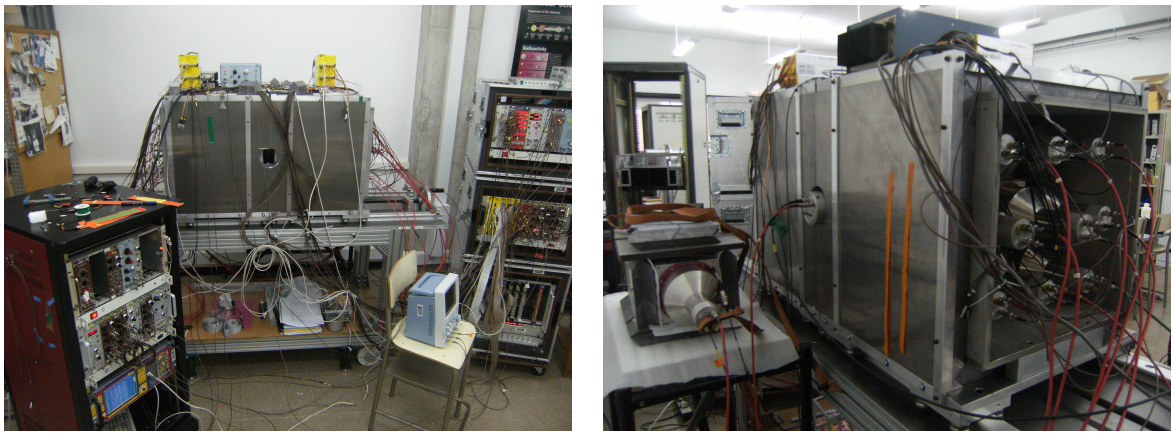

Figure 4.6: DTAS18 configuration mounted with the shielding around it.

The shielding is made of two 600 mm × 600 mm × 500 mm hollow structures each composed of 210 lead bricks of 50 mm thickness. These structures cover the inner part of the shielding, that is in direct contact with the NaI(Tl) modules, and which consists of 15 mm stainless steel sheets. The lead is, in turn, covered by two 5 mm thickness aluminium structures. The whole assembly of shielding and modules laid on an aluminium table with two rails with eight steel sliding rail carriers that enable the separation of DTAS into two independent structures, each of them containing half of the detectors, so that possible manipulations at the centre of the detector could be done easily. The shielding reduces the counting rate of DTAS by one-order-of-magnitude, as can be seen in Figure 4.7.

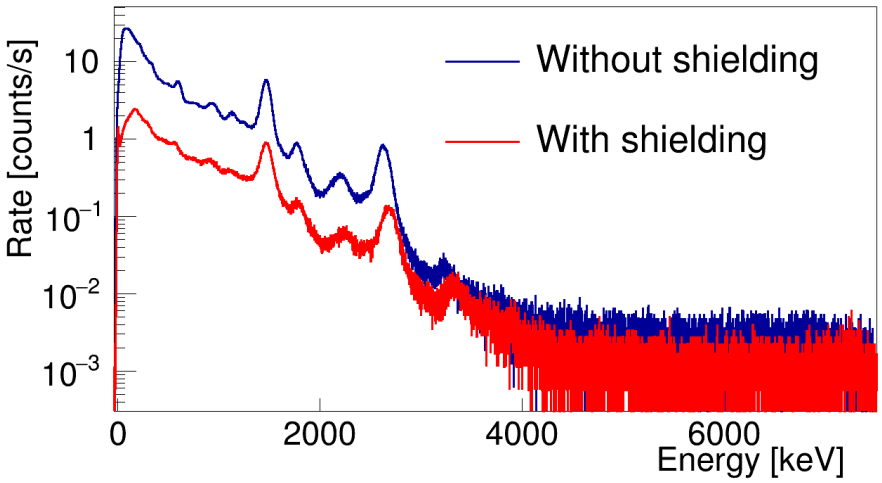

Figure 4.7: Influence of the shielding on the environmental background counting rate of DTAS for the sixteen-module configuration.

In order to analyse data from DTAS we have to reconstruct accurately, for each event, the energy deposited in the full spectrometer and its multiplicity, M_m (defined as the number of modules that fire above the threshold). The full energy released in the spectrometer has to be reconstructed by summing the energy deposited in the individual modules, either

electronically or via software. The electronic chain to process the signals from the modules was designed with this idea in mind. The details of all the electronics are presented in the Appendix A. For DTAS we use Mesytec MSI-8p preamplifiers [165] for both the anodes and the dynodes of the modules. After the preamplifier, dynodes are split into two branches; one branch is sent to a CAEN N625 Quad Linear FAN-in FAN-out [166], and the other to Mesytec MSCF-16 [165] shapers. The anodes are used with a new self-triggering digital acquisition system in test. The dynode signals sent to the FAN-in FAN-out are summed in this module, and one of the outcoming signals is processed in an ORTEC 671 amplifier [163] to produce the sum energy signal sent to the analog to digital converter (ADC), a CAEN V785 [166]. Another output from the FAN-in FAN-out is used to construct a timing signal sent to a time to digital converter (TDC), with an ORTEC 474 Timing Filter Amplifier, and an ORTEC 584 Constant Fraction Discriminator [163]. The output individual energy and timing signals from the MSCF-16 shapers are sent to individual channels of the ADC and TDC respectively.

4.2.1 Hardware sum

The hardware sum corresponds to the signal from the FAN-in FAN-out. In order to obtain this sum properly we need to match the gains of the PMTs of the modules by adjusting the HV, so that all individual signals are aligned. It has to be noted that aligned hereafter means having the same amplitude for the same energy.

It is worth mentioning that for the hardware sum, apart from the FAN-in FAN-out, we tested a CAEN N407 ADDER [166] and a home-made adder which consisted of 20 lemo connectors welded together and two lemo outputs. It was observed, as reported in the manuals [167, 168], that the linearity of the ADDER goes up to 400 mV (∼7 MeV in our case) while in the FAN in FAN out it goes up to 1.6 V (∼27 MeV). On the other hand, although the home-made adder showed linearity in the whole range studied, it was dismissed because it introduced reboots when the dynode signals were split in two. As a consequence, the FAN-in FAN-out was chosen for the hardware sum. An example of the hardware sum for both the sixteen- and the eighteen-module configurations is presented in Figure 4.8 for three calibration sources of ^{137}Cs, ^{22}Na and ^{60}Co.

The adjustment of the HV to align all the modules was done bearing in mind the desired energy range. In particular, we aimed to achieve an energy range of 15-20 MeV. This value

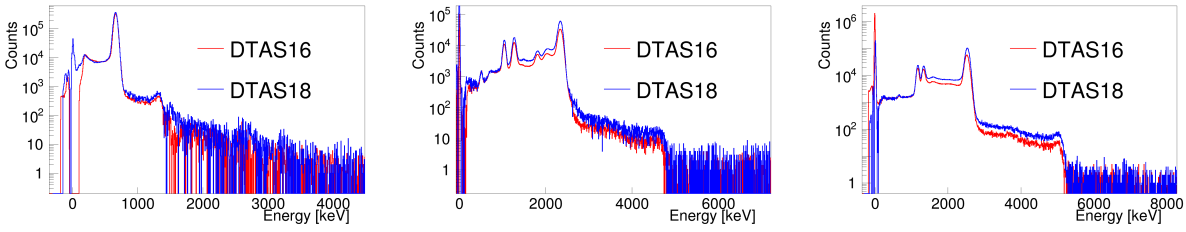

Figure 4.8: Hardware sum of calibration sources for DTAS16 and DTAS18 configurations. From left to right: ^{137}Cs, ^{22}Na and ^{60}Co. Spectra have been normalized to the low energy region.

was chosen because the first experiments with DTAS, explained in Chapter 6, included some β-decays with Q_β values of more that 8 MeV. In order to distinguish clearly the first-order pileup, a distortion that will be treated in next sections, a range of at least twice the Q_β is recommended both for the hardware sum and for the spectra of the individual modules. Such a wide range required lowering substantially the gain of the PMT (once the gains of the electronic amplification chains had been lowered). Several saturation effects distorting the spectra were observed. On the one hand, there was an intrinsic saturation in the electronic chain due to the maximum signal provided by the preamplifier that, in the case of the MSI-8p is 1.5 V (∼25 MeV). On the other hand, the PMTs also showed a saturation phenomenon which depends on the HV applied, as shown in Figure 4.9 left for the affected modules. The energy where the saturation appears increases when the HV applied is reduced, as shown in Figure 4.9 right, hence the HV values of the modules were lowered in order to place this saturation beyond the saturation of the preamplifier.

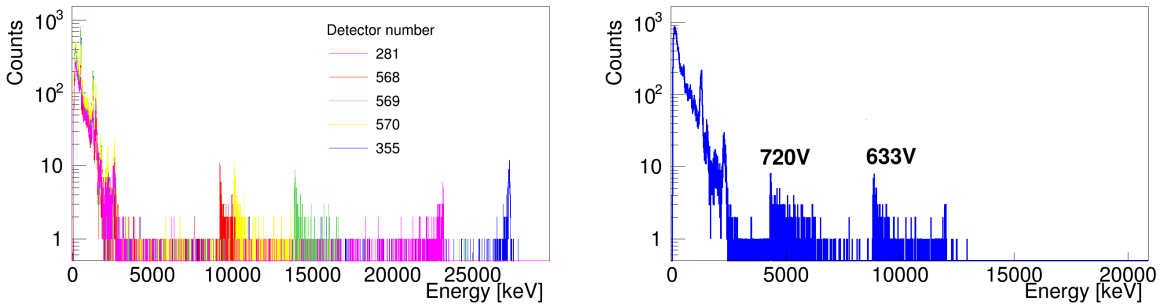

Figure 4.9: Saturation problems associated with the PMT of the modules of DTAS. The figure on the left shows all the modules affected by the saturation of the PMT, while in the figure on the right the effect of decreasing the HV can be seen.

The software sum is reconstructed offline from the individual signals processed with the shapers. In the following subsections a method to correct dynamical changes in the gain of the modules will be shown, as well as the way to perform properly the alignment and the software sum of these signals.

4.2.2 Gain correction system

A system to correct changes in the gain of the modules has been developed. These changes may be due to temperature oscillations [169], drift of the PMTs and fluctuations in the HV supply. The system is based on correcting the gain of each module by checking the position of a light pulser peak. An additional external reference detector is used to monitor the stability of the light pulser generator. The following elements are employed in this system:

- An external reference well type NaI(Tl) detector of 3" diameter × 3" length manufactured by Saint Gobain [170]. The well has 15 mm diameter and 40 mm depth. The detector mounted on a 3" diameter ETI 9305 PMT is shown in Figure 4.10.
- A 490 nm light pulse generator model 6010 from BNC [171].

- A borosilicate glass bundle of 20 optical fibres, each of 2 mm diameter and 2 m length, manufactured by FiberTech [172]. The fibres are terminated with SMA type connectors.
- A weak ^{137}Cs source of $\sim$ 300 Bq.

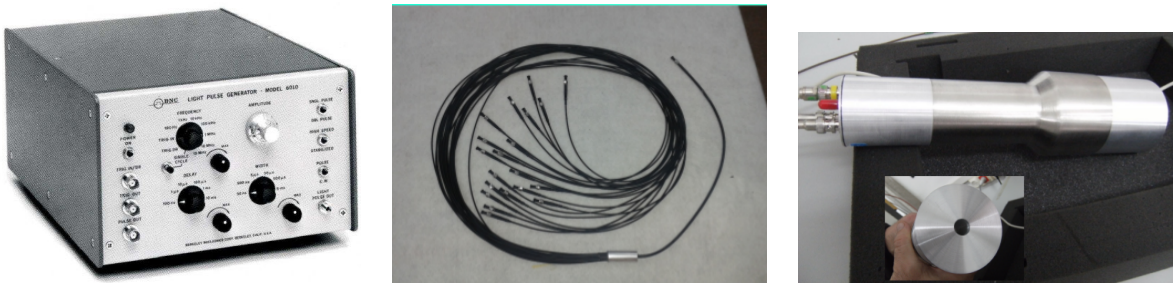

Figure 4.10: Gain correction system elements: light Pulser (left), optical fibres (middle) and NaI(Tl) reference well type detector (right). The inset in the figure with the reference detector shows a view of the front face with the hole where the weak ^{137}Cs source is placed.

The fibre bundle is used to distribute the light pulse from the light generator to the reference detector and to each of the eighteen modules. The ^{137}Cs source is placed inside the well of the reference detector. The reference detector is surrounded by lead shielding and is placed close to DTAS. Since both the reference detector and DTAS have shielding, this weak source does not affect the DTAS measurements. The aim of the source is to correct for gain changes in the reference detector by checking the position of the 661.7 keV peak. The position of the light peak in the reference detector is used to correct for variations of the light intensity of the light pulse generator, whereas the positions of the light peaks in each of the eighteen modules allow a gain correction in the individual modules of DTAS. The correction is calculated for short periods of time, and the procedure will be mathematically detailed in the next subsection. Examples of the spectra from the reference detector and an individual module of DTAS showing the light pulser peaks can be seen in Figure 4.11.

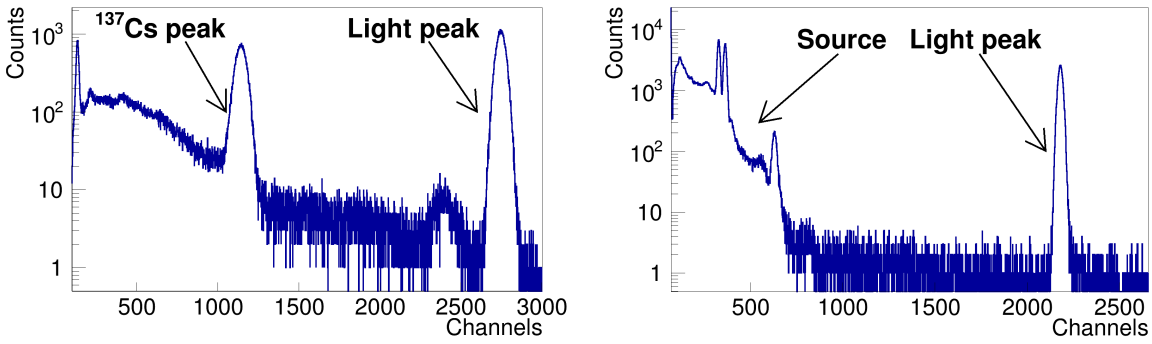

Figure 4.11: Individual DTAS detector spectrum with the light pulser peak in a ^{60}Co measurement (right). Reference detector spectrum with the 661.7 keV peak from the weak ^{137}Cs source, and the light pulser peak (left).

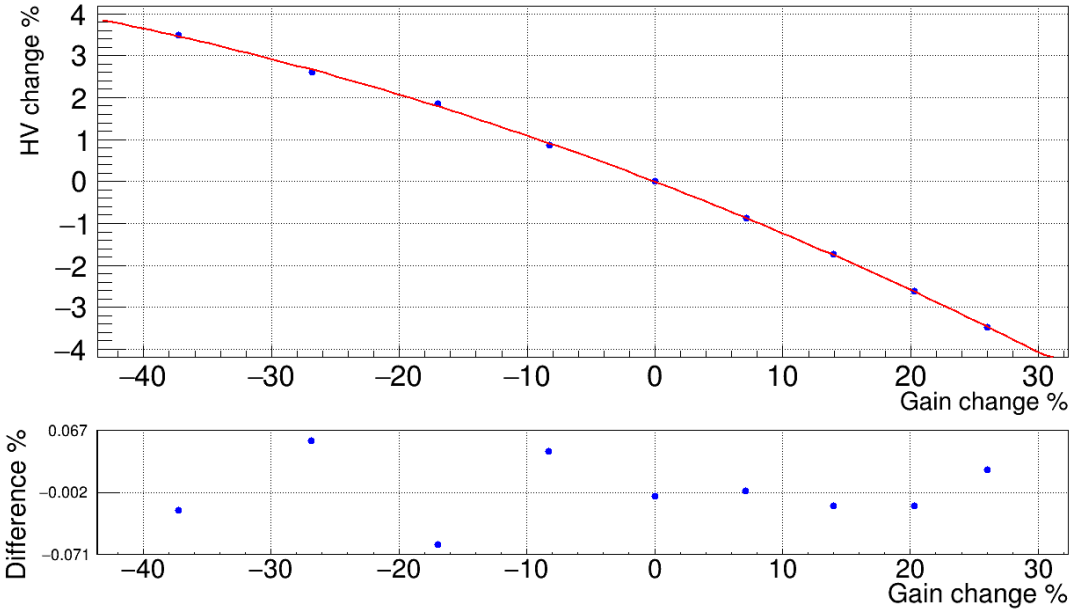

Figure 4.12: High voltage change as a function of the gain change for one module.

In order not to disturb the measured individual spectra, the light peaks due to the light pulser have to be located outside the energy region of interest. When choosing an optical fibre for each module, we took into account that each of the 20 fibres in the bundle does not transport the same amount of light, nor do each of the modules convert the same amount of incident light into the same signal amplitude in the PMT. For both reasons, in order to place all the light peaks in the same region, we assigned the fibres that transport more light to the worst modules in terms of light conversion. A rough ranking of fibres and modules was obtained by plugging the same fibre to all the modules and by plugging all the fibres to the same module.

Apart from applying the gain correction offline, the gain correction system could also be used for maintaining aligned the signals of the modules by applying HV corrections to the PMTs. This possibility requires information about the dependence of the gain on the HV for each module. The two peaks from a ^{22}Na source (at 511 keV and 1274.5 keV) were employed to calculate the gain for different values of the HV around the operational value. Data were fitted with a quadratic function: $\Delta_{HV}(\%) = a + b\Delta_{GAIN}(\%) + c\Delta^2_{GAIN}(\%)$ as can be seen in Figure 4.12.

Although we have tested this online correction, it was not used in the actual measurements, since we were only interested in the software sum in order to get information about the multiplicities.

4.2.3 Alignment and software sum

Just as for the hardware sum, before performing the software sum the amplitudes of the signals stored for each event must be properly aligned, as we mentioned above. Although amplitudes were aligned before the FAN-in FAN-out for the hardware sum, and even though

the gains of the shapers are set to a common value, the final amplitudes stored are not aligned, due to slight variations in gain and offset of the individual electronic channels. Therefore, a careful offline alignment procedure is required.

The first idea for this alignment was to convert signal amplitude (proportional to light collected) into energy for each of the individual channels. This conversion between light collected and energy is what we will call energy calibration. A solution like this has been successfully adopted for a 12-fold segmented BaF_2 spectrometer in previous works [73, 74, 108]. Nevertheless, we soon realized that it can not be applied in the case of a segmented detector made of NaI(Tl) because of the non-proportionality of the light yield in this material [173, 174]. The reason is that, as pointed out in [18], the positions of full energy peaks due to γ-ray cascades are shifted with respect to single γ-ray peaks of the same energy. For a γ-cascade of two γ-rays (γ-multiplicity, M_γ=2) the shift is approximately 30 keV (in energy units), while for M_γ=3 it is 60 keV and so on. However, in the case of a segmented detector the situation is even more complicated, and the shift depends not only on the γ-multiplicity, M_γ, but also on the number of modules where the energy is deposited, M_m. These shifts approximately follow the numbers in Table 4.2 based on [18], where the first row corresponds to the behaviour of a single NaI(Tl) crystal spectrometer like LUCRECIA at ISOLDE [175] or the LBNL spectrometer used at GSI [23].

M_γ	1	2	3	4
M_m				
1	0	+30	+60	+90
2	−30	0	+30	+60
3	−60	−30	0	+30
4	−90	−60	−30	0

Table 4.2: Shift in keV of the sum peaks due to the non-proportionality light yield in a segmented NaI(Tl) spectrometer with the individual modules calibrated in energy before the software sum.

For a single crystal spectrometer the non-proportionality is not a problem as far as this effect is included in the MC simulations in the way detailed in [18]. Likewise, it does not represent any problem for the hardware sum of a segmented NaI(Tl) spectrometer, since signals are aligned in amplitude and any energy calibration is always applied after the sum of the individual signals. However, the consequence of aligning the individual modules with an energy calibration before summing the total energy, is that the resolution of the sum peaks is worsened due to the displacement of the different multiplicities contributing to the sum. The non-proportionality of the light yield in NaI(Tl) is known to have an important contribution to the resolution of single crystal detectors [176, 177], but this is an additional effect for multi-crystal detectors. In Figure 4.13 these shifts are shown for a measurement of ^{22}Na (M_γ=3) and for the corresponding MC simulation of this source that includes the non-proportionality as in [18]. In both cases an energy calibration has been applied to all the individual modules before summing. The vertical black line corresponds to 2296.5 keV, the sum of the energies of the three γ-rays involved: 511 keV, 511 keV and 1274.5 keV. The sum peaks of the different multiplicities are not aligned, showing

a displacement in agreement with Table 4.2. Only M_m=3 is aligned with the nominal sum, since it corresponds to a 0 keV shift in Table 4.2, with three γ-rays detected in three crystals. Note that the experimental spectra are not background subtracted, whereas the MC is only widened by the light function from [18], without taking into account the experimental resolution.

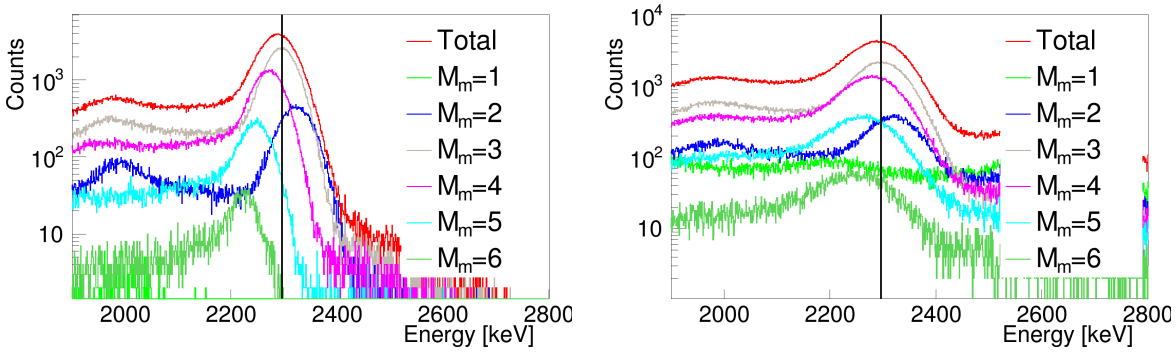

Figure 4.13: ^{22}Na software sum of the light produced in the individual detectors performed with the signals aligned in energy. Both the MC (left) and the experimental measurement (right) show the shifts from Table 4.2. The vertical black line corresponds to the sum of the energies of the three γ-rays involved.

In summary, in order not to worsen the resolution, we have to align the amplitudes of the individual modules, thus reproducing with our software sum the same behaviour of the hardware sum, and, equivalently, of a single crystal detector. More precisely, we have to avoid any calibration of the light collected that involves two or more parameters, since it introduces an artificial offset due to the non-proportionality. We have, however, to remove the offset introduced by the electronic chain and the ADC. In this way the amplitude of a signal is simply represented by the ADC channel minus the ADC offset. The ADC offset is represented by a_j, with $j = 0...18$, with $j = 0$ being the reference detector and $j = 1...18$ the DTAS modules. To determine the ADC offset for each channel we use the position of the peak due to the electronic noise.

To align the amplitudes we need to determine the gain for each module. The gain is obtained from the position of the two peaks from a calibration run with a ^{22}Na source (511 keV and 1274.5 keV). The alignment is performed choosing one arbitrary module as a reference, and considering a limited number of consecutive events. The number of events should be sufficiently large to determine the peak positions accurately and sufficiently small to limit the effect of PMT variations during this time. We have verified that 1 million events (that corresponds to approximately 4 minutes for a normal counting rate of 4-5 kHz in DTAS), fulfil this condition.

After the alignment, the parameters involved in the gain correction system are determined. The reference position of the light pulser peak for each module, L_j, is calculated, with $j = 1...18$. Analogously, the ^{137}Cs peak and the light pulser initial peak positions for the reference well type detector, P_0 and L_0 respectively, are also determined to complete the set of parameters involved in the procedure of gain correction and software sum

construction.

We define $L_j^{'}$ as the new light peak position of module j, b_j as the gain change factor of module j, and C as the factor of the change in the light production. In order to avoid the influence of possible changes in gain and to guarantee a reasonably good fit (with a Gaussian function plus a step function plus a linear background) 1 million events are used, as mentioned above. Hence, for each 1 million events of any measurement performed in the same conditions as the reference run used for the initial alignment, the mathematical procedure described below is followed in order to calculate the gain corrections and sum all the amplitudes stored in each event:

- The new position of the ^{137}Cs peak for the reference detector, $P_0^{'}$, is determined, as well as $L_0^{'}$.
- The change in the gain of the PMT of the reference detector is calculated:

$$b_0 = \frac{P_0 - a_0}{P_0^{'} - a_0} \tag{4.1}$$

- The possible change in the light produced by the light pulse generator, C, is calculated:

$$C = \frac{L_0 - a_0}{b_0(L'_0 - a_0)} \tag{4.2}$$

- $L_j^{'}$ is determined for each of the DTAS modules, and with this value the gain change is calculated taking into account the change of intensity of the light source from Equation 4.2:

$$b_j = \frac{L_j - a_j}{C(L_j^{'} - a_j)} \tag{4.3}$$

- With the b_j factors we can recalibrate the amplitudes of all 1 million events in the set and calculate the software sum for each event.

As a result of applying this procedure, the software sum is obtained, as can be seen in Figure 4.14 for a ^{60}Co source. At this point an energy calibration can be applied (a conversion between light collected and energy) by using single peaks (M_γ=1), as in the case of the hardware sum.

The software sum reconstructed in this way exhibits the same behaviour as the hardware sum in terms of the non-proportionality light yield, as shown in Figure 4.15 for two calibration sources. In both cases the detector behaves as a single crystal detector in terms

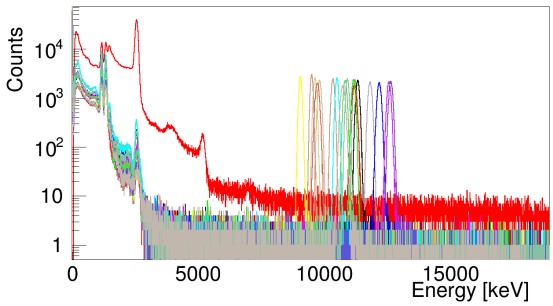

Figure 4.14: Software sum of a ^{60}Co source with the signals of all the modules aligned. The eighteen light peaks can be seen together.

of the position of the sum peak. The main differences are related to a slightly better resolution in the software sum with respect to the hardware sum due to the gain corrections, and a completely different shape in the pileup region that will be commented on in the next section.

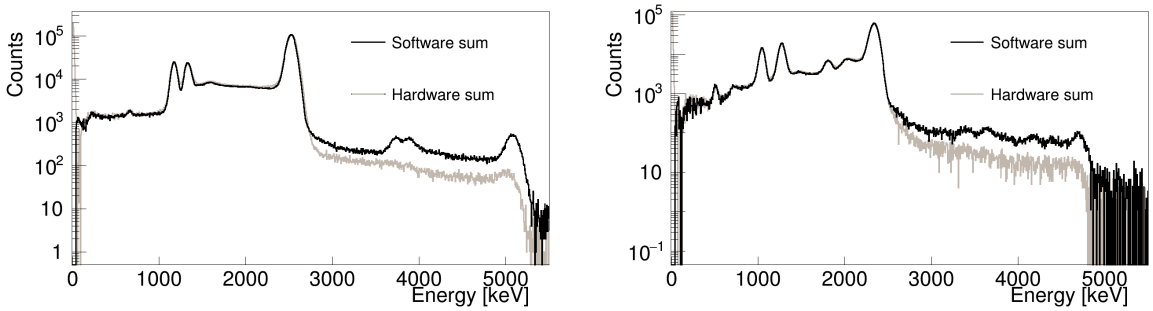

Figure 4.15: Comparison of the hardware sum and the software sum in DTAS for a ^{60}Co source (left) and a ^{22}Na (right) source.

Moreover, in order to ensure that the treatment of the non-proportionality is correct, we can check the spectra of the multiplicities after this process. In Figure 4.16, we show the quality of the alignment of the different multiplicity spectra achieved with this method for a ^{22}Na source (M_γ=3) and a ^{60}Co source (M_γ=2), in contrast to the results shown in Figure 4.13. The vertical black lines correspond to the sum peak positions calculated with the shift associated with single crystals according to [18] (first row of Table 4.2): 2296.5 keV+60 keV for the ^{22}Na source, and 2505.7 keV+30 keV for the case of the ^{60}Co.

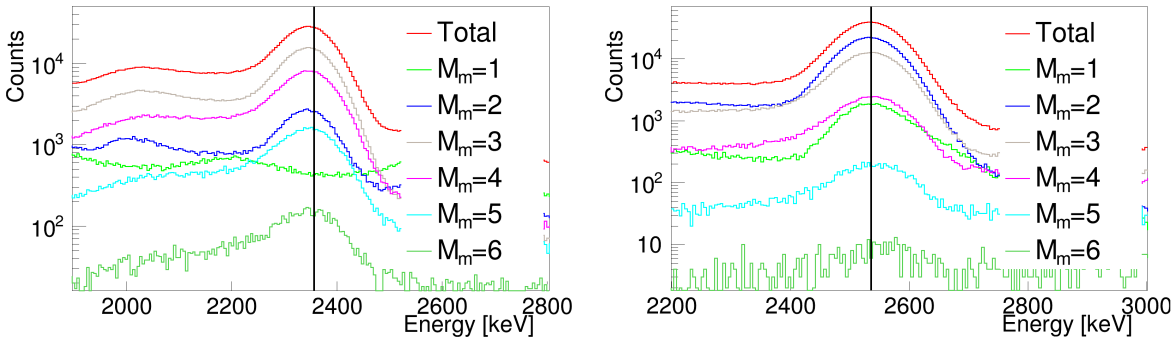

Figure 4.16: Multiplicity study of a ^{22}Na source (left) and a ^{60}Co source (right). Vertical black lines show the corresponding energy of the sum peak with the shift associated with single crystals.

4.3 Commissioning at IGISOL

The two main goals of this thesis are the characterization of the DTAS detector, and the measurement and analysis of several β-decays of interest. At this point both objectives converge, given that the commissioning with radioactive beams was done at the upgraded IGISOL IV in Jyväskylä in a campaign of measurements. In this section, we will describe only the technical details concerning the characterization of the DTAS and the ancillary detectors involved in the set-up and, therefore, important for the MC response function. We will focus on the Physics and motivations of the experiments in Chapter 6, where the IGISOL facility and JYFLTRAP will be explained in detail. The information concerning the electronic chain used at IGISOL for the DTAS spectrometer and the ancillary detectors is summarized in Appendix A.

The decay of some nuclei of interest measured in the experiments will be used for the calibrations, together with a set of laboratory sources. A total of five sources were measured at IGISOL for the characterization of the DTAS detector: a ^{22}Na β^+/EC source, a ^{137}Cs β^- source, a ^{60}Co β^- source, a combined ^{152}Eu-^{133}Ba source (the ^{152}Eu has two branches: one β^- and other EC/β^+, and the ^{133}Ba is EC/β^+), and a ^{24}Na β^- source produced at IGISOL by means of a (p, 2p) reaction on natural Mg. All these calibration sources will be used to characterize the performance of the DTAS spectrometer. For this, the calculation of all the contaminants will be carried out, especially the environmental background and the summing-pileup.

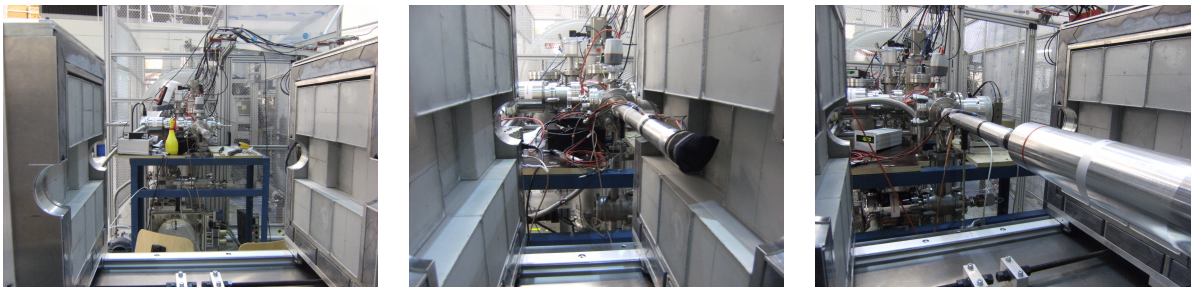

(a) (b) (c)

Figure 4.17: Set-up of the DTAS at IGISOL with DTAS open in two halves. From left to right: (a) DTAS detector in position, (b) DTAS detector, beam pipe and plastic detector screwed on at the end of it, (c) full set-up with the HPGe detector behind the plastic β-detector.

The DTAS detector was used in the eighteen-module configuration and the position of each module was decided taking into account the individual resolutions (Table 4.1 and Figure 4.3). By carrying out MC simulations we could find out the expected counting rates for each detector and we concluded that the positions associated with the lowest counting rates are the eight corners of the assembly, hence they were occupied by the modules with the worst energy resolutions. A hole of 10 cm was left between the central modules to place a HPGe detector from one side and the beam pipe with a β-detector from the other. The two central modules were separated by 16 cm instead of 10 cm in order to decrease their counting rates, so that they were comparable to the others. The complete set-up is shown in Figure 4.17.

A β-detector was used with the idea of tagging the β-decay events. The β-γ coincidences are used to clean the spectrum, as will be explained later. At IGISOL two different new β-detectors were used with DTAS. Both of them were scintillator plastic detectors, and they are shown in Figure 4.18.

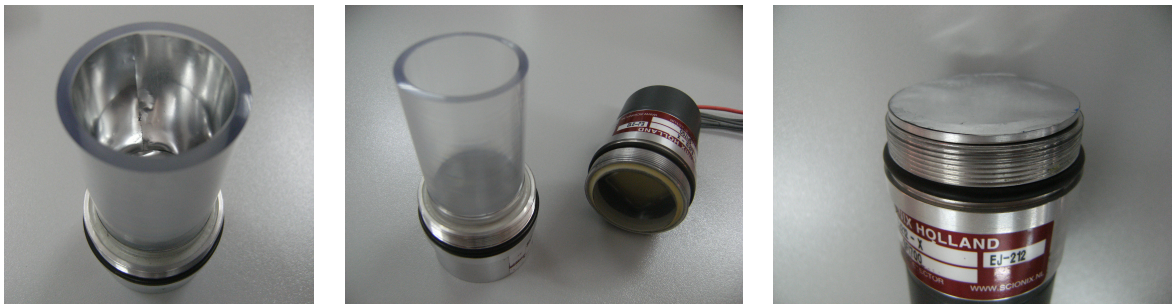

Figure 4.18: View of the plastic β-detectors used in conjunction with DTAS. The vase-shaped detector (left), the disk detector (right) and both detectors together (middle) are presented.

The main characteristics of the two β-detectors are detailed here:

- The vase-shaped detector is a cylinder of 35 mm external diameter, 50 mm length

and a wall thickness of 3 mm, made of EJ200 plastic scintillator, and manufactured by Scionix [159]. The bottom of the vase is optically glued to a 10 mm length Poly(methyl methacrylate) (PMMA) light guide with two diameters: the front one equal to the plastic detector diameter and the rear one of 39 mm. The optical coupling between the light guide and the PMT was made with optical grease. We used a segmented 2×2 multi-anode Hamamatsu PMT R7600U-M4 [178] with an effective area of 18 mm×18 mm, bi-alkali photocathode and 10-stage metal channel dynode structure, operated at an overall voltage of -800 V. The inner walls of the plastic detector were covered by a thin aluminized-mylar reflector in order to improve the light collection.

- The disk detector is a 35 mm diameter and 3 mm thickness disk made of EJ212 plastic scintillator, and also manufactured by Scionix [159]. It was covered by a thin aluminized-mylar reflector held to the frontal face of the detector by an aluminium ring. It is optically coupled to a 9 mm length PMMA light guide of two diameters, analogously to the other detector. Again, the optical coupling between the rear part and the PMT was done with optical grease. The same Hamamatsu PMT was used with this detector.

A HPGe detector completed the set-up with the mission of identifying possible contaminants in the measurements. The detector used was a High Purity Coaxial Germanium γ-ray detector Canberra GC7020, operated at a bias voltage of +4000 V, with 89 mm endcap diameter, 74 mm crystal diameter and 63 mm crystal length. The window is made of aluminium with a window-crystal distance of 6 mm [179].

For the present purposes it is worth mentioning that two experimental set-ups were used at IGISOL corresponding to two different experiments, as will be explained in Chapter 6. The main differences are summarized below:

- Experiment 1 was performed with the vase-shaped plastic β-detector and without a tape transport system.

- Experiment 2 was performed with the disk plastic β-detector and with a tape transport system.

Furthermore, during the second experiment it was necessary to open the shielding at some point because of a technical problem (the tape station was replaced). Due to this fact, the optical fibres were unplugged and the reference positions of the light peaks slightly changed. For this reason we distinguish between the two sets of reference values in the second experiments (Exp2 and Exp2* in Tables 4.3 and 4.4), both of them equivalent in terms of energy calibration after multiplying the total software sum corresponding to one of them by a global gain factor of 0.99412.

Module	#	HV Exp1 [V]	HV Exp2 [V]	a_j	L_j Exp1	L_j Exp2	L_j Exp2*
0		800	800	76	2256.56	2672.44	2780.16
1	285	702	702	58	2519.74	2554.93	2553.8
2	281	493	494	63	2072.2	2099.74	2093.66
3	282	559	560	66	2089.97	2122.66	2116.44
4	353	568	568	57	2209.4	2239.17	2231.23
5	568	596	598	92	2045.69	2066.89	2059.94
6	356	537	540	50	2400.08	2431.74	2423.27
7	286	575	573	56	2074.92	2102.68	2100.98
8	571	457	458	58	2421.95	2455.03	2451.02
9	288	746	747	83	2391.07	2419.38	2416.83
10	569	650	651	51	2406.78	2442.41	2437.1
11	355	600	600	76	2603.55	2640.31	2633.67
12	283	528	529	46	1929.49	1962.42	1953.69
13	287	526	525	61	2686.26	2719.09	2766.57
14	570	572	572	64	2262.89	2287.41	2254.81
15	284	534	535	73	2302.11	2340.58	2452.97
16	289	653	653	66	2680.91	2740.03	2732.05
17	290	504	505	58	2331.15	2359.45	2436.54
18	354	625	627	61	2301.52	2325.47	2364.49

Table 4.3: Reference values for the DTAS individual detectors at IGISOL experiments. For each module the serial number according to the module data sheet, the operational HV value, the ADC offset (a_j) and the positions of the light peak are presented. Detector 0 corresponds to the well-type external reference detector.

Exp1	Exp2	Exp2*
1066.70	1067.01	1040.54

Table 4.4: Reference values for the ^{137}Cs peak in the reference detector at IGISOL experiments (in channels).

4.3.1 Background and contaminants

In all the measurements of the calibration sources there is a natural contamination: the room background. This background is dominated by a continuum region at low energies, and it shows the characteristic peaks at 1460.8 keV (^{40}K) and at 2614.5 keV (^{208}Tl), as well as the neutron capture peak in the ^{127}I of the NaI(Tl) crystals at around 6.83 MeV. The ambient background was measured in a separated run, and in order to subtract this contamination, it was normalized taking into account the measured live times. The live time was obtained by integrating the 100 Hz light pulser peak for the 18 individual modules and averaging these values. The normalization factor calculated with the ratio of the live

times is presented in Tables 4.5 and 4.6. From the comparison of the background subtracted spectra of the sources with the MC simulations presented in the next chapter, we found that this factor was not accurate, and it was empirically modified by the factor in the fourth column in Tables 4.5 and 4.6.

Source	Rate [kHz]	Live t [s]	Back
^{22}Na	4.18	5852.26	0.9927
^{137}Cs	18.77	995.13	0.7976
^{60}Co	6.90	662.48	0.9645
^{24}Na	14.27	1330.51	0.8356
^{152}Eu-^{133}Ba	44.36	176.36	1.
Background	3.16	41426.6	-

Table 4.5: Normalization parameters for the background in Experiment 1. The counting rates are calculated by integrating the software sum spectra and dividing by the live time. The last column corresponds to the correction of the normalization factor for the background subtraction as a fraction of unity, obtained after comparison with MC simulations.

Source	Rate [kHz]	Live t [s]	Back
^{22}Na	3.94	2473.56	0.987166
^{137}Cs	22.64	483.35	0.816311
^{60}Co	6.97	662.40	0.950746
^{24}Na	12.98	1113.54	0.895325
^{152}Eu-^{133}Ba	43.98	199.74	1.
Background	2.90	7283.48	-

Table 4.6: Normalization parameters for the background in Experiment 2. The counting rates are calculated by integrating the software sum spectra and dividing by the live time. The last column corresponds to the correction of the normalization factor for the background subtraction as a fraction of unity, obtained after comparison with MC simulations.

Apart from the contamination of the environmental background, other contaminants are taken into account in some of the sources. A natural Mg target was used to produced ^{24}Na with the ^{25}Mg(p, 2p)^{24}Na reaction. However, the reactions ^{25}Mg(p, α)^{22}Na and ^{25}Mg(p, 2α)^{18}F also produced ^{22}Na and ^{18}F, that are treated as contaminants in the ^{24}Na spectra. The experimental ^{22}Na spectrum is subtracted by checking the 1022 keV peak. ^{18}F contributes as a contaminant only in Experiment 1, since $T_{1/2}$=109.77 m and this activity had already disappeared for the Experiment 2. This contribution has been calculated by means of MC simulations. Finally, a contamination of ^{137}Cs of unknown origin is found in the measurements of the ^{60}Co. This contamination does not seem to be due to an impurity in the source employed, since it was also seen in the ^{60}Co source used in commissioning at IFIC. It is not related to the weak source employed with the well-type reference detector, either, because the contamination was seen uniformly in all of the modules, and not preferentially in those close to the reference detector. In view of these facts, we simply treated it as a contaminant that is subtracted.

The calibration sources with all the contaminants normalized for both experiments can be seen in Figure 4.19.

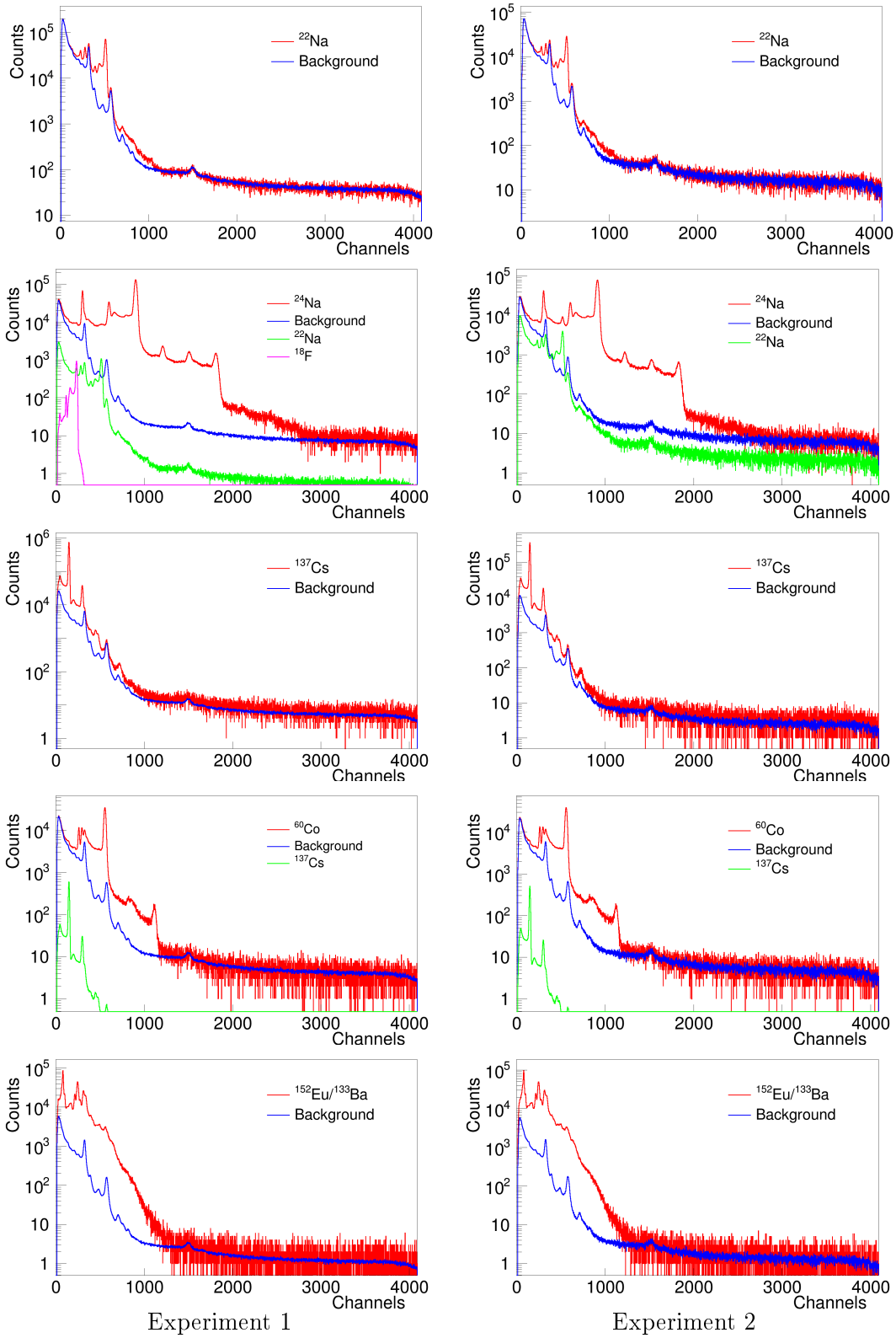

Figure 4.19: Spectra from the calibration sources with the corresponding contaminants normalized.

4.3.2 Summing-Pileup calculation

An important source of contamination in the measured spectra is the random superposition of electronic signals within the time length of the ADC gate, due to the statistical nature of the decays, as depicted in Figure 4.20. This superposition affects the pulse shape of a single module that arrives within the ADC gate length, leading to the so-called pulse-pileup [180]. This affects individual crystals as well as the hardware sum of the detector if two or more signals of successive decays overlap (see Figure 4.15). Furthermore, in a segmented detector there is another source of distortion, namely, the random sum of the signals detected in different modules and corresponding to different decays that are, however, stored in the same event. This affects the software sum, since the sum is distorted even if the signals are detected in different modules. In a real situation, the distortion involves both processes, the pulse-pileup (that we will simply call pileup) and the random summing (that will be simply called summing, but has to be distinguished from the traditional use of this term in spectroscopy). We have developed a method to treat the distortion of spectra due to both effects that was already used in previous works [73,74,108], and will be detailed here.

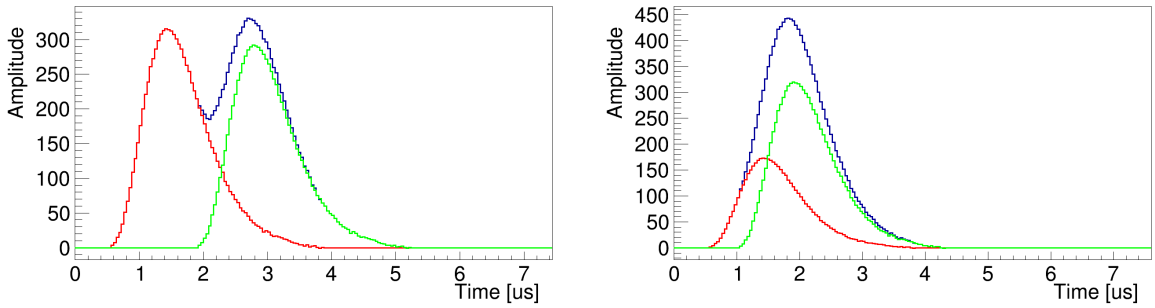

Figure 4.20: Examples of first order pileup (blue) of two experimental pulses (red and green). The shape of the pulses correspond to that of our electronic chain (see Appendix A).

Procedure

The evaluation of the summing-pileup contamination is based on the event structure of the experimental data, and on the true pulse shape of the individual modules after the MSCF-16 shapers (the true pulse shape can be seen in Figure A.1 of the Appendix A). For the first order calculation, two arbitrary random events are read, and the time difference between them is sampled randomly within the ADC gate length. If an individual detector has fired in both events, two pulses with their corresponding amplitude are summed, and the maximum within the effective ADC gate (5.6 μs in our case) is taken, according to [180]. If, on the contrary, the individual detector has fired only in one event, it contributes to the random summing evaluation. The total summing-pileup is the sum of all contributions, as depicted in Figure 4.21.

It is worth mentioning that, in the particular case of our spectrometer, the majority of the summing-pileup events contaminating our measurement come from the random

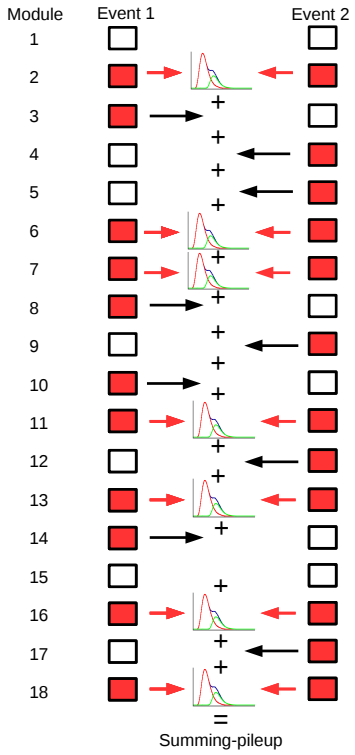

Figure 4.21: First order summing-pileup scheme. The red squares represent a signal over the threshold stored in the ADC for this module in this event. When the same module fires in the two events used for the summing-pileup reconstruction, it is processed as a pulse pileup. In any other case, the signals are added giving rise to the summing contribution.

summing contribution, as shown in Figure 4.22 for a ^{60}Co source, where the total summing-pileup contains around 87% events with only random summing, 1% with only pileup, and 12% where both contributions are summed as in Figure 4.21. The preponderance of the summing component increases with the counting rate.

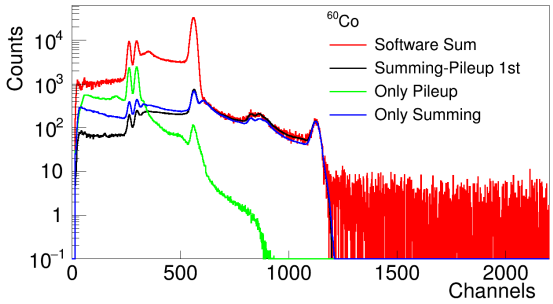

Figure 4.22: First order summing-pileup for the ^{60}Co source. The contributions of the pulse pileup and the random summing are separated to show the region where they are affecting the spectrum.

First order summing-pileup contributions have been calculated for all the calibration sources employed at IGISOL. The normalization factors for comparison with experimental

spectra are obtained from the theoretical expression of Equation (4.4), which is based on the expression obtained for pileup order n in [180], but adapted to a segmented detector. Here α_i are the individual counting rates of the 18 crystals and τ_p is the length of the effective ADC gate (6 μs minus the peaking time of the individual detector signal, which is ~ 0.4 μs, as shown in Figure A.1 of the Appendix A).

$$N^n_{theo} = \sum_{i=1}^{18} e^{-\alpha_i \tau_p}(1 - e^{-\alpha_i \tau_p})^n \tag{4.4}$$

When the counting rate is high (approximately above 10 kHz), second order contributions must be evaluated. This is the case for the ^{24}Na source and the ^{137}Cs source, whereas for the ^{152}Eu-^{133}Ba source even the third order contribution was needed in order to reproduce the measured spectrum. The procedure in those cases represents just an extension of the method already described. In the second order contribution, for example, three events are taken each time, instead of two.

Pileup calculation with the MC simulations of the sources

It was observed that we are unable to reproduce the shape of the summing-pileup contribution for sources with high counting rates, as was the case for the ^{137}Cs and ^{152}Eu-^{133}Ba sources. This is because in these sources, a large fraction of the events that are used for the calculation are already distorted. The ideal solution to overcome this problem, consists of using undistorted events of the source convoluted with background events. However, we can not distinguish whether an event corresponds to the decay of the source, the background, the pileup or any other source of signals. The only possibility one could think of is to use MC simulated events. For this purpose, we simulated the sources with Geant4, as explained in Section 5.2, and we stored the information in a ROOT TTRee [181] equivalent to the ones of the experimental measurements. Moreover, we introduced the corresponding width (see Table 5.2 in Section 5.2.1, Chapter 5), and we convert the light channels of the MC into experimental channels by taking into consideration the energy calibration of the experiment and the MC contained in Tables 4.7 and 4.8, and Table 5.1, respectively.

In this case, the same procedure explained in the previous section is used with little differences. In particular, only the source-source and source-background summing-pileup contributions are calculated. For this reason the first event is always chosen from the source (MC simulation) and the second is taken either from the source, or from the background experimental file. The proportion between source and background for the second event is roughly fixed by the counting rates, and it is a parameter that can be adjusted by looking at the resulting spectra.

The use of MC files to reconstruct the summing-pileup contribution has been proved to be successful, as will be shown in the next section.

Summing-pileup of the calibration sources

The procedure described in the previous sections has been applied to reproduce the spectra of the calibration sources in the two experiments carried out at IGISOL. First order contri-

butions have been calculated for all the sources. The second order contribution was needed in ^{24}Na and ^{137}Cs sources (and may be considered for ^{60}Co, while turns out to be negligible in ^{22}Na), whereas for the ^{152}Eu-^{133}Ba source, even the third order contribution was needed in order to reproduce the experiment. As mentioned above, the summing-pileup of ^{137}Cs and ^{152}Eu-^{133}Ba is reconstructed by using MC simulations, instead of using the experimental source file. For all the calibration sources we focused on the summing-pileup of the background subtracted spectra. For this reason, the summing-pileup of the environmental background is properly subtracted from the summing-pileup evaluation of the sources.

The contribution of the summing-pileup for each of the calibration sources in Experiment 1 and Experiment 2 is shown in Figure 4.23.

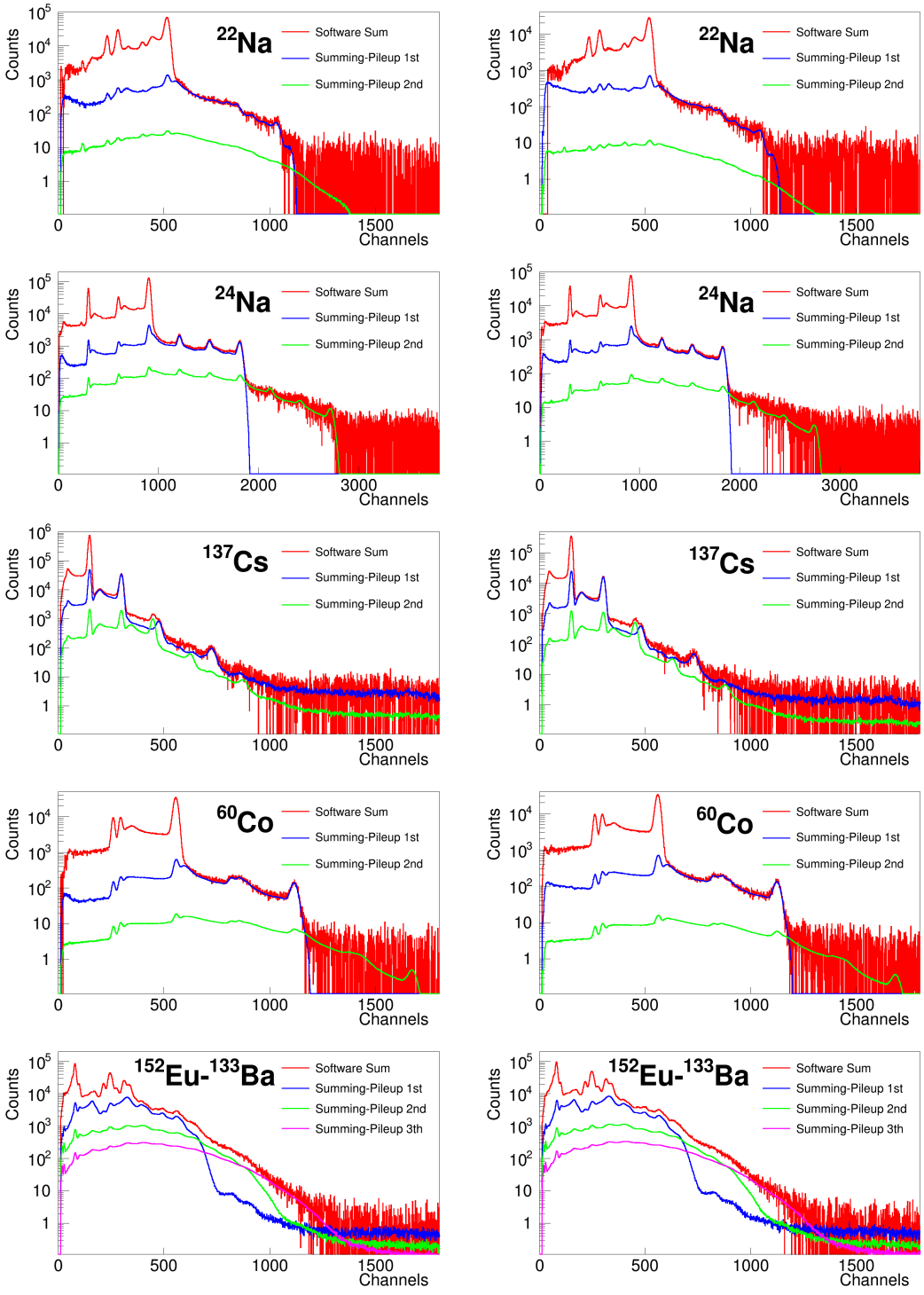

Figure 4.23: Summing-pileup contributions for all the calibration sources in Experiment 1 and Experiment 2.

4.3.3 Energy and sigma calibrations

The energy calibration of DTAS in the experiments at IGISOL was carried out with the main peaks of the set of calibration sources. For the energy calibration the following peaks were taken into account:

- 661.7 keV from ^{137}Cs
- 1274.5 keV from ^{22}Na
- 1173.2 keV and 1332.5 keV from ^{60}Co
- 2754.007 keV and 1368.626 keV from ^{24}Na
- 121.78 keV from ^{152}Eu (the branch going to ^{152}Sm)
- 6921 keV corresponding to neutron capture in ^{127}I (from ^{137}I measurement)

On the basis of the ideas explained when discussing the non-proportionality of the light yield in NaI(Tl) in Section 4.2.3, all the peaks involved in the calibration are single peaks, except the neutron capture peak. The reason to consider this peak is to have a reference point at high energies. The energy is accurately calculated with the corresponding shift by means of MC simulations, as will be discussed in Section 5.2.6 of Chapter 5.

The fitting function energy (E) vs. channels (x) used for the calibration, consists of a piecewise function with three parts, where continuity between the three regions is required:

$$E(x) = \begin{cases} a_c + b_c x + c_c x^2 & , \quad x < p_1 \\ a_{l1} + b_{l1} x & , \quad p_1 \leq x < p_2 \\ a_{l2} + b_{l2} x & , \quad x \geq p_2 \end{cases} \tag{4.5}$$

The quality of the fit for the calibration of Experiment 1 is shown in Figure 4.24, and the parameters obtained from the fit are collected in Table 4.7.

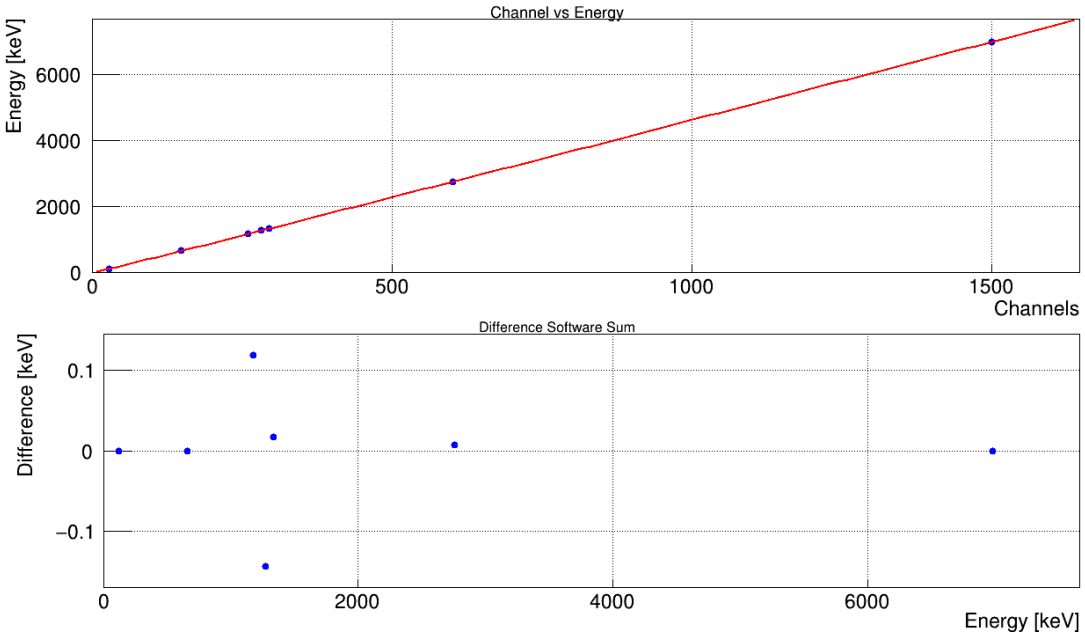

Figure 4.24: Energy vs. channel calibration in Experiment 1.

The quality of the fit for the calibration of Experiment 2 is shown in Figure 4.25, and the parameters obtained from the fit are collected in Table 4.8.

a_c	b_c	c_c	p_1	a_{l1}	b_{l1}	p_2	a_{l2}	b_{l2}
-3.948274	4.452063	0.000138	200	-37.752847	4.648770	1100	-10.864595	4.624326
-2.531447	4.432063	0.000138	200	-37.752847	4.635770	1100	-25.164447	4.624326

Table 4.7: Energy calibration parameters for Experiment 1. The second row is the calibration slightly changed by hand after comparison with the MC response and maintaining continuity.

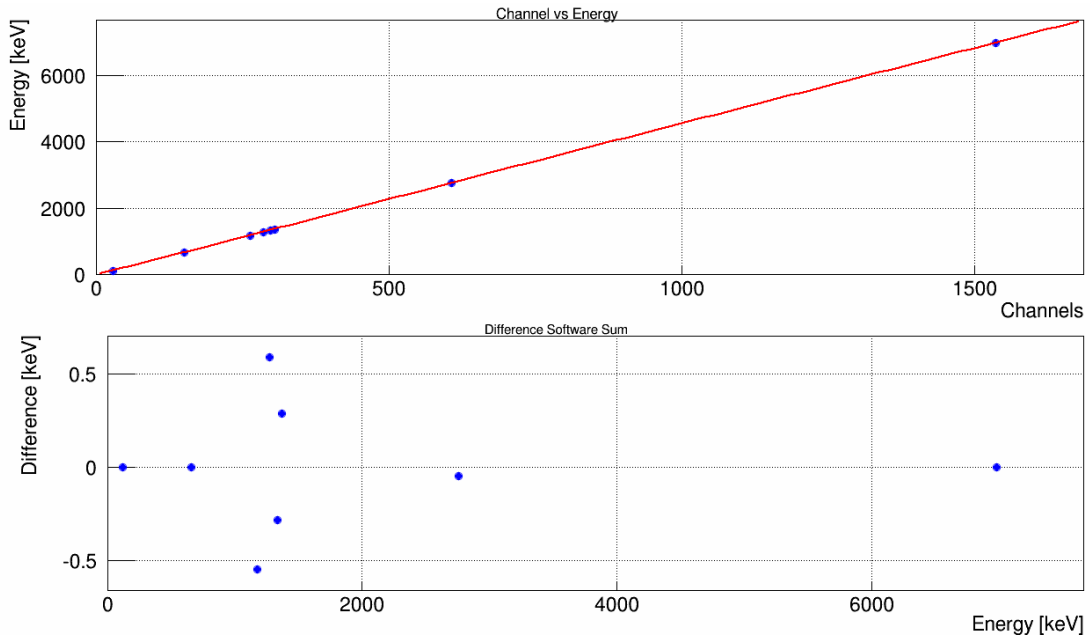

Figure 4.25: Energy vs. channel calibration in Experiment 2.

a_c	b_c	c_c	p_1	a_{l1}	b_{l1}	p_2	a_{l2}	b_{l2}
-5.443292	4.398366	0.000270	200	-34.034511	4.595265	1100	2.107407	4.562409
-5.454711	4.388366	0.000270	200	-34.034511	4.585265	1100	-8.892911	4.562409

Table 4.8: Energy calibration parameters for Experiment 2. The second row is the calibration slightly changed by hand after comparison with the MC response and maintaining continuity.

On the other hand, it is important to obtain the dependence of the resolution with energy in order to apply the corresponding width to the MC. The sigma calibration is performed according to the expression:

$$\sigma^2(E) = a + bE + cE^2 \tag{4.6}$$

The fit for the sigma calibration involves the same peaks than the energy calibration except the neutron peak and the 121.78 keV peak from ^{152}Eu. The resulting fit for Experiment 1 is shown in Figure 4.26, and the parameters obtained from the fit are collected in Table 5.2 (Section 5.2.1, Chapter 5).

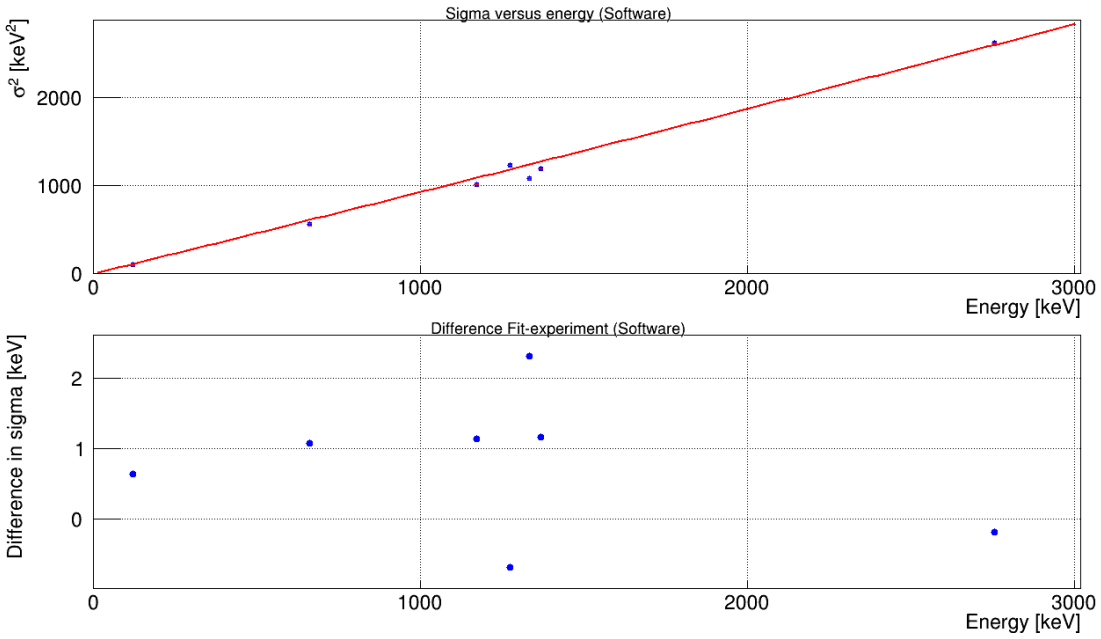

Figure 4.26: σ^2 vs. energy calibration for Experiment 1.

The fit for the sigma calibration of Experiment 2 is shown in Figure 4.27, and the parameters obtained from the fit are collected in Table 5.2 (Section 5.2.1, Chapter 5).

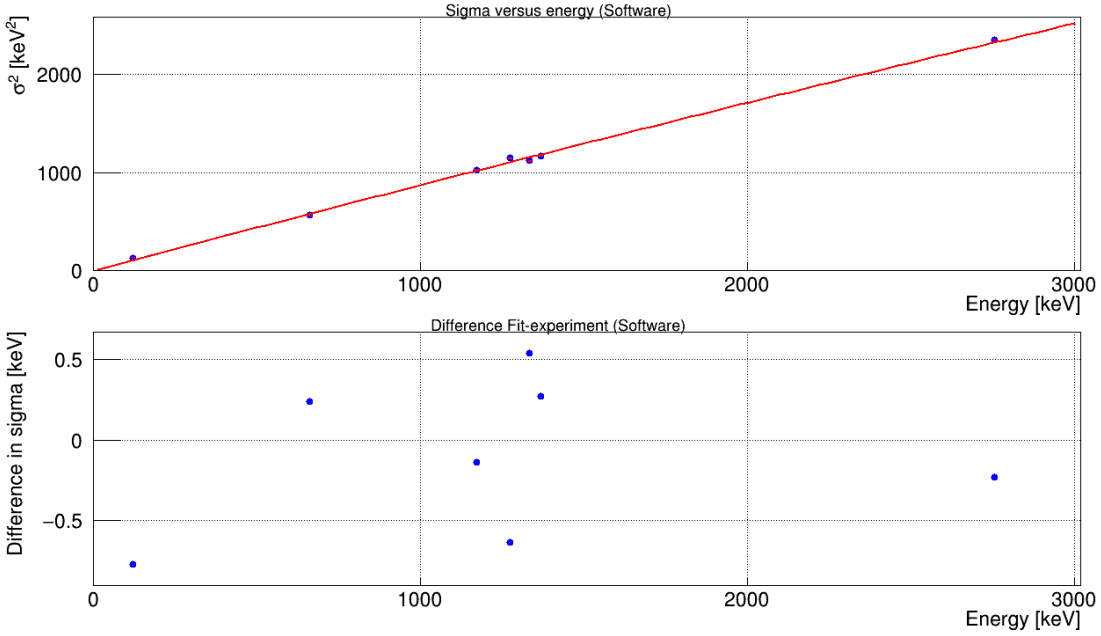

Figure 4.27: σ^2 vs. energy calibration for Experiment 2.

Chapter 5

MC response

> Cuando me siento con humor creo que podría demostrar tanto que dos más dos son cinco como que solo puede haber un Dios
>
> *When I really get going I could just as easily prove that twice two is five as that there can be only one God*
>
> Robert Musil

In this chapter, a careful comparison of MC simulations with the experimental measurements of calibration sources is carried out. The aim of this study, as explained in Chapter 2, is to validate the MC code that will be used for the calculation of the response function in a TAGS analysis. This validation is done for the geometry of the two experiments performed at IGISOL using the calibration sources mentioned in Chapter 4. For all the simulations the package Geant4 [156] is employed. In particular, the version geant4.9.6.p03 is used with the Livermore PhysicsList library.

5.1 Geometry

The first step before performing any MC calculation consists in the implementation of the geometry of the set-up, including as accurately as possible the composition and the thickness of the different materials, as well as the positions of the different components of the set-up. In this sense, the geometry of the DTAS modules, the beam pipe, the tape system, the plastic detector with its corresponding light guide and photomultiplier, the HPGe detector, and part of the shielding are included in the simulation code, as can be seen in Figures 5.1 and 5.2. The resulting geometry must be validated by comparing the simulations of the calibration sources with the experimental measurements. The simulation of the calibration sources is done taking also into account the geometry of their encapsulation, described in the data sheet of the sources when it exists, or obtained from direct measurement of their dimensions.

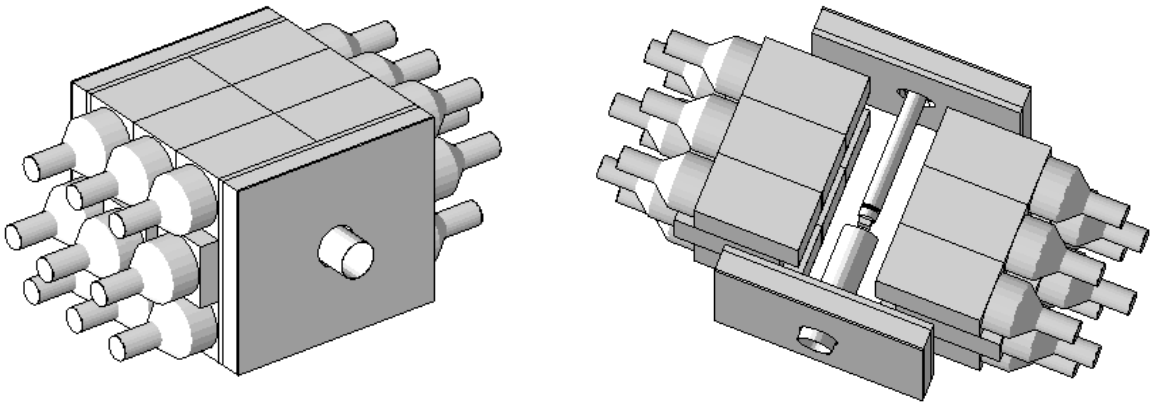

Figure 5.1: Geometry of the set-up included in the MC with the DTAS detector surrounded by part of the shielding (the part that can be seen by the sources). In the picture on the right the DTAS is open and the shielding separated to distinguish the different elements, in particular the beam pipe and the HPGe detector can be seen.

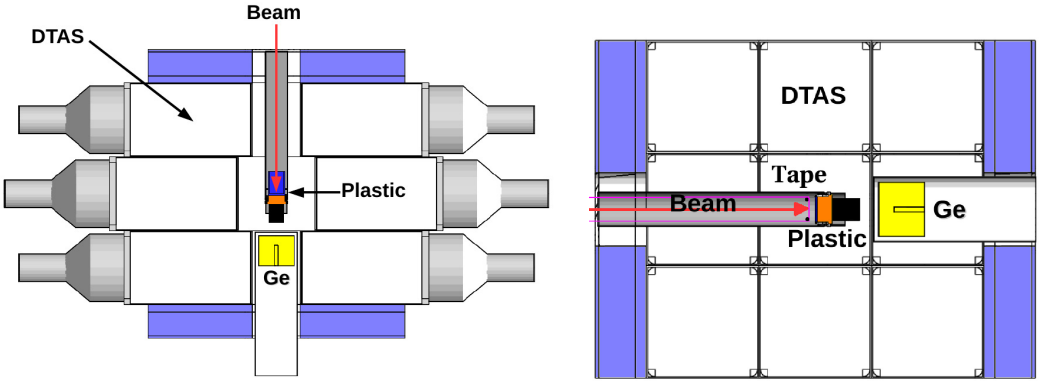

Figure 5.2: A lateral cut for Experiment 2 (right) and a horizontal cut of Experiment 1 (left) are shown. The DTAS detector (in white) surrounded by the shielding (in violet), the beam pipe (in grey), and the HPGe detector (in yellow) are depicted. The plastic β-detectors (in blue) with the light guide (in orange) and the PMT (in black) are also shown. Note that in Experiment 2 the tape and the rollers are also included.

5.2 DTAS detector

5.2.1 Light non-proportionality and calibrations

The reproduction of the non-proportionality light yield in NaI(Tl) is achieved as in previous works [18, 141] by using Equation 5.1 from [18] at the level of the SteppingAction in the MC code.

$$\frac{L}{E_e} = \frac{a_1(1 - e^{-a_2 E_e}) + a_3 E_e + a_4 E_e^2}{a_5 + a_6 E_e + a_7 E_e^2} \tag{5.1}$$

with

$$\{a_i\} = \{1.6(2), 0.058(8), 0.580(4), 0.00490(2), 0.25(2), 0.479(4), 0.00494(2)\}$$

It implies that the spectra obtained from the simulation are in light channels, so that an energy calibration similar to the one performed in section 4.3.3 must be done. In addition, the light function in equation 5.1 introduces a width in the spectra that has to be taken into account before widening the MC spectra to compare with the experiment.

With respect to the energy calibration, a piecewise function with the form of equation 4.5 is used, but only with one linear region (the neutron peak is not included). At low energies, five γ-rays are simulated corresponding to 100, 200, 300, 400 and 500 keV. Since these simulations at low energy exhibit large fluctuations, they are widened before calculating the centroids by applying a Gaussian instrumental width. This means that they are only used in the energy calibration, but not in the sigma calibration. The rest of the peaks for the calibration are obtained from the simulation of the calibration sources. The resulting parameters for the geometries of Experiment 1 and Experiment 2 are listed in Table 5.1. Since the results are essentially equivalent for both geometries, the parameters for Experiment 2 will be used. The fit is plotted in Figure 5.3.

a_c	b_c	c_c	p_1	a_{l1}	b_{l1}
-10.011706	0.943695	0.000001	704.827469	-34.233098	0.976482
-10.012381	0.943837	0.000001	758.550407	-34.475398	0.976681

Table 5.1: MC energy calibration parameters. The first row corresponds to Experiment 1 whereas the second row is that corresponding to Experiment 2.

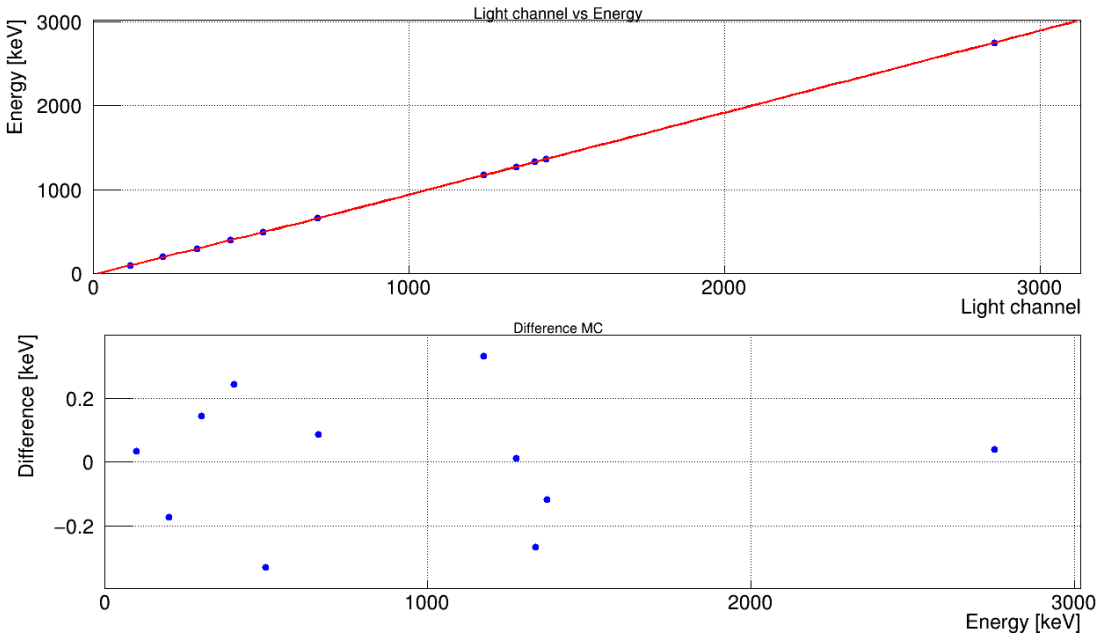

Figure 5.3: Energy vs. light channel calibration Experiment 2.

Regarding the width of the MC due to the light function, as mentioned above, equation 4.6 is used again to calibrate sigma with the energy. For consistency, the same sigma calibration has been assumed for both Experiment 1 and Experiment 2, since it does not

depend on the set-up details, but only on the NaI(Tl) crystals. The fit for Experiment 2 can be shown in Figure 5.4. The parameters from the fit are given in Table 5.2, as well as the final width that has to be applied to the MC simulations in light in order to match the experiment. The final width calibration corresponds to a slight variation of the parameters obtained in order to better reproduce the measured spectra with the simulation.

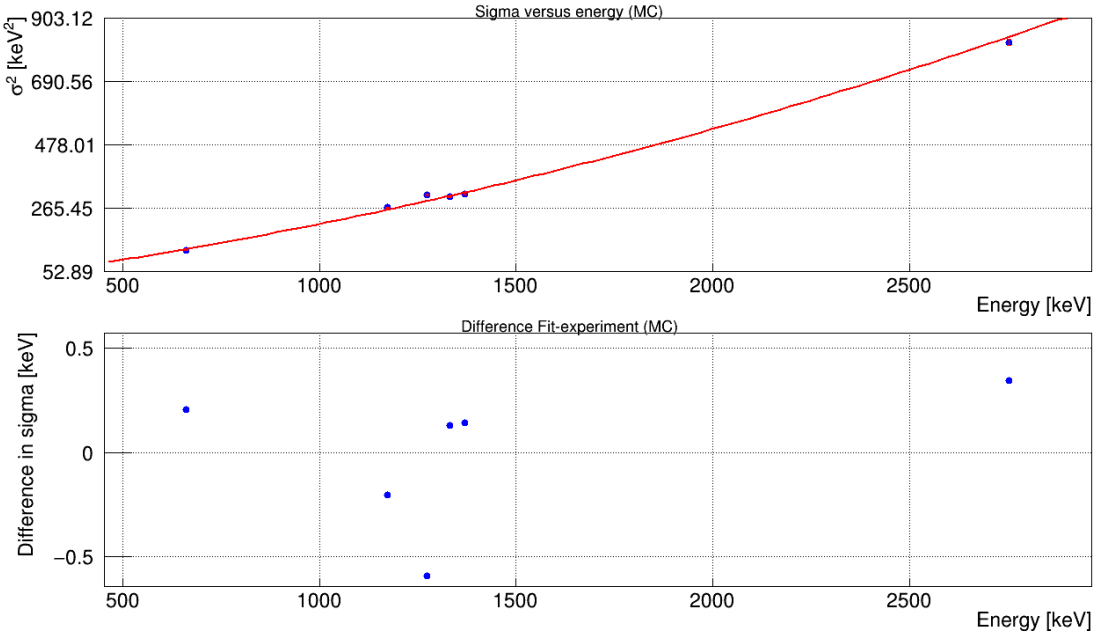

Figure 5.4: MC σ^2 vs Energy calibration Experiment 2.

Calculation	a	b	c
$\sigma^2_{exp}(E)$	0.0	0.889212	-0.000016
$\sigma^2_{MC}(E)$	0.0	0.161295	0.000052
$\sigma^2_{exp}(E) - \sigma^2_{MC}(E)$	0.0	0.727917	-0.000068
Final $\sigma^2_{exp}(E) - \sigma^2_{MC}(E)$	0.0	0.70336	0.000000678584

Table 5.2: Sigma vs energy calibration parameters (experimental and MC) for Experiment 2. The last row is the calibration slightly changed by hand after comparing the experimental spectra with MC simulations.

5.2.2 Efficiency

The efficiency of the detector for γ-rays and β-particles can be studied my means of MC simulations once the measured spectra for the different calibration sources are well reproduced by the simulations (as will be shown in Section 5.2.4 below). In Figure 5.5 the efficiency for the eighteen-module configuration at IGISOL for γ-rays and β-particles is shown. In order to make a comparison with the sixteen-module configuration in realistic experimental conditions, the same geometry is simulated inside DTAS: the beam pipe, the plastic scintillator β-detector with its PMT, and the HPGe detector. In both cases the

total efficiencies are above 80% over all the range, while the peak efficiency at 1 MeV is 56% for the sixteen-module configuration and 66% for the eighteen-module configuration. The difference in the efficiency for detecting β-particles between both configurations is largely due to the impact of the aluminium frames used in the sixteen-module configuration.

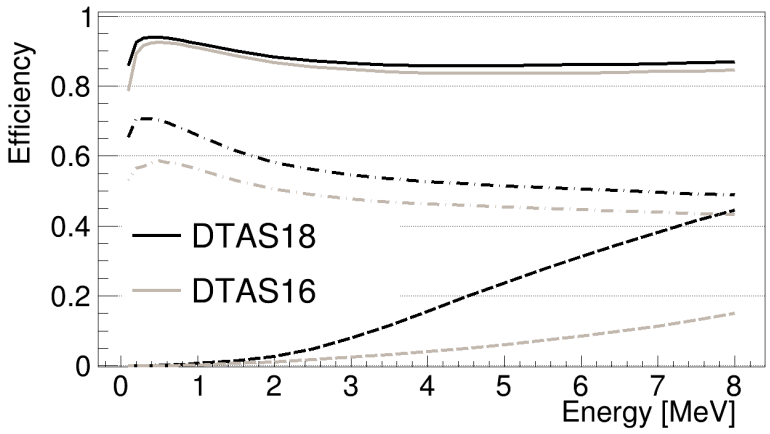

Figure 5.5: Efficiencies of the DTAS detector both in the sixteen-module configuration and in the eighteen-module one. Total γ-efficiency (solid lines) and peak γ-efficiency (dashed-dotted lines) are represented. The efficiency for β-particles (dashed lines) is also included. No threshold condition has been taken into account.

5.2.3 Threshold

The accurate determination of the value of the threshold is needed for the MC simulations. The energy threshold depends essentially on the electronic noise and a lot of effort was spent during the set-up of DTAS to minimize it. It is important to lower as much as possible the detection threshold since this will affect the low energy region of the sum spectrum. Moreover, for some decays one could expect very low energy transitions (100 keV or lower).

The strongest evidence we found to identify the threshold of DTAS was a peak in the spectra of the single modules in the region of 80 keV for the ^{152}Eu-^{133}Ba combined source, which is supposed to correspond to the 79.6142 keV and 80.9979 keV doublet from the *EC* decay of ^{133}Ba. However, we suspect that these peaks are, up to a certain point, partially cut. We tried to play with the threshold applied to the MC simulation and compare with the experimental measurement in order to determine the value with more accuracy. As a result, we concluded that the 79.6142 keV could be cut without distorting the comparison, but not the 80.9979 keV peak, as shown in Figure 5.6 right. For this reason, we chose 80.9 keV, just below the 80.9979 keV peak, as a threshold value we are confident of for the individual modules.

There is an important difference between the hardware sum and the software sum, and it is clearly revealed with the ^{152}Eu-^{133}Ba source, in particular with the ^{152}Eu $\rightarrow$ ^{152}Sm *EC* branch. In this branch, the *EC* process leads to the emission of the X-ray of 40.12 keV with the largest probability, and this X-ray could be summed with the de-excitation γ-cascade. In the hardware sum all the individual signals are summed at the level of the

preamplifiers, and this X-ray is, indeed, summed with the γ-rays from the de-excitation cascade. Nevertheless, in the software sum, where the individual signals are recorded and then added off-line, we observed that this X-ray is cut in the individual modules, and thus the cascade is shifted to lower energies. This shift between the hardware sum and the software sum can be observed in Figure 5.6 left, where the application of the threshold in the MC explains the shift.

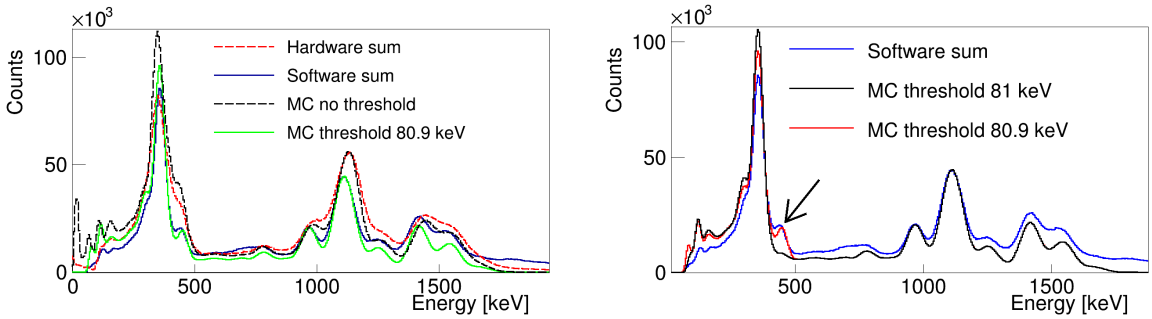

Figure 5.6: Study of the threshold of the DTAS detector with MC simulations (note that no summing-pileup contribution is considered). In the right hand figure the effect of cutting the γ-ray of 80.9979 keV from the ^{152}Eu-^{133}Ba source in the MC is shown in comparison with the experimental spectrum. The left figure shows the ^{152}Eu-^{133}Ba hardware sum of the DTAS compared with a MC simulation without any threshold, where no shift is observed, in comparison with the software sum of the DTAS compared with a MC simulation with 80.9 keV threshold, where a shift with respect to the hardware spectrum is found due to the non detection of the 40.12 keV X-ray. The application of the threshold reproduces the shift in the software spectrum.

It is worth mentioning that applying a threshold of 80.9 keV to our simulations is not enough to reproduce the shape of the spectra at low energies due to an additional effect. In reality, only the threshold of the individual modules is below 80.9 keV. The threshold of the hardware sum of DTAS, which is the one that fires the trigger, is higher (around 90 keV). It means that when less than 90 keV is deposited in a module, the trigger will fire only if enough energy is deposited in other modules so that the hardware sum accounts for more than 90 keV to be above the global threshold. This is connected to the detection of the X-ray of 40.12 keV from the EC branch of ^{152}Eu in the hardware sum when it is summed with other signals (with a γ-cascade). For the software sum, this implies that two different thresholds have to be taken into account in the MC simulations: a threshold for the individual modules (80.9 keV), and a global threshold for the sum. The main inconvenience arrives when calculating the response function for a decay in a TAGS analysis, since the response of the spectrometer is constructed by the convolution of monoenergetic simulations, as explained in Chapter 2. If we apply the global threshold before convoluting, we are distorting all those responses where signals below 90 keV are summed to give more than 90 keV. A possible solution is to apply a global threshold after the convolution. It is important to note that this global threshold has only an impact on the quality of the comparison with the experiment, and does not distort the spectra.

When a timing condition between DTAS and the plastic detector is required, it has been

found that the global energy threshold is slightly higher than in the singles case (DTAS without any condition), as shown in Figure 5.7. It has been estimated to be around 110 keV, and this effect may be important for our sensitivity to ground state to ground state transitions. An explanation for this can be found based on Figure 5.7, where a study of the β-γ spectrum for the ^{24}Na calibration source is performed depending on the timing conditions required. First, it can be seen that a coincidence requiring only signals above the energy thresholds of both DTAS and plastic detectors leads to a lower effective threshold than a coincidence with an additional condition in a TAC spectrum between DTAS and the plastic detector (when most of the environmental background contamination is then rejected). Secondly, a coincidence requiring signals above the energy thresholds of both detectors for those events where the time of the plastic is zero, gives essentially coincidences with environmental background. This can be understood since a zero value for the time of the plastic means a signal below the threshold of the Constant Fraction of the plastic, which is generally associated with noise (all the more reason in those cases dominated by a ground state to ground state transition, where the majority of β-particles should be well above the threshold). Finally, a coincidence requiring signals above the energy thresholds for those events where the time of DTAS is zero, gives coincidences with environmental background and β penetration in DTAS. Due to the fact that our ADC trigger is the OR of all detectors, as explained in Appendix A, when a signal is below the threshold of the Constant Fraction of DTAS, but the plastic detector fires, the energy deposited in DTAS is also stored. The result of this is a reduction of the effective threshold in DTAS when no positive time is required.

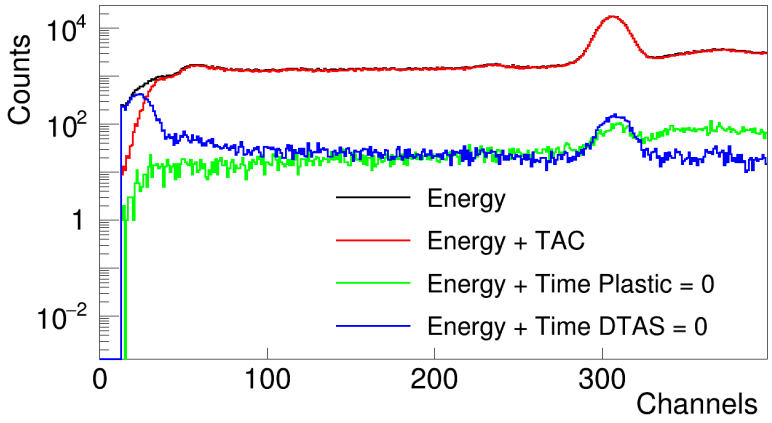

Figure 5.7: Study of the effective threshold at low energies depending on the detector that triggers the ADC (time $>$ 0). See text for details.

For the analysis of the decays presented in this work, in general β-gated spectra will be analysed, with conditions on the spectrum of the TAC between DTAS and the plastic β-detector. It means a threshold for the individual modules of 80.9 keV and 110 keV for the total sum. For the calibration sources and for those analyses performed with spectra in singles, without coincidences, the global threshold will be 90 keV.

5.2.4 Reproduction of the sources

The simulations of the sources have been performed using the DECAYGEN event generator [146] to simulate the primary particles of the decays according to the information available (γ and β-intensities, branching ratios, etc). The RadioactiveDecay of Geant4 was also tested and compared with the event generator, finding some discrepancies in the X-ray response because of the simplified treatment of atomic relaxation in the DECAYGEN generator.

In Figure 5.8 the comparison of the measurements with the MC for the calibration sources employed at IGISOL is shown. All the contaminants in the experimental spectra mentioned in Section 4.3.1 have been subtracted, and the summing-pileup calculated in Section 4.3.2 has been added to the MC. A nice agreement can be observed for all the sources in both experiments.

Another way to calculate the MC response is from the simulation of individual γ-rays and β electrons involved in the decay of each source. Each response is widened by the instrumental resolution and then they are convoluted according to the branching ratios. This procedure is the one we use to construct the response function in order to obtain the β-intensity from deconvolution of TAGS spectra, as described in Chapter 2, thus this comparison is even more meaningful. The resulting comparison of experiment and MC is shown in Figure 5.9, and it improves the reproduction of the shape of the sum peaks. Because of the large number of individual MC responses needed for the complex ^{152}Eu-^{133}Ba source, its comparison was not addressed.

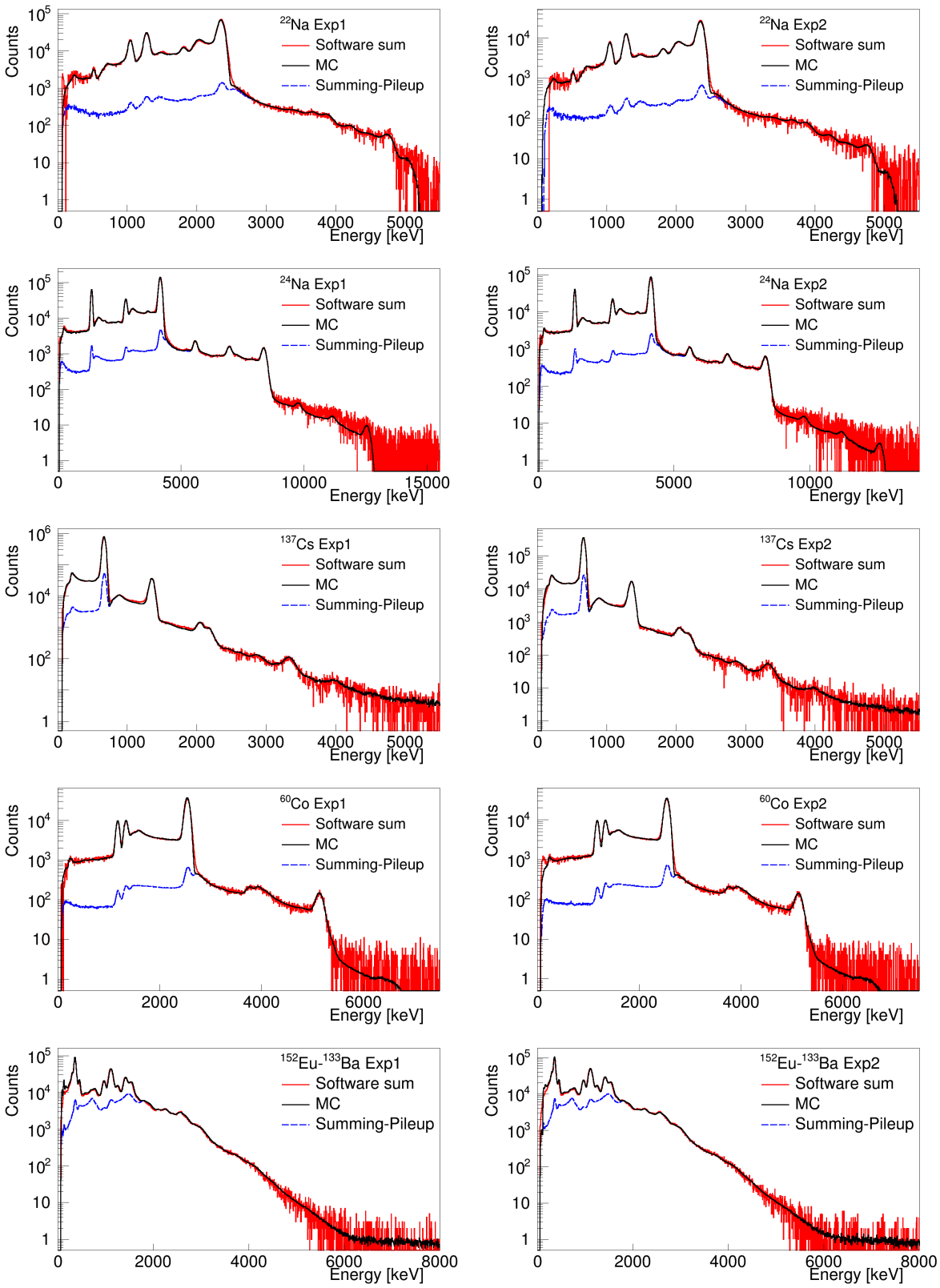

Figure 5.8: Comparison of experiment and MC using the DECAYGEN event generator [146] for the calibration sources used at IGISOL in Experiment 1 (Exp1) and Experiment 2 (Exp2).

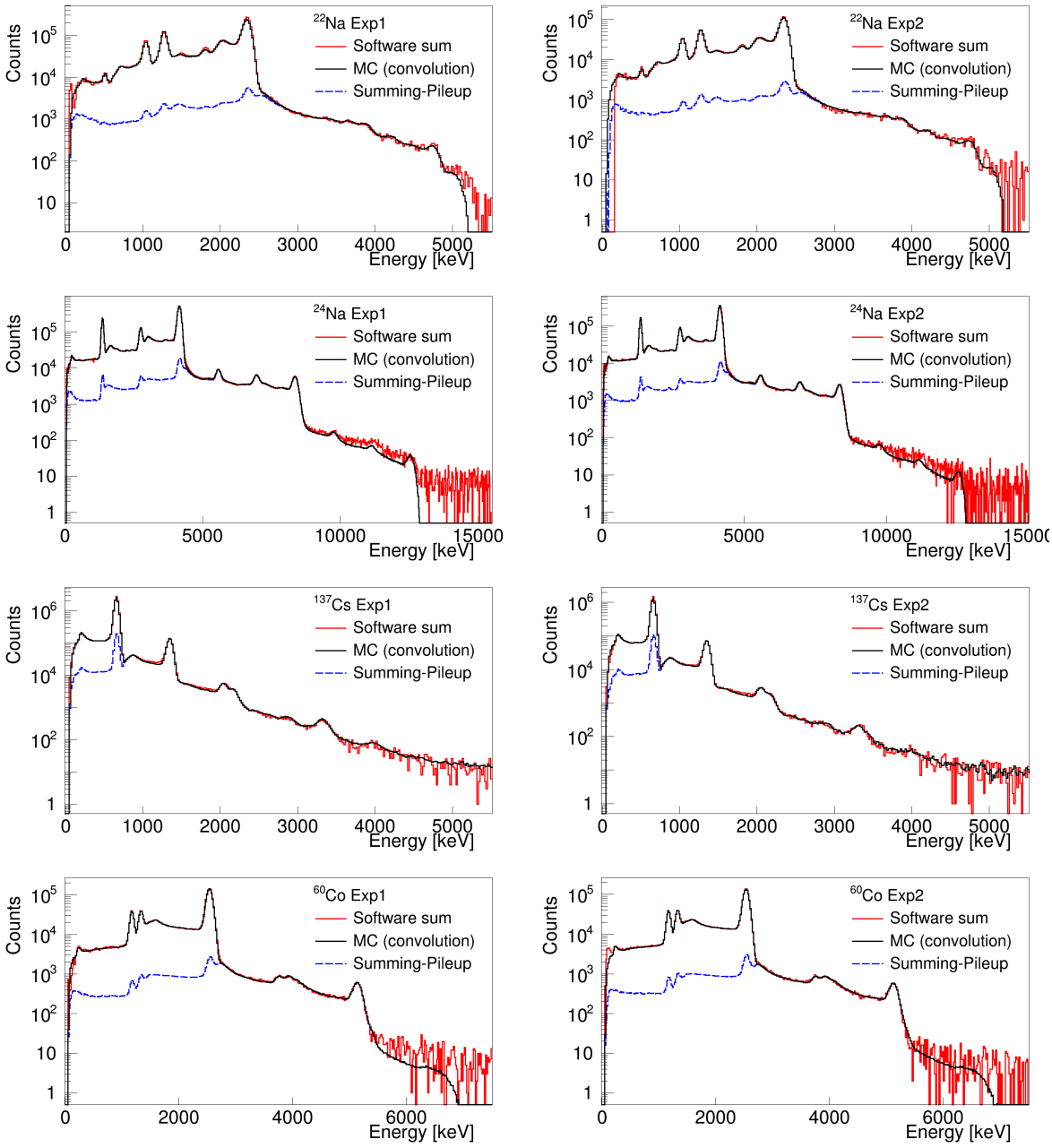

Figure 5.9: Comparison of experiment and MC response calculated from convolution of individual responses for the calibration sources used at IGISOL in Experiment 1 (Exp1) and Experiment 2 (Exp2).

5.2.5 Reproduction of the multiplicities

The segmentation of the DTAS detector brings the opportunity to do a more detailed study of the sources and a more thorough test of the MC simulations by comparing the different multiplicities for each calibration source. For this purpose, the same calibration, the same normalization factors and the same summing-pileup procedure have been applied for the multiplicities. The good reproduction of the multiplicities can be seen in Figures 5.10, 5.11, 5.12, 5.13, and 5.14. In the case of the ^{152}Eu-^{133}Ba source, from multiplicity 4 the spectra are totally dominated by summing-pileup. Due to the difficulties associated with

the reproduction of the summing-pileup contribution for this source, the multiplicities are not well reproduced.

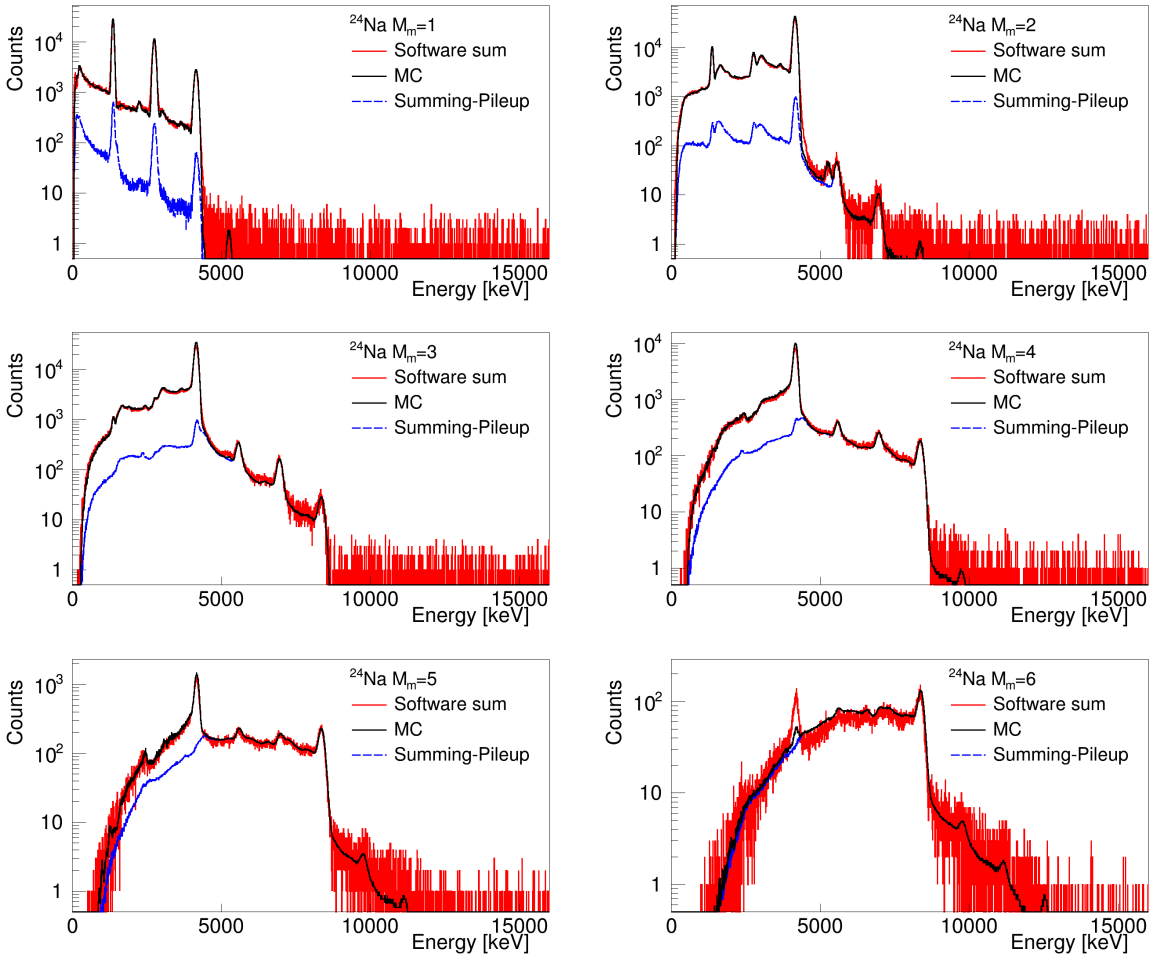

Figure 5.10: ^{24}Na MC-Experiment comparison for multiplicities 1-6.

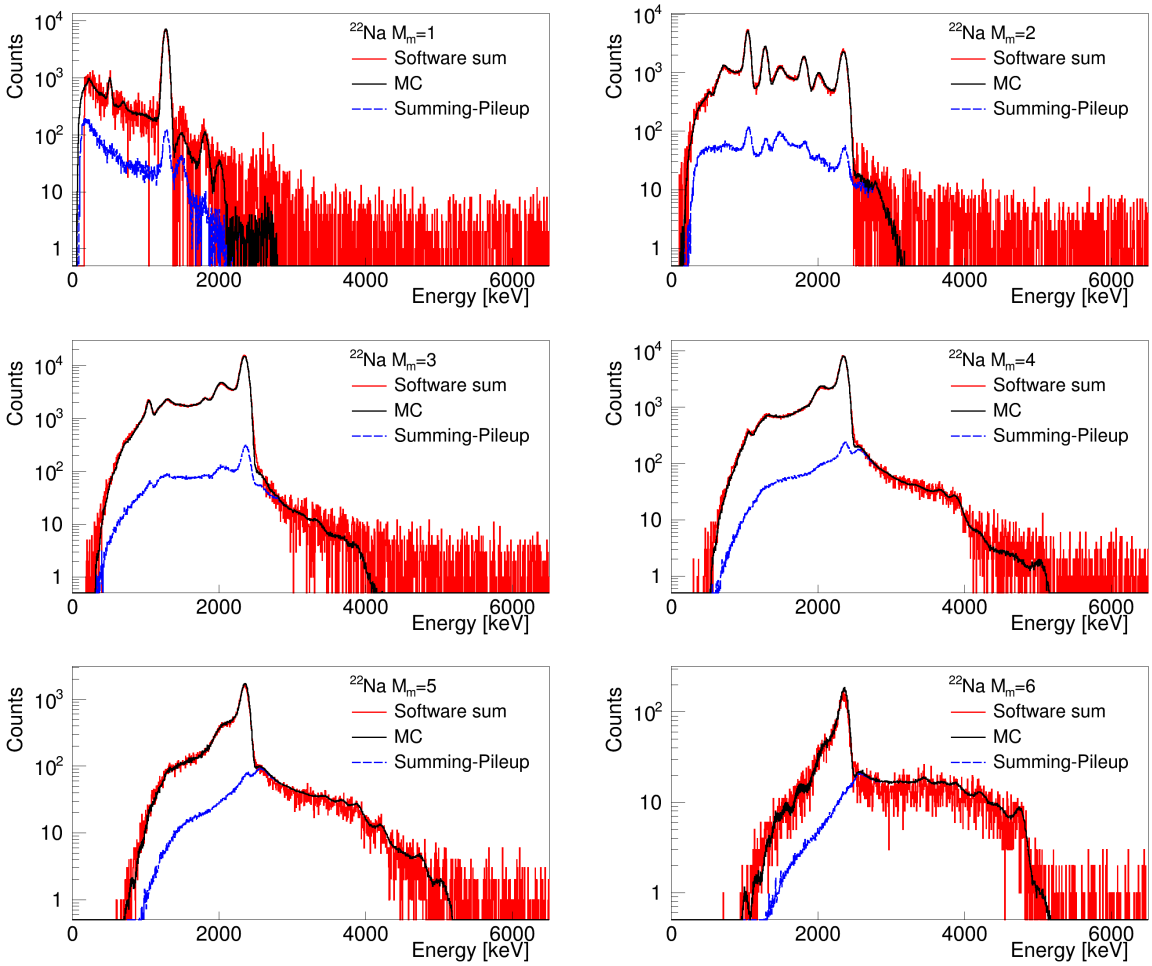

Figure 5.11: ^{22}Na MC-Experiment comparison for multiplicities 1-6.

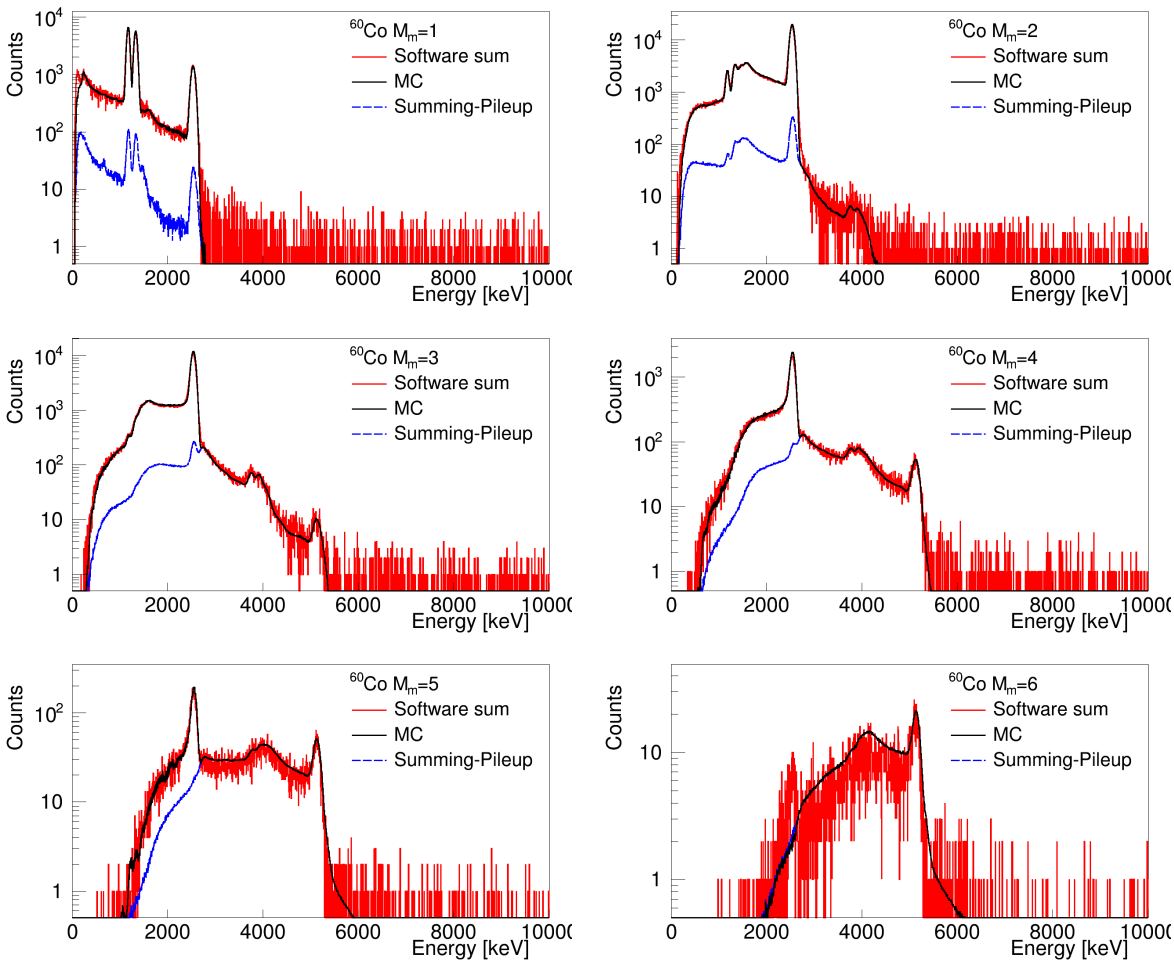

Figure 5.12: ^{60}Co MC-Experiment comparison for multiplicities 1-6.

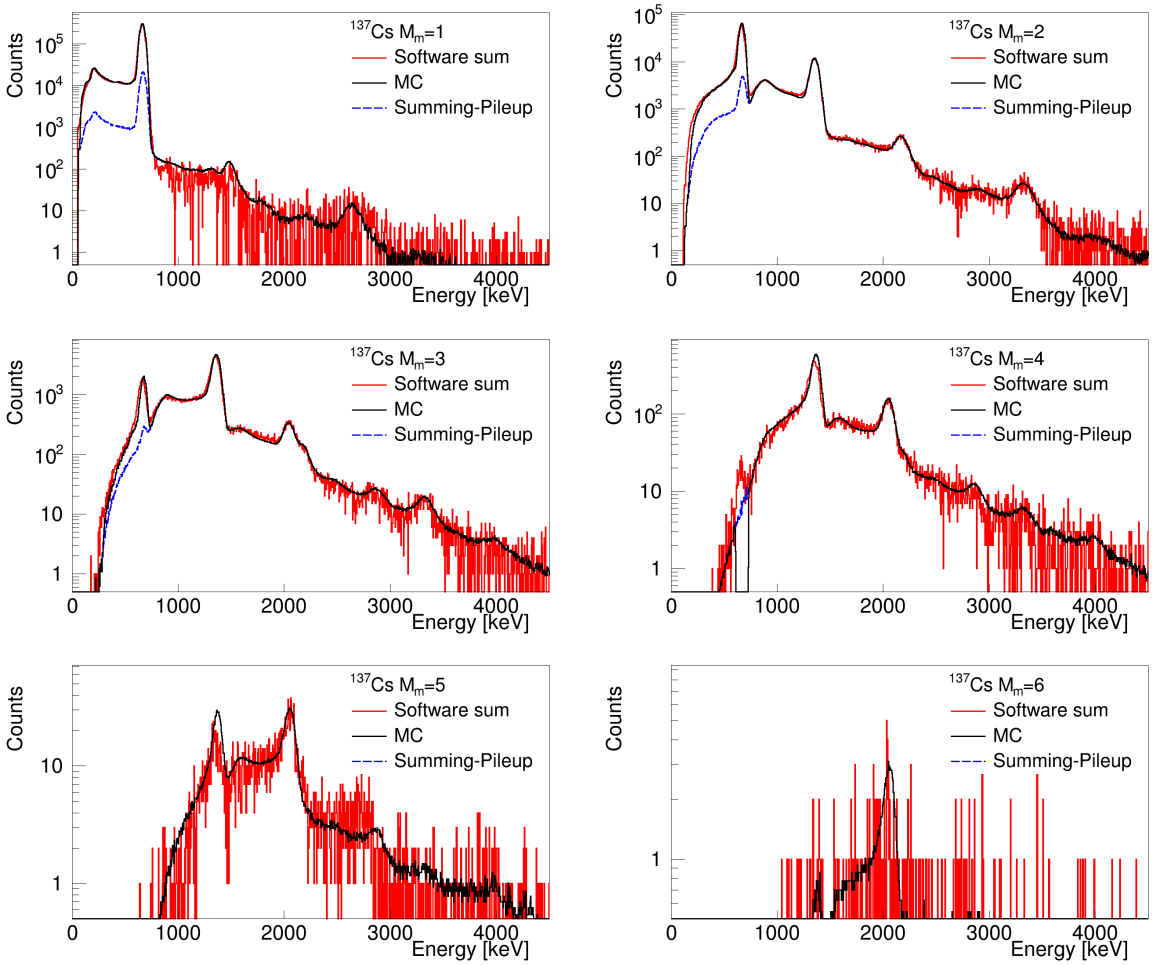

Figure 5.13: ^{137}Cs MC-Experiment comparison for multiplicities 1-6.

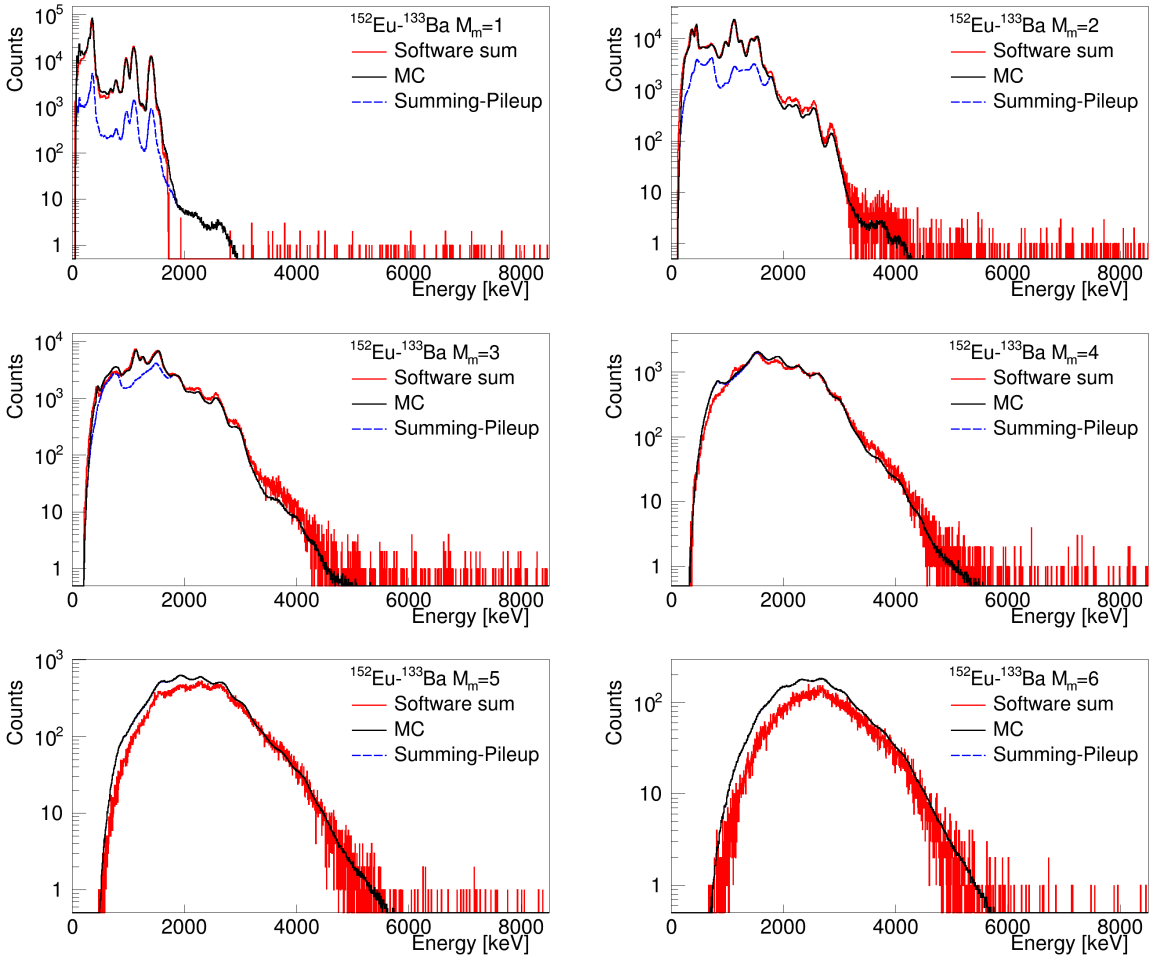

Figure 5.14: ^{152}Eu-^{133}Ba MC-Experiment comparison for multiplicities 1-6.

5.2.6 Neutron simulations

The competition between β-delayed neutrons and β-delayed γ-rays for very exotic neutron rich nuclei, as explained in Chapter 1 Section 1.3.2, will be a difficulty for DTAS. In this case neutrons will also interact with the scintillator crystals producing γ-rays, either in an inelastic reaction or after neutron capture. The γ de-excitation after the neutron decay will be indistinguishable from decay γ-rays. For this reason, it is critical to be able to reproduce this neutron contribution that will play an important role as a contaminant in the TAGS deconvolution procedure explained in Chapter 2. As a result of the interaction of neutrons with DTAS, a peak at 6.83 MeV can be observed in Figure 5.15 which comes from neutron capture in the ^{127}I of the NaI(Tl) crystals, while below 2 MeV inelastic interactions dominate. On the other hand, this neutron capture peak gives us the possibility to improve our energy calibration at high energies by including it in the calibration as in Section 4.3.3 of Chapter 4.

This contribution can be evaluated with MC simulations, following the line of previous works [32,73,74,182]. In these works, instead of using the standard γ-ray cascade generator of Geant4, which uses the often incomplete information from the nuclear databases, it is

replaced by a generator that uses the statistical model in order to be able to describe realistically the multiplicity and energy distribution of neutron capture γ-cascades [182]. For the present simulations we have used the library ENDF-VII0 converted into the G4NDL data format [183].

The capability of the MC to reproduce the neutron interaction with DTAS was confirmed by studying some cases of β-delayed neutron emitters of interest measured at IGISOL. In particular, we have simulated three decays: the decay of ^{137}I, with Q_β=6.027 MeV and S_n=4.025 MeV, the decay of ^{138}I, with Q_β=7.992 MeV and S_n=5.660 MeV, and the decay of ^{95}Rb, with Q_β=9.2286 MeV and S_n=4.348 MeV. An event generator was implemented [74] that reproduces the neutron spectra obtained from the ENDF/B VII.1 database, based on the thesis of M.C. Brady [184]. The generator reproduces the known sequence β-neutron-γ in the decay. This requires the reconstruction of the β-intensity distribution from the measured neutron spectra and using the information on neutron branchings into the excited levels in the final nucleus, I_n, and the associated γ-branchings, I_γ, retrieved from ENSDF [150]. As a result, the shape of the neutron capture peak was reproduced for each of the cases, as can be seen in Figure 5.15 for the β-gated experimental measurements of the three decays mentioned, confirming the potential of MC simulations to evaluate this contamination. In the simulation a time window for accumulation of the energy deposited by the multiple neutron interactions was applied. This window takes into account the delay between neutron induced γ-rays and the prompt decay γ-rays. We found that a window of 0.4-1 μs between the β-detector and DTAS gives the best reproduction of the spectra.

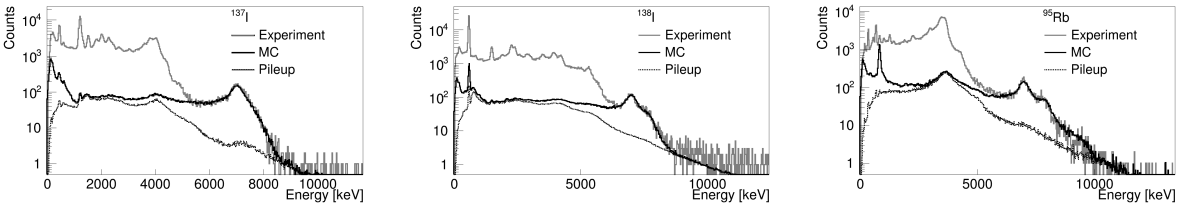

Figure 5.15: Neutron simulations for the β-delayed neutron emitters measured in the commissioning of DTAS at IGISOL, ^{137}I, ^{138}I and ^{95}Rb. Experimental β-gated spectra (in grey) and the simulations of the response of DTAS to the β-delayed neutron emission (in black) are shown. The summing-pileup contribution (dotted lines) is taken into account for the normalization.

The interaction of the ambient neutron background (with the accelerator off) with DTAS has been also studied. For this, the cosmic ray induced neutron spectra measured at PTB (free-in-air) from [185] was used, and the resulting comparison of the MC with the experiment can be seen in Figure 5.16 left. In this case the time window for energy deposition was set to 6 μs which is equal to the ADC gate length, since there is no β-coincidence requirement. This difference in time with respect to the β-gated cases, implies that neutrons interacting with DTAS within the β-gated window are in proportion faster than in a larger window, since they have less time to moderate. As a result the position of the neutron capture peak is shifted to higher energies in β-gated spectra, as shown in

the experimental spectra comparison of Figure 5.16 right.

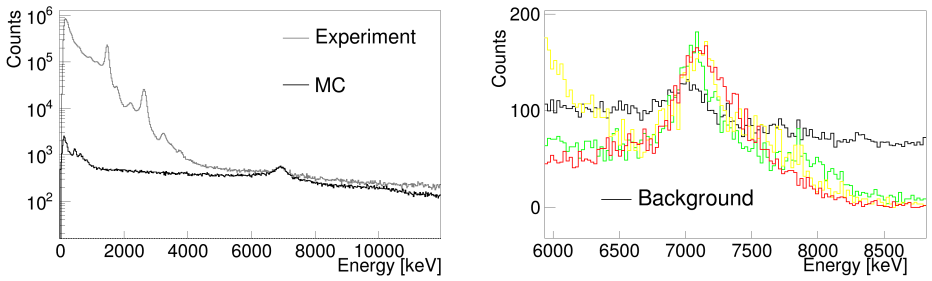

Figure 5.16: Neutron simulations of the interaction of the environmental neutron background distribution with DTAS (left), and comparison of experimental neutron background spectrum (black) and β-gated spectra (red, green, yellow) for β-delayed neutron emitters (right).

5.3 Plastic β-detectors

In β-decay experiments, β-detectors are frequently used in coincidence with neutron and/or γ detectors in order to clean the measurement by selecting only the events coming from the decays. This method of rejecting the background has been traditionally applied mainly with silicon detectors and plastic scintillator detectors. For this reason, together with the DTAS detector, as it was described in section 4.3, a plastic scintillator β-detector was used at IGISOL to clean the measurements by requiring β-γ coincidences. In particular, as previously mentioned, a different β-detector was used in each of the two experiments.

In the case of a TAGS analysis it is also crucial to know accurately the β-detection efficiency, which depends strongly on the endpoint energy of the β-branches, affecting the β-gated spectrometer response. Because of the continuum nature of β radiation, the low energy noise discrimination threshold results in a large variation of efficiency over a wide endpoint energy range. Therefore, it turns out to be important to reproduce with simulations the β-detector experimental measurements in order to identify the threshold, and calculate adequately the β-efficiency.

The first step in the characterization of the β-detector is to include thoroughly the geometry in the Geant4 code. This work was already done for the DTAS simulations, since all the material of the set-up affects the responses calculated for a TAGS analysis. Both β-detectors were used with the same PMT. The geometry of the PMT was included following the data sheet description [186] and the information provided by Hamamatsu [187]. The photocathode structure and estimated thickness of the dead material were based on Chapter 7 of reference [188]. The geometry implemented in the MC code for the two detectors is depicted in Figures 5.17 and 5.18.

The detectors were characterized with a a set of calibration sources (^{22}Na, ^{60}Co and ^{24}Na), as well as with the measurements of the decays studied in the experiments. In the first experiment, the sources were placed at the bottom of the vase-shaped detector, held by a cylinder of 3M reflector material introduced inside the detector. During the exper-

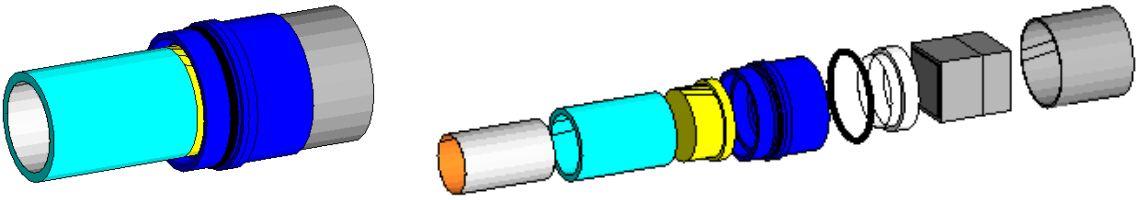

Figure 5.17: Geometry of the cylindrical plastic β-detector included in the MC simulations. General view (left) and separated components (right) are shown. The following elements are depicted: scintillator material (light blue), light guide (yellow), aluminium support (dark blue), o-ring (black), internal plastic holder (white), PMT plus PMT plastic holder (grey), and aluminized-mylar internal reflector (light grey and orange).

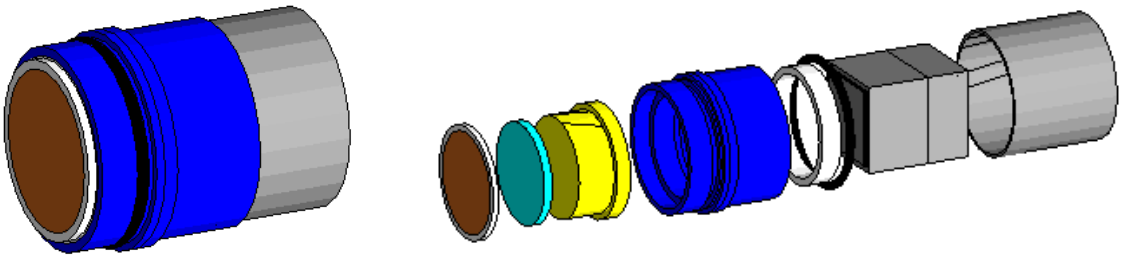

Figure 5.18: Geometry of the plastic disk β-detector included in the MC simulations. General view (left) and separated components (right) are shown. The following elements are depicted: scintillator material (light blue), light guide (yellow), aluminium support (dark blue), o-ring (black), internal plastic holder (white), PMT plus PMT plastic holder (grey), and aluminized-mylar frontal reflector (light grey and orange).

iment, nuclei were implanted on the aluminized-mylar reflector that covered the bottom of the detector. In the simulations, the internal aluminized-mylar cover is included, as well as the 3M reflector cylindrical support that was used to hold the sources. The 3M reflector composition was estimated based on the details given in [189]. In the second experiment, sources were placed onto a circular piece of aluminized-mylar reflector hold by an aluminium ring. During the experiments, as will be explained in Chapter 6, nuclei were implanted on a tape, and the aluminized-mylar reflector was maintained in front of the detector. This piece is also included in the MC, as shown in Figure 5.18.

5.3.1 Experiment 1

When a β-γ coincidence condition is required the statistics is reduced, since the total efficiencies of the two kind of detectors -close to 100% for DTAS, as shown in Figure 5.5- have to be multiplied by the corresponding efficiency of the β-detector. For this reason, it is important to maximize the β-detection efficiency in order to maximize the statistics. A simple and convenient way to maximize the β-detection efficiency, minimizing at the same time the γ sensitivity, is to build a hollow cylinder of thin plastic scintillator material surrounding the source [190–192]. Closing one end of the cylinder with scintillator

material is a practical way to allow the attachment of a photomultiplier tube (PMT) for light readout, while leaving the other end free for transporting the radioactivity inside the detector. This geometry resembles the shape of a vase and can have a geometrical efficiency close to 100% for sources at the bottom of the vase. This is the origin of the design of the β-detector used in the first experiment. It was built for experiments in conjunction with DTAS [32] and BELEN [193], aimed at the study of the decay of exotic nuclei, where the production of the isotopes of interest is low, thus the maximization of the efficiency is a critical requirement.

However, a detector with such a geometry has a different response depending on the interaction point of the β-particle. This is related to the different light collection efficiency for interactions in the lateral walls of the cylinder and in the bottom, where the PMT is coupled. This effect entails a reduced amount of light collected in the photocathode of the PMT from the lateral walls with respect to the bottom. As a result, the shape of the recorded β-spectrum is modified, and also makes it difficult to quantify the threshold. This affects dramatically the efficiency curve of the β-detector, as already mentioned. Therefore the quantification of the efficiency as a function of the endpoint energy cannot be done on the basis of the energy deposited in the detector alone, as we will see, and has to take into account the generation and transport of the light in the detector.

The task of simulating the light response includes the production in the scintillator material and the transport of the resulting photons until they are absorbed in the photocathode of the PMT. The properties of the scintillator were taken from the EJ200 data sheet [194]: scintillator yield of 10 photons/keV, fast time constant of 0.9 ns and a refraction index of n=1.58. The refraction index of the PMMA and the PMT glass window were set to 1.49 and 1.47 respectively. It is of great importance to define properly the optical interfaces in Geant4 [195,196], since the result of the simulation is sensitive to the properties of the optical interfaces between the different materials [197]. We defined as dielectric-dielectric all the surfaces where we expected transmission and as dielectric-metal all those where we expected reflection (in our case the interface between the plastic and the aluminized-mylar). All the surfaces were assumed to be polished. The reflectivity of the reflector was set to 1. In order to count the number of photons collected in the photocathode, i.e. photons that suffer an absorption process there, we assigned to the photocathode a constant absorption length of 10^{-9} m.

We compare in Figure 5.19 the experimental spectrum with the simulation of the energy deposited and of the light collected, both for calibration sources (^{60}Co, ^{22}Na and ^{24}Na) and for the ^{100}Tc decay. We have used the DECAYGEN event generator [146] to simulate the primary particles of the decays according to the information available (γ and β-intensities, branching ratios, etc). MC spectra have been represented in experimental channels by applying a linear calibration in order to be able to perform a comparison with energy and light simulations at the same time. The calibration factor has been chosen to fit the low energy region up to about 500 experimental channels, whereas a normalization factor is used to match the number of counts. As can be observed, while the simulated energy distribution fails to reproduce the measured spectrum, the simulated light distribution matches the

experiment well, especially at low energies, where we are interested in identifying the threshold as will be explained later. In particular, a low energy bump can be distinguished coming from the interaction of the β-particles in the lateral walls of the detector. Only a small fraction of the light produced there reaches the PMT, thus producing the bump. The higher part of the light distribution above this bump is largely due to the interactions in the bottom of the vase.

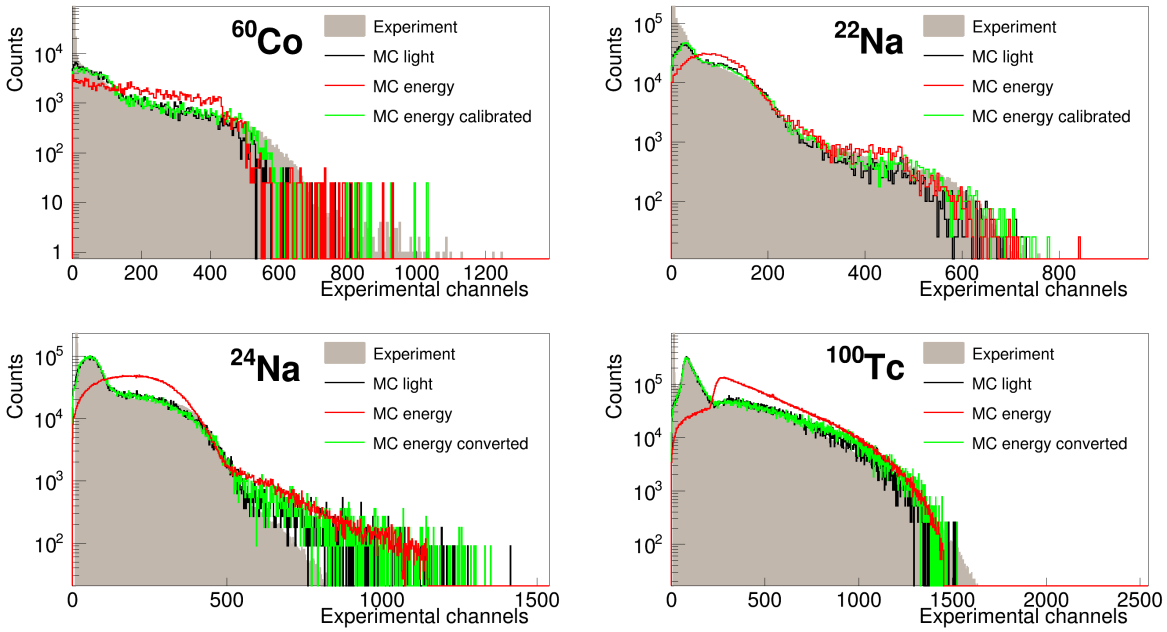

Figure 5.19: Comparison between the experimental and the MC spectra for ^{60}Co, ^{22}Na, ^{24}Na and ^{100}Tc. Experiment (grey filled) is compared with simulations of energy deposited (red), light collected (black), and energy deposited converted into light with the procedure explained in the text (green).

Apart from all the uncertainties in the optical parameters needed for the simulations with optical photons, an important issue is that they are computationally very demanding. We needed 17 hours of CPU time to perform a 10^5 events simulation with optical photons in an Intel Core i7-4770 CPU @ 3.40 Hz $\times$ 8 Mb cache with 15.6 GB memory and 8 threads, in contrast to the 50 seconds for a 10^5 events simulation of the energy deposited. This introduces a disadvantage for the particular case of the TAGS technique, since systematic β distribution simulations have to be performed up to the Q_β of the decay to construct the response function of the spectrometer, as described in Chapter 2. For this reason a method of avoiding the simulation of optical photons has been developed. This method is based on a relationship found between the energy deposited at different locations in the scintillator material and the light collected in the photocathode. As can be seen in Figure 5.20, when we plot light collected versus energy deposited for the ^{100}Tc simulation, most of the points lie in two well separated regions, depending on whether the energy is deposited in the bottom of the detector or in the lateral walls. These regions show a nearly linear dependence.

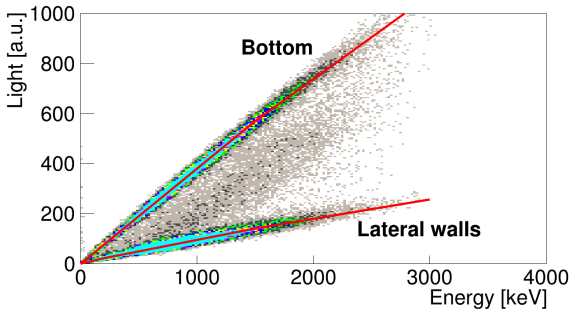

Figure 5.20: Simulation of the light collected vs. energy deposited for the cylindrical plastic detector in the ^{100}Tc measurement. Two different regions are distinguished and the calibration curves with the parameters from Table 5.3 are represented in red. The events in between both regions correspond to a 10% of those coming from the bottom, where less light than expected is collected.

This relationship enables us to reproduce the experimental spectra just with the information of the energy deposited and the interaction point. For this we consider two functions, one for the energy deposited in the bottom and the other for the lateral walls. Each of these two functions, in turn, consists of a piecewise function with two quadratic regions:

$$L = \begin{cases} a_1 + b_1 E + c_1 E^2 & , \quad E \leq k \\ \\ a_2 + b_2 E + c_2 E^2 & , \quad E > k \end{cases} \tag{5.2}$$

where L is the light, E the energy and k the energy value that separates both regions, where continuity is required.

The calibration coefficients obtained for Equation 5.2 in the case of the lateral walls and of the bottom of the detector, are reported in Table 5.3, and they correspond to the red lines drawn in Figure 5.20.

Part	a_1 [a.u]	b_1 [a.u. keV^{-1}]	c_1 [a.u. keV^{-2}]	k [keV]	a_2 [a.u.]	b_2 [a.u. keV^{-1}]	c_2 [a.u. keV^{-2}]
Lateral	0.0	0.1	0.0001	150	2.3625	0.1	-0.000005
Bottom	0.0	0.38	0.0	1500	22.5	0.38	-0.00001

Table 5.3: Energy-light calibration parameters for the lateral walls and the bottom of the cylinder following the Eq. 5.2. The parameter k separates two different energy regions.

In order to apply the conversion procedure it is not enough to use the calibration coefficients in Table 5.3. We explain, with the help of Figure 5.21, the different steps necessary to reproduce the light collection simulation with energy deposited. This figure shows a simulation of 10^4 events of mono-energetic electrons of 1 MeV interacting with the cylindrical detector. First, we use the calibration coefficients from Table 5.3 to convert

energy into light. As already mentioned, it does not reproduce light simulations, as can be seen in Figure 5.21 (a). Second, a Gaussian spread, empirically found to be proportional to $E^{3/4}$, is introduced, as shown in Figure 5.21 (b), in order to reproduce the width of the peaks produced by the interaction of the mono-energetic electrons. Finally, for 10% of the events interacting with the bottom of the detector we introduce a random loss of light collected. This corresponds to events in between both regions in Figure 5.20. For this, we change the slope of the calibration with a random linear interpolation between the slope of the bottom and the slope of the lateral walls. It improves the comparison with light simulations, as can be seen in Figure 5.21 (c). The result of following these steps, combining the calibration in Table 5.3 with the corrections explained here, is good agreement between light simulations, energy simulations converted to light, and experimental measurements, as can be observed in Figure 5.19 for both the calibration sources and the ^{100}Tc decay.

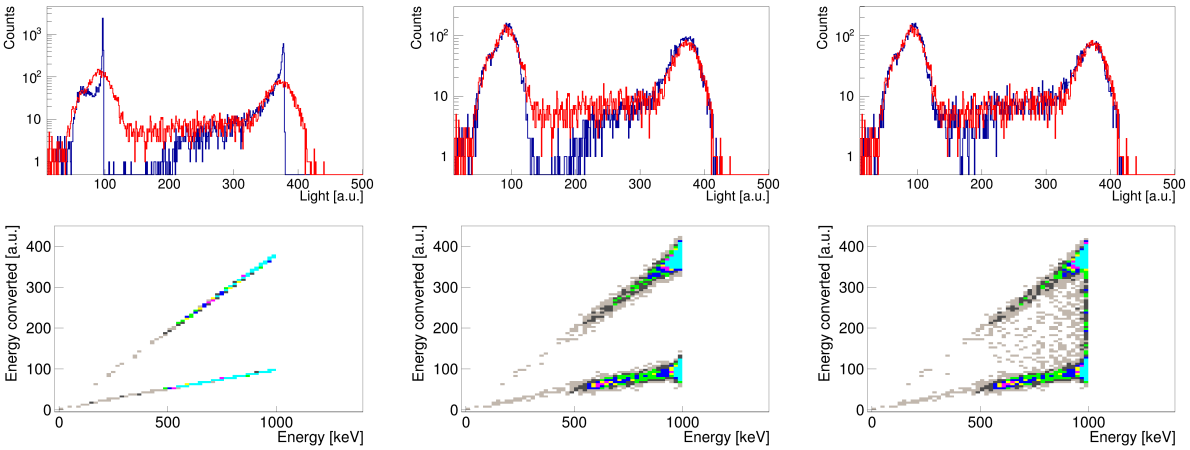

Figure 5.21: Figures (a), (b) and (c) represent different steps necessary to reproduce the simulated light collection with the results of the simulated energy deposition (for more details see the text). In the upper panel the simulation of optical photons (black) is compared with the energy converted into light (grey) for mono-energetic electrons of 1 MeV interacting with the detector. The lower panel shows the corresponding relationship between energy converted into light and energy deposited for this case.

In order to apply this procedure to calculate the β-responses for a TAGS analysis, we have to convert the threshold in signal amplitude, or equivalently in light collected, into a threshold in energy, according to the calibration in Table 5.3. A threshold value in light of 11 a.u. set just above the noise has been identified by comparison with experimental measurements in Figure 5.22, where the low energy region of the spectra in Figure 5.19 is shown. Note that light units are used instead of experimental channels in order to carry out this identification process.

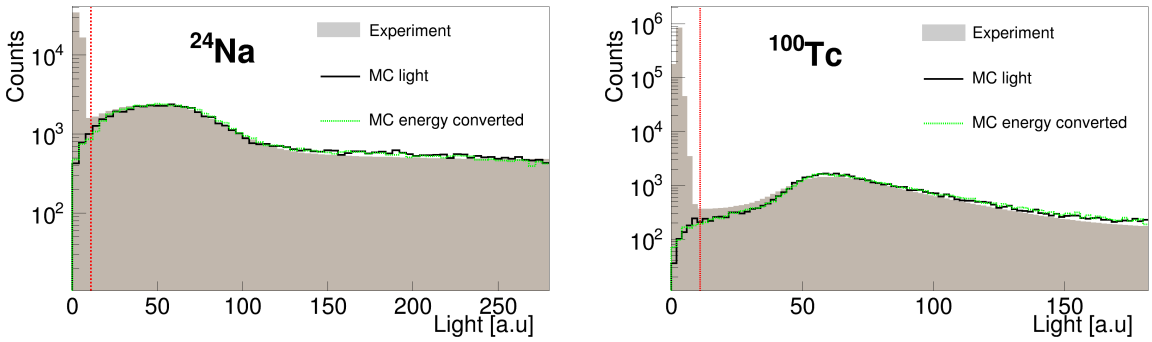

Figure 5.22: Zoom at low energies of the comparison between the experimental and the MC spectra in light units for ^{24}Na (up) and ^{100}Tc (bottom). Experiment (grey filled) is compared with simulations of light collected (solid black), and energy deposited converted into light with the procedure explained in the text (dotted green). The threshold value of 11 a.u is depicted with a vertical dotted red line.

Due to the effect of the different light collection in the two regions of the detector, this threshold corresponds to 29 keV in the bottom, whereas for the lateral walls of the detector it is 96 keV. To verify this equivalence, we simulated four end-points of the ^{100}Tc decay, namely 3203 keV, 2072 keV, 1151 keV and 543 keV, and we calculated the efficiency above this threshold value for the light simulation and for the energy converted into light. Both efficiencies are in very good agreement, as shown in Figure 5.23, with relative differences of $\sim$0.1%.

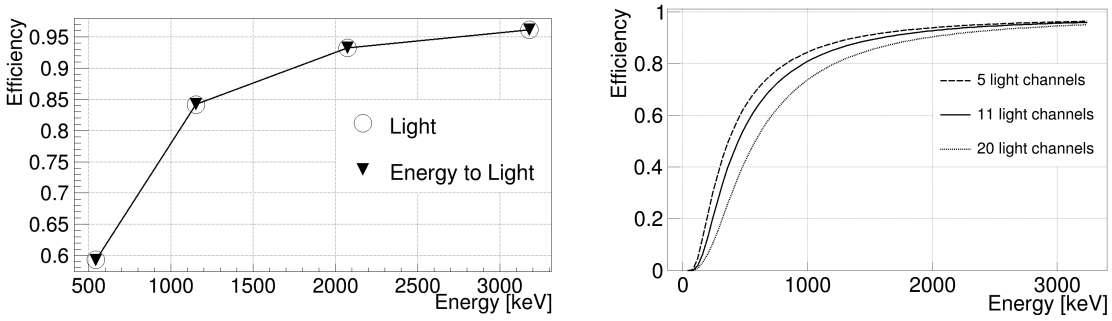

Figure 5.23: Efficiency of the cylindrical plastic detector for different β^- end-points. The results for light simulations (circles) are compared with the calculation using our procedure for converting energy deposited into light collected (triangles).

5.3.2 Experiment 2

Although the geometry of the β-detector in Experiment 2 is more conventional, a study of light simulations was also done in order to validate its behaviour. As a result, it was found that simulations of energy deposited are in agreement with experimental spectra for this case, while simulations of light collected do not improve the situation. The level of agreement achieved can be seen in Figure 5.24. This comparison makes possible to obtain

a calibration in energy for the experimental spectra and to identify the threshold (Table 5.4). For this, the maximum of the mean energy loss peak for the 3 mm thickness disk was used as the reference value (∼590 keV).

Threshold (exp) [channels]	Threshold (E) [keV]	a [keV]	b [keV^{-1}]
70	71	-43/0.38	1/0.38

Table 5.4: Parameters of the beta detector in Experiment 2. The first two values correspond to the threshold of the detector in experimental channels and energy, respectively. The last two columns contain the calibration parameters to convert experimental channels (C) into energy (E): E=a+bC. The intercept of the calibration contains the ADC offset for this channel: ADC$_{offset}$=43.

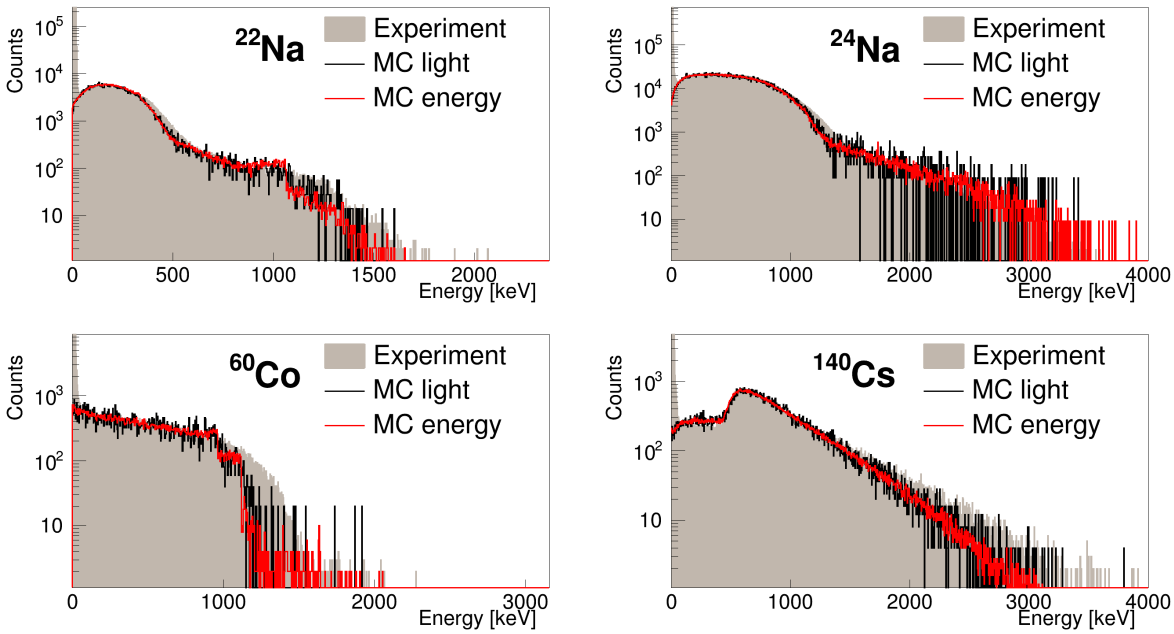

Figure 5.24: Comparison between the experimental and the MC spectra for ^{60}Co, ^{22}Na, ^{24}Na and ^{140}Cs. Experiment (grey filled) is compared with simulations of energy deposited (red) and light collected (black). Note that energy simulations (red) are performed with 10^6 events, while the rest correspond to 10^5.

Again, it is of great importance to study the efficiency depending on the threshold. For this purpose, we represent in Figure 5.25 the β-efficiency for several values around the threshold of 71 keV deduced from the comparison between the experimental and the MC spectra. For the estimation of the uncertainties in all the analyses presented in Chapters 8, 9, 10, 11, 12, 13, 14, we have studied the influence of a change in the threshold value of ±10 keV. The differences in the β-intensity distributions introduced by this change are small compared with the other sources of systematic uncertainty that will be considered.

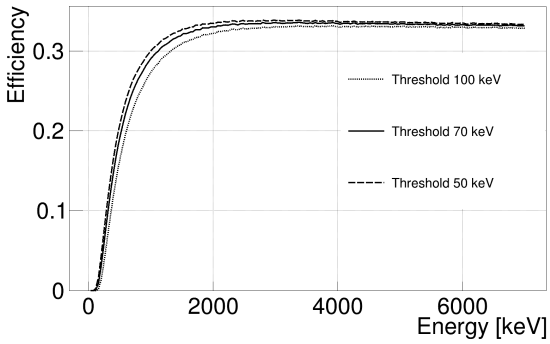

Figure 5.25: Efficiency of the plastic detector in Experiment 2 depending on the threshold.

Part III

Experiments and results

Chapter 6

The experiments

> Solamente hay dos opciones: si el resultado confirma la hipótesis, has hecho una medición. Si el resultado es contrario a la hipótesis, entonces has hecho un descubrimiento
>
> *There are two possible outcomes: if the result confirms the hypothesis, then you've made a measurement. If the result is contrary to the hypothesis, then you've made a discovery*
>
> Enrico Fermi

In the last decade, several TAGS experiments have been performed at the Accelerator Laboratory of the University of Jyväskylä, preceding those described here [25–28]. The reason to work at the ISOL facility IGISOL of Jyväskylä is twofold. First, the possibility to produce refractory elements that can be extracted from the fission ion guide as will be explained in this chapter. Secondly, the great advantage of counting on the help of the double Penning Trap system to purify the beams before doing spectroscopy. In this chapter we will describe the IGISOL facility, as well as the experimental cases of interest that were measured, and we will explain in detail the experimental set-up used for these measurements.

6.1 IGISOL IV

The Ion Guide Isotope Separator On-Line (IGISOL) technique has been used for nuclear structure studies since the 1980s. Over the years it has experienced several upgrades [198] until the current phase IGISOL-4 [199]. In fact, the last upgrade meant a movement to a new building, in order to gain space for experimental set-ups, improve the access with laser beams to the target area and take advantage of the new MCC30/15 cyclotron. Nowadays, IGISOL-4 looks as in Figure 6.1. The two beam lines corresponding to the two available accelerators are depicted: the one corresponding to the K=130 heavy-ion cyclotron (up to 130 MeV), and the new MCC30/15cyclotron, which accelerates protons (18-30 MeV) and deuterons (9-15 MeV). Both accelerators deliver beams to the IGISOL target chamber, where the reactions of interest are produced. A beam dump is placed behind the reaction

chamber. From this point onward, the extraction and purification capabilities of IGISOL are exploited, as will be explained below.

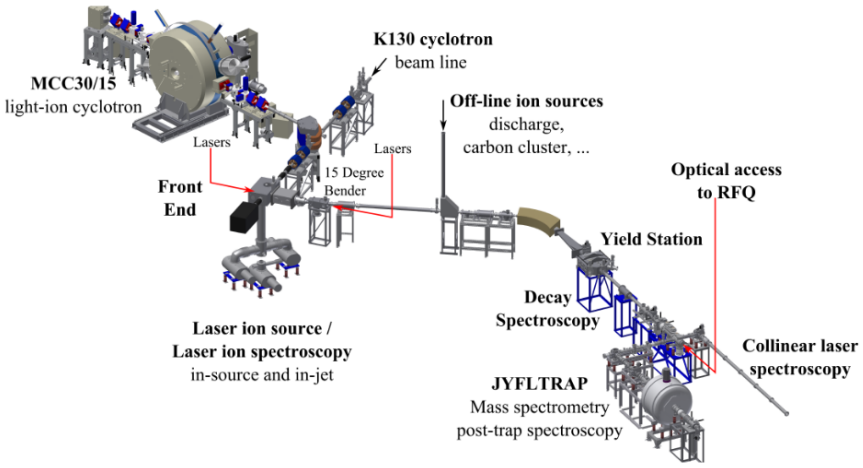

Figure 6.1: Layout of the IGISOL facility. From [200].

6.1.1 Fission Ion Guide

The Fission Ion Guide technique is based on the survival in helium buffer gas of primary ions from fission. A schematic view of the procedure is presented in Figure 6.2. The fission process is produced in the reaction chamber by protons impinging on a natural uranium target of 7.9 μm at 7 degrees with respect to the direction of the beam. Here we will just concentrate on proton induced fission, which was the technique used in this work, however, the new MCC30/15 cyclotron is planned to be used to convert high intensity proton beams into neutrons for neutron-induced fission studies. The primary recoil ions generated in the fission process are thermalized in helium, where they recombine to form singly charged ions, and then they are transferred by a helium flow through a differential pumping system into the mass separator. This differential pumping system consists of a sextupole ion guide (SPIG) that gathers the fission products in the direction of the axis, and accelerates them by static potentials. After that, ions are extracted and accelerated in steps up to 30 kV, and they are driven to the mass separator where the extracted ions are mass-separated with a 55° dipole magnet with a mass resolving power $R = M/\Delta M$ =500.

The helium buffer gas is the key feature of this technique, since the extraction process is independent of the chemistry of the elements involved, so that refractory elements can also be extracted. The time scale of this extraction is of the order of milliseconds. As is to be expected, the purity of the gas plays a critical role, and impurity levels below sub-parts-per-billion are required [202]. For this reason a gas purification and transport system is used [199].

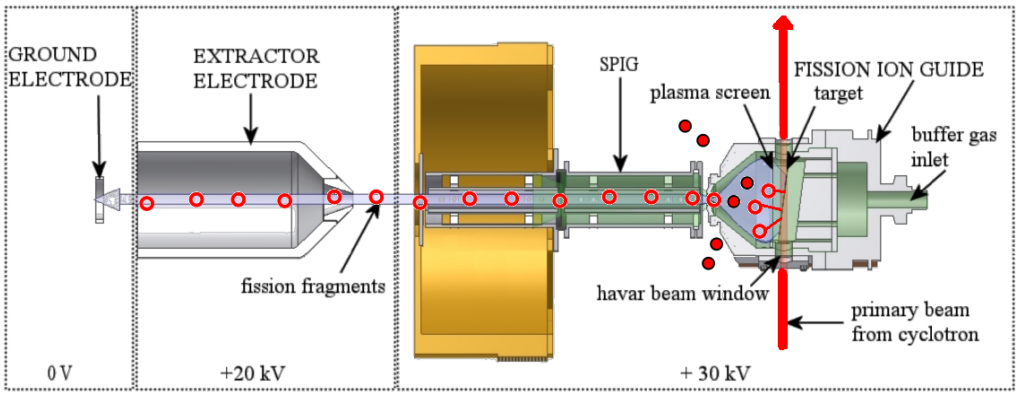

Figure 6.2: Scheme of the technique of the fission ion guide at IGISOL from [201].

6.1.2 JYFLTRAP

JYFLTRAP is an ion trap system available at IGISOL for cooling, bunching and isobaric purification of radioactive ion beams produced in the reaction chamber and separated in the mass separator. It is devoted to mass measurements of stable and radioactive ions, and moreover it can be used as a very high resolution mass separator for post-trap experiments. The system globally consists of two main elements: the ion beam cooler and the double Penning-trap system, and it is depicted in Figure 6.3.

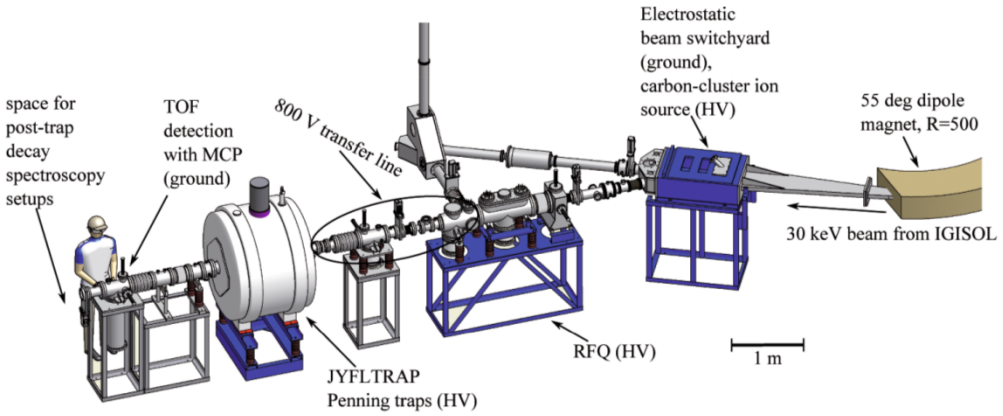

Figure 6.3: Layout of the JYFLTRAP double Penning-trap system. From [203].

Ion beam cooler

The aim of the ion beam cooler is to improve the optical properties of the ion beams for an efficient injection into the JYFLTRAP Penning trap. First, the beam is decelerated with an electrostatic lens system and injected into a closed radio frequency quadrupole (RFQ). The RFQ confines ions in the radial direction by applying a high frequency quadrupole field. The axial confinement is achieved by static electric potentials. The RFQ is filled with helium buffer gas at low pressure, so that ions lose energy in collisions with atoms. It represents a fast cooling method that is also independent of the physical and chemical

properties of the ions. The deceleration down to 100 eV can be achieved with a three electrode deceleration stage that also acts as a differential pumping system. Once they are cooled, they are collected in a potential well and they are extracted periodically from the RFQ to the Penning traps (or to the collinear laser spectroscopy station, instead) with an energy spread of $\sim$1 eV and a temporal spread of $\sim$15 μs.

Penning traps

Penning traps are devices that use electric and magnetic fields to confine and store ions in vacuum. A charged particle that moves in a homogeneous magnetic field, assumed to be along the z direction, describes cyclotron oscillations with frequency $\omega_C = \frac{qB}{m}$, where q is the charge of the ion and m its mass. This circular movement confines the ions in the plane orthogonal to the magnetic field. The Penning trap technology is based on the superposition of a static quadrupolar electrostatic potential along the field lines to avoid ions escaping, thus confining them. The electric potential used for JYFLTRAP [203] is presented in (x, y, z) coordinates in Equation 6.1.

$$\Phi(x, y, z) = \frac{U_0}{4d^2}(2z^2 - x^2 - y^2) \tag{6.1}$$

This potential can be generated by three hyperbolic electrodes: a central one and two at the endcaps, as represented in Figure 6.4 (however, in the case of JYFLTRAP all electrodes are cylindrical, because they are easier to manufacture and they allow a better vacuum [203]). U_0 is the positive potential difference between the central electrode and one electrode of the endcap, and d is a characteristic distance of the trap $d = \sqrt{2z_0^2 + r_0^2}$ (approximately half of the distance between both endcap electrodes), r_0 being the inner radius of the central electrode, and $2z_0$ the distance between the endcap electrodes.

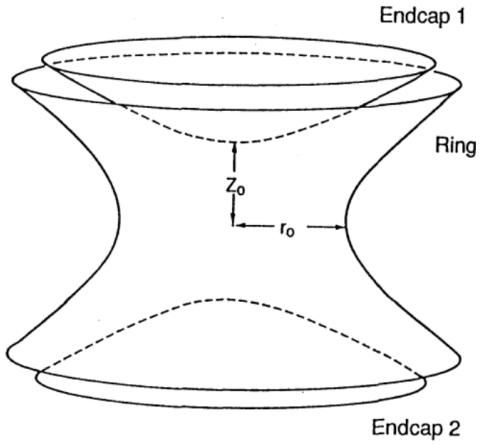

Figure 6.4: Scheme of a Penning trap from [204].

The total force experienced by the ions moving in the trap, is the combination of the magnetic force due to the magnetic field, and the electric force created by the potential Φ:

$$\overrightarrow{F} = \overrightarrow{F}_m + \overrightarrow{F}_e = q\overrightarrow{v} \wedge \overrightarrow{B} - \overrightarrow{\nabla} q\Phi \tag{6.2}$$

Newton's equation for coordinate z is a simple harmonic oscillator, with the frequency ω_z presented in Equation 6.3. This frequency corresponds to one of the three different eigenmotions for charged particles in the trap; in particular this is associated with the motion along the magnetic field lines, the so called axial motion, and the frequency is known as the axial frequency.

$$\omega_z = \sqrt{\frac{qU_0}{md^2}} \tag{6.3}$$

The remaining two eignemotions, known as radial motions, correspond to modes in the plane perpendicular to the magnetic field. They are obtained by diagonalizing Newton equations for components x and y. The two solutions of the resulting differential equation are presented in equation 6.4. The negative solution is known as the magnetron frequency, and is almost independent of the mass, whereas the positive one corresponds to cyclotron oscillations perturbed by the quadrupolar potential and is known as the reduced cyclotron frequency.

$$\omega_+ = \frac{\omega_C}{2} + \sqrt{\frac{\omega_C^2}{4} - \frac{\omega_z^2}{2}} \qquad \text{and} \qquad \omega_- = \frac{\omega_C}{2} - \sqrt{\frac{\omega_C^2}{4} - \frac{\omega_z^2}{2}} \tag{6.4}$$

The sum of the square of the three characteristic frequencies gives the Brown-Gabrielse invariance theorem relationship [205]:

$$\omega_c^2 = \omega_-^2 + \omega_+^2 + \omega_z^2 \tag{6.5}$$

The confinement of the ions is ensured only if all frequencies are real numbers, and it establishes a minimum value for the magnetic field: $B^{>}|\frac{2mU_0}{qd^2}|$.

The movement of an ion in a Penning trap results in a superposition of the three eigenmodes, as depicted in Figure 6.5.

In the case of JYFLTRAP, two cylindrical Penning traps are placed inside the same 7 Tesla superconducting solenoid. The relative homogeneity of the magnetic field created by the solenoid is $\Delta B/B \simeq$0.4 ppm [203]. A schematic view of the two traps, the purification trap and the precision trap, is shown in Figure 6.6. The operation of the trap consists of applying RF signals to different trap electrodes in order to manipulate the three eigenmodes explained above. For example, dipolar excitations can be used to excite the magnetron frequency ω_- or the reduced cyclotron frequency ω_+ without affecting the other two modes, in order to move the ions away from the centre by enlarging the radius of the motion.

The purification trap is the closest to the RFQ, it is filled with helium gas and used for isobaric purification of the beam. In this trap, the magnetron frequency is excited with multipole RF fields applied typically for 10 ms, increasing the radius of all ions to more than 1 mm so that after extraction no ion could pass trough the narrow electrode (2 mm) restricting the gas flow between the two traps [203]. After the magnetron excitation, a quadrupole RF field excites the cyclotron frequency ω_C of the ions of interest, moving them back to the centre of the trap, due to the conversion of the magnetron motion into a cyclotron motion, which is cooled much faster in the presence of a buffer gas. A mass

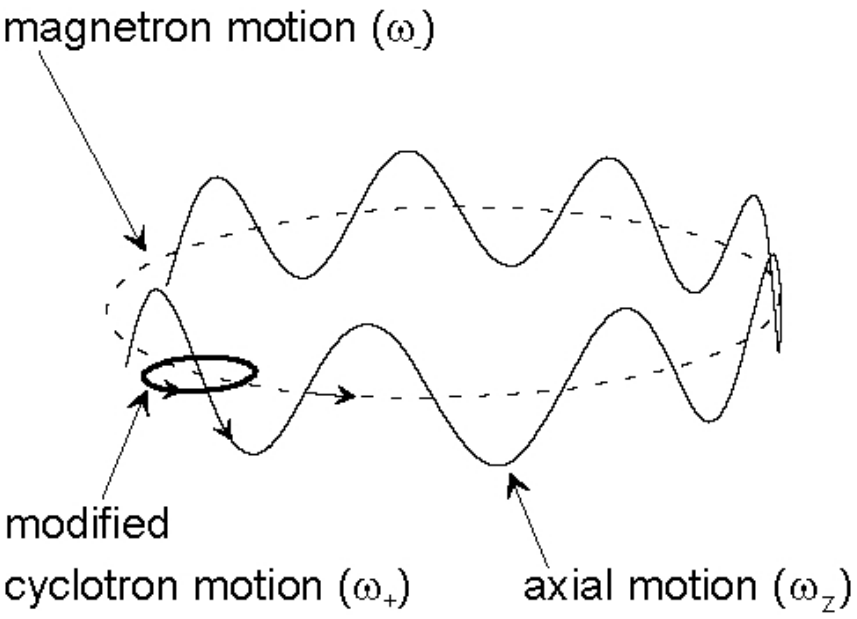

Figure 6.5: Superposition of motions in a Penning trap from [206].

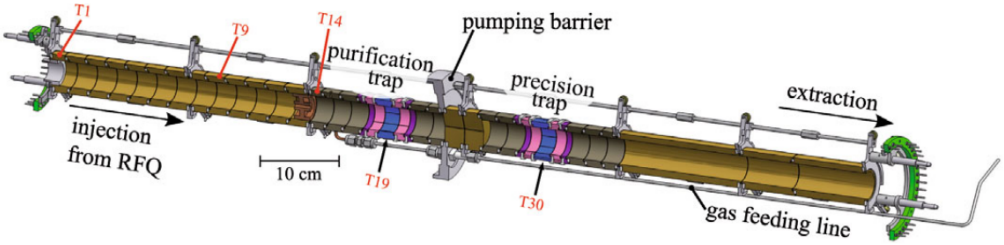

Figure 6.6: Scheme of the JYFLTRAP double Penning-trap. From [203].

resolving power $M/\Delta M \sim 10^5$ has been achieved with this trap [203].

The precision trap (geometrically equivalent to the previous one), is devoted to high precision mass measurements, as well as for high resolution beam purification with $M/\Delta M \sim 10^6$ [203]. This high resolution cleaning can only be applied after a pre-purification with the purification trap. For this, the strategy consists of leaving the ions of interest unexcited while exciting the contaminant ions with a RF field using the Ramsey method [207], increasing their cyclotron orbit. Ramsey technique employs a short RF pulse (20-50 ms) followed by a waiting period which depends on the half life of the ion of interest, and again the RF pulse with the same duration [203]. The ion bunch is sent back to the purification trap in order to be re-cooled and re-centred. During this process, the ions of interest gain some cyclotron motion. When they are centred again, the bunch is sent to the precision trap for extraction to decay spectroscopy experiments.

6.2 Experimental set-up

The experimental campaign performed in 2014 with the DTAS detector covered two experiments, Experiment 1 (I153) [208] and Experiment 2 (I154) [209], and took place between 6th February and 6th March 2014. The experimental set-up was placed after JYFLTRAP, in the post-trap spectroscopy area, as can be seen in Figure 6.7 (a) in order to take advantage of the purity of the beams provided by the Penning traps system. As described in Chapter 4 and shown in Figure 6.7 (b) and (c), the set-up consisted of: the DTAS detector in the 18-module configuration, a plastic β-detector, a HPGe detector, and a tape transport system for Experiment 2. A discussion of the two different plastic detectors used, one for each experiment, as well as pictures of them, were presented in Section 4.3 from Chapter 4. It has to be noted that two aluminium collimators were used after the trap, the closest to the trap with 10 mm, and the closest to the endcup with 5 mm diameter (this last one shown in Figure 6.7 (d)).

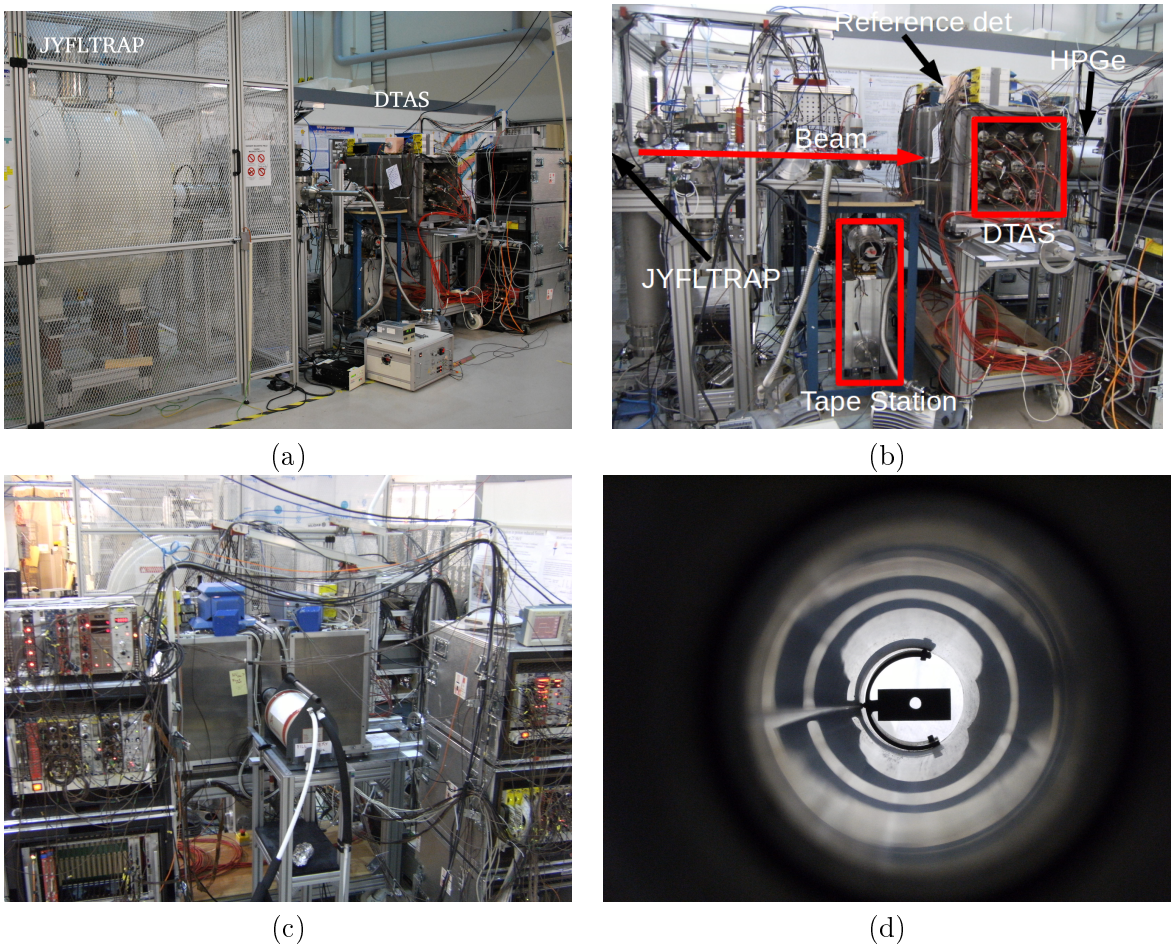

(a) (b)

(c) (d)

Figure 6.7: Complete set-up of DTAS experiments at IGISOL. In (a) the placement of the set-up with respect to JYFLTRAP can be seen. A lateral view of the set-up is presented in (b) with the main elements highlighted. A frontal view of the set-up is shown in (c) and a picture of the last collimator used in the beam pipe is given in (d).

6.2.1 Electronics

All the details related to the electronic chains for the readout of the detectors and the acquisition of the data are presented in the Appendix A.

6.2.2 Tape station system

A tape transport system was used in the second experiment in order to remove the activity from the set-up. In the first experiment it was not needed, since a decay to a stable nucleus was studied. This tape system was mounted to implant the species of interest in the centre of DTAS, in front of the β plastic detector. In Figure 6.8 left, the first rollers of the tape transport system are shown. They are off axis so that the beam extracted from JYFLTRAP passes between them and is implanted onto the backward side of the tape at the end of the tube shown in Figure 6.8 right, which is the part of the tape transport system placed in front of the β detector at the centre of DTAS.

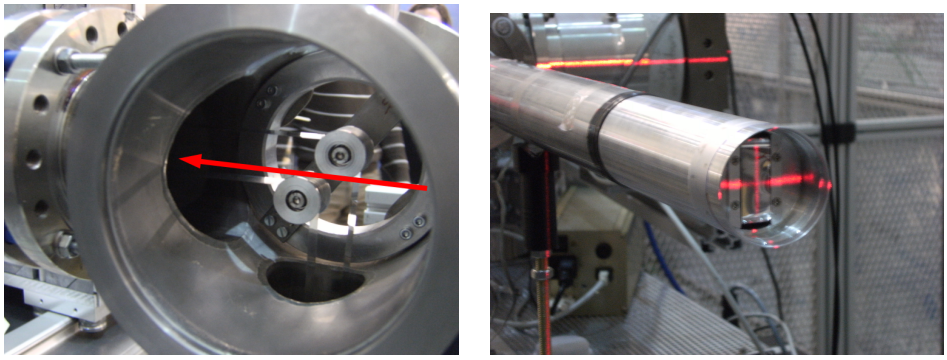

Figure 6.8: View of the tape transport system. Left picture shows the rollers outside the set-up of DTAS (red arrow indicates the direction of the beam), while right picture shows the rollers inside DTAS, close to the endcap, where implantation takes place.

The cycle of the tape system was synchronized with JYFLTRAP and the DACQ. As depicted in Figure 6.9, the cycle started with an implantation waiting time of around $1\times T_{1/2}$ of the decay of interest to check the background level. In the last 0.45 s of this interval the cooling system of JYFLTRAP was loaded. After that, an implantation time period of around $4\times T_{1/2}$ was followed by the tape movement to remove the activity implanted. There is a veto signal for the DACQ of 1.8 s during the movement of the tape. After the cycle, the time stamp values of the DACQ were set to zero. The waiting time, as well as the implantation time were selected for each decay as multiples of 0.45 s, which is the length of the cycles of JYFLTRAP. The last trap-cycle of the implantation time always corresponds to a cycle without cooling in JYFLTRAP.

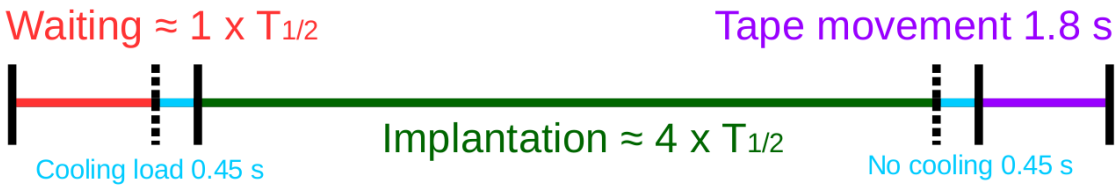

Figure 6.9: Scheme of the tape cycle.

6.3 Experimental measurements

Details of the production of the nuclear species of interest in each of the experiments will be given now.

6.3.1 Experiment 1: (p,n) reaction

The aim of Experiment 1 (I153) [208] was to measure the β-decay of ^{100}Tc into ^{100}Ru in order to improve the experimental knowledge of the double-β decay system of $A = 100$ presented in Chapter 1 Section 1.3.1.

^{100}Tc nuclei were produced from a Mo target (97.42% enrichment of ^{100}Mo) by means of a (p,n) reaction with protons of 10 MeV from the MCC30 cyclotron that were slowed down to 8 MeV with a degrader:

$$\mathrm{p} + {}^{100}_{42}\mathrm{Mo} \rightarrow {}^{100}_{43}\mathrm{Tc} + \mathrm{n}$$

The choice of the energy was based on a study performed with the TALYS nuclear reaction code [155] in the range of 6-15 MeV in steps of 500 keV [210]. In the light of these calculations, 8 MeV was chosen, since at this energy the cross section is maximum for the production of ^{100}Tc, while having a negligible contamination of ^{99}Tc and ^{100}Mo, as shown in Figure 6.10.

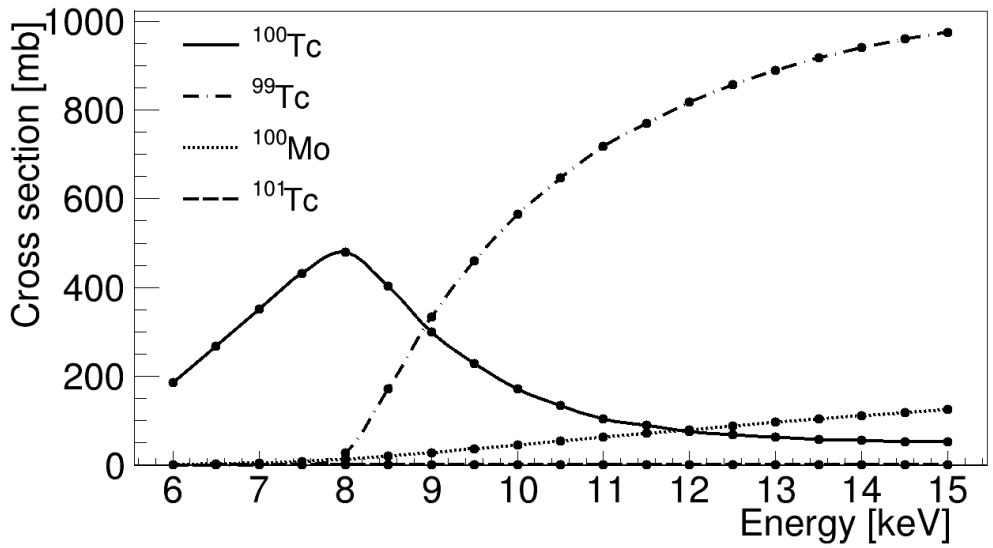

Figure 6.10: Cross section for the ^{100}Mo(p,n)^{100}Tc reaction based on a study performed with TALYS [210].

6.3.2 Experiment 2: proton induced fission reaction

Experiment 2 (I154) [209] was focused on the study of fission fragments of interest for decay heat calculations, antineutrino spectrum calculations and β-delayed neutron emission studies, as explained in Chapter 1.

As described in Subsections 6.1.1 and 6.1.2, the fission process is produced in the reaction chamber by protons impinging on a natural uranium target. Ions are separated in the mass separator, and then the nuclear species of interest is selected with JYFLTRAP. These nuclei are extracted and implanted on the tape according to the cycle chosen for each case, as it was explained in Subsection 6.2.2.

A summary of the main data for each decay is presented in Table 6.1. The table includes the parent half-life and Q_β value, the daughter half-life, and the length of the measuring cycle. Also included is the total time dedicated to each measurement and the average rate of β particles detected. The measuring time is obtained by integrating the 100 Hz light pulser peak for the 18 individual modules and averaging these values. Finally, the counting rate is obtained with the number of β-particles and the corresponding measuring time. The number of β-particles is obtained from the integral of the β spectrum of the plastic detector above the threshold without correcting for pileup and other contaminants (daughter/grand-daughter/grand-parent activity, etc.).

In Figure 6.11 we present plots of the intensity of ions extracted from the JYFLTRAP as a function of the frequency (which is proportional to the ion mass) for each of the experimental settings of JYFLTRAP. These plots show the amount of isobaric contamination and the separation between them. The isotope of interest is selected for extraction by choosing the appropriate frequency. As can be deduced from the figure, this separation has a high degree of purity, except for the cases with isomers, where the mass difference is not large enough to be resolved.

Nucleus	$T_{1/2}$ [s]	Q_β [keV]	Daughter	$T_{1/2}$ [s]	Cycle [s]	Time [s]	Rate [β/s]
^{103}Tc	54.2	2662	^{103}Ru	3.39×10^{6}	13.5 + 120.15	7413.84	58.6
^{103}Mo	67.5	3635	^{103}Tc	54.2	13.5 + 120.15	4146.35	375.3
^{140}Cs	63.7	6220	^{140}Ba	1.1×10^{6}	19.8 + 127.35	12382.9	10.8
^{100gs}Nb	1.5	6386	^{100}Mo	2.24×10^{26}	7.2 + 28.35	2163.74	741.6
^{100m}Nb	2.99	6700	^{100}Mo	2.24×10^{26}	no cycle	12506.5	8.8
^{102gs}Nb	4.3	7210	^{102}Mo	678	2.7 + 4.5	3892.5	164
^{102m}Nb	1.3	7305	^{102}Mo	678	4.5 + 17.1	5511.48	132.6
^{137}I	24.5	6027	^{137}Xe	229.08	24.3 + 99.45	7617.48	135.1
^{95}Rb	0.3777	9228	^{95}Sr	23.9	0.9 + 2.7	5972.33	34

Table 6.1: Measurements of Experiment 2. The cycle is the waiting time plus the implantation time, as explained in Subsection 6.2.2.

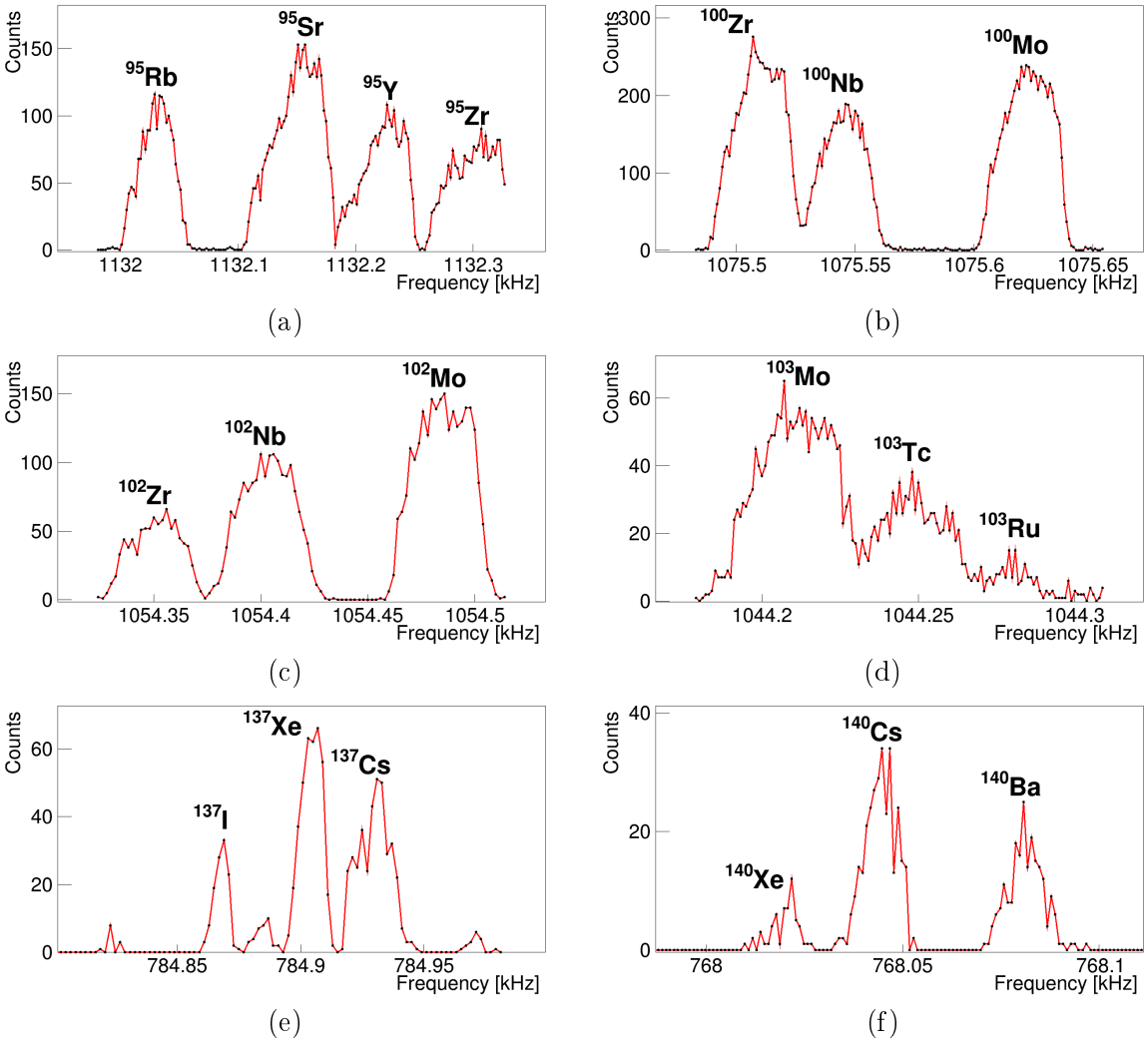

Figure 6.11: JYFLTRAP mass scans of Experiment 2 with DTAS at IGISOL.

Chapter 7

^{100}Tc decay

> La ciencia, hijo mío, está formada por errores, pero por errores que vale la pena cometer, porque conducen poco a poco hasta la verdad
>
> *Science, my lad, is made up of mistakes, but they are mistakes which it is useful to make, because they lead little by little to the truth*
>
> Julio Verne

In this chapter, the β-decay of ^{100}Tc into ^{100}Ru will be discussed. The relevance of this decay for double β-decay studies was presented in Chapter 1 Section 1.3.1. The experimental measurements were described in Chapter 6, and here the TAGS analysis and the results will be presented.

7.1 Experimental spectra

7.1.1 β-gated spectrum

The resulting software sum for the total 21 hours of measuring time corresponding to 96 experimental runs, is presented as the blue line in Figure 7.1 left, and it is dominated by the environmental background. In order to clean the spectrum and select only those events coming from the β-decay, coincidences with β-particles were required, as shown by the red line in Figure 7.1. For this purpose we used the vase-shaped plastic detector presented in Chapter 4. The β-spectrum and the efficiency curve of the detector were presented in Figures 5.19 and 5.23 in Chapter 5 respectively. Due to the geometry of this detector, a careful characterization with MC simulations using optical photons was needed in order to understand and reproduce the shape of the resulting β-spectra and calculate accurately how the β-efficiency depends on the β-end point energy, as described in Section 5.3.1 of Chapter 5.

The β-γ coincidence condition requires that both DTAS and plastic detector signals are above the respective noise discrimination thresholds. In addition, their timing signals are also taken into consideration. For this, a TAC-like spectrum (TAC: time-to-amplitude-converter) is constructed between the global timing signal of DTAS (obtained from the

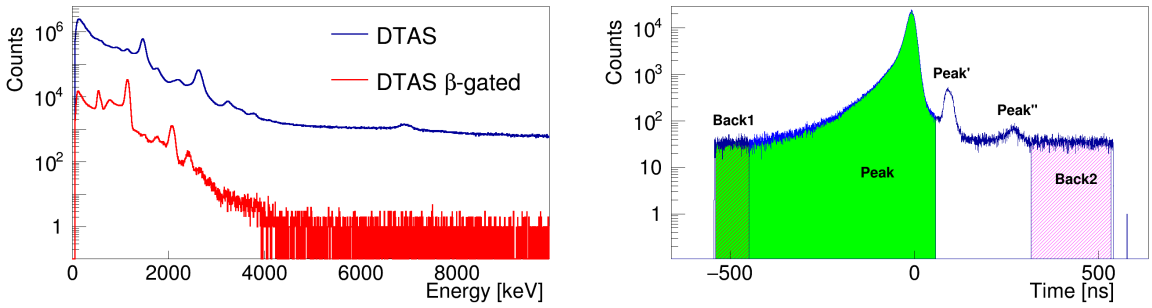

Figure 7.1: Comparison between the β-gated spectrum and the raw spectrum of DTAS for the decay of ^{100}Tc (left). TAC DTAS-β plastic detector for the measurement of the decay of ^{100}Tc (right).

Quad Linear Fan in-Fan out, as explained in Appendix A) and the global timing signal of the plastic detector, both stored as a TDC amplitude. The resulting TAC spectrum for the measurement of the decay of ^{100}Tc is shown in Figure 7.1 right, and it was calibrated with an ORTEC 462 Time Calibrator [163] with 10 ns time period. This TAC presents several structures apart from the main peak of the coincidence highlighted in green. The structure labelled as Peak' contains essentially environmental background events, whereas Peak" contains a few events from the decay of ^{100}Tc (0.5% of the statistics in the main peak). Furthermore, two flat regions are considered where environmental background events are located.

7.1.2 Singles spectrum

Before entering into the details of the β-gated analysis, it is worth mentioning that background measurements were performed between runs of ^{100}Tc in order to perform an analysis of the singles spectrum (without coincidence condition) which needs to be background subtracted. The spectra corresponding to all these runs of background were checked to be equivalent. The normalization factor of the background was calculated with the ratio of the live times, as explained in Chapter 4 Section 4.3.1. The resulting background subtracted singles spectrum is compared with the β-gated spectrum (which is also subtracted from the small amount of random coincidences with background that will be mentioned later) in Figure 7.2 left. From the comparison of the singles and β-gated spectra, we obtain a β detection efficiency of 88.3%. This number has not been corrected for the summing-pileup contribution in each of the spectra. Since the spectrum in singles shows large statistical fluctuations after the subtraction, we have considered only the analysis of the β-gated spectrum.

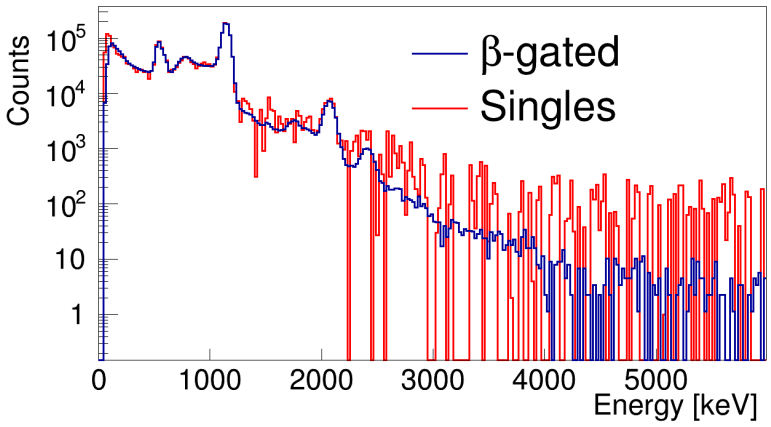

Figure 7.2: Comparison between the β-gated spectrum and the background subtracted singles spectrum for ^{100}Tc. The β-gated spectrum has been scaled to the singles spectrum.

7.1.3 Contaminants

With respect to the sources of contamination, in this case, although we are considering coincidences with the β-detector, the large ground state feeding intensity of this decay, which is around 90% as we shall see later, together with the high efficiency of the set-up gives rise to a non-negligible number of random coincidences of the β-particles with the environmental background in DTAS. The background spectrum used for the subtraction is obtained from gates in the two regions shown in Figure 7.1 right (Back1 and Back2). It was shown that the best subtraction was achieved with a combination of both gates with equal weights. This contamination is normalized by checking the two main peaks of the environmental background at 1460.8 keV and at 2614.5 keV.

Apart from subtracting the environmental background, there is the contribution of the summing-pileup of signals. The procedure explained in 4.3.2 was followed, taking the first event for the summing-pileup calculation with the same β coincidence as the software sum of the decay. The normalization of this contribution is obtained with expression (4.4). In Figure 7.3 the normalized contaminant spectra are presented together with the β-gated spectrum.

Since we are subtracting background from the ^{100}Tc β-gated spectrum, we have to subtract the background summing-pileup from the summing-pileup calculation for ^{100}Tc in order not to consider this contamination twice.

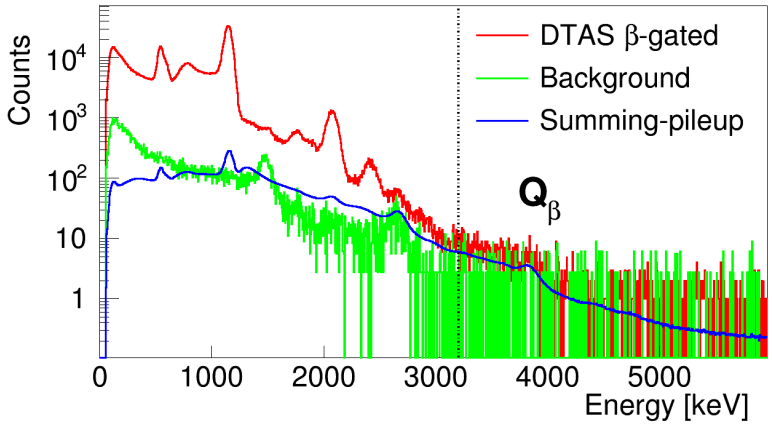

Figure 7.3: Relevant histograms for the analysis of the decay of ^{100}Tc. β-gated experimental spectrum (red) and contribution of the contaminants: environmental background (green) and summing-pileup (blue).

7.2 Branching ratio matrix

According to the recommendations of RIPL-3 [145], the level scheme of ^{100}Ru is complete up to the level at 3.072 MeV. From this level to the Q_β=3.204 MeV, a continuum region with 40 keV bins is used based on the statistical model as explained in Chapter 2. We have also considered a cut in the known level scheme up to the level at 2.387 MeV. The parameters used for the statistical model calculation are extracted from RIPL-3 [145] and summarized in Table 2.1.

The Hartree-Fock-Bogoliubov (HFB) plus combinatorial nuclear level density (HFB+c) [149,212] available at RIPL-3 [145] has been used, as explained in Chapter 2, with C and P parameters 0.01596 and 0.33071, respectively. The resulting accumulated number of levels is presented in Figure 7.4 in comparison with the experimental distribution.

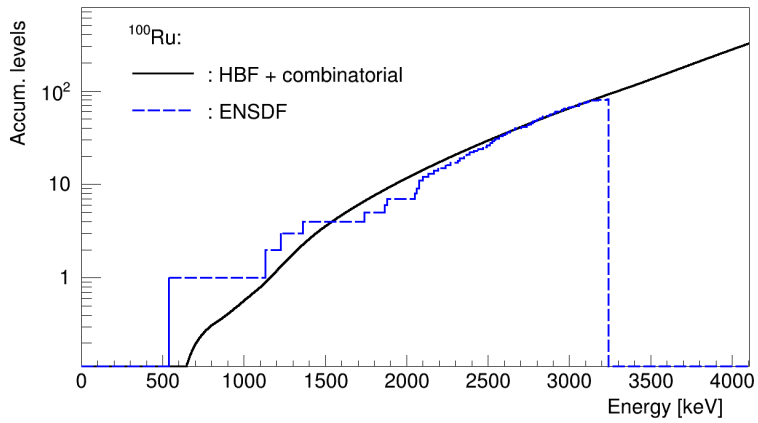

Figure 7.4: Accumulated number of levels in ^{100}Ru calculated with the HFB plus combinatorial approach (solid black) compared with the experimental information from ENSDF (dashed blue).

Once the branching ratio matrix is constructed, the response function $R_{ij}(B)$ is calculated recursively from single particle MC responses as explained in Chapter 2.

7.3 Analysis and results

The deconvolution was carried out with the response matrix obtained and the normalized contaminants. The expectation maximization (EM) algorithm explained in Chapter 2 was applied to extract the β-feeding distribution. We have found that there is no noticeable difference if we consider the known level scheme up to 3.072 MeV or up to 2.387 MeV, as can be seen in Figure 7.5, where both β-intensity distributions are compared. Moreover, from the analysis it was concluded that allowing feeding only to states observed in the high-resolution measurement of the β-decay was enough to obtain a good reproduction of the spectrum. However, the fit at high energies in the analysis with the known part up to 3.072 MeV is improved if we consider an additional 2^+ level at 2.934 MeV (as shown in Figure 7.6) that was not seen in previous β^- decay studies, but was seen in electron capture studies from ^{100}Rh [213]. The improvement of the fit with β-intensity at this energy is also seen in the analysis performed with the known level scheme up to 2.387 MeV, where the last level populated in the continuum is at 2.940 MeV. The level at 2.934 MeV, according to the information from ENSDF [213], de-excites with a single γ-ray of 2934 keV to the ground state and has spin-parity values of 1^+ or 2^+. In the RIPL-3 database [145], a spin-parity assignment of 2^+ is suggested and this was our assumption in the analysis. However, we also tested the 1^+ spin-parity assignment as a possibility for this level, with very similar results. The quality of the final analysis can be checked by the comparison of the experimental spectrum with the spectrum reconstructed with the β-intensities obtained in the analysis, as presented in Figure 7.7. As in all the cases presented in the following chapters, the reconstructed spectrum is obtained by multiplying the response function with the final accepted feeding distribution in the analysis. The residuals represent the relative differences of the reconstructed spectrum with respect to the experimental spectrum.

For the evaluation of the uncertainties in the β-intensities resulting from the analysis of all the cases studied in this work, we will follow the philosophy of [74], and the space of solutions with β-intensity distributions compatible with the data will be considered as the systematic uncertainty of the analysis (in all the cases statistical errors are negligible in comparison). Thus, different sources of systematic error were considered for the β-intensities presented in Table 7.1. First, the normalization factors of the contaminants were varied and the impact on the β-intensities evaluated. We have found that the reproduction of the experimental spectrum allows a change of up to $\pm$50% for the normalization factor of the background, and $\pm$10% for the summing-pileup. The impact of the effect of the β-detector efficiency has also been studied by changing the threshold value in the MC simulation by $\pm$30%. Finally, the Maximum Entropy (ME) algorithm explained in Chapter 2 has been applied instead of the EM algorithm in order to check the influence of the method of de-convolution.

In addition, we have investigated the sensitivity of the β-detector to γ-rays. This can introduce distortions in the β-gated TAGS spectrum. For a realistic estimation, we made a

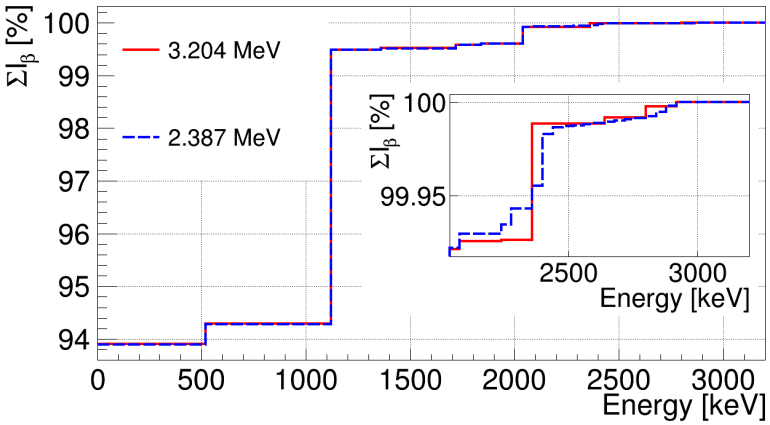

Figure 7.5: β-intensity distribution extracted from the TAGS analysis with a cut in the known level scheme at 3.072 MeV compared to the distribution with a cut at 2.387 MeV. A zoom in the last MeV of the Q_β window is shown in the inset to see the differences between both analysis.

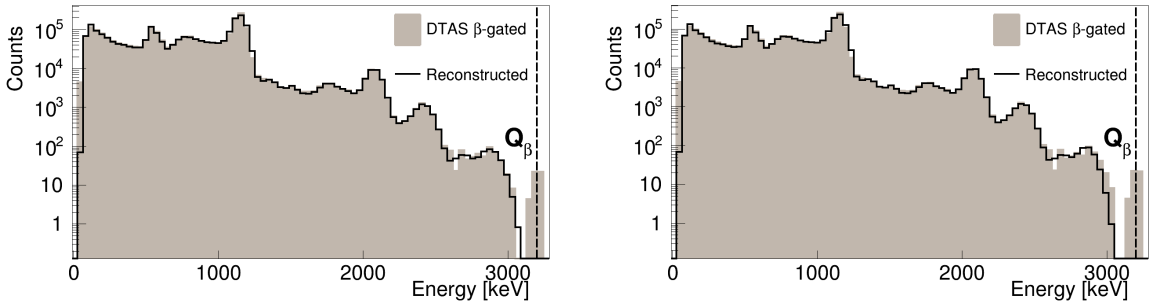

With new level Without new level

Figure 7.6: Result of the analysis of the ^{100}Tc decay: β-gated experimental spectrum after subtracting the contaminants (filled grey) is compared with the reconstructed spectrum after the analysis (black). An slight improvement at high energies when a further level is included in the analysis is shown.

MC simulation with decay cascades generated with the DECAYGEN event generator [146]. As input to this event generator we used the branching ratio matrix and the β-intensity distribution from our analysis. The output consists of an event file where the primaries are labelled and can be identified. By simulating the β-particles and γ-rays from the event file, and comparing with a simulation with only β-particles, we deduced that around 0.2% of the counts in the total simulation for the ^{100}Tc are coming from the interaction of γ-rays with our plastic detector.

By combining all these sources of uncertainty, we have estimated the systematic error of the analysis, as presented in Table 7.1 and shown in Figure 7.8 left. The information of the I_β from ENSDF [213] is compared with the result of the analysis in Figure 7.8 left. The evaluation of ENSDF is based on high resolution studies [53,54,214]. In Table 7.1 we present the I_β values and log ft values corresponding to this comparison. The accumulated strength is also evaluated in both cases and compared in Figure 7.8 right.

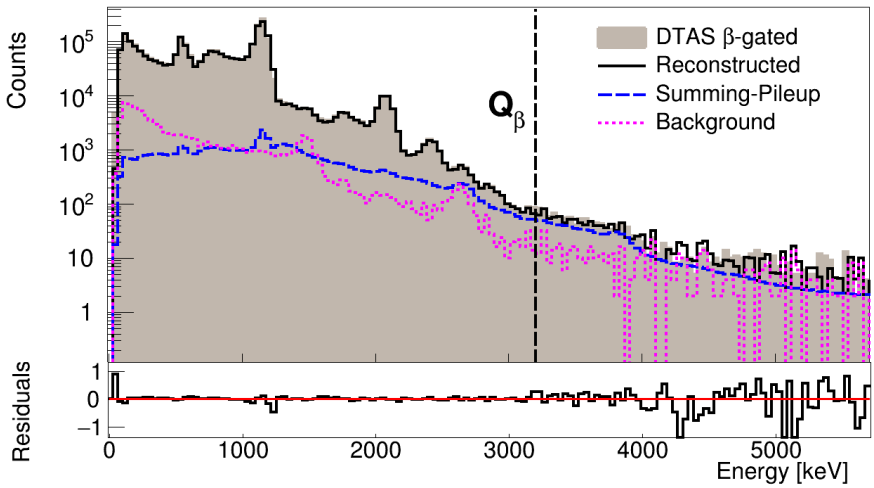

Figure 7.7: Result of the analysis of the ^{100}Tc decay: β-gated experimental spectrum after subtracting the contaminants (filled grey) is compared with the reconstructed spectrum after the analysis (black). The contamination from background (pink) and summing-pileup (blue) are also shown.

Energy [MeV]	J^P	I_β ENSDF [%]	I_β DTAS [%]	log ft ENSDF	log ft DTAS	log ft theory
0.000	0_1^+	93.3(1[a])	93.9(5)	4.591(6)[b]	4.588(6)	4.63
0.539	2_1^+	0.75(14)	0.39(5)	6.35(9)[b]	6.63(6)	5.88
1.130	0_2^+	5.36(13)	5.20(40)	5.04(1)	5.05(4)	6.06
1.362	2_2^+	0.030(4)	0.026(8)	7.1(1)	7.15(14)	7.35
1.741	0_3^+	0.066(3)	0.062(6)	6.34(2)	6.37(5)	-
1.865	2_3^+	0.030(4)	0.029(3)	6.54(6)	6.55(5)	-
2.052	0_4^+	0.36(5)	0.31(2)	5.21(6)	5.27(3)	5.30
2.099	2_4^+	0.0073(7)	0.0045(40)	6.83(5)	7.04(40)	-
2.241	2_5^+	0.0013(7)	0.0006(5)	7.36(20)[b]	7.69(80)	-
2.387	0_5^+	0.063(4)	0.062(6)	5.41(3)	5.42(5)	5.27
2.660	2_6^+	0.0046(10)	0.0032(30)	5.9(1)	6.1(10)	6.24
2.838	2_7^+	0.006(3)	0.006(1)	5.2(2)	5.22(8)	5.73
2.934	2_8^+	-	0.0024(9)	-	5.18(20)	5.64

Table 7.1: I_β and log ft values obtained with DTAS compared with the information from ENSDF [213]. The theoretical calculated values are also listed, and they have been computed by using the 'linear' model by adopting the value g_A=0.40. The experimental 0^+ state at 1.741 MeV is missing, since it is likely to be a three-phonon state in terms of structure, and such states are outside the model space of the theoretical framework used for the computations.

[a] for further discussion see text.

[b] This log ft value has been calculated with the log ft program of the National Nuclear Data Center (NNDC) [215] that uses ENSDF evaluated data as input (the β-intensity from the third column). It differs slightly from the log ft value of the evaluation [213].

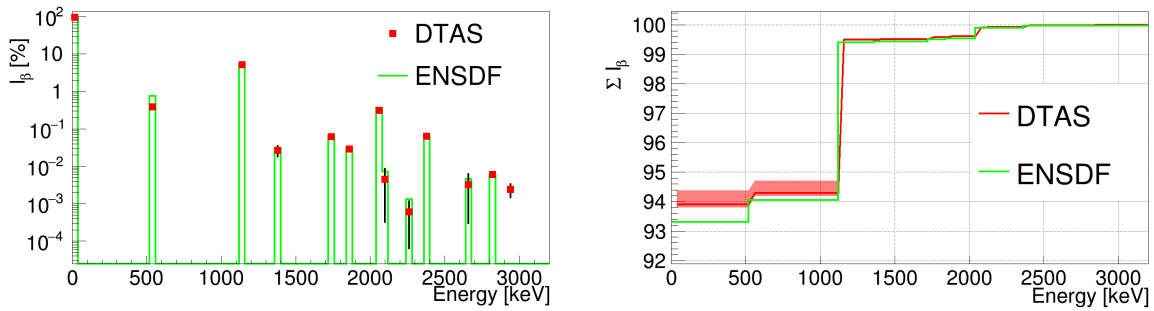

Figure 7.8: Left figure shows the β-intensities of the decay of ^{100}Tc from ENSDF (green) and from the TAGS analysis (red). Right figure shows the corresponding comparison of the accumulated β-intensity distributions.

Finally, as a crosscheck of the consistency of the analysis, we have also calculated the I_γ values de-exciting the main levels populated in the decay, using our branching ratio matrix and our I_β distribution. The result is presented in Table 7.2 and it shows a nice agreement with the high-resolution γ-intensities.

Energy [keV]	I_γ ENSDF	I_γ DTAS
539.48	0.066	0.060
1130.25	0.054	0.052
1362.21	0.001	0.001
1740.95	0.001	0.001
2051.51	0.004	0.003
2387.12	0.001	0.001

Table 7.2: Absolute γ-intensities de-exciting the main levels populated in the decay of ^{100}Tc (per 100 decays)

Furthermore, the segmentation of the spectrometer allows us to check the reproduction of the multiplicy spectra and the individual-module spectra of DTAS. For this, we carried out a simulation using the DECAYGEN event generator [146] with the branching ratio matrix and the β-intensity distribution from our analysis as input. The reproduction of the first six multiplicities is shown in Figure 7.9. The reproduction is quite reasonable in all the cases, although an excess of multiplicity $M_m = 1$ is observed at the energy of the extra level level at 2.934 MeV. This suggests that if there is some feeding to a level at these energies, then it de-excites by emission of more than a single γ-ray, or it has a non-negligible conversion coefficient.

In the context of the study of the multiplicities, the reproduction of the spectra of the individual modules has also been investigated. Since there are symmetrical positions in DTAS, we do not need to study the spectra of the 18 modules, and three geometrically distinguishable modules can be chosen: one of the two central modules of the horizontal central plane, a module placed in one of the corners, and a module located between two modules placed in the corners. The good reproduction of the spectra can be seen in Figure

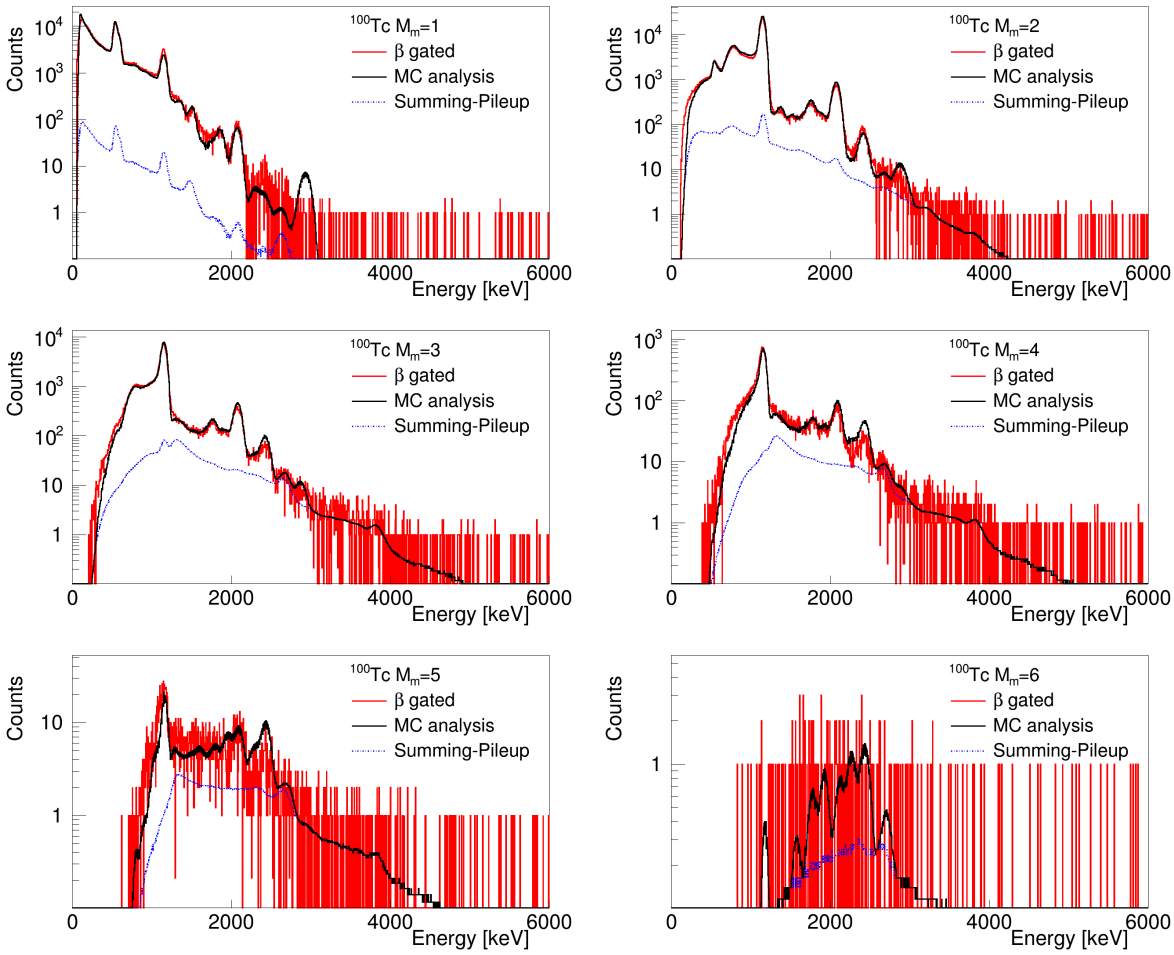

Figure 7.9: Experimental spectra for different multiplicities for the decay of^{100}Tc compared with the MC simulation performed with an event generator for multiplicities from 1 to 6.

7.10.

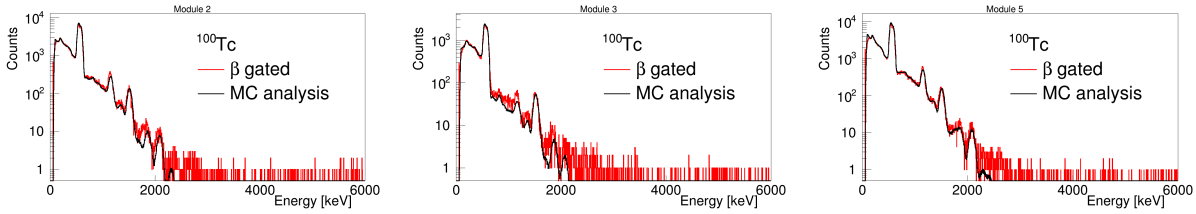

Figure 7.10: ^{100}Tc experimental spectra for the three geometrically distinguishable individual modules compared with the MC.

7.4 Discussion

From the data compiled in Tables 7.1 and 7.2, it can be concluded that the TAGS results are very similar to the high resolution results in this case. Apart from a weak feeding to a new level, the new TAGS data imply a slightly larger ground state feeding and a

smaller population of the first 2^+ state. The discrepancy of the β-intensity to this last level is outside the quoted errors in both the compiled data from ENSDF and the errors determined for this work. The largest β-intensity uncertainty in our analysis corresponds to the level at 2.66 MeV because it is strongly affected by the subtraction of the environmental background (the ^{208}Tl peak at 2614.5 keV).

Concerning the ground state feeding, it should be noted that the quoted value in ENSDF, 93.3(1)%, has a quite small error. In the only high-resolution reference that gives absolute γ-intensities with errors [53], the γ-ray with 100% relative intensity (539.6 keV) is measured with an absolute intensity of 6.6(6)%. Using this number we have evaluated the ground state feeding intensity, and obtained 93.3(6)%, where the error is calculated by applying the conventional method for error propagation. If we consider the updated error given by the same authors in a subsequent publication [214], with 6.6(5)%, a ground state feeding intensity of 93.3(4)% is obtained. In both cases, the error is larger than the ENSDF value, and our value of 93.9(5)% is in reasonable agreement with them. It is worth mentioning that in the EC decay study from [51], a 6.6(3)% absolute intensity is obtained for the 539.6 keV γ-ray. An evaluation of the ground state feeding intensity by combining this error and the relative intensities from [53] gives a value of 93.3(2)%. Furthermore, we have also calculated the ground state feeding by applying a β-γ counting method described in Appendix D. Our calculation with this method gives a value of 92.8(2)%, closer to the value from high-resolution measurements. However, we should note that with this ground state feeding intensity we do not obtain as good reproduction of the low energy part of the TAGS spectrum as with the value reported in Table 7.1.

Due to the importance of this decay for double β-decay calculations, the decay data obtained have been compared with new calculations performed by J. Suhonen and O. Civitarese in the QRPA framework, following the line of previous works [216–218]. The results obtained by J. Suhonen and O. Civitarese are presented in Table 7.1. These calculations are in good agreement with TAGS results for the ground state feeding and for the level at 2.052 MeV. The ratio of β-intensities calculated from the difference between experimental and theoretical $\log ft$ values in Table 7.1 gives differences in β-intensity of less than 10% for these two levels. The rest of the calculations lead to differences in β-intensities of between 30% and 70% with respect to the TAGS results, except for the 2_1^+ and 0_2^+ states in ^{100}Ru, where discrepancies are a factor of 6 and 10 respectively. These deviations from the measured β-decay rates could be due to the small deformation (shape softness) of both the mother and daughter nuclei. Concerning the interesting 2ν double β-decay there is a slight conflict regarding the adopted effective value of the axial-vector coupling constant $g_{\rm A}$. On the one hand, the β-decay calculations presented here are performed by adopting the value $g_{\rm A} = 0.4$ from the linear model of a global Gamow-Teller β-decay study. The other model of that study, with constant $g_{\rm A} = 0.6$, yields a poorer reproduction of the results for the present decay transitions. On the other hand, the constant $g_{\rm A} = 0.6$ model works better for the 2ν double β-decay, reproducing almost exactly the ^{100}Mo 2ν double β-decay half-life and many other 2ν double β-decay half-lives.

Chapter 8

^{103}Tc decay

La ciencia no debe contentarse con ideas, que son precisamente signos, sino que debe llegar a la verdad singular de las cosas

True learning must not be content with ideas, which are, in fact, signs, but must discover things in their individual truth

Umberto Eco

In this chapter the β-decay of an important fission fragment, ^{103}Tc, into ^{103}Ru will be studied. The experimental measurements were described in Chapter 6, and here the TAGS analysis and the results will be presented.

8.1 Experimental spectra

8.1.1 β-gated spectrum

The resulting software sum for the total statistics (run numbers 312-321) is presented as the blue line in Figure 8.1 left, and it is dominated by the environmental background. The environmental background of all measurements from Experiment 2 is different from the one of Experiment 1, since a lot of neutrons are produced in the target by the fission process, and they interact with the NaI(Tl) crystals as explained in Chapter 5 Section 5.2.6. For this reason, the neutron capture peak in the background of Experiment 2 is more prominent and more complex (with several structures). In order to clean the measurements from this background, coincidences between DTAS and a plastic β-detector disk were required in this case, as explained in Chapter 4. The efficiency curve of the detector was presented in Figure 5.25 from Chapter 5, and the measured β-spectrum is shown in Appendix D. Analogously to Chapter 7, a β-γ coincidence condition with a gate on the TAC spectrum is required. The gate is presented in green in Figure 8.1 right, and it covers the main peak of the TAC, while the secondary peak corresponds to a few background events likely due to random electronic noise.

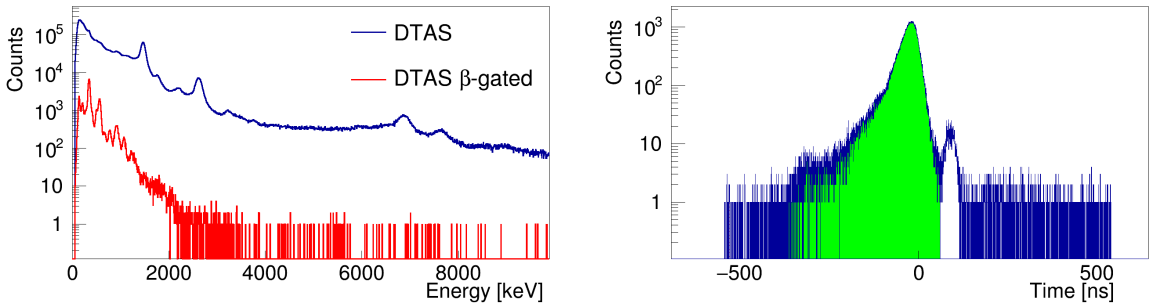

Figure 8.1: Comparison between the β-gated spectrum and the raw spectrum of DTAS for the decay of ^{103}Tc (left). The TAC DTAS-β plastic detector for the measurement of the decay of ^{103}Tc (right).

8.1.2 Contaminants

In the experiment, two different cycle conditions were used. Runs 312-317 correspond to a measurement with a cycle of 120.15 s collecting time (1.8 s tape + (30.0+0.45) s waiting + (266+1)×0.45 s implantation). However, runs 318-321 where measured without cycle, in accumulation mode. In Figure 8.2 left, both spectra are compared, and no difference is observed.

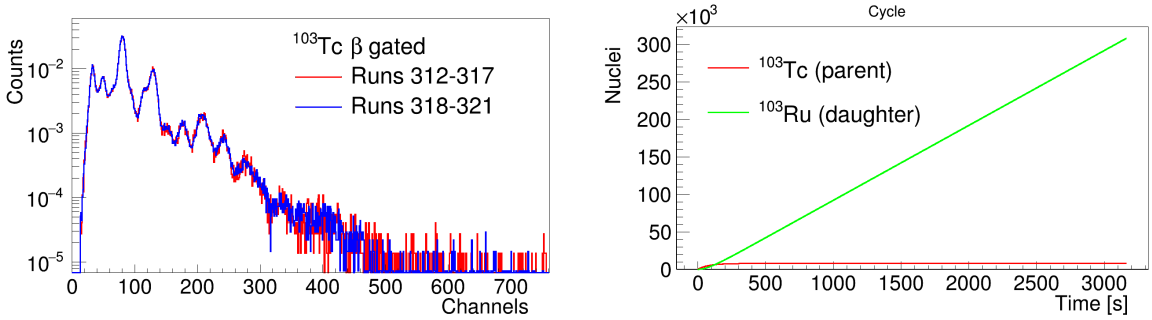

Figure 8.2: The comparison of the DTAS β-gated spectra for runs 312-317 (with cycle) and runs 318-321 (without cycle) is presented in the left. Possible contamination due to the continuous implantation is studied in right, where the number of nuclei accumulated in the center of DTAS for ^{103}Tc and its daughter, ^{103}Ru, are calculated using the Bateman equations.

The only possible difference between the two spectra could come from the contamination of the decay of the daughter, ^{103}Ru $\rightarrow$ ^{103}Rh, which populates 92% of the time a level at 536.8 keV in ^{103}Rh that in practical terms de-excites mainly with a γ-ray of 497 keV. We do not see such peak in the software sum nor in in the individual spectra. Using the half-life of this decay, 39.247 d, we can calculate with Bateman equations the contamination associated to an implantation time of 3164.49 s, which is obtained by integrating the light pulser for runs 318-321. The result is shown in Figure 8.2 right, and it corresponds to a negligible 0.05% contamination of ^{103}Ru $\rightarrow$ ^{103}Rh in the measurement of the decay of ^{103}Tc. The expressions for the solutions of Bateman equations are presented in Appendix

B.

After discarding any contamination from the daughter activity, the only contaminant is the summing-pileup of signals. In Figure 8.3 this contribution is presented normalized with the theoretical expression from Equation (4.4).

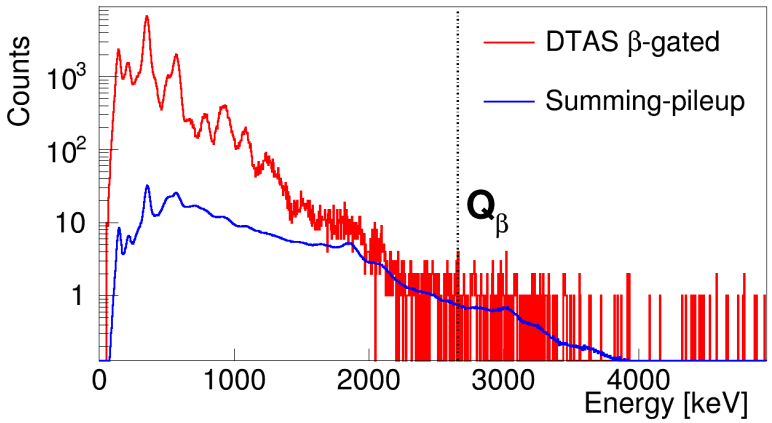

Figure 8.3: Relevant histograms for the analysis of the decay of ^{103}Tc. β-gated experimental spectrum (red) and contribution of the summing-pileup (blue).

8.2 Branching ratio matrix

According to RIPL-3 the level scheme of ^{103}Ru is complete up the excitation energy of 954 keV (39 levels). However, the level at 911 keV does not have information about the γ-intensities de-exciting it. For this reason, we took 30 levels, up to the level at 907 keV, as the known part of the level scheme for our analysis. For those levels with no spin-parity assignment, we used the values chosen by RIPL-3, as it is summarized in Table 8.1. It has to be noted that RIPL-3 assigns the parity randomly (with equal probabilities) when parity of a level is not known. Spins are assigned first checking the γ-transitions to levels with known spins, and then determining a spin distribution from 10 or more experimentally known spins (when it is possible).

Energy [keV]	J^P ENSDF	J^P RIPL
407.08	$3/2^+$,$5/2^+$	$3/2^+$
475.9	-	$3/2^+$
562.87	$3/2^+$,$5/2^+$	$3/2^+$
568.17	-	$5/2^-$
697.2	$7/2^+$,$9/2^+$	$7/2^+$
774.77	$3/2^+$,$5/2^+$	$3/2^+$
873.71	$3/2^+$,$5/2^+$	$5/2^+$
903.05	$\leq 5/2^+$	$5/2^+$
905.36	$3/2^+$,$5/2^+$	$5/2^+$
907.64	$\leq 5/2^+$	$5/2^+$

Continues on the next page.

Energy [keV]	J^P ENSDF	J^P RIPL
931.3	3/2,5/2	$3/2^+$
940.5	-	$3/2^-$
954.4	3/2	$3/2^+$

Table 8.1: Levels with no spin-parity assignment for ENSDF and the assignment from RIPL (up to 954.4 keV excitation energy).

The parameters used in the branching ratio matrix calculation are presented in Table 2.1. The HFB+c level density data [149,212] available at RIPL-3 [145] are used (see Figure 8.4) with C and P correction parameters -0.54818 and -0.77398 respectively.

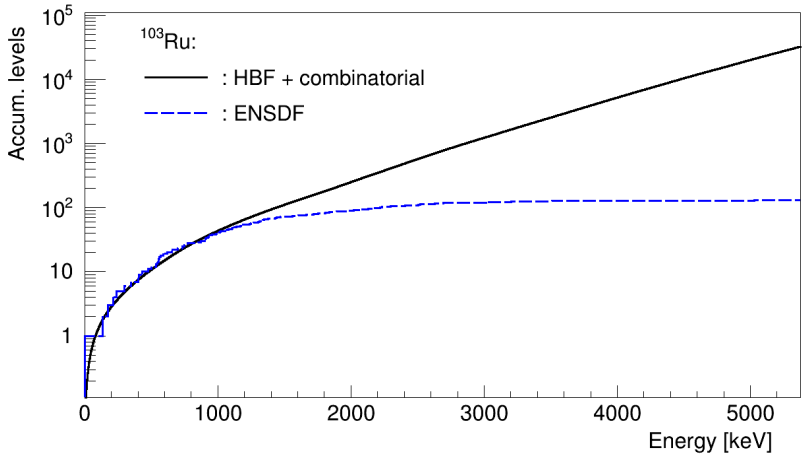

Figure 8.4: Accumulated number of levels in ^{103}Ru. The blue line is obtained from ENSDF and the black line corresponds to the Hartree-Fock-Bogoliubov calculation by Goriely downloaded from RIPL-3.

8.3 Analysis and results

The analysis was carried out by applying the expectation maximization (EM) algorithm explained in Chapter 2 with the response matrix obtained. Only direct feeding to levels with spin-parity $3/2^+$, $5/2^+$ and $7/2^+$ was permitted. These are allowed transitions assuming a $5/2^+$ ground state for ^{103}Tc, which is the spin-parity value given in ENSDF and RIPL-3. However, in H. Niizeki *et al.* [219], a $7/2^+$ is also considered.

Since the threshold of the individual modules of DTAS is 80.9 keV, the first excited state, a $5/2^+$ level which has a very low excitation energy, 3.03 keV, is not seen. It is considered together with the ground state, and direct feeding to this first excited level is forbidden. Feeding to the third excited state, a $1/2^+$ level at 174.26 keV was reported in [219], although it is a forbidden transition. We did not allow feeding to this level because the study of the multiplicities that will be presented later showed a worse reproduction of

the experimental spectra when including this level, although the fit of the total spectrum slightly improves if it is included.

Surprisingly, in the analysis we observed that the result was almost insensitive to the value of the ground state feeding intensity (ground plus first excited state). In Figure 8.5 right it is shown how the relative β-intensities of the excited states are almost independent of the g.s. β-intensity up to $I_{g.s.} = 80\%$. The only reference value from the bibliography is coming from the work of H. Niizeki *et al.* [219], where a $I_{g.s.} = 41 \pm 10\%$ is obtained. In the ENSDF evaluation [220] a $I_{g.s.} = 34 \pm 8\%$ is reported. The difference is due to the intensity of the 346.4 keV γ-ray used for normalization: H. Niizeki *et al.* deduced a 16% intensity for this γ-ray, whereas a 18.4% is obtained in a fission yield measurement [221]. The reason to our insensitivity seems to be related to the shape of the response corresponding to the end-point of the g.s. to g.s. transition. In Figure 8.5 left the MC response of this transition is compared to the experimental spectrum. From this comparison it is clear that the slope of the energy dependence of the MC response is similar to the one of the total spectrum, giving an explanation for this phenomenon.

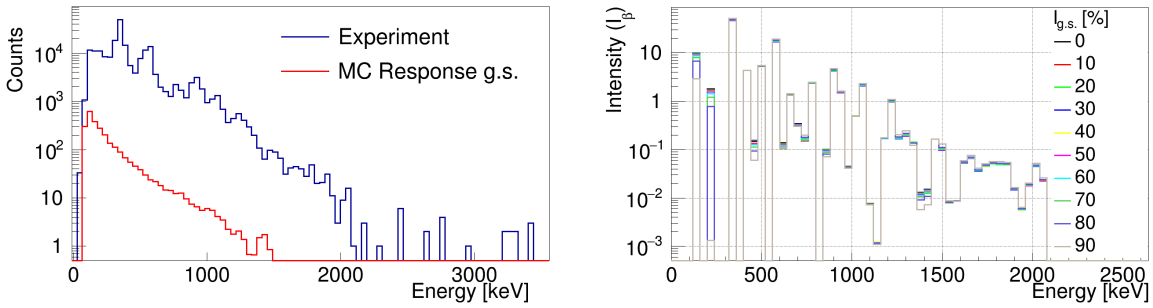

Figure 8.5: Experimental β-gated spectrum compared with the MC response of DTAS for the ground state (left). The right figure presents the relative β-intensities of the decay of ^{103}Tc for different fixed values of the g.s. β-intensity.

In order to obtain absolute intensities, the $I_{g.s.}$ can be calculated by means of the β-γ counting method for TAGS data explained in Appendix D. Since this method uses the β-intensity distribution to excited levels to compute some corrections, we have applied this procedure fixing the g.s. feeding to 0%,10%,...,90%. As can be observed in Figure 8.5 right, the effect of an absolute value for $I_{g.s.}$ on the relative I_β intensities for the excited levels is small. We have then calculated the mean of all these values weighted by the χ^2, obtaining as a result $I_{g.s.} = 46\%$. For the final deconvolution we fixed $I_{g.s.}$ to this value. The quality of reproduction of the spectrum is shown in Figure 8.6, and the resulting I_β are presented in Figure 8.7 in comparison with the ENSDF values.

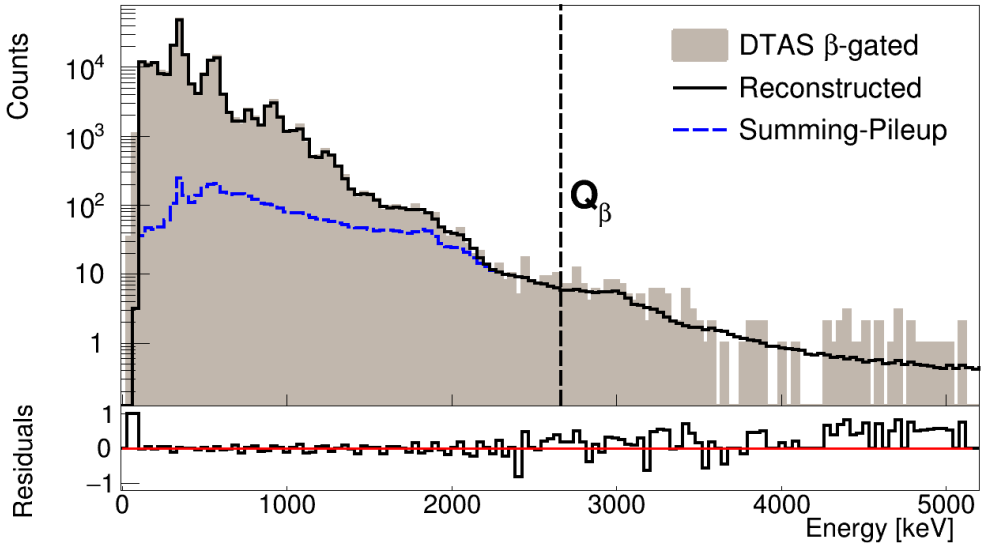

Figure 8.6: Result of the analysis of the decay of ^{103}Tc. The total spectrum is compared with the reconstructed one after the analysis.

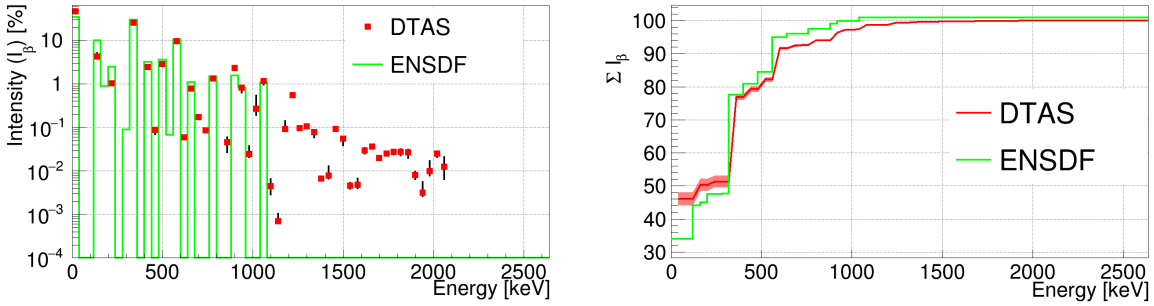

Figure 8.7: β-intensities of the decay of ^{103}Tc with error bars coming from the uncertainty of all the sources of error.

Regarding the reproduction of the multiplicities, we observed large discrepancies for $M_m = 1$. We found that the spectrum was quite sensitive to the normalization of the $M1$ PSF (original value σ=0.6294, according to Table 2.1). The reproduction of M_m=1 for the original value is compared with σ=15 in Figure 8.8. After studying the effect of this parameter in all the multiplicity spectra, a value of 6 has been chosen for the final analysis. The reproduction of the first four multiplicities can be seen in Figure 8.9.

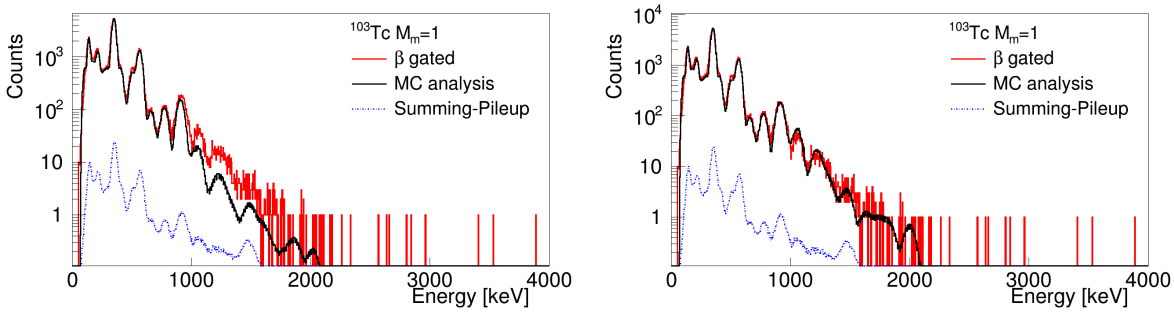

Figure 8.8: $M_m = 1$ reproduction for the decay of ^{103}Tc. The effect of the normalization of the $M1$ is studied. The spectrum for the original value σ=0.6294 (left) is compared with σ=15 (right).

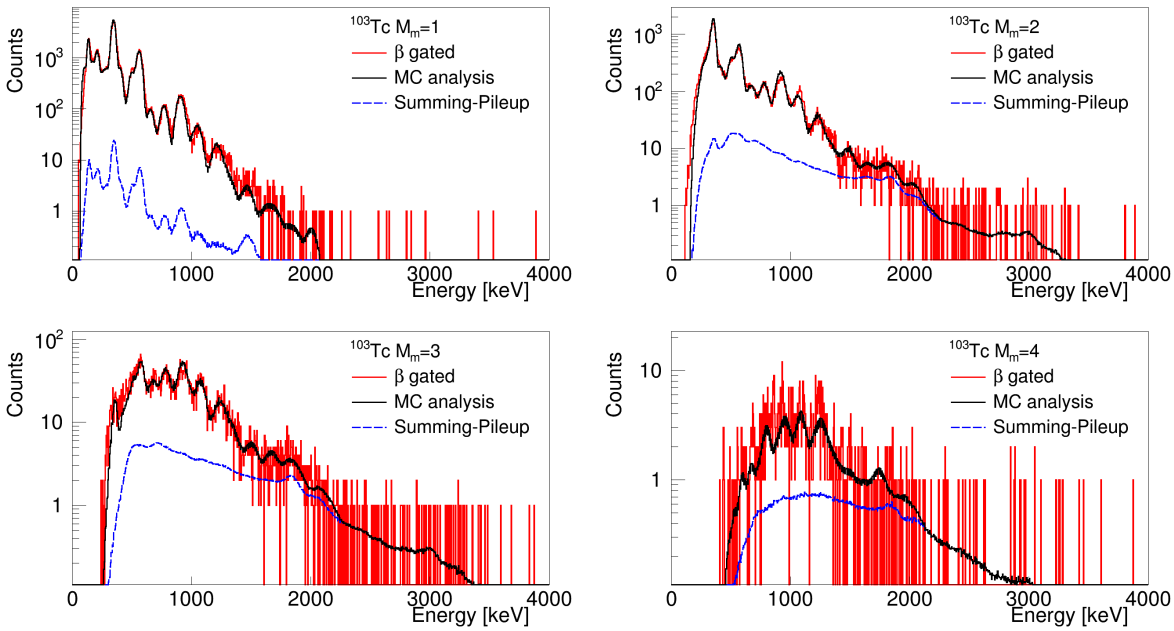

Figure 8.9: Experimental spectra for different multiplicities for the decay of ^{103}Tc compared with the MC simulation performed with an event generator for multiplicities from 1 to 4.

The reproduction of the individual crystals of DTAS (one central, one in the middle of a row, and one in a corner) is also shown in Figure 8.10. No pileup contribution has been calculated in this case.

I_γ intensities are calculated with the branching ratio matrix used in the analysis and the final β-intensity distribution. The resulting intensities are compared with the experimental ones in Table 8.2, and they are in agreement.

Energy [keV]	I_γ ENSDF	I_γ DTAS
3.03	0.000	0.113
136.079	0.170	0.118
174.32	0.028	0.023

Continues on the next page.

Energy [keV]	I_γ ENSDF	I_γ DTAS
213.52	0.033	0.021
297.83	0.001	0.014
346.383	0.284	0.260
404.44	0.009	0.015
406.19	0.028	0.014
432.1	0.001	0.000
475.9	0.000	0.001
501.06	0.035	0.030
554.6	0.001	0.000
557.7	0.000	0.001
562.9	0.094	0.091
568.17	0.000	0.003
591.98	0.005	0.004
622.00	0.000	0.001
661.73	0.010	0.008
697.20	0.000	0.002
748.80	0.000	0.001
774.87	0.014	0.013
903.05	0.000	0.005
905.32	0.015	0.007
907.64	0.000	0.012
940.7	0.008	0.008

Table 8.2: Absolute γ-intensities de-exciting the main levels populated in the decay of ^{103}Tc (per 100 decays). The second column corresponds to the intensities obtained from high resolution data [220]. The third column gives the intensities obtained with DTAS for the reference analysis.

Errors have been estimated on the one hand by changing $\pm$ 10% the normalization factor of the summing-pileup to see its influence in the analysis. On the other hand, the error of the g.s. feeding calculation has been determined by estimating the error in the ratio between the number of counts that is used in the β-γ counting method, as explained in Appendix D, obtaining a final value of I_0=46(2)%. The influence of this error in the deconvolution has also been taken into account. Moreover, the effect of different values of the $M1$ normalization parameter has been also taken into account. A positive parity for the level at 568.17 keV has also been considered, due to the already mentioned random criterion of RIPL-3 for parity assignment. Finally, the ME algorithm has been applied in order to evaluate the impact of the deconvolution method. The combined effect of all these sources of error is represented in Figure 8.7, as well as summarized in Table 8.3. Note that above the last level of the known level scheme used for the analysis, the values from the bibliography [220] listed in Table 8.3 correspond to integral values over our energy bins.

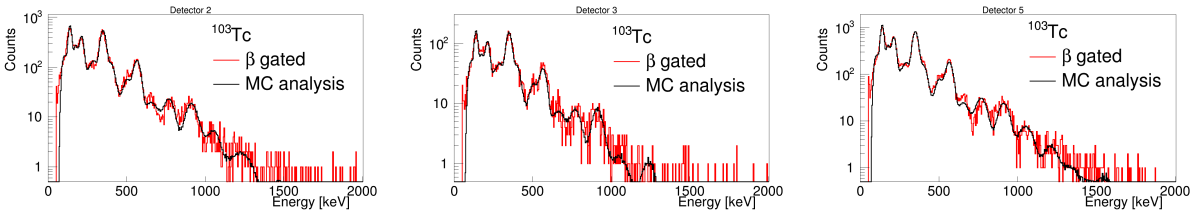

Figure 8.10: ^{103}Tc experimental spectra for the three geometrically distinguishable individual crystals compared with the MC.

Due to the insensibility to the ground state feeding intensity, we also include in Table 8.3 for comparison an evaluation of the relative β-intensities normalized to 100%. The average value and the dispersion given in the Table 8.3 have been obtained when fixing $I_{g.s.} = 10\% - 70\%$ (right part of Figure 8.5 excluding the extreme cases of $I_{g.s.}$=80% and 90%), and considering all the sources of error mentioned.

Energy [keV]	I_β ENSDF [%]	I_β relative DTAS [%]	I_β DTAS [%]
0.000	34(8)	0.000	$46.000^{+2.000}_{-2.000}$
2.810	-	-	-
136.079	10.1(17)	$7.925^{+1.604}_{-4.373}$	$4.279^{+0.835}_{-0.188}$
174.260	$\leq$0.9	-	-
213.560	2.5(5)	$1.884^{+0.235}_{-1.870}$	$1.018^{+0.052}_{-0.052}$
238.200	-	-	-
297.480	0.09(6)	-	-
346.380	30(4)	$47.287^{+3.710}_{-0.861}$	$25.535^{+0.977}_{-0.974}$
404.150	0.37(16)	$2.357^{+0.130}_{-0.023}$	$1.273^{+0.048}_{-0.048}$
406.080	2.8(4)	$2.089^{+0.030}_{-0.227}$	$1.128^{+0.044}_{-0.044}$
432.060	0.057(15)	-	-
475.900	-	$0.163^{+0.027}_{-0.107}$	$0.088^{+0.005}_{-0.019}$
501.150	3.6(5)	$5.259^{+0.203}_{-0.053}$	$2.840^{+0.105}_{-0.105}$
548.210	-	-	-
554.580	0.068(16)	-	-
557.700	-	-	-
562.870	9.9(14)	$16.863^{+1.738}_{-0.292}$	$9.106^{+0.342}_{-0.342}$
568.170	-	-	-
591.970	0.52(9)	$0.632^{+0.009}_{-0.047}$	$0.341^{+0.015}_{-0.015}$
622.000	-	$0.109^{+0.009}_{-0.043}$	$0.059^{+0.005}_{-0.003}$
653.700	-	-	-
661.550	1.10(17)	$1.429^{+0.073}_{-0.041}$	$0.772^{+0.032}_{-0.032}$
697.200	-	$0.319^{+0.012}_{-0.091}$	$0.172^{+0.011}_{-0.015}$
735.200	-	$0.004^{+0.000}_{-0.002}$	$0.002^{+0.000}_{-0.000}$
736.890	-	-	-
748.800	-	$0.155^{+0.042}_{-0.055}$	$0.084^{+0.004}_{-0.006}$

Continues on the next page.

Energy [keV]	I_β ENSDF [%]	I_β relative DTAS [%]	I_β DTAS [%]
774.770	1.49(21)	$2.457^{+0.061}_{-0.123}$	$1.327^{+0.055}_{-0.066}$
873.710	-	$0.084^{+0.025}_{-0.035}$	$0.046^{+0.014}_{-0.019}$
903.050	-	$0.872^{+0.036}_{-0.085}$	$0.471^{+0.020}_{-0.046}$
905.360	1.56(22)	$1.275^{+0.135}_{-0.108}$	$0.689^{+0.026}_{-0.058}$
907.640	-	$2.162^{+0.375}_{-0.162}$	$1.168^{+0.203}_{-0.087}$
940.000	0.82(13)	$1.520^{+0.125}_{-0.356}$	$0.821^{+0.065}_{-0.192}$
980.000	-	$0.045^{+0.023}_{-0.015}$	$0.024^{+0.012}_{-0.004}$
1020.000	-	$0.493^{+0.495}_{-0.134}$	$0.266^{+0.268}_{-0.072}$
1060.000	1.07(15)	$2.141^{+0.194}_{-0.366}$	$1.156^{+0.047}_{-0.198}$
1100.000	-	$0.008^{+0.003}_{-0.005}$	$0.005^{+0.002}_{-0.002}$
1140.000	-	$0.001^{+0.001}_{-0.001}$	$0.001^{+0.000}_{-0.000}$
1180.000	-	$0.171^{+0.087}_{-0.014}$	$0.092^{+0.047}_{-0.008}$
1220.000	-	$1.007^{+0.066}_{-0.027}$	$0.544^{+0.022}_{-0.022}$
1260.000	-	$0.175^{+0.035}_{-0.029}$	$0.095^{+0.005}_{-0.003}$
1300.000	-	$0.197^{+0.057}_{-0.008}$	$0.106^{+0.005}_{-0.005}$
1340.000	-	$0.143^{+0.013}_{-0.038}$	$0.077^{+0.007}_{-0.019}$
1380.000	-	$0.012^{+0.002}_{-0.008}$	$0.007^{+0.001}_{-0.001}$
1420.000	-	$0.014^{+0.009}_{-0.008}$	$0.008^{+0.005}_{-0.001}$
1460.000	-	$0.167^{+0.021}_{-0.010}$	$0.090^{+0.011}_{-0.006}$
1500.000	-	$0.101^{+0.029}_{-0.029}$	$0.054^{+0.006}_{-0.015}$
1540.000	-	$0.008^{+0.001}_{-0.002}$	$0.005^{+0.001}_{-0.001}$
1580.000	-	$0.009^{+0.003}_{-0.002}$	$0.005^{+0.002}_{-0.001}$
1620.000	-	$0.054^{+0.012}_{-0.007}$	$0.029^{+0.005}_{-0.004}$
1660.000	-	$0.067^{+0.013}_{-0.008}$	$0.036^{+0.003}_{-0.005}$
1700.000	-	$0.037^{+0.006}_{-0.002}$	$0.020^{+0.002}_{-0.001}$
1740.000	-	$0.046^{+0.008}_{-0.005}$	$0.025^{+0.003}_{-0.002}$
1780.000	-	$0.051^{+0.012}_{-0.006}$	$0.027^{+0.004}_{-0.004}$
1820.000	-	$0.050^{+0.012}_{-0.007}$	$0.027^{+0.004}_{-0.004}$
1860.000	-	$0.049^{+0.012}_{-0.013}$	$0.026^{+0.004}_{-0.007}$
1900.000	-	$0.015^{+0.004}_{-0.003}$	$0.008^{+0.002}_{-0.001}$
1940.000	-	$0.006^{+0.005}_{-0.001}$	$0.003^{+0.002}_{-0.001}$
1980.000	-	$0.018^{+0.013}_{-0.004}$	$0.010^{+0.007}_{-0.002}$
2020.000	-	$0.046^{+0.008}_{-0.008}$	$0.025^{+0.002}_{-0.004}$
2060.000	-	$0.023^{+0.018}_{-0.011}$	$0.013^{+0.008}_{-0.006}$

Table 8.3: I_β intensities of the decay of ^{103}Tc.

Chapter 9

^{103}Mo decay

Por un inmortal poder, todas las cosas, lejanas o cercanas, están ocultamente ligadas entre sí, de modo que no puedes arrancar una flor sin perturbar las estrellas

All things by immortal power, near or far, hiddenly to each other linked are, that thou canst not stir a flower without troubling of a star

Francis Thompson

In this chapter the β-decay of an important fission fragment, ^{103}Mo, into ^{103}Tc will be studied. The experimental measurements were described in Chapter 6, and here the TAGS analysis and the results will be presented.

9.1 Experimental spectra

9.1.1 β-gated spectrum

The resulting software sum for the total statistics measured (runs 307-311) is presented as the blue line in Figure 9.1 left, and it is dominated by the environmental background.

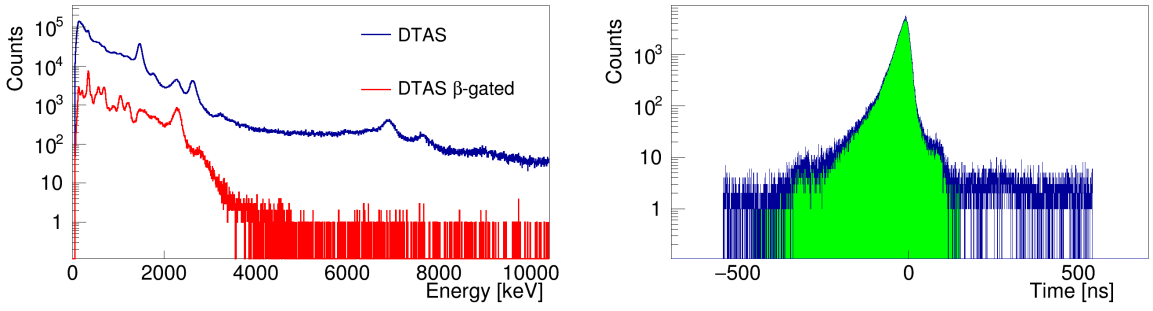

Figure 9.1: Comparison between the β-gated spectrum and the raw spectrum of DTAS for the decay of ^{103}Mo (left). The TAC DTAS-β plastic detector for the measurement of the decay of ^{103}Mo (right).

In order to reject background events, a β-γ coincidence is required with a gate in the TAC spectrum. This gate is presented in green in Figure 9.1 right, and it covers the main

peak of the TAC.

9.1.2 Singles spectrum

The background subtraction of the singles DTAS spectrum gives a reasonable spectrum in this case in terms of statistical fluctuations, as shown in Figure 9.2 where it is compared with the β-gated spectrum multiplied by a factor that gives an average β-efficiency of 32.5%. Consequently, an analysis without coincidence with the β-detector and, therefore, independent of the β-efficiency, can be performed in this case.

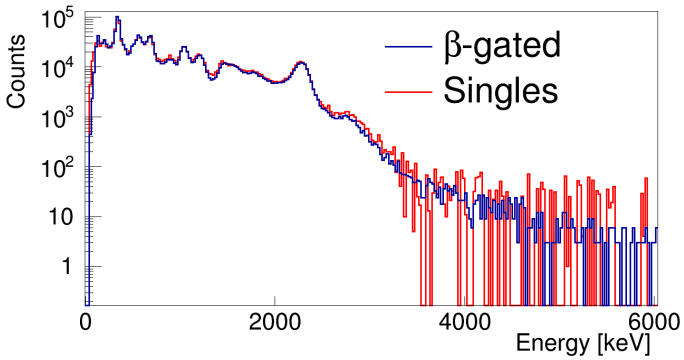

Figure 9.2: Comparison between β-gated spectrum and background subtracted singles spectrum for ^{103}Mo.

9.1.3 Contaminants

The contaminants of both the β-gated spectrum and the singles spectrum are discussed here. In this case, the decay of the daughter nucleus, ^{103}Tc, is a contaminant for the analysis of the decay of ^{103}Mo. The normalization of the daughter is calculated with the Bateman equation assuming a constant implantation rate, as detailed in Appendix B. A daughter contamination of 28.1% is obtained with this procedure (see Figure 9.3). However, the peak at 346 keV coming from the decay of ^{103}Tc is not removed completely, and the subtraction factor has to be increased up to a value of 36.9%. The subtraction was carried out with the spectrum measured and studied in Chapter 8. For the spectrum in singles a MC simulation of the decay of the daughter, based on the result of the analysis presented in Chapter 8, is used due to the large statistical fluctuations introduced by the subtraction of environmental background in the singles ^{103}Tc spectrum. The contribution of the daughter is shown normalized in Figure 9.4.

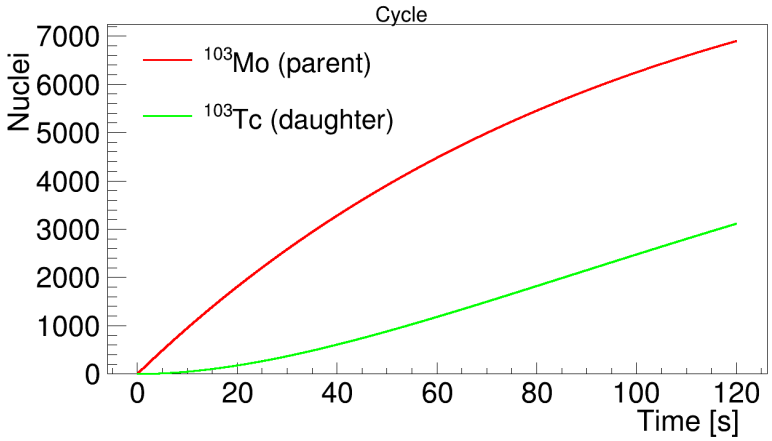

Figure 9.3: Cycle of implantation of ^{103}Mo on the tape. The number of parent and daughter nuclei is represented as a function of time during the cycle.

Concerning the summing-pileup of signals, it is calculated as explained for previous cases, and in Figure 9.4 this contribution is presented normalized with the theoretical expression from Equation (4.4).

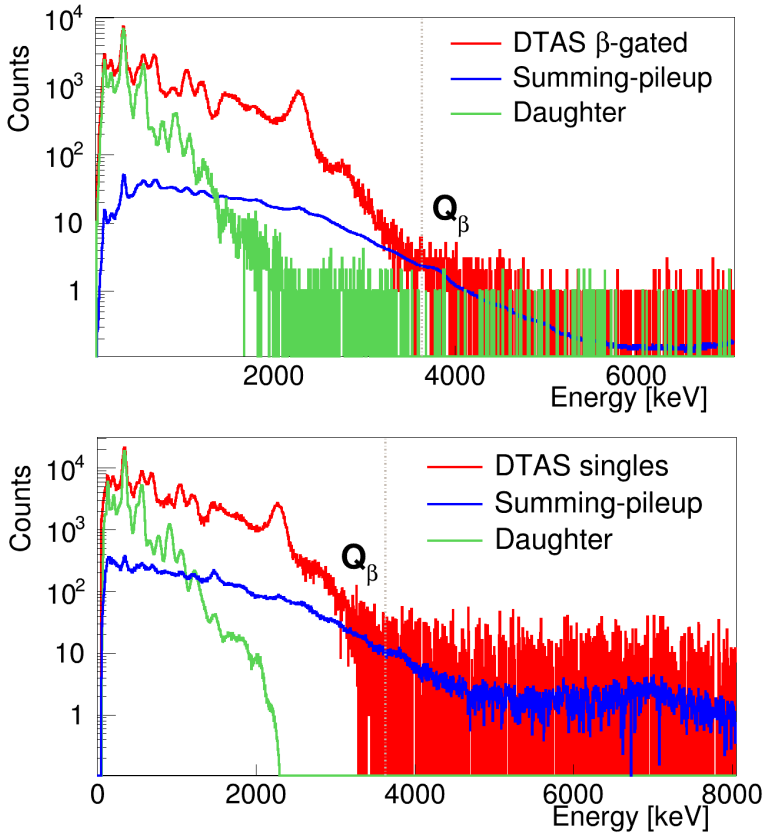

Figure 9.4: Relevant histograms for the analysis of the decay of ^{103}Mo. Summing-pileup (blue) and daughter activity (green) are shown normalized for the β-gated spectrum and the background subtracted singles spectrum (red).

9.2 Branching ratio matrix

According to RIPL-3 [145] the level scheme of ^{103}Tc is complete up to an excitation energy of 691.69 keV (19 levels). However, the information regarding the I_γ intensities is only complete up to 259 keV excitation. In order to include the rest of the levels, we take the I_γ intensities from the only previous β-decay study, the thesis of G.Tittel [222]. As will be shown in Figure 9.7, a known level scheme up to the level at 691.69 keV is not enough to reproduce the structures that appear up to approximately 1.3 MeV. For this reason, we have extended the known level scheme up to the level at 1219.85 keV, using also the γ-intensities from that β-decay study. However, there is still a lack of experimental information for the γ-intensities of some of the adopted levels that were not seen in β-decay. The first possibility is to eliminate those levels without assigned intensities that were not seen in [222]. Particularly. this affects to 6 levels up to 1219.85 keV: 362, 557, 595, 663, 848, 1158 keV. It has to be noted, that these are high spin levels identified with Euroball in a fusion reaction ^{37}Cl $+^{176}$Yb [223]. A second possibility that we have exploited is to consider them by employing the theoretical branching ratios from [224], calculated in the framework of the particle-rotor model. When there was a conflict between the energies of the theoretical calculation [224] and the experimental values from ENSDF [220], we chose the experimental energies of the levels, and we changed appropriately the energies of the γ-rays in order to connect with other levels.

The spin-parity of the ground state of the parent is defined as $(3/2^+)$ in ENSDF. $3/2^+$ is recommended by RIPL-3, whereas $1/2^+$ is also considered in the only reference of this decay [222]. In our analysis a $3/2^+$ option is preferred, allowing direct feeding just to $1/2^+$, $3/2^+$ and $5/2^+$ (allowed transitions). However, the $1/2^+$ option will also be considered, with allowed feeding to $1/2^+$ and $3/2^+$ levels.

For those levels in ^{103}Tc with no spin-parity assignment, we used the values chosen by RIPL-3 [145] when available. Levels at 887.20, 1085.95 and 1219.85 keV do not have a spin-parity value at RIPL-3 either. These three levels seem to be directly populated in the decay, since we have to allow direct feeding to them in the analysis in order to reproduce the spectrum; for this reason they are chosen to be $5/2^+$ levels at the first attempt, although the possibilities $1/2^+$ and $3/2^+$ are also considered for levels at 887.20 and 1085.95 keV, with all possible combinations of these values. The resulting spin-parities for the levels in ^{103}Tc are summarized in Table 9.1.

Energy [keV]	J^P ENSDF	J^P used
362.00	$(7/2^-)$	$7/2^-$
383.20	$3/2, 5/2, 7/2^-$	$5/2^-$
469.83	$3/2^+, 5/2^+$	$5/2^+$
557.00	$(11/2^+)$	$11/2^+$
595.00	$(9/2^-)$	$9/2^-$
620.77	-	$5/2^-$
662.00	$(13/2^+)$	$13/2^+$
686.60	-	$9/2^+$
687.62	$3/2^+, 5/2, 7/2$	$7/2^+$
691.59	$1/2^+, 3/2, 5/2^-$	$5/2^-$
848.00	$(11/2^-)$	$11/2^-$
887.20	-	$5/2^+$
1085.95	-	$5/2^+$
1158.00	$(13/2^-)$	$13/2^-$
1219.85	$5/2^+, 7/2, 9/2^+$	$5/2^+$

Table 9.1: Levels with no spin-parity assignment for ENSDF and our choice (up to 1219.85 keV).

In the level scheme constructed, some of the γ-rays have rather low energy, therefore we have evaluated the conversion coefficient of these transitions employing the NNDC tool [225], and assuming the most probable multipolarity. The values obtained are presented in Table 9.2. We have included these values in the construction of the branching ratio matrix.

E_γ [keV]	Multipolarity	α_{total}
45.8	M1	2.61
83.4	E1	0.225
93.0	M1	0.344
95.0	M1	0.324
172.0	M1	0.0635
176.0	M1	0.0597

Table 9.2: Conversion coefficients calculated for the level scheme of ^{103}Tc.

A very important issue of this analysis is related to the energy threshold. As discussed in Section 5.2.3 of Chapter 5, the energy threshold for the individual modules of DTAS is below 81 keV, whereas the total sum has a threshold of 90 keV for the singles spectra and 110 keV for the β-gated spectra. The first excited state at 45.8 keV is below the threshold of DTAS. The second excited state at 83.4 keV is not seen directly in the β-gated software sum, but it is summed in the cascades. This level can be seen clearly in the individual spectra, while in the total spectrum it is cut, as shown in Figure 9.5. In our analysis, the β-intensity feeding these two levels will be considered together with the ground state, since the response for the decay to any of the three levels is essentially equivalent.

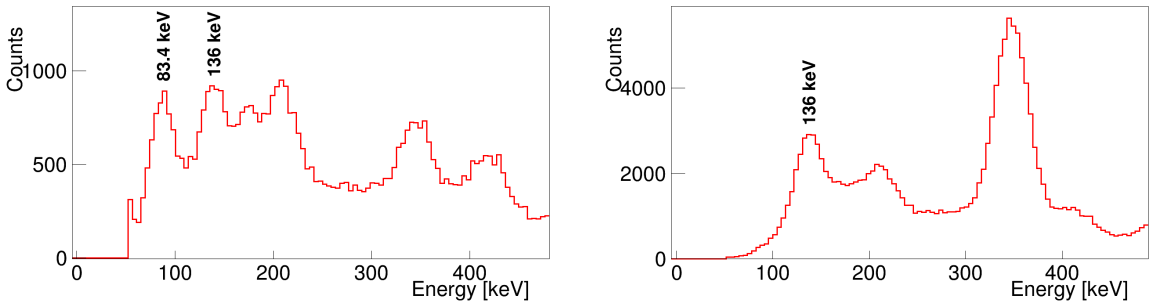

Figure 9.5: The presence of the 83.4 keV peak is investigated in the individual module β-gated spectra (the spectrum of a module is shown in left figure) and in the total DTAS β-gated spectrum for multiplicity 1, $M_m = 1$ (shown in right figure).

The level density data from HFB+c calculations [149, 212] available at RIPL-3 [145] is used (see Figure 9.6). The correction parameters are shown in Table 9.3 (first row). In order to match better the experimental accumulated level density at low energies, we have changed the C factor in the second row of Table 9.3, whereas in the third row we have changed the P factor.

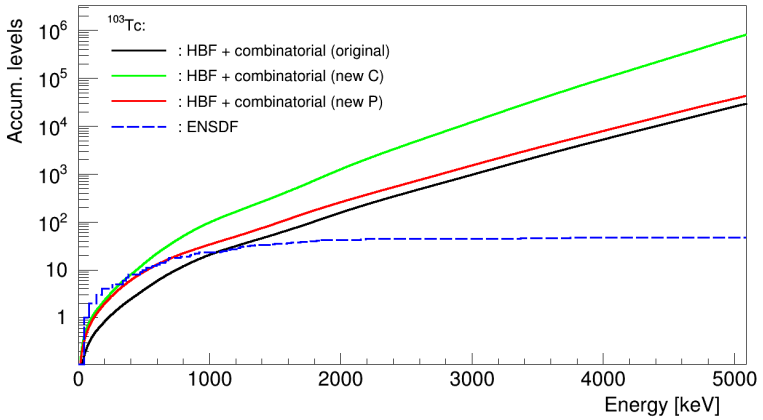

Figure 9.6: Accumulated number of levels in ^{103}Tc. The blue line is obtained from ENSDF and the black line corresponds to the Hartree-Fock-Bogoliubov calculation downloaded from RIPL-3. In addition, a new correction factor C (green) and a new correction factor P (red) have been considered since they show a better agreement at low energies with the experimental distribution.

C	P
0.0	-0.34394
1.5	-0.34394
0.0	-0.60000

Table 9.3: Correction factors C and P for the HFB+c level density distribution for ^{103}Tc (first row), together with two alternative values used in order to match better the experimental accumulated number of levels at low energies (second an third rows).

The remaining parameters involved in the branching ratio matrix and response function calculation, in particular the γ-strength function parameters, are presented in Table 2.1.

9.3 Analysis and results

Apart from allowed transitions, we found that in order to get a better fit, we have to consider also first forbidden transitions to levels at 519.22 keV ($3/2^-$) and 691.6 keV ($5/2^-$), and a second forbidden transition to 687.6 keV (which means that very probably it is not a $7/2^+$ as suggested by RIPL-3).

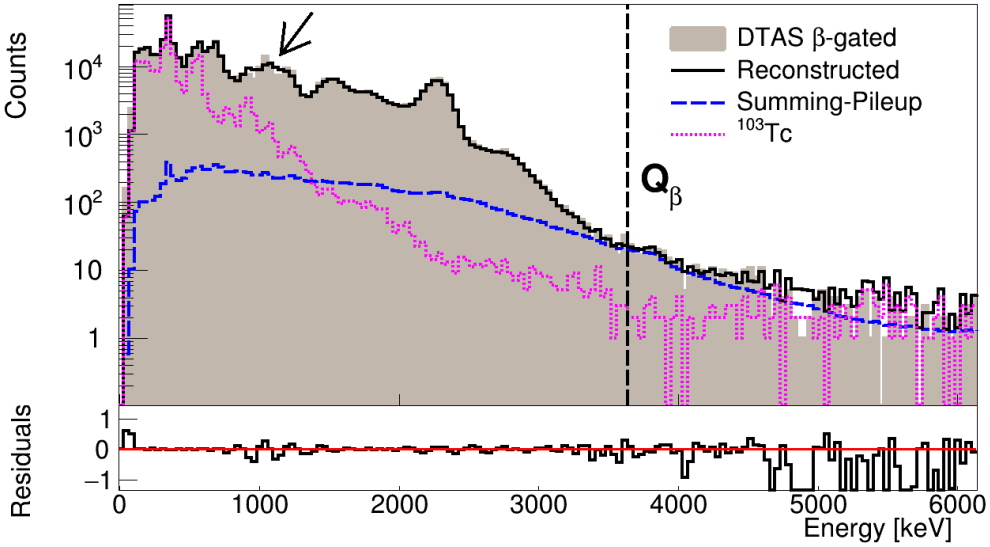

Figure 9.7: Result of the analysis of the decay of ^{103}Mo with a known level scheme up to 691.69 keV. The total spectrum is compared with the reconstructed one after the analysis.

As already discussed in the previous section, the use of the level scheme suggested in RIPL-3 leads to a poor reproduction of the measured spectrum, especially in the region just below 1.3 MeV (Figure 9.7) and here we extended the level scheme up to 1219.85 keV. We observed that adding the six high spin levels seen with Euroball [223] did not improve the fit. Likewise, changing the spin and parity values of levels at 887.20, 1085.95 and 1219.85 keV did not have an impact in the analysis. What turned out to improve the fit was the change in the γ-intensities de-exciting the level at 1085.95 keV. It de-excites with three possible γ-rays of 616 keV, 1040.2 keV and 1085.95 keV, with relative intensities 6.7, 100 and 76 respectively. The last intensity looks suspicious for two reasons: first, because we see a prominent peak at 1040 keV in the experiment, as if the de-excitation of the 1085.95 keV was essentially dominated by a cascade of 1040.2 keV followed by 45.85 keV (that is below the detection threshold and is, therefore, missed); second, because the corresponding experimental germanium spectrum from [222] shows a common peak for the γ-ray of 1081 keV (coming from level 1219.85 keV) and this of 1085.05 keV. It is clear from the coincidence spectrum, that the level at 1085.95 keV exists, since the γ-rays 1040 keV and 45.85 keV are seen in coincidence, however, the intensity of the 1085.95 keV γ-ray seems

to be overestimated. We obtained the best fit of our experimental spectrum changing the relative intensity for this γ-transition to 20 instead of 76.

On the other hand, although the modified correction factors of the level density seem to match better the low energy part of the accumulated number of levels distribution, a better fit is obtained with the original one. It may be related to the poor experimental knowledge of the number of levels for this case.

Finally it has to be mentioned that we found problems to reproduce properly the region of the prominent peak at 2280 keV. Later in the study of the multiplicities, it will be shown that $M_m = 1$ is dominant around 2280 keV. For this reason, we found that the best fit of this experimental region was obtained increasing the proportion of single γ-transitions with respect to cascade transitions from this region to the ground state. We tried three ways of doing this: a) considering first forbidden transitions to the levels in the part of the branching ratio matrix corresponding to the unknown region, b) increasing the normalization of the $M1$ γ-strength function by a factor of 10, and c) decreasing the Lorentzian function centroid energy of the $M1$ γ-strength function to 0.8 MeV. Under all these conditions, we obtained a good fit both for the β-gated spectrum and for the singles spectrum, as can be seen in Figure 9.9. A comparison of the β intensity distributions obtained from these two fits is shown in Figure 9.8.

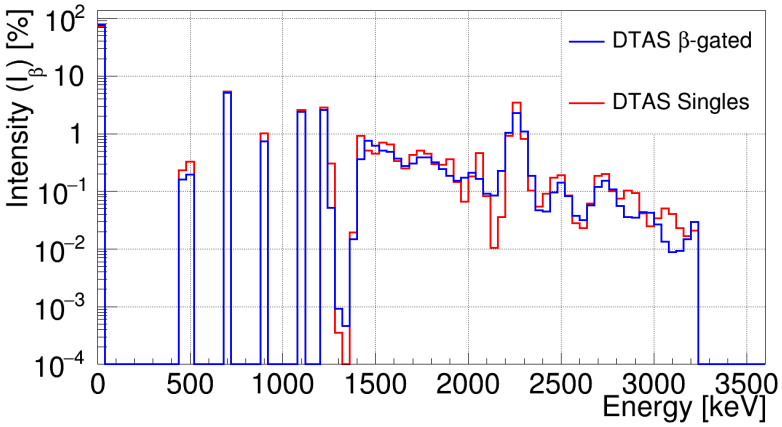

Figure 9.8: The β-intensity distribution of the decay of ^{103}Mo from the analysis of the β-gated spectrum and the analysis in singles, are compared.

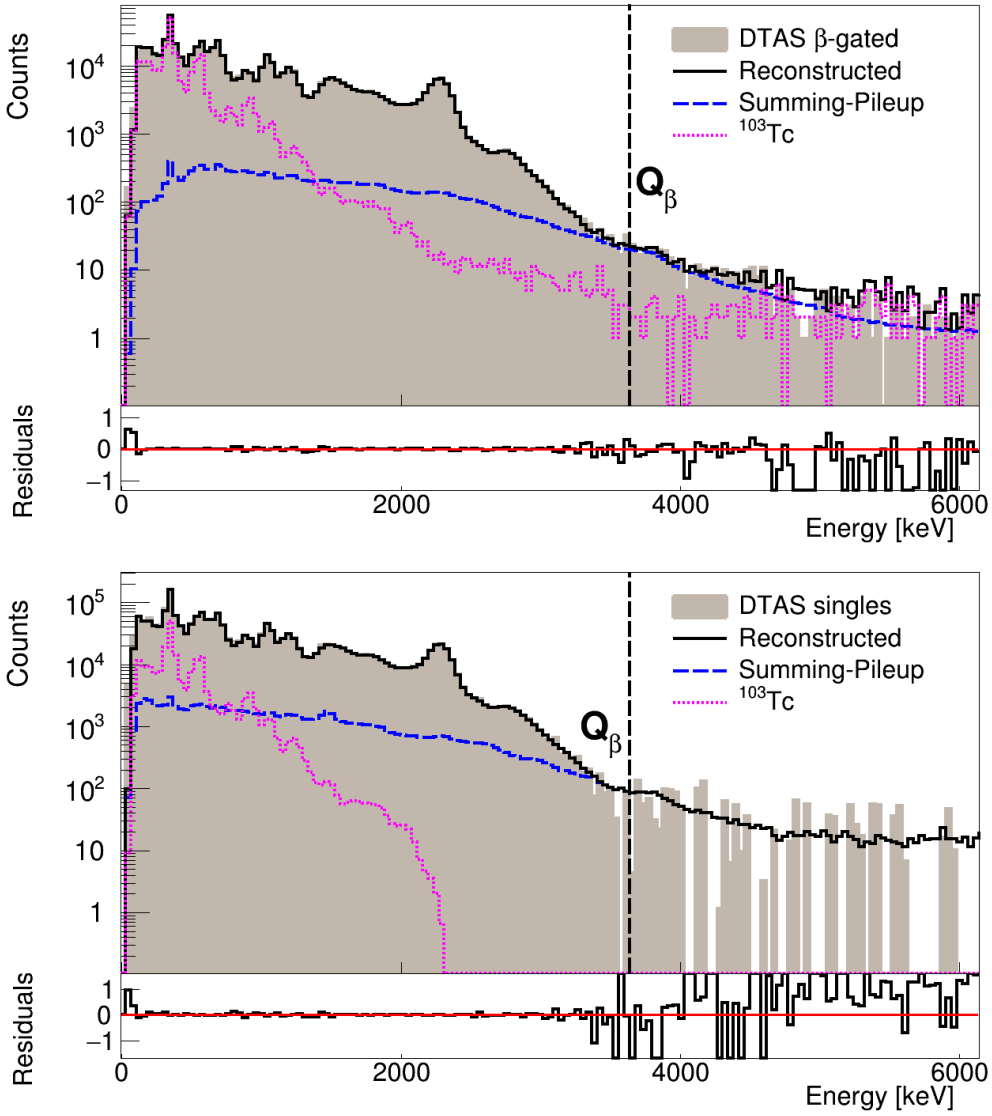

Figure 9.9: Result of the analysis of the decay of ^{103}Mo. The total spectrum is compared with the spectrum reconstructed one after the analysis for the β-gated analysis and the analysis in singles.

Regarding the reproduction of the multiplicities, we have observed a deficit in multiplicity M_m=1 and an overestimation of higher multiplicities, specially $M_m = 3$, as shown in Figure 9.10. This is related to the quality of the global fit in the region of the peak at 2280 keV that was discussed above. Among the three possibilities to improve this fit, the only one that gave a more reasonable reproduction of the multiplicities is c) (decreasing the Lorentzian function centroid energy of the $M1$). In Figure 9.11 the reproduction of the first six multiplicities can be seen.

We have also investigated the reproduction of the three geometrically distinguishable individual crystals of DTAS (one central, one in the middle of a row, and one in a corner). A reasonable agreement was found, as shown in Figure 8.10. It has to be noted that no summing-pileup contribution has been calculated in this case.

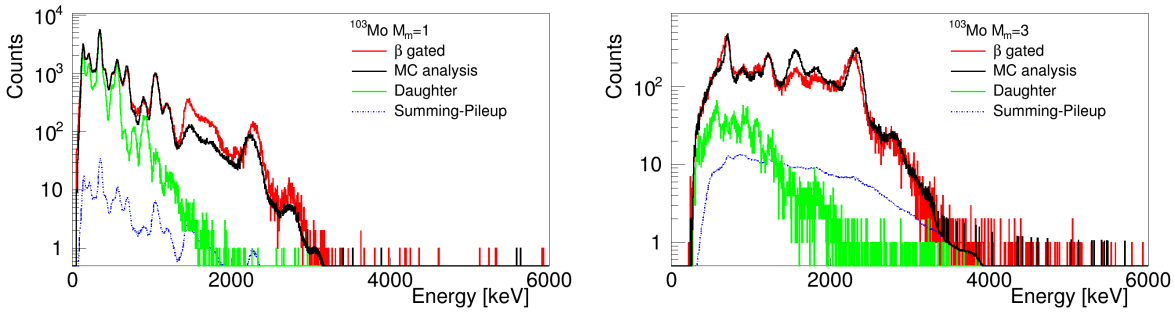

Figure 9.10: Poor reproduction of multiplicities 1 and 3 in the decay of ^{103}Mo.

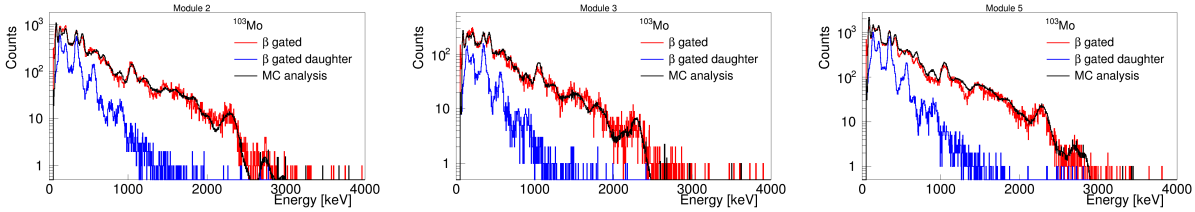

Figure 9.12: ^{103}Mo experimental spectra for the three geometrically distinguishable individual crystals compared with the MC.

The evaluation of the β-intensity distribution and the errors have been done by combing all the possibilities in the branching ratio matrix construction with a known level scheme up to the level at 1219.85 keV, as well as changing the normalization of the contaminants. The effect on the branching ratio matrix of different values of the spin an parity have been considered, including the possibility of $1/2^+$ for the ground state of the parent; the effect of not considering the conversion coefficients, and the change in the γ-intensity of the γ-ray of 1085.95 keV have also been included. Moreover, the three different sets of correction factors for the HFB+c level density were also taken into account. Concerning the normalization factors of the contaminants, we observed that a changed of 10% in the summing-pileup and daughter activity normalization factors still gave a good fit. Furthermore, the singles analysis was also included in the evaluation, as well as the analysis with the Maximum Entropy (ME) algorithm. The resulting β-intensity distribution with errors is shown in Figure 9.13 and listed in Table 9.4. As usual, the largest contribution to the errors is coming from the normalization factors of the contaminants, especially from the daughter contamination in this case, which affects dramatically the low energy region and thus the sensitivity to the ground state to ground state transition. In Figure 9.13, a comparison with the high resolution (HR) values from [222] is shown. It has to be noted that no evaluated β-intensities were available up to now [220]. For this comparison, we have fixed the ground state feeding intensity to the one obtained with DTAS, and we have considered the conversion coefficients from Table 9.2 in order to carry out the intensity balance, thus deducing feeding probabilities that could be compared with ours.

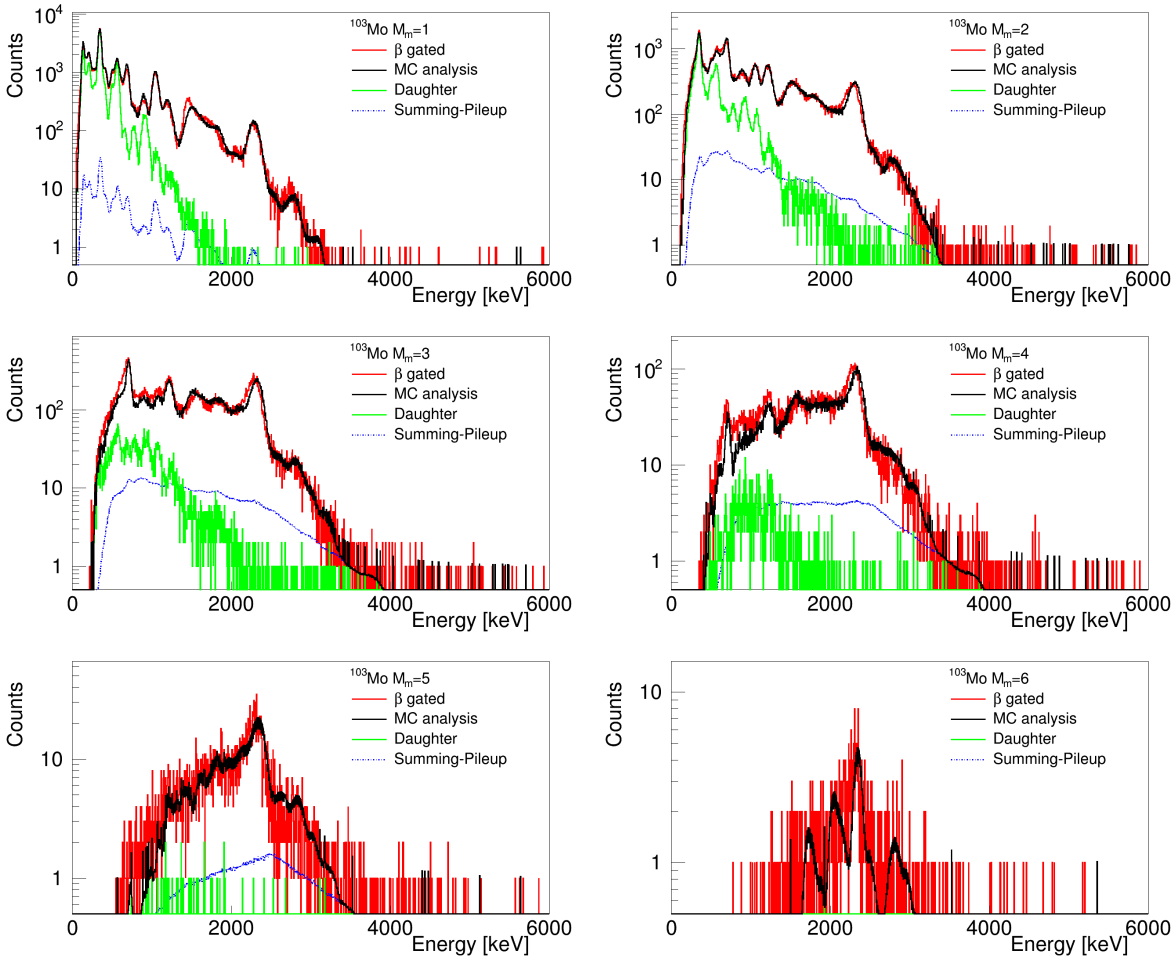

Figure 9.11: Experimental spectra for different multiplicities for the decay of ^{103}Mo compared with the MC simulation performed with an event generator for multiplicities from 1 to 6.

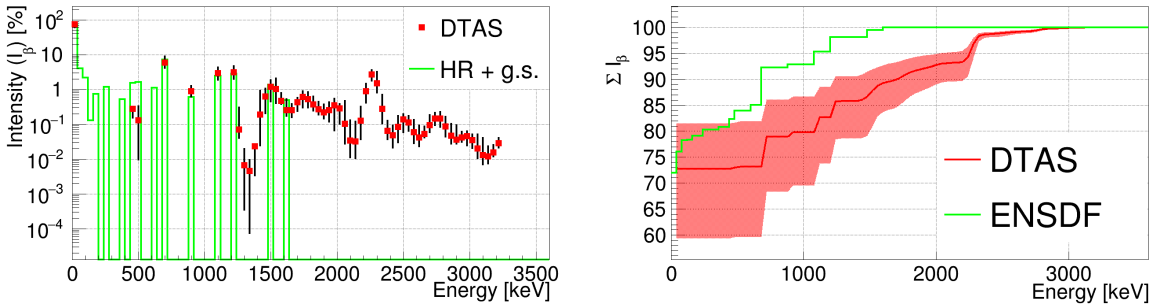

Figure 9.13: β-intensities of the decay of ^{103}Tc with error bars coming from the uncertainty of all the sources of error.

Energy [keV]	I_β DTAS [%]
0.000	$72.720^{+8.791}_{-13.430}$
469.770	$0.276^{+0.032}_{-0.124}$

Continues on the next page.

Energy [keV]	I_β DTAS [%]
519.220	$0.130^{+0.194}_{-0.120}$
687.600	$2.008^{+1.739}_{-0.859}$
691.590	$3.759^{+1.181}_{-0.814}$
887.200	$0.886^{+0.364}_{-0.271}$
1085.950	$2.894^{+1.356}_{-1.005}$
1219.850	$3.062^{+1.597}_{-1.055}$
1260.000	$0.070^{+0.231}_{-0.030}$
1300.000	$0.007^{+0.013}_{-0.006}$
1340.000	$0.004^{+0.005}_{-0.004}$
1380.000	$0.023^{+0.004}_{-0.023}$
1420.000	$0.185^{+0.729}_{-0.182}$
1460.000	$0.624^{+0.437}_{-0.603}$
1500.000	$1.167^{+0.656}_{-0.713}$
1540.000	$1.006^{+1.080}_{-0.609}$
1580.000	$0.461^{+0.320}_{-0.351}$
1620.000	$0.249^{+0.265}_{-0.240}$
1660.000	$0.250^{+0.130}_{-0.244}$
1700.000	$0.425^{+0.143}_{-0.190}$
1740.000	$0.599^{+0.630}_{-0.301}$
1780.000	$0.518^{+0.303}_{-0.326}$
1820.000	$0.370^{+0.247}_{-0.123}$
1860.000	$0.263^{+0.215}_{-0.073}$
1900.000	$0.217^{+0.147}_{-0.149}$
1940.000	$0.252^{+0.173}_{-0.219}$
1980.000	$0.343^{+0.352}_{-0.276}$
2020.000	$0.280^{+0.125}_{-0.178}$
2060.000	$0.101^{+0.358}_{-0.101}$
2100.000	$0.033^{+0.095}_{-0.033}$
2140.000	$0.032^{+0.087}_{-0.032}$
2180.000	$0.126^{+0.191}_{-0.126}$
2220.000	$0.880^{+0.555}_{-0.880}$
2260.000	$2.645^{+0.961}_{-0.886}$
2300.000	$1.506^{+1.639}_{-0.698}$
2340.000	$0.275^{+0.412}_{-0.275}$
2380.000	$0.065^{+0.061}_{-0.065}$
2420.000	$0.047^{+0.044}_{-0.047}$
2460.000	$0.084^{+0.090}_{-0.080}$
2500.000	$0.138^{+0.265}_{-0.079}$
2540.000	$0.111^{+0.060}_{-0.046}$
2580.000	$0.059^{+0.072}_{-0.058}$
2620.000	$0.041^{+0.050}_{-0.041}$

Continues on the next page.

Energy [keV]	I_β DTAS [%]
2660.000	$0.052^{+0.033}_{-0.050}$
2700.000	$0.092^{+0.092}_{-0.056}$
2740.000	$0.146^{+0.162}_{-0.053}$
2780.000	$0.144^{+0.078}_{-0.061}$
2820.000	$0.086^{+0.075}_{-0.070}$
2860.000	$0.046^{+0.057}_{-0.044}$
2900.000	$0.036^{+0.058}_{-0.029}$
2940.000	$0.041^{+0.050}_{-0.010}$
2980.000	$0.045^{+0.068}_{-0.021}$
3020.000	$0.034^{+0.017}_{-0.024}$
3060.000	$0.020^{+0.031}_{-0.019}$
3100.000	$0.013^{+0.028}_{-0.012}$
3140.000	$0.012^{+0.011}_{-0.007}$
3180.000	$0.015^{+0.010}_{-0.004}$
3220.000	$0.029^{+0.037}_{-0.007}$

Table 9.4: I_β intensities of the decay of ^{103}Mo.

Finally, the g.s. feeding intensity is compatible within the errors with the value obtained by applying the β-γ counting method of Appendix D, which gives a result of 58(13)%. In both cases, the uncertainty in the normalization of the daughter, leads to those large errors.

Chapter 10

^{140}Cs decay

Hay más cosas en el cielo y en la tierra, Horacio, que todas las que pueda soñar tu filosofía

There are more things in heaven and earth, Horatio, than are dreamt of in your philosophy

William Shakespeare

In this chapter the β-decay of an important fission fragment, ^{140}Cs, into ^{140}Ba will be studied. The study of this decay, apart from being relevant from the point of view of the antineutrino spectrum calculation, as mentioned in Chapter 1, represents a cross-check for TAGS analysis techniques because it was already measured with this technique at the INEL ISOL facility by Greenwood et al. [131,226]. The experimental measurements were described in Chapter 6, and here our TAGS analysis and results will be presented.

10.1 Experimental spectra

10.1.1 β-gated spectrum

The experimental DTAS singles spectrum corresponding to the total statistics of runs 374-386 is presented in Figure 10.1 left, where the β-gated spectrum is also shown.

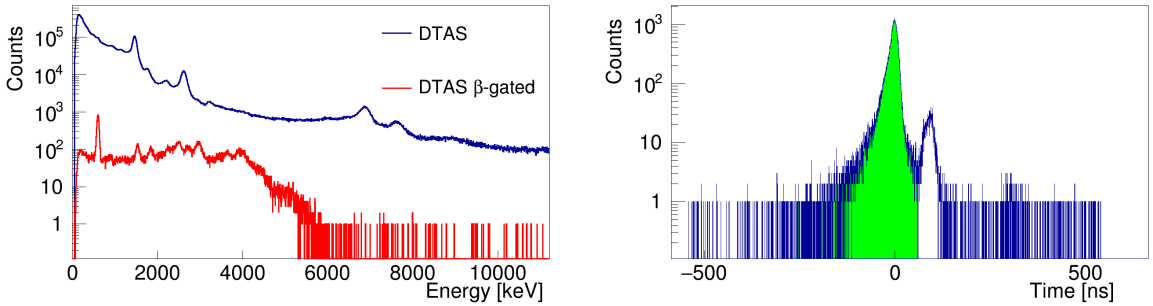

Figure 10.1: Comparison between the β-gated spectrum and the raw spectrum of DTAS for the decay of ^{140}Cs (left). The TAC spectrum DTAS-β plastic detector for the measurement of the decay of ^{140}Cs (right).

The window applied on the β-γ TAC spectrum is shown in Figure 10.1 right. The

secondary peak of the TAC, excluded from the coincidence, contains less that 1000 counts of background.

10.1.2 Contaminants

Since the half-life of the daughter is 12.75 d (compared with 63.7 s for ^{140}Cs, as presented in Table 6.1), its decay does not contribute to the spectrum and the only contaminant of this decay is the summing-pileup of signals. In Figure 10.2 this contribution is presented normalized with the theoretical expression from Equation (4.4). Due to the low counting rate it is a small contribution.

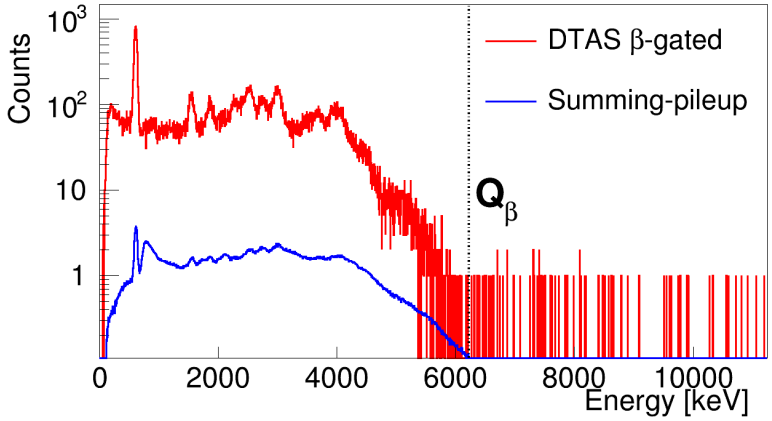

Figure 10.2: Relevant histograms for the analysis of the decay of ^{140}Cs. β-gated experimental spectrum (red) and contribution of the summing-pileup (blue).

10.2 Branching ratio matrix

According to RIPL-3 [145] the level scheme of ^{140}Ba is complete up to 2.52 MeV excitation energy (18 levels). In the construction of the branching ratio matrix and response function for the decay of ^{140}Cs, we will consider these 18 levels as the known part at low excitation energies. Those levels without assigned spin-parity values are summarized in Table 10.1, and for our analysis the recommended values from RIPL-3 [145] will be employed.

Energy [keV]	J^P ENSDF	J^P used
1951.6	(3^+)	3^+
2138.23	$3^{(+)}$	3^+
2152.1	(5^-)	5^-
2204.2	2^+, 3	3^+
2309.51	2^+, 1	2^+
2320.51	(3, 4^+)	3^+
2429.52	1, 2^+	1^+
2468.3	(8^+)	8^+

Continues on the next page.

Energy [keV]	J^P ENSDF	J^P used
2521.81	$(1, 2^+)$	2^+

Table 10.1: Levels with no spin-parity assignment for ENSDF and our choice (up to 2521.8 keV).

With respect to the unknown part of the level scheme, the statistical model will be used as described in Chapter 2. For this, the γ-strength function parameters presented in Table 2.1 will be used. The level density data from HFB+c calculations [149,212] available at RIPL-3 [145] and presented in Figure 10.3 will be used. The correction parameters for the level density distribution are shown in Table 10.2, where we present an additional set of correction factors. The new C and P values match better the low energy region where we trust the known level scheme, as can be seen in Figure 10.3.

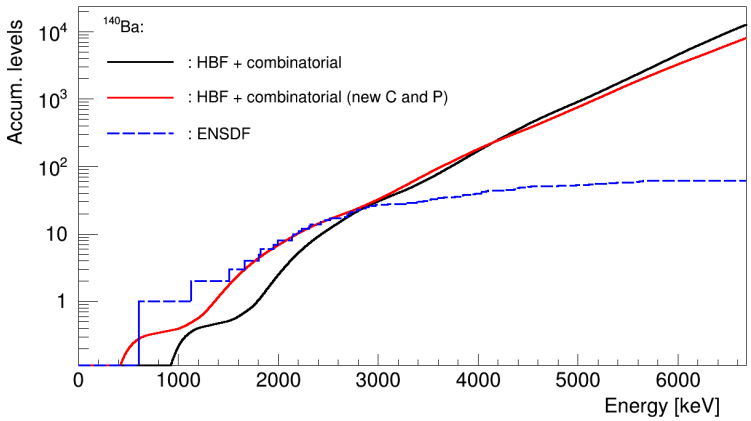

Figure 10.3: Accumulated number of levels in ^{140}Ba. The blue line is obtained from ENSDF and the black line corresponds to the Hartree-Fock-Bogoliubov calculation downloaded from RIPL-3. In addition, a new C and P factors (red) have been tested to obtain a better agreement at low energies with the known part.

C	P
0.0	0.72951
-0.5	0.2

Table 10.2: Correction factors for the HFB+c level density distribution for ^{140}Ba (first row). In order to match better the experimental accumulated number of levels at low energies, we have changed the C and P factors (second row).

10.3 Analysis and results

In the analysis we allowed direct feeding from the 1^- ground state of ^{140}Cs to 0^-, 1^- and 2^- levels in ^{140}Ba (allowed transitions), as well as to 0^+, 1^+, 2^+ and 3^+ levels (first forbidden transitions).

The quality of the reproduction of the measured spectrum is shown in Figure 10.4, and the resulting I_β distribution is presented in Figure 10.5. It is compared with the distribution obtained previously with TAGS by Greenwood *et al.* [131], using another method of analysis and a different set-up, and with the distribution from high resolution measurements [227]. It can be seen how *Pandemonium* affects the high resolution data [228,229], overestimating the β-intensity at low energies. Moreover, it also shows that our data and data from Greenwood *et al.* are in good agreement.

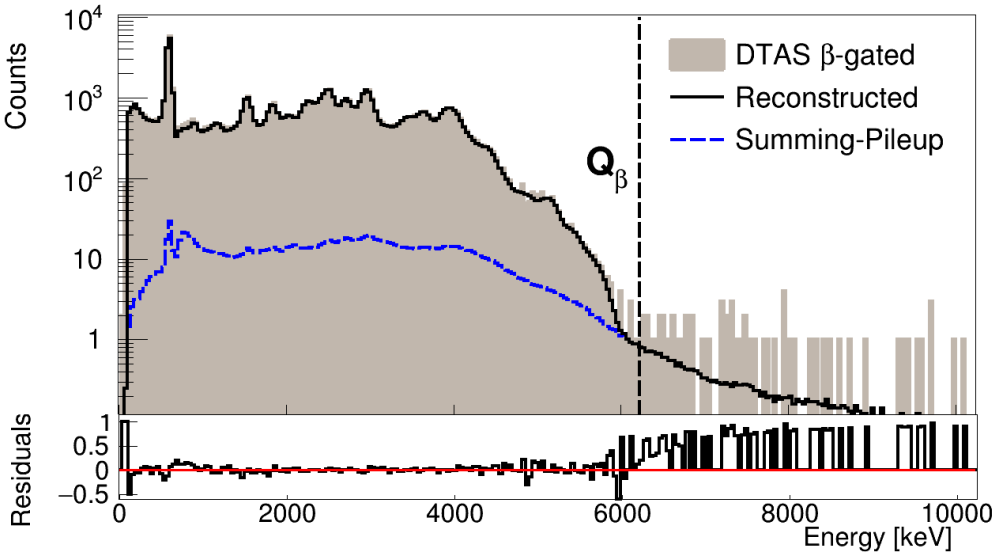

Figure 10.4: Result of the analysis of the decay of ^{140}Cs. The total spectrum is compared with the reconstructed one after the analysis.

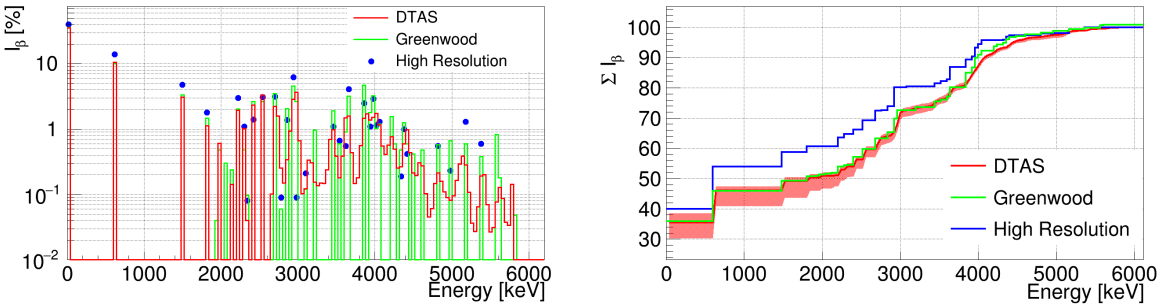

Figure 10.5: β-intensities of the decay of ^{140}Cs with error bars coming from different sources of systematic error investigated.

Several sources of systematic error were investigated. We found that a good reproduction of the spectrum is compatible with a change in the normalization factor of the summing-pileup of a $\pm 100\%$ (note that it is a small contribution for this measurement, due to the low counting rate). We have also evaluated the β-feeding distributions considering the following systematic effects: primary levels fed by allowed transitions or by first forbidden transitions in the unknown part of the response function, the original HFP+c

level density correction factors or the new ones, and changes in the first bin of the spectrum considered in the analysis (which affects especially the sensitivity to the ground state feeding intensity). We also considered the effect of using the ME algorithm instead of the EM. Finally, we have considered a modified branching ratio matrix that reproduces better the experimental γ-intensities known from high resolution measurements [227], as presented in Table 10.3.

Energy [keV]	I_γ ENSDF	I_γ DTAS	I_γ DTAS*
602.31	0.529	0.482	0.524
1130.55	0.029	0.068	0.028
1510.63	0.086	0.059	0.072
1802.84	0.059	0.132	0.050
1823.78	0.024	0.016	0.022
1951.63	0.002	0.006	0.003
1993.58	0.024	0.012	0.009
2138.25	0.016	0.005	0.006
2204.2	0.008	0.004	0.007
2237.22	0.058	0.021	0.030
2309.82	0.017	0.013	0.008
2320.78	0.006	0.003	0.004
2429.51	0.020	0.025	0.025
2521.85	0.038	0.034	0.028

Table 10.3: Absolute γ-intensities de-exciting the main levels populated in the decay of ^{140}Cs (per 100 decays). The second column corresponds to the intensities obtained from high resolution data [227]. The third column gives the intensities obtained with DTAS for the reference analysis, whereas the intensities obtained with a modified branching ratio matrix are presented in the fourth column (DTAS*).

It is worth mentioning that both sets of correction factors for the level density give almost the same results, and both assumptions concerning the primary levels fed in the unknown part also lead to very similar fits, although the first forbidden option reproduces better the γ-intensities and the different multiplicities presented in Figure 10.6. As a result, our reference analysis is associated with a response function constructed with the original level density corrections and first forbidden transitions feeding the unknown part of the level scheme. The result of all the combinations of the different variations described for the analysis, gives the systematic error evaluation that we show in Figure 10.5, and is included in Table 10.4, where the values from high resolution [227] and Greenwood *et al.* [131] are also listed. Note that above the last level of the known level scheme used for the analysis, the values from the bibliography listed in Table 10.4 correspond to integral values over our energy bins. When comparing the results from Greenwood *et al.* with our results in Table 10.4 one should note that in their analysis the region of the decay at high excitation energies is fitted with the introduction of discrete pseudo-levels, different from our approach of a binned continuum. For this reason, the best way to compare the results

is using the accumulated β-intensities as in Figure 10.5.

Energy [keV]	I_β HR [%]	I_β Greenwood [%]	I_β DTAS [%]
0.000	40(4)	35.9(17)	$35.497^{+2.993}_{-5.366}$
602.370	14(3)	10.07	$10.547^{+0.640}_{-2.265}$
1510.680	4.8(6)	3.36	$3.073^{+0.189}_{-0.643}$
1823.800	1.8(2)	1.46	$1.122^{+1.177}_{-0.039}$
1951.610	-	0.04	-
1993.660	-	0.48	$0.609^{+0.230}_{-0.145}$
2061.200	-	0.3	-
2138.240	-	0.24	$0.144^{+0.649}_{-0.051}$
2152.100	-	-	-
2204.210	0.2(1)	0.6	$0.114^{+0.541}_{-0.082}$
2237.240	2.8(4)	1.44	$1.815^{+0.176}_{-0.478}$
2309.520	1.1(1)	0.48	$1.023^{+0.187}_{-0.362}$
2320.510	0.08(7)	0.097	$0.040^{+0.448}_{-0.006}$
2429.520	0.08(7)	2.64	$2.330^{+0.300}_{-0.060}$
2468.300	-	-	-
2521.810	3.1(3)	2.64	$3.241^{+0.287}_{-0.737}$
2540.000		-	$0.113^{+0.694}_{-0.056}$
2580.000	-	-	$0.001^{+0.066}_{-0.000}$
2620.000	-	-	$0.001^{+0.054}_{-0.000}$
2660.000	-	-	$0.101^{+0.234}_{-0.028}$
2700.000	3.16(31)	3.480	$2.236^{+0.117}_{-0.682}$
2740.000	-	-	$1.586^{+0.604}_{-0.068}$
2780.000	0.09(6)	0.060	$0.255^{+0.299}_{-0.007}$
2820.000	-	-	$0.150^{+0.108}_{-0.006}$
2860.000	1.38(24)	2.050	$0.343^{+0.172}_{-0.105}$
2900.000	-	-	$0.940^{+0.046}_{-0.158}$
2940.000	6.2(5)	4.550	$2.869^{+0.218}_{-0.550}$
2980.000	0.09(7)	2.640	$3.668^{+0.603}_{-0.436}$
3020.000	-	-	$0.666^{+0.529}_{-0.014}$
3060.000	-	-	$0.103^{+0.196}_{-0.006}$
3100.000	0.21(9)	0.120	$0.123^{+0.073}_{-0.010}$
3140.000	-	-	$0.337^{+0.143}_{-0.120}$
3180.000	-	-	$0.305^{+0.092}_{-0.028}$
3220.000	-	0.960	$0.155^{+0.097}_{-0.009}$
3260.000	-	-	$0.137^{+0.073}_{-0.015}$
3300.000	-	-	$0.149^{+0.107}_{-0.022}$
3340.000	-	-	$0.148^{+0.077}_{-0.016}$
3380.000	-	-	$0.240^{+0.145}_{-0.014}$
3420.000	-	-	$0.699^{+0.039}_{-0.136}$

Continues on the next page.

Energy [keV]	I_β HR [%]	I_β Greenwood [%]	I_β DTAS [%]
3460.000	1.1(1)	1.920	$0.974^{+0.155}_{-0.293}$
3500.000	-	-	$0.383^{+0.175}_{-0.015}$
3540.000	0.66(21)	0.600	$0.180^{+0.235}_{-0.007}$
3580.000	-	-	$0.384^{+0.268}_{-0.092}$
3620.000	0.55(7)	0.900	$1.480^{+0.073}_{-0.394}$
3660.000	4.1(4)	3.180	$1.594^{+0.262}_{-0.352}$
3700.000	-	-	$0.440^{+0.255}_{-0.012}$
3740.000	-	-	$0.147^{+0.206}_{-0.006}$
3780.000	-	-	$0.181^{+0.162}_{-0.007}$
3820.000	-	-	$0.558^{+0.092}_{-0.105}$
3860.000	2.50(31)	4.730	$1.476^{+0.086}_{-0.525}$
3900.000	-	-	$1.710^{+0.078}_{-0.246}$
3940.000	1.1(2)	1.800	$1.381^{+0.330}_{-0.074}$
3980.000	2.9(3)	3.240	$1.507^{+0.119}_{-0.115}$
4020.000	1.14(14)	1.020	$1.730^{+0.085}_{-0.367}$
4060.000	1.3(1)	1.200	$1.166^{+0.202}_{-0.133}$
4100.000	-	-	$0.553^{+0.172}_{-0.013}$
4140.000	-	-	$0.411^{+0.148}_{-0.011}$
4180.000	-	-	$0.568^{+0.028}_{-0.069}$
4220.000	-	1.560	$0.767^{+0.048}_{-0.252}$
4260.000	-	0.600	$0.494^{+0.108}_{-0.038}$
4300.000	-	-	$0.253^{+0.124}_{-0.006}$
4340.000	0.19(3)	0.480	$0.266^{+0.135}_{-0.039}$
4380.000	0.99(9)	1.260	$0.597^{+0.023}_{-0.134}$
4420.000	0.42(8)	0.600	$0.984^{+0.071}_{-0.387}$
4460.000	-	-	$0.440^{+0.150}_{-0.056}$
4500.000	-	0.420	$0.214^{+0.169}_{-0.013}$
4540.000	-	-	$0.196^{+0.071}_{-0.070}$
4580.000	-	-	$0.304^{+0.030}_{-0.122}$
4620.000	-	0.480	$0.276^{+0.060}_{-0.117}$
4660.000	-	-	$0.104^{+0.040}_{-0.010}$
4700.000	-	-	$0.045^{+0.053}_{-0.009}$
4740.000	-	-	$0.061^{+0.051}_{-0.029}$
4780.000	-	-	$0.147^{+0.030}_{-0.052}$
4820.000	0.55(6)	0.580	$0.215^{+0.035}_{-0.074}$
4860.000	-	-	$0.159^{+0.017}_{-0.032}$
4900.000	-	-	$0.110^{+0.017}_{-0.013}$
4940.000	-	-	$0.089^{+0.018}_{-0.017}$
4980.000	0.23(6)	0.660	$0.081^{+0.021}_{-0.016}$
5020.000	-	-	$0.096^{+0.022}_{-0.016}$
5060.000	-	-	$0.164^{+0.026}_{-0.037}$

Continues on the next page.

Energy [keV]	I_β HR [%]	I_β Greenwood [%]	I_β DTAS [%]
5100.000	-	-	$0.293^{+0.185}_{-0.006}$
5140.000	-	-	$0.389^{+0.205}_{-0.032}$
5180.000	1.3(1)	0.600	$0.283^{+0.164}_{-0.032}$
5220.000	-	-	$0.109^{+0.081}_{-0.014}$
5260.000	-	-	$0.037^{+0.058}_{-0.007}$
5300.000	-	-	$0.027^{+0.047}_{-0.005}$
5340.000	-	-	$0.065^{+0.040}_{-0.009}$
5380.000	0.6(1)	0.380	$0.193^{+0.080}_{-0.067}$
5420.000	-	-	$0.202^{+0.110}_{-0.066}$
5460.000	-	-	$0.070^{+0.079}_{-0.011}$
5500.000	-	-	$0.027^{+0.059}_{-0.008}$
5540.000	-	-	$0.031^{+0.038}_{-0.012}$
5580.000	-	0.820	$0.076^{+0.041}_{-0.026}$
5620.000	-	0.180	$0.129^{+0.052}_{-0.064}$
5660.000	-	-	$0.087^{+0.040}_{-0.025}$
5700.000	-	-	$0.038^{+0.047}_{-0.006}$
5740.000	-	-	$0.034^{+0.053}_{-0.014}$
5780.000	-	-	$0.143^{+0.117}_{-0.101}$
5820.000	-	0.048	-

Table 10.4: I_β intensities of the decay of ^{140}Cs.

The g.s. feeding intensity obtained with DTAS is very close to the value obtained by Greenwood *et al.* [131]. It is worth noting that the value from [131] (35.9(17)%) is supposed to be obtained from a β-γ counting method for TAGS data proposed in [134], although in that work a 36.9(17) was quoted. We have also evaluated the β-intensity to the ground state by applying the β-γ counting method of Appendix D, and a 35.1(6)% is obtained. All of these values are in agreement within the quoted errors.

Looking at the multiplicities in Figure 10.6, an excess in multiplicity $M_m = 1$ is found in the region where the statistical model is employed. This excess is observed for all the combinations performed for the error evaluation. With the modified branching ratio matrix that improves the reproduction of I_γ, this excess is reduced, as shown in Figure 10.7, at the expense of worsening the rest of the multiplicities.

We have also tried different changes in the γ-strength factors employed in the response function construction in order to improve this reproduction. Specifically, for the reference response a possible solution could be decreasing the $M1$ and $E2$ normalization (because these transitions connect 1^+, 2^+, 3^+ levels with the 0^+ ground state). Such a change did improve the reproduction of $M_m = 1$, although the most effective change was found to be decreasing the Lorentzian centroid energy of the $E1$ PSF by a factor of around 30%. Unfortunately, in every scenario an improvement of $M_m = 1$ turned out to be linked to a poorer reproduction of the rest of multiplicities. It is worth mentioning that an $E1$ Pygmy dipole resonance structure, associated with 1^- levels at high energies, has been pointed out

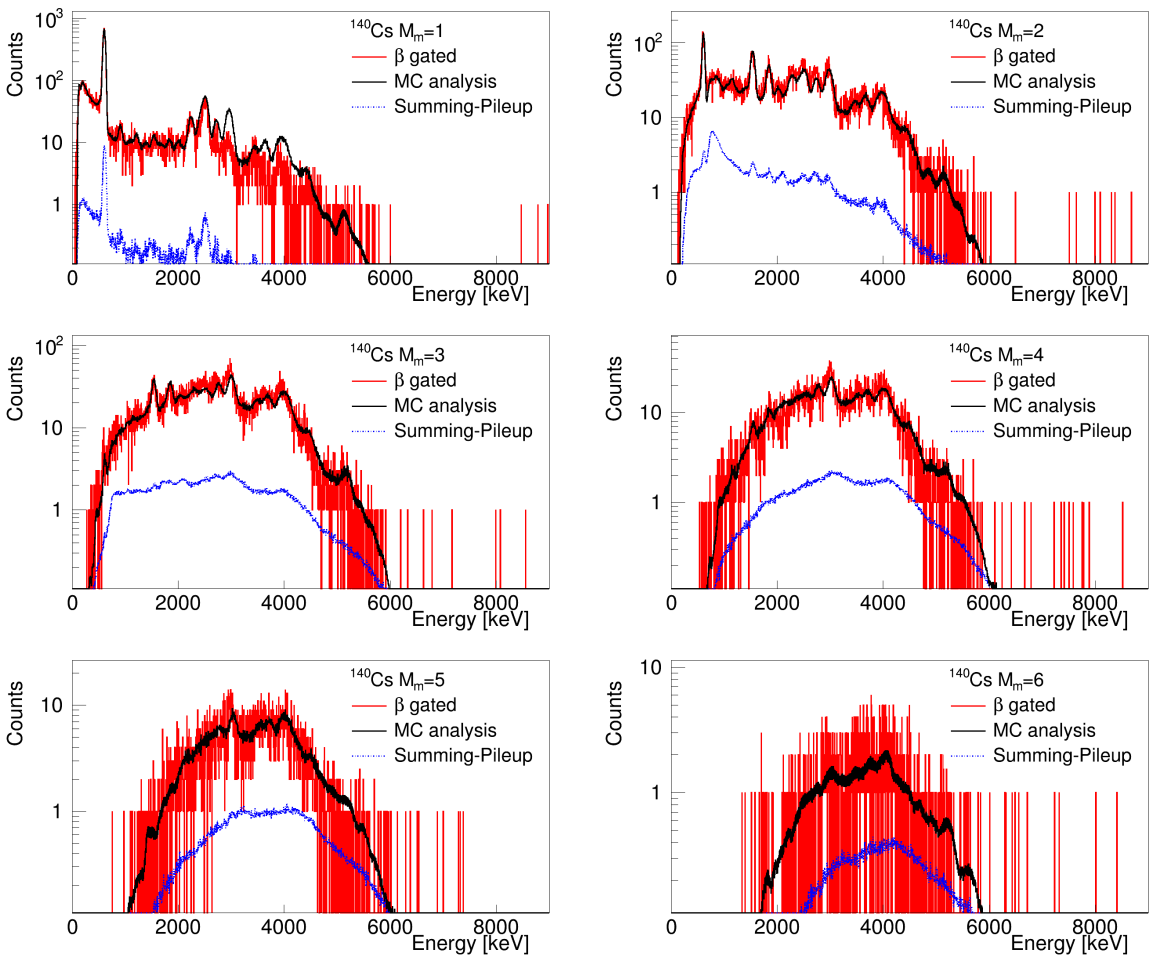

Figure 10.6: Experimental spectra for different multiplicities for the decay of ^{140}Cs compared with the MC simulation performed with an event generator for multiplicities from 1 to 6.

to play a role inside the Q_β of the decay of ^{140}Cs [230]. This could introduce additional effects in the $E1$ shape that we have considered by adding another generalized Lorentzial peak at 8 MeV to the $E1$ γ-strength function employed (see Figure 10.8 right). As a result, a slight improvement in the reproduction of $M_m = 1$ is achieved, when modifying the branching ratio matrix to improve the I_γ reproduction, as shown in Figure 10.8 left.

Finally, the reproduction of the individual modules has also been studied, as displayed in Figure 10.9, finding a good agreement between the experimental spectra and the MC performed with an event generator that uses as input the result of the reference analysis.

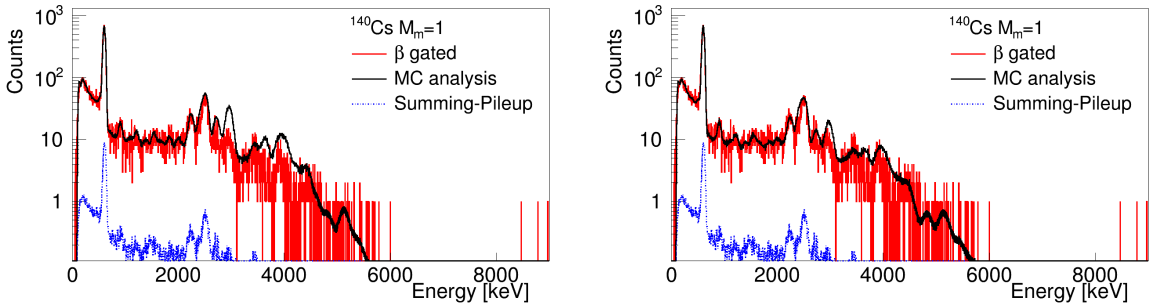

Figure 10.7: ^{140}Cs multiplicity spectra 1 for the reference response function and for the response constructed with the modified branching ratio matrix that improves the I_γ reproduction.

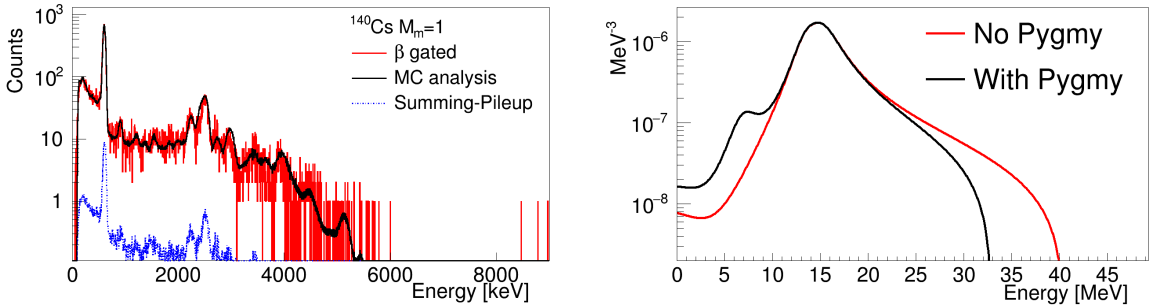

Figure 10.8: ^{140}Cs $M_m = 1$ multiplicity spectra when a $E1$ Pygmy dipole resonance is considered and the branching ratio matrix is modified to improve the I_γ reproduction (left). The $E1$ γ-strength function for ^{140}Ba with and without considering the $E1$ Pygmy dipole resonance are depicted (right).

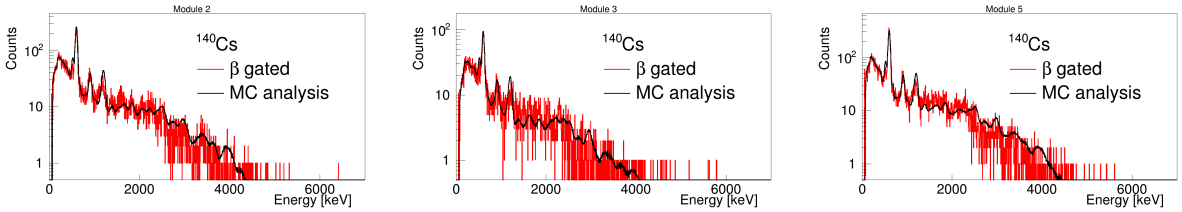

Figure 10.9: ^{140}Cs experimental spectra for the three geometrically distinguishable individual crystals (one central, one in the middle of a row, and one in a corner) compared with the MC.

Chapter 11

^{100}Nb decay

El científico no estudia la naturaleza porque es útil, sino porque le cautiva, y le cautiva porque es bella

The scientist does not study nature because it is useful to do so. He studies it because he takes pleasure in it, and he takes pleasure in it because it is beautiful

Henri Poincaré

In this chapter the β-decay of ^{100}Nb into ^{100}Mo will be studied. This is a very important decay from the point of view of reactor antineutrino spectrum calculations, as was pointed out in Chapter 1, Section 1.3.4. In the measurement of ^{100}Nb, special care was taken in order to distinguish experimentally between the decay of the two isomeric states depicted in Figure 11.1.

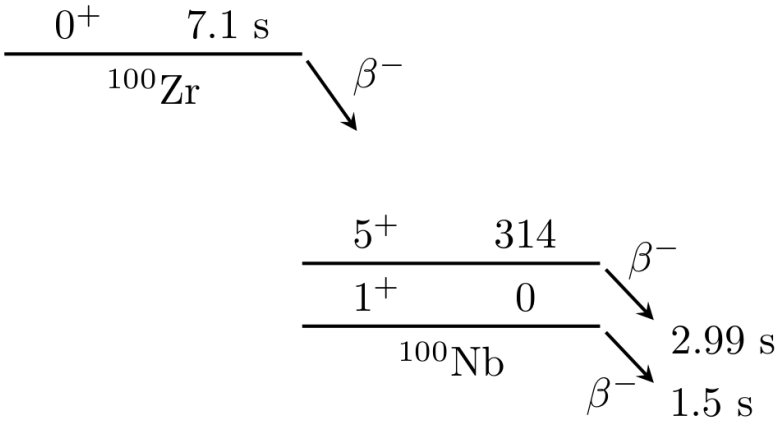

Figure 11.1: Scheme of the two β-decaying isomers in ^{100}Nb. Spin-parities and energies (in keV) of both isomeric states, as well as the half-life of their β-decay are presented. The decay of the ground state of the parent, ^{100}Zr, is also depicted.

The low-spin isomer was populated through the decay of the parent, by selecting ^{100}Zr in JYFLTRAP, since the $0^+ \rightarrow 1^+$ transition is strongly favoured with respect to the $0^+ \rightarrow 5^+$ transition. The high-spin isomer, assumed to be a 5^+ based on [231], was obtained from the

direct measurement of ^{100}Nb ions selected in the trap where both isomers are present. In this case the low-spin isomer from the other measurement is considered to be a contaminant to be subtracted. Moreover, we tried to isolate the high-spin component by using the high precision Ramsey cleaning purification technique [207] explained in Chapter 6.

11.1 Experimental spectra

In this section, the measured spectra corresponding to the three different experimental conditions mentioned above will be shown, i.e., the measurement of the combined decays of ^{100}Zr and ^{100gs}Nb, the measurement of the decay of ^{100m}Nb selected with the Ramsey cleaning technique, and the combined measurement of the decays of both isomers, ^{100gs}Nb and ^{100m}Nb.

11.1.1 β-gated spectrum

The resulting singles spectrum for the total statistics obtained for each of the three different measurements is compared with the β-gated spectrum in Figures 11.2 (runs 295-299), 11.3 (runs 300-304) and 11.4 (runs 279, 281-283, 285-293). The time coincidence window on the β-γ TAC spectrum used in each case is indicated. The secondary peak in Figure 11.3 corresponds to 700 counts from the decay, whereas the one in Figure 11.4 corresponds to 1400 background counts.

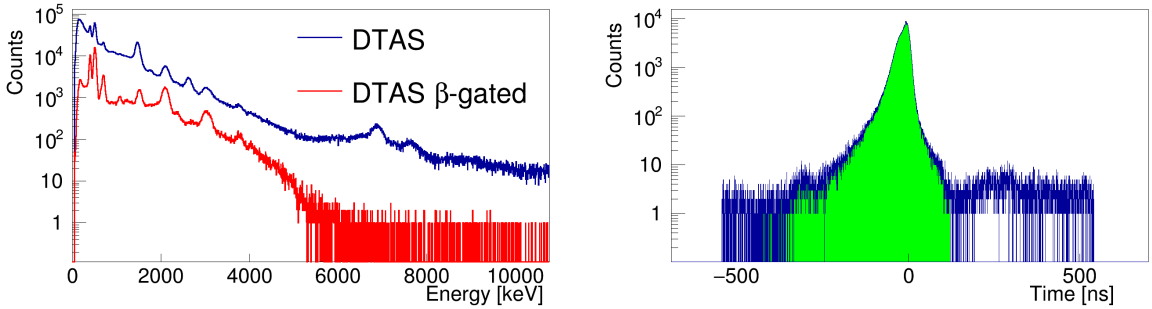

Figure 11.2: Comparison between the β-gated spectrum and the singles spectrum of DTAS for the combination of the decays of ^{100}Zr and ^{100gs}Nb (left). The TAC spectrum between DTAS-β plastic detector for this measurement (right) with the coincidence window highlighted in green.

The three corresponding β-gated spectra are compared in Figure 11.5, where a MC simulation of the decay of ^{100}Zr is also shown. This MC simulation has been obtained with the DECAYGEN event generator [146] using the information from ENSDF [213]. However, a discussion about the completeness of this information will be presented in this chapter based on our measurements.

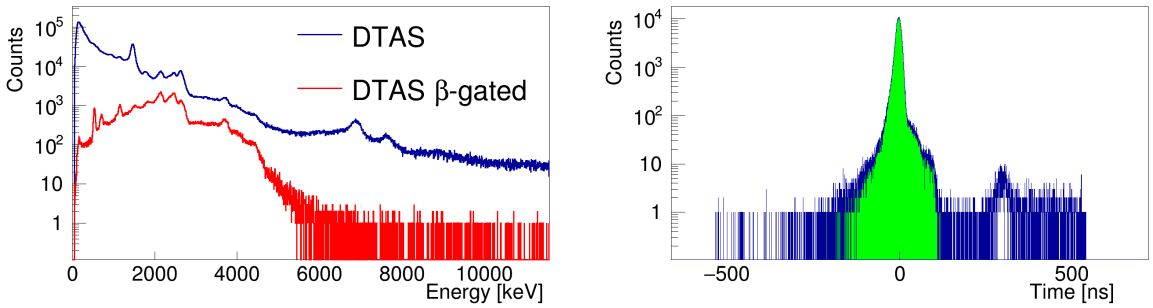

Figure 11.3: Comparison between the β-gated spectrum and the singles spectrum of DTAS for the combination of the decays of ^{100gs}Nb and ^{100m}Nb (left). The TAC spectrum between DTAS-β plastic detector for this measurement (right) with the coincidence window highlighted in green.

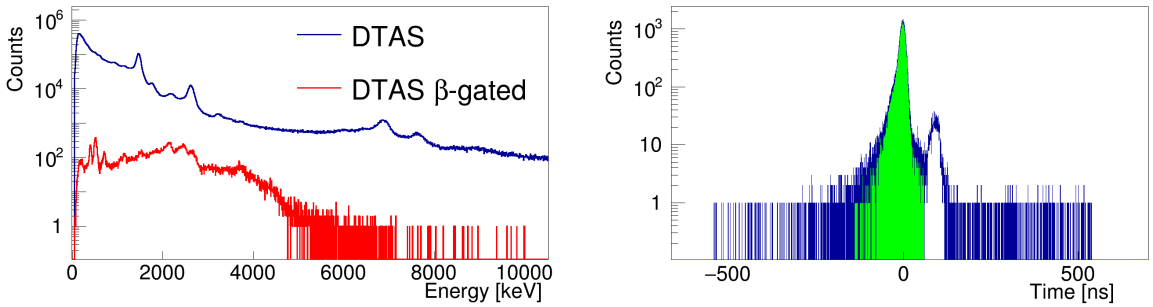

Figure 11.4: Comparison between the β-gated spectrum and the singles spectrum of DTAS for the decay of ^{100m}Nb (measured with the Ramsey cleaning technique), and TAC spectrum between DTAS-β plastic detector (left). The TAC DTAS-β plastic detector for this measurement (right) with the coincidence window highlighted in green.

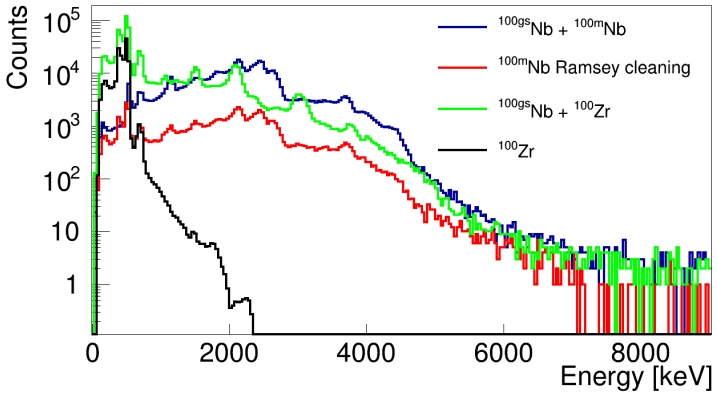

Figure 11.5: Experimental β-gated spectra of the different measurements of the decays of ^{100gs}Nb and ^{100m}Nb: the measurement of the combined decays of ^{100}Zr and ^{100gs}Nb (green), the measurement of the decay of ^{100m}Nb selected with the Ramsey cleaning technique (red), and the combined measurement of the decays of both isomers, ^{100gs}Nb and ^{100m}Nb (blue).

11.1.2 Contaminants

The contaminants for each of the three different measurements will be discussed here.

^{100gs}Nb

From the first measurement, ^{100gs}Nb will be analysed by considering the decay of ^{100}Zr as a contaminant. The normalization of the contaminant is obtained from the γ-ray at 400 keV coming from the decay of ^{100}Zr$\rightarrow^{100}$Nb. The summing-pileup contribution is normalized with the theoretical expression from Equation (4.4). The normalized contaminant spectra are shown in Figure 11.6.

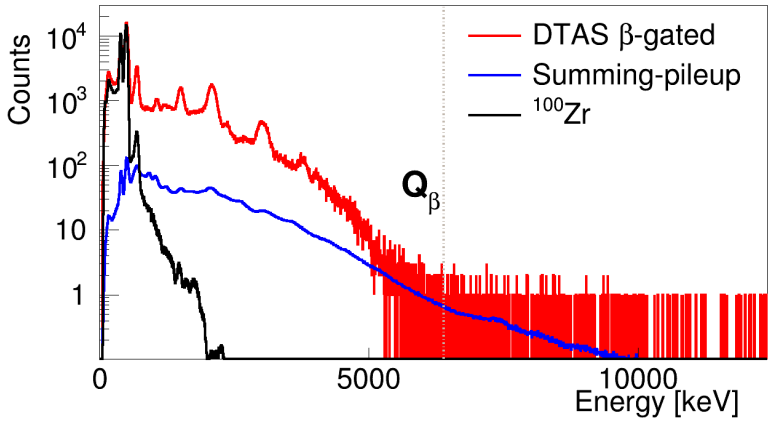

Figure 11.6: Relevant histograms for the analysis of the decay of ^{100gs}Nb. β-gated experimental spectrum (red), contamination from the decay of the parent, ^{100}Zr (black), and the summing-pileup contribution (blue).

^{100m}Nb

Two different strategies were adopted to study this branch, as already mentioned. The first strategy was to measure both isomers together by selecting the frequency of JYFLTRAP associated with ^{100}Nb, as shown in the mass scan of Figure 6.11 of Chapter 6. In this measurement, the high-spin component was favoured in the proton-induced fission process, and the low-spin component was treated as a contaminant. It was normalized by checking the peak at 695.2 keV associated with a level populated only in the decay of ^{100gs}Nb, as well as adjusting the low energy part of the spectrum produced by the penetration of β-particles in the spectrometer, mainly due to the ground state to ground state transition that is only allowed for the decay of the low-spin isomer. The low-spin component in this case represents just 9.4% of the total spectrum free from summing-pileup. In Figure 11.7 the contributions of the contaminants normalized are shown, with the corresponding summing-pileup contribution normalized theoretically.

The second strategy consisted in using a high resolution purification technique in the JYFLTRAP system, based on the use of the purification trap first for isobaric cleaning, followed by the precision trap for isomeric cleaning [207] as described in Chapter 6. The

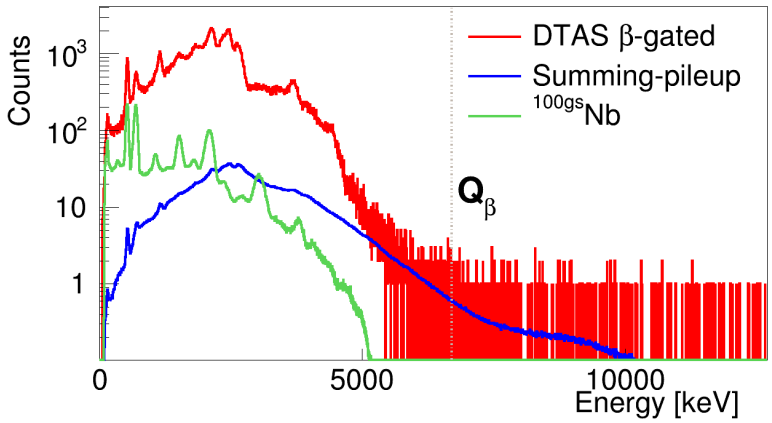

Figure 11.7: Relevant histograms for the analysis of the decay of ^{100m}Nb. β-gated experimental spectrum (red), spectrum of the contamination from the decay of ^{100gs} (green), and the summing-pileup contribution (blue).

study of the resulting spectrum free from summing-pileup gives a contamination of 16.5% from the low-spin isomer. A 9.3% contribution from the decay of ^{100}Zr is also found, probably due to an accidental overlap between the frequency selected in the purification process for ^{100m}Nb and the repeating frequency corresponding to ^{100}Zr, as reported in [232]. The contributions of the low-spin isomeric branch and of the decay of ^{100}Zr were normalized as mentioned before. The β-gated spectrum and the normalized contaminants including the summing-pileup are presented in Figure 11.8, where the summing-pileup contribution is normalized with the theoretical expression from Equation (4.4). A small background contamination is also taken into account, since the low statistics of this measurement leads to a relative enhancement of the random background contribution that affects the analysis close to Q_β.

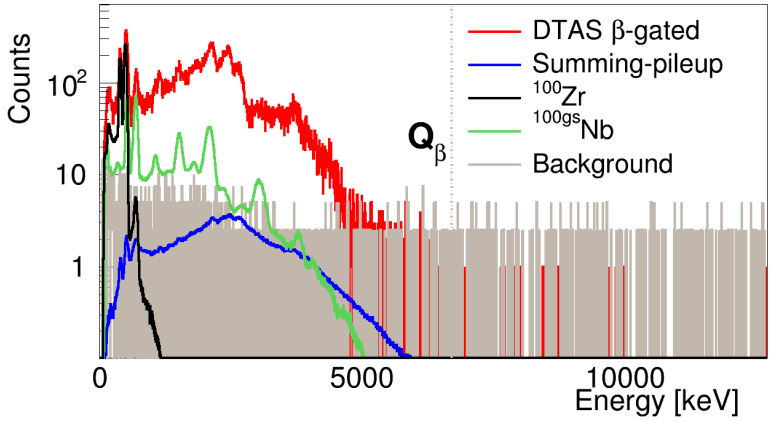

Figure 11.8: Relevant histograms for the analysis of the decay of ^{100m}Nb. β-gated experimental spectrum (red), spectrum of the contamination from the decay of ^{100gs} (green), spectrum of the contamination from the decay of the parent, ^{100}Zr (black), summing-pileup contribution (blue), and spectrum of the small background contamination (gray).

11.2 Branching ratio matrix

According to the recommendations of RIPL-3 [145], the level scheme of ^{100}Mo is complete up to the level at 2339.8 keV. From this level to the Q_β, a continuum region with 40 keV bins is used based on the statistical model as explained in Chapter 2. Those levels without assigned spin-parity values are summarized in Table 11.1, and for our analysis the recommended values from RIPL-3 [145] will be employed.

Energy [keV]	J^P ENSDF	J^P used
1607.36	(3^+)	3^+
1766.48	(2^+)	2^+
1771.44	(4^+)	4^+
1977.33	$(1, 2^+)$	1^+
2042.76	$(2)^+$	2^+
2189.53	(≤ 4)	4^+
2201.18	(2^-)	2^-
2289.4	$(4, 5^+)$	4^+
2310.1	(4^+)	4^+
2320.3	(≤ 4)	4^-
2339.8	(5^-)	5^-

Table 11.1: Levels with no spin-parity assignment in the ENSDF database and our adopted values (up to 2339.8 keV).

The level density data from HFB+c calculations [149, 212] available at RIPL-3 [145] were used (see Figure 12.7). The correction parameters C and P for the level density distribution are 0.0 and 0.15081 respectively.

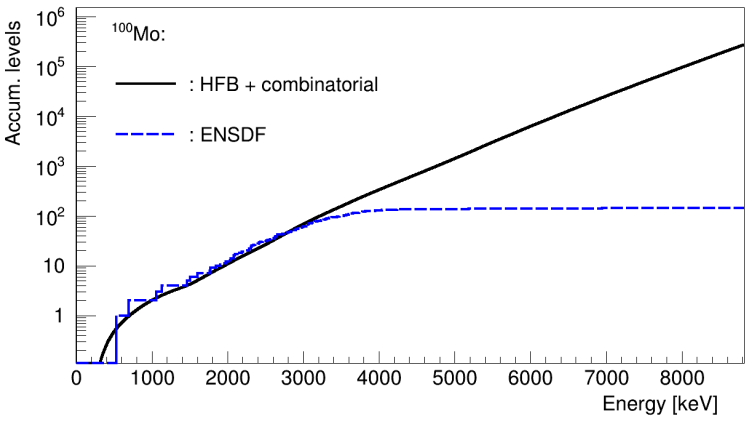

Figure 11.9: Accumulated number of levels as a function of the excitation energy for ^{100}Mo. The blue line is obtained from ENSDF and the black line corresponds to the Hartree-Fock-Bogoliubov calculation downloaded from RIPL-3.

The γ-strength function parameters involved in the branching ratio matrix and response

function calculation are presented in Table 2.1.

11.3 Analysis and results

In this section, the analysis of each of the three measurements will be addressed, and the results for the β-intensity distributions of the decays involved will be evaluated.

11.3.1 ^{100}Zr decay

The β-decay of ^{100}Zr is a contaminant in our measurements of the decay of ^{100}Nb. In theory, if this decay was well known, it could be simply simulated and subtracted. However it is likely that this is not the case since the Q_β of this decay is 3.421 MeV and the last level populated in β-decay that was seen experimentally is at 704.1 keV [233]. Thus a TAGS measurement of this decay with DTAS seems appropriate. However given that the half-life of ^{100gs}Nb is much shorter than the half-life of ^{100}Zr (see Figure 11.1) it is difficult to minimize the contribution of ^{100gs}Nb. One possibility would have been to use separate accumulation and measuring cycles as was done in the measurements of Rudstam *et al.* [234]. However, this was not done due to a lack of time, and only one cycle length was used to measure the mixed decay of ^{100}Zr and ^{100gs}Nb with DTAS. In view of this situation, a method to disentangle both decays from this single measurement has been developed and it is described in Appendix C. The method uses different time windows within the full length of the implantation cycle (28.35 s for this measurement), and the activities for both decays are calculated from the Bateman equations, as described in Appendix B, to assign the contribution of each of the decays to the total spectrum. The resulting β-gated DTAS spectra for the different time windows are presented in Figure 11.10. The corresponding weights for the ^{100gs}Nb contribution as a fraction of unity for these times are 0.07, 0.12, 0.20, 0.26, 0.30, 0.33, 0.41, 0.44 and 0.46 respectively. The MC simulation performed with the available information from ENSDF [213] as input is also presented in Figure 11.10 and scaled to be compared with the spectrum with the largest ^{100}Zr contribution. From this comparison it seems that the amount of missing β-intensity would not be large for the decay of ^{100}Zr.

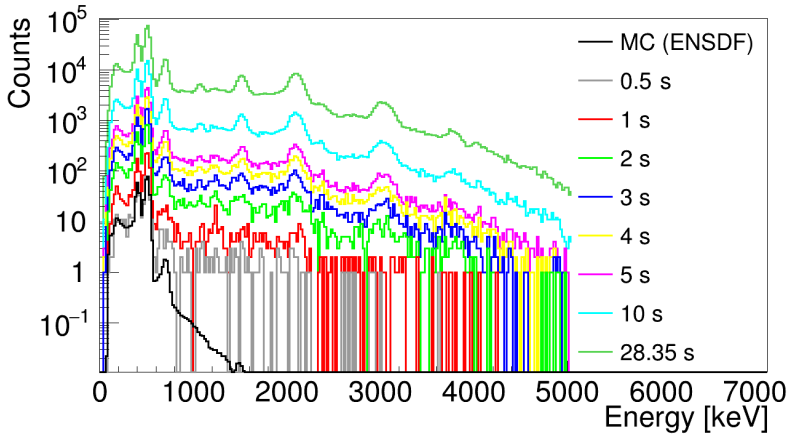

Figure 11.10: Comparison of the spectra for ^{100}Zr implantation for different time windows set within the total length of the cycle (28.35 s). The MC simulation with the available information from ENSDF is also presented and scaled to be compared with the spectrum with the shortest time window.

With one pair of spectra from Figure 11.10 we could apply the procedure explained in Appendix C to carry out the decomposition. In an attempt to improve the separation we have performed the decomposition for every pair of spectra, and then we computed the average of all the combinations (weighted by a factor dependent on the statistics of the original spectra). It has to be noted that this procedure is not applied directly to the spectra shown in Figure 11.10, but to these spectra after subtracting the corresponding summing-pileup contribution. Consequently, the resulting spectrum extracted for the decay of ^{100}Zr, shown as the grey histogram in Figure 11.11, is clean from the point of view of contaminants.

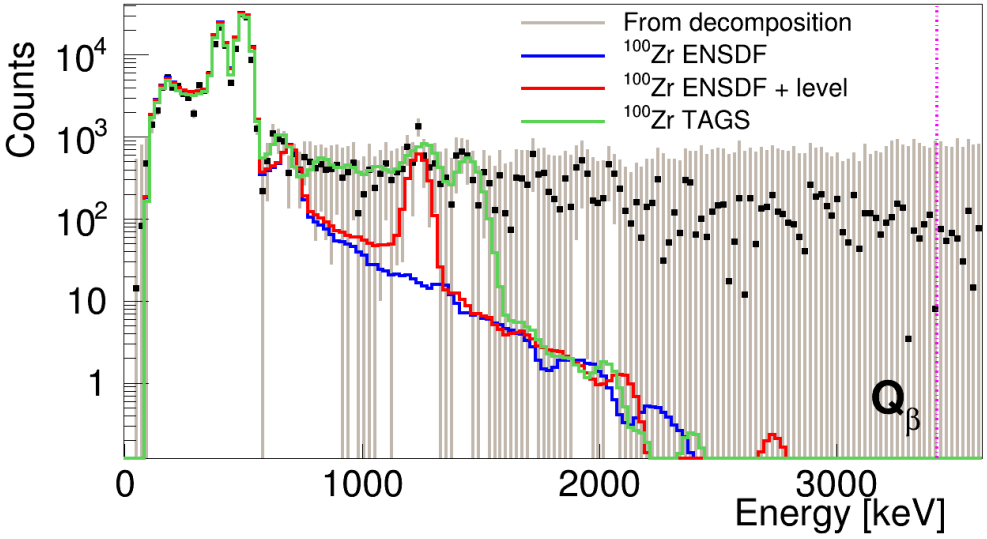

Figure 11.11: Spectrum of the decay of ^{100}Zr extracted with different time windows (grey) as explained in the text. The spectrum is compared with MC simulations of the decay of ^{100}Zr assuming different β-intensity distributions (see text).

One possibility for our purposes would be to treat the extracted ^{100}Zr spectrum as a contaminant for the study of the decay of ^{100gs}Nb. However, due to the large fluctuations in the spectrum obtained from the decomposition procedure, we prefer to use a MC simulation that reproduces the extracted spectrum. This will ensure good statistics as well as the possibility to study properly the multiplicities and the individual module spectra.

We compare in Figure 11.11 the extracted spectrum with the MC simulation that was already shown in Figure 11.10. As can be seen the known β-intensity reproduces the spectrum up to the last level known experimentally [233], but there is a clear indication of a small contribution from decays to states at higher energy.

A study of the ^{100}Mo(t,^{3}He)^{100}Nb reaction [235] identified levels in ^{100}Nb up a level at 1260(30) keV. Introducing in the simulation a level at 1240 keV with a β-intensity of 1% reproduces the peak observed in the extracted spectrum at this energy as can be seen in Figure 11.11. We assumed that this level de-excites with a mono-energetic γ-ray. It has to be noted that by adding feeding to this level, the known intensities are renormalized so that the distribution sums to 100%.

Finally we also made a TAGS analysis of the spectrum obtained. In addition, this option gave an estimate of the complete β-intensity distribution for the decay of ^{100}Zr, important from the point of view of reactor decay-heat calculations and nuclear structure. The level scheme of ^{100}Nb used for the analysis included all those levels from ENSDF [213] identified up to 703.6 keV, ignoring the 5^+ isomer. Levels with no spin-parity assignment are listed in Table 11.2, where the 1^+ assignment is taken from RIPL-3 [145], while the three 0^+ are our choices.

Energy [keV]	J^P ENSDF	J^P used
471.38	(1^+)	1^+
498.1	$0^+, 1^+, 3^+$	0^+
653.9	$0^+, 1^+, 3^+$	0^+
703.6	$0^+, 1^+, 3^+$	0^+

Table 11.2: Levels with no spin-parity assignment for ENSDF and our adopted values (up to 703.6 keV) for ^{100}Nb.

The PSF parameters needed to calculate the branching ratio matrix for the unknown part of the level scheme and the response function calculation are presented in Table 2.1. The level density from HFB+c calculations [149, 212] available at RIPL-3 [145] are used (see Figure 11.12). Due the lack of experimental information, there are no correction parameters.

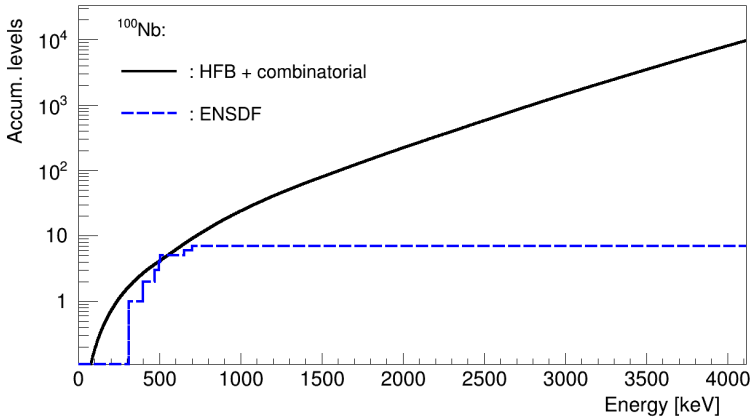

Figure 11.12: Accumulated number of levels. The blue line is obtained from ENSDF and the black line corresponds to the Hartree-Fock-Bogoliubov calculation downloaded from RIPL-3.

We have analyzed the extracted spectrum up to 1.5 MeV. Above this energy the spectrum fluctuations are consistent with zero counts. The study of the ^{100}Mo(t,^{3}He)^{100}Nb reaction [235] identified levels in ^{100}Nb up to 1300 keV without any information on spin-parity values and with large uncertainties in energy. In this analysis we restricted the feeding in the continuum to a limited number of bins. Up to 1.3 MeV we have associated those bins with the levels observed in [235], as presented in Table 11.5. Above that energy we allowed feeding to three additional bins necessary to reproduce the features of the spectrum. Moreover, due to the very limited sensitivity of this analysis, we fixed the ground state feeding intensity to the 45% value from [233]. It is worth mentioning that the ground state feeding intensity of this decay will affect the ground state feeding intensity of the decay of ^{100}Nb, as will be discussed later. The quality of the reproduction of the spectrum with the β-intensity distribution obtained can be seen in Figure 11.13. The confirmation of intensity to a level at 1.26 MeV seems the most clear conclusion of this exercise.

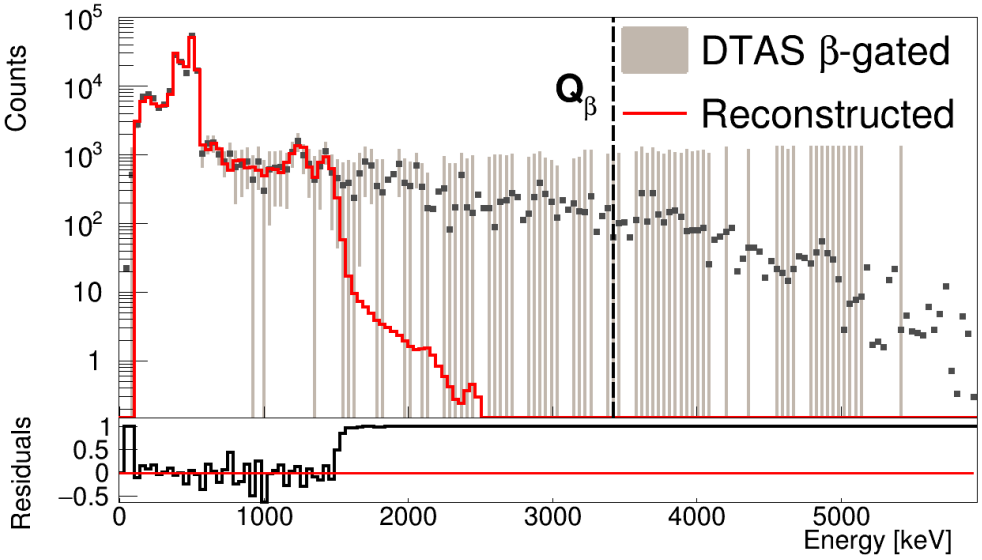

Figure 11.13: Result of the analysis of the decay of ^{100}Zr. The total spectrum is compared with the reconstructed one after the analysis.

Unlike previous cases, the uncertainty in the β-intensity distribution due to the statistical uncertainty in the data is significant. This is the only error quoted in Table 11.3. We have not attempted to evaluate the systematic errors given the quality of the data. Obviously, the values listed in Table 11.3 suffer larger uncertainties that are difficult to evaluate, exceeding the purposes of this rough analysis, and they have to be taken just as an estimate.

Energy [keV]	I_β ENSDF [%]	I_β DTAS [%]
0.00	45(4)	45 (fixed)
400.49	19(3)	17.25(11)
471.38	1.7(5)	-
498.10	0.80(15)	9.39(5)
504.26	33(4)	22.59(12)
653.90	0.12(6)	0.94(9)
703.60	0.74(16)	0.070(10)
740.00-720(20)	-	-
780.00-784(20)	-	-
820.00-820(20)	-	0.30(7)
860.00-865(20)	-	0.20(5)
900.00-893(20)	-	-
940.00-945(20)	-	0.27(9)
1060.00-1040(20)	-	0.34(10)
1100.00-1075(20)	-	-
1140.00-1136(20)	-	-
1180.00-1180(25)	-	0.57(10)

Continues on the next page.

Energy [keV]	I_β ENSDF [%]	I_β DTAS [%]
1260.00-1260(30)	-	1.6(2)
1300.00-1300(30)	-	0.010(2)
1380.	-	0.010(3)
1420.	-	1.2(2)
1460.	-	0.35(7)

Table 11.3: I_β intensities obtained in the analysis for the decay of ^{100}Zr. Notice that only statistical errors are presented. From energy 740 keV upwards only feeding to selected bins in the continuum was allowed. The chosen bins were associated with energy levels identified in [235].

As a conclusion, for the analysis of ^{100gs}Nb we will consider three possible alternative contributions for the ^{100}Zr contamination. The corresponding spectra are calculated with the DECAYGEN event generator [146] using: the ENSDF [213] decay scheme (lower limit), the modification of the ENSDF decay scheme with the addition of 1% feeding to a level at 1240 keV (intermediate value), and the results of the TAGS analysis (upper limit). The three spectra are shown in Figure 11.11.

11.3.2 ^{100gs}Nb decay

For the analysis of the decay of the low-spin isomer, we considered allowed transitions to the levels up to 2339.8 keV plus forbidden transitions to levels at 1136 keV (4^+), 1607.36 keV (3^+), 1908.28 keV (3^-) and 2189.53 keV (4^+). Except for the level at 1136 keV, with firm spin-parity assignment, the spin-parity of the the three remaining levels is compatible with a 3^- assignment (first forbidden transitions). Thus a branching ratio matrix with the 3^- assignment was also considered for the study of the systematic errors. Feeding to all these levels was seen in high resolution measurements, with the exception of the level at 1908.28 keV. The reported intensity to the level at 1136 keV is questionable due to the proximity to the peak in the decay of ^{100}Zr. For this reason, we studied the effect of allowing and not allowing feeding to this level. Finally, feeding to the level at 2189.53 keV can be replaced by feeding to the level at 2201.12 keV (2^-), not seen in high resolution measurements, obtaining a very similar fit. This possibility was tried when studying the systematic errors in the analysis. The quality of the reproduction of the measured spectrum with the accepted I_β distribution is shown in Figure 11.14, and the β-intensity distribution obtained can be seen in Figure 11.15 left compared with the values available at ENSDF.

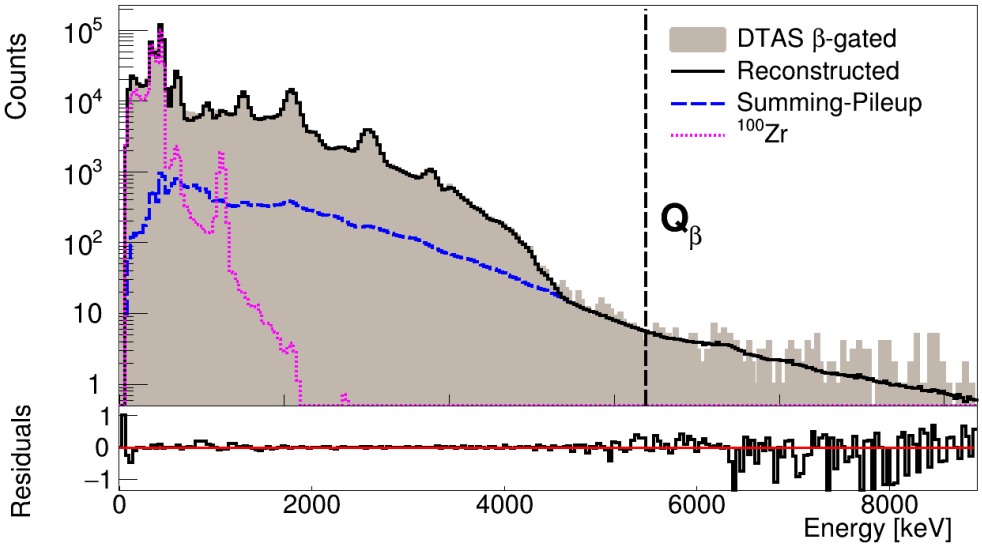

Figure 11.14: Result of the analysis of the decay of ^{100gs}Nb. The total spectrum is compared with the reconstructed one after the analysis.

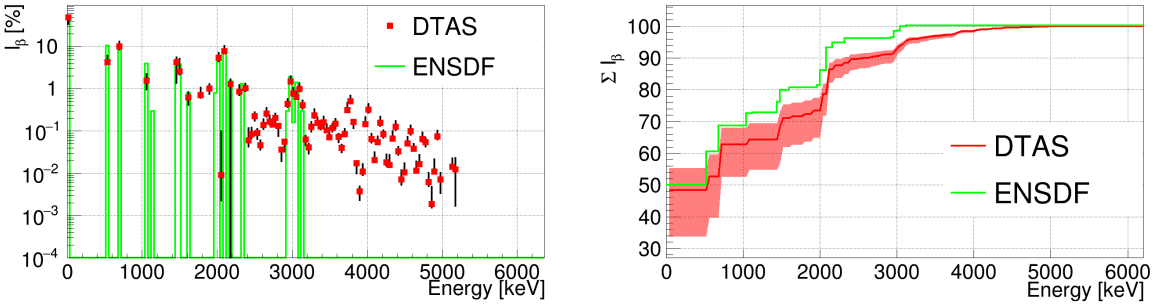

Figure 11.15: β-intensities of the decay of ^{100gs}Nb with error bars coming from the uncertainty of all the sources of error.

Systematic errors have been evaluated by considering all the possibilities mentioned for the branching ratio matrix. Moreover, an optimization of the reproduction of the γ-intensities led to a modified branching ratio matrix that has also been taken into consideration. The initial γ-intensities and the ones obtained with the modified branching ratio matrix are presented in Table 11.4. The original γ-intensities from the TAGS analysis are not far from the high resolution values [213], and the fit barely changes with this modified branching ratio matrix.

Energy [keV]	I_γ ENSDF	I_γ DTAS	I_γ DTAS*
535.663	0.457	0.450	0.457
695.21	0.088	0.122	0.114
1063.92	0.1253	0.124	0.125
1136.17	0.0055	0.005	0.005
1463.94	0.0618	0.068	0.067
1504.79	0.0367	0.027	0.027
1607.41	0.0101	0.008	0.008
1977.14	0.008	0.001	0.008
2037.55	0.0469	0.054	0.054
2086.37	0.0715	0.077	0.077
2189.7	0.0154	0.013	0.013
2320.4	0.013	0.001	0.001

Table 11.4: Absolute γ-intensities de-exciting the main levels populated in the decay of ^{100gs}Nb (per 100 decays). The second column corresponds to the intensities obtained from high resolution data [213]. The third column gives the intensities obtained with DTAS for the reference analysis, whereas the intensities obtained with a modified branching ratio matrix are presented in the fourth column (DTAS*).

Furthermore, for the evaluation of the errors, the three possible shapes discussed in Subsection 11.3.1 for the contamination of the decay of ^{100}Zr were used. For each of them, a change in the normalization factor of around 10% was shown to be compatible with a reasonable fit. The fit was also compatible with a change in the normalization of the summing-pileup of 20%. The effect of the lowest bin included in the fit was also investigated, showing a large impact in the sensitivity to the ground state feeding intensity, comparable to the impact of the change in the subtraction of the parent activity. Finally, the ME algorithm was used instead of the EM one to check the influence in the analysis. The β-intensities and the evaluated systematic errors are presented in Table 11.5 and plotted in Figure 11.15 right in comparison with ENSDF values [213]. Note that above the last level of the known level scheme used for the analysis, the values from the bibliography listed in Table 11.5 correspond to integral values over our energy bins.

Energy [keV]	I_β ENSDF [%]	I_β DTAS [%]
0.000	50(7)	$48.442^{+6.835}_{-14.787}$
535.561	10.5(18)	$4.231^{+1.756}_{-0.421}$
695.109	8.2(12)	$10.048^{+2.975}_{-1.621}$
1063.776	3.9(9)	$1.557^{+0.637}_{-0.610}$
1136.090	$\simeq$0.3	-
1463.900	3.3(7)	$4.189^{+1.356}_{-2.822}$
1504.620	3.7(6)	$2.571^{+2.555}_{-0.412}$
1607.360	$\simeq$0.8	$0.621^{+0.217}_{-0.205}$
1766.480	-	$0.710^{+0.341}_{-0.107}$

Continues on the next page.

Energy [keV]	I_β ENSDF [%]	I_β DTAS [%]
1908.280	-	$0.993^{+0.279}_{-0.235}$
1977.330	≃0.8	$0.000^{+0.001}_{-0.000}$
2037.480	4.7(7)	$5.357^{+1.574}_{-0.949}$
2042.760	-	$0.009^{+0.090}_{-0.007}$
2086.300	7.2(12)	$7.634^{+2.675}_{-0.970}$
2189.530	≃1.5	$1.287^{+0.365}_{-1.287}$
2286.450	-	$0.856^{+0.356}_{-0.148}$
2320.300	≃1.3	-
2380.000	-	$1.039^{+0.283}_{-0.173}$
2420.000	-	$0.060^{+0.057}_{-0.018}$
2460.000	-	$0.083^{+0.038}_{-0.016}$
2500.000	-	$0.223^{+0.056}_{-0.048}$
2540.000	-	$0.090^{+0.021}_{-0.025}$
2580.000	-	$0.046^{+0.014}_{-0.010}$
2620.000	-	$0.139^{+0.048}_{-0.027}$
2660.000	-	$0.260^{+0.087}_{-0.043}$
2700.000	-	$0.169^{+0.063}_{-0.026}$
2740.000	-	$0.140^{+0.050}_{-0.015}$
2780.000	-	$0.200^{+0.058}_{-0.041}$
2820.000	-	$0.132^{+0.005}_{-0.057}$
2860.000	-	$0.036^{+0.000}_{-0.016}$
2900.000	-	$0.055^{+0.006}_{-0.022}$
2940.000	≃0.3	$0.432^{+0.127}_{-0.065}$
2980.000	≃1.9	$1.461^{+0.520}_{-0.193}$
3020.000	≃0.16	$0.772^{+0.270}_{-0.103}$
3060.000	≃1.4	$0.635^{+0.188}_{-0.084}$
3100.000	-	$0.989^{+0.341}_{-0.147}$
3140.000	≃0.3	$0.409^{+0.118}_{-0.072}$
3180.000	-	$0.063^{+0.014}_{-0.017}$
3220.000	-	$0.041^{+0.009}_{-0.012}$
3260.000	-	$0.127^{+0.035}_{-0.031}$
3300.000	-	$0.236^{+0.091}_{-0.034}$
3340.000	-	$0.155^{+0.053}_{-0.019}$
3380.000	-	$0.129^{+0.037}_{-0.019}$
3420.000	-	$0.158^{+0.058}_{-0.031}$
3460.000	-	$0.104^{+0.041}_{-0.012}$
3500.000	-	$0.071^{+0.028}_{-0.007}$
3540.000	-	$0.117^{+0.031}_{-0.020}$
3580.000	-	$0.148^{+0.047}_{-0.034}$
3620.000	-	$0.073^{+0.013}_{-0.018}$
3660.000	-	$0.040^{+0.007}_{-0.008}$

Continues on the next page.

Energy [keV]	I_β ENSDF [%]	I_β DTAS [%]
3700.000	-	$0.083^{+0.027}_{-0.009}$
3740.000	-	$0.310^{+0.155}_{-0.013}$
3780.000	-	$0.502^{+0.190}_{-0.058}$
3820.000	-	$0.165^{+0.015}_{-0.048}$
3860.000	-	$0.017^{+0.000}_{-0.007}$
3900.000	-	$0.004^{+0.001}_{-0.001}$
3940.000	-	$0.011^{+0.006}_{-0.002}$
3980.000	-	$0.145^{+0.065}_{-0.008}$
4020.000	-	$0.316^{+0.115}_{-0.049}$
4060.000	-	$0.064^{+0.022}_{-0.011}$
4100.000	-	$0.020^{+0.011}_{-0.003}$
4140.000	-	$0.054^{+0.021}_{-0.004}$
4180.000	-	$0.156^{+0.061}_{-0.025}$
4220.000	-	$0.083^{+0.022}_{-0.014}$
4260.000	-	$0.018^{+0.010}_{-0.003}$
4300.000	-	$0.016^{+0.011}_{-0.001}$
4340.000	-	$0.065^{+0.033}_{-0.004}$
4380.000	-	$0.126^{+0.045}_{-0.023}$
4420.000	-	$0.033^{+0.009}_{-0.006}$
4460.000	-	$0.007^{+0.005}_{-0.002}$
4500.000	-	$0.010^{+0.007}_{-0.001}$
4540.000	-	$0.050^{+0.023}_{-0.003}$
4580.000	-	$0.098^{+0.036}_{-0.017}$
4620.000	-	$0.038^{+0.012}_{-0.004}$
4660.000	-	$0.011^{+0.008}_{-0.001}$
4700.000	-	$0.016^{+0.011}_{-0.000}$
4740.000	-	$0.064^{+0.028}_{-0.009}$
4780.000	-	$0.054^{+0.014}_{-0.011}$
4820.000	-	$0.006^{+0.004}_{-0.001}$
4860.000	-	$0.002^{+0.003}_{-0.000}$
4900.000	-	$0.011^{+0.010}_{-0.000}$
4940.000	-	$0.074^{+0.028}_{-0.012}$
4980.000	-	$0.007^{+0.003}_{-0.004}$
5140.000	-	$0.014^{+0.008}_{-0.000}$
5180.000	-	$0.012^{+0.011}_{-0.011}$

Table 11.5: I_β intensities of the decay of ^{100gs}Nb.

The g.s. feeding intensity calculated with DTAS is compatible within the errors with the value from ENSDF. However, the value obtained by applying the β-γ counting method of Appendix D, which gives a result of 41.3(16)%, suggests that the β-intensity to the ground state feeding could be lower than the value from ENSDF.

The reproduction of the multiplicities is shown in Figure 11.16. As can be observed the multiplicity M_m=1 spectrum is not well reproduced in the continuum region while there is quite good agreement for higher multiplicities. We investigated the impact of changes in the γ-strength function parameters from Table 2.1. The best reproduction of the spectrum for $M_m = 1$ was achieved when the centroid energy of $E2$ γ-strength functions was increased and the normalization of $M1$ γ-strength functions was decreased. However, these changes distorted the rest of the multiplicities. A change in the parameters of the $E2$ γ-strength functions alone did not worsen the other multiplicities, but was not found to be enough to reproduce the $M_m = 1$ spectrum.

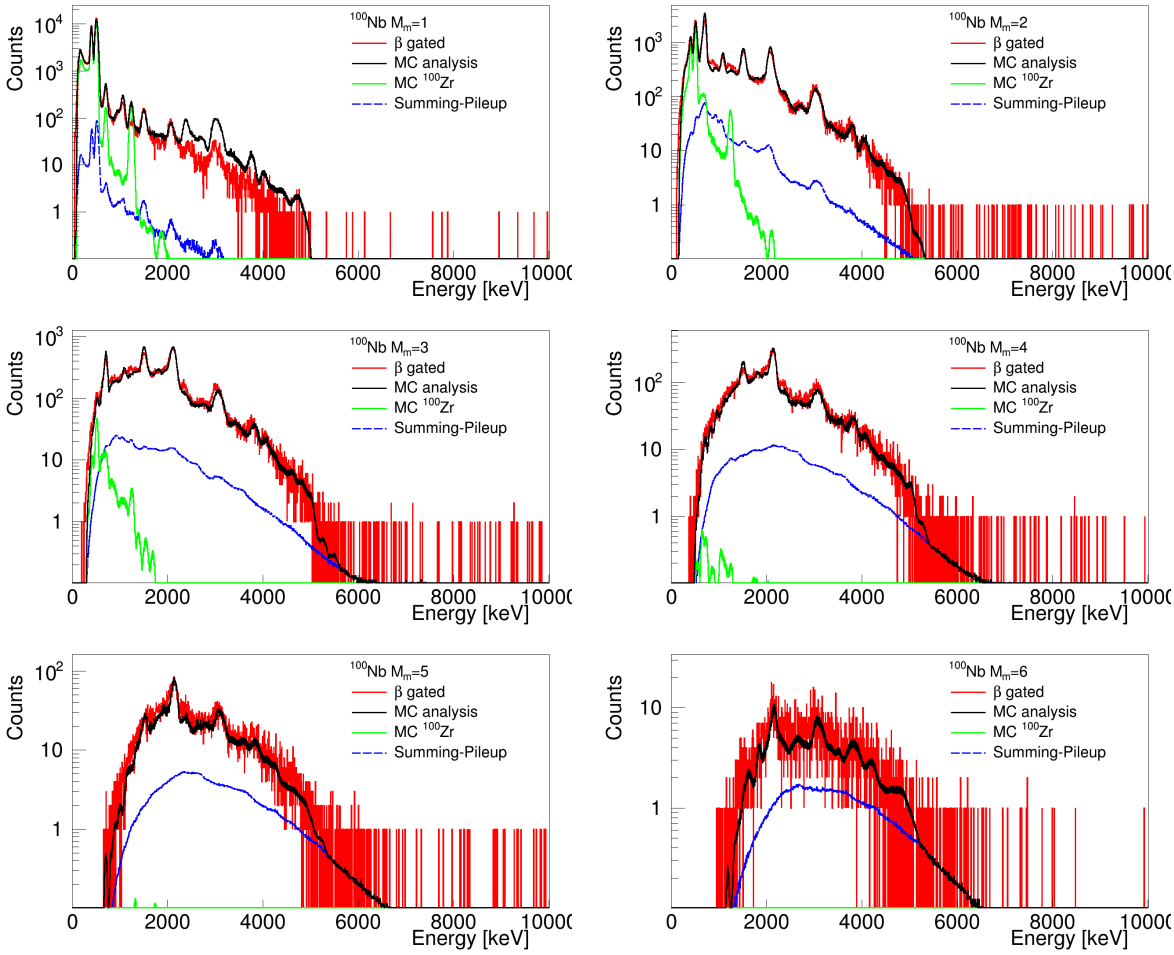

Figure 11.16: Experimental spectra for different multiplicities for the decay of ^{100gs}Nb compared with the MC simulation performed with an event generator for multiplicities from 1 to 6.

We have also considered an $E1$ Pygmy dipole resonance at 8 MeV, as in the case of ^{140}Cs (Chapter 10). The change in the γ-strength function is depicted in Figure 11.17 right. An improvement in the reproduction of $M_m = 1$ is achieved, as shown in Figure 11.17 left, although the rest of the multiplicities (specially $M_m = 2$) are worsened.

Finally, the reproduction of the individual modules has also been studied, as presented in Figure 11.18, where a good agreement between the experimental spectra and the MC

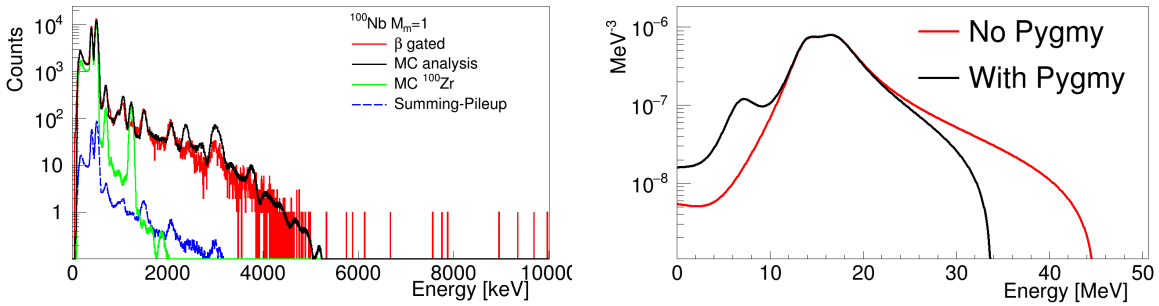

Figure 11.17: ^{100}Nb multiplicity spectra 1 when a $E1$ Pygmy dipole resonance is considered (left). The $E1$ γ-strength function for ^{100}Mo with and without considering the $E1$ Pygmy dipole resonance are depicted (right).

simulation based on the analysis is shown.

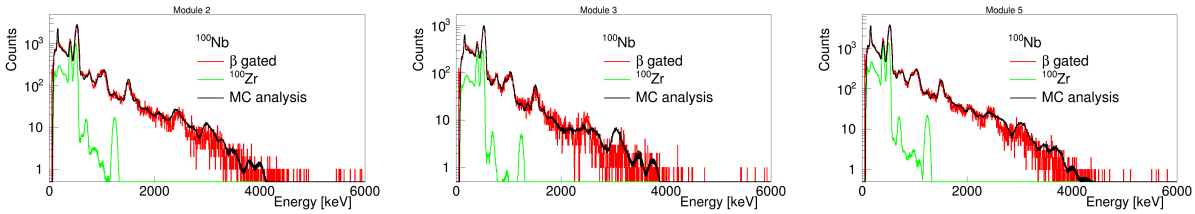

Figure 11.18: ^{100gs}Nb experimental spectra for the three geometrically distinguishable individual crystals compared with the MC.

11.3.3 ^{100m}Nb decay

^{100m}Nb decay (combined measurement)

The combined measurement of both isomers is used to study the β-decay of the 5^+ isomeric state. The results of the analysis of the decay of ^{100gs}Nb presented in the previous section is employed to simulate this contamination, as explained in Section 11.6.

The analysis was carried out by considering allowed transitions to 4^+, 5^+ and 6^+ states in ^{100}Mo. In this case the fit is significantly improved when a modified branching ratio matrix, calculated to reproduce the γ-intensities for low energy levels coming from high resolution data [231,236], is used. In Table 11.6 the γ-intensities obtained with the initial branching ratio matrix and the initial feeding distributions are compared with those that we obtained with the modified branching ratio matrix. The resulting fit of the experimental spectrum with this branching ratio matrix is presented in Figure 11.19.

Energy [keV]	I_γ ENSDF	I_γ DTAS	I_γ DTAS*
535.667	0.95	0.909	0.959
695.23	0.0361	0.025	0.021
1063.93	0.1406	0.296	0.141
1136.08	0.6935	0.353	0.691
1463.91	0.08455	0.046	0.043
1607.38	0.09785	0.132	0.081
1771.41	0.09595	0.044	0.023
1847.08	0.0646	0.037	0.023
2103.07	0.26315	0.153	0.261
2289.2	0.01805	0.070	0.047
2310.16	0.0931	0.066	0.042

Table 11.6: Absolute γ-intensities de-exciting the main levels populated in the decay of ^{100m}Nb (per 100 decays). The second column corresponds to the intensities obtained from high resolution data [213]. The third column gives the intensities obtained with DTAS for the reference analysis, whereas the intensities obtained with a modified branching ratio matrix are presented in the fourth column (DTAS*).

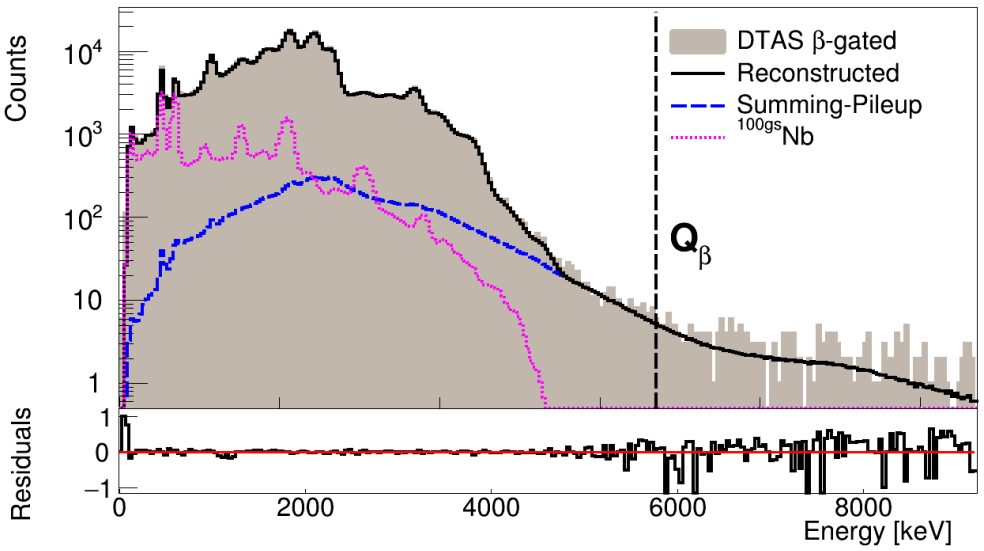

Figure 11.19: Result of the analysis of the decay of ^{100m}Nb. The total spectrum is compared with the reconstructed one after the analysis.

As in previous cases, the systematic error due to changes in the normalization factors of the contaminants was estimated (by 10% for both the summing-pileup and the contamination of the low-spin isomer). The original branching ratio matrix and the modified one are taken into account in the evaluation of the errors, and the ME algorithm is also used instead of the ME. The β-intensity distribution with errors is shown in Figure 11.20 and listed in Table 11.7. Note that above the last level of the known level scheme used for the analysis, the values from the ENSDF [213] listed in Table 11.7 correspond to integral

values over our energy bins.

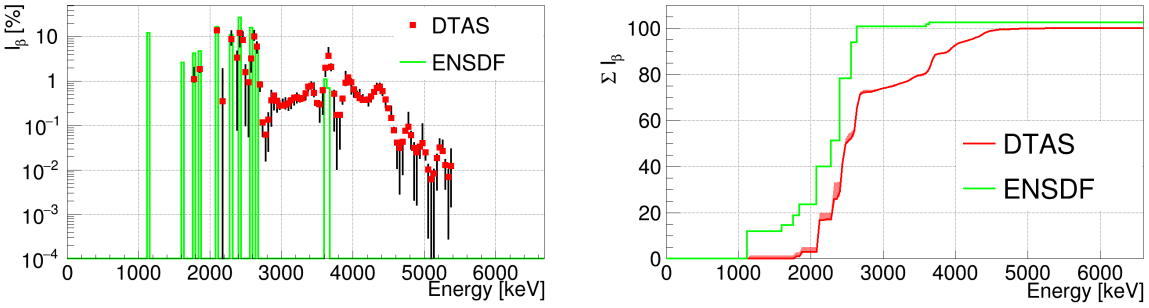

Figure 11.20: β-intensities of the decay of ^{100m}Nb with error bars coming from the uncertainty of all the sources of error.

Energy [keV]	I_β ENSDF [%]	I_β DTAS [%]
1136.090	12(7)	-
1607.360	<2.6	-
1771.440	4.2(13)	$1.099^{+0.901}_{-0.148}$
1847.070	4.7(9)	$1.877^{+0.256}_{-0.307}$
2103.170	16.6(25)	$13.752^{+1.130}_{-0.282}$
2189.530	-	$0.348^{+1.500}_{-0.348}$
2289.400	1.8(4)	$4.594^{+2.256}_{-2.279}$
2310.100	9.3(11)	$4.123^{+2.313}_{-0.647}$
2380.000	-	$3.352^{+1.286}_{-3.273}$
2420.000	27(3)	$12.195^{+1.503}_{-6.308}$
2460.000	-	$8.359^{+4.335}_{-0.870}$
2500.000	-	$1.566^{+0.729}_{-1.466}$
2540.000	-	$0.941^{+0.001}_{-0.885}$
2580.000	15.8(13)	$3.223^{+0.007}_{-1.617}$
2620.000	-	$10.040^{+3.543}_{-1.684}$
2660.000	6.7(9)	$5.898^{+1.526}_{-1.604}$
2700.000	-	$0.826^{+0.025}_{-0.240}$
2740.000	-	$0.118^{+0.004}_{-0.059}$
2780.000	-	$0.062^{+0.003}_{-0.046}$
2820.000	-	$0.133^{+0.055}_{-0.106}$
2860.000	-	$0.365^{+0.247}_{-0.268}$
2900.000	-	$0.475^{+0.009}_{-0.248}$
2940.000	-	$0.357^{+0.041}_{-0.155}$
2980.000	-	$0.281^{+0.073}_{-0.051}$
3020.000	-	$0.278^{+0.105}_{-0.022}$
3060.000	-	$0.295^{+0.114}_{-0.060}$
3100.000	-	$0.315^{+0.082}_{-0.095}$
3140.000	-	$0.368^{+0.036}_{-0.124}$

Continues on the next page.

Energy [keV]	I_β ENSDF [%]	I_β DTAS [%]
3180.000	-	$0.422^{+0.048}_{-0.130}$
3220.000	-	$0.428^{+0.105}_{-0.103}$
3260.000	-	$0.396^{+0.020}_{-0.055}$
3300.000	-	$0.413^{+0.001}_{-0.054}$
3340.000	-	$0.534^{+0.007}_{-0.148}$
3380.000	-	$0.738^{+0.002}_{-0.132}$
3420.000	-	$0.782^{+0.157}_{-0.101}$
3460.000	-	$0.544^{+0.350}_{-0.090}$
3500.000	-	$0.322^{+0.028}_{-0.047}$
3540.000	-	$0.297^{+0.002}_{-0.176}$
3580.000	-	$0.619^{+0.004}_{-0.440}$
3620.000	1.1(3)	$1.975^{+0.015}_{-0.699}$
3660.000	0.7(3)	$3.692^{+1.840}_{-0.121}$
3700.000	-	$2.082^{+0.327}_{-0.363}$
3740.000	-	$0.515^{+0.098}_{-0.439}$
3780.000	-	$0.172^{+0.010}_{-0.161}$
3820.000	-	$0.172^{+0.011}_{-0.143}$
3860.000	-	$0.400^{+0.014}_{-0.096}$
3900.000	-	$0.919^{+0.708}_{-0.128}$
3940.000	-	$1.194^{+0.067}_{-0.056}$
3980.000	-	$0.939^{+0.160}_{-0.422}$
4020.000	-	$0.648^{+0.069}_{-0.212}$
4060.000	-	$0.485^{+0.093}_{-0.002}$
4100.000	-	$0.410^{+0.221}_{-0.010}$
4140.000	-	$0.379^{+0.099}_{-0.007}$
4180.000	-	$0.374^{+0.003}_{-0.032}$
4220.000	-	$0.389^{+0.009}_{-0.112}$
4260.000	-	$0.447^{+0.015}_{-0.107}$
4300.000	-	$0.560^{+0.022}_{-0.025}$
4340.000	-	$0.701^{+0.170}_{-0.011}$
4380.000	-	$0.737^{+0.132}_{-0.009}$
4420.000	-	$0.592^{+0.076}_{-0.112}$
4460.000	-	$0.387^{+0.056}_{-0.133}$
4500.000	-	$0.241^{+0.029}_{-0.012}$
4540.000	-	$0.146^{+0.121}_{-0.003}$
4580.000	-	$0.077^{+0.012}_{-0.002}$
4620.000	-	$0.041^{+0.004}_{-0.030}$
4660.000	-	$0.031^{+0.003}_{-0.028}$
4700.000	-	$0.042^{+0.003}_{-0.035}$
4740.000	-	$0.076^{+0.004}_{-0.003}$
4780.000	-	$0.094^{+0.098}_{-0.003}$

Continues on the next page.

Energy [keV]	I_β ENSDF [%]	I_β DTAS [%]
4820.000	-	$0.061^{+0.011}_{-0.031}$
4860.000	-	$0.031^{+0.009}_{-0.029}$
4900.000	-	$0.025^{+0.005}_{-0.023}$
4940.000	-	$0.033^{+0.003}_{-0.015}$
4980.000	-	$0.040^{+0.067}_{-0.003}$
5020.000	-	$0.025^{+0.003}_{-0.008}$
5060.000	-	$0.010^{+0.003}_{-0.010}$
5100.000	-	$0.006^{+0.002}_{-0.006}$
5140.000	-	$0.008^{+0.002}_{-0.008}$
5180.000	-	$0.019^{+0.003}_{-0.015}$
5220.000	-	$0.032^{+0.017}_{-0.002}$
5260.000	-	$0.027^{+0.020}_{-0.002}$
5300.000	-	$0.013^{+0.004}_{-0.009}$
5340.000	-	$0.007^{+0.003}_{-0.007}$
5380.000	-	$0.012^{+0.017}_{-0.011}$

Table 11.7: I_β intensities of the decay of ^{100m}Nb.

Finally, the reproduction of the multiplicities and the spectra of the individual modules has also been studied, and can be seen in Figures 11.21 and 11.22. The excess in $M_m = 1$ is due to the contribution to the spectrum of the low-spin isomer. A deficit of counts for multiplicities M_m=5 and M_m=6 is also found. One can also observe that individual spectra are not so well reproduced as in other cases (Figure 11.22).

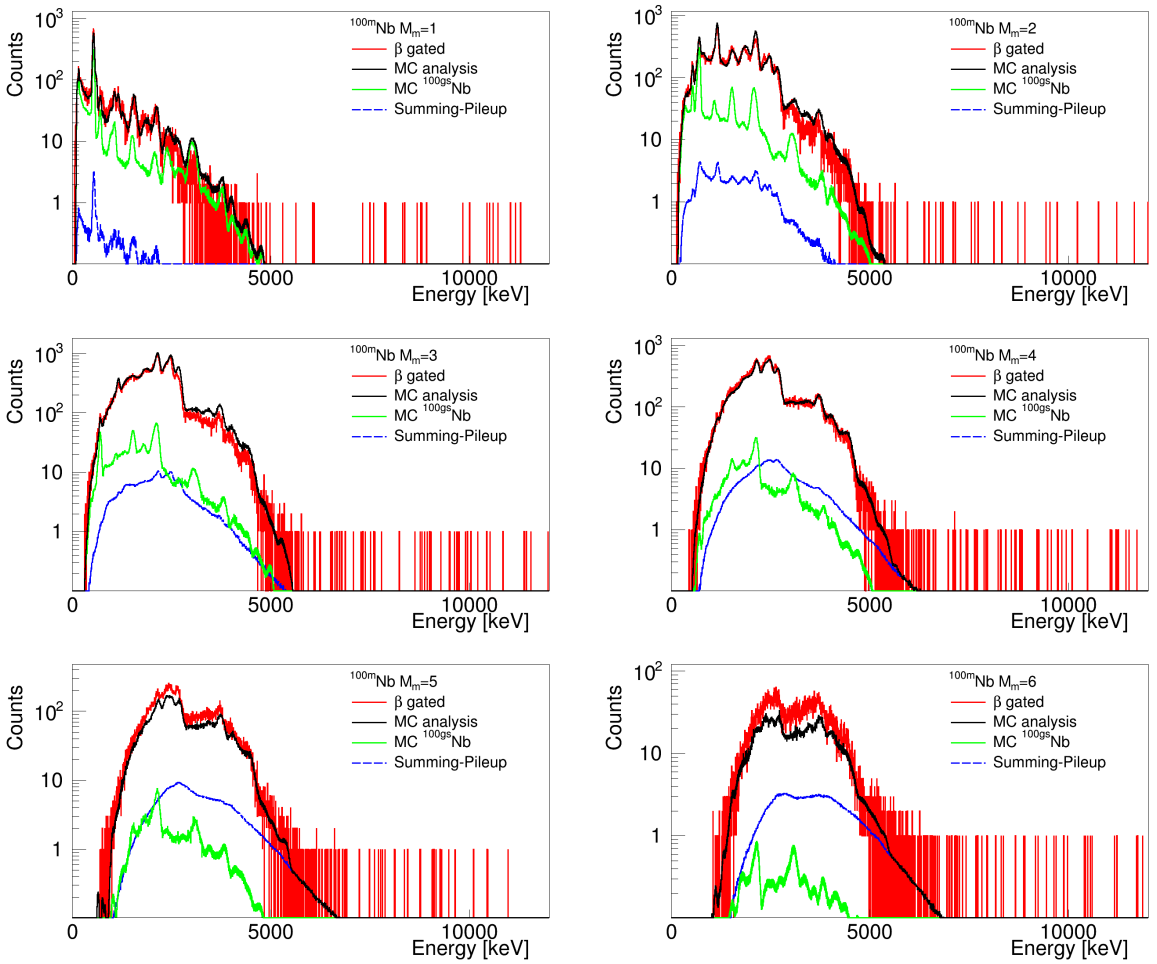

Figure 11.21: Experimental spectra for different multiplicities for the decay of ^{100m}Nb compared with the MC simulation performed with an event generator for multiplicities from 1 to 6.

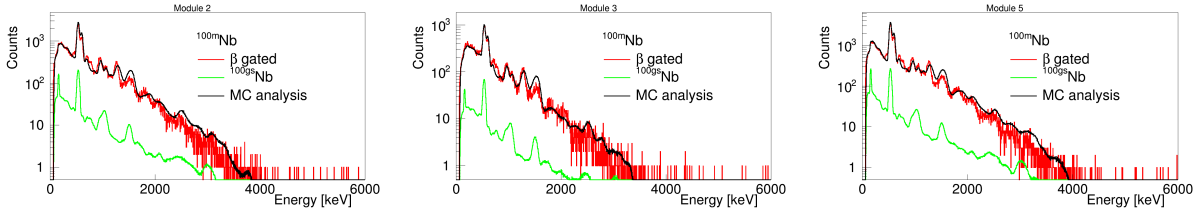

Figure 11.22: ^{100m}Nb experimental spectra for the three geometrically distinguishable individual crystals compared with the MC.

^{100m}Nb decay (Ramsey cleaning)

In the case of the measurement with the Ramsey cleaning technique, the statistics is considerably lower than in the previous case, and many contaminants play a role in the analysis, as discussed in Section 11.6. For all these reasons, the analysis of this experimental spectrum is not considered as reliable as the previous one, and we will simply use it as a

cross-check.

Again, the analysis was carried out by considering allowed transitions to 4^+, 5^+ and 6^+ states in ^{100}Mo. The modification of the branching ratio matrix in order to improve the reproduction of the γ-intensities turned out to have a clear impact in the quality of the fit, as in the combined measurement of both isomers described above.

Energy [keV]	I_γ ENSDF	I_γ DTAS	I_γ DTAS*
535.667	0.95	0.911	0.960
695.23	0.0361	0.025	0.020
1063.93	0.1406	0.288	0.142
1136.08	0.6935	0.368	0.698
1463.91	0.08455	0.047	0.041
1607.38	0.09785	0.106	0.089
1771.41	0.09595	0.050	0.035
1847.08	0.0646	0.040	0.028
2103.07	0.26315	0.164	0.261
2289.2	0.01805	0.042	0.041
2310.16	0.0931	0.069	0.068

Table 11.8: Absolute γ-intensities de-exciting the main levels populated in the decay of ^{100m}Nb (per 100 decays). The second column corresponds to the intensities obtained from high resolution data [213]. The third column gives the intensities obtained with DTAS for the reference analysis, whereas the intensities obtained with a modified branching ratio matrix are presented in the fourth column (DTAS*).

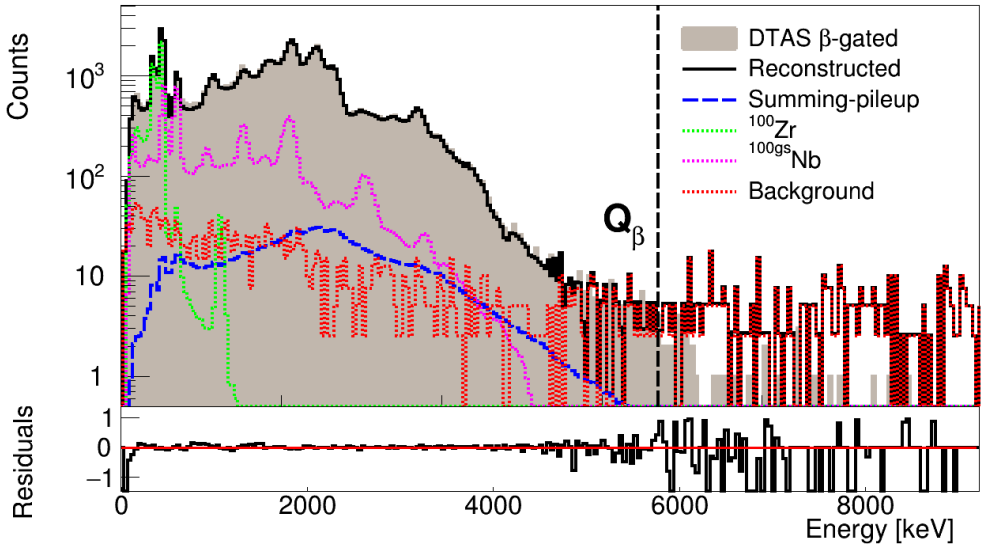

Figure 11.23: Result of the analysis of the decay of ^{100m}Nb. The β-gated spectrum is compared with the reconstructed one after the analysis.

Instead of evaluating systematic errors for this analysis, we just compare in Figure

11.24 the β-intensity distribution with the one coming from the combined measurement of both isomers (and with the feeding intensities from ENSDF [213]). A quite reasonable agreement is found, and we interpret this result as a check on the consistency of the β-intensity distribution presented in Table 11.5.

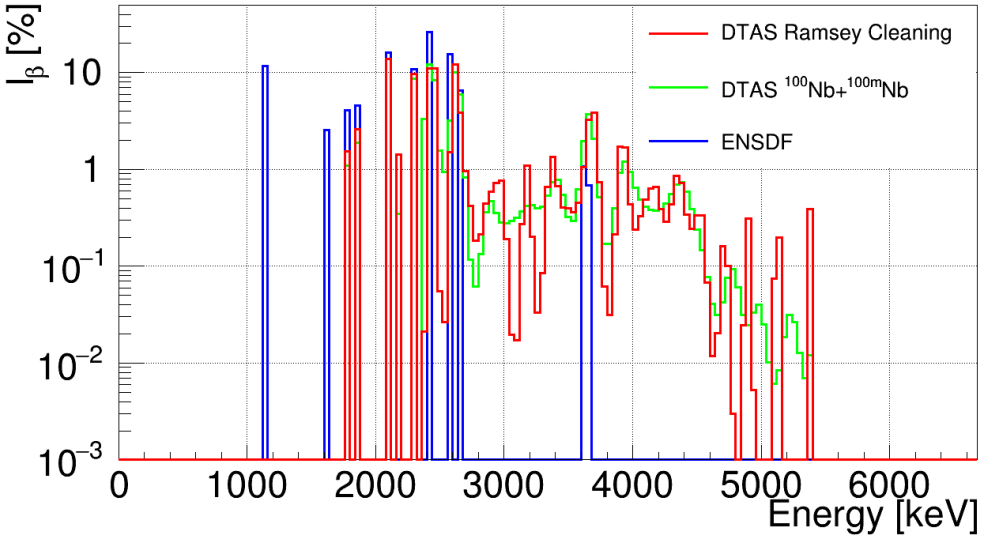

Figure 11.24: Comparison of the β-intensity distributions obtained with DTAS for the decay of ^{100m}Nb from the two different measurements (combined measurement of low-spin and high-spin isomers, and measurement with Ramsey cleaning technique.

Chapter 12

^{102}Nb decay

A los hombres les encanta maravillarse. Esta es la semilla de la ciencia

Men love to wonder, and that is the seed of science

Ralf Waldo Emerson

In this chapter the β-decay of ^{102}Nb, into ^{102}Mo will be studied. This is an important decay from the point of view of reactor antineutrino spectrum and decay heat calculations, as mentioned in Chapter 1. As in the case of ^{100}Nb, presented in Chapter 11, special care was taken in order to distinguish experimentally between the decay of the two isomeric states depicted in Figure 12.1. The difference in excitation energy between both isomers is 95 keV according to the NUBASE evaluation of 2012 [237] (130 keV in NUBASE 2003 [238] and 94.5 keV in the recent NUBASE 2016 [239]), in good agreement with the value of 93(23) keV measured at IGISOl in [233].

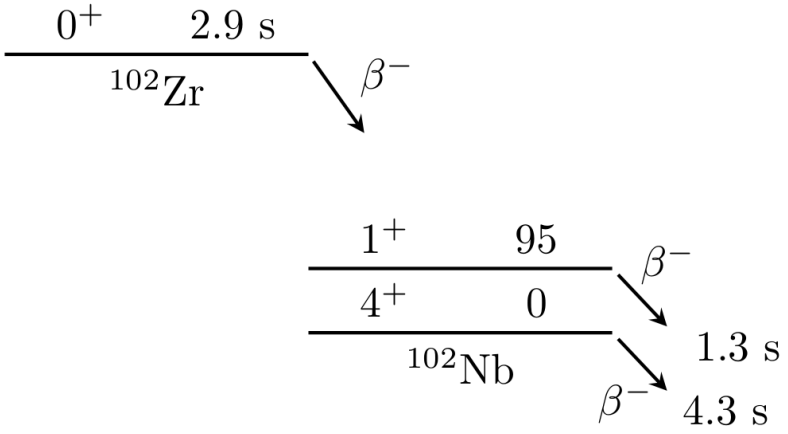

Figure 12.1: Scheme of the two isomers in ^{102}Nb. Spin-parity and energy (in keV) of both isomeric states, as well as the half-life of their β-decay are presented. The decay of the ground state of the parent, ^{102}Zr, is also depicted.

In the measurements with DTAS, the low-spin isomer (^{102m}Nb) was populated through the decay of the parent. This was done by extracting and implanting ^{102}Zr from JYFLTRAP, since the $0^+ \rightarrow 1^+$ transition is extremely favoured with respect to the $0^+ \rightarrow 4^+$

transition. The high-spin isomer (^{102gs}Nb), was obtained from the direct measurement of ^{102}Nb ions selected in the trap where both isomers are present. In this case the low-spin isomer is considered a contaminant to be subtracted from the other measurement.

12.1 Experimental spectra

In this section, we will show the measured spectra corresponding to the combined measurement of the decays of ^{102}Zr and ^{102m}Nb, as well as the spectra of the combined measurement of the decays of both isomers, ^{102gs}Nb and ^{102m}Nb.

12.1.1 β-gated spectrum

The resulting singles spectrum for the total statistics obtained for the two measurements is compared with the β-gated spectrum in Figures 12.2 (runs 358-361 and 365-368) and 12.3 (runs 353-357). The time coincidence window on the β-γ TAC spectrum used in each case is indicated. The secondary peak of the TAC spectrum in Figure 12.2 corresponds to 1100 background counts, while the one in Figure 12.3 corresponds to 800 counts from the decay.

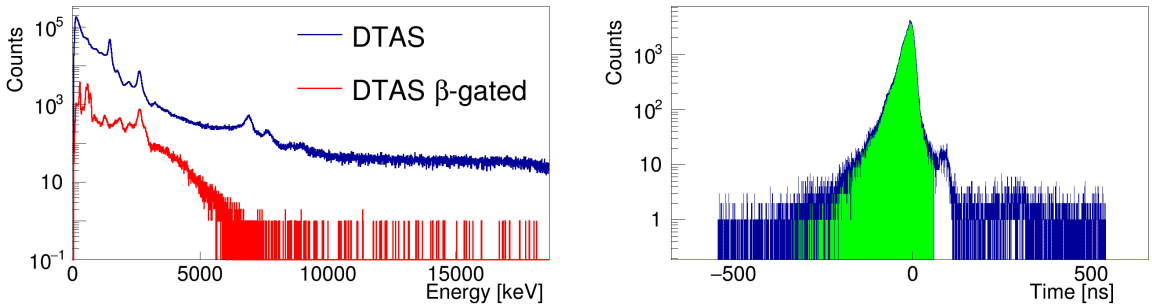

Figure 12.2: Comparison between the β-gated spectrum and the singles spectrum of DTAS for the combination of the decays of ^{102}Zr and ^{102m}Nb (left). The TAC spectrum between DTAS-β plastic detector for this measurement (right) with the coincidence window highlighted in green.

The β-gated spectra for both measurements are compared in Figure 12.4, where the MC simulation of the decay of ^{102}Zr is also shown. Details about this MC simulation will be given in Section 12.3.1.

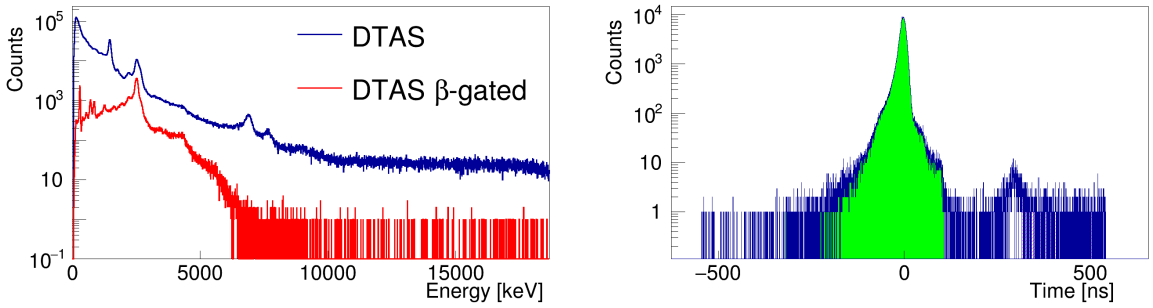

Figure 12.3: Comparison between the β-gated spectrum and the singles spectrum of DTAS for the combination of the decays of ^{102gs}Nb and ^{102m}Nb (left). The TAC spectrum between DTAS-β plastic detector for this measurement (right) with the coincidence window highlighted in green.

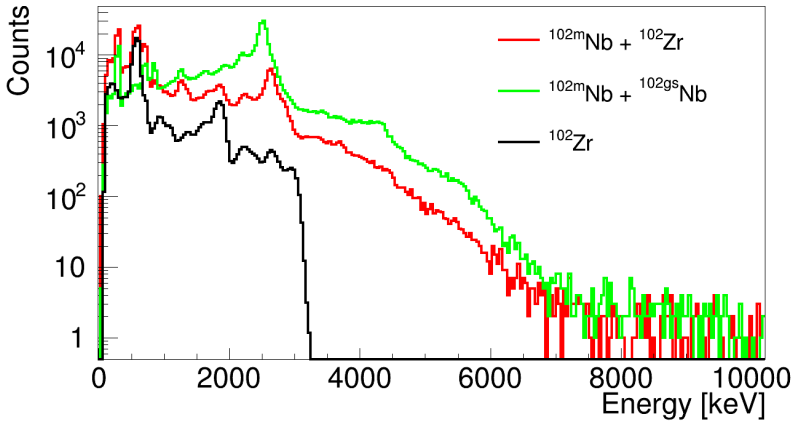

Figure 12.4: Experimental β-gated spectra of the different measurements of the decays of ^{102gs}Nb and ^{102m}Nb: the combined measurement of the decays of ^{102}Zr and ^{102m}Nb (red), the combined measurement of the decays of both isomers, ^{102gs}Nb and ^{102m}Nb (green), and the MC simulation of the decay of ^{102}Zr (black).

12.1.2 Contaminants

From the combined measurement of the decays of ^{102}Zr and ^{102m}Nb, the decay of ^{102m}Nb will be studied by considering ^{102}Zr as a contaminant. On the other hand, from the combined measurement of the decays of the two niobium isomers, the decay of ^{102gs}Nb will be studied by considering ^{102m}Nb as a contaminant. All the contaminants for each of the two different measurements will be studied here.

^{102m}Nb

A MC simulation of the decay of ^{102}Zr is used, as will be discussed in Section 12.3.1. The normalization of the contaminant is obtained from the γ-rays of 599.48 keV and 535.13 keV. These γ-rays are emitted in the de-excitation of the 599.48 keV level, which is strongly populated in the decay of ^{102}Zr$\rightarrow^{102}$Nb. The summing-pileup contribution is normalized with the theoretical expression from Equation (4.4). The contaminants normalized are

shown in Figure 12.5.

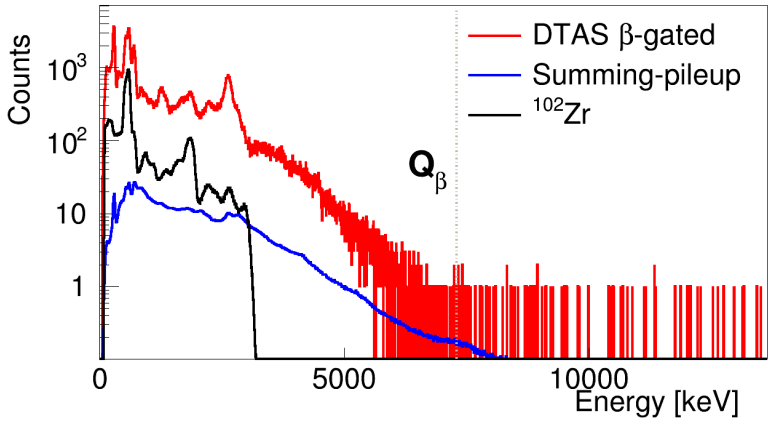

Figure 12.5: Relevant histograms for the analysis of the decay of ^{102m}Nb. β-gated experimental spectrum (red), contamination from the decay of the parent, ^{102}Zr (black), and summing-pileup contribution (blue).

^{102gs}Nb

As in the case of ^{100}Nb (see Chapter 11), the high-spin component was favoured in the proton-induced fission process, and the low-spin component (^{102m}Nb) was treated as a contaminant to study the decay of the high-spin isomer. The spectrum of the decay of low-spin isomer was calculated by means of a MC simulation. For this we used the DECAYGEN event generator [146] and the results of the TAGS analysis for ^{102m}Nb as input. The resulting spectrum was normalized by using the peak associated to the level at 698.26 keV, a 0^+ level that is only populated in the decay of ^{102m}Nb. The low-spin component in this case represents just a 19.7% of the total spectrum free from summing-pileup. In Figure 12.6 the contaminants normalized are shown, including the summing-pileup contribution.

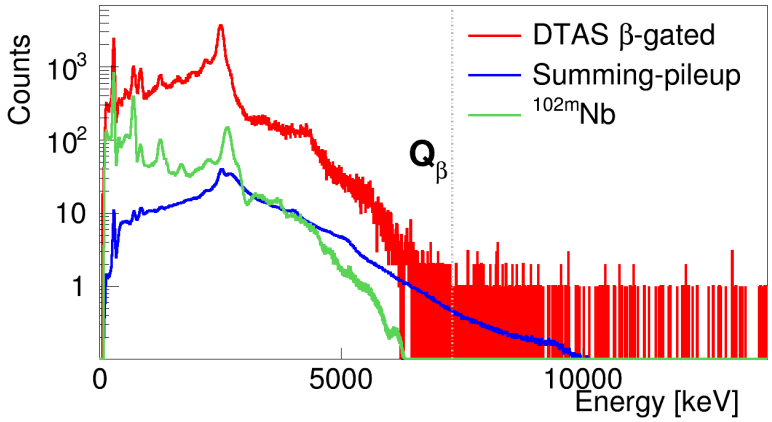

Figure 12.6: Relevant histograms for the analysis of the decay of ^{102gs}Nb. β-gated experimental spectrum (red), contamination from the decay of ^{102m}Nb (green), and summing-pileup contribution (blue).

12.2 Branching ratio matrix

According to the recommendations of RIPL-3 [145], the level scheme of ^{102}Mo is considered complete up to the level at 1398.39 keV. From this level up to the Q_β, a continuum region with 40 keV bins is used with branching ratios based on the statistical model as explained in Chapter 2. The levels in the complete decay scheme without assigned spin-parity values are summarized in Table 12.1, together with the recommended values from RIPL-3 [145] which we employed in our analysis..

Energy [keV]	J^P ENSDF	J^P used
1144.5	(2^+)	2^+
1245.54	(3^+)	3^+
1398.39	(4^+)	4^+

Table 12.1: Levels with no spin-parity assignment for ENSDF and our choice (up to 1398.39 keV).

The level density data from HFB+c calculations [149,212] available at RIPL-3 [145] are used (see Figure 12.7). The correction parameters C and P for the level density distribution are presented in Table 12.2. We also used a different P factor adjusted to match better the experimental accumulated number of levels at low energies.

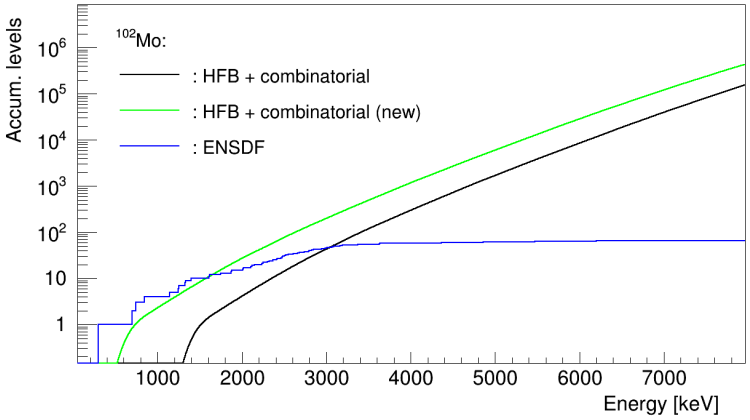

Figure 12.7: Accumulated number of levels in ^{102}Mo. The blue line is obtained from ENSDF and the black line corresponds to the Hartree-Fock-Bogoliubov calculation downloaded from RIPL-3. In addition, we show the distribution with a different P correction factor (green) that reproduces better the experimental distribution at low energies.

C	P
0.0	1.17951
0.0	0.4

Table 12.2: Correction factors for the HFB+c level density distribution for ^{102}Mo (first row). In order to match better the experimental accumulated number of levels at low energies, we have changed the P factor (second row).

The γ-strength function parameters involved in the branching ratio matrix and response function calculation are presented in Table 2.1.

12.3 Analysis and results

12.3.1 ^{102}Zr decay

The β-decay of ^{102}Zr is a contaminant in our measurements of the decay of ^{102m}Nb. As in the case of ^{100}Zr discussed in Chapter 11, one can suspect that the knowledge of this decay is incomplete, since the Q_β is 4.717 MeV and the last level populated in β-decay that was seen experimentally is at 940.5 keV [233]. Thus a TAGS measurement of this decay with DTAS seems appropriate. Unfortunately, given that the half-life of ^{102m}Nb is much shorter than the half-life of ^{102}Zr (see Figure 12.1) it is difficult to minimize the contribution of ^{102m}Nb. The method described in Appendix C to disentangle both decays from a single measurement has been applied (as in the case of ^{100}Zr presented in Chapter 11). The resulting β-gated DTAS spectra for the different time windows used for this procedure are presented in Figure 12.8.

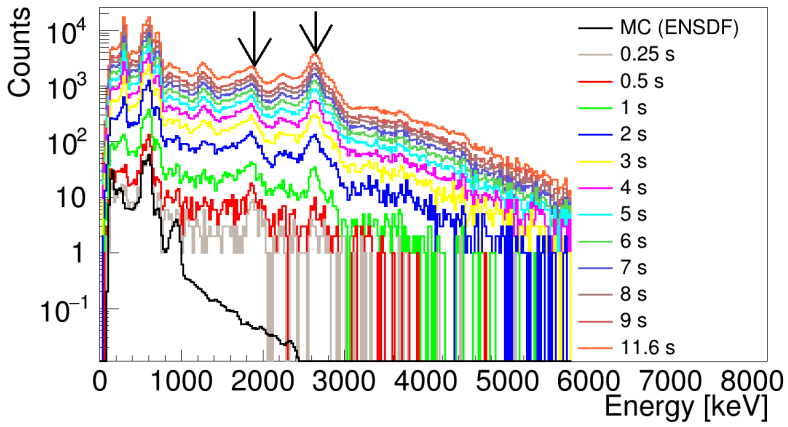

Figure 12.8: Comparison of the DTAS β-gated spectra for ^{102}Zr implantation with different time windows set within the total length of the cycle (11.6 s). The MC simulation with the available information from ENSDF is also presented and scaled to be compared with the spectrum with the shortest time window. The arrows indicate two peaks that clearly grow with different tendencies, thus proving the contribution of the decay of ^{102}Zr at these energies.

The corresponding weights for the ^{102m}Nb contribution as a fraction of unity for the time windows in Figure 12.8 are 0.041, 0.078, 0.137, 0.223, 0.281, 0.322, 0.352, 0.375, 0.393, 0.401, 0.418 and 0.439 respectively. A MC simulation performed with the DECAYGEN event generator [146] using the available information from ENSDF [240] based on [233] as input is also presented in Figure 12.8. The simulation is scaled to be compared with the spectrum with the largest ^{102}Zr contribution (the shortest time window). From this comparison it seems that indeed there is new β-intensity above 940.5 keV.

The spectrum of ^{102}Zr is obtained analogously to the case of ^{100}Zr (explained in Chapter 11), and it is shown as the grey histogram in Figure 12.9.

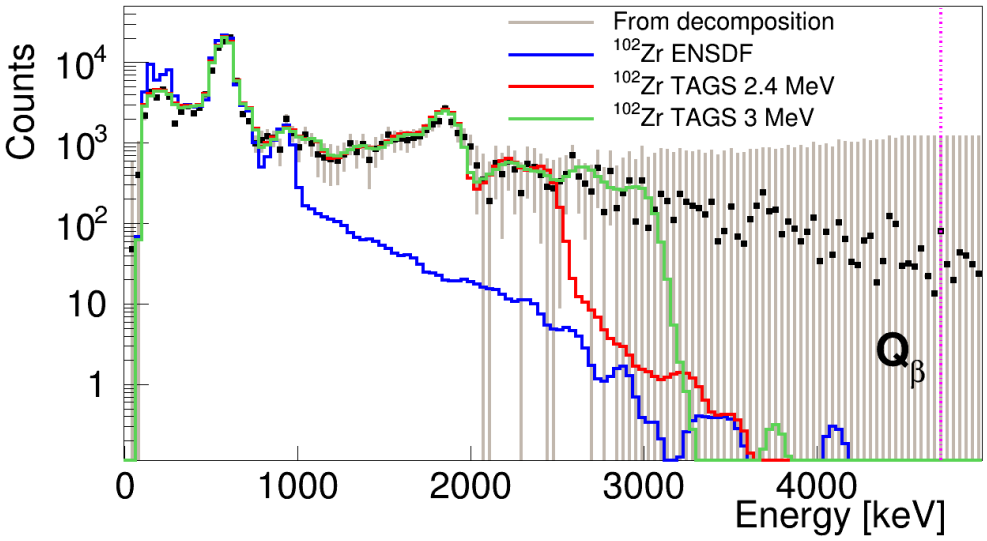

Figure 12.9: Spectrum of the decay of ^{102}Zr extracted with different time windows (grey) as explained in the text. The spectrum is compared with MC simulations of the decay of ^{102}Zr assuming different β-intensity distributions (see text).

As in the case of ^{100}Zr (Chapter 11), the spectrum obtained from the decomposition procedure for the decay of ^{102}Zr exhibits large fluctuations. In order to subtract it as a contaminant for the analysis of ^{102m}Nb, we prefer to use a MC simulation based on the this extracted spectrum. This also ensures the possibility to study properly the multiplicities and the individual module spectra. The β-intensity information for the MC simulation of the decay of ^{102}Zr was obtained from a TAGS analysis of the spectrum extracted from the decomposition procedure in Figure 12.9. This analysis is also interesting since this decay is important from the point of view of reactor decay-heat calculations and nuclear structure. The level scheme of ^{102}Nb used for the analysis included all those levels identified in the β-decay study from [233] up to the level at 940.5 keV, as presented in Table 12.3.

Energy [keV]	J^P ENSDF	J^P used
0.00 +x	1^+	1^+
20.37 +x	-	1^+
64.39 +x	(2^+)	2^+
93.95 +x	-	2^+
156.36 +x	-	2^+
160.72 +x	-	2^+
246.31 +x	-	1^-
258.43 +x	-	1^-
430.70 +x	-	1^-
599.49 +x	1^+	1^+
705.08 +x	(1)	1^+
940.50 +x	(1)	1^+

Table 12.3: Levels with no spin-parity assignment for ENSDF and our adopted values (up to 940.5 keV) for ^{102}Nb. The energy offset x is expected to be 95 keV according to the NUBASE evaluation of 2012 [237].

The PSF parameters needed to calculate the branching ratio matrix for the unknown part of the level scheme are presented in Table 2.1. The level density from HFB+c calculations [149,212] available at RIPL-3 [145] are used. Due the lack of experimental information, there are no correction parameters. As can be seen in Figure 12.10 the calculation does not fit the experimental information when the level scheme from [233] is used.

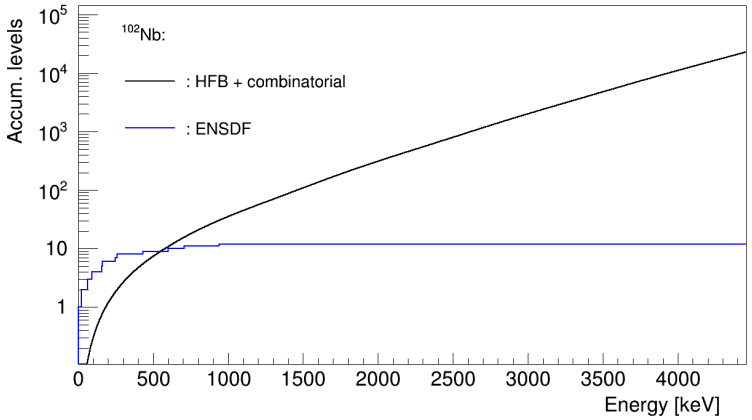

Figure 12.10: Accumulated number of levels. The blue line is obtained from ENSDF (only based on [233]), and the black line corresponds to the Hartree-Fock-Bogoliubov calculation downloaded from RIPL-3.

We have analyzed the extracted spectrum up to 2.98 MeV. Above this energy the spectrum fluctuations are consistent with zero counts. As discussed for ^{100}Zr in Chapter 11, due to the poor sensitivity associated to the extracted spectrum with this procedure, the ground state feeding intensity is fixed to 59%, the value obtained in [233]. In order

to reproduce the clear peak at 1860 keV, we needed no modify the branching ratio matrix manually, forcing the levels of this region to go directly to the ground state. Otherwise, these levels de-excite through many other levels, and the peak is widened due to the shifts produced by the missing low energy γ-rays that are below the energy threshold. It implies that this peak may correspond in reality to a level 64 keV above, since due to our energy threshold we can not distinguish whether the cascade goes through the low energy levels (at 20.27 keV and 64.39 keV). The assumption of direct de-excitation to the ground state should be improved in the light of the multiplicity study of the decay of ^{102m}Nb that will be discussed later.

The β-intensity distribution obtained in the analysis is presented in Table 12.4 together with the results from high resolution [240] based on [233]. The quality of the reproduction of the spectrum with the β-intensity distribution obtained is presented in Figure 12.11. As in the case of the analysis of ^{100}Zr (Chapter 11) the uncertainty in the β-intensity distribution due to the statistical uncertainty in the data is significant. This is the only error quoted in Table 12.4, although the values listed suffer larger uncertainties that are difficult to evaluate in this case.

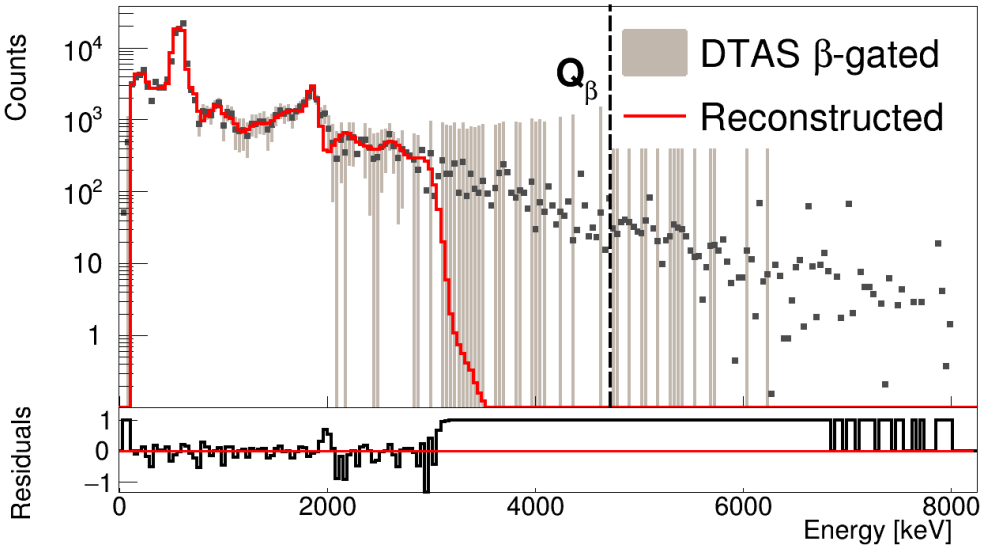

Figure 12.11: Result of the analysis of the decay of ^{102}Zr. The total spectrum is compared with the one reconstructed one after the analysis.

Energy [keV]	I_β ENSDF [%]	I_β DTAS [%]
0.000	59(3)	59 (fixed)
20.370	2.1(14)	-
64.390	2.1(21)	-
93.950	0.8(5)	-
156.360	1.3(7)	-
160.720	<0.7	0.276(12)
246.310	2.2(8)	0.560(5)

Continues on the next page.

Energy [keV]	I_β ENSDF [%]	I_β DTAS [%]
258.430	2.4(2)	-
430.700	0.26(9)	0.0494(4)
599.490	25(2)	22.01(7)
705.080	3.3(7)	2.926(15)
940.500	1.7(3)	0.645(6)
980.000	-	0.405(3)
1020.000	-	0.0278(2)
1060.000	-	0.1625(12)
1100.000	-	0.858(7)
1140.000	-	0.0966(8)
1180.000	-	0.01825(16)
1220.000	-	0.00756(7)
1260.000	-	0.00389(4)
1300.000	-	0.01484(14)
1340.000	-	0.2167(19)
1380.000	-	0.451(4)
1420.000	-	0.0902(8)
1460.000	-	0.01947(16)
1500.000	-	0.0318(3)
1540.000	-	0.2026(16)
1580.000	-	0.554(4)
1620.000	-	0.382(3)
1660.000	-	0.1656(11)
1700.000	-	0.1571(10)
1740.000	-	0.545(4)
1780.000	-	1.817(11)
1820.000	-	0.0535(4)
1860.000	-	3.32(2)
2220.000	-	1.200(10)
2260.000	-	0.01353(11)
2300.000	-	0.01187(10)
2340.000	-	0.0746(6)
2380.000	-	0.378(3)
2420.000	-	0.291(3)
2460.000	-	0.0609(6)
2500.000	-	0.0216(2)
2540.000	-	0.0341(3)
2580.000	-	0.1390(12)
2620.000	-	0.391(3)
2660.000	-	0.403(3)
2700.000	-	0.287(2)

Continues on the next page.

Energy [keV]	I_β ENSDF [%]	I_β DTAS [%]
2740.000	-	0.243(2)
2780.000	-	0.1889(17)
2820.000	-	0.1072(10)
2860.000	-	0.0585(6)
2900.000	-	0.0544(5)
2940.000	-	0.1371(14)
2980.000	-	0.840(9)

Table 12.4: I_β intensities obtained in the analysis for the decay of ^{102}Zr. Notice that only statistical errors are presented.

As in Chapter 11, for the analysis of ^{102m}Nb we will use MC spectra calculated with the DECAYGEN event generator [146] using two possibilities: the TAGS analysis up to 2.98 MeV presented before, and a more conservative TAGS analysis up to 2.42 MeV. Both MC spectra are shown in Figure 12.9. We did not use the MC simulation with ENSDF information because we found that it was not able to give a reasonable subtraction at low energies in the combined spectrum of ^{102}Zr and ^{102m}Nb. This could be due to the excess deduced at low energies from the comparison in Figure 12.9 when the simulations are scaled to match the prominent peaks in the region of 600 keV.

12.3.2 ^{102m}Nb decay

For the analysis of the decay of the low-spin isomer, we considered allowed transitions to positive parity levels with spins 0,1 and 2. We needed to include direct feeding at around 1330 keV in order to improve the fit at this energy. However, although there is a 0^+ level at 1334.5 keV, which would be easily fed in the decay, no γ-rays have been seen from this level, identified in a ^{100}Mo(t,p) reaction. For this reason, it was not included in the branching ratio matrix calculation. Instead of including a fictitious level, we have used the decay pattern of the 6^+ level at 1327.9 keV.

The quality of the reproduction of the measured spectrum with the accepted I_β distribution is shown in Figure 12.12, and the β-intensity distribution obtained can be seen in Figure 12.13 left. No previous β-decay data were known to compare with, and for the same reason we were not able to optimized the branching ratio matrix by checking the γ-intensities.

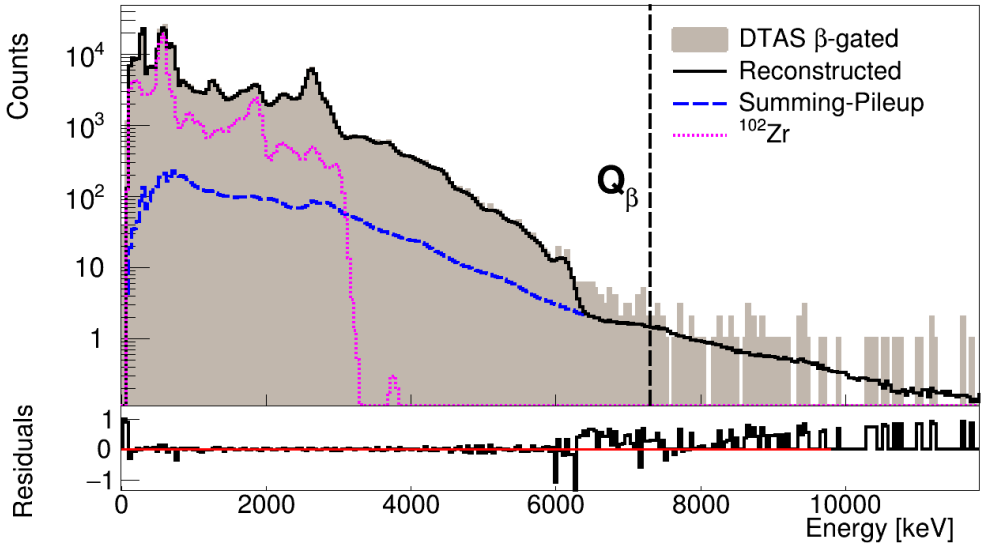

Figure 12.12: Result of the analysis of the decay of ^{102m}Nb. The total spectrum is compared with the reconstructed one after the analysis.

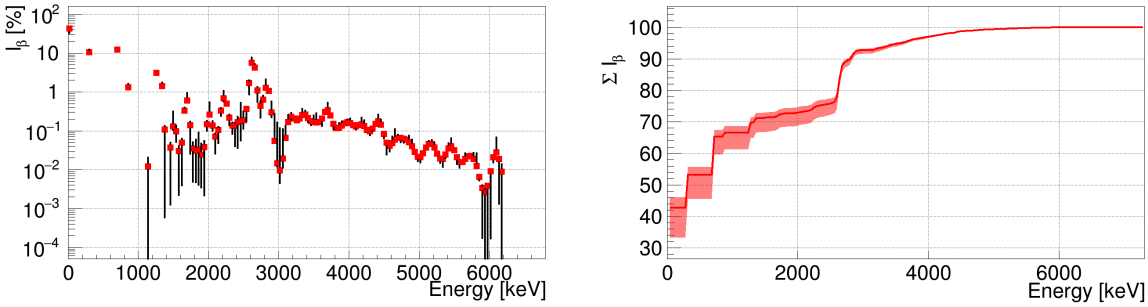

Figure 12.13: β-intensities of the decay of ^{102m}Nb with error bars coming from the uncertainty of all the sources of error.

Systematic errors have been evaluated by considering changes in the normalization factor of the contaminants. An acceptable fit was compatible with a change in the normalization of the summing-pileup of 30%, and with a 5% for the contamination of the decay of ^{102}Zr. The two possible shapes discussed in Subsection 12.3.1 for the contamination of the decay of ^{102}Zr were used, both coming from our TAGS analysis (the simulation with the information from ENSDF did not allow a good subtraction). The effect of the lowest bin included in the fit was also investigated, showing a large impact in the sensitivity to the ground state feeding intensity. Finally, the ME algorithm was used instead of the EM one to check the influence of the deconvolution method in the results of the analysis. The β-intensities and the evaluated systematic errors are presented in Table 12.5 and plotted in Figure 12.13 right.

Energy [keV]	I_β DTAS [%]
0.000	$42.683^{+3.297}_{-9.514}$
296.610	$10.478^{+1.841}_{-0.761}$
698.260	$12.113^{+2.024}_{-0.527}$
847.890	$1.313^{+0.284}_{-0.087}$
1144.500	$0.012^{+0.008}_{-0.012}$
1249.740	$3.076^{+0.508}_{-0.204}$
1327.910	$1.401^{+0.344}_{-0.093}$
1398.390	$0.106^{+0.025}_{-0.106}$
1460.000	$0.037^{+0.012}_{-0.035}$
1500.000	$0.128^{+0.183}_{-0.025}$
1540.000	$0.097^{+0.036}_{-0.046}$
1580.000	$0.030^{+0.010}_{-0.027}$
1620.000	$0.049^{+0.013}_{-0.045}$
1660.000	$0.327^{+0.063}_{-0.017}$
1700.000	$0.588^{+0.347}_{-0.077}$
1740.000	$0.138^{+0.033}_{-0.113}$
1780.000	$0.034^{+0.016}_{-0.030}$
1820.000	$0.030^{+0.028}_{-0.026}$
1860.000	$0.033^{+0.056}_{-0.029}$
1900.000	$0.024^{+0.023}_{-0.021}$
1940.000	$0.038^{+0.017}_{-0.036}$
1980.000	$0.145^{+0.037}_{-0.047}$
2020.000	$0.261^{+0.282}_{-0.030}$
2060.000	$0.134^{+0.040}_{-0.036}$
2100.000	$0.070^{+0.015}_{-0.044}$
2140.000	$0.103^{+0.021}_{-0.055}$
2180.000	$0.324^{+0.057}_{-0.084}$
2220.000	$0.679^{+0.380}_{-0.110}$
2260.000	$0.498^{+0.080}_{-0.028}$
2300.000	$0.218^{+0.039}_{-0.080}$
2340.000	$0.134^{+0.026}_{-0.053}$
2380.000	$0.133^{+0.027}_{-0.093}$
2420.000	$0.165^{+0.060}_{-0.129}$
2460.000	$0.182^{+0.342}_{-0.126}$
2500.000	$0.185^{+0.126}_{-0.072}$
2540.000	$0.361^{+0.058}_{-0.191}$
2580.000	$1.676^{+0.284}_{-0.809}$
2620.000	$5.638^{+1.961}_{-0.368}$
2660.000	$4.199^{+0.969}_{-0.265}$
2700.000	$1.070^{+0.249}_{-0.517}$

Continues on the next page.

Energy [keV]	I_β DTAS [%]
2740.000	$0.439^{+0.146}_{-0.225}$
2780.000	$0.623^{+0.167}_{-0.040}$
2820.000	$1.275^{+0.789}_{-0.087}$
2860.000	$1.063^{+0.162}_{-0.065}$
2900.000	$0.295^{+0.276}_{-0.076}$
2940.000	$0.054^{+0.216}_{-0.005}$
2980.000	$0.014^{+0.147}_{-0.002}$
3020.000	$0.010^{+0.107}_{-0.005}$
3060.000	$0.019^{+0.090}_{-0.008}$
3100.000	$0.065^{+0.066}_{-0.007}$
3140.000	$0.167^{+0.088}_{-0.012}$
3180.000	$0.229^{+0.055}_{-0.034}$
3220.000	$0.203^{+0.032}_{-0.017}$
3260.000	$0.182^{+0.029}_{-0.021}$
3300.000	$0.205^{+0.032}_{-0.014}$
3340.000	$0.250^{+0.115}_{-0.018}$
3380.000	$0.256^{+0.069}_{-0.019}$
3420.000	$0.210^{+0.033}_{-0.044}$
3460.000	$0.174^{+0.027}_{-0.035}$
3500.000	$0.166^{+0.078}_{-0.012}$
3540.000	$0.164^{+0.117}_{-0.012}$
3580.000	$0.164^{+0.026}_{-0.020}$
3620.000	$0.205^{+0.031}_{-0.073}$
3660.000	$0.300^{+0.045}_{-0.021}$
3700.000	$0.338^{+0.192}_{-0.023}$
3740.000	$0.244^{+0.036}_{-0.017}$
3780.000	$0.151^{+0.023}_{-0.041}$
3820.000	$0.116^{+0.018}_{-0.008}$
3860.000	$0.118^{+0.041}_{-0.009}$
3900.000	$0.135^{+0.037}_{-0.010}$
3940.000	$0.155^{+0.025}_{-0.012}$
3980.000	$0.166^{+0.029}_{-0.012}$
4020.000	$0.158^{+0.047}_{-0.011}$
4060.000	$0.138^{+0.020}_{-0.010}$
4100.000	$0.129^{+0.019}_{-0.023}$
4140.000	$0.138^{+0.020}_{-0.010}$
4180.000	$0.147^{+0.066}_{-0.010}$
4220.000	$0.130^{+0.055}_{-0.009}$
4260.000	$0.105^{+0.016}_{-0.007}$
4300.000	$0.097^{+0.014}_{-0.020}$
4340.000	$0.113^{+0.017}_{-0.018}$

Continues on the next page.

Energy [keV]	I_β DTAS [%]
4380.000	$0.150^{+0.022}_{-0.010}$
4420.000	$0.173^{+0.084}_{-0.012}$
4460.000	$0.141^{+0.049}_{-0.010}$
4500.000	$0.083^{+0.013}_{-0.020}$
4540.000	$0.049^{+0.008}_{-0.025}$
4580.000	$0.041^{+0.006}_{-0.012}$
4620.000	$0.047^{+0.023}_{-0.003}$
4660.000	$0.059^{+0.051}_{-0.004}$
4700.000	$0.065^{+0.013}_{-0.005}$
4740.000	$0.065^{+0.010}_{-0.014}$
4780.000	$0.062^{+0.009}_{-0.014}$
4820.000	$0.058^{+0.009}_{-0.004}$
4860.000	$0.050^{+0.023}_{-0.004}$
4900.000	$0.039^{+0.020}_{-0.003}$
4940.000	$0.028^{+0.004}_{-0.002}$
4980.000	$0.021^{+0.003}_{-0.005}$
5020.000	$0.021^{+0.003}_{-0.006}$
5060.000	$0.026^{+0.004}_{-0.002}$
5100.000	$0.037^{+0.005}_{-0.002}$
5140.000	$0.046^{+0.008}_{-0.003}$
5180.000	$0.046^{+0.012}_{-0.003}$
5220.000	$0.037^{+0.012}_{-0.002}$
5260.000	$0.026^{+0.004}_{-0.002}$
5300.000	$0.019^{+0.003}_{-0.004}$
5340.000	$0.018^{+0.003}_{-0.007}$
5380.000	$0.024^{+0.003}_{-0.004}$
5420.000	$0.034^{+0.013}_{-0.002}$
5460.000	$0.039^{+0.025}_{-0.003}$
5500.000	$0.031^{+0.004}_{-0.002}$
5540.000	$0.021^{+0.003}_{-0.007}$
5580.000	$0.016^{+0.002}_{-0.004}$
5620.000	$0.015^{+0.002}_{-0.001}$
5660.000	$0.018^{+0.008}_{-0.001}$
5700.000	$0.022^{+0.003}_{-0.001}$
5740.000	$0.022^{+0.003}_{-0.002}$
5780.000	$0.019^{+0.008}_{-0.001}$
5820.000	$0.012^{+0.014}_{-0.001}$
5860.000	$0.006^{+0.001}_{-0.001}$
5900.000	$0.003^{+0.001}_{-0.003}$
5940.000	$0.003^{+0.000}_{-0.003}$
5980.000	$0.004^{+0.001}_{-0.004}$

Continues on the next page.

Energy [keV]	I_β DTAS [%]
6020.000	$0.009^{+0.001}_{-0.009}$
6060.000	$0.021^{+0.003}_{-0.006}$
6100.000	$0.028^{+0.039}_{-0.002}$
6140.000	$0.019^{+0.003}_{-0.017}$
6180.000	$0.009^{+0.005}_{-0.009}$

Table 12.5: I_β intensities of the decay of ^{102m}Nb.

The ground state feeding intensity was also calculated by means of the β-γ counting method of Appendix D, and a $I_{g.s.}$ =43.5(24)% was obtained, in agreement with the value from the TAGS analysis, $42.7^{+3.3}_{-9.5}$%.

The reproduction of the multiplicities is shown in Figure 12.14. As can be observed, the good agreement is deteriorated by the multiplicity spectra of the ^{102}Zr contaminant. This is due to the simple assumption made in the branching ratio matrix calculation of this decay in order to reproduce the peak at 1860 keV. As explained in Section 12.3.1, we forced the branching ratio matrix to connect the levels of this region directly with the ground state. A more realistic assumption that improves notably the multiplicity reproduction is obtained by forcing only an 11% of the transitions from the levels of this region to decay to the ground state. The remainder branching ratios are adjusted to reproduce multiplicity M_m=2,3,4.

Finally, the reproduction of the spectra of the individual modules has also been studied, as presented in Figure 12.15, and a good agreement between the experimental spectra and the MC simulation based on the analysis is found.

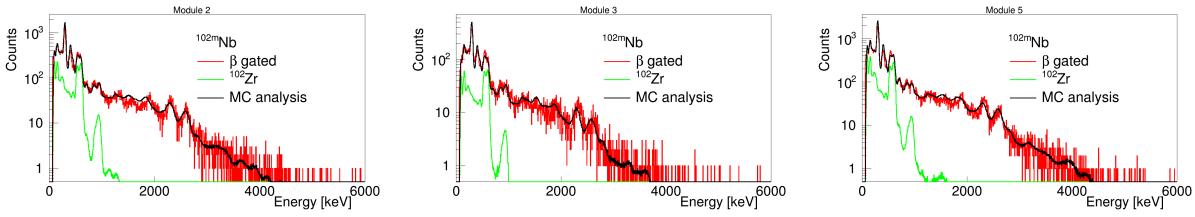

Figure 12.15: ^{102m}Nb experimental spectra for the three geometrically distinguishable individual crystals compared with the MC.

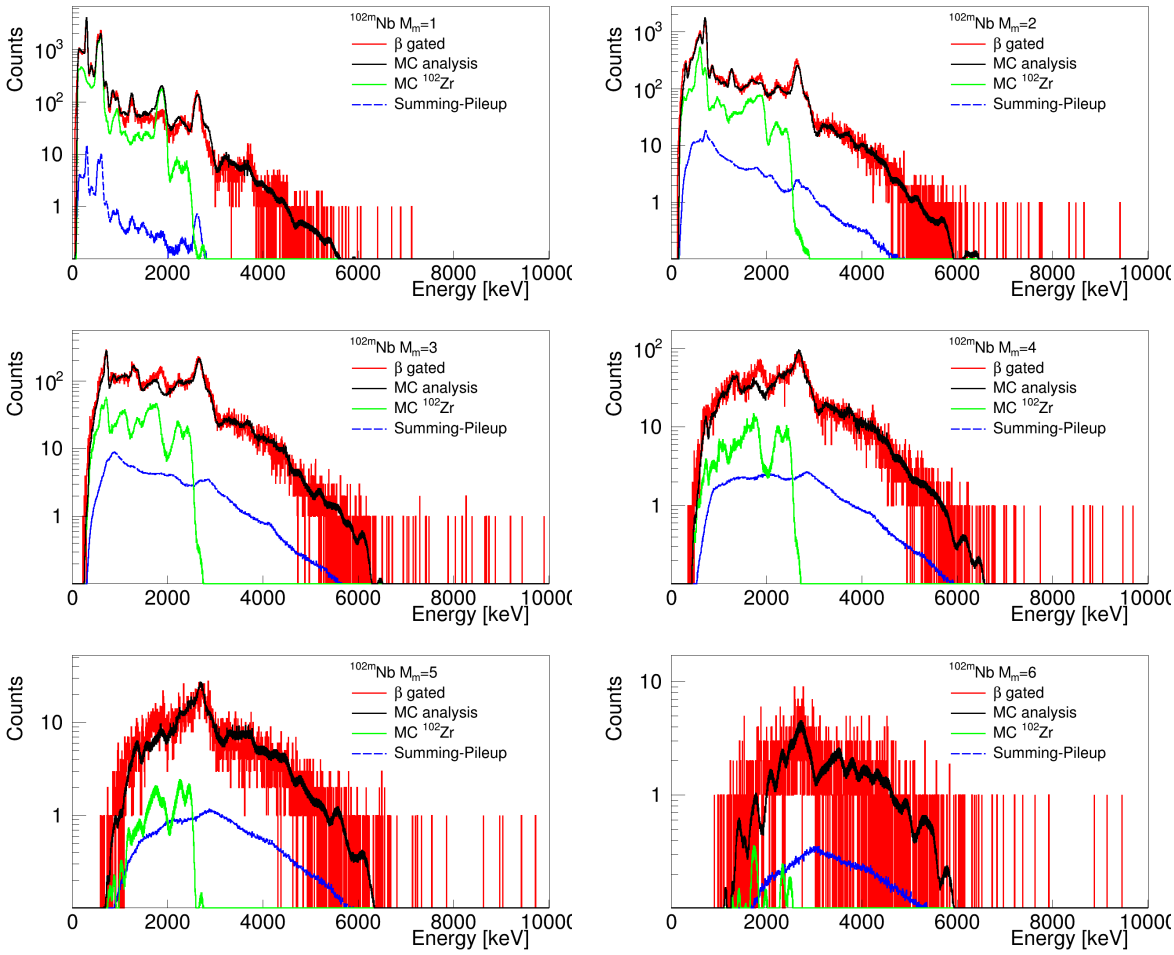

Figure 12.14: Experimental spectra for different multiplicities for the decay of ^{102m}Nb compared with the MC simulation performed with an event generator for multiplicities from 1 to 6.

12.3.3 ^{102gs}Nb decay

The analysis was carried out permitting direct feeding to levels with spin-parity assignment 3^+, 4^+ and 5^+ (allowed transitions). In the known part of the level scheme it means direct feeding only to levels at 743.7 keV (4^+) and at 1245.54 keV (3^+) excitation.

In this case, as in ^{100m}Nb (Chapter 11), the reproduction of the γ-intensities known from high resolution experiments [240] is crucial to improve the fit. The γ-intensities with the original branching ratio matrix and the ones obtained with the modified branching ratio matrix are compared in Table 12.6 with the high resolution values.

Energy [keV]	I_γ ENSDF	I_γ DTAS	I_γ DTAS*
295.92	0.7938	0.880	0.790
697.05	0.01862	0.039	0.010
743.03	0.196	0.295	0.188
847.48	0.5047	0.132	0.492
1244.95	0.2303	0.048	0.227
1249.1	0.02156	0.019	0.005
1327.13	0.01176	0.019	0.006
1397.85	0.07938	0.024	0.008

Table 12.6: Absolute γ-intensities de-exciting the main levels populated in the decay of ^{102gs}Nb (per 100 decays). The second column corresponds to the intensities obtained from high resolution data [240]. The third column gives the intensities obtained with DTAS for the base analysis, whereas the intensities obtained with a modified branching ratio matrix are presented in the fourth column (DTAS*).

If the branching ratio matrix is not modified, the best fit requires considering direct feeding to the 2^+ level at 847 keV. However, a modified branching ratio matrix has been considered for the adopted analysis, and the resulting fit of the experimental spectrum is presented in Figure 12.16. The accepted I_β distribution is shown in Figure 11.15 left compared with the values available at ENSDF [240].

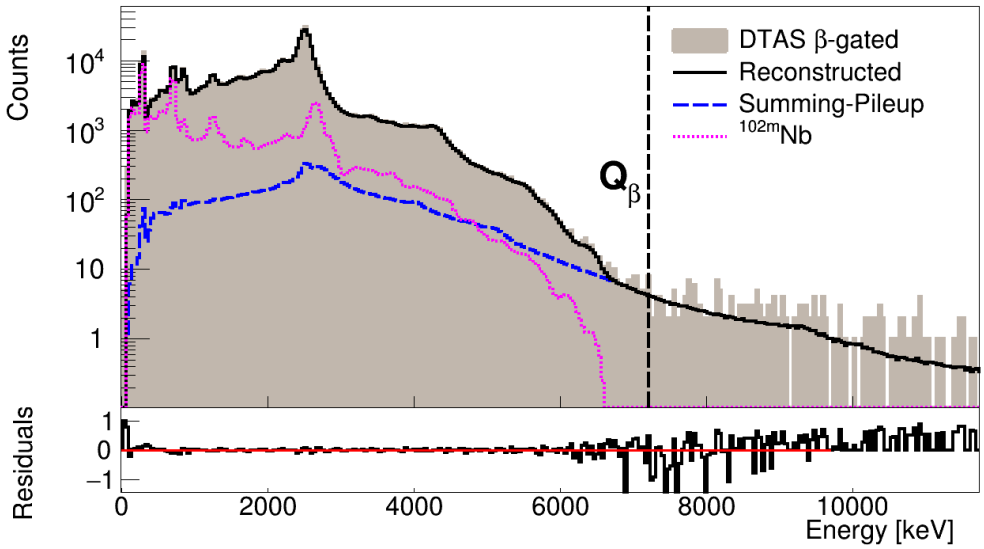

Figure 12.16: Result of the analysis of the decay of ^{102gs}Nb. The total spectrum is compared with the reconstructed one after the analysis.

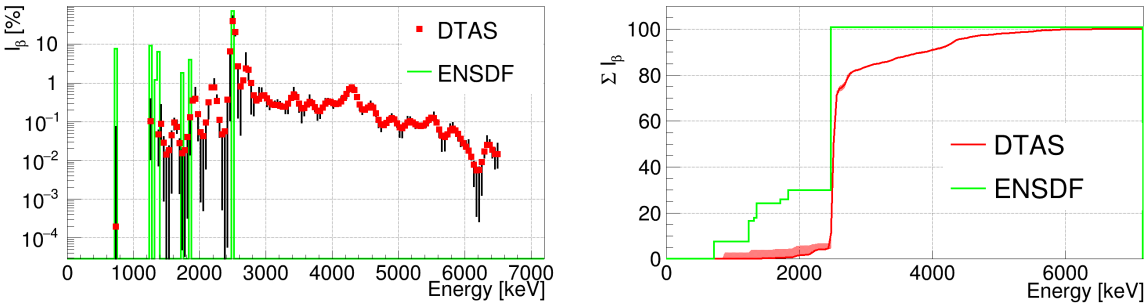

Figure 12.17: β-intensities of the decay of ^{102gs}Nb with error bars coming from the uncertainty of all the sources of error.

As in previous cases, systematic errors have been evaluated by changing the normalization factors of the contaminants while preserving a reasonable fit. The fit was compatible with a change in the normalization of the summing-pileup of 20%, and with a change of 20% for the contamination of ^{102m}Nb. In addition, the measured contamination of ^{102m}Nb has been used, instead of a MC simulation. This gave a better fit at low energies, but introduced many fluctuations at high energies. However, it allowed to study the impact of the shape of the spectrum of ^{102}Zr in this analysis. The two possible spectra used for the analysis of ^{102m}Nb (see Sections 12.3.1 and 12.3.2) were subtracted from ^{102m}Nb, and these clean spectra were used in the analysis of ^{102gs}Nb. Finally, the impact of using the ME algorithm instead of the EM was also studied. After considering all these sources of uncertainty, the β-intensities and the evaluated systematic errors are presented in Table 12.7 and plotted in Figure 12.17 right in comparison with ENSDF values [240]. Note that above the last level of the known level scheme used for the analysis, the values from the bibliography listed in Table 12.7 correspond to integral values over our energy bins.

Energy [keV]	I_β ENSDF [%]	I_β DTAS [%]
743.730	7.6(23)	$0.0002^{+0.0732}_{-0.0002}$
1245.540	9(3)	$0.102^{+0.950}_{-0.092}$
1327.910	1.2(3)	-
1398.390	6.3(11)	$0.047^{+0.016}_{-0.043}$
1420.000	-	$0.087^{+0.181}_{-0.086}$
1460.000	-	$0.028^{+0.012}_{-0.027}$
1500.000	-	$0.014^{+0.004}_{-0.014}$
1540.000	-	$0.018^{+0.005}_{-0.018}$
1580.000	-	$0.044^{+0.108}_{-0.043}$
1620.000	-	$0.093^{+0.181}_{-0.031}$
1660.000	-	$0.073^{+0.035}_{-0.023}$
1700.000	-	$0.028^{+0.014}_{-0.026}$
1740.000	1.8(7)	$0.015^{+0.014}_{-0.015}$
1780.000	-	$0.018^{+0.017}_{-0.018}$
1820.000	-	$0.040^{+0.024}_{-0.040}$

Continues on the next page.

Energy [keV]	I_β ENSDF [%]	I_β DTAS [%]
1860.000	3.9(7)	$0.130^{+0.051}_{-0.116}$
1900.000	-	$0.349^{+0.164}_{-0.013}$
1940.000	-	$0.389^{+0.355}_{-0.010}$
1980.000	-	$0.155^{+0.011}_{-0.122}$
2020.000	-	$0.053^{+0.001}_{-0.052}$
2060.000	-	$0.042^{+0.003}_{-0.041}$
2100.000	-	$0.093^{+0.007}_{-0.087}$
2140.000	-	$0.315^{+0.022}_{-0.195}$
2180.000	-	$0.762^{+0.048}_{-0.416}$
2220.000	-	$0.770^{+0.486}_{-0.494}$
2260.000	-	$0.343^{+0.127}_{-0.260}$
2300.000	-	$0.111^{+0.011}_{-0.092}$
2340.000	-	$0.047^{+0.005}_{-0.047}$
2380.000	-	$0.057^{+0.005}_{-0.056}$
2420.000	-	$0.367^{+0.022}_{-0.367}$
2460.000	-	$6.554^{+0.204}_{-6.446}$
2500.000	71(6)	$39.554^{+12.643}_{-0.985}$
2540.000	-	$20.689^{+1.452}_{-4.315}$
2580.000	-	$2.678^{+0.093}_{-2.551}$
2620.000	-	$0.810^{+0.070}_{-0.765}$
2660.000	-	$1.161^{+0.214}_{-0.242}$
2700.000	-	$2.353^{+3.443}_{-0.386}$
2740.000	-	$2.150^{+0.225}_{-0.993}$
2780.000	-	$0.990^{+0.060}_{-0.832}$
2820.000	-	$0.470^{+0.020}_{-0.328}$
2860.000	-	$0.349^{+0.027}_{-0.021}$
2900.000	-	$0.385^{+0.348}_{-0.057}$
2940.000	-	$0.464^{+0.257}_{-0.079}$
2980.000	-	$0.475^{+0.065}_{-0.067}$
3020.000	-	$0.396^{+0.010}_{-0.149}$
3060.000	-	$0.316^{+0.009}_{-0.112}$
3100.000	-	$0.277^{+0.007}_{-0.047}$
3140.000	-	$0.268^{+0.059}_{-0.055}$
3180.000	-	$0.267^{+0.086}_{-0.060}$
3220.000	-	$0.257^{+0.066}_{-0.057}$
3260.000	-	$0.243^{+0.016}_{-0.043}$
3300.000	-	$0.244^{+0.005}_{-0.082}$
3340.000	-	$0.292^{+0.004}_{-0.129}$
3380.000	-	$0.405^{+0.005}_{-0.052}$
3420.000	-	$0.500^{+0.249}_{-0.038}$
3460.000	-	$0.433^{+0.109}_{-0.036}$

Continues on the next page.

Energy [keV]	I_β ENSDF [%]	I_β DTAS [%]
3500.000	-	$0.290^{+0.004}_{-0.113}$
3540.000	-	$0.217^{+0.004}_{-0.122}$
3580.000	-	$0.222^{+0.004}_{-0.080}$
3620.000	-	$0.274^{+0.042}_{-0.022}$
3660.000	-	$0.319^{+0.151}_{-0.030}$
3700.000	-	$0.299^{+0.061}_{-0.025}$
3740.000	-	$0.236^{+0.018}_{-0.051}$
3780.000	-	$0.190^{+0.013}_{-0.081}$
3820.000	-	$0.188^{+0.004}_{-0.067}$
3860.000	-	$0.228^{+0.004}_{-0.012}$
3900.000	-	$0.289^{+0.101}_{-0.019}$
3940.000	-	$0.328^{+0.063}_{-0.021}$
3980.000	-	$0.322^{+0.006}_{-0.041}$
4020.000	-	$0.295^{+0.008}_{-0.074}$
4060.000	-	$0.280^{+0.008}_{-0.033}$
4100.000	-	$0.291^{+0.055}_{-0.010}$
4140.000	-	$0.330^{+0.095}_{-0.004}$
4180.000	-	$0.402^{+0.017}_{-0.005}$
4220.000	-	$0.520^{+0.045}_{-0.121}$
4260.000	-	$0.679^{+0.065}_{-0.099}$
4300.000	-	$0.764^{+0.129}_{-0.009}$
4340.000	-	$0.644^{+0.139}_{-0.008}$
4380.000	-	$0.424^{+0.021}_{-0.035}$
4420.000	-	$0.271^{+0.017}_{-0.075}$
4460.000	-	$0.207^{+0.015}_{-0.054}$
4500.000	-	$0.202^{+0.014}_{-0.024}$
4540.000	-	$0.229^{+0.021}_{-0.002}$
4580.000	-	$0.253^{+0.075}_{-0.003}$
4620.000	-	$0.229^{+0.044}_{-0.004}$
4660.000	-	$0.164^{+0.003}_{-0.026}$
4700.000	-	$0.110^{+0.006}_{-0.040}$
4740.000	-	$0.084^{+0.006}_{-0.027}$
4780.000	-	$0.081^{+0.005}_{-0.011}$
4820.000	-	$0.092^{+0.006}_{-0.003}$
4860.000	-	$0.110^{+0.019}_{-0.003}$
4900.000	-	$0.121^{+0.035}_{-0.003}$
4940.000	-	$0.112^{+0.021}_{-0.003}$
4980.000	-	$0.089^{+0.003}_{-0.016}$
5020.000	-	$0.071^{+0.006}_{-0.031}$
5060.000	-	$0.067^{+0.007}_{-0.028}$
5100.000	-	$0.078^{+0.006}_{-0.004}$

Continues on the next page.

Energy [keV]	I_β ENSDF [%]	I_β DTAS [%]
5140.000	-	$0.094^{+0.039}_{-0.004}$
5180.000	-	$0.101^{+0.027}_{-0.004}$
5220.000	-	$0.095^{+0.003}_{-0.010}$
5260.000	-	$0.085^{+0.004}_{-0.017}$
5300.000	-	$0.078^{+0.006}_{-0.003}$
5340.000	-	$0.076^{+0.008}_{-0.002}$
5380.000	-	$0.079^{+0.010}_{-0.003}$
5420.000	-	$0.090^{+0.013}_{-0.018}$
5460.000	-	$0.110^{+0.015}_{-0.019}$
5500.000	-	$0.127^{+0.013}_{-0.002}$
5540.000	-	$0.123^{+0.049}_{-0.002}$
5580.000	-	$0.094^{+0.016}_{-0.002}$
5620.000	-	$0.061^{+0.007}_{-0.021}$
5660.000	-	$0.043^{+0.007}_{-0.026}$
5700.000	-	$0.040^{+0.007}_{-0.022}$
5740.000	-	$0.047^{+0.007}_{-0.007}$
5780.000	-	$0.059^{+0.025}_{-0.002}$
5820.000	-	$0.065^{+0.028}_{-0.002}$
5860.000	-	$0.059^{+0.006}_{-0.001}$
5900.000	-	$0.047^{+0.006}_{-0.015}$
5940.000	-	$0.036^{+0.005}_{-0.013}$
5980.000	-	$0.028^{+0.004}_{-0.004}$
6020.000	-	$0.022^{+0.010}_{-0.002}$
6060.000	-	$0.018^{+0.015}_{-0.002}$
6100.000	-	$0.012^{+0.002}_{-0.002}$
6140.000	-	$0.008^{+0.001}_{-0.006}$
6180.000	-	$0.005^{+0.001}_{-0.005}$
6220.000	-	$0.006^{+0.002}_{-0.005}$
6260.000	-	$0.009^{+0.002}_{-0.008}$
6300.000	-	$0.017^{+0.003}_{-0.005}$
6340.000	-	$0.025^{+0.017}_{-0.002}$
6380.000	-	$0.025^{+0.008}_{-0.003}$
6420.000	-	$0.019^{+0.003}_{-0.007}$
6460.000	-	$0.014^{+0.006}_{-0.008}$
6500.000	-	$0.015^{+0.012}_{-0.008}$

Table 12.7: I_β intensities of the decay of ^{102gs}Nb.

The reproduction of the multiplicities is shown in Figure 12.18, and the reproduction of the spectra of the individual modules is presented in Figure 12.19. A good agreement between the experimental spectra and the MC simulation based on the adopted analysis is observed for the multiplicities, and a reasonable reproduction is achieved for the individual

modules. However, the peak associated with the γ-ray of 1632.7 keV, coming from the de-excitation of the structure at 2.8 MeV, is not well reproduced for the individual modules. It is worth mentioning that these comparisons worsen considerably when using the original branching ratio matrix.

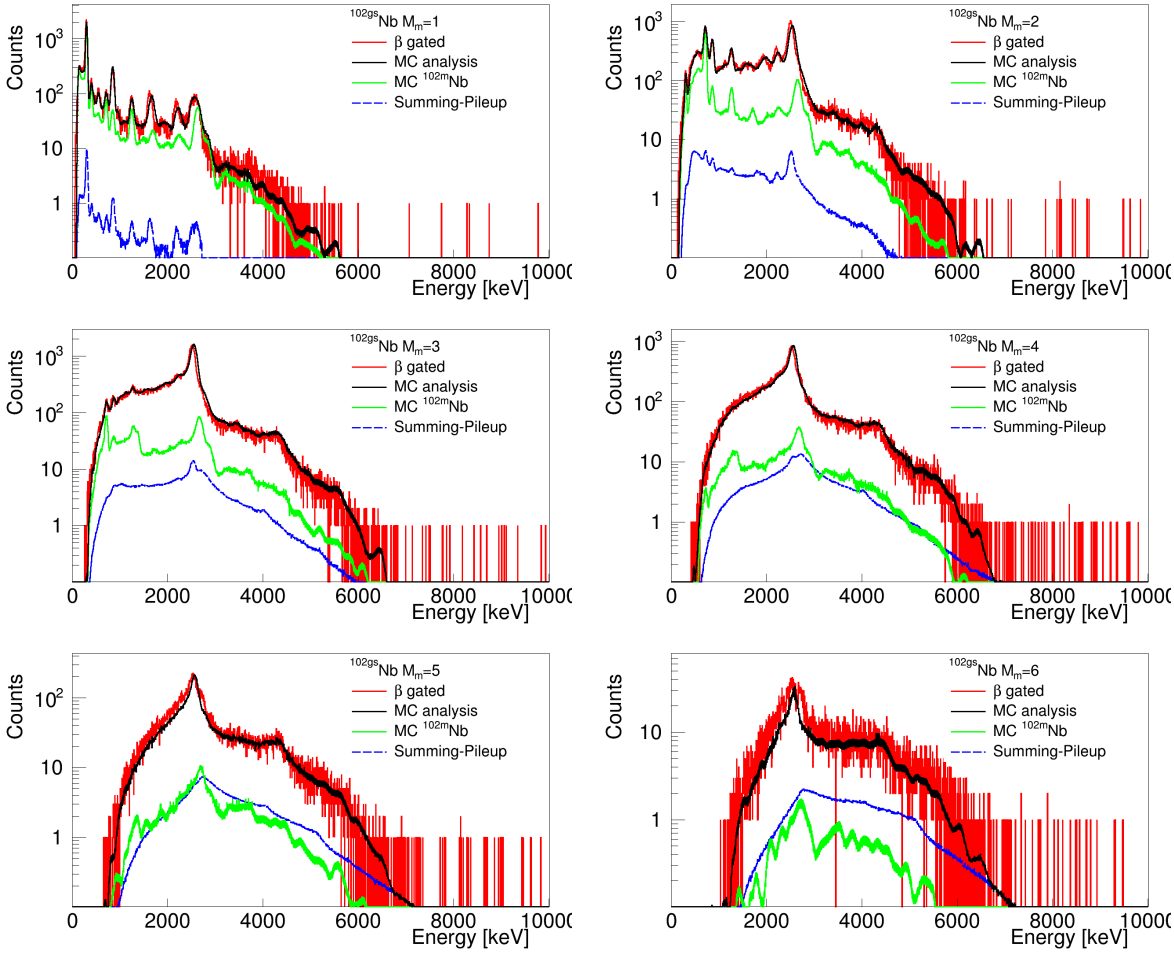

Figure 12.18: Experimental spectra for different multiplicities for the decay of ^{102gs}Nb compared with the MC simulation performed with an event generator for multiplicities from 1 to 6.

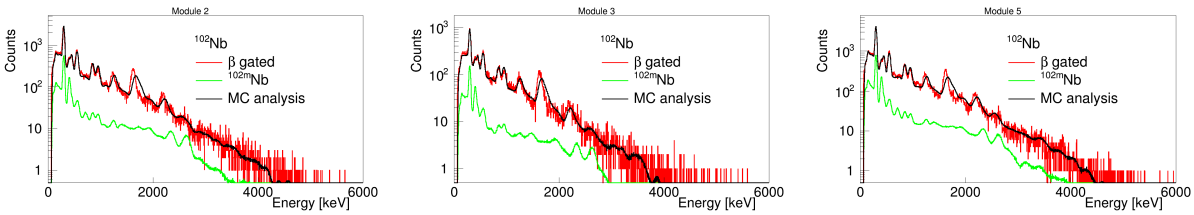

Figure 12.19: ^{102gs}Nb experimental spectra for the three geometrically distinguishable individual crystals compared with the MC.

Chapter 13

^{137}I decay

Donde quiera que algo esté en juego,
ahí se produce la revelación del mundo

Wherever something is at stake, there is the revelation of the world

Nancy H. Kleinbaum

In this chapter we report on the study of the β-decay of ^{137}I into ^{137}Xe, with Q_β=6.027 MeV and S_n=4.025 MeV. Apart from being an important fission fragment contributing to the decay heat and to the antineutrino spectrum calculation, it is also interesting from the point of view of β-delayed neutron emission, as mentioned in Chapter 1 Section 1.3.2, since $Q_\beta > S_n$. The experimental details about the production and measurement of this decay were described in Chapter 6.

13.1 Experimental spectra

13.1.1 β-gated spectrum

The resulting singles spectrum and β-gated spectrum for the sum of all the runs (runs 213-220) are presented in Figure 13.1 left. In Figure 13.1 right, the gate in the TAC spectrum between DTAS and the plastic detector is shown in green.

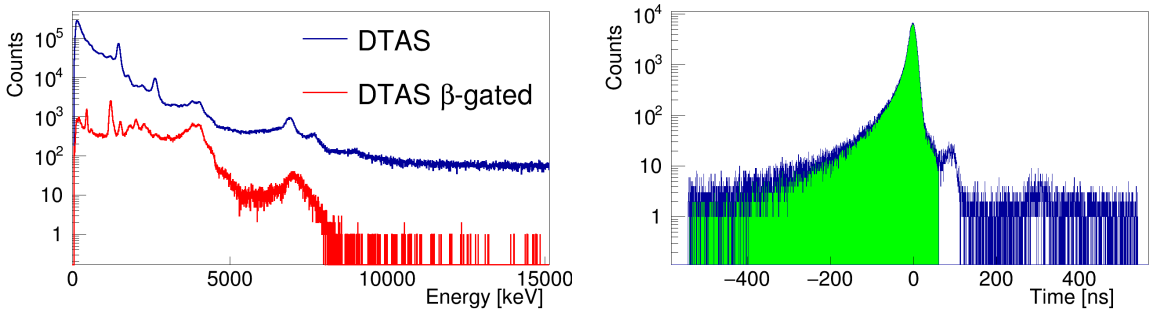

Figure 13.1: Comparison between the β-gated spectrum and the singles spectrum of DTAS for the decay of ^{137}I (left). The TAC spectrum between DTAS-β plastic detector for the measurement of the decay of ^{137}I (right).

13.1.2 Singles spectrum

The background subtraction of the singles DTAS spectrum gives a reasonable spectrum in this case in terms of statistical fluctuations, as shown in Figure 13.2 where it is compared with the β-gated spectrum multiplied by a factor that gives an average β-efficiency of 29.2%. Consequently, an analysis without coincidence with the β-detector and, therefore, independent of the β-efficiency, can be performed in this case.

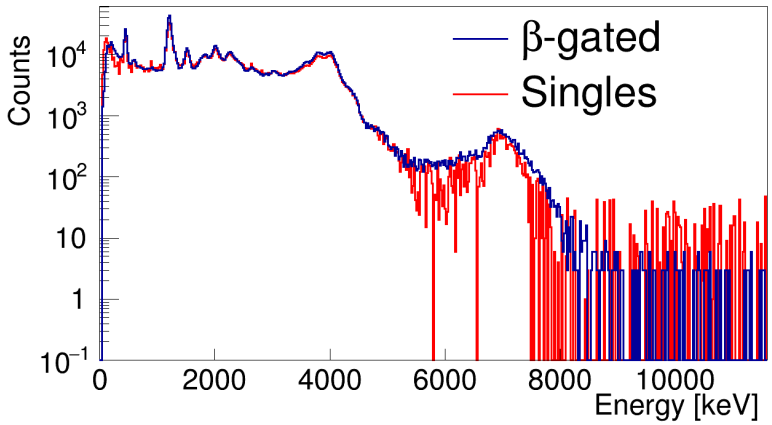

Figure 13.2: Comparison between the β-gated spectrum and background subtracted singles spectrum for ^{137}I.

13.1.3 γ-neutron discrimination

Due to the importance of the interaction of β-delayed neutrons with DTAS, as discussed in Section 5.2.6 from Chapter 5, it will be a relevant contamination in our experimental spectra. If the timing resolution would had been good enough, γ-neutron discrimination through timing could have been applied in order to clean the spectra of neutrons, since decay neutrons travel much more slowly than decay γ-rays and, in general, need time to slow down before interacting with NaI(Tl). The TAC spectra between DTAS and the plastic detector shown so far were constructed with the global timing signal of DTAS. As explained in Appendix A, this signal comes from the hardware sum of the individual modules. This makes it more difficult to distinguish an event due to prompt γ-rays from an event due to β-delayed γ-rays, since everything is entangled because of the electronic sum (an event with a prompt γ-ray detected in one module and a delayed γ-ray in another module-coming from the interaction of a neutron with NaI(Tl)- will produce a slow global timing signal). A better way will be explored here, where we use the timing signals of the individual modules provided by the Mesytec shapers (see Appendix A for details). In general one expects a better timing resolution from individual modules, and more importantly, there is a sizeable probability that γ-rays from delayed neutrons and from prompt decays do not interact in the same module. By setting a narrow window in the TAC spectra for the individual modules we can separate prompt γ-rays from delayed γ-rays (neutrons). For convenience we have aligned the timing signals of the individual modules, by applying an

offset to them, to make the peak of the different TAC spectra between each module and the plastic detector lie in the same position, as shown in Figure 13.3.

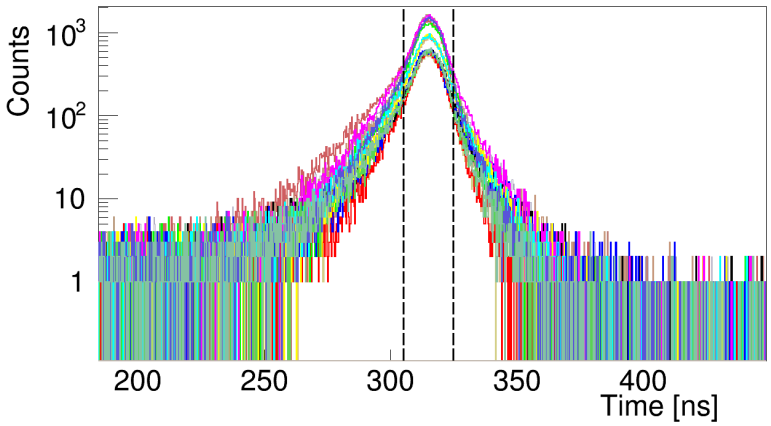

Figure 13.3: Individual TACs between each module and the plastic detector aligned for the decay of ^{137}I, where a narrow prompt gate to select only γ-rays is shown.

A narrow gate of 20 ns was applied to all individual TAC spectra to select prompt γ events before constructing the software sum. One disadvantage of using individual timing signals is that they have a higher threshold, in general, than the global timing signal, since these individual timing branches were not optimized so carefully in the commissioning of DTAS. When applying a narrow gate of 20 ns, this threshold is even higher, around 250 keV. In Figure 13.4 we compare the resulting DTAS spectrum with the 20 ns gate, with the spectra using a wide open gate (full range of the TAC spectra) or using a gate only in the tails of the TAC spectra. It is clear that neutrons are indeed rejected, but so are some low energy signals. In the spectrum with a gate in the tails there are more counts at low energy than in the spectrum with a gate in the full range. This can be understood since normally many low energy signals deposited in the individual modules are summed with other signals and do not appear in the low energy region, but at higher energies. All these effects show the price we have to pay with this procedure: an enlargement of the energy threshold and a distortion in the spectrum, due to the poor timing resolution of the sum of the modules against the plastic detector ($\sim$20 ns). Anyway, we will perform an analysis with this γ-neutron discrimination strategy, in order to evaluate differences with respect to the analysis where neutrons are included as contaminants.

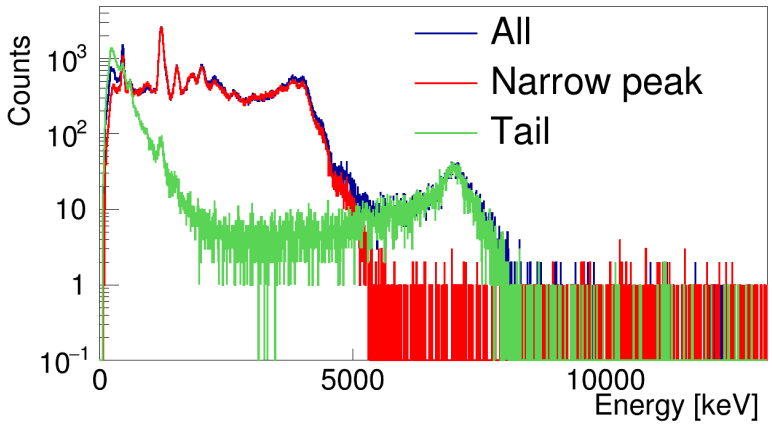

Figure 13.4: Different gates in the TAC spectra of the individual modules for the decay of ^{137}I.

13.1.4 Contaminants

In this case, the decay of the daughter, ^{137}Xe is a contaminant in the measurement. The normalization of this activity was calculated with the Bateman equation assuming constant implantation rate as in Appendix B. From this we obtain that ^{137}Xe represents 9.83% of the total activity, and the cycle is shown in Figure 13.5.

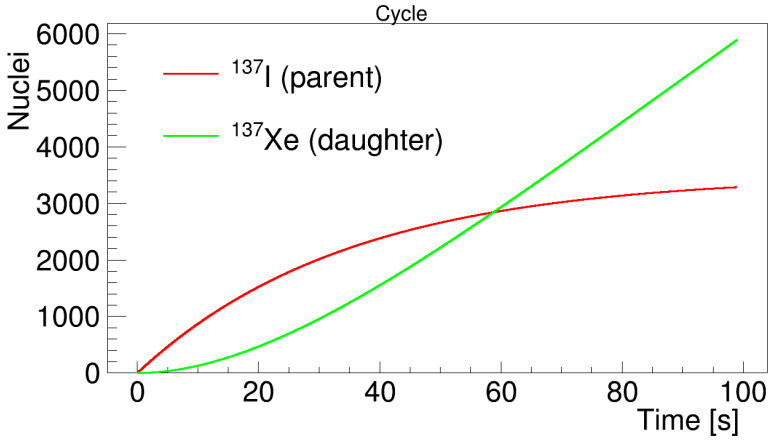

Figure 13.5: Cycle of implantation of ^{137}I on the tape. The number of parent and daughter nuclei is represented as a function of time during the cycle.

However this calculated normalization factor turned out to be too large, and we needed to reduce the value to half in order to obtain an adequate subtraction. The value was adjusted using the 455.5 keV peak of the decay of ^{137}Xe. The resulting daughter spectrum, normalized according to this modified factor can be seen in green in Figure 13.7. In the analysis of the β-gated spectrum with a narrow gate of 20 ns in the TAC spectra of the individual modules, the same gate has been applied for the ^{137}Xe contamination.

The β-delayed neutron decay branch (β-n branch) has been simulated with Geant4 and the special event generator according to the details given in Chapter 5 Section 5.2.6.

The neutron spectrum from ENDF/B-VII.0 used to produce the event generator file for the simulation is shown in Figure 13.6, and it represents the β-intensity accompanied by neutron emission in this case, since only the ground state of ^{136}Xe is populated.

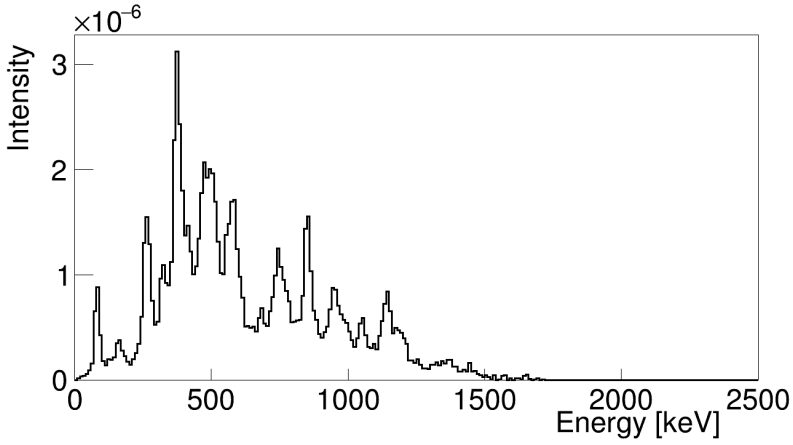

Figure 13.6: Spectrum of the β-delayed neutrons for the decay of ^{137}I.

We found that a time window for energy deposition of 400 ns between the plastic detector and the DTAS was needed in the MC simulation in order to normalize the neutron spectrum using the P_n value. A value of P_n=7.33% is taken from the average weighted value evaluated by the IAEA [241] (other values that will be used for the estimation of errors are 7.14% [242] and 7.76% [193]). The normalization factor $N_{\beta n}$ was calculated using Equation (13.1):

$$N_{\beta n} = N_{\beta \gamma} \times \varepsilon_n \times \frac{P_n}{100 - P_n} \tag{13.1}$$

where $N_{\beta\gamma}$, the number of decays followed by γ emission, is obtained from the TAGS analysis. Since this number depends on $N_{\beta n}$, it is improved iteratively. ε_n is the efficiency of DTAS to detect the β-delayed neutron branch of the decay of ^{137}I. This efficiency is obtained from the β-gated MC simulation and its value is 11.2%. It is worth mentioning that increasing the time window for energy deposition in the simulation from 400 ns to 1 μs the efficiency increases to 11.9%, and the normalization with the P_n value overestimates the amount of neutrons. For the calculation of the β-delayed neutron contribution to the singles spectrum we used a time window for energy deposition of 6 μs, equivalent to the ADC gate length, giving an efficiency of 44.8% (in a longer time window more neutrons are moderated, thus increasing the number of interactions with DTAS).

Finally, the summing-pileup contamination shown in Figure 13.7 has been calculated and normalized in the same way as for the previous cases. In the analysis of the β-gated spectrum with a narrow gate of 20 ns in the TAC spectra of the individual modules, the same gate has been applied for the summing-pileup calculation.

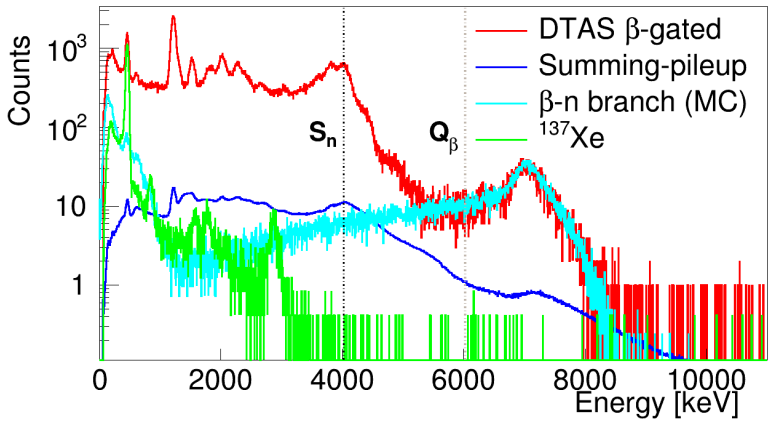

(a)

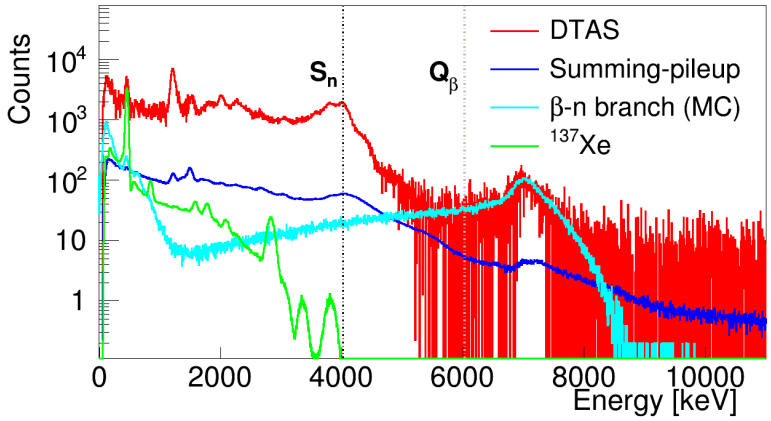

(b)

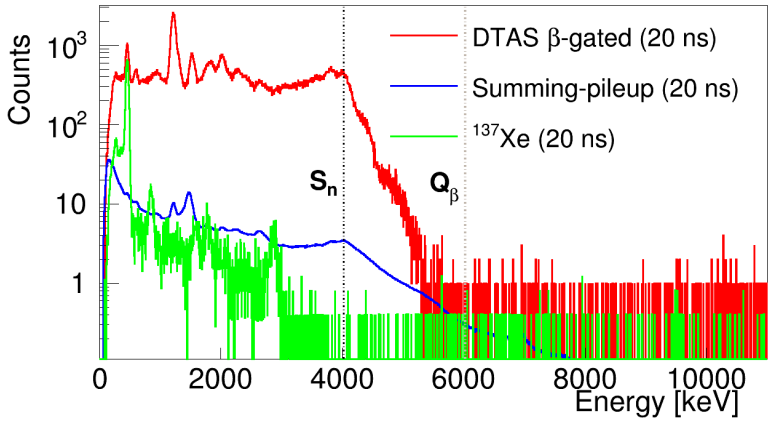

(c)

Figure 13.7: Relevant histograms for the analysis of the decay of ^{137}I: (a) β-gated spectra, (b) singles spectra and (c) β-gated spectra with a narrow (20 ns) window in the individual TAC spectra.

13.2 Branching ratio matrix

According to RIPL-3 the level scheme of ^{137}Xe is complete up to an excitation energy of 2726.140 keV (60 levels). We take these 60 levels as the first option for the known part of the level scheme in our analysis. For those levels with no spin-parity assignment, we used the values chosen by RIPL, as summarized in Table 13.1. A second possibility up to the level at 2244.1 keV for the known part has been considered, where the agreement between the level density used and the experimental number of levels is optimum, as will be shown later. The last possibility considered in the analysis is a known level scheme up to the level at 1534.32 keV.

Energy [keV]	J^P ENSDF	J^P RIPL
1461.28	(1/2,3/2)	$1/2^-$
1512.16	-	$5/2^-$
1668.13	(1/2,3/2)	$1/2^+$
1715.55	$3/2^-$,$5/2^-$,$7/2^-$	$3/2^-$
1752.65	-	$9/2^-$
1766.17	$3/2^-$,$5/2^-$,$7/2^-$	$3/2^-$
1796.08	-	$11/2^-$
1808.75	-	$7/2^+$
1820.56	-	$5/2^-$
1849.69	$3/2^-$,$5/2^-$,$7/2^-$	$7/2^-$
1837.13	-	$7/2^-$
1879.26	-	$7/2^+$
1898.3	-	$7/2^+$
1926.4	-	$11/2^-$
1991.18	-	$7/2^+$
1997.06	-	$7/2^+$
2010.8	-	$5/2^-$
2013.1	-	$3/2^-$
2029.9	-	$9/2^+$
2088	-	$7/2^+$
2089.67	-	$5/2^+$
2099.97	-	$9/2^+$
2114.0	-	$5/2^+$
2144.32	-	$5/2^-$
2147.0	-	$11/2^-$
2155.11	-	$5/2^-$
2191.19	-	$5/2^+$
2196.15	(1/2,3/2)	$1/2^-$
2229.97	-	$5/2^-$
2237.76	-	$11/2^+$
2244.09	-	$11/2^-$

Continues on the next page.

Energy [keV]	J^P ENSDF	J^P RIPL
2281.59	-	$7/2^-$
2345.65	-	$11/2^+$
2356.38	-	$5/2^+$
2368.32	-	$7/2^-$
2380.30	-	$11/2^-$
2422.7	-	$11/2^+$
2444.0	-	$9/2^+$
2452.4	(1/2,3/2)	$1/2^+$
2474.84	-	$7/2^+$
2566.90	-	$3/2^+$
2571.09	-	$7/2^-$
2608.80	-	$7/2^+$
2629.7	-	$15/2^+$
2671.59	-	$3/2^+$
2676.3	-	$9/2^+$
2726.14	-	$7/2^+$

Table 13.1: Levels with no spin-parity assignment for ENSDF and our choices of spin-parity based on RIPL-3.

The level density data from HFB+c calculations [149, 212] available at RIPL-3 [145] are used, as shown in Figure 13.8 where the calculated level density is compared with the experiment. We noticed that the level density correction factors in RIPL-3 did not reproduce the available experimental information, therefore we have calculated new corrections that are presented in Table 13.2. The reason for these new correction is twofold. First, according to the information available in RIPL-3 [145], the highest level used for the fit in the calculation of the correction factors is the one at 1808.75 keV. At this energy the accumulated number of levels is 16 (including the g.s.). With the original corrections, the accumulated number of levels obtained at this energy is 13, whereas with the new corrections we obtain 15. Secondly and more importantly, the experimental number of resonances in ^{137}Xe in the region 4.03-4.53 MeV, just above the neutron separation energy S_n, according to B. Fogelberg et al. [243] is $\leq$4 $1/2^+$ levels, (24 $\pm$ 8) $1/2^-$ levels and (16 $\pm$ 5) $3/2^-$ levels. With the original correction factors, in the range 4.0-4.5 MeV, we obtain 618 $1/2^+$ levels, 12630 $1/2^-$ levels, and 24722 $3/2^-$ levels. On the other hand, with the new corrections, we obtain 2.6 $1/2^+$ levels, 12 $1/2^-$ levels, and 24 $3/2^-$ levels.

C	P
2.96189	1.09479
-1.02	0.69

Table 13.2: Correction factors for the HFB+c level density distribution for ^{137}Xe (first row). In the second row, we have changed the factors to reproduce the experimental information both at low and high energies.

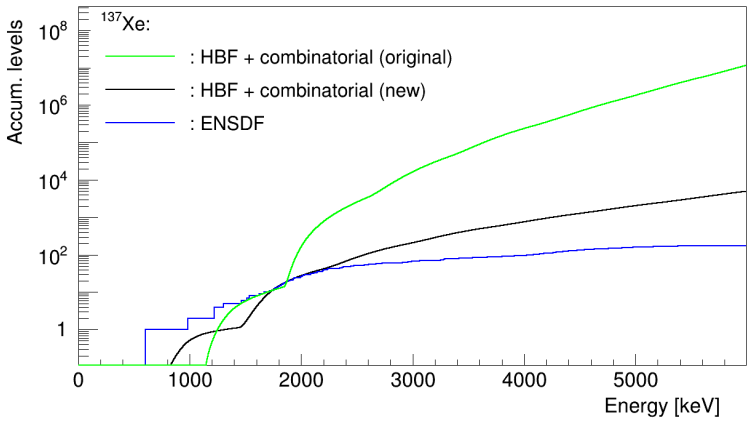

Figure 13.8: Accumulated number of levels as a function of excitation energy for ^{137}Xe. The blue line is obtained from ENSDF and the green line corresponds to the Hartree-Fock-Bogoliubov calculation downloaded from RIPL-3 with the original correction factors. The black line is obtained after changing the C and P factors to reproduce the experimental information both at low and high energies (see text).

The γ-strength function parameters are presented in Table 2.1. The level density parameter $a(S_n)$ used in the calculations of the $E1$ strength is 7.1184 from EGSM calculations at RIPL, but in the literature many other values are found, as discussed in [244]. A careful fit to this parameter was carried out by B. Fogelberg *et al.* [245] obtaining 12.3 MeV^{-1}, which will be our reference value. On the other hand, TALYS [155] gives a value of 16.46067. These three values will be taken into account when evaluating the errors.

13.3 Analysis and results

For the analysis we consider the ground state of ^{137}I as a $7/2^-$ level decaying by allowed transitions ($5/2^+$, $7/2^+$ and $9/2^+$) and first forbidden transitions ($3/2^-$, $5/2^-$, $7/2^-$, $9/2^-$ and $11/2^-$). Using allowed transitions alone does not give a good fit to the spectrum.

With these assumptions some levels without an original parity assignment may remain excluded because of the parity choice from RIPL-3 (a random choice, as already mentioned), e.g. $3/2^+$ levels. We also allowed feeding to these levels in our analysis.

The three possibilities for the known part of level scheme have been investigated for the analysis of the β-gated spectrum (CUT1 up to 2726.1 keV, CUT2 up to 2244.1 keV, and CUT3 up to 1534.3 keV). A comparison of the β-intensities obtained for the three cases is presented in Figure 13.9. Essentially, the choice of the limit for the known part of the level scheme is found to be equivalent, although the best χ^2 is obtained with CUT1. Moreover, CUT1 reproduces better the spectra for different multiplicities, as will be discussed later. For these reasons, CUT1 will be the option used for the rest of the discussion.

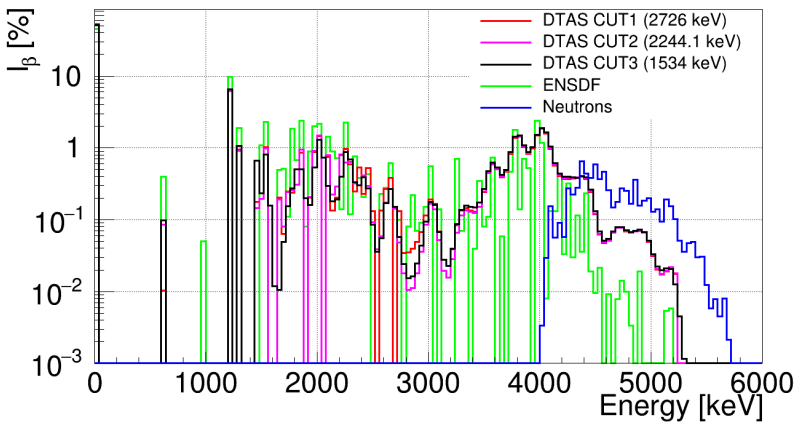

Figure 13.9: Comparison of the β-intensities obtained for the decay of ^{137}I with three different known level schemes.

The branching ratio matrix was modified in order to reproduce the γ-intensities at low energies obtained in high resolution studies [243–245]. The original intensities as well as the ones obtained after the modification are listed in Table 13.3 for CUT1.

Energy [keV]	I_γ ENSDF	I_γ DTAS	I_γ DTAS*
601.05	0.048	0.062	0.049
986.2	0.0046	0.009	0.008
1218	0.128	0.071	0.127
1220.07	0.035	0.067	0.045
1302.73	0.04937	0.039	0.047
1512.16	0.0124	0.017	0.011
1534.32	0.0324	0.021	0.033
1668.13	0.005	0.003	0.003
1715.55	0.00518	0.006	0.004
1752.56	0.0018	0.011	0.007
1766.17	0.01586	0.006	0.006
1796.08	0.01003	0.006	0.004
1808.75	0.0079	0.004	0.005
1820.56	0.0023	0.008	0.005
1841.49	0.0008	0.005	0.004
1849.69	0.0095	0.013	0.010
1873.13	0.0184	0.010	0.006
1879.26	0.00492	0.004	0.004
1898.34	0.00078	0.001	0.000
1926.44	0.0015	0.004	0.002
1936.05	0.0106	0.000	0.003
1991.18	0.0117	0.004	0.008
1997.06	0.0109	0.007	0.004

Continues on the next page.

Energy [keV]	I_γ ENSDF	I_γ DTAS	I_γ DTAS*
2010.8	0.0015	0.004	0.006
2013.05	0.0012	0.008	0.005
2029.86	0.0205	0.006	0.007
2087.97	0.0026	0.008	0.003
2089.67	0.00217	0.003	0.001
2099.97	0.0086	0.003	0.003
2113.99	0.0011	0.003	0.002
2144.32	0.00194	0.004	0.002
2147	0.0027	0.003	0.002
2155.11	0.00442	0.004	0.002
2191.19	0.0038	0.001	0.001
2196.15	0.0034	0.002	0.002
2229.97	0.001	0.004	0.002
2237.76	0.0016	0.008	0.008
2244.09	0.0228	0.012	0.021
2281.59	0.0012	0.011	0.008
2345.65	0.00353	0.000	0.000
2356.28	0.0042	0.003	0.003
2368.32	0.00285	0.007	0.004
2380.3	0.00092	0.004	0.003
2422.7	0.0021	0.003	0.003
2444.01	0.0024	0.002	0.001
2474.84	0.00189	0.002	0.001
2566.93	0.00092	0.001	0.001
2571.09	0.0014	0.002	0.001
2629.7	0.00853	0.000	0.000
2671.59	0.0034	0.003	0.003
2676.3	0.00269	0.001	0.000
2726.14	0.00096	0.001	0.001

Table 13.3: Absolute γ-intensities de-exciting the main levels populated in the decay of ^{137}I (per 100 decays). The second column corresponds to the intensities obtained from high resolution data [242]. The third column gives the intensities obtained with DTAS for the reference analysis, whereas the intensities obtained with a modified branching ratio matrix are presented in the fourth column (DTAS*).

The quality of the fits obtained for CUT1 with the β-gated spectrum, the singles spectrum and the β-gated spectrum with γ-neutron discrimination is presented in Figure 13.10. A comparison of the β-intensities is shown in Figure 13.11.

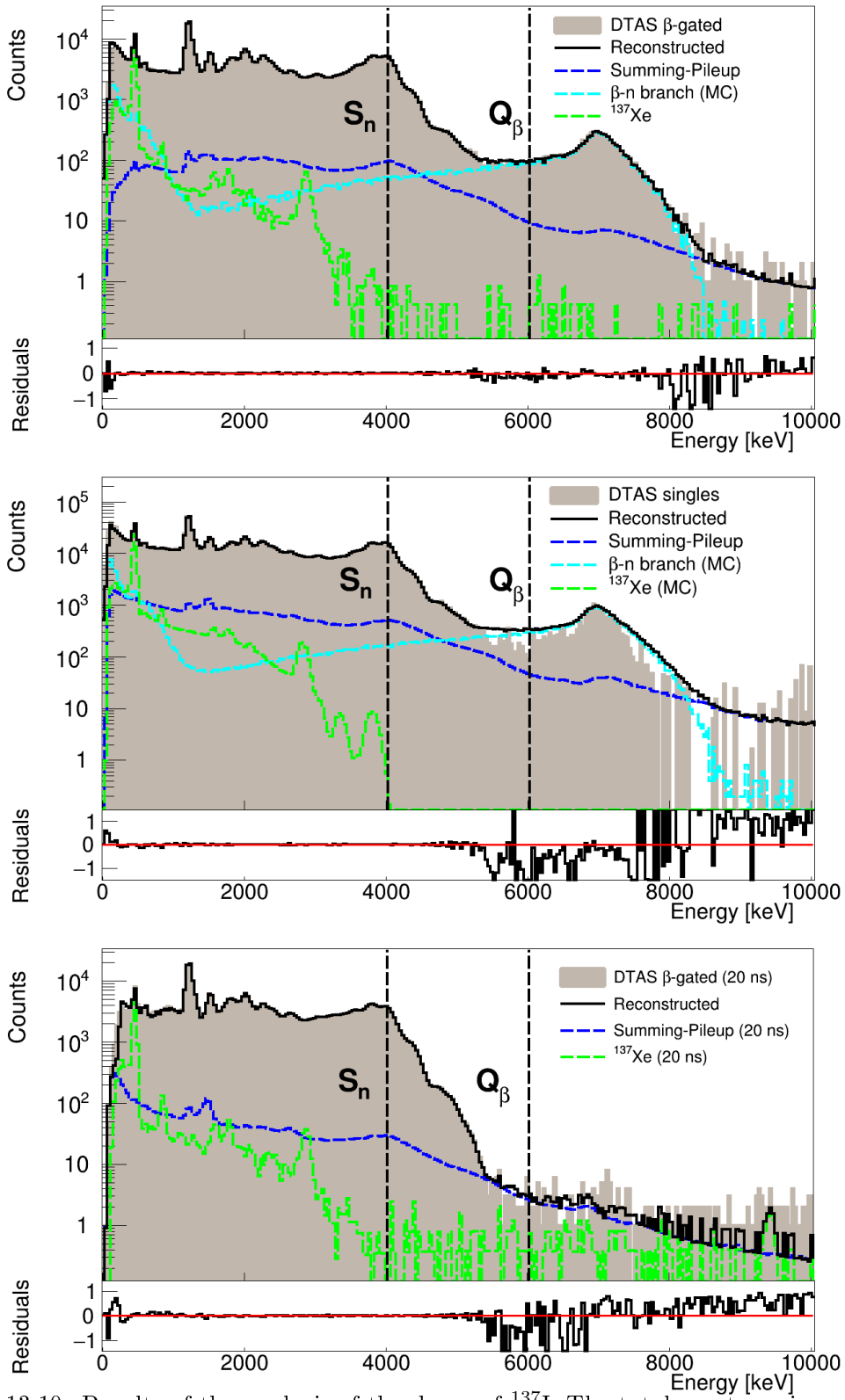

Figure 13.10: Results of the analysis of the decay of ^{137}I. The total spectrum is compared with the reconstructed one after the analysis for the β-gated spectrum (top), the singles spectrum (middle) and the β-gated spectrum with a 20 ns window in the individual TAC spectra (bottom).

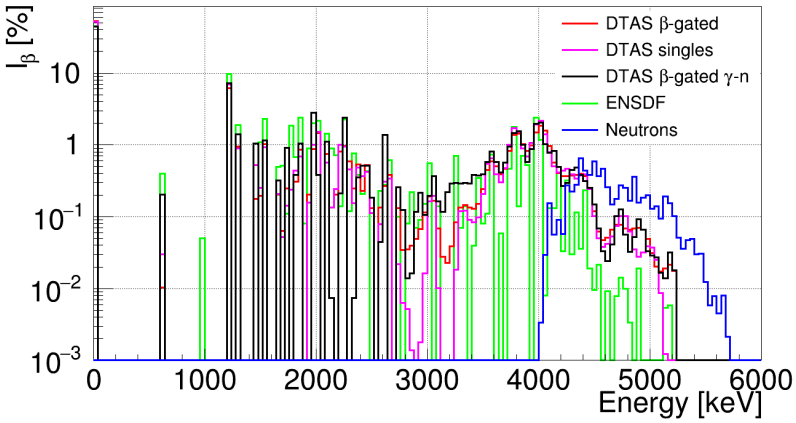

Figure 13.11: Comparison of the β-intensities obtained for the decay of ^{137}I for the β-gated spectrum, the singles spectrum and the β-gated with γ-neutron discrimination.

The evaluation of systematic errors in the β-intensities was done only for the analysis of the β-gated spectrum including the β-delayed neutron contamination. The reference analysis corresponds to CUT1 with $a(S_n)$ =12.3 MeV^{-1} and the new correction parameters for the level density in Table 13.2. As in previous cases, the normalization factors of the parameters were changed until the fit was no longer considered acceptable. The summing-pileup was changed by a factor of 30%, the daughter contribution was changed by 10%, and the neutron contribution was normalized according to other P_n values (7.14% and 7.76%, instead of 7.33%). Moreover, three possible $a(S_n)$ parameters were used (B. Fogelberg *et al.* [245], EGSM and TALYS) to calculate the $E1$ γ-strength function, and both sets of corrections for the level densities were also considered. The original branching ratio matrix and the modified one reproducing better the γ-intensities were considered. The first bin included in the analysis was also varied by ± 1 in order to see the effect on the ground state feeding intensity determination. Finally, a branching ratio matrix and response function were calculated assuming a spin-parity of $7/2^-$ for the ground state in the parent (a value of $(7/2^+)$ is given in ENSDF based on systematics [242]). Allowed and first forbidden transitions were taken into account, and the fit was comparable to that obtained with spin-parity $7/2^+$. Similarly, spin-parity $5/2^-$ was also tried and gave a reasonable fit, but $5/2^+$ did not reproduce the spectrum. As a result, the uncertainty in the β-intensity distribution shown in Figure 13.12 and listed in Table 13.4 was obtained, where a comparison with ENSDF values [242] is made. The β-intensity distribution is normalized to 100%-P_n (ENSDF uses $P_n = 7.1\%$ [242]). Note that above the last level of the known level scheme used for the analysis, the values from the bibliography listed in Table 13.4 correspond to integral values over our energy bins.

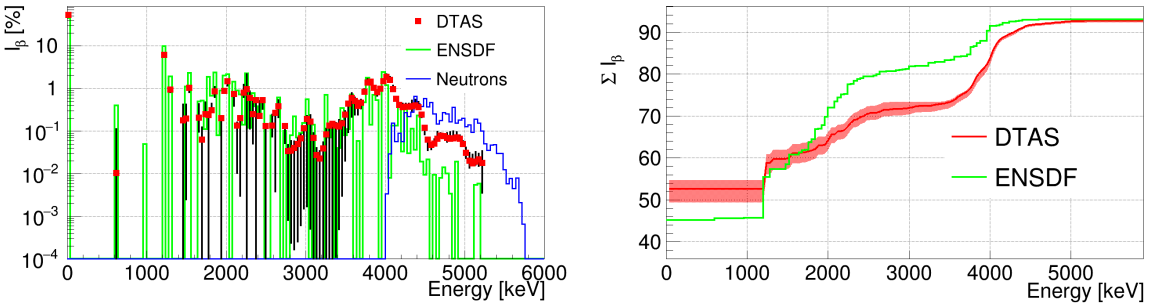

Figure 13.12: β-intensities for the decay of ^{137}I with error bars coming from the uncertainty of all the sources of error investigated.

Energy [keV]	I_β ENSDF [%]	I_β DTAS [%]
0.000	45.2(5)	$52.557^{+2.182}_{-3.204}$
601.050	<0.4	$0.010^{+0.100}_{-0.010}$
986.200	<0.05	-
1218.000	8.900	$3.233^{+2.865}_{-0.340}$
1220.070	0.900	$2.930^{+0.228}_{-2.930}$
1302.730	1.900	$0.947^{+0.138}_{-0.130}$
1461.280	-	$0.177^{+0.242}_{-0.177}$
1512.160	1.100	$0.197^{+0.221}_{-0.195}$
1534.320	2.300	$1.022^{+0.151}_{-0.209}$
1621.100	-	-
1668.130	0.500	$0.205^{+0.221}_{-0.109}$
1715.550	0.520	$0.063^{+0.059}_{-0.063}$
1752.560	0.110	$0.246^{+0.222}_{-0.017}$
1766.170	0.860	$0.089^{+0.057}_{-0.089}$
1796.080	1.000	$0.147^{+0.010}_{-0.147}$
1808.750	0.450	$0.144^{+0.039}_{-0.005}$
1820.560	0.230	$0.164^{+0.132}_{-0.007}$
1841.490	≈0.080	$0.220^{+0.056}_{-0.220}$
1849.690	0.490	$0.145^{+0.063}_{-0.142}$
1873.130	1.330	$0.142^{+0.097}_{-0.054}$
1879.260	0.490	$0.345^{+0.419}_{-0.021}$
1898.300	0.080	-
1926.400	0.150	-
1935.200	-	-
1936.250	0.750	$0.201^{+0.011}_{-0.201}$
1991.180	0.940	$0.542^{+0.130}_{-0.179}$
1997.060	1.080	$0.341^{+0.160}_{-0.021}$
2010.800	0.150	$0.356^{+0.263}_{-0.347}$
2013.100	0.120	$0.423^{+0.172}_{-0.423}$

Continues on the next page.

Energy [keV]	I_β ENSDF [%]	I_β DTAS [%]
2029.800	1.900	$0.691^{+0.208}_{-0.159}$
2088.000	1.450	$0.212^{+0.021}_{-0.183}$
2089.670	0.220	$0.094^{+0.017}_{-0.094}$
2099.970	0.860	$0.229^{+0.021}_{-0.134}$
2114.000	1.450	$0.209^{+0.476}_{-0.171}$
2144.320	0.190	$0.044^{+0.017}_{-0.044}$
2147.000	0.270	$0.048^{+0.004}_{-0.048}$
2155.110	0.440	$0.041^{+0.030}_{-0.041}$
2191.190	0.380	$0.050^{+0.026}_{-0.049}$
2196.150	0.340	$0.153^{+0.010}_{-0.153}$
2204.000	-	-
2229.970	0.100	$0.101^{+0.095}_{-0.089}$
2237.760	0.040	$0.701^{+0.351}_{-0.091}$
2244.090	2.280	$0.968^{+1.176}_{-0.968}$
2281.590	0.120	$0.595^{+0.252}_{-0.483}$
2345.650	0.350	-
2356.280	0.420	$0.246^{+0.030}_{-0.196}$
2368.320	0.290	$0.299^{+0.045}_{-0.299}$
2380.300	0.090	$0.238^{+0.277}_{-0.238}$
2422.700	0.210	$0.227^{+0.278}_{-0.023}$
2444.000	0.240	$0.198^{+0.077}_{-0.198}$
2452.400	0.430	$0.174^{+0.047}_{-0.174}$
2474.840	0.190	$0.155^{+0.158}_{-0.044}$
2490.380	-	$0.131^{+0.017}_{-0.131}$
2566.900	0.090	$0.133^{+0.107}_{-0.084}$
2571.090	0.140	-
2608.800	0.280	$0.267^{+0.017}_{-0.263}$
2629.700	0.280	-
2671.590	0.340	$0.309^{+0.220}_{-0.154}$
2676.300	0.270	$0.075^{+0.016}_{-0.075}$
2726.140	0.100	$0.090^{+0.017}_{-0.043}$
2740.000	0.100	$0.040^{+0.009}_{-0.035}$
2780.000	-	$0.034^{+0.013}_{-0.033}$
2820.000	0.080	$0.035^{+0.024}_{-0.035}$
2860.000	0.220	$0.040^{+0.018}_{-0.039}$
2900.000	0.070	$0.049^{+0.018}_{-0.049}$
2940.000	0.090	$0.067^{+0.016}_{-0.067}$
2980.000	0.153	$0.116^{+0.013}_{-0.114}$
3020.000	0.560	$0.192^{+0.033}_{-0.190}$
3060.000	-	$0.166^{+0.073}_{-0.166}$
3100.000	0.140	$0.068^{+0.020}_{-0.068}$

Continues on the next page.

Energy [keV]	I_β ENSDF [%]	I_β DTAS [%]
3140.000	-	$0.028^{+0.013}_{-0.028}$
3180.000	-	$0.023^{+0.012}_{-0.023}$
3220.000	-	$0.039^{+0.016}_{-0.039}$
3260.000	0.700	$0.084^{+0.031}_{-0.084}$
3300.000	0.070	$0.134^{+0.019}_{-0.134}$
3340.000	0.140	$0.147^{+0.019}_{-0.147}$
3380.000	-	$0.135^{+0.021}_{-0.135}$
3420.000	0.040	$0.129^{+0.055}_{-0.128}$
3460.000	0.350	$0.152^{+0.024}_{-0.149}$
3500.000	0.080	$0.245^{+0.052}_{-0.225}$
3540.000	0.060	$0.443^{+0.052}_{-0.348}$
3580.000	0.730	$0.593^{+0.189}_{-0.380}$
3620.000	-	$0.501^{+0.107}_{-0.260}$
3660.000	0.059	$0.388^{+0.027}_{-0.147}$
3700.000	-	$0.461^{+0.080}_{-0.125}$
3740.000	0.470	$0.827^{+0.139}_{-0.105}$
3780.000	1.790	$1.380^{+0.272}_{-0.144}$
3820.000	0.140	$1.426^{+0.212}_{-0.131}$
3860.000	0.710	$1.025^{+0.075}_{-0.080}$
3900.000	0.530	$0.820^{+0.059}_{-0.144}$
3940.000	-	$0.992^{+0.072}_{-0.048}$
3980.000	2.420	$1.483^{+0.219}_{-0.040}$
4020.000	1.181	$1.850^{+0.301}_{-0.049}$
4060.000	0.008	$1.566^{+0.312}_{-0.077}$
4100.000	0.133	$0.970^{+0.182}_{-0.080}$
4140.000	0.069	$0.572^{+0.068}_{-0.050}$
4180.000	0.407	$0.405^{+0.032}_{-0.028}$
4220.000	0.033	$0.364^{+0.080}_{-0.016}$
4260.000	0.009	$0.370^{+0.071}_{-0.012}$
4300.000	0.030	$0.376^{+0.061}_{-0.024}$
4340.000	0.114	$0.381^{+0.132}_{-0.079}$
4380.000	0.036	$0.398^{+0.150}_{-0.011}$
4420.000	0.005	$0.368^{+0.119}_{-0.023}$
4460.000	0.019	$0.243^{+0.033}_{-0.034}$
4500.000	0.010	$0.120^{+0.005}_{-0.036}$
4540.000	0.021	$0.062^{+0.003}_{-0.027}$
4580.000	-	$0.047^{+0.004}_{-0.010}$
4620.000	0.009	$0.051^{+0.014}_{-0.000}$
4660.000	-	$0.066^{+0.030}_{0.000}$
4700.000	0.008	$0.077^{+0.013}_{-0.002}$
4740.000	0.014	$0.077^{+0.010}_{-0.010}$

Continues on the next page.

Energy [keV]	I_β ENSDF [%]	I_β DTAS [%]
4780.000	0.010	$0.069^{+0.021}_{-0.014}$
4820.000	0.003	$0.066^{+0.028}_{-0.004}$
4860.000	-	$0.068^{+0.029}_{-0.001}$
4900.000	0.019	$0.071^{+0.023}_{-0.001}$
4940.000	-	$0.065^{+0.014}_{-0.005}$
4980.000	-	$0.049^{+0.009}_{-0.006}$
5020.000	-	$0.031^{+0.010}_{-0.008}$
5060.000	-	$0.020^{+0.010}_{-0.006}$
5100.000	-	$0.017^{+0.010}_{-0.002}$
5140.000	0.005	$0.019^{+0.013}_{-0.003}$
5180.000	0.006	$0.022^{+0.008}_{-0.007}$
5220.000	-	$0.018^{+0.016}_{-0.014}$

Table 13.4: I_β intensities for the decay of ^{137}I.

The ground state feeding intensity was also calculated by means of the β-γ counting method of Appendix D, and $I_{g.s.}$ =52.5(7)% was obtained, very similar to the value from the analysis. These two values are larger than the quoted number at ENSDF. It is also worth mentioning that B. Fogelberg *et al.* [243] reported a β-intensity of 47% to the ground state.

The reproduction of the spectra for different multiplicities is shown in Figure 13.13 for the reference analysis. The agreement is quite reasonable for all of them. Some problems in the reproduction for $M_m = 1$ are found. However, any of the possible changes in the response function investigated for the evaluation of errors worsened the spectrum for $M_m = 1$. Furthermore, CUT2 and CUT3 were unable to reproduce part of the structure in the spectrum for $M_m = 1$.

Finally, the reproduction of the individual modules has also been studied, as presented in Figure 13.14, and the MC simulation based on the analysis agrees with the experimental spectra.

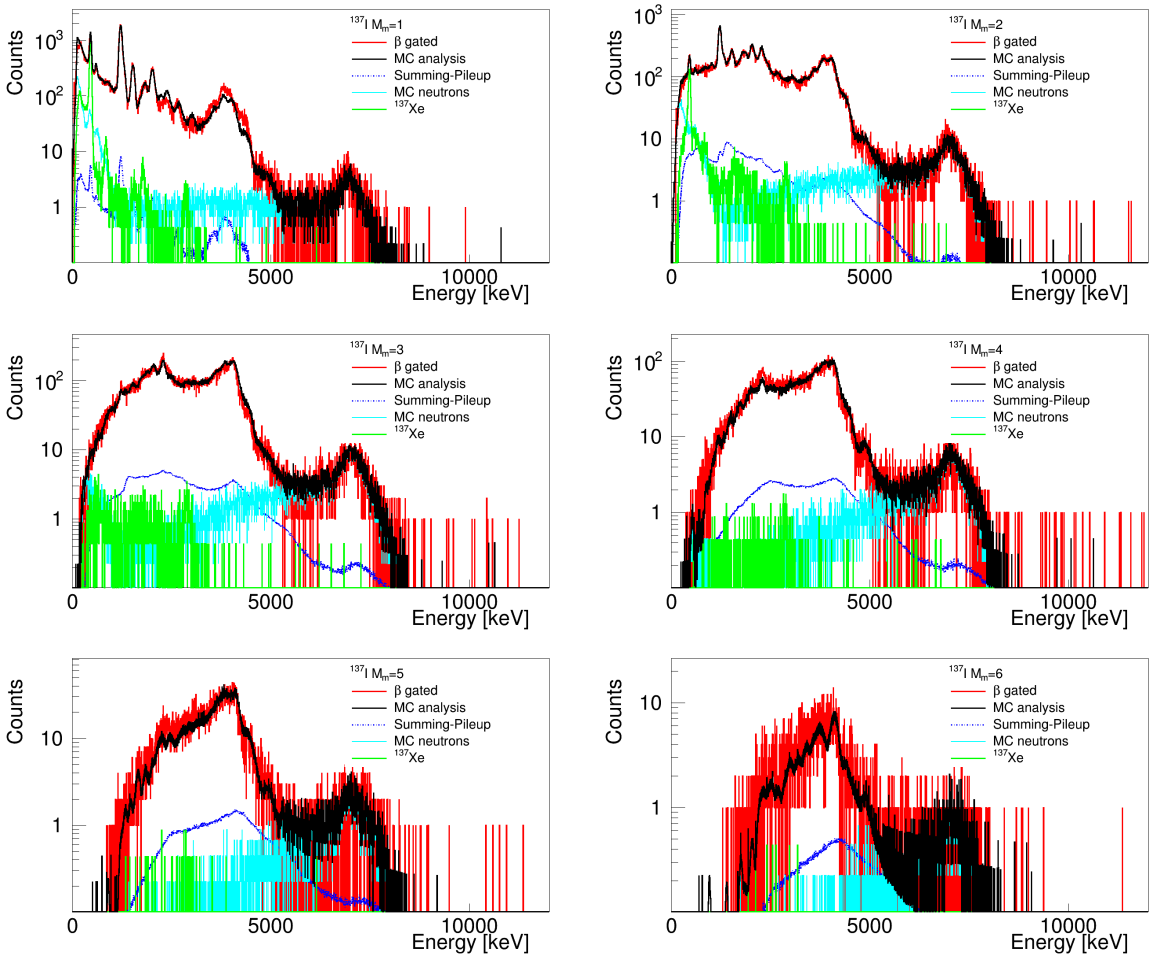

Figure 13.13: Experimental spectra for different multiplicities for the decay of ^{137}I compared with the MC simulation performed with an event generator for multiplicities from 1 to 6.

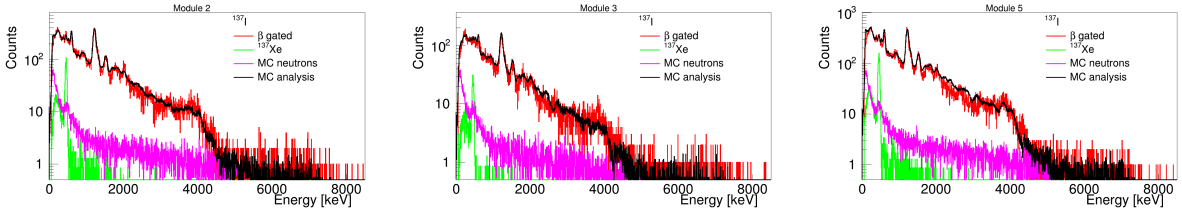

Figure 13.14: ^{137}I experimental spectra for the three geometrically distinguishable individual crystals compared with the MC.

Chapter 14

^{95}Rb decay

Lo que hoy está probado, ayer apenas era un sueño

What is now proved was once only imagined

William Blake

In this chapter the β-decay of ^{95}Rb into ^{95}Sr is reported. This fission fragment contributes to both reactor decay heat and the reactor antineutrino spectrum. It is also important from the point of view of β-delayed neutron emission, as the case of ^{137}I explained in Chapter 14, since Q_β=9.228 MeV and ^{95}Sr has S_n=4.348 MeV. The experimental measurements were described in Chapter 6, and here the TAGS analysis and the results will be presented.

14.1 Experimental spectra

14.1.1 β-gated spectrum

The resulting singles and β-gated spectra for the sum of all the experimental runs (runs 139-144, 146-147, 150-152, 154-157, 180-182, 242-245) are presented in Figure 14.1 left. In Figure 14.1 right, the gate in the TAC between DTAS and the plastic detector is marked in green.

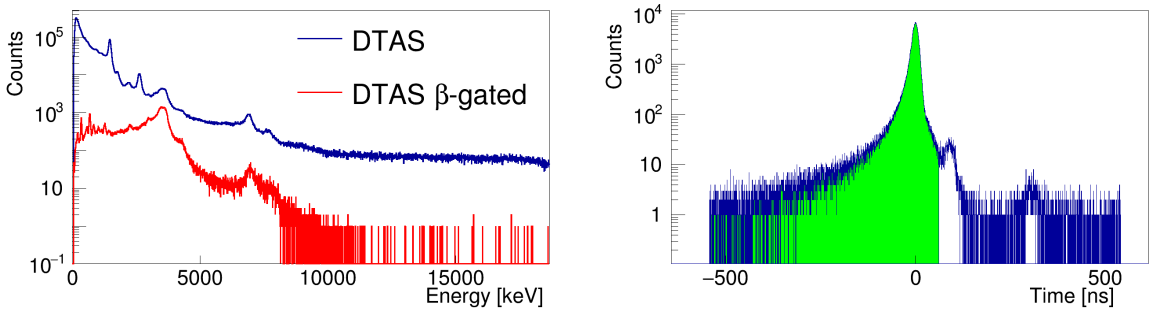

Figure 14.1: Comparison between the β-gated spectrum and the singles spectrum of DTAS for the decay of ^{95}Rb (left). The TAC spectrum between DTAS-β plastic detector for the measurement of the decay of ^{95}Rb (right).

14.1.2 γ-neutron discrimination

Similarly to the decay of ^{137}I, a narrow gate of 20 ns has been selected in all individual TAC spectra before reconstructing the software sum, in order to select prompt γ interactions (see Figure 14.2).

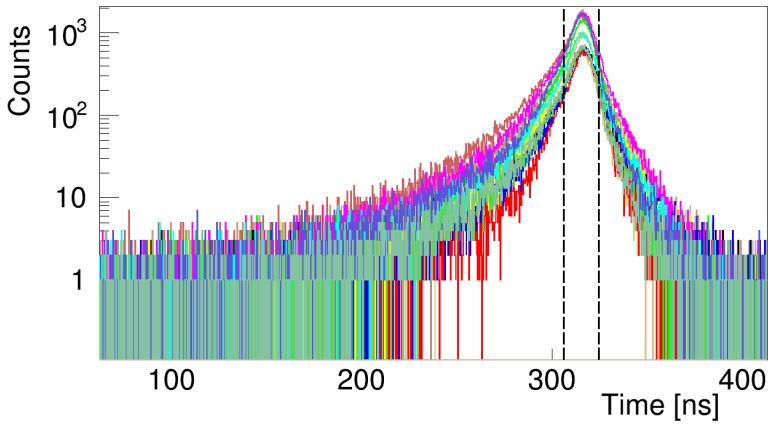

Figure 14.2: Aligned TAC spectra between each module of DTAS and the plastic detector for the decay of ^{95}Rb, where a narrow gate (20 ns) to select prompt γ-rays is shown by the vertical dashed lines.

The comparison of the resulting spectra with the narrow gate in the individual TAC spectra, with a gate in the full range, and with a gate only in the tails of the TAC spectra is shown in Figure 14.3.

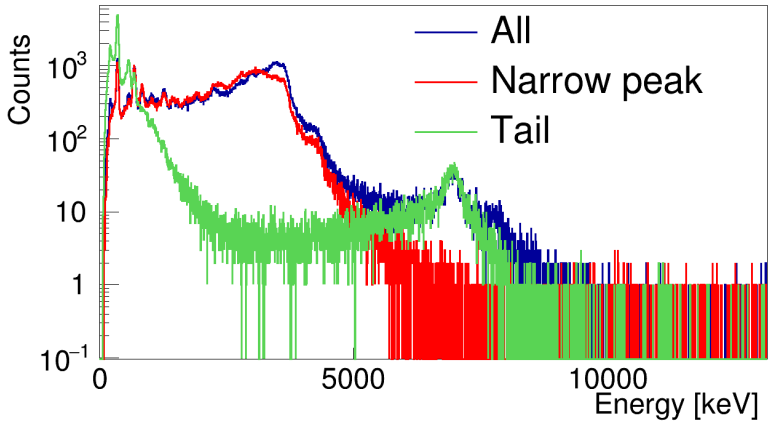

Figure 14.3: Spectra from different gates on the TACs of the individual modules for the decay of ^{95}Rb.

As in the case of ^{137}I, the threshold is increased with the narrow gate, and low energy signals are cut. In this case the distortion of the spectrum is larger, when compared with the β-gated spectrum with neutrons, showing the limitations of this procedure with poor timing resolution. Moreover, in this case, β-delayed neutrons are not populating only the ground state in ^{94}Sr, but also excited states. Due to the de-excitation by means of γ-rays of these excited states, γ-rays are also emitted in the β-delayed neutron branch, which

constitutes a prompt component that is not rejected with the gate in the TACs. In the next subsection details of the calculation of the β-delayed neutron contribution with MC simulations will be given.

14.1.3 Contaminants

In this case, the decay of the daughter, ^{95}Sr, and also the granddaughter, ^{95}Y, with $T_{1/2}$ =10.3 m, are contaminants in the measurement. The normalization of their activities is calculated with the Bateman equation assuming a constant implantation rate as in Appendix B. The cycle is shown in Figure 14.4, and contaminant fractions of 3.13% and 0.38% are obtained for the daughter and the granddaughter respectively. These two contaminants have been measured experimentally, and a contamination of 3.96% of ^{95}Y in ^{95}Sr is also taken into account before subtracting them from ^{95}Rb. The contaminants are shown in Figure 14.7 normalized by these factors after the subtraction of their corresponding summing-pileup contributions (evaluated and normalized as in all previous cases). The summing-pileup evaluation for ^{95}Rb is also shown in Figure 14.7. In the analysis of the β-gated spectrum with a narrow gate of 20 ns in the TAC spectra of the individual modules, the same gate has been applied for all the contaminants.

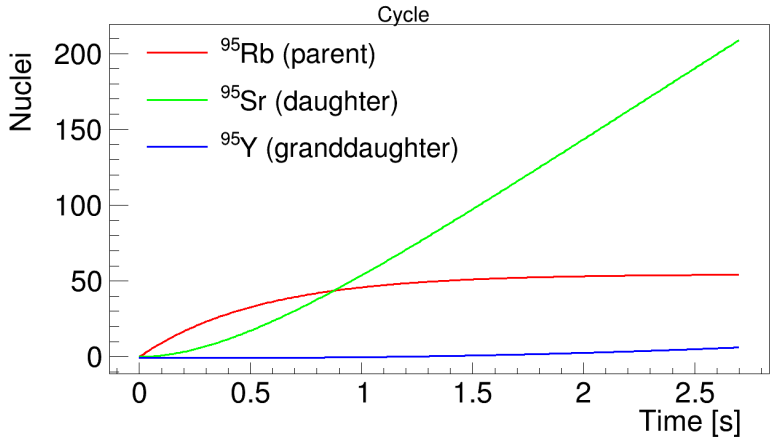

Figure 14.4: Cycle of implantation of ^{95}Rb on the tape. The number of parent, daughter and granddaughter nuclei is represented as a function of time during the cycle.

The β-delayed neutron branch contamination (β-n branch) has been simulated with Geant4 and the special event generator according to the details given in Chapter 5 Section 5.2.6. The neutron spectrum was obtained from ENDF/B-VII.0, coming from [184] and completed at high energies with QRPA and Hauser-Feshbach theoretical calculations [246]. It is shown in Figure14.5.

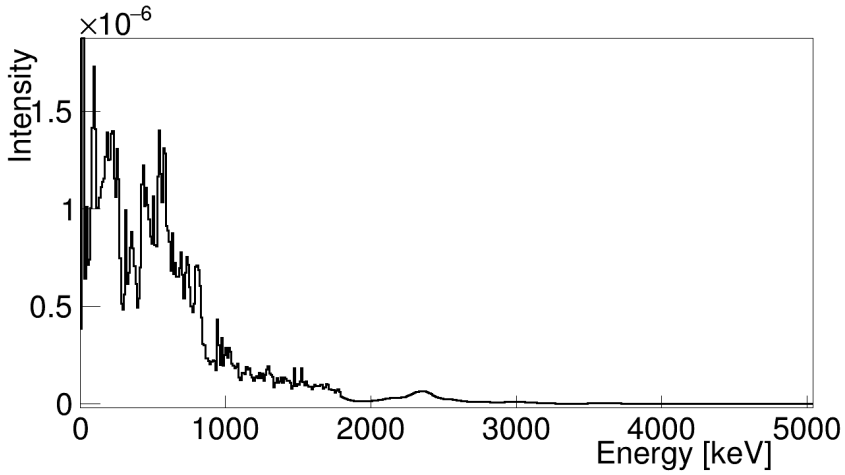

Figure 14.5: Spectrum of the β-delayed neutrons of the decay of ^{95}Rb.

There are several measurements concerning the neutron branching I_n to the different levels in ^{94}Sr [247–249]. The reference values available at ENSDF come from the thesis of H. Gabelmann [249]. However, we have observed that our experimental spectrum is clearly more compatible with the intensities coming from the previous experiment of K.-L. Kratz *et al.* [247], as shown in Figure 14.6. The two sets of I_n values studied are listed in Table 14.6. In [247] it is mentioned that $\leq$2% intensity is expected above 2.650 MeV.

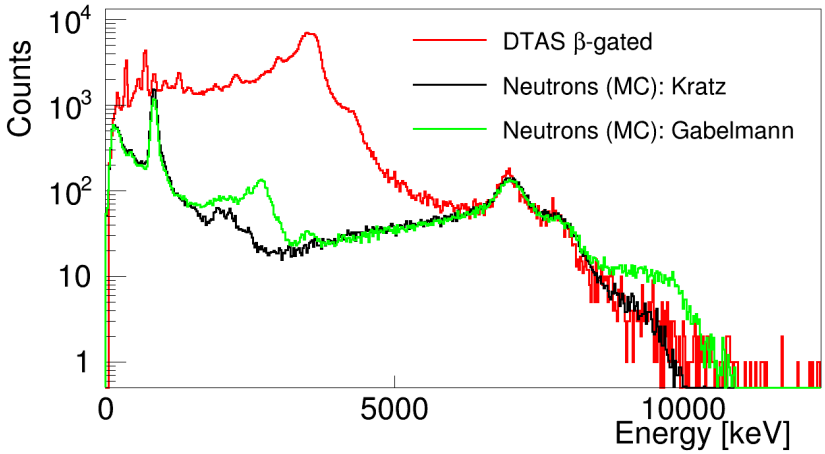

Figure 14.6: Comparison of the effect of the two I_n distribution discussed in the text for the simulation of the β-delayed neutron branch in ^{95}Rb with DTAS. The MC spectra are normalized to the experimental β-gated TAGS spectrum of the decay of ^{95}Rb.

Energy [MeV]	I_n ENSDF [%]	I_n Kratz [247] [%]
0.000	0.676	0.665
0.837	0.209	0.288
1.927	0.005	0.013
2.146	0.005	0.012
2.415	0.020	0.009
2.604	0.019	0.007
2.614	0.013	0.003
2.650	0.010	0.002
2.703	0.013	0.000
2.711	0.008	0.000
2.740	0.009	0.000
2.930	0.009	0.000
3.439	0.010	0.000

Table 14.1: β-delayed neutron intensities for the decay of ^{95}Rb to ^{94}Sr.

A time window for energy deposition of 1 μs between the plastic detector and the DTAS was needed in this case in order to normalize the β-delayed neutron branch contamination using the evaluated value P_n=8.87% [241] with Equation (13.1) (a slightly different value of 8.7% is quoted in ENSDF [250]). In this case the β-gated detection efficiency calculated from the MC simulation, ε_n, is 21.5%. For the case of the β-gated spectrum with a narrow window (20 ns) in the individual TAC spectra, we used a time window of 20 ns also in the simulation to evaluate the contribution of the prompt γ-rays of the β-delayed branch. The normalization in this case is done by looking at the clear peak of 837 keV. In Figure 14.7 the MC simulation of the β-delayed branch is presented together with the rest of contaminants.

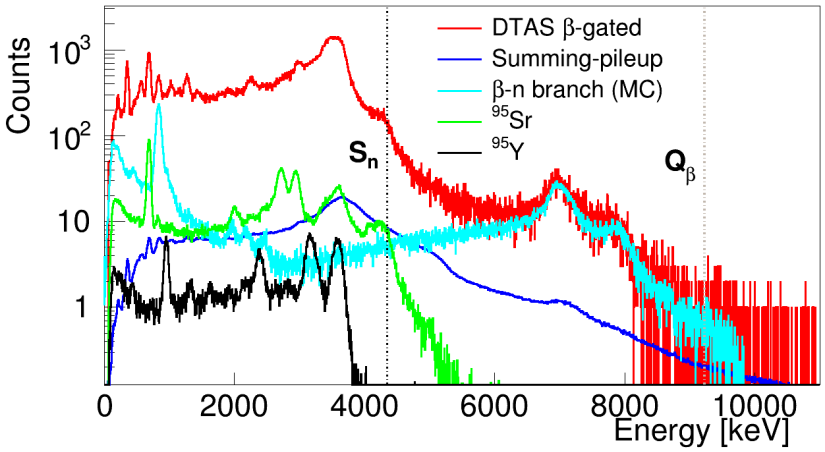

(a)

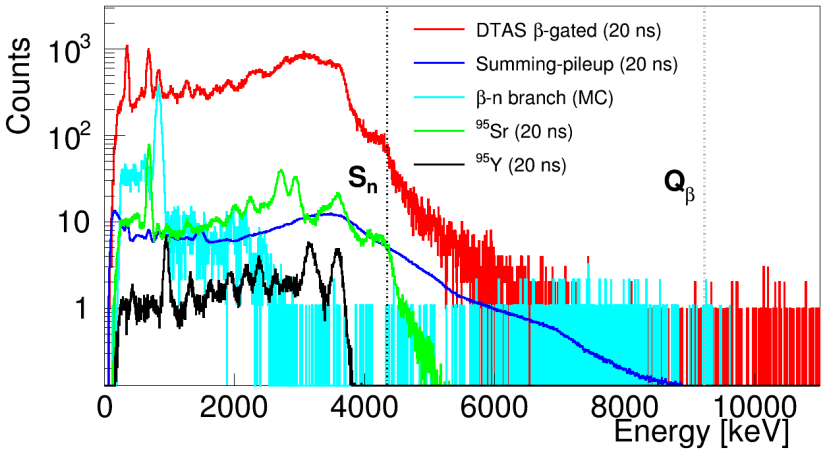

(b)

Figure 14.7: Relevant histograms for the analysis of the decay of ^{95}Rb: (a) β-gated spectra, (b) β-gated spectra with the narrow gate (20 ns).

14.2 Branching ratio matrix

According to RIPL-3 the level scheme of ^{95}Sr is complete up to 1259.7 keV in excitation energy (10 levels). We take these ten levels as the known part of the level scheme for our analysis. For those levels with no spin-parity assignment, we used the values assigned by RIPL-3, as summarized in Table 14.2.

Energy [keV]	J^P ENSDF	J^P used
352.02	$(3/2)^+$	$3/2^+$
556.08	$(7/2)^+$	$7/2^+$
680.70	$3/2^+$, $5/2^+$	$5/2^+$
1003.70	$1/2^+$, 3/2, 5/2	$1/2^+$
1012.25	$1/2^+$, $3/2^+$, $5/2^+$	$3/2^+$
1121.01	$3/2^+$, $5/2^+$, $7/2^+$	$3/2^+$
1238.80	$(9/2^+)$	$9/2^+$
1247.24	1/2, 3/2, 5/2	$5/2^-$
1259.66	$1/2^+$, 3/2, 5/2	$3/2^+$

Table 14.2: Levels with uncertain spin-parity assignments for ENSDF in ^{95}Sr and our choice of spin-parities for levels up to 1259.66 keV.

The level density data from HFB+c calculations [149, 212] available at RIPL-3 [145] are used (see Figure 14.8). The correction parameters for the level density distribution are shown in Table 14.3. Apart from the original values a new set of C and P parameters, giving a better reproduction of the number of levels at low energies, is included. In this case, there is no experimental information from neutron resonances to verify the level density at high energies.

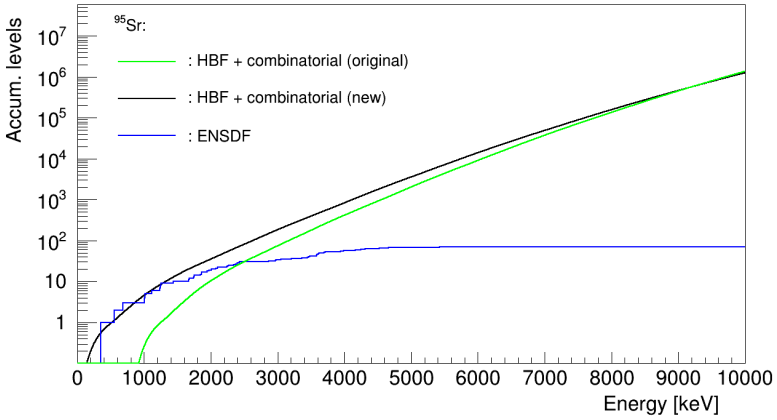

Figure 14.8: Accumulated number of levels in ^{95}Sr as a function of excitation energy. The blue line is obtained from ENSDF and the green line corresponds to the Hartree-Fock-Bogoliubov calculation downloaded from RIPL-3 with the original correction parameters, whereas the black one corresponds to new correction parameters that match better the experimental level density at low energies.

C	P
0.0	0.78795
-0.3	0.0

Table 14.3: Correction factors C and P for HFB+c level density distribution for ^{95}Sr. Original values (first row) and improved values (second row) are presented.

Regarding the rest of the parameters involved in the branching ratio matrix and response function calculation, especially the γ-strength function parameters, they are presented in Table 2.1.

14.3 Analysis and results

For the analysis, allowed transitions (to levels $3/2^-$, $5/2^-$ and $7/2^-$), and first forbidden transition (to levels $1/2^+$, $3/2^+$, $5/2^+$, $7/2^+$ and $9/2^+$) are considered from the $5/2^-$ ground state of ^{95}Rb.

It was clearly observed that the original correction parameters for the level density reproduced the experimental spectrum better, and they have been used throughout. The quality of the fit is shown in Figure 14.9.

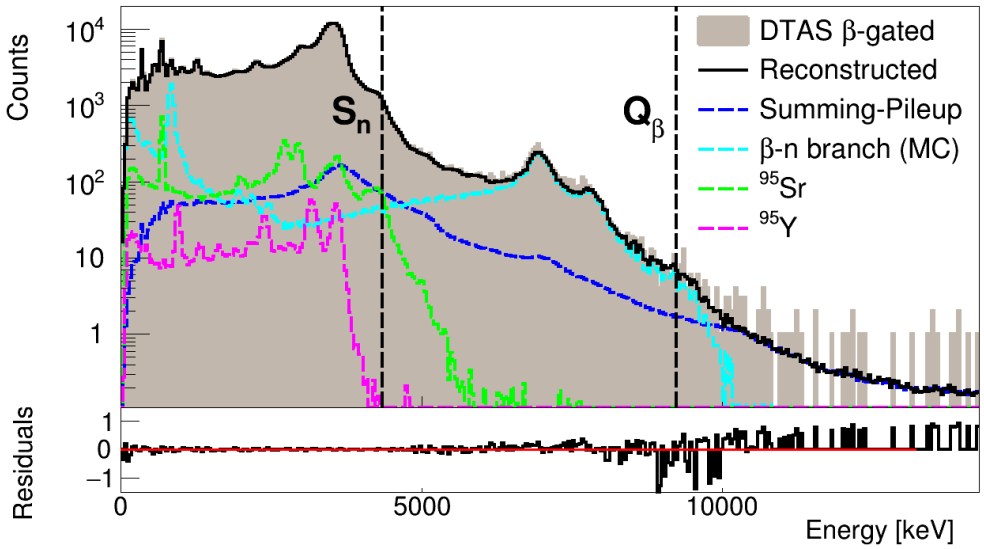

Figure 14.9: Result of the analysis of the decay of ^{95}Rb. The β-gated spectrum is compared with the reconstructed one after the analysis.

Moreover, the reproduction of the γ-intensities was investigated, as presented in Table 14.4, where the experimental values from high resolution measurements [251] are compared with the values obtained from the TAGS analysis. A modified branching ratio matrix was able to reproduce better the γ-intensities from high resolution measurements (see Table 14.4), although it gave a worse fit of the total spectrum.

Energy [keV]	I_γ ENSDF	I_γ DTAS	I_γ DTAS*
352.01	0.490	0.658	0.490
556.06	0.151	0.253	0.153
680.7	0.244	0.263	0.241
1003.7	0.025	0.028	0.048
1012.25	0.058	0.070	0.121
1121.01	0.074	0.062	0.102
1238.91	0.017	0.047	0.076
1247.24	0.006	0.015	0.028
1259.65	0.079	0.054	0.083

Table 14.4: Absolute γ-intensities de-exciting the main levels populated in the decay of ^{95}Rb (per 100 decays). The second column corresponds to the intensities obtained from high resolution data [250]. The third column gives the intensities obtained with DTAS for the reference analysis, whereas the intensities obtained with a modified branching ratio matrix are presented in the fourth column (DTAS*).

The systematic error due to the normalization factor of contaminants was investigated in the usual fashion. Due to the large contribution of the contamination of the β-delayed neutron branch at high energies, the summing-pileup normalization could be changed by a factor 100%, and the activities of daughter and granddaughter were changed by a factor 50% without noticing a distortion in the spectrum. The normalization of the neutron contribution was changed by considering the error in P_n=8.87(29)% [241]. The impact of both sets of correction factors for the level density, as well as the modified branching ratio matrix that reproduces the γ-intensities were also taken into account. Finally, as usual, the ME deconvolution method was used instead of EM to check the impact on the β-intensity distribution. All these effects were combined to give the quoted systematic uncertainty. In Figure 14.10, the β-intensity distribution obtained is compared with the values from ENSDF [250], and the corresponding numbers with errors are listed in Table 14.5. The β-intensity distribution obtained with DTAS is normalized to 100%-P_n, whereas the intensities from ENSDF are normalized to 77.941% [250] due to the lack of experimental information. Note that above the last level of the known level scheme used in the analysis, the values from the bibliography listed in Table 14.5 correspond to integral values over our energy bins.

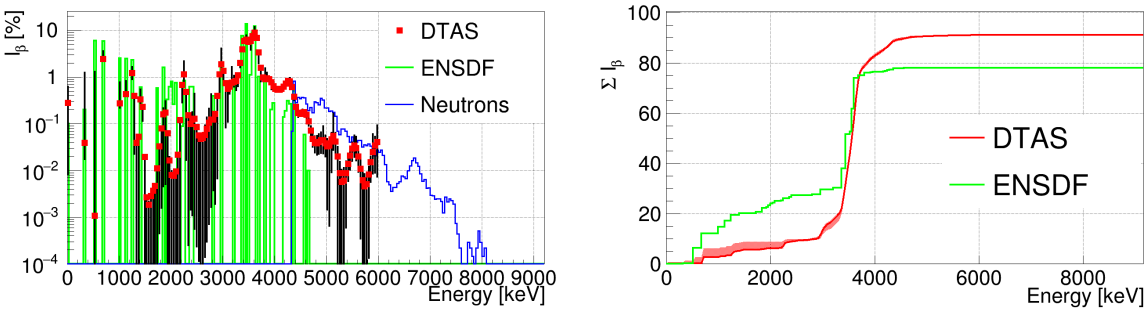

Figure 14.10: β-intensities for the decay of ^{95}Rb with error bars coming from the uncertainty of all the sources of error.

Energy [keV]	I_β ENSDF [%]	I_β DTAS [%]
0.000	$\leq$0.1	$0.276^{+0.343}_{-0.268}$
352.020	$\leq$0.2	$0.039^{+1.207}_{-0.021}$
556.080	6.000(12)	$0.001^{+1.303}_{-0.001}$
680.700	5.900(16)	$2.401^{+1.141}_{-0.211}$
1003.700	0.740(24)	$0.077^{+0.085}_{-0.056}$
1012.250	1.800(5)	$0.193^{+0.418}_{-0.046}$
1121.010	2.500(6)	$0.427^{+0.393}_{-0.016}$
1238.800	-	-
1247.240	2.300(12)	$0.455^{+0.132}_{-0.453}$
1259.660	2.300(12)	$0.761^{+0.870}_{-0.109}$
1300.000	-	$0.391^{+0.012}_{-0.368}$
1340.000	-	$0.039^{+0.001}_{-0.039}$
1380.000	-	$0.052^{+0.001}_{-0.052}$
1420.000	0.600(5)	$0.330^{+0.220}_{-0.116}$
1460.000	-	$0.229^{+0.007}_{-0.114}$
1500.000	-	$0.019^{+0.001}_{-0.019}$
1540.000	-	$0.003^{+0.000}_{-0.003}$
1580.000	-	$0.002^{+0.000}_{-0.002}$
1620.000	-	$0.003^{+0.000}_{-0.003}$
1660.000	-	$0.004^{+0.001}_{-0.004}$
1700.000	-	$0.005^{+0.001}_{-0.005}$
1740.000	0.580(13)	$0.011^{+0.001}_{-0.011}$
1780.000	-	$0.033^{+0.002}_{-0.032}$
1820.000	-	$0.079^{+0.005}_{-0.077}$
1860.000	1.620(46)	$0.159^{+0.055}_{-0.155}$
1900.000	-	$0.171^{+0.134}_{-0.166}$
1940.000	0.330(6)	$0.063^{+0.006}_{-0.063}$
1980.000	0.620(9)	$0.016^{+0.003}_{-0.016}$
2020.000	0.800(10)	$0.008^{+0.002}_{-0.008}$

Continues on the next page.

Energy [keV]	I_β ENSDF [%]	I_β DTAS [%]
2060.000	0.260(7)	$0.008^{+0.001}_{-0.008}$
2100.000	0.750(11)	$0.010^{+0.000}_{-0.010}$
2140.000	-	$0.022^{+0.001}_{-0.022}$
2180.000	-	$0.120^{+0.002}_{-0.120}$
2220.000	0.089(21)	$0.678^{+0.010}_{-0.396}$
2260.000	0.830(22)	$1.126^{+1.029}_{-0.477}$
2300.000	-	$0.479^{+0.013}_{-0.462}$
2340.000	-	$0.151^{+0.006}_{-0.150}$
2380.000	0.620(10)	$0.098^{+0.006}_{-0.097}$
2420.000	0.620(12)	$0.122^{+0.054}_{-0.121}$
2460.000	-	$0.127^{+0.308}_{-0.126}$
2500.000	-	$0.085^{+0.003}_{-0.085}$
2540.000	-	$0.056^{+0.002}_{-0.056}$
2580.000	-	$0.047^{+0.004}_{-0.047}$
2620.000	-	$0.049^{+0.016}_{-0.049}$
2660.000	-	$0.058^{+0.035}_{-0.057}$
2700.000	-	$0.077^{+0.059}_{-0.077}$
2740.000	-	$0.106^{+0.106}_{-0.105}$
2780.000	-	$0.123^{+0.310}_{-0.121}$
2820.000	0.390(7)	$0.122^{+0.021}_{-0.118}$
2860.000	-	$0.162^{+0.018}_{-0.160}$
2900.000	-	$0.391^{+0.045}_{-0.384}$
2940.000	-	$1.145^{+0.115}_{-0.681}$
2980.000	1.980(26)	$1.877^{+2.183}_{-0.619}$
3020.000	-	$1.350^{+0.020}_{-0.618}$
3060.000	-	$0.730^{+0.027}_{-0.648}$
3100.000	-	$0.550^{+0.018}_{-0.440}$
3140.000	-	$0.621^{+0.035}_{-0.186}$
3180.000	-	$0.751^{+0.901}_{-0.191}$
3220.000	0.720(9)	$0.788^{+0.268}_{-0.175}$
3260.000	-	$0.813^{+0.072}_{-0.290}$
3300.000	-	$1.089^{+0.125}_{-0.463}$
3340.000	-	$1.995^{+0.162}_{-0.404}$
3380.000	7.700(12)	$3.894^{+0.210}_{-0.098}$
3420.000	-	$5.890^{+0.613}_{-0.092}$
3460.000	13.580(29)	$6.289^{+1.482}_{-0.100}$
3500.000	-	$5.676^{+0.279}_{-0.276}$
3540.000	1.100(14)	$5.822^{+0.314}_{-2.027}$
3580.000	9.060(38)	$7.411^{+0.423}_{-1.194}$
3620.000	12.240(21)	$8.878^{+2.990}_{-0.120}$
3660.000	-	$6.872^{+0.884}_{-0.085}$

Continues on the next page.

Energy [keV]	I_β ENSDF [%]	I_β DTAS [%]
3700.000	1.010(15)	$3.385^{+0.081}_{-1.422}$
3740.000	-	$1.555^{+0.033}_{-0.748}$
3780.000	-	$0.976^{+0.033}_{-0.029}$
3820.000	0.950(12)	$0.889^{+0.650}_{-0.038}$
3860.000	-	$0.933^{+0.293}_{-0.045}$
3900.000	-	$0.900^{+0.041}_{-0.190}$
3940.000	0.200(5)	$0.763^{+0.032}_{-0.218}$
3980.000	0.280(5)	$0.631^{+0.027}_{-0.064}$
4020.000	-	$0.554^{+0.055}_{-0.026}$
4060.000	-	$0.529^{+0.065}_{-0.026}$
4100.000	-	$0.531^{+0.068}_{-0.025}$
4140.000	-	$0.557^{+0.048}_{-0.023}$
4180.000	0.140(3)	$0.615^{+0.041}_{-0.055}$
4220.000	0.190(4)	$0.714^{+0.047}_{-0.134}$
4260.000	0.309(25)	$0.816^{+0.050}_{-0.032}$
4300.000	0.264(24)	$0.801^{+0.162}_{-0.020}$
4340.000	-	$0.607^{+0.092}_{-0.020}$
4380.000	0.500(6)	$0.376^{+0.021}_{-0.060}$
4420.000	-	$0.230^{+0.019}_{-0.074}$
4460.000	-	$0.170^{+0.018}_{-0.031}$
4500.000	-	$0.160^{+0.023}_{-0.019}$
4540.000	-	$0.172^{+0.029}_{-0.022}$
4580.000	0.059(20)	$0.178^{+0.022}_{-0.024}$
4620.000	-	$0.157^{+0.022}_{-0.024}$
4660.000	0.010(5)	$0.112^{+0.020}_{-0.022}$
4700.000	-	$0.070^{+0.017}_{-0.018}$
4740.000	-	$0.047^{+0.015}_{-0.015}$
4780.000	-	$0.039^{+0.015}_{-0.015}$
4820.000	-	$0.038^{+0.016}_{-0.016}$
4860.000	-	$0.041^{+0.019}_{-0.018}$
4900.000	-	$0.044^{+0.020}_{-0.021}$
4940.000	-	$0.044^{+0.045}_{-0.021}$
4980.000	-	$0.038^{+0.017}_{-0.018}$
5020.000	-	$0.033^{+0.014}_{-0.031}$
5060.000	-	$0.034^{+0.014}_{-0.034}$
5100.000	-	$0.046^{+0.019}_{-0.037}$
5140.000	-	$0.055^{+0.110}_{-0.028}$
5180.000	-	$0.042^{+0.021}_{-0.023}$
5220.000	-	$0.020^{+0.012}_{-0.020}$
5260.000	-	$0.009^{+0.007}_{-0.009}$
5300.000	-	$0.006^{+0.005}_{-0.006}$

Continues on the next page.

Energy [keV]	I_β ENSDF [%]	I_β DTAS [%]
5340.000	-	$0.006^{+0.005}_{-0.006}$
5380.000	-	$0.009^{+0.007}_{-0.008}$
5420.000	-	$0.014^{+0.009}_{-0.008}$
5460.000	-	$0.021^{+0.010}_{-0.010}$
5500.000	-	$0.029^{+0.010}_{-0.013}$
5540.000	-	$0.034^{+0.022}_{-0.015}$
5580.000	-	$0.030^{+0.023}_{-0.014}$
5620.000	-	$0.020^{+0.010}_{-0.010}$
5660.000	-	$0.011^{+0.007}_{-0.011}$
5700.000	-	$0.006^{+0.005}_{-0.006}$
5740.000	-	$0.005^{+0.004}_{-0.005}$
5780.000	-	$0.005^{+0.003}_{-0.005}$
5820.000	-	$0.008^{+0.004}_{-0.008}$
5860.000	-	$0.015^{+0.005}_{-0.009}$
5900.000	-	$0.025^{+0.035}_{-0.016}$
5940.000	-	$0.034^{+0.019}_{-0.025}$
5980.000	-	$0.041^{+0.051}_{-0.033}$

Table 14.5: I_β intensities of the decay of ^{95}Rb.

The reproduction of the multiplicities is shown in Figure 14.11 for the reference analysis. The agreement is very good for all of them, except for $M_m = 1$. At least in part the discrepancies could be due to the very limited information available to construct the known part of the level scheme for the response function calculation, which is restricted to energies below 1259.6 keV. It seems that the level at 2.236 MeV in ^{95}Sr is populated and is likely to de-excite by means of a single γ-ray, because we see a clear peak at this energy for $M_m = 1$. However, the statistical model tends to smooth the feeding and several structures in the $M_m = 1$ spectrum are poorly resolved.

Finally, the reproduction of the individual modules has also been studied, as presented in Figure 14.12, and the MC simulation based on the analysis agrees with the experimental spectra.

As a test of the γ-neutron discrimination, and in order to cross-check the β-intensity distribution obtained, the analysis of the β-gated DTAS spectrum with the gate discriminating between neutrons and γ-rays has also been undertaken. The quality of the fit can be seen in Figure 14.13, and a comparison of the feeding distribution obtained and the one from the analysis of the spectrum with neutrons is presented in Figure 14.14.

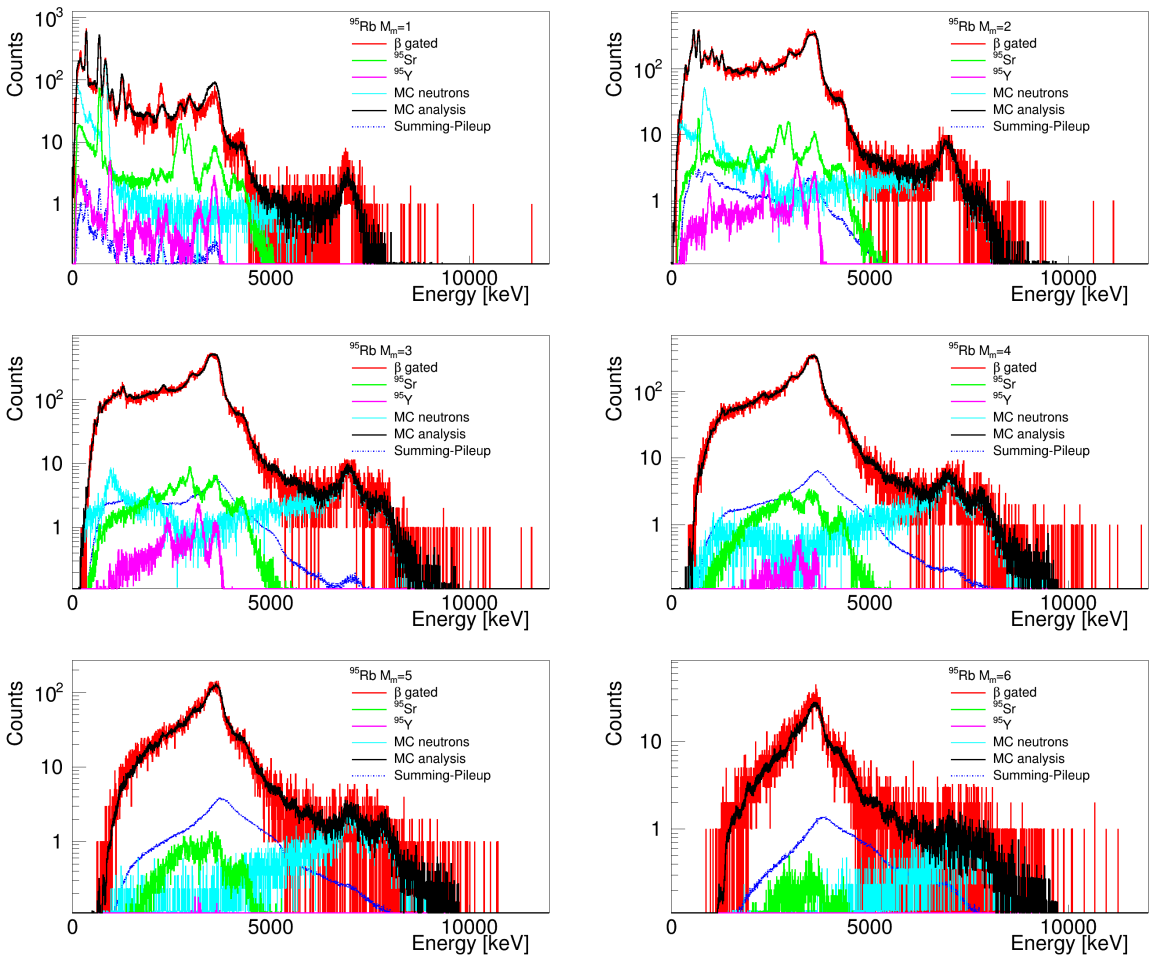

Figure 14.11: Experimental spectra for different multiplicities for the decay of ^{95}Rb compared with the MC simulation performed with an event generator for multiplicities from 1 to 6.

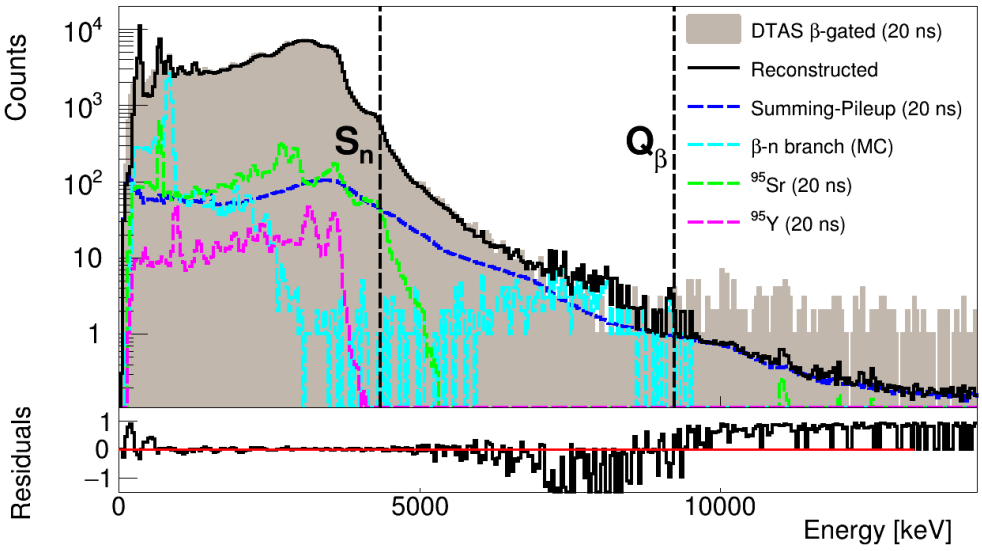

Figure 14.13: Result of the analysis of the decay of ^{95}Rb. The total spectrum is compared with the reconstructed one after the analysis.

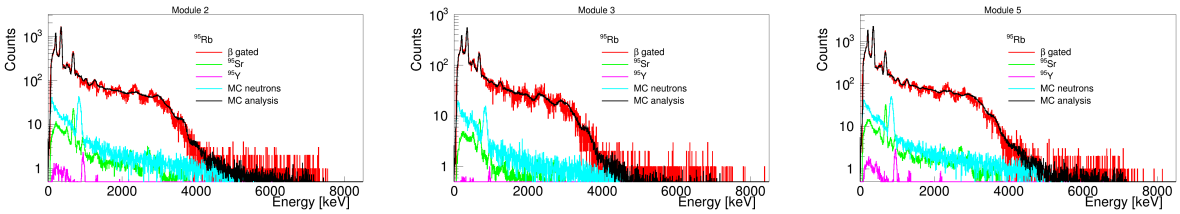

Figure 14.12: ^{95}Rb experimental spectra for the three geometrically distinguishable individual crystals compared with the MC.

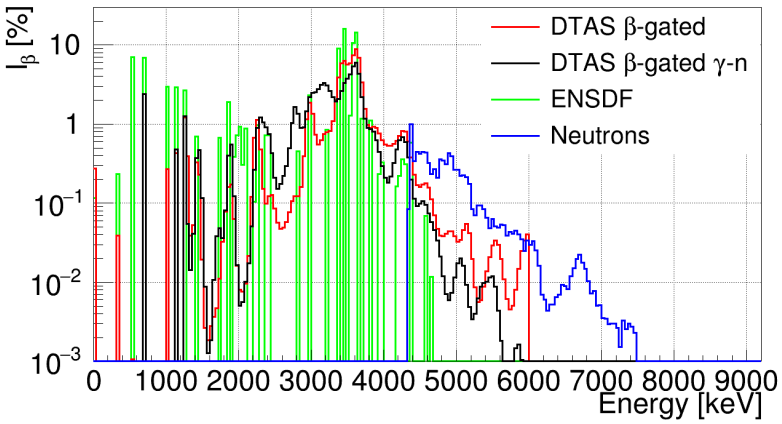

Figure 14.14: Comparison of the β-intensities obtained for the decay of ^{95}Rb for the β-gated spectrum and the β-gated spectrum with γ-neutron discrimination.

Part IV

Summary and appendixes

Summary and conclusions

Daría todo lo que sé por la mitad de lo que ignoro

I would give everything I know for half of what I ignore

René Descartes

In this final part of the thesis, we will discuss the impact on the calculated reactor decay heat and reactor antineutrino spectrum of the results obtained for all of fission fragments studied here. At this point, we will link the experimental β-intensities obtained in previous chapters with the motivations reported in Chapter 1. We will also comment on the γ-neutron competition from neutron unbound states in the case of β-delayed neutron emitters. Finally, the relevance of the results for Mo and Zr isotopes for the shapes of the nuclear ground states of the parent nuclei will be discussed.

Average energies

The β-intensity distributions obtained in this work for fission fragments have been used to evaluate the average γ and β energies in these decays and they are listed in Table IV.1. They were computed using Equation 1.31, presented in Chapter 1. In this equation, the mean energy of the β-particles emitted when level i is fed, $\langle E_{\beta i} \rangle$, was calculated employing subroutines from the $\log ft$ program of NNDC [215].

Uncertainties in Table IV.1 come from the evaluation of the average energies for all the space of solutions obtained for each case. The maximum positive and negative differences with respect to the average energies associated with the adopted β-intensity distribution, are quoted as the uncertainties. The same information that is summarized in Table IV.1 is graphically depicted in Figure IV.1. In both cases, the values obtained in this work are compared with the reference databases ENDF/B-VII.1 and JEFF-3.11. Differences are observed in all of the cases except for ^{103}Tc, where the relatively low amount of new intensity detected at high excitation energies is compensated by an enlargement of the ground state to ground state feeding intensity. For the remainder cases, the expected tendency due to the *Pandemonium* effect is found: average γ energies increase while average β energies decrease. The tendency has the opposite direction for ^{103}Mo, where average energies are available in the databases in spite of the lack of experimental information. In fact, no evaluation of β-intensities was available for the decay of ^{103}Mo [220]. Likewise, no

previous intensities or average energies were available for ^{102m}Nb.

According to the values quoted in Table IV.1, the largest differences are found for ^{100m}Nb, ^{102gs}Nb and ^{95}Rb, with an increase of $\overline{E}_\gamma$ around 30%, and a reduction of $\overline{E}_\beta$ around 15% for the niobium isotopes and 8% for the rubidium.

For the case of the β-delayed neutron emitters (^{137}I and ^{95}Rb), the contribution of the β-delayed neutron branch was taken into account for the evaluation of the average energies, in concordance with the average energies from the databases.

The decays of ^{100,102}Zr were not included in the evaluation of average energies, since the β-intensity distributions reported in this work represent an estimate only.

Nucleus	Energy	DTAS [keV]	JEFF-3.11 [keV]	ENDF/B-VII.1 [keV]
^{103}Tc	Gamma	254^{+168}_{-112}	248	248
	Beta	981^{+52}_{-78}	977(98)	977(98)
^{103}Mo	Gamma	402^{+205}_{-132}	628	981(28)
	Beta	1372^{+62}_{-96}	1301	1175(44)
^{140}Cs	Gamma	1841^{+158}_{-47}	1675	1796(28)
	Beta	1881^{+22}_{-74}	1961(69)	1947
^{100gs}Nb	Gamma	936^{+256}_{-133}	708	708(37)
	Beta	2432^{+64}_{-123}	2484(209)	2539(213)
^{100m}Nb	Gamma	2760^{+3}_{-28}	2056	2213(69)
	Beta	1709^{+13}_{-2}	2039	1999(198)
^{102gs}Nb	Gamma	2776^{+6}_{-51}	2094	2094(97)
	Beta	1945^{+25}_{-3}	2276(169)	2300(169)
^{102m}Nb	Gamma	1022^{+162}_{-61}	-	-
	Beta	2831^{+29}_{-78}	-	-
^{137}I	Gamma	1521^{+73}_{-68}	1212	1135(20)
	Beta	1948^{+32}_{-34}	1861	1920(26)
^{95}Rb	Gamma	3482^{+32}_{-23}	2629	2162(42)
	Beta	2586^{+11}_{-16}	2824	2296(110)

Table IV.1: Average β and γ energies obtained from the TAGS analysis presented in this thesis compared with values from JEFF-3.11 and ENDF/B-VII.1.

Finally, the values of the average energies have been used to evaluate their impact on the decay-heat summation calculations explained in Chapter 1, following the line of previous TAGS measurements already mentioned [74,89,252]. It should be noted that the importance of each decay is linked to the corresponding fission yield. The preliminary results from calculations performed by A. A. Sonzogni using the ENDF/B-VII.1 database as reference calculation is shown in Figure IV.2. The ratio of the γ and β components of the decay-heat time evolution for ^{235}U and ^{239}Pu with respect to the reference calculation are depicted in this figure, showing a remarkable impact due to the inclusion of our data, with an increase in the ratio for the γ component of more than 6% and a decrease close to 2% for the β component for both fissioning systems. The main contributor to this difference is the decay of ^{100m}Nb that increases by 9% and 10% the ratio of the γ component in ^{235}U and ^{239}Pu respectively, while decreasing by 3% the β component in both cases. The impact of ^{100gs}Nb is, however, quite modest, increasing by around 1% the ratio of the γ component and decreasing the ratio of the β component by less than 0.5% for both ^{235}U

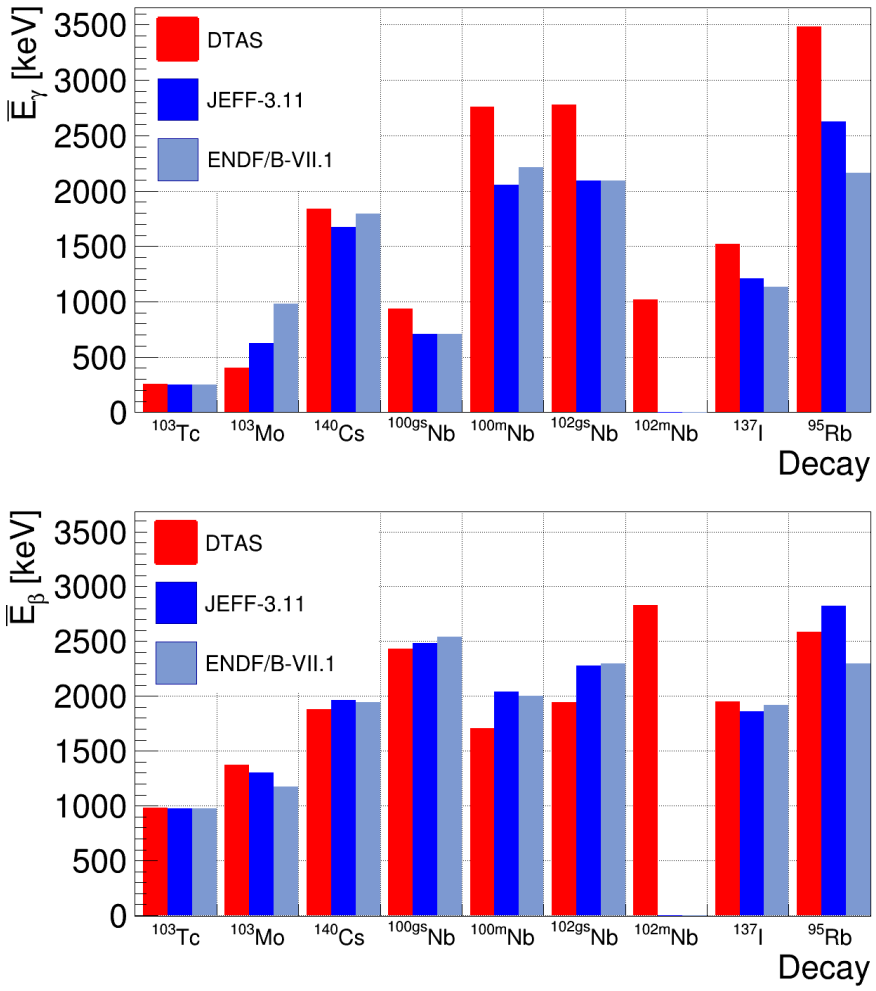

Figure IV.1: Average β and γ energies obtained from the TAGS analysis presented in this thesis compared with values from JEFF-3.11 and ENDF/B-VII.1.

and ^{239}Pu. Concerning the other two isomers studied, they also affect the calculation at around 10 s: ^{102gs}Nb increases by $<$2% the γ component and decreases the β component by around 0.5% for both fissioning systems, while ^{102m}Nb decreases by $<$3% the γ component and increases almost by 1% the β component in both ^{235}U and ^{239}Pu. Around 100 s, the data for ^{103}Mo decrease the γ component by 1% and 3% for ^{235}U and ^{239}Pu respectively, and the ratio for the β component is increased by 0.5% and 1% respectively. The impact of ^{103}Tc and ^{140}Cs is negligible, whereas ^{137}I only affects slightly the γ component of the calculation for ^{235}U, with an increase of around 0.7% between 10 s and 100 s. Finally, ^{95}Rb increases the γ component in both calculations around 3% below 1 s, and reduces the ratio of the β component by $<$0.5% for them.

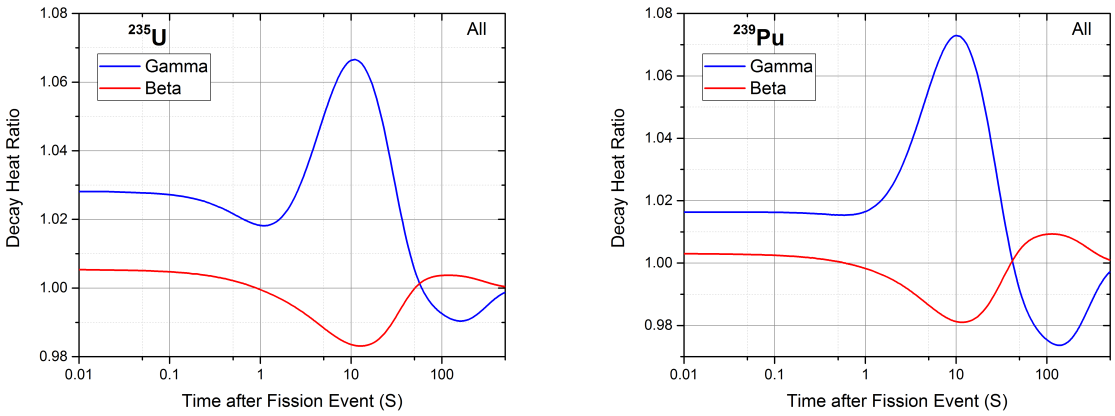

Figure IV.2: Ratio of the reactor decay-heat as a function of time when the data obtained in the present work replace the previous knowledge in the ENDF/B-VII.1 database. This preliminary calculation was performed by A. A. Sonzogni (NNDC, Brookhaven National Laboratory) for the γ and β components of the decay-heat for ^{235}U and ^{239}Pu.

β spectra and antineutrino spectra

We also used the β-intensity distributions obtained in this work to calculate the β energy distributions and the antineutrino distributions, according to Equation (IV.1):

$$\begin{aligned} S_\beta(E_\beta) &= \int_0^{Q_\beta} I_\beta(E_x) s_\beta(Q_\beta - E_x, E_\beta) dEx \\ S_{\overline{\nu}}(E_{\overline{\nu}}) &= \int_0^{Q_\beta} I_\beta(E_x) s_{\overline{\nu}}(Q_\beta - E_x, E_{\overline{\nu}}) dEx \end{aligned} \tag{IV.1}$$

where for the transition to each state E_x, $s_\beta(Q_\beta - E_x, E_\beta)$ and $s_{\overline{\nu}}(Q_\beta - E_x, E_{\overline{\nu}})$ are the shapes of the β and antineutrino energy distributions. These shapes are calculated with subroutines from the $\log ft$ program of NNDC [215], and only allowed shapes are considered.

In Figure IV.3 the β spectra for the decays studied in previous chapters are presented. The distributions calculated with the data from ENSDF are also included for comparison, showing a shift to higher energies with respect to the TAGS data. This trend, observed for all the cases except for ^{103}Tc, is a visual way to show the reduction of the average β energies associated with the *Pandemonium* systematic error, as commented on in previous section. Note that for the β-delayed neutron emitters, ^{137}I and ^{95}Rb, the β spectra with and without considering the β-delayed branch are also included in the comparison.

In addition, we have evaluated the β spectra for the decay of ^{140}Cs with the β intensity distribution from Greenwood *et al.* [131], obtaining a shape very similar to the one calculated with our data, as expected from the level of agreement of the β-intensity distributions shown in Chapter 10.

For those cases where β spectra were measured by Tengblad *et al.* at OSIRIS-ISOLDE [130], a meaningful comparison between our calculated β spectra and their experimental

data can be made. This is the case for ^{140}Cs, ^{137}I and ^{95}Rb. Differences in shape are observed in this comparison for the three isotopes, as shown in Figure IV.3. This is especially remarkable in ^{95}Rb. This is also seen when comparing in Table IV.2 our average β energies with the ones obtained from the direct β spectra measurements [130]. In addition, average γ energies were also measured by Rudstam *et al.* at OSIRIS in [234], and differences between the present values and both β and γ average energies collected by Rudstam *et al.* in [234] can be seen in Table IV.2. These deviations are not new, and they have been already highlighted in two recent publications [74,252]. A problem with the normalization of the average decay γ energies was pinpointed in [252], but the source of the remaining discrepancies has not been clarified and further comparisons are needed. New direct measurements of β spectra would benefit the discussion, and a proposal in this line has been accepted at IGISOL [253].

Nucleus	Rudstam [234]		DTAS		Rudstam-DTAS	
	$\overline{E}_\gamma$ [keV]	$\overline{E}_\beta$ [keV]	$\overline{E}_\gamma$ [keV]	$\overline{E}_\beta$ [keV]	$\Delta\overline{E}_\gamma$ [keV]	$\Delta\overline{E}_\beta$ [keV]
^{95}Rb	3370(220)	2850(150)	3482^{+32}_{-23}	2586^{+11}_{-16}	-112	+264
^{137}I	1230(150)	2050(40)	1521^{+73}_{-68}	1948^{+32}_{-34}	-291	+102
^{140}Cs	1270(50)	1860(40)	1841^{+158}_{-47}	1881^{+22}_{-74}	-571	-21

Table IV.2: Comparison of our average γ and β energies (including the β-delayed branch for β-delayed neutron emitters) with the average energies from [234].

The calculation of the antineutrino spectra is presented in Figure IV.4. As in the case of the β spectra, the distributions with the data from ENSDF are also included for comparison. In the case of ^{140}Cs we also include the calculation using the data from Greenwood *et al.* [131]. Similarly to the β spectra, differences are found between the shapes obtained with our data and with ENSDF, showing a shift of our spectra to lower energies.

The first estimate of the impact of the new antineutrino spectra presented in Figure IV.4 in the reactor antineutrino spectrum was evaluated by means of summation calculations performed by M. Fallot and M. Estienne (Subatech, Nantes), based on the procedure explained in [133]. For each of the four main fissile isotopes in a PWR reactor (see Section 1.3.4 of Chapter 1), Figure IV.5 shows the preliminary ratio between the antineutrino spectrum calculated with the inclusion of all the decay data obtained with DTAS, and the spectrum calculated with the previous knowledge of these decays. These previous data came from JEFF-3.11 (decays of ^{100gs,100m}Nb, ^{102m}Nb, ^{103}Tc and ^{103}Mo), ENDF/B-VII.1. (decay of ^{102gs}Nb) and Rudstam *et al.* (decays of ^{95}Rb, ^{137}I and ^{140}Cs). The impact of our new data is quite remarkable in the energy region of the reactor antineutrino shape distortion explained in Chapter 1, especially for the Pu isotopes.

The impact of ^{103}Tc is negligible, while ^{103}Mo increases the ratio more than 1% for the plutonium isotopes, especially for ^{239}Pu. The new data for ^{100gs,100m}Nb increase the ratio $< 1\%$ for the four isotopes, and the impact of ^{95}Rb and ^{137}I is to decrease the ratio $< 1\%$ for all of them. ^{140}Cs introduces an increase of the ratio of around 2% in all the isotopes, except in ^{235}U, where it is around 1%. Finally, the most important effect is found

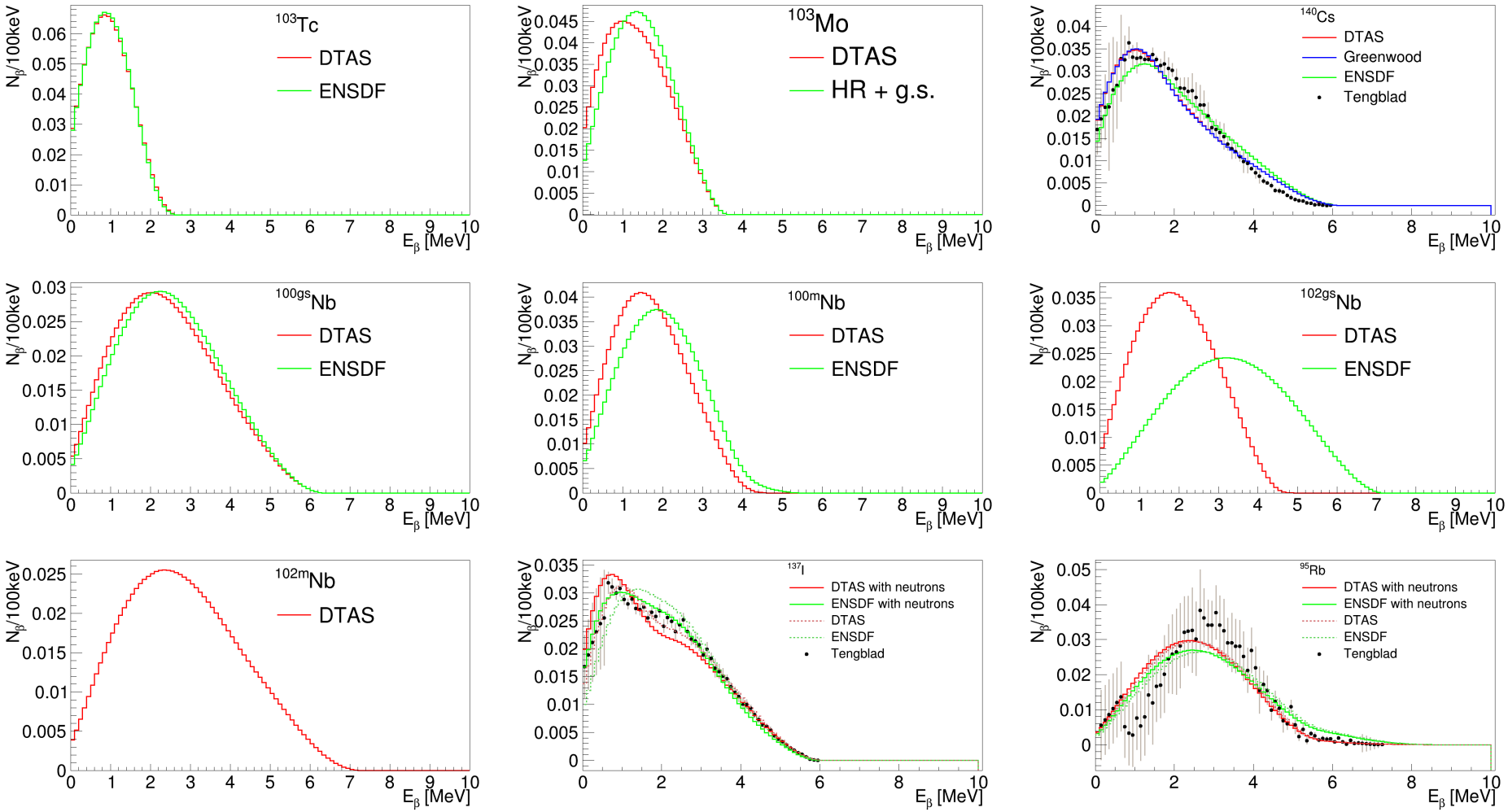

Figure IV.3: β spectra calculated with the β intensity distributions obtained with DTAS compared to the spectra calculated with the data from ENSDF, and with the data of Tengblad *et al.* when possible.

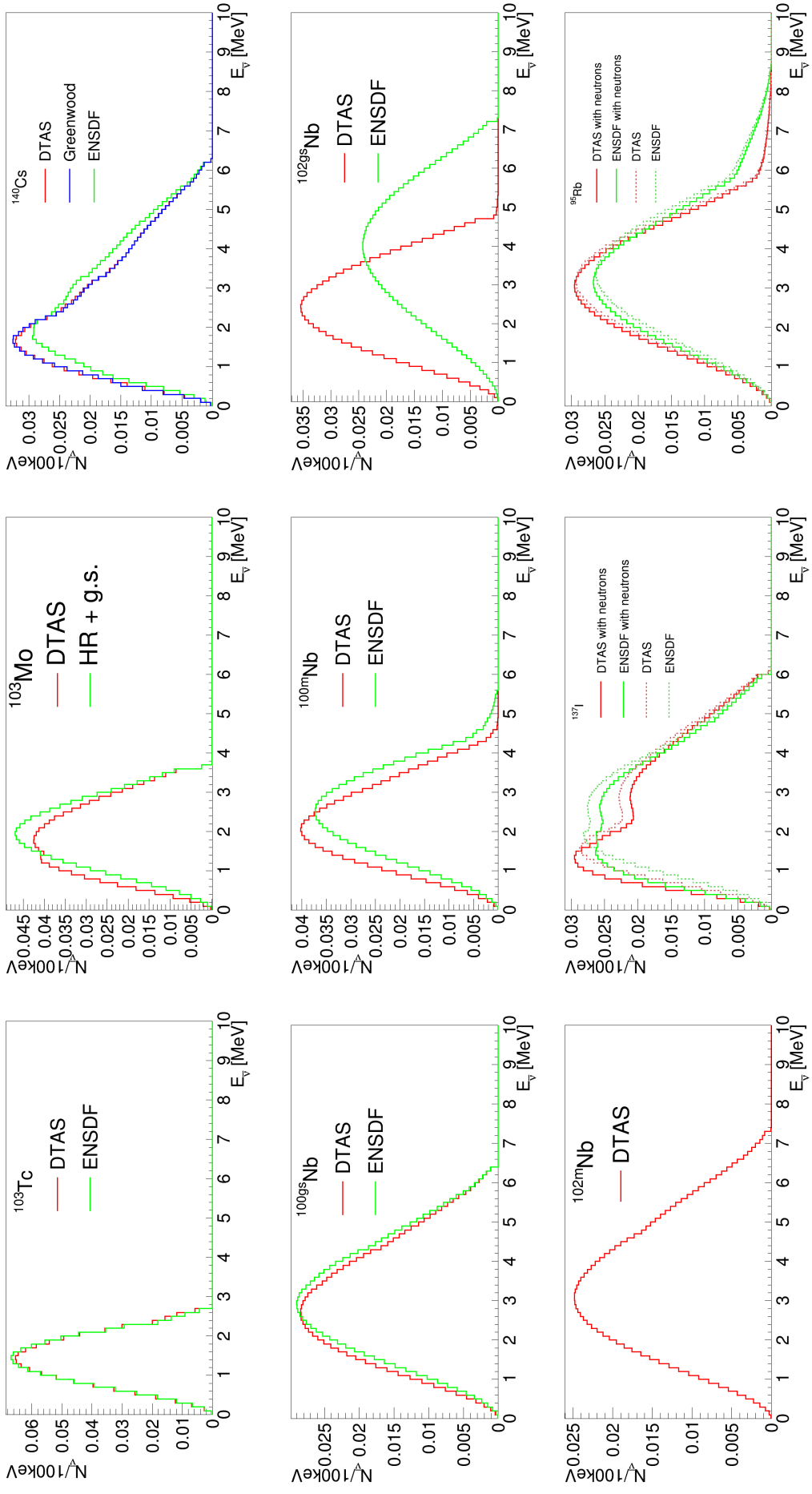

Figure IV.4: Antineutrino spectra calculated with the β intensity distributions obtained with DTAS compared to the spectra calculated with the data from ENSDF.

for ^{102gs}Nb, that decreases by 3% the ratio for uranium isotopes and by 4% for plutonium isotopes, and for ^{102m}Nb that increases by 1% the ratio for ^{238}U, by 2% for ^{235}U, by 4% for ^{241}Pu and by 7% for ^{239}Pu.

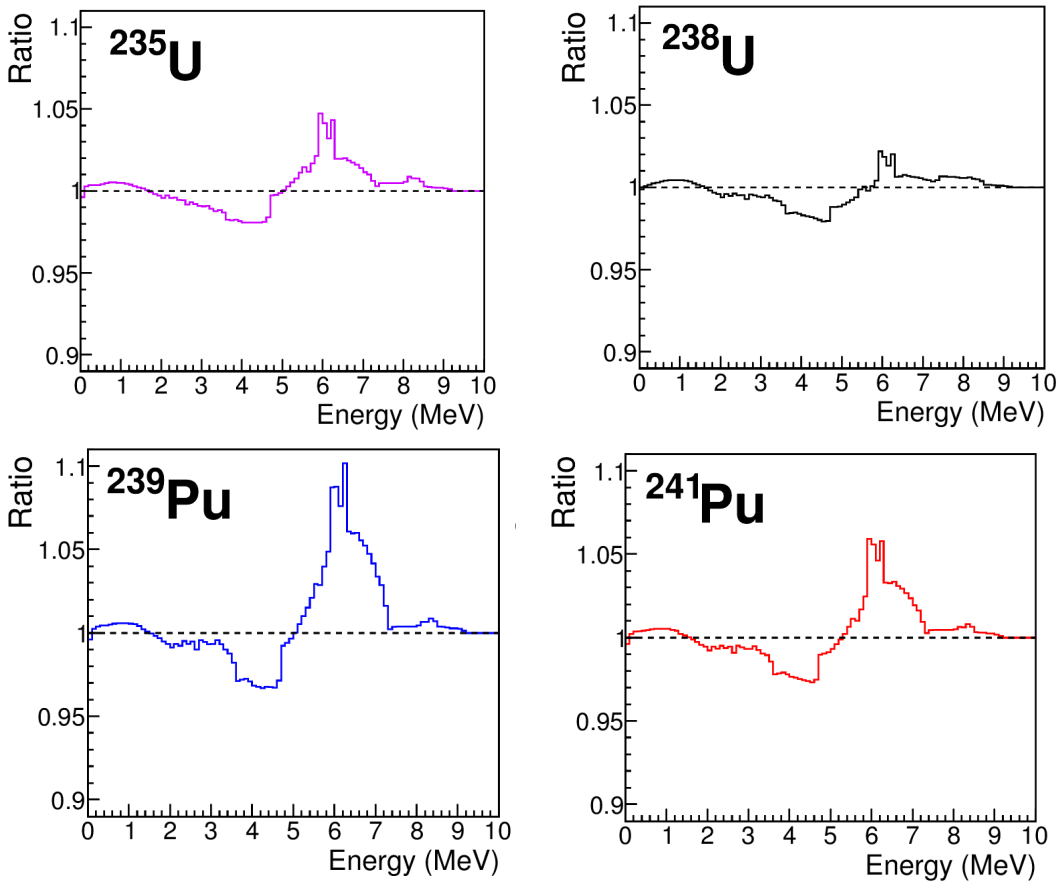

Figure IV.5: Ratio of reactor antineutrino spectra as a function of energy when the data obtained in the present work replace previous knowledge of the decays studied with DTAS. This preliminary calculation was performed by M. Fallot and M. Estienne (Subatech, Nantes) for the four main fissile isotopes in a PWR reactor: ^{235}U, ^{238}U, ^{239}Pu and ^{241}Pu.

γ-neutron competition

In the case of the two β-delayed neutron emitters studied in this work, ^{137}I (Chapter 13) and ^{95}Rb (Chapter 14), a significant amount of $I_{\beta\gamma}$ is observed above S_n. In order to compare with the P_n value (the neutron emission probability) we can define P_γ according to Equation (IV.2), as the integrated $I_{\beta\gamma}$ above S_n:

$$P_\gamma = \int_{S_n}^{Q_\beta} I_{\beta\gamma} dE_x \tag{IV.2}$$

The results are summarized in Table IV.3, where P_γ is compared with the P_n value (from [241]). Thus, the β-intensity leading to levels de-exciting by means of γ-rays represents 55% of the total β-intensity above S_n for ^{137}I and 26% for ^{95}Rb. The situation in both cases is similar to that found in the decay of ^{87,88}Br [73, 74] and can be understood as

a nuclear structure effect. The allowed decay of ^{137}I populates positive parity states with J=5/2, 7/2, 9/2. The decay of the $7/2^+$ and $9/2^+$ states to the 0^+ g.s. of ^{136}Xe requires the emission of neutrons with large orbital angular momentum (l=4 or higher even angular momentum values) and is, therefore, hindered. The same happens in ^{95}Rb, where negative parity states with J=3/2, 5/2, 7/2 are populated. Below S_n+837 keV, the energy of the 2^+ first excited state of ^{94}Sr, the $5/2^-$ and $7/2^-$ states can only decay to the 0^+ g.s. by l=3 neutron emission, which is hindered. In addition, a sizeable *Pandemonium* effect is seen, since P_γ for ^{137}I and ^{95}Rb is respectively 3 and 5 times higher than the quoted values from ENSDF.

Nucleus	P_γ ENSDF [%]	P_γ DTAS [%]	P_n [%]
^{137}I	2.76	$8.88^{+1.96}_{-1.53}$	7.33(38)
^{95}Rb	0.57	$3.08^{+0.87}_{-1.03}$	8.87(29)

Table IV.3: Integral $I_{\beta\gamma}$ above S_n (P_γ) obtained with DTAS in comparison with the value from ENSDF and with the neutron emission probability, P_n.

All possible solutions compatible with the data have been used to evaluate the systematic uncertainties in Table IV.3. For this, the maximum positive and negative difference with respect to the adopted β-intensity distribution were considered as the uncertainties due to the β-intensity. Among the possible solutions we also included the analysis with a narrow gate of 20 ns to separate the prompt contribution from the delayed neutron interactions, and in the case of ^{137}I, the analysis in singles has also been included. In [74] several other possible sources of uncertainty were investigated, related to the redistribution of counts around S_n (energy calibration, width calibration, etc.). Here we will only evaluate the one that was found to be more important in [74], i.e. the uncertainty in the first bin considered in the integration. This uncertainty corresponds to 20% for ^{137}I, and 26% for ^{95}Rb. The final uncertainties quoted in Table IV.3 are the quadratic sum of the two sources of error considered.

In line with previous calculations for ^{87,88}Br and ^{94}Rb, we have evaluated the ratio $I_{\beta\gamma}/(I_{\beta\gamma}+I_{\beta n})$ as a function of the excitation energy above S_n. This ratio is equivalent to the average ratio of the widths: $\langle\Gamma_\gamma/(\Gamma_\gamma+\Gamma_n)\rangle$, which has been highlighted as a very interesting link between β-decay and (n,γ) reactions [73–76], as explained in Chapter 1. This average ratio of widths is calculated in the Hauser-Feshbach formalism (HFF) [71] as described in detail in [74, 75]. As explained in [74, 75], the ingredients for these Hauser-Feshbach calculations are the Nuclear Level Density (NLD) and the Photon Strength Functions (PSF) for the daughter nucleus of the β-decay, and the Neutron Transmission Coefficients (NTC) for the daughter nucleus of the β-delayed branch. The first two are the same used for the construction of the branching ratio matrix of the TAGS analysis, whereas NTC are obtained from optical model calculations performed with TALYS-1.8 [155]. Only the neutron transmission to the 0^+ ground state of ^{136}Xe is considered (the only state populated in the β-delayed branch), while several levels are considered in ^{94}Sr. In Table IV.4 the levels populated in the β-delayed branch of ^{95}Rb are summarized, and spin-parity

values from RIPL-3 [145] have been selected for those levels with unassigned values (the β-intensities to these levels were discussed in Table 14.1).

Energy [MeV]	J^P ENSDF	J^P used
0.000	0^+	0^+
0.837	2^+	2^+
1.927	$3^{(-)}$	2^-
2.146	4^+	4^+
2.415	(3^-)	3^-
2.604	(4^-)	4^-
2.614	(2,3,4)	4^-
2.650	$4^{(+)}$	4^+
2.703	(2,3,4)	2^-
2.711	(2,3,4)	2^+
2.740	(4^-)	4^-
2.930	(2,3,4)	4^-
3.439	(2,3,4)	2^+

Table IV.4: Levels of ^{94}Sr populated in the β-delayed neutron branch. Spin-parity values from ENSDF and the adopted values used, based on the information in RIPL-3, are presented

For the calculation of the average ratio of widths we used the Monte Carlo method explained in [74]. A direct comparison between the experimental ratio of β-intensities and the average ratio of widths is possible, since the average is taken over all levels of a given J^π within an energy bin of 40 keV (the experimental binning width). In addition, Porter-Thomas fluctuations on neutron and γ widths are introduced. In Figure IV.6 the comparison between the experimental $I_{\beta\gamma}/(I_{\beta\gamma}+I_{\beta n})$ and the Hauser-Feshbach calculation of $\langle\Gamma_\gamma/(\Gamma_\gamma+\Gamma_n)\rangle$ is shown. The large P_γ in ^{137}I is clearly understood attending to the hindrance of $l=4$ neutron emission from $7/2^+$ and $9/2^+$ states needed to populate the 0^+ ground state in ^{136}Xe. Analogously, in the decay of ^{95}Rb, $l=3$ neutron emission from $5/2^-$ and $7/2^-$ states to populate the ground state in ^{94}Sr is very suppressed. However, the γ de-excitation is not so dominant above S_n as in ^{137}I due to the possible emission of $l=1$ neutrons from $3/2^-$ states to populate the ground state in ^{94}Sr.

As in the evaluation of systematic uncertainties in the P_γ values of Table IV.3, the filled regions depicted in Figure IV.6 correspond to the envelope of the ratio calculated for all possible solutions compatible with the data. The structure at 5.6 MeV in the case of ^{95}Rb is not reproduced with the Hauser-Feshbach calculations. Although it is not covered by the systematic uncertainties, we think that it is a consequence of the limitations in the reproduction of the β-delayed neutron branch with MC simulations, which did not produce a satisfactory subtraction for the TAGS analysis.

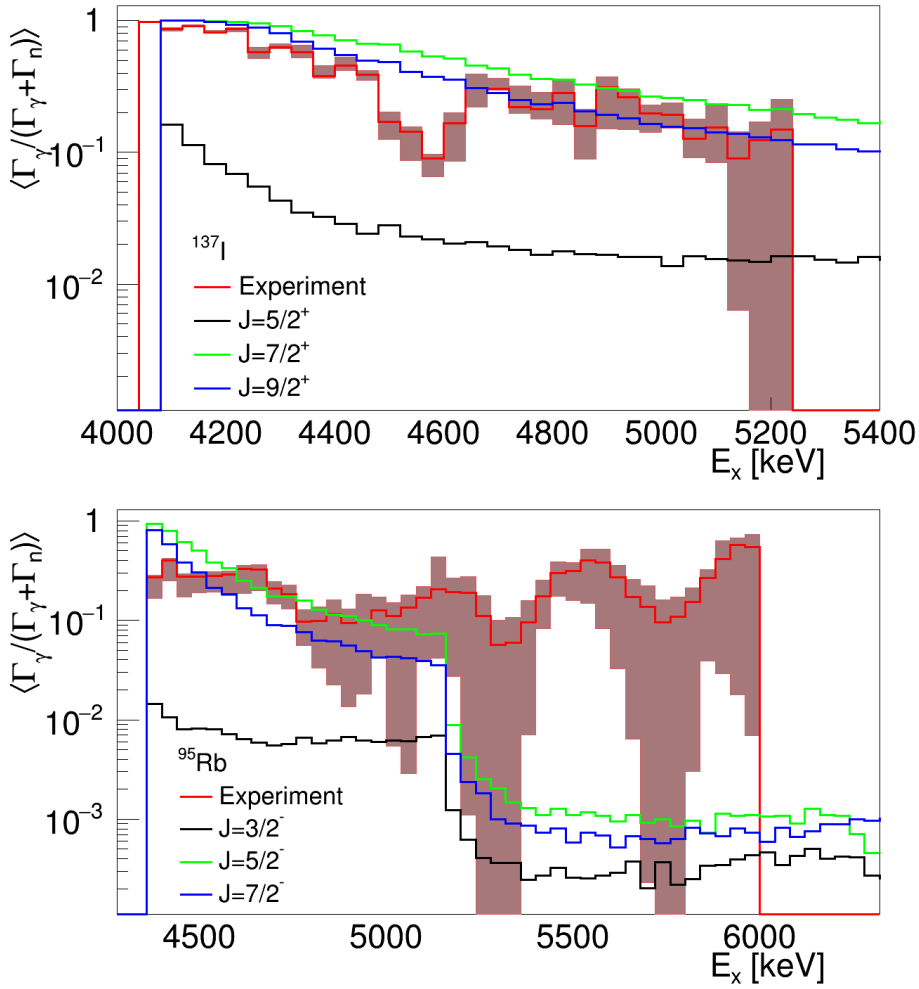

Figure IV.6: Experimental average γ to total width compared with Hauser-Feshbach calculations for allowed β-decays in the case of ^{137}I (top) and ^{95}Rb (bottom).

Extra: shape studies

The total absorption technique has been used to study shape effects in the parent nucleus, based on the measured B(GT) strength distribution in the daughter [175, 254–257]. Although it was not the aim of any of the measurements presented in this work, for some cases we could try to shed light on the shape of the parent nucleus in the decay. The justification for this approach in the present case relies on the theoretical work of Sarriguren *et al.* [258, 259] in the A =100 - 120 region of neutron rich isotopes of molybdenum and zirconium. Zirconium isotopes are known to have a phase transition around ^{100}Zr from spherical ground states to deformed ground states [260]. Recently a quantum phase transition has been predicted in this region [261], and shape coexistence in ^{96}Zr has been deduced [262].

In order to provide experimental information to be compared with theoretical calculations, we have evaluated the β-strength distribution for the decays of ^{103}Mo and ^{100,102}Zr. For this we made use of Equation (1.22), employing subroutines from the log ft program of

NNDC [215]. Bearing in mind that our TAGS analysis of the zirconium isotopes give just an estimate, we thought that our limited sensitivity in these two cases was enough to distinguish between the very different prolate and oblate patterns obtained in the theoretical calculations [258,259].

Concerning the theoretical calculations, details about the model are given in [258] and a thorough description is beyond the scope of this work. Just it should be noted that they are based on the proton-neutron quasiparticle random-phase approximation. This microscopic approach uses a Hartree-Fock mean field obtained with Skyrme interactions to generate single-particle energies, wave functions, and occupation probabilities. In particular, the SLy4 Skryme force is used. A quenching factor of 0.77 is included in these calculations: $(g_A/g_V)_{eff} = 0.77(g_A/g_V)$.

It is important to note that the results for ^{100,102}Zr from [258] will be directly used in our comparison. However, the calculations of molybdenum isotopes in [258,259] did not include ^{103}Mo, and it has been calculated by P. Sarriguren for this work.

Experimental B(GT) distributions are compared with the theoretical calculations in Figure IV.7. Calculations have been scaled by the quenching factor for the comparison. The shaded regions correspond to the envelope of the B(GT) distributions for all possible solutions compatible with the data.

Although the calculations in [259] predict very close minima for the oblate and prolate configurations in the potential energy curves of ^{100,102}Zr, the comparison with the experimental B(GT) distribution in both cases is better described with prolate shapes.

With respect to ^{103}Mo, in general the experimental distribution is better described with an oblate shape. However, since molybdenum isotopes exhibit shape coexistence in this region [263], it is difficult to come to a firm conclusion from the comparison. The only conclusion is that an oblate component is seemingly needed to understand the experimental distribution. Moreover, in the oblate calculation a $7/2^+$ level is obtained as a ground state for ^{103}Tc, although experimentally it is a $5/2^+$ supported by the large ground state to ground state feeding intensity observed (73% in our case, as presented in Chapter 9). The first theoretical $5/2^+$ appears at 279 keV, so that all energies could be shifted to consider this state as the ground state. This is not so critical in the prolate calculation, with a shift of 70 keV. The result of applying these shifts is a larger discrepancy with respect to the experimental distribution for the oblate calculation. However, it has to be noted that the amount of strength predicted at the energy of the ground state in both prolate and oblate configurations is enormous in comparison with experiment. No ground state feeding intensity can lead to this value, and it is due to the fact that the half-life (67.5 s) is not reproduced in the calculation, which gives 39.2 s for the prolate case and 24.4 s for the oblate case. A change in the parameters of the interaction could account for these discrepancies.

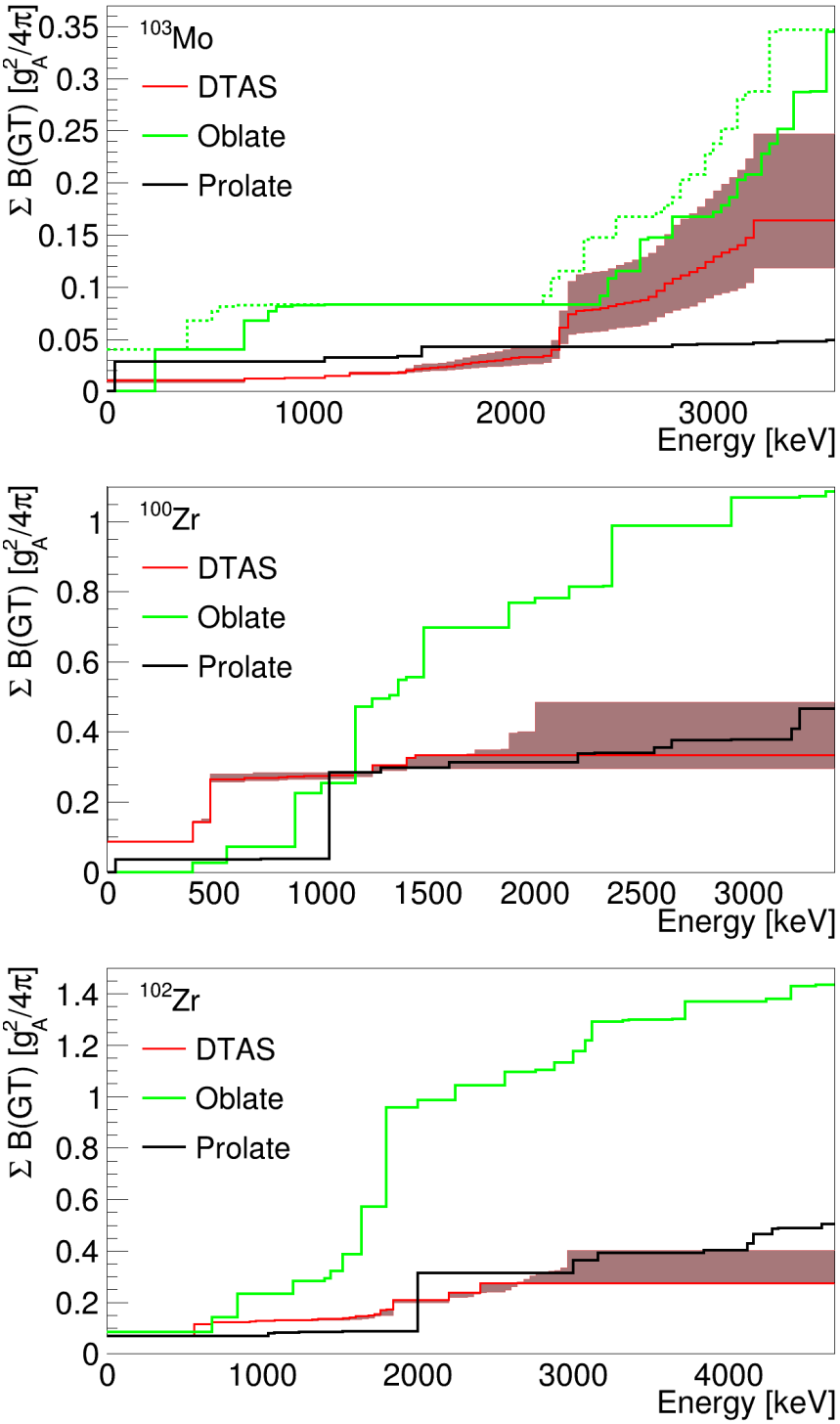

Figure IV.7: Comparison of the experimental accumulated B(GT) distribution (red) with the theoretical distributions for oblate (green) and prolate (black) configurations. Calculations performed by P. Sarriguren (data for ^{100,102}Zr from [258]). The green dotted line in the comparison for ^{103}Mo represents the oblate distribution after correcting the calculated strength with a shift in energy.

Outlook

In this work the β-decays of some nuclei of interest in neutrino physics, nuclear structure and reactor calculations have been investigated by means of the TAGS technique. For this, the new DTAS spectrometer has been used for the first time at IGISOL, in combination with new plastic β-detectors.

The whole set-up has been carefully characterized. In the characterization of the DTAS detector a gain stabilization system was successfully employed, and we have been able to deal with the non-proportionality light yield effects in a NaI(Tl) multi-crystal spectrometer in order to reconstruct properly the sum of the total energy deposited in the spectrometer, taking into account the effect of the segmentation. The summing-pileup distortion of the spectrum was successfully taken into account using a revision of a method previously developed, and for high-rate measurements an improvement in this method has been introduced with the help of MC simulation. A detailed Geant4 MC simulation of the DTAS detector has been performed, including its response to neutrons and the reproduction of the spectra for different multiplicities. Concerning the vase-shaped β-detector used in one of the measurements at IGISOL, MC simulations with optical photons have been shown to reproduce the shape of the experimental β spectra when energy deposited simulations turned out to be insufficient. Furthermore, a method to directly convert the energy deposited into the equivalent amount of light has been developed, and successfully applied to the TAGS analysis of the β^- decay of ^{100}Tc.

The results of the analysis for the decay of ^{100}Tc confirmed the β-intensities obtained with HPGe detectors using the high-resolution technique, particularly the large β-intensity of the most important branch of the decay, going to the ground state of ^{100}Ru. The remainder of the β-intensities obtained were shown to be in reasonable agreement with previous results. The decay data have been discussed in the framework of the QRPA calculations, because of their impact in double β-decay calculations. These calculations were in good agreement with TAGS results for the ground state feeding, but showed deviations from the measured β-decay rates that could be due to the effect of small deformation of both the mother and daughter nuclei. A conflict regarding the adopted effective value of the axial-vector coupling constant g_{A} was pointed out, since the best reproduction of the results for the single β-decay and the best reproduction of the ^{100}Mo 2ν double β-decay half-life was obtained with different g_{A} values.

The TAGS analysis of nine important fission products have been presented in this work. For each case the reproduction of the multiplicity spectra, the individual spectra and the γ-intensities were investigated, and a thorough study of the systematic uncertainties was carried out. In all cases new β-intensity has been observed, and two completely new β-intensity distribution were obtained, namely for ^{103}Mo and $^{102\mathrm{m}}$Nb. In the decay of ^{103}Tc the differences with respect to previous β-intensity distributions were not very remarkable, but the lack of sensitivity to the ground state feeding intensity triggered the re-evaluation of a β-γ counting method for ground state feeding calculation with TAGS data. This procedure has been applied to seven cases showing a reasonable agreement with the value from the deconvolution for most of them. A deeper discussion about the estimation of

the uncertainties in this method would be advisable. In addition, the application of this method to other cases (some from the same campaign of measurements at IGISOL, but also from the previous campaign [74, 108, 252]) is needed to consolidate this procedure.

Among the fission products studied, there were two challenging measurements from the point of view of the isomers: ^{100gs,100m}Nb, and ^{102gs,102m}Nb. Similar strategies were adopted in both cases to disentangle them, and a TAGS analysis of each of the isomers was possible. Additionally, a rough analysis of the decays of ^{100,102}Zr was extracted from these measurements by using a method to separate two components of a decay chain from a single measurement. The β-intensity distributions of these Zr isotopes allowed us to study the nuclear shapes of the parent nuclei. A reasonable agreement with prolate configurations was observed for both cases when compared with theoretical calculations. The shape of ^{103}Mo was also investigated, finding strong indications of an oblate component.

The impact of the β-intensity distributions obtained for the fission fragments of this work on summation calculations, both for the reactor decay heat and the reactor anti-neutrino spectrum, was studied. Differences with respect to the values available in the databases for the average γ and β energies have been pointed out, as well as differences in the shapes of the β and antineutrino spectra for each case. Preliminary summation calculations of the antineutrino spectrum and the decay-heat have been performed by M. Fallot and M. Estienne (Subatech, Nantes) and by A. A. Sonzogni (NNDC, Brookhaven National Laboratory), respectively. A remarkable impact of the present TAGS data has been found in both the decay-heat and the antineutrino spectrum calculations. The decays of ^{100m}Nb and ^{102m}Nb seem to introduce the largest differences.

For the β-delayed neutron emitters ^{137}I and ^{95}Rb, the β-intensity distributions served to address important topics such as the γ-neutron competition.

Finally, the results collected in this thesis widen the field of the TAGS technique with new frontiers to investigate. Apart from the β-γ counting method already mentioned, further efforts should be made to evaluate the possibilities concerning the sensitivity of the DTAS measurements to the I_n distributions of the β-delayed neutron branches. Likewise, the sensitivity of the multiplicities to the photon strength function parameters may lead to new applications in the domain of nuclear collective excitations.

To conclude, the new DTAS spectrometer has taken its first steps at IGISOL. However, this detector was originally designed for FAIR, and it is aimed at new experiments, especially at fragmentation facilities. The excellent performance of DTAS in this work, enabled the planning of future measurements both at RIKEN, with an approved proposal [264], and GSI, with a submitted proposal [265]. These future experiments will obviously benefit from the work presented here, but many new challenges will also be faced at fragmentation facilities. The MC characterization of DTAS coupled to the complex AIDA detector will be one of these challenges, as will be the identification of the β-gated spectrum and all the contaminants for the selected cases. Anyway, the success of such new measurements will be within reach as long as the capabilities of DTAS and the powerful analysis tools of the Valencia group walk together.

Resumen en castellano

La solución al misterio siempre es inferior al misterio. El misterio participa de lo sobrenatural y aun de lo divino; la solución, del juego de manos

The solution of a mystery is always inferior to the mystery. The mystery has a touch of the supernatural and even of the divine about it; while the solution, of sleight of hand

Jorge Luis Borges

Introducción

Motivación

La desintegración β es un proceso en el cual el núcleo de un elemento químico X, con Z protones y N neutrones, ${}^{A}_{Z}\mathrm{X}_{N}$, se transforma en el núcleo del elemento con $Z \pm 1$ protones, manteniéndose $A = N + Z$ constante. Se trata de un proceso radioactivo en el que un neutrón padre se convierte en un protón (hablamos entonces de desintegración β^-) o viceversa (β^+), emitiendo en cada caso una pareja de leptones (un e^-/e^+ junto a un $\overline{\nu}_e/\nu_e$ para β^-/β^+). En la Ecuación (IV.3) ambos procesos aparecen esquemáticamente representados junto a la captura electrónica (EC), la cual representa un tercer modo de desintegración β similar al proceso β^+.

$$\begin{aligned} \beta^- &: {}^{A}_{Z}\mathrm{X}_{N} \rightarrow {}^{A}_{Z+1}\mathrm{X}_{N-1} + e^- + \overline{\nu}_e \\ \beta^+ &: {}^{A}_{Z}\mathrm{X}_{N} \rightarrow {}^{A}_{Z-1}\mathrm{X}_{N+1} + e^+ + \nu_e \\ EC &: {}^{A}_{Z}\mathrm{X}_{N} + e^- \rightarrow {}^{A}_{Z-1}\mathrm{X}^{*}_{N+1} + \nu_e \end{aligned} \tag{IV.3}$$

Desde los años 30 del siglo XX, cuando se empezó a tener una visión clara de este proceso, los estudios de desintegración β han reportado una gran cantidad de valiosa información para la formalización y entendimiento de la estructura nuclear. En el marco de la llamada Teoría de Fermi [2], basada en un formalismo relativista en el que la interacción responsable de la desintegración β se considera puntual, pueden relacionarse estructura nuclear y observables experimentales. En concreto, las funciones de onda de los estados

cuánticos del núcleo final (núcleo hijo) e inicial (núcleo padre) toman parte en el cálculo de la probabilidad de transición reducida, B(GT) (para las transiciones más habituales en las cuales los dos leptones emitidos tienen espines intrínsecos paralelos, llamadas desintegraciones Gamow-Teller (GT) [3]). En la Ecuación (IV.4) las B(GT) de todas las posibles transiciones entre estados iniciales y finales promediadas en intervalos de energía ΔE, aparecen relacionadas con tres observables experimentales: Q_β, $T_{1/2}$ e $I_\beta(E_x)$. El primer observable, Q_β, es la ventana de energías en la que pueden producirse las transiciones. El segundo observable, $T_{1/2}$, es la vida media y está ligada con el ritmo al que se producen las desintegraciones en el tiempo. Finalmente, el tercer observable, las intensidades β, $I_\beta(E_x)$, representa las probabilidades con las que se producen transiciones a los estados finales con energía E_x. Son precisamente estas probabilidades y su determinación experimental el objeto de este trabajo.

$$S_\beta(E_x) = \sum_{E_f \in \Delta E} \frac{\frac{1}{\Delta E} I_\beta(E_x)}{f(Q_\beta - Ex, Z) T_{1/2}} = \frac{1}{6146 \pm 7} \left(\frac{g_A}{g_V}\right)^2 \sum_{E_f \in \Delta E} \frac{1}{\Delta E} B(GT)_{i \to f} \quad \text{(IV.4)}$$

TAGS: espectroscopía de absorción total

Tradicionalmente, las intensidades β se han determinado midiendo los rayos γ emitidos en la des-excitación del núcleo hijo tras la desintegración β. Estudiando cuidadosamente las intensidades de esos rayos γ, sus energías y si son detectados en coincidencia unos con otros, el objetivo es determinar las cascadas γ a través de los distintos niveles excitados del núcleo hijo mediante las cuales tiene lugar su des-excitación al estado fundamental. Haciendo un balance de las intensidades que entran y salen de cada nivel, pueden, en principio, extraerse las probabilidades con las que han sido poblados en la desintegración β del núcleo padre. Para ello, típicamente se utilizan detectores de alta resolución en energía (generalmente detectores de germanio) y este hecho conlleva un problema intrínseco en estas medidas, debido a la limitada eficiencia de este tipo de detectores. Dicho problema se traduce en un error sistemático cuando se deducen las intensidades β, debido a las altas posibilidades de no detectar alguno de los rayos γ de las cascadas, haciendo que el balance de intensidades γ sea erróneo. Este efecto, conocido como *Pandemonio* [17], se agrava cuanto más alejados de las estabilidad son los núcleos que se estudian, pues sus esquemas de niveles son normalmente más complejos y las cascadas γ se fragmentan en múltiples caminos con múltiples rayos γ implicados. La consecuencia directa de este efecto es una sobre-estimación de las probabilidades de poblar niveles a bajas energías de excitación en el núcleo hijo, quedando parte de la intensidad β que va a altas energías de excitación sin detectar.

El panorama en la determinación experimental de intensidades β a través de la medida de rayos γ afortunadamente no acaba con el efecto *Pandemonio*, y el problema puede aproximarse con una filosofía diferente, que es la adoptada en el presente trabajo. Así, en vez de utilizar detectores de alta resolución energética con una eficiencia modesta, pueden usarse detectores de alta eficiencia con una resolución energética modesta en lo que se conoce como Espectroscopía γ de Absorción Total (TAGS por sus siglas en inglés). Esta técnica se

basa en la utilización de cristales centelleadores de gran tamaño cubriendo la mayor parte posible del ángulo sólido total de cara a maximizar la eficiencia. De este modo, los detectores utilizados se comportan como calorímetros, en los que en lugar de medir los rayos γ individuales, se registra la suma de toda la cascada γ. El procedimiento para extraer la información sobre las intensidades β en el caso de un detector ideal, consistiría en mirar directamente las intensidades de los picos suma medidos, y éstas darían la probabilidad con la que se puebla el nivel a la energía de cada pico suma. No obstante, la vida real impone sus reglas, y pese a la alta eficiencia de los detectores utilizados (cercana al 90 % en muchos casos), en un espectro real encontramos picos de escape, zonas de continuo debidas a interacciones Compton, así como efectos de distorsión producidos por la resolución energética. Por todo ello, la determinación de las intensidades β se lleva a cabo a través de un proceso de deconvolución del espectro experimental con la función de respuesta del detector [18]. Para ello es preciso resolver el problema inverso definido matemáticamente en la Ecuación (IV.5):

$$d_i = \sum_{j}^{levels} R_{ij}(B) f_j + C_i \tag{IV.5}$$

donde d_i es el número de cuentas del canal i del espectro experimental, f_j es el número de eventos que pueblan el nivel j en el núcleo hijo, C_i es la contribución de todos los contaminantes al canal i y $R_{ij}(B)$ es la función de respuesta del detector, la cual representa la probabilidad de que al poblar el nivel j del núcleo hijo se registre una cuenta en el canal i del espectro experimental. Esta función de respuesta se calcula mediante simulaciones Monte Carlo (MC) [18] y es única para cada detector y cada esquema de niveles [137], al depender de la matriz de razones de ramificación. El cálculo de la matriz de razones de ramificación se basa parcialmente en la información disponible para los niveles a baja excitación (obtenida de la bibliografía asumiendo que se conoce bien). Desde el último nivel conocido incluido hasta Q_β, se utiliza un continuo con bines de 40 keV cuyas razones de ramificación se calculan mediante el modelo estadístico [146].

La resolución matemática del problema inverso presentado en la Ecuación IV.5 se efectúa utilizando distintos algoritmos de deconvolución. En concreto, en este trabajo se ha utilizado el algoritmo de Esperanza-Maximización (EM) basado en el teorema de Bayes, siguiendo la formulación matemática propuesta por el grupo de Valencia [137]. El algoritmo de Máxima Entropía (ME) [137] ha sido, asimismo, utilizado en todos los análisis de este trabajo con el fin de estudiar el impacto del método de deconvolución en las intensidades β obtenidas.

Aplicaciones

Actualmente existen en Física nuclear innumerables temas de gran interés. De entre todos ellos, en los últimos años se han identificado algunos en los que la técnica de absorción total puede aportar resultados de elevado impacto al determinar las intensidades β libres del efecto *Pandemonio*. A continuación se procede a detallar brevemente las aplicaciones en las que esas intensidades resultan de especial valor, y que han motivado las medidas

presentadas en este trabajo.

- Desintegración doble β

  Este proceso tiene lugar en algunos núcleos ${}^{A}_{Z}\mathrm{X}_{N}$ cuando se desintegran directamente a ${}^{A}_{Z\pm2}\mathrm{X}_{N\mp2}$, debido a que el núcleo intermedio ${}^{A}_{Z\pm1}\mathrm{X}_{N\mp1}$ tiene menor energía de ligadura y la desintegración β no es posible [33]. Se trata de un proceso extremadamente lento, con vidas medias de 10^{18}-10^{22} años [34]. Hoy en día la desintegración doble β se considera una puerta a nueva Física si se llegan a encontrar hallazgos del modo sin neutrinos, que significaría que neutrino y antineutrino son la misma partícula [36, 37]. Las desintegraciones doble β con neutrinos (las únicas medidas experimentalmente hasta el momento) se consideran una fuente de aprendizaje para acotar las propiedades del hipotético modo sin neutrinos, puesto que los elementos de matriz involucrados son similares [39]. En ese sentido, una de las formas de validar los parámetros usados en los modelos teóricos para cálculos de sistemas emisores doble β, es a través de las medidas de las desintegraciones simples en las que el núcleo intermedio es el padre. En esta línea, la desintegración simple ${}^{100}\mathrm{Tc} \rightarrow {}^{100}\mathrm{Ru}$ es de gran interés, ya que forma parte del sistema doble β ${}^{100}\mathrm{Mo} \rightarrow {}^{100}\mathrm{Ru}$. Dicha desintegración simple ha sido estudiada únicamente en experimentos de alta resolución [53, 54] y en este trabajo se presenta la primera medida con la técnica TAGS. La intención es buscar intensidad β no detectada hasta ahora que tenga un impacto en los parámetros usados en cálculos de sistemas emisores doble β.

- Desintegración β con emisión retardada de neutrones

  Lejos de la estabilidad, cuando la ventana accesible de energías en la desintegración β supera la energía de separación de neutrones S_n, en la des-excitación desde los niveles de mayor energía compiten la emisión de rayos γ y la emisión de neutrones. El proceso de emisión retardada de neutrones juega un papel primordial en los distintos escenarios astrofísicos considerados hoy en día para la síntesis de elementos pesados más allá del hierro [63]. Se piensa que estos núcleos se producen por capturas neutrónicas merced a ingentes flujos de neutrones procedentes de violentos fenómenos como las explosiones supernova. Una vez agotado el flujo de neutrones, las desintegraciones β con emisión retardada de neutrones marcan la ruta hacia la estabilidad.

  Los cálculos teóricos de las abundancias químicas en el sistema solar dependen íntimamente de esta maraña de desintegraciones β con emisión retardada de neutrones y de los parámetros que las caracterizan, como son las masas de los núcleos implicados, las vidas medias o las probabilidades de emisión retardada de neutrones, P_n. La comparación de estos parámetros obtenidos mediante modelos teóricos [67, 68] con valores experimentales se queda corta a la hora de validar el buen comportamiento de dichos modelos. Por este motivo, una comparación de la distribución de intensidades β resulta mucho más fructífera, y la técnica TAGS es la única que permite obtener estas distribuciones completas para núcleos alejados de la estabilidad. Además, últimamente se ha puesto de manifiesto la conexión entre el proceso de captura neutrónica y la desintegración β con emisión retardada de neutrones [73–76]. Para

poder extraer conclusiones firmes de esta conexión, se precisa de una sensibilidad adecuada a las intensidades que pueblan los niveles a más alta energía de excitación, por encima de S_n, lo que de nuevo resulta posible gracias a la técnica TAGS. Por estos motivos, dos emisores retardados de neutrones de importancia, ^{137}I y ^{95}Rb, han sido estudiados en este trabajo.

- Cálculo del calor residual de un reactor

  La energía producida por la desintegración β de los productos de fisión generados en un reactor nuclear se conoce como calor residual, y representa una porción importante de la energía liberada durante el funcionamiento del mismo, así como la fuente primordial de energía cuando éste se apaga.

  El cálculo del calor residual más generalizado hoy en día se efectúa mediante un método de suma [80,86], tal y como se presenta en la Ecuación (IV.6):

$$f(t) = \sum_i (\overline{E}_{\beta,i} + \overline{E}_{\gamma,i} + \overline{E}_{\alpha,i}) \lambda_i N_i(t) \tag{IV.6}$$

  donde $f(t)$ es la potencia en función del tiempo, $\overline{E}_i$ es la energía promedio del núcleo i (con las componentes β, γ y α), λ_i es la constante de desintegración del núcleo i, y $N_i(t)$ es el número de núcleos de tipo i en el tiempo t. Las intensidades β están involucradas en el cálculo de $\overline{E}_\gamma$ y $\overline{E}_\beta$.

  El principal inconveniente de este método está asociado a la ausencia de datos nucleares para algunos núcleos y a la incompletitud de los datos disponibles para otros. Como es de esperar, muchas de las intensidades β empleadas en el cálculo pueden sufrir el efecto *Pandemonio* [17] y por ello la Agencia Internacional de la Energía Atómica (IAEA por sus siglas en inglés) realizó un listado con las medidas prioritarias que se recomendaba hacer con la técnica TAGS [85]. El impacto de las primeras medidas llevadas a cabo en esta línea conllevó una mejora dramática en la reproducción de las medidas experimentales de referencia con los cálculos suma [89]. En este trabajo, las desintegraciones de varios fragmentos de fisión de la más alta prioridad en el marco de esta problemática seguirán sus pasos.

- Determinación del espectro de antineutrinos de un reactor nuclear

  Los reactores nucleares son ricas fuentes de antineutrinos (se producen en promedio seis antineutrinos por fisión) que se vienen utilizando en los últimos tiempos para experimentos donde se estudia el fenómeno de la oscilación de neutrinos. Los experimentos actuales basados en neutrinos de reactores, utilizan en sus análisis la predicción del espectro de antineutrinos emitido por el reactor [94–96]. El flujo total de neutrinos emitidos viene dado por la Ecuación (IV.7):

$$S_{total}(E_{\overline{\nu}_e}) = \sum_k f_k S_k(E_{\overline{\nu}_e}) \tag{IV.7}$$

donde k representa el tipo de combustible, f_k es su contribución al número total de fisiones, y S_k es el correspondiente espectro de referencia de antineutrinos por fisión. En los reactores de agua a presión (PWR por sus siglas en inglés) que se usan en los experimentos de oscilación de neutrinos, el 99 % de los antineutrinos proviene de cuatro combustibles: ^{235}U, ^{238}U, ^{239}Pu y ^{241}Pu. Los espectros de referencia, $S_k(E_{\overline{\nu}})$, para estos cuatro núcleos pueden obtenerse con dos métodos distintos. El primero está basado en medidas del espectro β total de cada uno de los cuatro combustibles [99–103]. Para cada uno se hace un ajuste con distintas contribuciones de los fragmentos de fisión involucrados, y cada una de las contribuciones obtenidas se convierte en el correspondiente espectro de antineutrinos [104]. El segundo método consiste en un cálculo suma [106, 107] similar al del calor residual.

Recientemente se han desatado varias problemáticas relacionadas con la incertidumbre de los dos métodos mencionados. Una tiene que ver con la revisión del flujo de antineutrinos calculado con estos métodos, que ha desvelado un déficit en el número de antineutrinos detectados en experimentos de oscilación frente a los predichos con los formalismos de oscilación manejados hoy en día [113]. Otra problemática se relaciona con la observación experimental de un exceso de antineutrinos frente a los cálculos obtenidos con estos métodos para los principales experimentos con antineutrinos de reactores [115–117]. Ambas polémicas parecen estar estrechamente vinculadas a la incertidumbre en el cálculo de $S_k(E_{\overline{\nu}})$. Nuevamente, y en especial para el método de suma, medidas experimentales con la técnica TAGS para las desintegraciones que dominan las regiones conflictivas del espectro de antineutrinos han sido fomentadas en los últimos tiempos, dando ya sus primeros resultados [108, 133]. En este trabajo se presentan las desintegraciones β de varios fragmentos de fisión que contribuyen notablemente al espectro total de antineutrinos de los reactores.

El nuevo espectrómetro DTAS

Con el objetivo de llevar a cabo estudios de desintegración β en la futura instalación de FAIR en GSI, el grupo de Valencia ha diseñado y construido un nuevo detector de absorción total [158]. Se trata de DTAS (Decay Total Absorption γ-Ray Spectrometer), un detector segmentado compuesto por un máximo de 18 cristales rectangulares de NaI(Tl) de dimensiones 150 mm × 150 mm × 250 mm [32] fabricado por Scionix [159]. Cada cristal tiene acoplado su propio fomultiplicador (PMT por su siglas en ingles) y está rodeado por teflón, silicona y un encapsulado de aluminio [32].

La segmentación del detector introduce una doble ventaja: por un lado la posibilidad de extraer información de los espectros de multiplicidades (siendo M_m la multiplicidad de un evento registrado en DTAS, definida como el número de módulos en los que se deposita energía), y por otro la flexibilidad del montaje experimental del detector. En relación con la última, dos configuraciones principales han sido consideradas: una con 16 módulos pensada para instalaciones de fragmentación, donde DTAS se use en combinación con el detector de implantación AIDA [160], y otra con 18 módulos para instalaciones tipo ISOL. Ambas

configuraciones se muestran en la Figura IV.8.

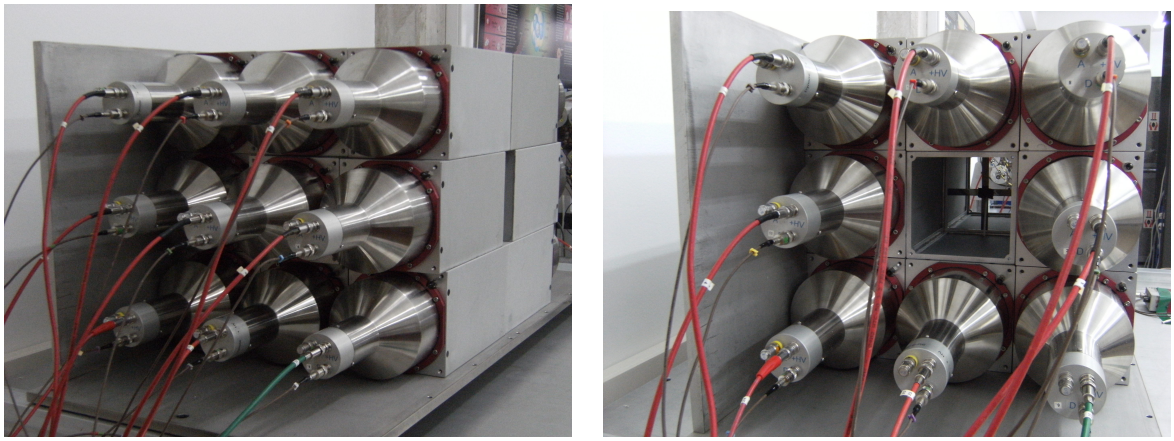

Figura IV.8: DTAS en su configuración de 16 módulos (derecha) y de 18 módulos (izqierda).

Con el objetivo de poder llevar a cabo medidas con DTAS, es necesario poder reconstruir, para cada evento, la energía total depositada en el detector y su multiplicidad M_m. Para ello se precisa sumar la energía depositada en los módulos individuales, bien electrónicamente o bien a posteriori mediante un procesado de los datos (suma software). Con esta idea en mente se ha diseñado la cadena electrónica que recoge y trata las señales de los módulos de DTAS. Para ello se han utilizado preamplificadores Mesytec MSI-8p [165] tanto para los ánodos como para los dínodos de los PMT de los módulos. Tras los preamplificadores, las señales de los dínodos han sido divididas en dos ramas: una rama ha sido enviada al módulo CAEN N625 Quad Linear FAN-in FAN-out [166] donde tiene lugar la suma electrónica de todas las señales, mientras que la otra rama ha sido llevada a módulos Mesytec MSCF-16 [165]. Los ánodos, por su parte, han sido usado con un sistema de adquisición de datos digital en pruebas. Una de las salidas del FAN-in FAN-out es procesada con un amplificador ORTEC 671 [163] para producir la señal de energía que se envía al ADC CAEN V785 [166]. La otra salida sirve para construir una señal temporal que se envía al TDC, mediante un ORTEC 474 TFA y un ORTEC 584 CFD [163]. Los módulos MSCF-16 proveen de una señal individual de tiempo y una de energía para cada módulo, las cuales son enviadas al TDC y ADC respectivamente.

Se ha puesto especial cuidado a la hora de alinear las ganancias de los módulos antes de sumar sus señales para reconstruir la energía total depositada. Este alineamiento se ha realizado ajustando los altos voltajes de los fotomultiplicadores, pero esto solo ha servido para el caso de la suma electrónica. En el caso de la suma software, las ganancias se han alineado desarrollando un algoritmo que permite trabajar cuidadosamente con las amplitudes registradas en el ADC. Esto ha permitido evitar los desplazamientos entre las distintas multiplicidades que se ha descubierto que ocasiona la no proporcionalidad de la luz producida en NaI(Tl) [173, 174] en un detector segmentado. El resultado del correcto alineamiento de los módulos y la correcta reconstrucción de la suma total a través de este algoritmo puede verse en la Figura IV.9.

Debido a oscilaciones térmicas [169] e inestabilidades en el alto voltaje aplicado a

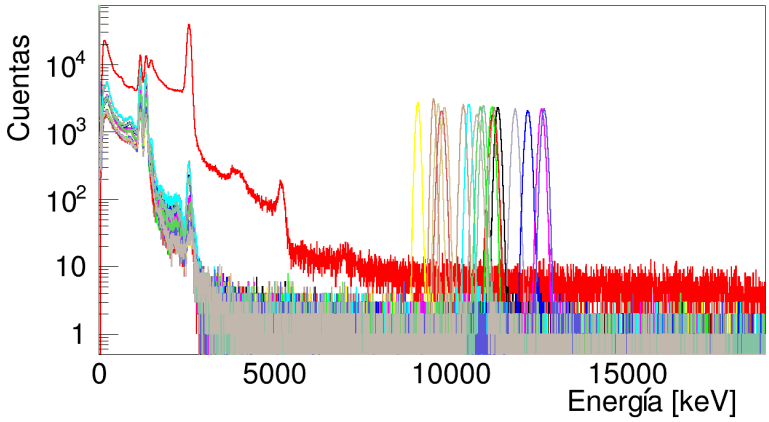

Figura IV.9: Módulos individuales de DTAS alineados mediante un algoritmo y suma software de toda la energía depositada en el detector para una fuente de calibración de ^{60}Co.

los PMT, la ganancia de los módulos individuales puede variar. Por ese motivo se ha desarrollado un sistema de corrección de ganancia basado en un generador de pulsos de luz modelo 6010 de BNC [171], un detector de referencia externo con un hueco donde colocar una fuente débil de ^{137}Cs, y un haz de fibras ópticas con el que llevar la señal de luz a cada módulo de DTAS y al detector de referencia. Los picos de luz en cada módulo permiten detectar cambios en su ganancia, mientras que el detector externo garantiza la detección de cualquier alteración en la cantidad de luz suministrada por el generador de pulsos, monitorizando la distancia entre su pico de luz y el pico característico de la fuente de ^{137}Cs.

Experimentos en IGISOL

En 2014 se llevaron a cabo en IGISOL, Jyväskylä (Finlandia) [199], los primeros experimentos con DTAS en una instalación de haces radioactivos. Por un lado, el experimento I153 [208] tuvo como objetivo medir la desintegración β del ^{100}Tc. Para ello, los núcleos de ^{100}Tc fueron producidos en una reacción (p,n) sobre un blanco de Mo, usando protones de 8 MeV procedentes del ciclotrón MCC30. Por otro lado, el experimento I154 [209] giró en torno a la medida de fragmentos de fisión producidos por protones incidiendo sobre un blanco de uranio natural. Los iones producidos fueron separados en el separador de masas de IGISOL. En ambos experimentos, el sistema de trampas de Penning JYFLTRAP [203] fue utilizado para purificar el haz que posteriormente era medido por DTAS.

El montaje experimental estaba constituido por el detector DTAS en su configuración de 18 módulos, rodeado de acero inoxidable, plomo y aluminio para reducir el fondo ambiental. En el centro de DTAS, enroscado al tubo del haz, se posicionó un detector plástico para partículas β, destinado a hacer coincidencias con DTAS (coincidencias γ-β). Se usaron dos detectores plásticos, uno con forma de vaso (para el experimento I153) y otro con forma de disco (para el experimento I154). Detrás del detector plástico en cada caso se colocó

un detector de germanio para identificar contaminantes en las medidas (actividades de los descendientes, isómeros, etc.). Finalmente, en el experimento I154 se empleó una unidad de cinta en la que implantar los núcleos de interés seleccionados en JYFLTRAP. La parte de la cinta donde tenía lugar la implantación se situaba justo enfrente del detector plástico. La cinta era movida de acuerdo con la vida media de la especie nuclear estudiada para no acumular actividad en el montaje experimental y potenciar la desintegración de interés dentro de cada cadena de desintegración. En el experimento I153 no fue necesaria la unidad de cinta y los núcleos de ^{100}Tc eran implantados directamente en el fondo del detector plástico con forma de vaso, debido a que el núcleo hijo, ^{100}Mo, es estable. En la Figura IV.10 se muestra una fotografía con el emplazamiento de DTAS detrás de JYFLTRAP, así como esquemas de los montajes experimentales de los dos experimentos.

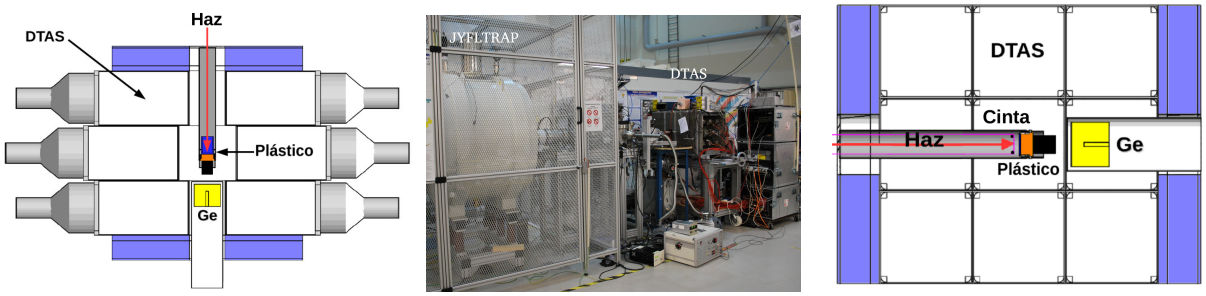

Figura IV.10: Corte lateral de la geometría del experimento I154 (derecha) y corte horizontal de la geometría del experimento I153 (izquierda): DTAS (en blanco) rodeado de plomo (en violeta), el tubo del haz (en gris) y el detector de germanio (en amarillo). También se muestran los detectores plásticos β (en azul) con su guía de luz (en naranja) y su PMT (en negro). En el experimento I154 el sistema de cinta también se muestra. La fotografía central muestra el emplazamiento del montaje experimental de DTAS detrás de JYFLTRAP.

Para poder llevar a cabo el análisis de los experimentos según la metodología de la técnica TAGS, ha de calcularse la función de respuesta de DTAS mediante simulaciones MC. Para ello es necesario validar el código MC utilizado, comparando simulaciones de fuentes de calibración con medidas experimentales de las mismas. Se utilizaron fuentes de ^{24}Na, ^{60}Co, ^{137}Cs, ^{22}Na y una fuente combinada de ^{152}Eu-^{133}Ba para realizar la calibración en energía de DTAS y llevar a cabo la comparación con las simulaciones. El paquete de simulación Geant4 [156] (versión geant4.9.6.p03) ha sido utilizado, con la librería de física Livermore e incluyendo la no proporcionalidad de la luz producida en NaI(Tl) según [18]. La geometría detallada de todo el montaje experimental se incluyó en las simulaciones y se ha estudiado de forma específica la respuesta del detector a neutrones, así como la reproducción de las distintas multiplicidades. Un ejemplo del nivel de reproducción de las fuentes de calibración con las simulaciones MC puede verse en la Figura IV.11. La distorsión provocada por el efecto del summing-pileup es tenida en cuenta en la comparación. Esta contribución es calculada mediante un procedimiento MC basado en la superposición de dos eventos guardados en el intervalo de la ventana del ADC, y se normaliza de acuerdo a una expresión teórica basada en [180].

Tal y como se ha mencionado, el uso de detectores β permite hacer coincidencias γ-β

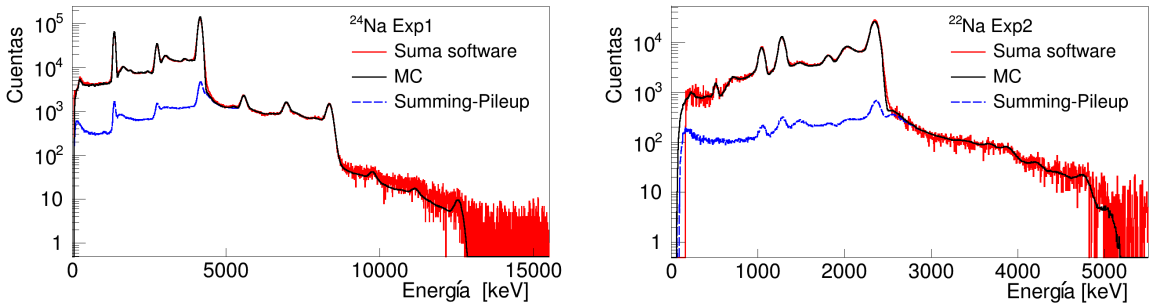

Figura IV.11: Comparación entre medidas experimentales de fuentes de calibración con DTAS y las correspondientes simulaciones MC. Fuente de ^{22}Na para el experimento I154 (derecha) y fuente de ^{24}Na para el experimento I153 (izquierda).

con DTAS destinadas a limpiar las medidas seleccionando únicamente eventos procedentes de la desintegración β. Para el análisis TAGS de un espectro en coincidencia con un detector β, resulta de vital importancia conocer de forma precisa la eficiencia de dicho detector β. Esta eficiencia tiene una dependencia muy grande con la energía del nivel que se puebla en la desintegración. Debido a la naturaleza continua de la radiación β, el umbral de detección a bajas energías afecta notablemente a la curva de eficiencia. Esta es la razón por la que conocer con la mayor precisión posible ese umbral de detección es básico de cara a cualquier análisis. Para identificarlo en el caso de los dos detectores plásticos usados en los experimentos de IGISOL, se han realizado simulaciones MC de fuentes de calibración y de algunas desintegraciones medidas. Gracias a ellas, se han podido calibrar ambos detectores y el umbral de detección ha podido ser identificado. Un ejemplo de la calidad de la reproducción de las medidas experimentales de los detectores plásticos con simulaciones MC puede verse en la Figura IV.12.

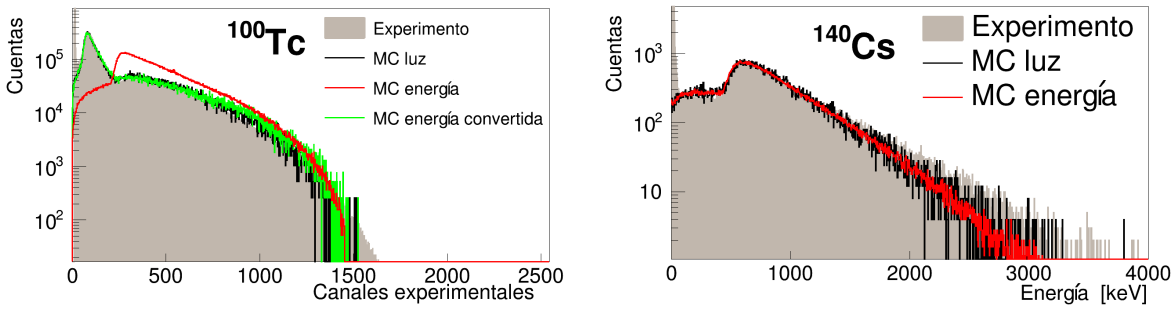

Figura IV.12: Comparación entre los espectros experimentales medidos con los detectores β usados en los experimentos de IGISOL y las correspondientes simulaciones MC (detector con forma de vaso: iquierda, detector con forma de disco: derecha).

En el caso del detector plástico con forma de vaso, el tipo de geometría ha requerido un estudio exhaustivo con simulaciones de fotones ópticos para poder reproducir la forma de los espectros experimentales. Para evitar el elevado peso computacional de las simulaciones de fotones ópticos, se ha desarrollado un método paramétrico de conversión de energía

depositada en luz recolectada, basado en el punto de deposición de la energía.

Resultados

A continuación se mencionarán los aspectos fundamentales de los análisis TAGS de las medidas llevadas a cabo en IGISOL con DTAS en coincidencia con el detector β. Resulta importante mencionar que el cálculo de errores en todos los casos se ha llevado a cabo siguiendo la filosofía de [74], de manera que todo el espacio de soluciones compatibles con los datos experimentales, produciendo un buen ajuste de los mismos, se considera como la incertidumbre sistemática asociada con la solución de referencia. Este espacio de soluciones se obtiene variando la normalización de los contaminantes, así como considerando variaciones pertinentes en la matriz de razones de ramificación. Los errores estadísticos son, en todos los casos, despreciables frente a las incertidumbres sistemáticas así calculadas.

- ^{100}Tc $\rightarrow$ ^{100}Ru (Q_β=3204 keV)

  Se ha observado que no era necesario incluir una parte continua en el esquema de niveles a la hora de construir la matriz de razones de ramificación. La contribución del summing-pileup y coincidencias aleatorias con el fondo ambiental han sido considerados como contaminantes. Los resultados obtenidos confirman los datos previos obtenidos en experimentos de alta resolución [53, 54]. No obstante, además de una ligera probabilidad de poblar un nivel que no se había visto antes de desintegración β, el análisis da como resultado una intensidad β al estado fundamental del hijo ligeramente mayor de la conocida (93.9(5) % frente a 93.3(1) %) y una menor población del primer nivel 2^+ (0.75(14) frente a 0.39(5)).

- ^{103}Tc $\rightarrow$ ^{103}Ru (Q_β=2662 keV)

  La parte conocida del esquema de niveles del hijo incluida en el análisis llega hasta 907 keV [145]. El único contaminante considerado es el summing-pileup. En este análisis se encuentra una increíble insensibilidad al valor de la intensidad β al estado fundamental del hijo (pudiendo variar de 10 % a 90 % produciendo un ajuste razonable del espectro). Este hecho parece deberse a que la forma de la respuesta a estado fundamental tiene la misma pendiente que el espectro total. Mediante un método de conteo basado en el trabajo de R. C. Greenwood *et al.* in [134], se ha podido obtener un valor I_0=46(2) % (frente a $I_{g.s.}$ = 34(8) % de la bibliografía [220]). Se extrae un poco de intensidad β no vista hasta ahora, pero las diferencias no son grandes respecto a los datos previos de esta desintegración.

- ^{103}Mo $\rightarrow$ ^{103}Tc (Q_β=3635 keV)

  El grado de conocimiento previo de esta desintegración y del esquema de niveles del núcleo hijo es muy escaso. Las intensidades γ de la única medida de desintegración β [222] han sido usadas para construir el esquema de niveles a bajas energías, cambiando a mano la intensidad de la transición de 1085.95 keV. El summing-pileup y la desintegración del hijo se han tomado en cuenta como contaminantes de esta medida.

Se ha encontrado intensidad β nueva y se ha llevado a cabo la primera evaluación de la distribución de intensidad de esta desintegración. El análisis del espectro sin coincidencia con el detector β, sustrayendo el fondo ambiental, confirma esta distribución de intensidad.

- ^{140}Cs $\rightarrow$ ^{140}Ba (Q_β=6220 keV)

  La parte conocida del esquema de niveles ha sido tomada hasta 2.52 MeV [145]. Como único contaminante se ha considerado el summing-pileup. Los resultados previos con la técnica TAGS obtenidos por Greenwood *et al.* [131] están en buen acuerdo con los resultados obtenidos con DTAS. Ambas medidas TAGS discrepan notablemente de las medidas de alta resolución, mostrando la influencia del efecto *Pandemonio*.

- ^{100gs}Nb $\rightarrow$ ^{100}Mo (Q_β=6386 keV)

  El isómero de bajo espín (1^+) se puebla a través de la desintegración del padre, el ^{100}Zr, cuyo estado fundamental es 0^+. Esto garantiza no poblar el isómero de alto espín (un 5^+). La contaminación de la desintegración del padre logra aislarse gracias a un método de separación de las componentes de una cadena de desintegración con una sola medida experimental. El esquema de niveles conocido del ^{100}Mo se considera completo hasta 2339.8 keV de energía de excitación [145]. Junto a la contaminación de la desintegración del padre se considera también el summing-pileup. Una cantidad reseñable de intensidad β nueva es obtenida en el análisis.

- ^{100m}Nb $\rightarrow$ ^{100}Mo (Q_β=6700 keV)

  Una medida conjunta de los dos isómeros de ^{100}Nb permite sustraer la componente de bajo espín y asilar la de alto espín. Como contaminantes se cuenta con el summing-pileup y la desintegración del ^{100gs}Nb. Para este caso también se encuentra una cantidad cuantiosa de intensidad β nueva.

- ^{102m}Nb $\rightarrow$ ^{102}Mo (Q_β=7210 keV)

  Análogamente al caso de los isómeros en ^{100}Nb, el isómero de bajo espín (1^+) se puebla a través de la desintegración del padre, el ^{102}Zr, cuyo estado fundamental es 0^+. Esto garantiza no poblar el isómero de alto espín (un 4^+). La contaminación de la desintegración del padre logra aislarse gracias a un método de separación de las componentes de una cadena de desintegración con una sola medida experimental. El esquema de niveles conocido del ^{102}Mo se considera completo hasta 1398.39 keV de energía de excitación [145]. Junto a la contaminación de la desintegración del padre se considera también el summing-pileup. La distribución de intensidad β obtenida en el análisis representa el primer resultado para este isómero.

- ^{102gs}Nb $\rightarrow$ ^{102}Mo (Q_β=7305 keV) Una medida conjunta de los dos isómeros de ^{102}Nb permite sustraer la componente de bajo espín y asilar la de alto espín. Como contaminantes se cuenta con el summing-pileup y la desintegración del ^{102m}Nb. Para este caso también se encuentra una cantidad cuantiosa de intensidad β nueva.

- ^{137}I $\rightarrow$ ^{137}Xe (Q_β=6027 keV)

  Al tratarse de un emisor retardado de neutrones, resulta necesario considerar la contribución de la rama que va por neutrones. Para ello se realiza un simulación MC de esta rama y se tiene en cuenta como un contaminante, normalizado al P_n, junto al summing-pileup y a la desintegración del hijo, cuya vida media hace que no pueda separarse de la desintegración del ^{137}I. El esquema de niveles conocido del núcleo hijo se considera completo hasta 2726.140 keV [145]. Una sorprendente cantidad de intensidad β por encima de S_n es detectada. Este hecho se confirma con un análisis del espectro sin coincidencia con el detector β, sustrayendo el fondo ambiental, así como con un análisis cortando toda la rama retardada de la desintegración con una condición temporal de 20 ns para la coincidencia β-γ.

- ^{95}Rb $\rightarrow$ ^{95}Sr (Q_β=9228 keV)

  Nuevamente se trata de un emisor retardado de neutrones, y la contribución de la rama que va por neutrones es simulada y normalizada al P_n. Esta contribución se considera como un contaminante junto al summing-pileup y a las desintegraciones del hijo y del nieto, cuyas vidas medias hacen que su desintegración se vea en esta medida. El esquema de niveles conocido del núcleo hijo se considera completo hasta la energía de excitación 1259.7 keV [145]. La cantidad de intensidad β por encima de S_n obtenido del análisis vuelve a ser muy significativa. Este hecho se confirma con un análisis cortando toda la rama retardada de la desintegración con una condición temporal de 20 ns para la coincidencia β-γ.

La calidad de los análisis finales puede comprobarse comparando los espectros experimentales con el espectro reconstruido con las intensidades β obtenidas en los análisis, tal y como se muestra en la Figura IV.13. Cada espectro reconstruido se obtiene multiplicando la correspondiente función de respuesta por la distribución de intensidades β de referencia en cada análisis.

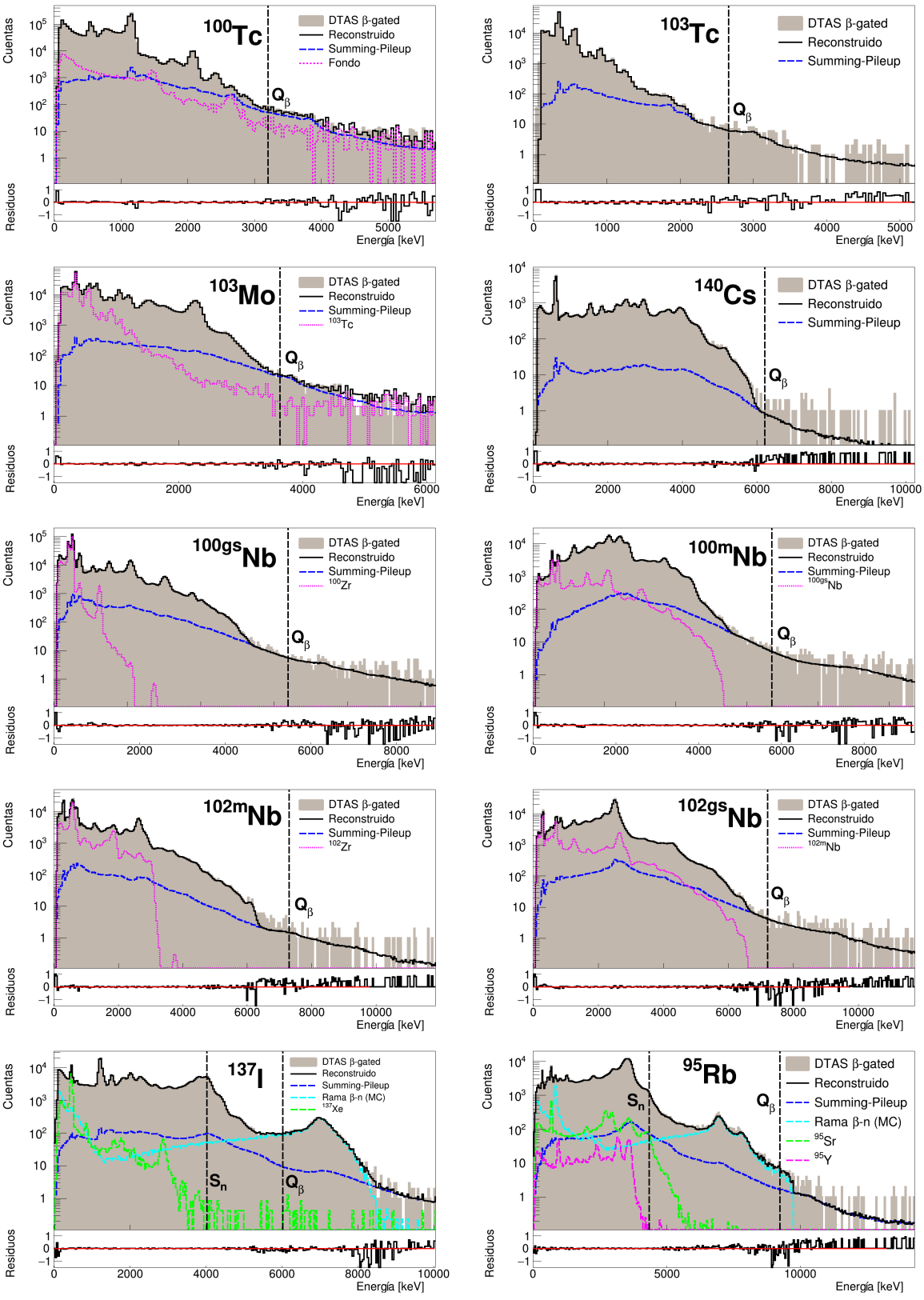

Figura IV.13: Espectro analizado comparado con el espectro reconstruido con las intensidades β obtenidas en el análisis para cada unos de los casos estudiados.

Conclusiones

- Desintegración doble β

  Los datos obtenidos para la desintegración del ^{100}Tc han sido comparados con cálculos teóricos QRPA (quasiparticle-random-phase-approximation) efectuados por J. Suhonen y O. Civitarese siguiendo la línea de sus trabajos anteriores [216–218]. Estos cálculos se muestran en concordancia con los resultados TAGS para la intensidad β que puebla el estado fundamental del ^{100}Ru y para el estado excitado a 2.052 MeV, con discrepancias de menos del 10 %. Para el resto de intensidades β, los cálculos presentan desviaciones mucho mayores, lo cual puede estar relacionado con el hecho de que el modelo empleado no contempla las deformaciones del núcleo padre y el núcleo hijo. Cuando los parámetros usados en esta comparación con la desintegración β simple del ^{100}Tc se transportan al estudio de la desintegración doble β con neutrinos del ^{100}Mo, se encuentra que la mejor reproducción de la vida media de esta desintegración es obtenida para un valor de la constante axial-vector de acoplamiento, g_A, diferente (0.4 para reproducir lo mejor posible la desintegración β del ^{100}Tc frente a 0.6 para reproducir la vida media de la desintegración doble β con neutrinos del ^{100}Mo). Se trata de un conflicto que ya había sido observado con anterioridad. Es por ello que el sistema $A = 100$- Mo, Tc y Ru - continúa siendo un desafío para los modelos nucleares que intentan describir satisfactoriamente ambos procesos.

- Desintegración β con emisión retardada de neutrones

  Como ya se ha comentado, la intensidad β obtenida para los emisores ratardados de neutrones por encima de S_n des-excitando mediante rayos γ, P_γ, es llamativamente grande, siendo un 55 % de la intensidad β total por encima de S_n para ^{137}I y un 26 % para ^{95}Rb. Los resultados se encuentran recogidos en la Tabla IV.5. La situación en ambos casos es similar a lo encontrado en la desintegración de ^{87,88}Br [73, 74] y puede ser entendida como una efecto de estructura nuclear. Las transiciones permitidas en la desintegración de ^{137}I pueblan estados de paridad positiva con J=5/2, 7/2, 9/2, de manera que conectar los estados $7/2^+$ y $9/2^+$ con el estado fundamental del ^{136}Xe (0^+) precisa de la emisión de neutrones con un momento angular orbital l=4 estando, por tanto, muy suprimida. Lo mismo sucede con el ^{95}Rb, en el que se pueblan estados de paridad negativa con J=3/2, 5/2, 7/2 y la emisión de neutrones con l=3 de momento angular es requerida para poblar el estado fundamental (0^+) del ^{94}Sr desde los estados $5/2^-$ y $7/2^-$.

Núcleo	P_γ ENSDF [%]	P_γ DTAS [%]	P_n [%]
^{137}I	2.76	$8.88^{+1,96}_{-1,53}$	7.33(38)
^{95}Rb	0.57	$3.08^{+0,87}_{-1,03}$	8.87(29)

Tabla IV.5: Integral de $I_{\beta\gamma}$ por encima de S_n (P_γ) obtenida con DTAS comparada con los valores de ENSDF y con la probabilidad de emisión de neutrones, P_n.

- Cálculo del calor residual de un reactor

  Las distribuciones de intensidad β obtenidas para los productos de fisión estudiados en este trabajo se han utilizado para evaluar las correspondientes energías promedio γ y β que intervienen en el cálculo del calor residual de acuerdo con la Ecuación (IV.6). Los resultados, comparados con las energías promedio disponibles en las principales bases de datos nucleares (ENDF/B-VII.1. y JEFF-3.11) se presenta en la Figura IV.14.

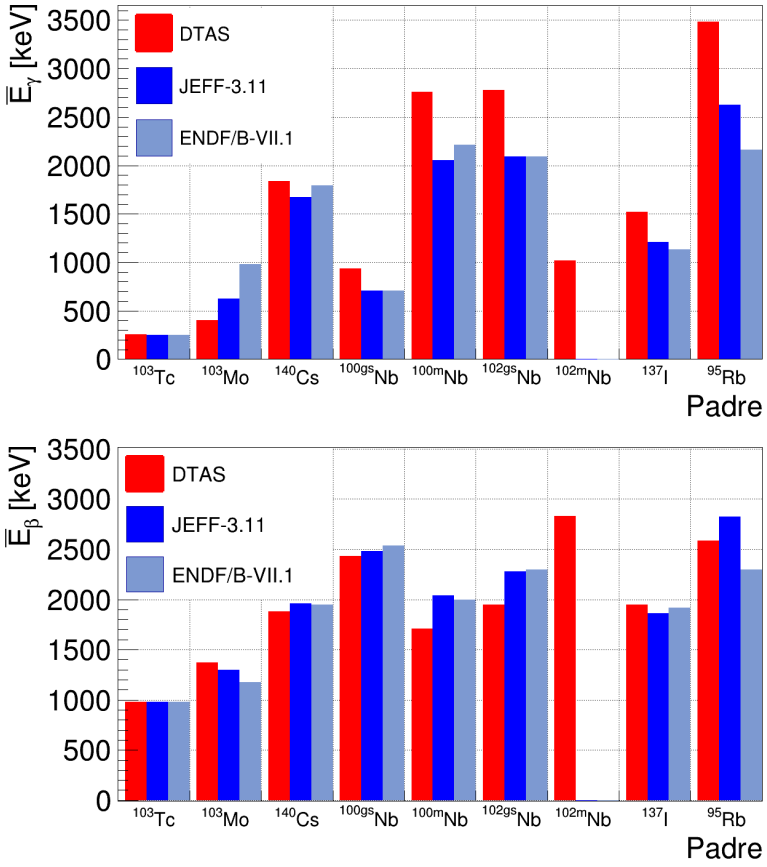

Figura IV.14: Energías promedio γ y β calculadas para las distribuciones de intensidad β de las desintegraciones estudiadas en este trabajo. Las correspondientes energías promedio de las bases de datos nucleares ENDF/B-VII.1. y JEFF-3.11 se muestran por comparación.

Como puede observarse, existen diferencias entre las energías promedio de este trabajo y las de las bases de datos, excepto para la desintegración del ^{103}Tc, donde la reducida cantidad de intensidad β nueva detectada se compensa con el incremento en la intensidad β al estado fundamental del núcleo hijo. Para el resto de los casos queda al descubierto la tendencia asociada al efecto *Pandemonio*: las energías promedio γ aumentan, mientras que las energías promedio β disminuyen. Para el ^{103}Mo esta tendencia tiene el sentido opuesto, aunque no está claro de dónde salen las energías promedio disponibles en las bases de datos para este caso, puesto que no hay información experimental sobre la distribución de intensidades β. Análogamente, tampoco hay información experimental sobre la distribución de intensidades β para

la desintegración del ^{102m}Nb, de forma que las energías medias no pueden compararse con valores previos.

Las mayores diferencias se observan para el ^{100m}Nb, el ^{102gs}Nb y el ^{95}Rb, con un aumento de $\overline{E}_\gamma$ que ronda el 30 %, y una disminución de $\overline{E}_\beta$ de aproximadamente el 15 % para los isótopos de niobio y de alrededor de un 8 % para el rubidio.

El impacto de estas nuevas energías medias en el cálculo del calor residual ha sido evaluado por A. A. Sonzogni con la base de datos ENDF/B-VII.1 en el marco del método de suma (Ecuación (IV.6)). Los resultados prliminares para ^{235}U y ^{239}Pu pueden verse en la Figura IV.15, con un aumento de la componente γ superior al 6 % y una dismunción de la componente β de casi un 2 % en ambos casos alrededor de 10 s.

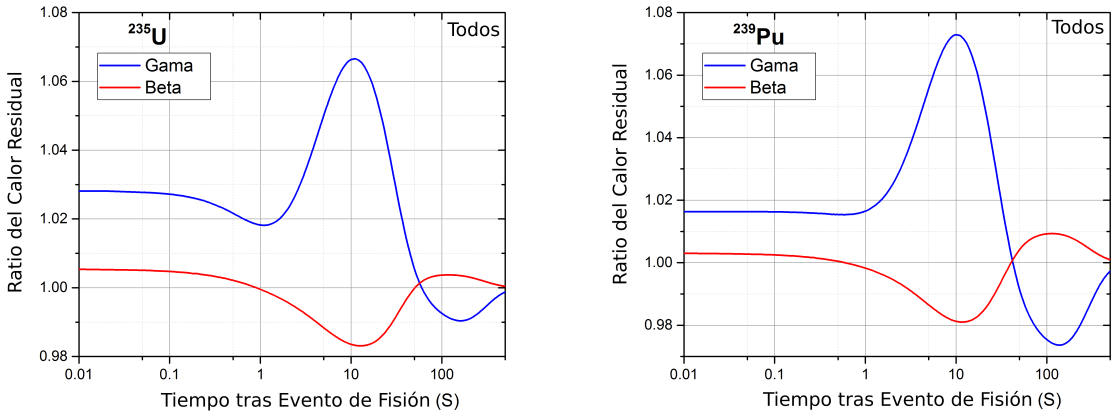

Figura IV.15: Cociente (en función del tiempo) entre el calor residual obtenido cuando los datos de este trabajo reemplazan los de la librería ENDF/B-VII.1 y el calor residual calculado con la librería original. Esta evaluación preliminar del impacto de los presentes resultados ha sido realizada por A. A. Sonzogni (NNDC, Brookhaven National Laboratory) para las componnetes γ y β del calor residual del ^{235}U y del ^{239}Pu.

- Determinación del espectro de antineutrinos de un reactor nuclear

  Las intensidades β obtenidas pueden usarse para evaluar la forma del espectro de antineutrinos asociado a cada una de las desintegraciones estudiadas, tal y como se muestra en la Figura IV.16. Estos espectros han sido evaluados también con los datos disponibles en ENSDF (así como con los datos previos de TAGS para el ^{140}Cs [131]). Como puede verse en la comparación de la Figura IV.16 existen claras diferencias en la forma de los espectros de antineutrinos, con una tendencia a que los espectros calculados con los datos de este trabajo se desplacen hacia menores energías, debido al efecto *Pandemonio*.

El impacto de estas diferencias en la forma de los espectros de antineutrinos ha sido evaluado por M. Fallot y M. Estienne (Subatech, Nantes) mediante el método de suma. Los resultados preliminares se muestran en la Figura IV.17, con un impacto bastante relevante

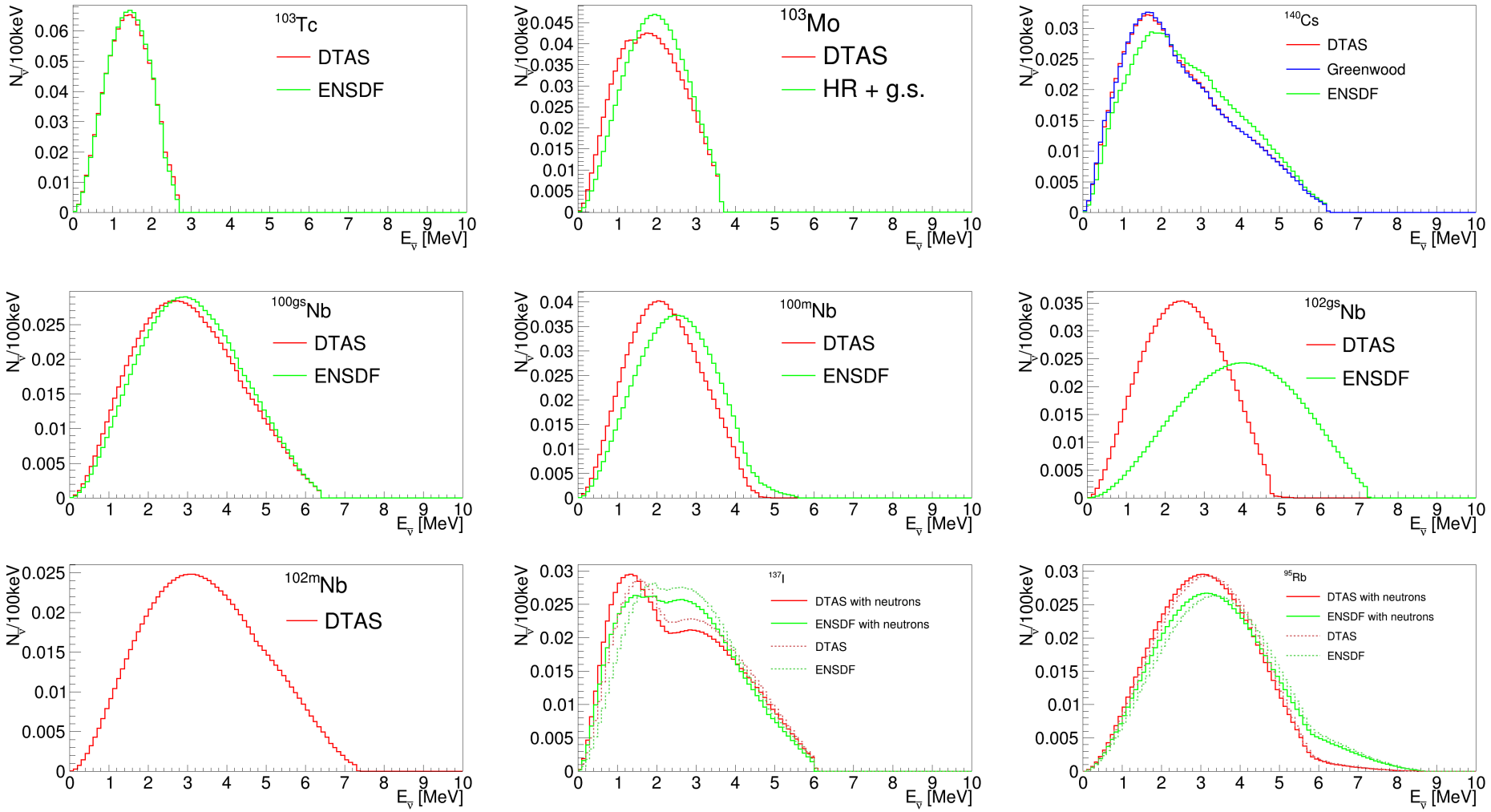

Figura IV.16: Espectro de antineutrinos para las desintegraciones β de los fragmentos de fisión estudiados. Comparación de la forma del espectro calculado con las intensidades β obtenidas en este trabajo y con los datos disponibles en ENSDF.

en los espectros de los cuatro isótopos principales del combustible de los reactores PWR, especialmente en los isótopos de plutonio.

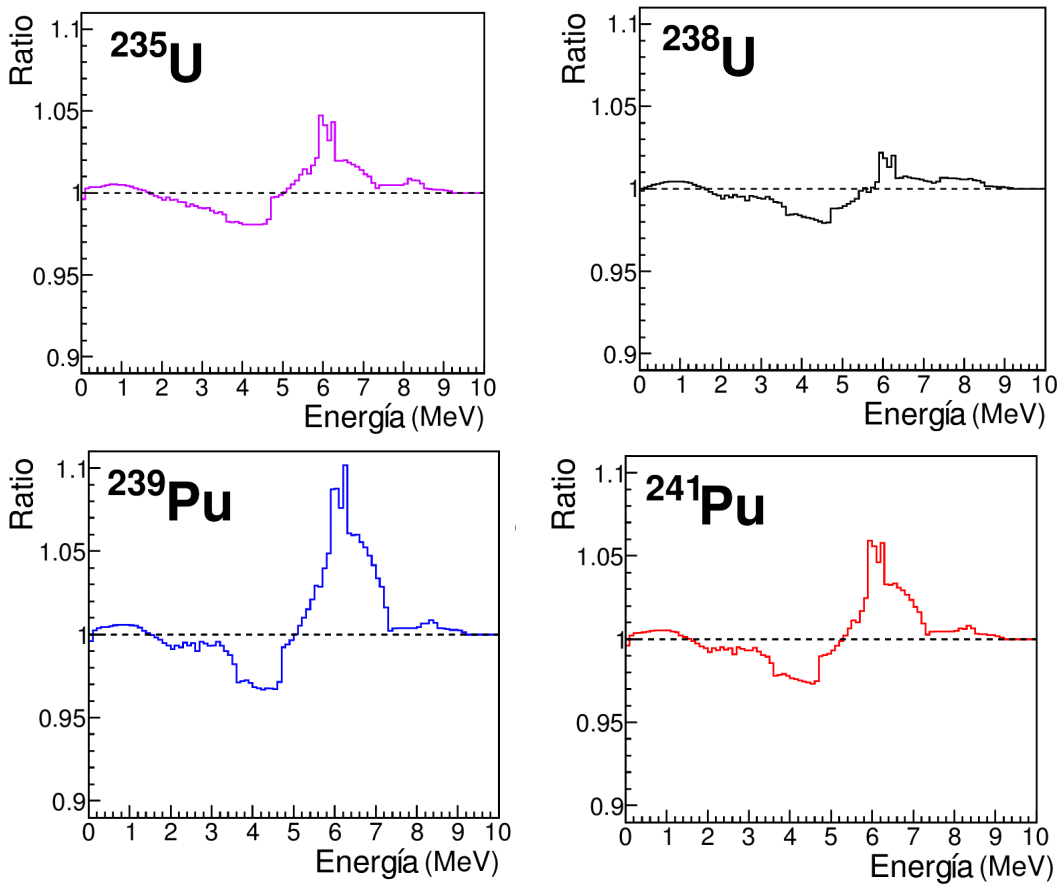

Figura IV.17: Cociente (en función de la energía) entre el espectro de antineutrinos obtenido cuando los datos de este trabajo reemplazan los datos previamente utilizados y el espectro original. Esta evaluación preliminar del impacto de los presentes resultados ha sido efectuada por M. Fallot y M. Estienne (Subatech, Nantes) para los principales isótopos que actúan como combustibles en reactores PWR: ^{235}U, ^{238}U, ^{239}Pu y ^{241}Pu.

Appendix A

Electronics

> Si tiras una rosa al río Hudson en sus misteriosas fuentes en las Adirondacks, podemos pensar en todos los sitios por los que pasará en su camino hasta el mar
>
> *If you drop a rose in the Hudson River at its mysterious source in the Adirondacks, think of all the places it journeys by as it goes out to sea forever*
>
> Jack Kerouac

In this appendix, details about the electronics of the experiments performed at IGISOL with DTAS are presented. A diagram with a schematic layout of the electronics is shown in Figure A.2. Tables A.1, A.2, A.3 and A.4 summarize the main settings of the electronic modules employed.

For the DTAS detector, in the first stage after the PMT, we used Mesytec MSI-8p preamplifiers [165] both for the anodes and the dynodes of the modules. The dynode signals were divided in two branches after the preamp, and one branch was processed with Mesytec MSCF-16 shapers [165], which provided energy and timing information for individual modules. The other branch was sent to a CAEN N625 Quad Linear Fan in-Fan out [166] that was used to add the signals from the individual modules. One output of the Fan in-Fan out was processed in an ORTEC 671 amplifier [163] to obtain the hardware sum energy signal. The other output of the Fan in-Fan out was used to generate a global timing signal with an ORTEC 474 Timing Filter Amplifier, and an ORTEC 584 Constant Fraction Discriminator [163]. This signal was used to trigger our Data Acquisition System (DACQ) and generate the gates for the ADC and the common start signal for the TDC. The anode signals were used in parallel with a new self-triggering system that was being tested, but was not used in the final analysis. The Light Pulser unit was connected by means of optical fibers to all the modules of DTAS, as well as to the external reference detector, as explained in Chapter 4. The Light Pulser was operated with gain 1.45, coarse width 500 ns and maximum fine width, coarse delay of 100 ns and maximum fine delay, and mode "Single pulse" with "Stabilized" and "Pulse" options. The light pulse generator was driven by a precision in-house built external clock running at a frequency of 100 Hz, with the external trigger (TTL) option. The reference detector was treated analogously to

an individual module of DTAS, with special settings in the shaper, and with a separated timing branch for the trigger.

With respect to the plastic detector, the four outputs of the Hamamatsu R7600U-M4 segmenetd PMT [178] were wired in pairs for simplicity. These two signals were integrated in CANBERRA 2005 preamplifiers [162], before being split into two branches for energy and timing reconstruction. In the energy branch the two preamplifier outputs were added and shaped with a CANBERRA 243 amplifier [162], whereas in the timing branch each preamplifier signal was processed independently with an ORTEC 474 Timing Filter Amplifier and an ORTEC 584 Constant Fraction Discriminator [163]. Both timing signals were combined in an ORTEC C04020 Quad 4-input Logic module [163] where a coincidence within a narrow time interval (20 ns) was required to fire the trigger of the data acquisition system. The coincidence requirement allowed the reduction of the noise level and lowered the energy threshold for β signals.

Finally, in the case of the HGe detector, the output of the preamp was shaped with a TENNELEC amplifier [162], while the timing branch was constructed with an ORTEC 474 Timing Filter Amplifier and an ORTEC 584 Constant Fraction Discriminator [163]. Additionally, a pulser signal was introduced in this detector. For this a BNC BH1 unit [171] was used with a positive signal of amplitude 2.5 V, delay 300 ns, fall time 50 us and options "Tail" and "Clamp OFF". This pulse generator was also driven by the external clock at a frequency of 100 Hz, with the external trigger (TTL) option.

Regarding the Data Acquisition System (DACQ), an analog system using a V785 Analog to Digital Converter (ADC) module from CAEN [166] and a V775 Time to Digital Converter (TDC) from CAEN [166], was running in parallel with a digital system operating with two SIS3316 modules and a SIS3100 control module from STRUCK [266]. The analog DACQ measured the amplitude of the shaped signals from all detectors arriving within a 6 μs gate in the ADC. Figure A.1 shows the position of the signals from the different types of detectors in relation to the common gate. The digital DACQ used signals directly from the preampliers. Both DACQ-s used different versions of the home-made GASIFIC data acquistion software, and they used as trigger signal the logic OR of all the detectors, as depicted in Figure A.2. The analog DACQ stored on disk events with energy and time information of: the 18 modules of DTAS, the hardware sum, the reference detector, the plastic detector and the HPGe detector. In addition, a clock signal from a SIS3302 module from STRUCK [266] was also stored providing a time mark (or time stamp) for each event, as well as five signals (1 MHz clock, accepted triggers, free triggers, pulser and trap extraction pulse) that were connected to a V830 scaler from CAEN [166]. The information was written in list-mode event files which were off-line converted into ROOT TTrees [181] for the analysis, with the information stored in leaves.

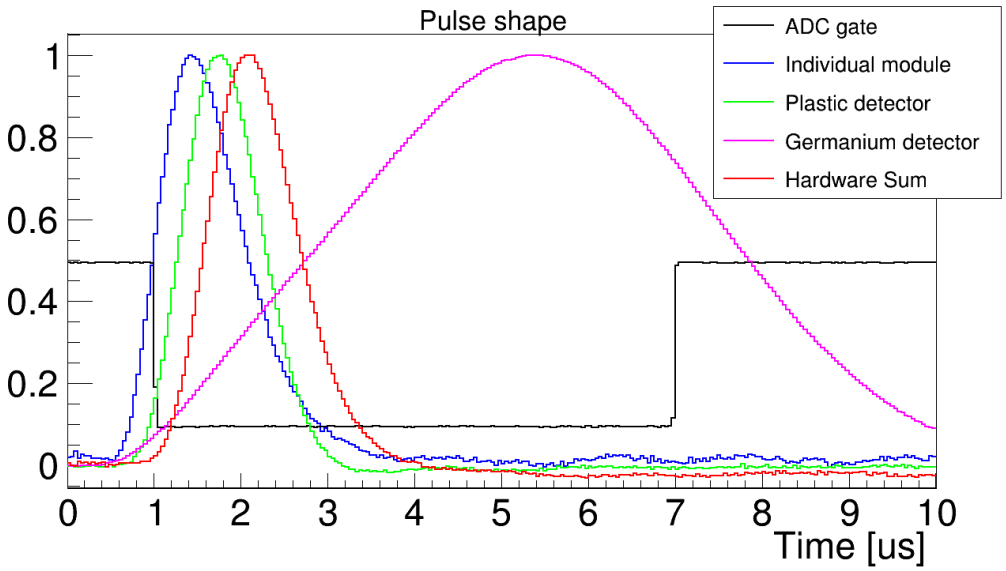

Figure A.1: Pulse shapes of all the detectors and ADC gate.

Shaper	Mode	Gain	Shap. t [μs]	PZ	BLR	Int. t [ns]	Coin. t [ns]	Threshold
1	Common	13	0.5	100	5	80	128	1
2	Single	9 and 14 (ref)	0.5	60	5	70	128	1,1,2,1,0,2

Table A.1: Settings Shapers.

Detector	DTAS	Plastic	HPGe
Coarse Gain	20	5	5
Fine Gain	0.64	0.5	0.9
Shap. t [μs]	0.5	1	4
Others	-	-	Triangular Shape

Table A.2: Settings Amplifiers.

Detector	DTAS	Ref	Plastic 1+2	Plastic 3+4	HPGe
Threshold	0.44	0.5	0.28	0.28	0.3
Delay [ns]	10 +3xTC412A	12 + 3xTC412A	16	16	60

Table A.3: Settings TFA-s.

Detector	DTAS	Ref	Plastic 1+2	Plastic 3+4	HPGe
Coarse Gain	10	20	6	6	4
Fine Gain	max	max	max	max	max
Int. t [ns]	200	200	50	50	200
Diff. t [ns]	100	50	50	50	100

Table A.4: Settings CFD-s.

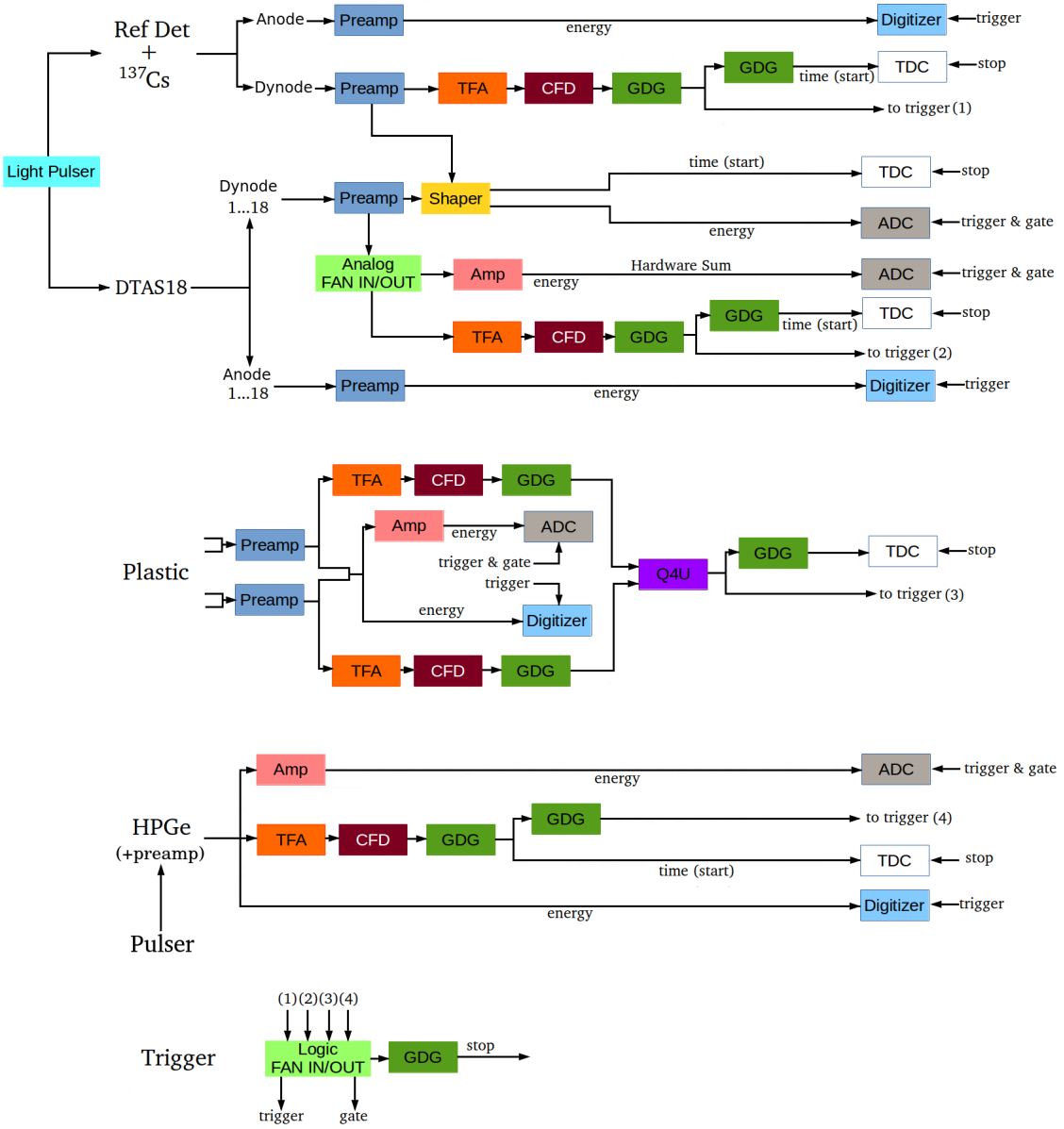

Figure A.2: Schematic diagram of the electronics of the set-up. The labels correspond to: Preamplifier (Preamp), Spectroscopic Amplifier (Amp), Timing Filter Amplifier (TFA), Constant Fraction Discriminator (CFD), Gate/Delay Generator (GDG), Time to Digital Converter (TDC), Analog to Digital Converter (ADC), Quad 4-Input Logic Unit (G4U).

Appendix B

Solving Bateman equations for a constant production rate

Nosotros que comprendemos la vida,
nos burlamos de los números

For us who understand life, figures are a matter of indifference

Antoine de Saint-Exupéry

In this appendix, the analytical solutions of Bateman equations for the particular case of a constant rate of production, R, of a certain nuclear specie, P, will be mathematically detailed. If we only take into account the parent P, the daughter Q, and the granddaughter S, with half-lives λ_1, λ_2 and λ_3 respectively, the following system of differential equations is obtained:

$$\begin{cases} \dfrac{dP(t)}{dt} = R - \lambda_1 P(t) & \text{(B.1a)} \\ \dfrac{dQ(t)}{dt} = \lambda_1 P(t) - \lambda_2 Q(t) & \text{(B.1b)} \\ \dfrac{dS(t)}{dt} = \lambda_2 Q(t) - \lambda_3 S(t) & \text{(B.1c)} \end{cases}$$

B.1 Parent

For the parent we assume a trial solution:

$$P(t) = Ae^{-\lambda_1 t} + B \tag{B.2}$$

and we require the initial condition $P(t=0) = 0$:

$$0 = A + B \Rightarrow A = -B \tag{B.3}$$

Now we go to Equation (B.1a) and we replace the solution from (B.2):

$$-\lambda_1 Ae^{-\lambda_1 t} = R - \lambda_1 (Ae^{-\lambda_1 t} + B)$$

By comparing the exponential terms we obtain:

$$B = \frac{R}{\lambda_1}$$

If we replace B in Equation (B.3), we obtain:

$$A = -\frac{R}{\lambda_1}$$

Therefore, the solution for Equation (B.1a) is:

$$\boxed{P(t) = \frac{R}{\lambda_1}(1 - e^{-\lambda_1 t})} \tag{B.4}$$

B.2 Daughter

For the daughter, we assume the following trial function in Equation (B.1b):

$$Q(t) = Ae^{-\lambda_1 t} + Be^{-\lambda_2 t} + C \tag{B.5}$$

with the initial condition $Q(t = 0) = 0$:

$$0 = A + B + C \Rightarrow B = -A - C \tag{B.6}$$

By replacing Equations (B.5) and (B.4) in (B.1b), we obtain:

$$\begin{aligned} -\lambda_1 Ae^{-\lambda_1 t} - \lambda_2 Be^{-\lambda_2 t} &= \lambda_1 \frac{R}{\lambda_1}(1 - e^{-\lambda_1 t}) - \lambda_2(Ae^{-\lambda_1 t} + Be^{-\lambda_2 t} + C) \\ &= R + e^{-\lambda_1 t}(-R - \lambda_2 A) - \lambda_2 Be^{-\lambda_2 t} - \lambda_2 C \end{aligned}$$

If we compare the exponential terms:

$$-\lambda_1 A = -R - \lambda_2 A \tag{B.7}$$

$$0 = R - \lambda_2 C \tag{B.8}$$

From Equation (B.7):

$$A = \frac{R}{\lambda_1 - \lambda_2}$$

From Equation (B.8):

$$C = \frac{R}{\lambda_2}$$

Taking this into account in Equation (B.6):

$$B = -A - C = -\frac{R}{\lambda_1 - \lambda_2} - \frac{R}{\lambda_2}$$

$$B = \frac{R\lambda_1}{\lambda_2(\lambda_2 - \lambda_1)}$$

Thus, the solution for Equation (B.1b) is:

$$\boxed{Q(t) = \frac{R}{\lambda_1 - \lambda_2}e^{-\lambda_1 t} + \frac{R\lambda_1}{\lambda_2(\lambda_2 - \lambda_1)}e^{-\lambda_2 t} + \frac{R}{\lambda_2}} \tag{B.9}$$

B.3 Granddaughter

For Equation (B.1c) we assume the trial function:

$$S(t) = Ae^{-\lambda_1 t} + Be^{-\lambda_2 t} + Ce^{-\lambda_3 t} + D \tag{B.10}$$

with the initial condition $S(t = 0) = 0$:

$$0 = A + B + C + D \Rightarrow C = -A - B - D \tag{B.11}$$

By replacing Equations (B.10) and (B.9) in B.1c, we obtain:

$$\begin{aligned} -\lambda_1 Ae^{-\lambda_1 t} - \lambda_2 Ae^{-\lambda_2 t} - \lambda_3 Ae^{-\lambda_3 t} = \lambda_2 \left(\frac{R}{\lambda_1 - \lambda_2}e^{-\lambda_1 t} + \frac{R\lambda_1}{\lambda_2(\lambda_2 - \lambda_1)}e^{-\lambda_2 t} + \frac{R}{\lambda_2} \right) \\ - \lambda_3(Ae^{-\lambda_1 t} + Be^{-\lambda_2 t} + Ce^{-\lambda_3 t} + D) \end{aligned}$$

By comparing the exponential terms:

$$-\lambda_1 A = \frac{\lambda_2 R}{\lambda_1 - \lambda_2} - \lambda_3 A \tag{B.12}$$

$$-\lambda_3 B = \frac{\lambda_1 R}{\lambda_2 - \lambda_1} - \lambda_3 B \tag{B.13}$$

$$0 = R - \lambda_3 D \tag{B.14}$$

From B.12:

$$A = \frac{\lambda_2 R}{(\lambda_1 - \lambda_2)(\lambda_3 - \lambda_1)}$$

From B.13:

$$B = \frac{\lambda_1 R}{(\lambda_2 - \lambda_1)(\lambda_3 - \lambda_2)}$$

From B.14:

$$D = \frac{R}{\lambda_3}$$

From the initial condition in Equation (B.11):

$$C = -A - B - D = -\frac{\lambda_2 R}{(\lambda_1 - \lambda_2)(\lambda_3 - \lambda_1)} - \frac{\lambda_1 R}{(\lambda_2 - \lambda_1)(\lambda_3 - \lambda_2)} - \frac{R}{\lambda_3}$$

$$C = R\left(\frac{1}{\lambda_2 - \lambda_1}\left(\frac{\lambda_3}{\lambda_3 - \lambda_1} - \frac{\lambda_1}{\lambda_3 - \lambda_2}\right) - \frac{1}{\lambda_3}\right)$$

If we replace in Equation (B.10), the solution of B.1c is:

$$\boxed{\begin{aligned} S(t) = {} & \frac{\lambda_2 R}{(\lambda_1 - \lambda_2)(\lambda_3 - \lambda_1)} e^{-\lambda_1 t} + \frac{\lambda_1 R}{(\lambda_2 - \lambda_1)(\lambda_3 - \lambda_2)} e^{-\lambda_2 t} + \\ & R\left(\frac{1}{\lambda_2 - \lambda_1}\left(\frac{\lambda_3}{\lambda_3 - \lambda_1} - \frac{\lambda_1}{\lambda_3 - \lambda_2}\right) - \frac{1}{\lambda_3}\right) e^{-\lambda_3 t} + \frac{R}{\lambda_3} \end{aligned}} \tag{B.15}$$

Appendix C

Decomposition of two spectra in a decay chain

Los efectos de las partículas radioactivas en el cuerpo humano (...) no son nada nuevo para los viejos amantes de la poesía

The effects of radioactive particles on the human body (...) are nothing new to old poetry-lovers

J. D. Sallinger

In this Appendix, a method to separate two components of a decay chain from a single measurement will be mathematically described. This method relies on the possibility of setting offline different lengths for the implantation cycle up to the length fixed in the experimental measurement. In the experiments performed with DTAS at IGISOL this was possible thanks to the study of the number of β particles detected in the plastic detector as a function of the clock signal, as shown in Figure C.1. This method is inspired in the work of Rudstam *et al.* [234] where measurements with different cycles were performed to separate the components of decay chains.

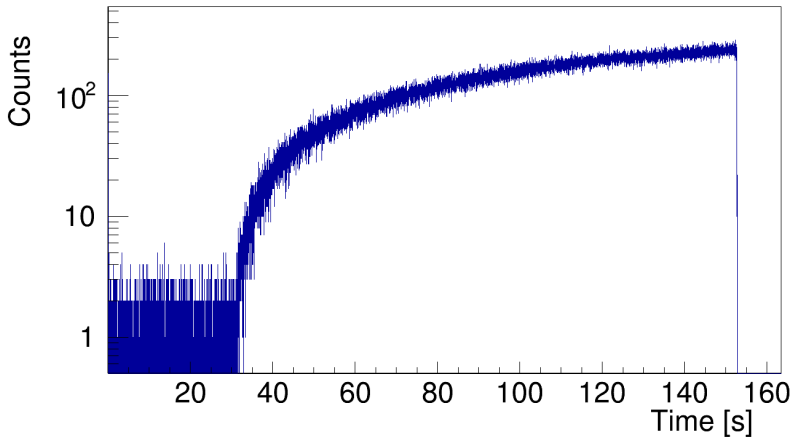

Figure C.1: Number of β particles detected in the plastic detector along the cycle for the measurement of the decay of ^{103}Mo.

If the decay chain has two components, two lengths of the implantation cycle are needed.

If the total spectrum for a given length has T_j counts in bin j, the aim of this procedure is to extract the number of counts corresponding to each of the two components, S_j^1 and S_j^2. The weights of these components, α_1 and α_2, are given by the Bateman equations discussed in Appendix B. For two cycle lengths, the following system of $2 \times N$ equations and $2 \times N$ variables is obtained, with N the number of experimental bins:

$$\begin{cases} T_j = \alpha_1 S_j^1 + (1-\alpha_1) S_j^2 & \text{(C.1a)} \\ T_j^{'} = \alpha_1^{'} S_j^1 + (1-\alpha_1^{'}) S_j^2 & \text{(C.1b)} \end{cases}$$

By simply getting S_j^1 on one side of equation C.1a and then replacing in equation C.1b, S_j^2 is obtained, so that S_j^1 can be straightforwardly evaluated too:

$$\begin{cases} S_j^1 = \dfrac{1}{\alpha_1}\left(T_j - (1-\alpha_1)\dfrac{T_j^{'} - \dfrac{\alpha_1^{'}}{\alpha_1} T_j}{1-\alpha_1^{'} - \dfrac{\alpha_1^{'}}{\alpha_1}(1-\alpha_1)} \right) & \text{(C.2a)} \\ S_j^2 = \dfrac{T_j^{'} - \dfrac{\alpha_1^{'}}{\alpha_1} T_j}{1-\alpha_1^{'} - \dfrac{\alpha_1^{'}}{\alpha_1}(1-\alpha_1)} & \text{(C.2b)} \end{cases}$$

It is important to note that this procedure requires the two total spectra to have the same number of counts, which implies applying a global scaling factor to one of them.

A very important question now is how to evaluate errors associated to the disentangled spectra. If we avoid the error in the calculation of the weights with Bateman equations, as well as the error in the length of the cycle (essentially related to the error in the timing calibration), statistical errors will be the most important. From this point of view, the errors associated to the Poisson statistics of the total spectra have to be propagated (σ_{T_j} and $\sigma_{T_j^{'}}$). For this, the original statistics of these spectra before scaling to the same number of counts has to be considered. The expressions for the statistical errors of the extracted spectra, $\sigma^2_{S_j^1}$ and $\sigma^2_{S_j^2}$, are presented in Equations (C.3a) and (C.3b).

$$\begin{cases} \sigma^2_{S_j^1} = \sigma^2_{T_j} \dfrac{1}{\alpha_1^2} \left(1 + \dfrac{\dfrac{\alpha_1^{'}}{\alpha_1}(1-\alpha_1)}{1-\alpha_1^{'} - \dfrac{\alpha_1^{'}}{\alpha_1}(1-\alpha_1)} \right)^2 + \sigma^2_{T_j^{'}} \dfrac{1}{\alpha_1^2} \left(\dfrac{1-\alpha_1}{1-\alpha_1^{'} - \dfrac{\alpha_1^{'}}{\alpha_1}(1-\alpha_1)} \right)^2 & \text{(C.3a)} \\ \sigma^2_{S_j^2} = \sigma^2_{T_j} \left(\dfrac{\dfrac{\alpha_1^{'}}{\alpha_1}}{1-\alpha_1^{'} - \dfrac{\alpha_1^{'}}{\alpha_1}(1-\alpha_1)} \right)^2 + \sigma^2_{T_j^{'}} \left(\dfrac{1}{1-\alpha_1^{'} - \dfrac{\alpha_1^{'}}{\alpha_1}(1-\alpha_1)} \right)^2 & \text{(C.3b)} \end{cases}$$

As a proof of the validity of this method, we have applied it to the experimental measurement of the decay of ^{103}Mo, where the activity of the daughter, ^{103}Tc, is a contaminant

(see Chapter 9 for details). Since the decay of ^{103}Tc was measured independently, as explained in Chapter 8, we can compare this measurement with the spectrum obtained from the decomposition method presented here.

The implantation time of the measurement of ^{103}Mo is 120.15 s, as presented in Figure C.1 (see also Table 6.1 of Chapter 6). The resulting β-gated DTAS spectra for the different time windows within this implantation time are presented in Figure C.2. The corresponding weights for the ^{103}Tc contribution as a fraction of unity for these times are 0.021, 0.040, 0.075, 0.107, 0.135, 0.160, 0.182, 0.203, 0.221, 0.238, 0.253 and 0.281 respectively.

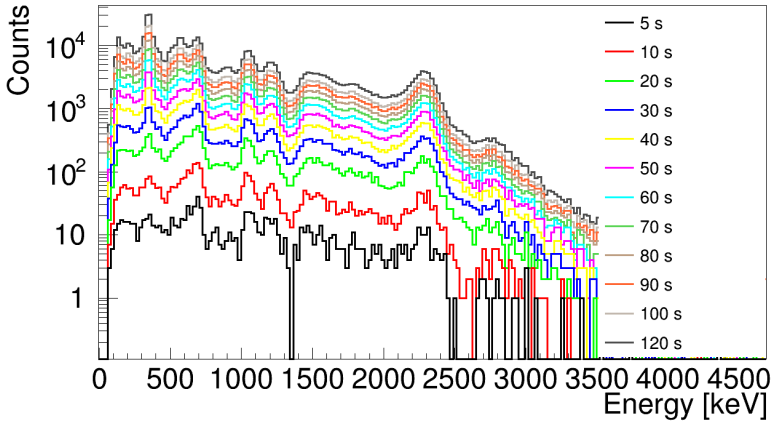

Figure C.2: Comparison of the spectra for ^{103}Mo implantation for different time windows set within the total length of the cycle (120.15 s).

With one pair of spectra from Figure C.2 we could undertake the decomposition. However, in an attempt to improve the separation we have done the decomposition for every pair of spectra, and then we computed the average of all the combinations (weighted by a factor dependent on the statistics of the original spectra). It has to be noted that this procedure is not applied directly to the spectra shown in Figure C.2, but to these spectra after subtracting the corresponding summing-pileup contribution. The resulting spectrum extracted with this method is shown in Figure C.3, and it is in good agreement with the experimental measurement (subtracted from the summing-pileup contribution). The agreement is excellent up to 600 keV, although from this energy onward the statistical fluctuations are dominant, showing the main limitation of this method.

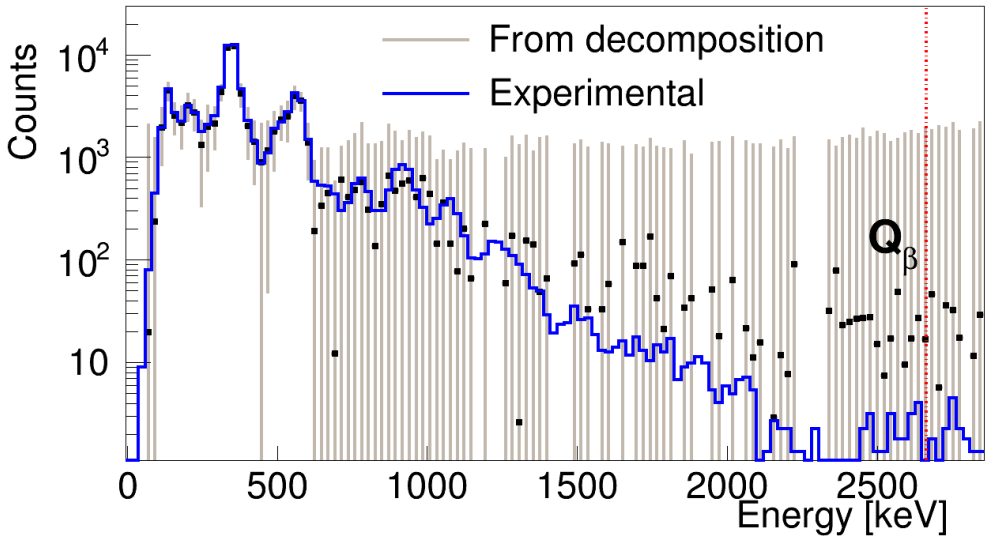

Figure C.3: Spectrum of the decay of ^{103}Tc (grey) extracted with different time windows from the measurement of the decay of ^{103}Mo as explained in the text. The spectrum is compared with the experimental measurement of the decay of ^{103}Tc (blue).

Appendix D

A β-γ counting method for g.s. feeding calculation

El pensamiento es solo un relámpago en medio de una larga noche. Pero ese relámpago lo es todo

Thought is only a gleam in the midst of a long night. But it is this gleam which is everything

Henri Poincaré

A β-γ counting method for ground state (g.s.) feeding calculation with TAGS data was proposed by R. C. Greenwood *et al.* in [134]. It was based on evaluating the experimental number of β particles detected above the threshold, and the experimental number of β-γ coincidences detected (corrected for the bremsstrahlung associated with the ground state branch). The connection between these two quantities with the β intensities and the detection efficiencies presented in that work for N decays could be written as follows:

$$\begin{aligned} N_\beta &= N\left(\varepsilon_\beta^0 I_0 + \sum_{i\geq 1}\varepsilon_\beta^i I_i\right) = N\left(\varepsilon_\beta^0 I_0 + \overline{\varepsilon}_\beta^*(1-I_0)\right) \\ N_{\beta TAS}^* &= N\left(\sum_{i\geq 1}\varepsilon_\beta^i I_i \sum_{i\geq 1}\varepsilon_{TAS}^i I_i\right) = N(1-I_0)\left(\overline{\varepsilon}_\beta^*\overline{\varepsilon}_{TAS}^*\right) \end{aligned} \tag{D.1}$$

where we define the average detection efficiencies for the decay to excited levels $\overline{\varepsilon}_\beta^* = \frac{\sum_{i\geq 1}\varepsilon_\beta^i f_i}{\sum_{i\geq 1} f_i}$ and $\overline{\varepsilon}_{TAS}^* = \sum_{i\geq 1}\varepsilon_{TAS}^i I_i$, being $f_i = NI_i$ the number of decays when level i is fed, with $\sum_{i\geq 1} f_i = N(1-I_0)$.

From the ratio between the two expressions in Equation (D.1), a formula for the computation of the ground state feeding probability is obtained, equivalent to the formula presented in [134]:

$$I_0 = \frac{1 - \dfrac{N_{\beta TAS}^*}{N_\beta}\dfrac{1}{\overline{\varepsilon}_{TAS}^*}}{1 + \dfrac{N_{\beta TAS}^*}{N_\beta}\dfrac{\varepsilon_\beta^0 - \overline{\varepsilon}_\beta^*}{\overline{\varepsilon}_\beta^*\overline{\varepsilon}_{TAS}^*}} \tag{D.2}$$

Recently, this method has been revisited by J. L. Tain *et al.* [267], reconsidering the assumptions in the evaluation of the number of β-γ coincidences as in Equation (D.3), so that the β penetration in the spectrometer is taken into account, and the efficiencies of β and TAGS detectors are not treated independently ($\overline{\varepsilon}^*_{\beta TAS} \neq \overline{\varepsilon}^*_{\beta}\overline{\varepsilon}^*_{TAS}$). As a result a new expression for $N_{\beta TAS}$ is obtained in Equation (D.3).

$$N_{\beta TAS} = N\left(\varepsilon^0_{\beta TAS} I_0 + \sum_{i\geq 1} \varepsilon^i_{\beta TAS} I_i\right) = N\left(\varepsilon^0_{\beta TAS} I_0 + \overline{\varepsilon}^*_{\beta TAS}(1 - I_0)\right) \tag{D.3}$$

where $\overline{\varepsilon}^*_{\beta TAS} = \dfrac{\sum_{i\geq 1} \varepsilon^i_{\beta TAS} f_i}{\sum_{i\geq 1} f_i}$.

The I_0 obtained with the ratio of N_β and the $N_{\beta TAS}$ from Equation (D.3) is presented in Equation (D.4).

$$I_0 = \frac{1 - \dfrac{N_{\beta TAS}}{N_\beta}\dfrac{\overline{\varepsilon}^*_{\beta}}{\overline{\varepsilon}^*_{\beta TAS}}}{1 + \dfrac{N_{\beta TAS}}{N_\beta}\dfrac{\varepsilon^0_\beta - \overline{\varepsilon}^*_\beta}{\overline{\varepsilon}^*_{\beta TAS}} - \dfrac{\varepsilon^0_{\beta TAS}}{\overline{\varepsilon}^*_{\beta TAS}}} \tag{D.4}$$

The different efficiencies can be obtained straightforwardly from the response function, and we employ the β intensities from the TAGS analysis performed with this response. The most delicate point arrives when one needs to evaluate the experimental number of β particles (N_β) and the experimental number of coincidences β-γ ($N_{\beta TAS}$). In fact, this will be the major source of error of this method. If we call σ_R the error of the ratio between the number of counts, the corresponding error in the ground state feeding intensity determination will be:

$$\sigma_{I_0} = \frac{\dfrac{\varepsilon^0_\beta - \overline{\varepsilon}^*_\beta}{\overline{\varepsilon}^*_{\beta TAS}} + \dfrac{\overline{\varepsilon}^*_\beta}{\overline{\varepsilon}^*_{\beta TAS}}\left(1 - \dfrac{\varepsilon^0_{\beta TAS}}{\overline{\varepsilon}^*_{\beta TAS}}\right)}{\left(1 + \dfrac{N_{\beta TAS}}{N_\beta}\dfrac{\varepsilon^0_\beta - \overline{\varepsilon}^*_\beta}{\overline{\varepsilon}^*_{\beta TAS}} - \dfrac{\varepsilon^0_{\beta TAS}}{\overline{\varepsilon}^*_{\beta TAS}}\right)^2}\sigma_R \tag{D.5}$$

We have evaluated the error in the determination of I_0 with Equation D.4. For this, we have produced different MC input files with the DECAYGEN event generator [146] corresponding to fixing different ground state feeding values for the decay of ^{103}Tc, from 10 to 90%. After simulating these files, we have applied Equation D.4 to the resulting MC spectra, taking into account the β intensity distributions and the response functions that were used to produce the event files. Assuming a 5% error in the determination of the ratio $\dfrac{N_{\beta TAS}}{N_\beta}$, the errors (absolute and relative) as a function of the ground state intensity are obtained, as shown in Figure D.1.

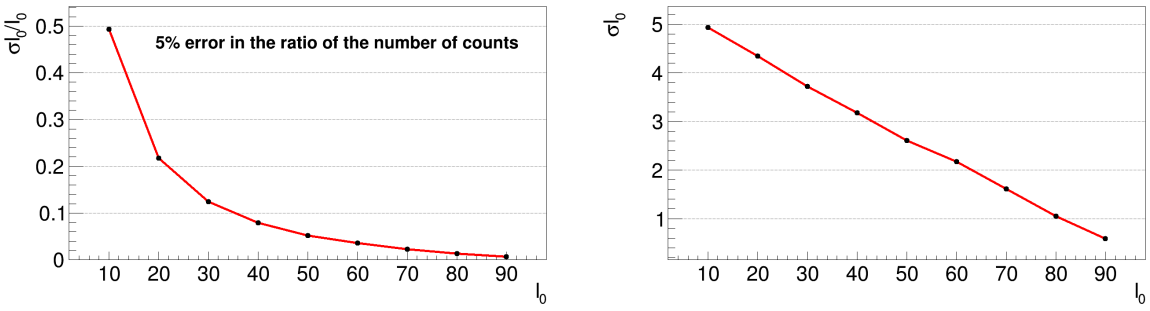

Figure D.1: Relative (left) and absolute (right) errors in the determination of the ground state feeding intensity (I_0) for the decay of ^{103}Tc as a function of I_0.

In the light of all these considerations, the ground state feeding intensities for the decays presented in this work have been evaluated. For this, $N_{\beta TAS}$ and N_β have been calculated as follows:

- $N_{\beta TAS}$ is taken as the number of counts of the clean β-gated DTAS spectrum, with an error coming from the difference due to the integration point: up to the Q_β or the full spectrum. For β-delayed neutron emitters this number of counts is divided by 1-P_n in order to take into account the amount of intensity that goes through neutron emission. We call $N'_{\beta TAS}$ to the number of counts of the β-gated DTAS spectrum corrected by adding two times the counts of the summing-pileup contribution, since they are β-γ coincidences not considered. The error in $N'_{\beta TAS}$ is coming from the propagation of the error of $N_{\beta TAS}$ and the error in the summing-pileup. The error in the number of counts of the summing-pileup has two contributions: the integration point and the uncertainty in the normalization, that depends on the analysis. When the error considered for the normalization factor is less than 50%, we take 50% because in the construction of the first order summing-pileup for β-gated spectra, we only require a coincidence condition with the β detector for the first of the two events, and hence the second event may not be a missing β-γ count.

- N_β is calculated as the number of counts of the singles spectrum of the β plastic detector above the threshold. A more precise number, N'_β, is obtained by subtracting all the contaminants (background, daughter/parent activity, etc.), and adding the missing counts from the pileup of this spectrum. The calculation of this pileup as well as the normalization of this contribution are performed in the way explained in [180]. The error in N'_β results from the propagation of the errors in the normalization factors of the contaminants. The errors for the background and pileup normalizations are fixed to a 20%, whereas for the rest of contaminants it will depend on the analysis.

  The spectra of the plastic β detector for all the cases studied in this work are shown in Figure D, with the corresponding contaminants normalized.

In Table D.1, a summary of the values obtained for each of the cases of interest is presented. The number of counts for each of the cases before and after taking into account

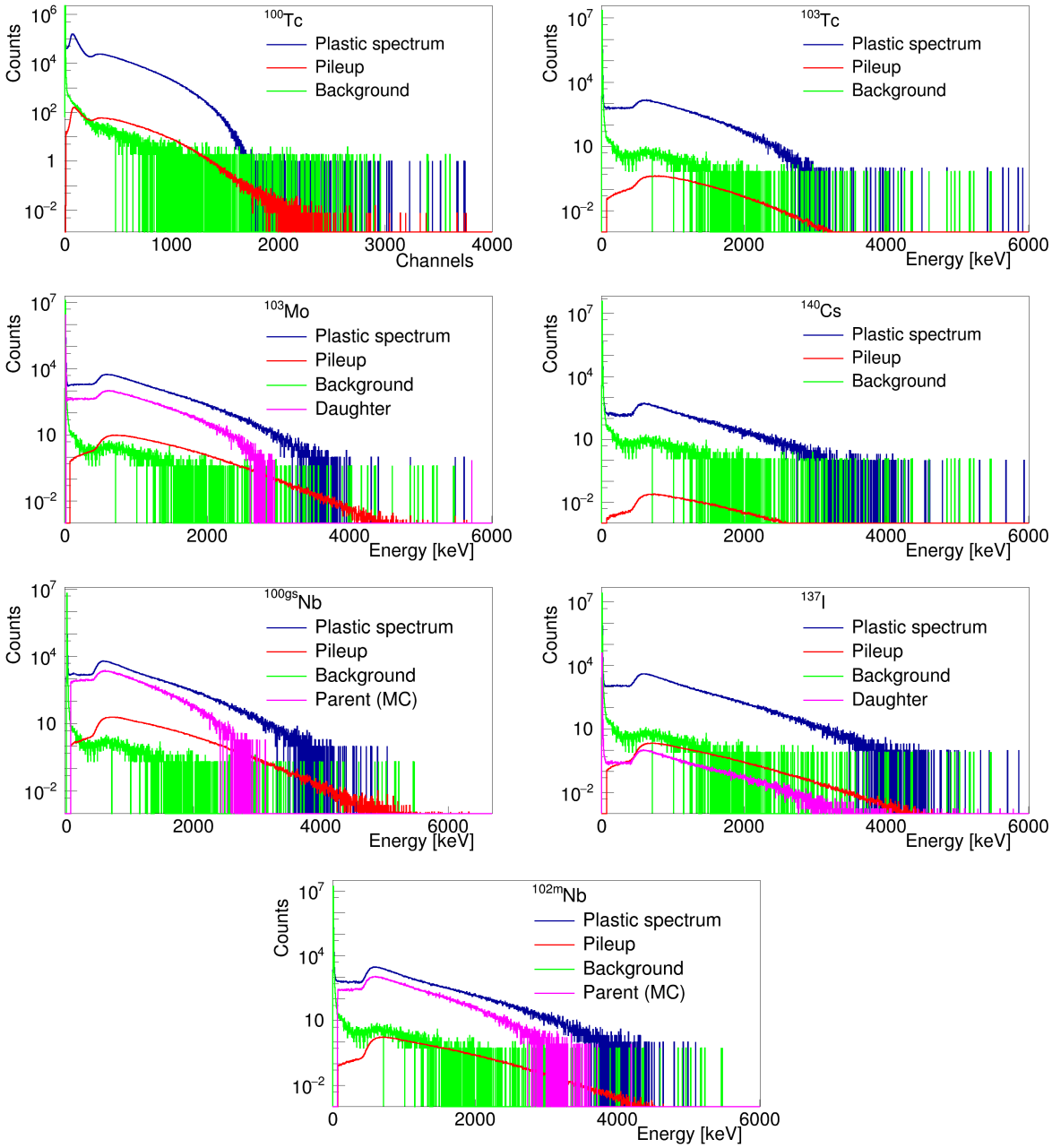

Figure D.2: Plastic detector spectra with the contaminants corresponding to each of the decays studied.

the contaminants, is shown. In the last two columns we give the values for the ground state feeding intensities from the TAGS analysis, the values calculated with the corrected formula (Equation (D.4)), and the values calculated with the original formula from Greenwood (Equation (D.2)). The last value does not have errors, and it corresponds to the direct application of Equation (D.2). We have observed that the corrected formula is less sensitive to the response function and feeding distribution employed for the calculation than the original one. To check it we have applied both expressions for each of the responses and each of the β intensity distributions used in the estimation of systematic errors for each analysis. The dispersion of values obtained in this way with the corrected formula is well

inside the error given here, coming from the number of counts.

Parent	$N_{\beta TAS}$	$N'_{\beta TAS}$	N_β	N'_β	Analysis [%]	Formula [%]
^{100}Tc	2280973(73)	2382641(50834)	24171300	24127100(27181)	93.9(5)	92.8(2) [93]
^{103}Tc	205326(39)	213938(2160)	434601	432183(545)	-	46(2) [46]
^{103}Mo	571353(20)	599553(7078)	1556110	983068(59648)	73(13)[a]	58(13) [60]
^{140}Cs	78754.3(333)	82083.7(341)	133205	128919(861)	35.5(50)	35.1(6) [35.1]
^{100gs}Nb	519532(2)	583419(55252)	1604560	959699(206108)	48(15)	41.3(16) [42]
^{102m}Nb	252011(6)	271029(4755)	730958	455492(13691)	42.7(95)	43.5(24) [43]
^{137}I	447621(3743)	468659(4597)	1029290	976625(5706)	52.6(30)	52.5(7) [52.8]

Table D.1: Ground state feeding intensity evaluation for the decays of this work. The last column presents the value calculated with Equation (D.4) (in brackets, the result obtained with Equation (D.2) is also listed). For details about the meaning of the rest of the columns see text.

[a] this number includes the I_β to the excited states that are below the threshold.

Bibliography

[1] W. Pauli, Rapports du Septieme Conseil de Physique Solvay, Brussels 103.

[2] E. Fermi, Z. Phys. 88 (1933) 161.

[3] G. Gamow, E. Teller, Phys. Rev. 49 (1936) 895.

[4] C. Patrignani, et al. (Particle Data Group), Chin. Phys. C 40 (2016) 100001.

[5] K. Krane, Introductory Nuclear Physics, John Wiley & Sons, 1988.

[6] R. Esiberg, Quantum Physics of Atoms, Molecules, Solids, Nuclei, and Particles, John Wiley & Sons, 1974.

[7] L. Ballentine, Quantum Mechanics. A Modern Development, World Scientific Publishing, 1998.

[8] B. Rubio, W. Gelletly, Lect. Notes Phys. 764 (2009) 99.

[9] K. Heyde, Basic Ideas and Concepts in Nuclear Physics. An Introductory Aproach, Institute of Physics (IOP) Publishing, 1994.

[10] Y. Fujita, PoS (ENAS 6) 031 (2011) 1.

[11] A. Bohr, B. R. Mottelson, Nuclear Structure I, World Scientific Publishing, 1998.

[12] P. G. Hansen, Advances in Nuclear Physics, Vol. 7, Plenum Press, 1973.

[13] C. L. Duke, et al., Nuclear Phys. A 151 (1970) 609.

[14] K. H. Johansen, et al., Nuclear Phys. A 203 (1973) 481.

[15] J. C. Hardy, et al., Nuclear Phys. A 509 (1990) 429.

[16] H. Abele, et al., Phys. Rev. Lett. 88 (2002) 211801.

[17] J. Hardy, et al., Phys. Lett. B 71 (2) (1977) 307.

[18] D. Cano-Ott, et al., Nucl. Instrum. and Methods A 430 (1999) 333.

[19] G. Alkhzarov, et al., Phys. Lett., B 157 (1985) 350.

[20] Y. V. Naumov, A. A. Bykov, I. N. Izosimov, Sov. J. Part. Nucl. 14(2) (1983) 175.

[21] R. Greenwood, et al., Nucl. Instrum. and Methods A 314 (1992) 514.

[22] I. N. Izosimov, et al., J. Phys. G: Nucl. Part. Phys. 24 (1998) 831.

[23] M. Karny, et al., Nucl. Instrum. and Methods B 126 (1997) 411.

[24] B. Rubio, J. Phys. G: Nucl. Part. Phys. 44 (2017) 084004.

[25] M. Dolores Jordán Martín, β-decay Total Absorption Spectroscopy measurements for decay heat calculations, Ph.D. thesis, University of Valencia, 2010.

[26] E. Valencia Marín, Beta strength measurements of delayed neutron emitters ^{87,88}Br, ^{94}Rb, Ph.D. thesis, University of Valencia, 2017.

[27] S. Rice, Decay Heat Measurements of Fission Fragments ^{86}Br, ^{91}Rb & ^{94}Sr Using Total Absorption Gamma-ray Spectroscopy, Ph.D. thesis, University of Surrey, 2014.

[28] A.-A. Zakari, Etude des propriétés de décroissance bêta de noyaux d'intérêt pour la physique des neutrinos, la structure nucléaire et la physique des rèacteurs, Ph.D. thesis, University of Nantes, 2015.

[29] G. Mukherjee, et al., Proceedings of the international thorium energy conference: gateway to thorium energy.

[30] A. Simon, et al., Nucl. Instrum. and Methods A 703 (2013) 16.

[31] M. Karny, et al., Nucl. Instrum. and Methods A 836 (2016) 83.

[32] J. L. Tain, et al., Nucl. Instrum. and Methods A 803 (2015) 36.

[33] J. Suhonen, O. Civitarese, Phys. Rep. 300 (1998) 123.

[34] S. Pirro, et al., Eur. Phys. J. A 27 (2006) 25.

[35] H. V. Klapdor-Kleingrothaus, et al., Modern Physics Letters A 16 (2001) 2409.

[36] F. T. Avignone III, et al., Rev. Mod. Phys. 80 (2008) 481.

[37] J. D. Vergados, et al., Rep. Prog. Phys. 75 (2012) 106301.

[38] K. Zuber, IPPP/05/56 DCPT/05/114.

[39] M. Aunola, J. Suhonen, Nuc. Phys. A 602 (1996) 133.

[40] P. Pirinen, J. Suhonen, Phys. Rev. C 91 (2015) 054309.

[41] S. J. Freeman, J. P. Schiffer, J. Phys. G: Nucl. Part. Phys. 39 (2012) 124004.

[42] J. S. Thomas, et al., Physical Review C 86 (2012) 047304.

[43] J. Hirsch, et al., Phys. Rev. C 51 (1995) 2252.

[44] A. Barabash, et al., Phys. Lett. B 345 (1998) 408.

[45] O. Civitarese, et al., Eur. Phys. J. A 16 (2003) 353.

[46] O. Civitarese, et al., Phys. Rev. C. 58 (1998) 1535.

[47] O. Civitarese, et al., Nuc. Phys. A. 653 (1999) 321.

[48] Q-value Calculator (QCalc), National Nuclear Data Center, Brookhaven National Laboratory, `http://www.nndc.bnl.gov/qcalc/`.

[49] R. Arnold, et al., Nuc. Phys. A. 781 (2007) 209.

[50] R. Arnold, et al., Nucl. Instrum. and Methods A 536 (2005) 79.

[51] S.K.L.Sjue, et al., Phys. Rev. C 78 (2008) 064317.

[52] J. Abad, et al., An. Fis. A 80 (1984) 9.

[53] K. Furutaka, et al., J. Nucl. Science and Technology 38 (2001) 1035.

[54] G. Berzins, et al., Phys. Rev. 187 (1969) 1618.

[55] J. Suhonen, Nuc. Phys. A. 700 (2002) 649.

[56] A. Barabash, Nuc. Phys. A 935 (2015) 52.

[57] J. Suhonen, O. Civitarese, Phys. Lett. B 725 (2013) 153.

[58] J. Suhonen, O. Civitarese, Nucl. Phys. A 924 (2014) 1.

[59] H. Bhang, et al., J. Phys. Conf. Ser. 375 (2012) 042023.

[60] K. Fushimi, et al., J. Phys. Conf. Ser. 203 (2010) 012064.

[61] P. Huber, P. Jaffke, Phys. Rev. Lett. 116 (2016) 122503.

[62] R. Roberts, et al., Phys. Rev. 55 (1939) 510.

[63] E. M. Burbidge, et al., Rev. Mod. Phys. 29 (1957) 547.

[64] S. E. Woosely, et al., Astrophys. J. 433 (1994) 229.

[65] C. Freiburghaus, et al., Astrophys. J. Lett. 525 (1999) L121.

[66] G. Marínez-Pinedo, AIP Conf. Proc. 1541 (2013) 32.

[67] P. Moeller, et al., Phys. Rev. C 67 (2003) 055802.

[68] I. N. Borzov, et al., Phys. Rev. C 67 (2003) 025802.

[69] S. Goriely, Phys. Lett. B 436 (1998) 10.

[70] A. Arcones, et al., Phys. Rev. C 83 (2011) 045809.

[71] W. Hauser, H. Feshbach, Phys. Rev. 87 (1952) 366.

[72] T. Rauscher, F.-K. Thielemann, At. Data Nucl. Data Tables 75 (2000) 1.

[73] J. L. Tain, et al., Phys. Rev. Lett. 115 (2015) 062502.

[74] E. Valencia, et al., Phys. Rev. C 95 (2017) 024320.

[75] J. L. Tain, et al., EPJ Web of Conferences.

[76] J. L. Tain, et al., JPS Conf. Proc. 14 (2017) 010607.

[77] A. Spyrou, et al., Phys. Rev. Lett. 117 (2016) 142701.

[78] A. Porta, et al., EPJ Web of Conferences 111 (2016) 08006.

[79] A. L. Nichols, ICTP Lecture Notes Series 20 (2005) 65.

[80] A. Algora, J. L. Tain, Decay Heat and Nuclear Data, Nuclear Reactors, Vol. Prof. Amir Mesquita (Ed.), InTech, 2012.

[81] J. K. Dickens, et al., Nucl. Sci. Eng. 74 (1980) 106.

[82] W. A. Schier, G. P. Couchell (1994).

[83] Y. Ohkawachi, A. Shono, Jour. Nucl. Sci. Technol. 2 (2002) 493.

[84] A. Tobias, Central Electricity Generating Board report RD/B/6210/R89.

[85] Assessment of Fission Product Decay Data for Decay Heat Calculations, NuclearScience NEA/WPEC-25, 2007.

[86] A. Algora, et al., Hyperfine Interact 223 (2014) 245.

[87] K. Way, E. P. Wigner, Phys. Rev. 73 (1948) 1318.

[88] A. Tobias, Progr. Nuc. Energy 5 (1980) 93.

[89] A. Algora, et al., Phys. Rev. Lett. 105 (2010) 202501.

[90] Decay Data Comparisons for Decay Heat and Inventory Simulations of Fission Events,CCFE-R(15)28/S1, 2015.

[91] Total Absorption Gamma-ray Spectroscopy for Decay Heat Calculations and Other Applications, IAEA report INDC(NDS)-0676, 2015.

[92] C. Patrignani, et al. (Particle Data Group), Chin. Phys. C 40 (2016) 100001.

[93] K. Zygmunt, Kamchatka 2 (2013) 105.

[94] Y. Abe, et al., Phys. Rev. Lett. 108 (2012) 131801.

[95] F. P. An, et al., Phys. Rev. Lett. 108 (2012) 171803.

[96] J. K. Ahn, et al., Phys. Rev. Lett. 108 (2012) 191802.

[97] A. Cucoanes, et al., arXiv:1501.00356 [hep-ex].

[98] W. Mampe, et al., Nucl. Instrum. and Methods 154 (1978) 127.

[99] K. Schreckenbach, et al., Phys. Lett. B 9 (1981) 251.

[100] F. von Feilitzch, et al., Phys. Lett. B 118 (1982) 162.

[101] K. Schreckenbach, et al., Phys. Lett. B 160 (1985) 325.

[102] A. A. Hahn, et al., Phys. Lett. B 218 (1988) 365.

[103] N. Haag, et al., Phys. Rev. Lett. 112 (2014) 122501.

[104] P. Huber, Phys. Rev. C 84 (2011) 024617.

[105] P. Vogel, Phys. Rev. D 29 (1984) 1918.

[106] T. A. Mueller, et al., Phys. Rev. C 83 (2011) 054615.

[107] A. A. Sonzogni, et al., Phys. Rev. C 91 (2015) 011301(R).

[108] A.-A. Zakari-Issoufou, et al., Phys. Rev. Lett. 115 (2015) 102503.

[109] P. Novella, Adv. High Energy Phys. 2015 (2015) 364392.

[110] P. Vogel, Phys. Rev. C 76 (2007) 025504.

[111] G. Mention, et al., Phys. Rev. D 83 (2011) 073006.

[112] D. W. Schmitz, Physics 9 (2016) 94.

[113] A. C. Hayes, et al., Phys. Rev. Lett. 112 (2014) 202501.

[114] F. P. An, et al., Phys. Rev. Lett. 118 (2017) 251801.

[115] J. H. Choi, et al., Phys. Rev. Lett. 116 (2016) 211801.

[116] F. P. An, et al., Phys. Rev. Lett. 116 (2016) 061801.

[117] Y. Abe, et al., J. High Energy Phys. 01 (2016) 163.

[118] A. C. Hayes, et al., Phys. Rev. D 92 (2015) 033015.

[119] D. A. Dwyer, T. J. Langford, Phys. Rev. Lett. 114 (2015) 012502.

[120] A. A. Sonzogni, et al., Phys. Rev. Lett. 116 (2016) 132502.

[121] M. Pequignot, et al., Nucl. Part. Phys. Proc. 265 (2015) 126.

[122] Y. J. Ko, et al., arXiv:1610.05134 [hep-ex].

[123] C. Buck, et al., Phys. Lett. B 765 (2017) 159.

[124] P. Huber, Phys. Rev. Lett. 118 (2017) 042502.

[125] P. H. E. Christensen, P. Jaffke, arXiv:1312.1959.

[126] A. A. Borovoi, L. A. Mikaelyan, Sov. At. Energy 44 (1978) 589.

[127] E. Christensen, et al., Phys. Rev. Lett. 113 (2014) 04250317.

[128] S. Oguri, et al., Nucl. Instrum. and Methods A 757 (2014) 33.

[129] M. Fallot, Nuclear Data Sheets 120 (2014) 137.

[130] O. Tengblad, et al., Nucl. Phys. A 503 (1989) 136.

[131] R. C. Greenwood, et al., Nucl. Instrum. and Methods A 390 (1997) 95.

[132] D. Jordan, et al., Phys. Rev. C 87 (2013) 044318.

[133] M. Fallot, et al., Phys. Rev. Lett. 109 (2012) 202504.

[134] R. C. Greenwood, D. A. Struttmann, K. D. Watts, Nucl. Instrum. and Methods A 317 (1992) 175.

[135] B. C. Rasco, et al., Phys. Rev. Lett. 117 (2016) 092501.

[136] M. Fallot, et al., submitted to EPJ Web of Conferences.

[137] J. L. Tain, D. Cano-Ott, Nucl. Instrum. and Methods A 571 (2007) 728.

[138] G. D'Agostini, Nucl. Instrum. and Methods A 362 (1995) 487.

[139] W. H. Richardson, J. Opt. Soc. Am. 62 (1972) 55.

[140] L. B. Lucy, Astron. J. 79 (1974) 745.

[141] E. Nácher González, Beta decay studies in the N≃Z and the rare-earth regions using Total Absorption Spectroscopy techniques, Ph.D. thesis, University of Valencia, 2004.

[142] C. Shannon, Bell Syst. Tech. J. 27 (1948) 379.

[143] J. S. (Ed.), Maximum Entropy and Bayesian Methods, Kluwer Academix Publishers, 1989.

[144] D. M. Collins, Nature 298 (1982) 49.

[145] R. Capote, et al., Nucl. Data Sheets 110 (2009) 3107.

[146] J. L. Tain, D. Cano-Ott, Nucl. Instrum. and Methods A 571 (2007) 719.

[147] P. G. Hansen, M. Uhl, Nucl. Phys. A 518 (1990) 13.

[148] A. V. Ignatyuk, Handbook for calculations of nuclear reaction data. Reference Input Parameter Library (RIPL), IAEA-TEDOC-1034 Ch.5.

[149] S. Goriely, et al., Phys. Rev. C 78 (2008) 064307.

[150] Evaluated Nuclear Structure Data Fle, http://www.nndc.bnl.gov/ensdf/.

[151] G. A. Bartholomew, et al., Advances in Nuclear Physics, Vol. 7, Plenum Press, 1973.

[152] J. Kopecky, M. Uhl, Phys. Rev. C 41 (1990) 1941.

[153] J. Kopecky, Handbook for calculations of nuclear reaction data. Reference Input Parameter Library (RIPL), IAEA-TEDOC-1034 Ch.6.

[154] S. Raman, C. W. Nestor Jr, P. Tikkanen, Atomic Data and Nuclear Data Tables 78 (2001) 1.

[155] A. Koning, S. Hilaire, M. Duijvestijn, R. Haight, M. Chadwick, T. K. (Eds.), Proceedings of the International Conference on Nuclear Data for Science and Technology, ND2004, AIP 769 (2005) 1154.

[156] S. Agostinelli, et al., Nucl. Instrum. and Methods A 506 (2003) 250.

[157] I. Lehmann, NUSTAR Week 2014.

[158] B. Rubio, Int. J. Modern Phys. E 15 (2006) 1979.

[159] SCIONIX Dedicated Scintillation Detectors.
URL http://scionix.nl/

[160] T. Davinson, et al., Technical Report for the Design, Construction and Commissioning of the Advanced Implantation Detector Array (AIDA)[link].
URL http://www.fair-center.eu/fileadmin/fair/publications_exp/aida_TDR.pdf

[161] T. Davinson, AIDA Update, NUSTAR meeting, GSI 25 February.

[162] Canberra.
URL http://www.canberra.com/

[163] ORTEC AMETEK.
URL http://www.ortec-online.com/

[164] Palmtop MCA.
URL http://w3.atomki.hu/atomki/Electr/palmtopmca_en.html

[165] Mesytec Detector Readout Systems.
URL http://www.mesytec.com/

[166] CAEN.
URL http://www.caen.it/

[167] CAEN 24 Channel Analog Adder Manual.
URL http://www.caen.it/servlet/checkCaenManualFile?Id=4992

[168] CAEN Quad Linear FAN-IN FAN-OUT.
URL http://www.caen.it/csite/CaenProd.jsp?parent=12&idmod=419#

[169] M. Moszyński, et al., Nucl. Instrum. and Methods A 568 (2006) 739.

[170] Saint-Gobain Crystals.
URL http://www.crystals.saint-gobain.com/

[171] BNC Berkeley Nucleonics Corp.
URL http://www.berkeleynucleonics.com/

[172] FTO FiberTech Optica.
URL https://fibertech-optica.com/

[173] D. Engelkemeir, Rev. Sci. Instr. 27 (1956) 589.

[174] S. Payne, et al., IEEE Transactions on Nuclear Science 56 (2009) 4.

[175] E. Nácher, et al., Phys. Rev. Lett. 92 (23) (2004) 232501.

[176] P. Dorenbos, et al., IEEE Transactions on Nuclear Science 42 (1995) 6.

[177] J. Valentine, et al., IEEE Transactions on Nuclear Science 45 (1998) 3.

[178] Hamamatsu.
URL http://www.hamamatsu.com

[179] G. K. Stefansson, CERN Summer Student Report.

[180] D. Cano-Ott, et al., Nucl. Instrum. and Methods A 430 (1999) 488.

[181] ROOT Data Analysis Framework.
URL https://root.cern.ch/

[182] J. L. Tain, et al., Nucl. Instrum. and Methods A 774 (2015) 17.

[183] E. Mendoza, et al., IEEE Transactions on Nuclear Science 61 (2014) 4.

[184] M. Brady, Evaluation and Application of Delayed Neutron Precursor Data, Los Alamos National Laboratory, 1989.

[185] I.A.E.A., Compendium of Neutron Spectra and Detector Responses for Radiation Protection Purposes, Vol. Supplement to Technical Reports Series No. 318, International Atomic Energy Agency, 2001.

[186] HAMAMATSU, MULTIANODE PHOTOMULTIPLIER TUBE R7600U-M4 SERIES.
URL https://www.hamamatsu.com/resources/pdf/etd/R7600U-M4_TPMH1318E.pdf

[187] D. Castrillo, private communication.

[188] HAMAMATSU, PHOTOMULTIPLIER TUBES: Basics and Applications, HAMAMATSU PHOTONICS K. K., 2007.

[189] L. Stuhl, et al., Nucl. Instrum. and Methods A 736 (2014) 1.

[190] A. Bey, et al., Eur. Phys. J. A 36 (2008) 121.

[191] A. Etilé, et al., Phys. Rev. C 91 (2015) 064317.

[192] D. Testov, et al., Nucl. Instrum. and Methods A 815 (2016) 96.

[193] J. Agramunt, et al., Nucl. Instrum. and Methods A 807 (2016) 69.

[194] ELJEN Technology EJ-200.
URL http://www.eljentechnology.com/products/plastic-scintillators/ej-200-ej-204-ej-208-ej-212

[195] P. Gumplinger, Optical Photon Processes in GEANT4 (2002).
URL http://geant4.slac.stanford.edu/UsersWorkshop/PDF/Peter/OpticalPhoton.pdf

[196] J. Nilsson, et al., Appl. Radiat. Isotopes 103 (2015) 15.

[197] J. Bea, et al., Nucl. Instrum. and Methods A 350 (1994) 184.

[198] I. D. Moore, et al., Hyperfine Interactions 223 (2014) 17.

[199] I. D. Moore, et al., Nucl. Instrum. and Methods B 317 (2013) 208.

[200] I. Pohjalainen, et al., 48th Annual Meeting of the Finnish Physical Society.

[201] H. Penttila, Workshop on Reactor Neutrinos, Brookhaven National Laboratory.

[202] T. Kessler, et al., Nucl. Instrum. and Methods B 266 (2008) 681.

[203] T. Eronen, et al., Eur. Phys. J. A 48 (2012) 1.

[204] Max Plack Institute for Nuclear Physics.
URL https://www.mpi-hd.mpg.de/blaum/high-precision-ms/ptms/basics.en.html

[205] L. Brown, G. Gabrielse, Rev. Mod. Phys. 58 (1986) 233.

[206] Ludwig-Maximillians-Universitat Munchen.
URL https://www.med.physik.uni-muenchen.de/research/nuclear-science/nuclear-masses/mlltrap/layout/traps/index.html

[207] T. Eronen, et al., Nucl. Instrum. and Methods B **266** (2008) 4527.

[208] A. Algora, J. L. Tain, Total absorption measurement of the β-decay of ^{100}Tc, Proposal for the JYFL Accelerator Laboratory, Experiment I153.

[209] M. Fallot, J. L. Tain, A. Algora, Study of nuclei relevant for precise predictions of reactor neutrino spectra, Proposal for the JYFL Accelerator Laboratory, Experiment I154.

[210] A. Algora, private communication.

[211] D. Veale, et al., BJU Int 115 (2015) 978.

[212] S. Goriely, M. Samyn, J. Pearson, Phys. Rev. C 75 (2007) 064312.

[213] B. Singh, Nuclear Data Sheets 109 (2008) 297.

[214] K. Furutaka, et al., J. Nucl. Radiochem. Sci. 6 (2005) 283.

[215] ENSDF Analysis Programs, LOGFT, National Nuclear Data Center, Brookhaven National Laboratory, `http://www.nndc.bnl.gov/nndcscr/ensdf_pgm/analysis/logft/unx/`.

[216] J. Suhonen, Nucl. Phys. A 563 (1993) 205.

[217] O. Civitarese, J. Suhonen, Nucl. Phys. A 575 (1994) 251.

[218] J. Suhonen, From Nucleons to Nucleus: Concepts of Microscopic Nuclear Theory, Springer, 2007.

[219] H. Niizeki, et al., Journal of the Physical Society of Japan 47 (1979) 26.

[220] D. D. Frene, Nuclear Data Sheets 110 (2009) 2081.

[221] J. K. Dickens, J. W. McConne11, Phys. Rev. C 23 (1981) 331.

[222] G. Tittel, Zerfallseigenschaften Kurzlebiger Neutronenreicher Molybdan-Isotope, Ph.D. thesis, Johannes Gutenberg-Universitat, Mainz, 1980.

[223] A. Bauchet, et al., Eur. Phys. J. A 10 (2001) 145.

[224] S. Zeghib, Can. J. Phys. 93 (2015) 862.

[225] ENSDF Analysis Programs, hsicc Hager-Seltzer Internal Conversion Coefficients, National Nuclear Data Center, Brookhaven National Laboratory, `http://www.nndc.bnl.gov/hsicc/`.

[226] R. G. Helmer, et al., Nucl. Instrum. and Methods A 353 (1994) 222.

[227] L. K. Peker, et al., Nuclear Data Sheets 51 (1987) 425.

[228] W. C. Schick, W. L. Talbert, Phys. Rev. C 9 (1974) 2328.

[229] S. J. Robinson, et al., J. Phys. G 12 (1986) 903.

[230] M. Scheck, et al., Phys. Rev. Lett. 116 (2016) 132501.

[231] J. Suhonen, G. Lhersonneau, Phys. Rev. C 64 (2001) 014315.

[232] C. Rodríguez-Triguero, et al., J. Phys. G 39 (2012) 015101.

[233] S. Rinta-Antila, et al., Eur. Phys. J. A 31 (2007) 1.

[234] G. Rudstam, et al., Atomic Data and Nuclear Data Tables 45 (1990) 239.

[235] F. Ajzenberg-Selove, et al., Phys. Rev. C 19 (1979) 2068.

[236] G. Menzen, et al., Z. Phys. A 327 (1987) 119.

[237] G. Audi, et al., Chin. Phys. C 36 (2012) 1287.

[238] G. Audi, et al., Nuclear Phys. A 729 (2003) 3.

[239] G. Audi, et al., Chin. Phys. C 41 (2016) 030001.

[240] D. D. Frenne, E. Jacobs, Nuclear Data Sheets 83 (1998) 535.

[241] D. Abriola, et al., IAEA Consultants Meeting on Beta Delayed Neutron Evaluation, Summary Report, INDC(NDS)-0599.

[242] E. Browne, J. K. Tuli, Nuclear Data Sheets 108 (2007) 2173.

[243] B. Fogelberg, H. Tovedal, Nuclear Physics A 345 (1980) 13.

[244] H. Ohm, et al., Z. Phys. A 296 (1980) 23.

[245] B. Fogelberg, et al., Phys. Rev. C 31 (1985) 2041.

[246] T. Kawano, et al., Phys. Rev. C 78 (2008) 054601.

[247] K.-L. Kratz, et al., Z. Phys. A 306 (1982) 239.

[248] P. Hoff, Nuclear Phys. A 359 (1981) 9.

[249] H. Gabelmann, Untersuchung des Beta-Verzogerten Neutronenzerfalls Neutronenreicher Brom-, Rubidium- und Caesiumisotope, Ph.D. thesis, Johannes Gutenberg-Universitat, Mainz, 1987.

[250] S. K. Basu, et al., Nuclear Data Sheets 111 (2010) 2555.

[251] K.-L. Kratz, et al., Z. Phys. A 312 (1983) 43.

[252] S. Rice, et al., Phys. Rev. C 96 (2017) 014320.

[253] A. Algora, M. Fallot, W. Gelletly, Study of beta shapes relevant for precise predictions of reactor neutrino spectra, Proposal for the JYFL Accelerator Laboratory.

[254] E. Poirier, et al., Phys. Rev. C 69 (2004) 034307.

[255] A. B. Pérez-Cerdán, et al., Phys. Rev. C 88 (2013) 014324.

[256] M. E. Estévez Aguado, et al., Phys. Rev. C 92 (2015) 044321.

[257] J. A. Briz, et al., Phys. Rev. C 92 (2015) 054326.

[258] P. Sarriguren, A. Algora, J. Pereira, Phys. Rev. C 89 (2014) 034311.

[259] P. Sarriguren, J. Pereira, Phys. Rev. C 81 (2010) 064314.

[260] P. Federman, S. Pittel, Phys. Rev. C 20 (1979) 820.

[261] T. Togashi, et al., Phys. Rev. Lett. 117 (2016) 172502.

[262] C. Kremer, et al., Phys. Rev. Lett. 117 (2016) 172503.

[263] F. Charlwood, et al., Phys. Lett. B 674 (2009) 23.

[264] A. Algora, Studies of the beta decay of ^{100}Sn and its neighbours with a Total Absorption Spectrometer (TAS), Proposal for the RIKEN Nishina center.

[265] J. L. Tain, A. I. Morales, Investigation of the βs-trength crossing N=126 and the formation of the 3rd r-process abundance peak, Proposal for GSI.

[266] Struck Innivative Systeme.
URL `http://struck.de/`

[267] J. L. Tain, et al., (unpublished).

Scientific production

Some of the results of this thesis have been already published in the following articles:

- V. Guadilla et al., Study of the β-decay of ^{100}Tc with Total Absorption γ-Ray Spectroscopy, Physical Review C, 96, 014319, 2017
- V. Guadilla et al., Characterization of a cylindrical plastic β-detector with Monte Carlo simulations of optical photons, Nuclear Instruments and Methods in Physics Research A, 854, 134-138, 2017
- J.L. Tain, V. Guadilla, E. Valencia, A. Algora et al., r Process (n,γ) Rate Constraints from the γ Emission of Neutron Unbound States in β-Decay, JPS Conf. Proc. 14 , 010607, 2017
- V. Guadilla et al., Study of the β Decay of Fission Products with the DTAS detector, ACTA PHYSICA POLONICA B, 48, 529-532, 2017
- V. Guadilla et al., First Measurements with the DTAS Detector, Springer Proceedings in Physics, 182, 173-175, 2016
- J.A. Briz, A.-A. Zakari-Issoufou, M. Fallot, A. Porta, A. Algora, J.L. Tain, E. Valencia, S. Rice, V. Guadilla et al., Total Absorption Spectroscopy of Fission Fragments Relevant for Reactor Antineutrino Spectra Determination, ACTA PHYSICA POLONICA B, 47, 755-762, 2016
- V. Guadilla et al., First experiment with the NUSTAR/FAIR Decay Total Absorption γ-Ray Spectrometer (DTAS) at the IGISOL IV facility, Nuclear Instruments and Methods in Physics Research B, 376, 334-337, 2016
- V. Guadilla et al., TAGS measurements of ^{100,100m}Nb for neutrino Physics with the new DTAS detector, accepted in EPJ Web of Conferences (proceedings of the International Conference on Nuclear Data for Science and Technology)
- J.L. Tain, V. Guadilla, E. Valencia, A. Algora et al., Strong γ-ray emission from neutron unbound states populated in β-decay: impact on (n, γ) cross-section estimates, accepted in EPJ Web of Conferences (proceedings of the International Conference on Nuclear Data for Science and Technology)
- M. Fallot, A. Porta, L. Le Meur, J. A. Briz, A. -A. Zakari-Issoufou, V. Guadilla et al., Total Absorption Spectroscopy of Fission Fragments Relevant for Reactor Antineutrino Spectra, accepted in EPJ Web of Conferences (proceedings of the International Conference on Nuclear Data for Science and Technology)

In addition, the student was involved in other works that led to the following publications:

- A.I. Morales, A. Algora, B. Rubio, K. Kaneko, S. Nishimura, P. Aguilera, S.E.A. Orrigo, F. Molina, G. de Angelis, F. Recchia, G. Kiss, V. H. Phong, J. Wu, D. Nishimura, H. Oikawa, T. Goigoux, J. Giovinazzo, P. Ascher, J. Agramunt, D.S. Ahn, H. Baba, B. Blank, C. Borcea, A. Boso, P. Davies, F. Diel, Zs. Dombrádi, P. Doornenbal, J. Eberth, G. de France, Y. Fujita, N. Fukuda, E. Ganioglu, W. Gelletly, M. Gerbaux, S. Grevy, V. Guadilla et al., Simultaneous investigation of the $T = 1$ ($J_\pi = 0^+$) and $T = 0$ ($J_\pi = 9^+$) β decays in ^{70}Br, Physical Review C, 95, 064327, 2017

- R. Caballero-Folch , I. Dillmann , J. Agramunt, J.L. Taín, C. Domingo-Pardo, A. Algora, J. Äysto , F. Calvino, L. Canete , G. Cortès, T. Eronen, E. Ganioglu, W. Gelletly, D. Gorelov, V. Guadilla et al., First evidence of multiple β-delayed neutron emission for isotopes with A>100, ACTA PHYSICA POLONICA B, 48, 517-522, 2017

- T. Goigoux, P. Ascher, B. Blank, M. Gerbaux, J. Giovinazzo, S. Grévy, T. Kurtukian Nieto, C. Magron, J. Agramunt, A. Algora, V. Guadilla et al., Two-proton radioactivity of ^{67}Kr, Physical Review Letters, 117, 162501, 2016

- B. Blank, T. Goigoux, P. Ascher, M. Gerbaux, J. Giovinazzo, S. Grévy, T. Kurtukian Nieto, C. Magron, J. Agramunt, A. Algora, V. Guadilla et al., New neutron-deficient isotopes from ^{78}Kr fragmentation, Physical Review C 93, 061301(R), 2016

- J.L. Tain , A. Algora , J. Agramunt, V. Guadilla et al., A decay total absorption spectrometer for DESPEC at FAIR, Nuclear Instruments and Methods in Physics Research A, 803, 36-46, 2015

- A. Algora, E. Valencia, J.L. Tain, M.D. Jordan, J. Agramunt, B. Rubio, E. Estevez, F. Molina, A. Montaner, V. Guadilla et al., Total Absorption Study of Beta Decays Relevant for Nuclear Applications and Nuclear Structure, NUCLEAR DATA SHEETS, 120, 12-15, 2014

- A. Montaner, J. L. Tain, J. Agramunt, A. Algora, V. Guadilla, E. Marín, S. Rice and B. Rubio, Characterization of a new modular decay total absorption gamma-ray spectrometer (DTAS) for FAIR, AIP Conference Proceedings, 1541, 179, 2013

- V. Guadilla, J. L. Tain, J. Agramunt, A. Algora, C. Domingo-Pardo and B. Rubio, Calibration of a DSSSD detector with radioactive sources, AIP Conference Proceedings, 1541, 173, 2013

- A. Algora, S. Rice, V. Guadilla, J.L Tain, E. Valencia et al., Total absorption studies of high priority decays for reactor applications, accepted in EPJ Web of Conferences (proceedings of the International Conference on Nuclear Data for Science and Technology)

The results of this thesis have been defended in several congresses with talks and posters.

Talks:

- International Conference on Nuclear Data for Science and Technology, Bruges (Belgium), 2016
- NUSTAR Annual Meeting 2016, GSI (Germany), 2016
- XXXV Reunión Bienal de La Real Sociedad Española de Física, Gijón (Spain), 2015
- International Scientific Meeting on Nuclear Physics, La Rábida (Spain), 2015
- NUSTAR Week 2014, HISPEC/DESPEC Collaboration meeting, Valencia (Spain), 2014

Posters:

- Zakopane Conference on Nuclear Physics, Zakopane (Poland), 2016
- XVII International Conference on Electromagnetic Isotope Separators and Related Topics (EMIS) Grand Rapids, (USA), 2015
- Euroschool on Exotic Beams, Flerov Laboratory of Nuclear Reactions (FLNR), Joint Institute for Nuclear Research (JINR), Dubna (Russia), 2013
- VII Encuentros de Física Nuclear, La Rábida (Spain), 2012
- XXXIV Reunión Bienal de La Real Sociedad Española de Física, Valencia (Spain), 2013
- International Scientific Meeting on Nuclear Physics, La Rábida (Spain), 2012

Participation in experiments

The student has participated in a variety of experiments in different research facilities:

- Experiment IS539 (ISOLDE) Shape effects in the vicinity of the Z=82 line: study of the β-decay of ^{182,184,186}Hg, CERN (Geneva, Switzerland)
- MINIBALL experiment: ^{56}Fe(p,n)^{56}Co, Maier-Leibnitz-Laboratorium (MLL) (Munich, Germany)
- Experiments I153 (Total absorption measurement of the beta decay of 100Tc) and I154 (Study of nuclei relevant for precise predictions of reactor neutrino spectra), IGISOL (Jyväskylä, Finland)
- Experiments I162 (Delayed neutron measurements for advanced reactor technologies and astrophysics) and I181 (Measurement of the beta-delayed two-neutron emitter 136Sb with the BELEN detector), IGISOL (Jyväskylä, Finland)
- Eurica campaign with ^{78}Kr beam, RIKEN (Tokyo, Japan)

- TETRA measurements of Rb isotopes, ALTO (Orsay, France)
- Experiment IS570 (ISOLDE) β-decay of the N=Z, rp-process waiting points: ^{64}Ge, ^{68}Se and the N=Z+2: ^{66}Ge, ^{70}Se for accurate stellar weak-decay rates, CERN (Geneva, Switzerland)
- Measurement of the γ-decay from high-lying states and giant resonances excited in ^{208}Pb, CCB (Kraków, Poland)

Agradecimientos
Acknowledgements

Además de tratarse de las páginas probablemente más leídas de este trabajo, los agradecimientos constituyen el verdadero resumen de todos estos años, el bagaje personal y la huella sentimental que han dejado en mí. No obstante, a pesar de que valoro con devoción las palabras, soy de los que ven en los actos una fuente infinitamente más potente de significado. En ese sentido, la propia tesis, el propio acto de sacarla adelante hasta sus últimas consecuencias, representa para mí el intento de saldar una deuda con todas las personas que me han ido guiando y ayudando en este apasionante camino.

Si esta tesis ha sido posible, con todas sus virtudes y defectos, es gracias a mis tutores, Alejandro y José Luis. En primer lugar, gracias por darme esta fantástica oportunidad, por confiarme el cuidado de una línea de investigación y unas ideas que vosotros habéis alumbrado. Me siento increíblemente afortunado de haber podido vivir todas las etapas de este proyecto, y eso es gracias a vuestra apuesta por mí desde el primer momento. He de reconocer que antes de iniciar mi doctorado, nunca imaginé que tendría tanta suerte con mis tutores. Sois dos grandísimos investigadores, a quienes respeto y admiro profundamente. Además, he de agradecer a Alejandro haber trascendido la frontera del director de tesis y haber sabido apoyarme y motivarme durante todo este tiempo. No hace falta vivir un mes contigo en Jyväskylä para empaparse de tu inconfundible ilusión, siempre con entretenidas anécdotas, apasionantes conversaciones sobre libros y detalles técnicos insospechados sobre el misterio de la natación. A José Luis le debo un ejemplo incomparable de meticuloso buen hacer y tenacidad. Agradezco eternamente tu puerta siempre abierta y tu curiosidad infinita. También agradezco tu paciencia conmigo y haberme demostrado que un científico como tú también sabe disfrutar de la naturaleza, el cine y la cultura. Una de las cosas que más valoro de los dos, es haberme dado una libertad absoluta para jugar e indagar, basada únicamente en el respeto, sin necesidad de exigencias ni jerarquías. Gracias por moldear el investigador que seré a partir de ahora. Vosotros tendréis y habéis tenido otros estudiantes, pero para mí siempre seréis mis únicos tutores. Gracias.

De forma natural, mis siguientes palabras van dirigidas al resto del grupo de Espectroscopía γ y de neutrones. En primer lugar le debo un sincero agradecimiento a Berta.

Aún recuerdo el día en que entré en tu despacho y empezó a fraguarse mi relación con todos vosotros. Gracias por tu apoyo e impulso desde el mismísimo comienzo. A Jorge, además de agradecerle su imprescindible trabajo, que ha hecho posible en buena medida esta tesis, le agradezco su entusiasmo y su inconfundible sentido del humor. Al grupo de atletas: Luis, César y Kike, por mostrarme con vuestro ejemplo que la vida tiene muchas facetas, y hacerlas compatibles es un arte. Os admiro como artistas y como personas. A Kike le dedico unas palabras más (ya que él nunca escatima ninguna). Como tu compañero de despacho he aprendido una ingente cantidad de cosas de ti, y la menor parte de ellas sobre física. Tu sentido del humor y tu apoyo han sido imprescindibles en todo esto. Quisiera aprovechar para agradecer a los demás compañeros de despacho que he tenido el gran ambiente en el que siempre he trabajado (salvo cuando la calefacción no funcionaba...): a Giuseppe, siempre con una llave de judo preparada, a Álvaro (Tolosa), siempre con un comentario inteligente e insospechado, y a todos los que han pasado por el despacho como visitantes. A Loli le dedico el tecnecio que le falta en su tesis. Tu legado me ha ayudado mucho en todo esto, ahora te deseo todo lo mejor como investigadora y como madre. A Sonja, Anabel, Ion, Ariel y Pablo, porque ha sido un honor y un auténtico placer coincidir con vosotros. Ana, con quien empecé estas andanzas en el máster hace casi seis años, gracias por todas las aventuras y desventuras (incluyendo absurdos papeleos y llamadas en Rusia). Te deseo mucho ánimo para la recta final, y te agradezco estos años de sincero compañerismo. A Ebhelixes, siempre original y siempre risueña, ojalá encuentres en tu tierra la fuerza necesaria para hacer justicia con tu trabajo y terminar tu tesis.

Quisiera aprovechar este momento para agradecer de forma rotunda y clara a todo el personal del IFIC por su increíble buen hacer durante todo este tiempo. Empezando por el servicio de limpieza, pasando por informática, mantenimiento y mecánica. De entre todos mención aparte merece Manolo (auto-proclamado herrero), de quien he aprendido y con quien he disfrutado incomparablemente. Hablar del personal de secretaría de nuestro instituto es hablar de eficacia, amabilidad y compromiso. Gracias a todos por ser un auténtico milagro para los que peleamos con papeles y trámites. No me olvido de la gente de divulgación, gracias por recordarme con vuestro ejemplo que lo que hacemos tiene un trasfondo apasionante, y que tenemos la responsabilidad de compartirlo con los demás.

I would like to express my deepest gratitude to all the members of the jury, for their commitment and their time. Special thanks to Bill, a fascinating person I have been honoured to meet during these years. Thank you for your support, your energy, and your always valuable English corrections.

This thesis would not have been possible without the dedicated work and effort of the people of the IGISOL accelerator facility, Sami, Tomi, Iain, Veli, Dimitry, Juuso, Heikki and Ari among many others. Thank you for your contribution, and for the nice atmosphere during the experiments. I would also like to thank all the people from the different facilities where I had the opportunity to participate in experiments, because most of the times I encountered kindness and hard-work. Special thanks to the people from Kraków, Adam Maj, Maria Kmiecik, Barbara Wasiłewska and Michał Ciemała, for their hospitality.

Two months of my work had as a backdrop the city of Nantes, and I am very grateful to the people from Subatech for their hospitality. Thank you Amanda, for taking care of me during that time. And lots of thanks to Jose Briz, a real champion, whose support, friendship and good mood were essential to enjoy that period. Many thanks to all the friendly students I met there, especially to Loïc, Lucía, Javi, Charlotte and Florian.

It would not be fair to forget the precious contribution to this thesis of Muriel Fallot, Alejandro Sonzogni, Jouni Suhonen, Osvaldo Civitarese and Pedro Sarriguren, whose calculations helped to shed light on the studies presented.

A los grandes maestros que he tenido tanto en el aula como en el dojo, por enseñarme a pensar y a sobrevivir. A Miguel Lorenzo, por abrirme la puerta a un mundo más rico y fascinante a través de tus clases de filosofía, por tu tiempo y tu amistad. Sin ánimo de caer en la injusticia, hay un puñado de profesores a quienes quisiera agradecer especialmente su pasión y su dedicación durante la carrera: a Mariano Santander, José Carlos Cobos y Marco Antonio Gigosos, de la Universidad de Valladolid, y a Guillermo García Alcaine, Ricardo Brito y David Gomez-Ullate de la Universiad Complutense de Madrid. Parte de lo que soy como científico os lo debo.

Cuando me quiero dar cuenta, mis siguientes palabras me llevan ya a un terreno resbaladizo en el que temo despistarme y dejar a gente sin nombrar. Pido perdón de antemano por cualquier desliz. Si algo me ha resultado extraordinariamente valioso durante mis años de doctorado, ha sido el estupendo grupo de estudiantes que hemos ido coincidiendo en el IFIC. Me gustaría empezar señalando a tres personas con quienes comenzó todo, los doctores Carlos, Pablo y Nacho. Hemos vivido todo este proceso juntos, entre carreras por el Turia, cervezas y chistes (sin entrar a valorar su calidad), y sobre todo viéndonos crecer y viéndonos tomar nuestros respectivos caminos, que espero siempre sepamos hacer converger. Gracias por vuestra amistad, uno de los grandes hallazgos de mi tesis. Dicho esto, hay otro buen número de amigos, compañeros y doctorandoms en general con quienes he disfrutado de este viaje entre la bruma del doctorado. Gracias a todos por regalarme conversaciones siempre alejadas de nuestras obligaciones y tantas veces acompañadas de deliciosos postres o regadas con cerveza. A Damián, y sus ciclos de sueño, a Miguel Ángel, con su compromiso político y su huerto, a Marçà, el doctor anti-sistema, a Javi y Davide, siempre pegados a una roca, a Javi Barrios, generoso amante de las estrellas, a Pablo y su sentido del humor vegetariano, a Rosa, del Toro, Martín, Ane, Dominik, Nuria, André, Giulia, Jonathan, Elena, Sebas y muchos más. Finalmente a mi gran amigo Dani, una de las personas que más me ha apoyado en los últimos años. Dani, tenemos aún mucho que aprender y disfrutar juntos. Espero saber estar a la altura a partir de ahora. ¡Tú puedes!

Me resisto a olvidarme de los compañeros nucleares de todos los rincones de España con los que he ido coincidiendo a lo largo de los años, haciendo que los congresos y escuelas resultaran agradables y divertidos: Roger, Samuel, Viki, Javi, Marta, Jorge, Jesús, Guillermo, Miguel, etc. Os deseo a todos la mejor de las suertes.

En estos años he tenido la suerte de ser acogido por los senderistas de AMR: Egon,

Nacho, Enrique, Maite y Pacho, quienes con su amor por la naturaleza y su energía han sabido alejarme del trabajo hasta alturas insospechadas. Gracias a todos y que no dejemos de hacer excursiones juntos.

A pesar de la distancia y de lo complicado de coincidir, hay ciertas personas a quienes debo mucho más que unas palabras. A mis amigos del colegio, Dani, Valles y Javi, por escuchar mis paranoias, y por haberme sabido apoyar en mi aventura como físico. A mis amigos de la carrera, en especial a Vasco, Ángela, Blade, Belén y Vero, con quienes he pasado grandes momentos en estos años, lametablemente siempre demasiado pocos, y tantas veces alrededor de un tablero. Gracias por todo. He dejado aparte a mi amigo, compadre, compinche y padrino de boda Mario. Hace tiempo me acompañaste a recuperar mi mochila, y cuando nos hemos querido dar cuenta la hemos llenado con nuestras tesis. Gracias por todo este tiempo. Espero que sean muchas las aventuras que nos aguarden.

Llegados a este punto, es el momento de los agradecimientos a la familia, pero temo que cualquier esfuerzo sea en vano. A mi familia le debo todo lo que soy, todo lo que me mueve y todo lo que hago, no solo esta tesis. A mis hermanas, Silvia e Irene, que jamás han dejado de apoyarme incondicionalmente en todas mis metas. Gracias por vuestro amor y vuestra comprensión. Estoy terriblemente orgulloso de vosotras. Simplemente sois las mejores hermanas del mundo y os quiero. A mis padres, José Félix y Amparo, que siempre han velado por mi futuro con cariño y preocupación, y que han sabido afrontar el vértigo y la distancia para dejarme caminar hacia mis sueños. Es imposible que os agradezca todo vuestro esfuerzo y el apoyo diario. Esta tesis es sobre todo para vosotros y por vosotros. GRACIAS. Al resto de mi familia, especialmente a los que han seguido más de cerca este proceso, José Ángel, Miguel, Luisa, Javi, Mada, Mariví, por hacerme llegar siempre vuestro apoyo. A mis abuelos y mis abuelas, que descansan en la paz de este universo fascinante, donde algún día volveremos a juntarnos en el llameante corazón de alguna estrella.

Chciałbym serdecznie podziękować mojej polskiej rodzinie za zaakceptowanie mnie nawet kiedy granica pomiędzy fizykiem i wariatem jest tak cienka.

Finalmente, el motivo. La clave. El sentido. La solución al enigma. La respuesta. El origen y el destino de mis pasos. Karolinka. Si no fuera por ti, nada de esto habría pasado. Gracias a ti, hacer el doctorado ha sido una experiencia maravillosa. Necesitaría otras trescientas páginas para explicar todo lo que te debo y fracasaría estrepitosamente. Gracias por enseñarme el camino y recorrerlo a mi lado. Gracias por tu amor. Gracias por hacerme feliz.